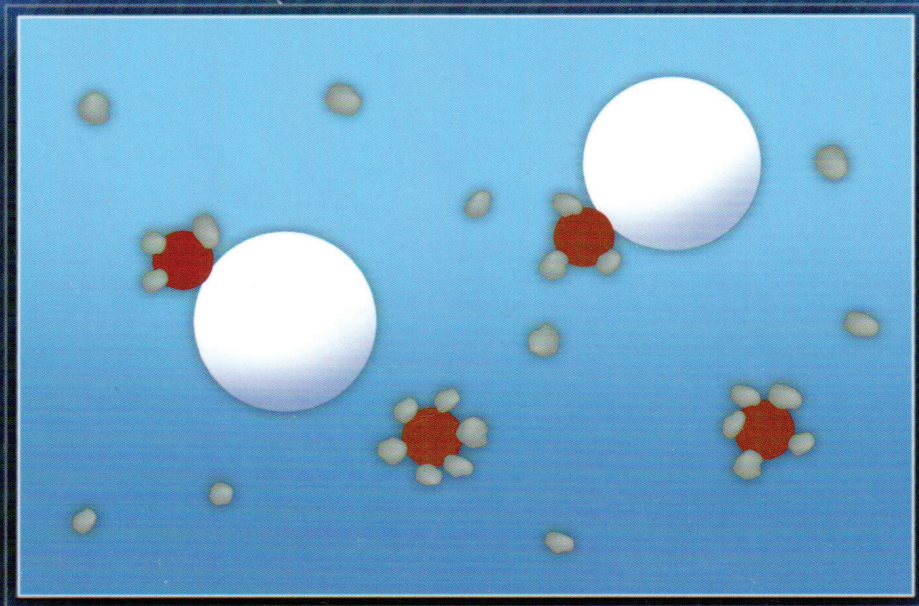


Handbook on Theory and Practice of Bitumen Recovery from Athabasca Oil Sands

Volume I: Theoretical Basis



Jacob H. Masliyah
Jan Czarnecki and Zhenghe Xu

Handbook on Theory and Practice on Bitumen Recovery from Athabasca Oil Sands

Volume I: Theoretical Basis

Jacob H. Masliyah

Jan Czarnecki and Zhenghe Xu

Copyright © 2020 Jacob H. Masliyah, Jan Czarnecki, and Zhenghe Xu, All rights reserved.

Cover design by Dean Pickup

Interior design for e-edition by Jan Czarnecki

Printed in Canada
2011 / 01

Library and Archives Canada has catalogued the print edition as follows:

Masliyah, Jacob H. (Jacob Heskell), 1942–
Handbook on theory and practice of bitumen
recovery from Athabasca Oil Sands / Jacob H. Masliyah,
Jan A. Czarnecki, and Zhenghe Xu.

Includes bibliographical references and indexes. Contents: v. 1.
Theoretical basis—v. 2. Industrial practice.

ISBN 978-1-926832-03-6 (v. 1)

1. Oil sands industry—Technological innovations—Alberta.
2. Secondary recovery of oil—Alberta. 3. Bitumen—Alberta.
I. Xu, Z. (Zhenghe) II. Czarnecki, Jan A. (Jan Adam) III. Title.

TN871.37.M38 2011 622'.33820971232 C2011-900185-3

eISBN 978-1-926832-68-5 (v.1)

Published in Canada and the United States by Kingsley Knowledge
Publishing

Content

Acknowledgements	X
Foreword	XI
List of Commonly-used Abbreviations	XVIII
Chapter 1: Introduction to the Athabasca Oil Sands	1
1.1 Geology	3
1.1.1 Origins of Oil Sands	3
1.1.2 The Athabasca Wabiskaw-McMurray Deposit	5
1.2 Alberta's Crude Bitumen Resource	7
1.2.1 Oil Sands Ore Characterization	7
1.2.2 Recovery Methods	9
1.2.3 Crude Bitumen Reserves: Definitions and Values	10
Initial In-Place Volume of Crude Bitumen	11
Ultimate In-Place Volume of Crude Bitumen	11
Ultimate Potential Recoverable Reserves of Crude Bitumen	11
Established Reserves of Crude Bitumen	12
Initial Established Reserves of Crude Bitumen	12
Remaining Established Reserves of Crude Bitumen	13
Synthetic Crude Oil Production	13
1.2.4 Crude Bitumen and Synthetic Crude Oil Under Active Development	15
1.3 Bitumen Production from the Athabasca Oil Sands: Historical Background	18
1.4 Driving Forces in Oil Sands Development	23
1.5 Bitumen Extraction and Upgrading Schemes	25
1.5.1 Extraction	25
1.5.2 Upgrading	27
1.5.3 Sulphur and Sulphur Dioxide Production	31
1.5.4 Greenhouse Gases (GHGs) and Energy Intensity	33
1.5.5 Water Use	39
1.6 References	47
Chapter 2: Basic Scientific Background	51
2.1 Surface and Colloid Science	51
2.2 Surface and Interfacial Tension	53
2.2.1 Introduction	53
2.2.2 Young-Laplace Equation	54
2.2.3 Superheating, Supercooling, and Ostwald Ripening	55
Superheating	55

Supercooling	56
Ostwald Ripening	57
2.2.4 Three-Phase Contact and Contact Angle	57
Contact Angle Hysteresis	59
2.2.5 Spreading	60
Adhesion and Cohesion Energies	60
Spreading Coefficient	61
2.3. Measurements of Surface and Interfacial Tension	62
2.3.1 Capillary Rise Method	62
2.3.2 Maximum Bubble Pressure Method	64
2.3.3 Wilhelmy Plate Method	65
2.3.4 Du Noüy Ring Method	66
2.3.5 Drop Shape Methods	67
2.3.6 Spinning Drop (or Spinning Bubble) Method	67
2.3.7 Drop Weight (or Volume) Method	68
2.3.8 Micropipette Method	68
2.4. Methods of Measuring Contact Angle	69
2.4.1 On Flat Surfaces	69
2.4.2 On Powders	69
2.5. Adsorption	69
2.5.1 Thermodynamics of Adsorption	70
Gibbs' Surface Excess and Dividing Plane Concepts	71
Gibbs' Adsorption Equation	72
2.5.2 Adsorption Isotherms	75
Langmuir's Adsorption Isotherm	75
The BET Isotherm	77
Henry's Isotherm	78
2.6. Electric Surface Phenomena	79
2.6.1 Origins of Surface Charge	79
2.6.2 Electrical Double Layer	81
2.6.3 Theory of Electrical Double Layer Structure	83
2.6.4 Electrokinetic Phenomenal	86
Electrophoresis	88
Streaming Potential	89
Electro-osmosis	89
Sedimentation Potential	90
2.6.5 Zeta Potential	90
2.7. Surface Forces	91
2.7.1 Van der Waals Forces	92
Dipole-Dipole Interaction	92
Dipole-Induced Dipole Interaction	92
Dispersive Interaction	93
2.7.2 Double Layer Overlapping Forces	96
2.7.3 DLVO Theory of Colloid Stability	98
Impact of Surface Potential	100

Impact of Electrolyte Concentration	101
Critical Coagulation Concentration (CCC)	102
Impact of Specific Ion Adsorption	103
2.8. Non-DLVO Interactions	104
2.8.1 Steric Repulsion	104
2.8.2 Polymer Bridging	105
2.8.3 Hydration Effects	106
2.8.4 Hydrophobic Interactions	106
2.9. Coagulation Kinetics	107
2.9.1 Stability Ratio	107
2.9.2 Theory of Rapid Coagulation	108
Smoluchowski's Theory	108
Smoluchowski's Continuity Equation	109
2.9.3 Slow Coagulation	112
2.10. Surfactants	113
2.10.1 Common Surfactant Types	113
2.10.2 HLB Scale	115
2.10.3 Micelles and Critical Micellization Concentration	116
Micelle Formation	116
Krafft Point	117
Factors Affecting the CMC	119
Thermodynamics of Micellization	120
2.10.4 Solubilization	121
2.10.5 Emulsification	121
2.10.6 Detergency and Flotation	122
Detergency	123
Flotation	124
2.11 Physical Constants and Basic SI Units	125
2.12 References	126
Chapter 3: Fluid Dynamics as Applied to Oil Sands Operations	129
3.1 Multiphase Flow and Applications	129
3.2 Drag on a Single Rigid Sphere	130
3.3 Bubbles and Drops	137
3.4 Ideal System: Multi-Particle System of the Same Species	142
3.5 Ideal System: Multi-Particle System Containing Different Species	154
3.6 Non-Ideal System: Multi-Particle System of the Same Species	156
3.7 Non-Ideal System: Multi-Particle System Containing Different Species	158
3.8 Modelling of a Gravity Separation Vessel	159
3.8.1 Modelling of a Bidisperse Suspension Separation	159
Model Verification	162
3.9 Inclined Plate Settlers (IPS)	165
3.9.1 Settling of Heavy Particles in an Inclined Plate Settler	166

3.9.2 Separation of Particles in an Inclined Plate Settler	168
3.10 Concluding Remarks	169
3.11 References	169
Chapter 4: Physical and Chemical Properties of Oil Sands	173
4.1 Oil Sands Composition: Bitumen, Mineral Solids, and Inorganic Ions . .	177
4.1.1 Bitumen Grade Distribution	177
4.1.2 Mineral Solids	179
Clays	182
Two-Layer Kaolinite Clays	185
Three-Layer Clays	188
Chlorite	190
Cation Exchange Capacity of Clays	190
Mineral Solids and Bitumen Grade	192
4.1.3 Electrolytes in Oil Sands	196
4.2 Bitumen Density	204
4.2.1 API Classifications of Oil Crude	204
4.3 Bitumen Dynamic Viscosity	207
4.4 Refractive Index of Bitumen	217
4.5 Specific Heat	218
4.6 Heat of Combustion	224
4.7 Thermal Conductivity	226
4.8 Chemical Aspects of Bitumen	227
4.8.1 Bitumen Characterization	228
Elemental Composition	229
Solubility and Adsorption	230
Chemical Structure	235
4.9. Interfacial Properties in Bitumen Recovery	235
4.9.1 Surface Tension	238
4.9.2 Interfacial Tension	242
4.9.3 Surfactant Chemistry	246
4.9.4 Natural Surfactants in Bitumen	255
Zeta Potential	256
4.10 References	259
Chapter 5: Slurry Preparation and Conditioning	267
5.1. Modelling of Lump Digestion in a Hydrotransport Pipeline	270
5.1.1 Conceptual Model	270
5.1.2 Model Development	271
Conservation of Mass	271
Conservation of Thermal Energy	274
Model for Lump Ablation	276
Lump Shear Stress	277

5.1.3 Comparison of Model to Experimental Measurements	278
5.1.4 Model Parametric Study Predictions	279
5.2 Bitumen Liberation	282
5.3 References	286
Chapter 6: Bitumen Recovery	289
6.1 Bitumen Liberation	289
6.2 Bitumen Aeration	294
6.2.1 Wettability of Solids	302
6.3 Bitumen Flotation	305
6.3.1 Induced Air Flotation	306
6.3.2 Flotation by Gas Nucleation/Precipitation	313
6.3.3 Flotation Machines	316
6.3.4 Flotation Circuits	320
6.4 Processability	323
6.4.1 Ore Processability	323
Impact of Ore Grade	323
Impact of Temperature	324
Impact of Ore Acidity	326
Impact of Solids Wettability	327
Impact of Water Chemistry	328
Effect of Clay and Calcium Addition on Bitumen Recovery	329
Sludging of the Separation Vessel	330
Slime Coating	331
Water Softening	335
Impact of Natural Surfactants	338
Bitumen-in-Water Emulsions	340
Segregating and Non-Segregating Slurry	341
6.5 Concluding Remarks	343
6.6 References	343
Chapter 7: Froth Treatment Fundamentals	349
7.1 Emulsions and Emulsion Stability	350
7.1.1 Introduction	350
7.1.2 Surfactant-Stabilized Emulsions	353
Winsor Emulsion Types	353
7.1.3 Impact of Fine Solids on Emulsion Stabilization	355
7.1.4 Emulsion Thin Liquid Films	359
Scheludko-Exerowa Thin Film Balance Technique	359
7.2. Emulsions in Petroleum Systems	360
7.2.1 Introduction	360
7.2.2 Asphaltenes	361
SARA Analysis	361

Asphaltene Chemistry	363
Molecular Mass of Asphaltenes	364
Asphaltene Aggregation	366
Asphaltene Molecular Structure	369
Archipelago Model	369
Island or Like-Your-Hand Model	371
Asphaltene Nano-Aggregation and Mullins' Model	372
7.2.3 Role of Naphthenic Acids and their Salts in Emulsion Stabilization	372
7.3 Fundamental Aspects of Paraffinic and Naphtha-Based Processes . . .	373
7.3.1 Learning from Past Research	374
Critical Dilution Ratio	374
7.3.2 Industrial Implications	378
Naphtha-Based Froth Treatment	378
Paraffinic Froth Treatment	379
7.3.3 Summary	380
7.4. Demulsifiers and Other Chemical Aids	381
7.4.1 Demulsifier Dosage	382
Flocculant-Type Chemicals.....	382
Coalescing-Type Chemicals.....	385
Commercial Compositions Versus 'Pure' Systems	385
7.5 Concluding Remarks	386
7.6 References	387
Chapter 8: Colloidal Science in Tailings Management	391
8.1 Impact of Water Chemistry	392
8.2 Characteristics of Fluid Fine Tailings	394
8.3 Hydrodynamics of Particle Aggregation	398
8.3.1 Coagulation	399
8.3.2 Flocculation	403
8.4 Rheology of Fine Particle Slurries	411
8.5 Non-Segregating Tailings	419
8.5.1 CT Process	421
8.5.2 Thickened Tailings (or Paste) Technology	424
8.6 Integration of Fines Flocculation with Bitumen Extraction	426
8.6.1 Stackable Deposits	430
8.6.2 Freeze-Thaw Process	430
8.6.3 Natural Drying	432
8.6.4 Centrifugation	434
8.6.5 Filtration	437
8.7 Concluding Remarks	448
8.8 References	449
Index	453

To our families:

Odette, Tamara, Larry, Ellie Liya, Ruth, Michael,
Jasmine, Judah, Daniel, and Nicole;

Helena, Andrzej, Weronika, Zosia, Adam, Jan, and Anna

Choyi and Paul

Acknowledgement

In 2011, the first volume of the Handbook on Theory and Practice of Bitumen Extraction from Athabasca Oil Sands was printed. It was enthusiastically received by researchers in the oil sands industry, government and University. At the time of its printing, we the co-authors, did not anticipate the need of having an electronic format for the handbook. With the hard copy of volume one coming close to being out of print, we decided to provide an electronic version. However, unknown to us, to convert the hard copy to an eBook was a major task. It was only through the persistence and dedication of Dr. Jan Czarnecki that such a conversion was feasible. We owe him much for the time he spent in the conversion process and in proof reading of the eBook.

We reiterate here our appreciation to our colleagues, oil sands industrial personnel and Alberta Government research laboratories for their unweathering support. We thank Drs. Yi Lu and Xiao He for their time for proof reading parts of the eBook. Last, but not least, we thank Mrs. Lisa Carreiro for her help to streamline the handling of the eBook.

Finally, we thank the University of Alberta for inclusion of the electronic version of the handbook in their open access repository Education & Research Archive (ERA).

Acknowledgements to printed edition

The generous financial support of Alberta Innovates – Energy and Environment Solutions (formerly the Alberta Energy Research Institute, AERI), the Canadian Oil Sands Network for Research and Development (CONRAD), and the Canadian Heavy Oil Association (CHOA) is much appreciated. Without such support we would not have been able to embark on the oil sands handbook project.

The Department of Chemical and Materials Engineering at the University of Alberta provided the necessary physical space and logistics to create a workable editorial office. Personal support from the Department Head, Dr. Fraser Forbes, is greatly appreciated.

We would also like to thank many of our colleagues who provided materials that are included in Volume I. To that end, we extend our gratitude to Barry Bara, Graham Cuddy, Hassan Hamza, Tadek Dabros, Randy Mikula, Robert Tipman, Brenda Wright, and many others. We would also like to thank Dr. Joe Zhou of Alberta Innovates – Technology Futures (formerly the Alberta Research Council) for his critical reading of part of the volume.

Last but not least, we would like to extend our very special thanks and appreciation to Ms. Marta Dabros for her meticulous editing of the text, checking of the references, drawings, and photographs, and for taking care of hundreds of administrative chores. Her devotion to the project is greatly appreciated.

Foreword

I was pleased to be asked by the main authors, Drs. Jacob Masliyah, Jan Czarnecki, and Zhenghe Xu, to write a brief foreword to the *Handbook on Theory and Practice of Bitumen Recovery from Athabasca Oil Sands*. They, along with the other contributors, have completed a monumental piece of work that has the potential to make a significant contribution to the path forward for oil sands development. The information contained in this handbook is the state-of-the-art technological and operational foundation upon which a growing sustainable and environmentally responsible oil sands industry can be built and vast socio-economic benefits can be realized, while providing energy security for Canada and North America.

To understand the significance of this handbook, one needs first to appreciate the significance of the oil sands as a critical strategic resource for Canada and, more broadly, the world. Technological breakthroughs have unlocked the tremendous potential of the oil sands as a secure and long-term source of crude oil from a politically stable nation. In order for such development to proceed in a sustainable and environmentally and socially responsible fashion, technological development, including the development of processes that significantly reduce the carbon footprint and water usage associated with oil sands production, as well as ongoing improvements in key areas such as tailings management and land reclamation, must continue to play a vital role. These advances are over and above the major progress already achieved in each of these areas.

This handbook is not a one-shot research document meant to ‘gather dust’ on library shelves, but rather a ‘live’ document that will be modified and augmented over time. In this way, it will remain a current and critical reference that engages the minds of students, researchers, engineers, and operational employees alike. It will provide the knowledge foundation for bright ideas and innovations, which are necessary if the spectacular potential of Alberta’s vast oil sands resource is to be reached.

Securing Canada’s Energy Future

“Securing Canada’s Energy Future”—that is the promise of the oil sands. The magnitude of the oil sands resource, largely found in Alberta, is vast. The proven crude oil reserves from Canada’s oil sands are 177 billion barrels—second only to Saudi Arabia. This is enough resource to double oil sands production (currently at 1.3 million barrels per day) and still provide Canada with a secure supply of crude oil for over 200 years.

Of course, the true potential of Canada’s oil sands resource is actually much greater. It has been estimated that approximately 315 billion barrels is recoverable using current technology, and an even larger metric is the total oil in place (1.7 trillion barrels), which is roughly equivalent to the total for the entire Middle East. About 20 % of the bitumen is accessible through surface mining methods in the Athabasca region near Fort McMurray, and 80 % requires in situ methods, such as the cyclic steam stimulation (CSS) process developed by Imperial Oil Ltd. at Cold Lake, Alberta, and the steam-assisted gravity drainage (SAGD) process developed by the Alberta

Oil Sands Technology and Research Authority (AOSTRA) and industry partners over the 1974–1999 period. There are other large-scale bitumen resources, for example, those held in carbonate formations, for which extraction technology has not yet been developed. There are also oil sand deposits present at depths too deep to allow for surface mining to be carried out economically, but not deep enough to be accessed using in situ technologies such as SAGD.

The oil sands are a resource of global strategic value. Even in today's difficult economic conditions, oil sands projects are proceeding, with international investment coming into Canada to support about \$140 billion in current and proposed projects. Growth in the oil sands has the potential to improve energy supply security for North America. For example, Athabasca oil sands crude already supplies approximately 20 % of the crude oil imports in the United States and can replace the U.S. market's declining supply of heavy oil from Mexico and Venezuela. The Rand Corporation estimates that the United States spends between \$67 and \$83 billion annually (12 %–18 % of the United States government's defense budget) protecting its interests (including oil shipping routes) in unstable oil-producing parts of the world. These concerns do not apply with Canada's oil sands; in fact, the opposite is true.

Technology is the Key to Unlocking the Potential

That there is a vast supply of oil in the oil sands has long been known. The local Aboriginal people used the gummy bitumen material to patch their canoes. As early as 1778, North West Company trader, Peter Pond, reported seeing bitumen deposits as he entered the Athabasca River watershed via the Clearwater River, where the city of Fort McMurray is currently located. In the 1880s, the Geological Survey of Canada initiated work to better define the bitumen deposits in the Athabasca region following an 1875 report on the resource potential in the area by GSC botanist John Macoun, originally sent to chart railway construction routes. The investigations, led by Drs. Robert Bell, R.G. McConnell, and George M. Dawson, led to the drilling of a number of wells over the ensuing years, including several by German count and entrepreneur Alfred Von Hammerstein in the early 1900s, which proved to be largely unsuccessful. It was believed at the time that the oil was contained in large pools below the sands.

In 1913, the Federal Department of Mines sent engineer Sidney Ells to conduct a more detailed survey of the oil sands. Ells established that the bitumen was trapped within the sand deposits and could not be accessed using traditional methods. His maps became the first comprehensive assessment of the resource. Ells remained devoted to the characterization and promotion of the oil sands.

During this time, Alberta's bitumen resource was largely viewed in terms of its potential as a paving material. With the outbreak of World War I, there was a renewed interest by the federal government in developing the nation's oil resource. The Scientific and Industrial Research Council of Alberta (now the Alberta Research Council) was established in 1921 to investigate the province's natural resources. A key area of study was the oil sands; the mystery that remained to be solved was how to extract the bitumen from the sand to unlock the area's huge energy potential. Although some of the earlier pioneers had suggested that the oil could be washed from the sand with water, a major technological breakthrough did not occur until the 1920s. In 1923, ARC chemist Dr. Karl A. Clark, working with Sidney M. Blair and David Pasternack,

explored a process that used hot water to separate (or “wash”) the bitumen from the sand, for which Clark received a patent in 1929. The hot-water extraction process was a truly transformative technological advance that, until recent years, was still in use by Syncrude and Suncor as the primary bitumen extraction technology.

Technology development on a major scale, such as that for the oil sands, is never simple and takes years of dedicated research and development activity. There is a rich history of early pilot plant operations and commercial experiments, including Dr. Clark’s Dunvegan plant (started in Edmonton and moved to Waterways in 1929) and the acquisition of the Bitumount lease by Robert Fitzsimmons in 1922, which led to the development of a hot water processing plant to produce a heavy oil residue marketed by the International Bitumen Corporation. Max Ball, a petroleum engineer from Denver, formed a company later called Abasand Oils Ltd., which in 1936 completed a plant that processed oil sands until it was destroyed by fire in 1941. With the impetus of World War II to find better ways to realize the fuel potential from the oil sands, Lloyd Champion purchased the Bitumount plant in 1942, renamed it Oil Sands Ltd., and upgraded the plant using technology and support from Dr. Clark and the Alberta Research Council. Taken over by the Alberta government, the Bitumount plant was not completed until 1949. It only operated long enough to prove the process worked and was then shut down. In the meantime, the Abasand plant was rebuilt between 1941 and 1944, but burned down again in 1945.

Following the end of World War II in 1945, until about 1970, there was a perceived oversupply of crude oil, which led to output restrictions on most wells in North America and a general reticence towards the acceleration of oil sands development. (The situation changed vastly with the Arab oil embargo in 1973 and the Iranian oil embargo in 1979, both of which highlighted the world’s vulnerability to supply disruptions and the rising energy demand associated with the rapidly growing population and increasing standards of living in the developing world.) As a result of the post-war oversupply problem, it was not until 1964 that the first large-scale commercial plant was approved for development by Great Canadian Oil Sands (GCOS, now Suncor), with support from Sun Oil Company (and its visionary CEO, Howard Pew). Interestingly, the plant, which became operational in 1967, was limited to a production of 31 500 barrels per day, and Syncrude’s competing application was denied because of the concern that it would flood the crude oil marketplace. Undaunted, Syncrude, at that time a consortium of Cities Services Ltd. (now Nexen Inc.), Imperial Oil Ltd., Gulf Oil, and Atlantic Richfield, incorporated in December 1964 despite the regulatory setback. Led by Syncrude’s first CEO, Frank Spragins, further technology advances were pursued, and approval for a Syncrude plant was finally granted in 1971 under Peter Lougheed’s new conservative government. Construction could not proceed until 1973, and the plant was completed in 1978; Mr. Spragins lived to see his dream become a reality, albeit for a short period, as he passed away two months after startup. The other major early large-scale commercial development was Imperial Oil’s Cold Lake phased bitumen development program (now comprised of 14 phases), which was a brilliant strategy to enable the development of very deep bitumen deposits on a scale that was financially feasible following the shelving of the Cold Lake megaproject in 1976. Imperial Oil

developed its cyclic steam stimulation, or “huff and puff,” technology over many years, starting with the Ethel and May pilot plants in 1959. Imperial Oil is now the largest bitumen producer in Canada.

The National Oil Sands Task Force: The Rest is History

Oil sands development was quite limited following the Syncrude startup, as both Suncor and Syncrude contended with major reliability issues and a very high operating cost structure. At the same time, the economy was quite weak, and global crude oil prices collapsed in 1986 (i.e., below \$10 per barrel). There were many who doubted that the oil sands would ever be economically viable. I was seconded to Syncrude (from Imperial Oil) and moved to Fort McMurray that summer, where I personally experienced the concern for the future of the oil sands, which was palpable in the community and in the plants.

An all-out effort was undertaken by the three major commercial operations (Esso in Cold Lake, and Suncor and Syncrude in Fort McMurray) to improve safety and operations reliability and to reduce the inherently high operating cost structure. Several megaprojects were proposed, but failed to proceed. Most notable, perhaps, was the OSLO Joint Venture, which was shelved in the early 1990s. Following that event, the profile of the oil sands as a critical national resource virtually disappeared. I recall speaking in Ottawa’s Centre Block to politicians who were surprised to hear that Syncrude was producing a full 10 % of Canada’s crude oil requirement. An editorial board member of a very prominent eastern Canadian newspaper asked if the oil sands had gone commercial yet. I used to joke that I was the CEO of the “best kept secret in Canada.”

By the mid-1990s, trends in operating results at the three major operating plants were positive due to a strong focus on safety, continuous improvement, and technical innovations. This, together with the lack of interest in major oil sands development by investors and key political and community leaders, particularly outside of Alberta, led to the formation of the multi-stakeholder National Oil Sands Task Force (NOSTF) by the Alberta Chamber of Resources (ACR) in 1993. The NOSTF report, issued in May 1995, put forward an exciting vision to triple oil sands production by 2025, which would require about \$21–\$25 billion investment in capital projects and would deliver huge socio-economic benefits nationwide (i.e., employment, including for Canada’s Aboriginal population; revenues for all orders of governments to fund highly valued social programs; and other significant economic spinoff benefits, particularly for Canada’s manufacturing heartland in Ontario and Quebec). The report also highlighted barriers that had to be overcome for this vision to be realized, and named several working groups to identify solutions. The Fiscal Terms Working Group designed the generic royalty scheme, which was adopted by Premier Ralph Klein’s government in late 1995, and the corporate income tax recommendations were included in the federal government’s spring 1996 budget. The fiscal regime was designed to reduce the up-front financial risk of investing in large oil sands megaprojects in return for a fair share of profits upon payback of the original investment.

The actual results speak for themselves, and have far exceeded the original NOSTF projections. In less than 10 years (versus the 30 years projected in the report), oil sands production had tripled 1995 levels. By 2010, 1995 levels had quadrupled. In June 1996, Prime Minister Jean Chretien, the Honourable Anne McLellan, Minister of Natural Resources, and the Honourable Pat Black (now Nelson), Alberta's Minister of Energy, met with more than a dozen industry CEOs in Fort McMurray to sign the *Declaration of Opportunity*. At that time, the proposed oil sands project investments totaled about \$6 billion. Today, the total is about \$140 billion for current or proposed projects.

New Technologies Have Led the Way

Prior to 1990, the vision for the development of the surface-mineable oil sands was many heat-integrated (between bitumen extraction and bitumen upgrading) megaprojects dotted all over northeastern Alberta. Even Syncrude was expected to operate for only 25 years, shutting down in 2003 after producing 1 billion barrels of oil. Once again, technology came to the rescue. Syncrude needed to be able to mine and extract the bitumen at very remote mine sites and then transport it to the Mildred Lake site so that the upgrading, utilities, and central services operations located there could continue to function. In this way, we could access the bitumen leases with the highest ore grade, best ore quality, and lowest amount of overburden (i.e., lowest bitumen supply cost and environmental impact). At the same time, we would avoid the major capital investment associated with dismantling the existing Mildred Lake Upgrader and the central facilities there and rebuilding them at a new site. This vision became fully operational in 2000 with the opening of the remote satellite Aurora Mine and extraction operation 35 km north of the Mildred Lake site. As a result, Syncrude did not shut down in 2003; has now produced over 2.2 billion barrels of high-quality sweet Syncrude blend; has been expanded to a design capacity of 350 000 barrels per day (from 200 000 barrels per day); and has access to enough bitumen reserves to produce at these rates for another 60 years (Syncrude's leases contain an estimated 12 billion barrels of recoverable oil).

I love to use this example of how purpose-focused research and development, or "beginning with the end in mind," can be made to work. A few years after I joined Syncrude, at one of the company's annual R&D Seminars, four research associates laid out the complex path for achieving the above change in vision from heat-integrated, standalone megaprojects to a central operation fed by remote bitumen mines. Reaching this goal involved the development of several enabling technologies and technology platforms, including hydrotransport, the key technology involved in cold water extraction. Hydrotransport technology reduced the energy required to produce a barrel of bitumen by 40 % and precluded, to a large extent, the need to heat-integrate the extraction and upgrading processes. The development of the satellite mines also led to the creation (with global suppliers) of the world's largest haul trucks (400 tonne capacity), hydraulic shovels, electric shovels, cyclofeeders, and mixing boxes, which replaced much more costly and environmentally intrusive equipment such as dragline, bucket-wheel, and conveyor systems. The final technology platform,

called Natural Froth Lubricity (NFL), developed with the support of research bodies external to Alberta, allowed for the pumping of bitumen froth (i.e., mixture containing bitumen, water, clay, sand, even rocks, etc.) over great distances through pipelines without the need for extensive capital for froth cleanup, diluent facilities, and other support services at the remote mine site. It was amazing to follow the development and testing of the many technology platforms over this approximately 10-year period, and then the final culmination of this effort with the opening of the Syncrude Aurora Mine in 2000.

Transformative in situ technology, which led to the development of the steam-assisted gravity drainage (SAGD) process, is also currently being employed on a major scale. The groundbreaking work behind this technology was largely performed at the Underground Test Facility jointly operated and financed by AOSTRA and its industry partners. Dr. Roger Butler of Imperial Oil was a leading proponent of this technology, and devised an innovative way of combining the cyclic steam stimulation process from Esso's Cold Lake operation with the horizontal well technology used in the conventional oil and gas industry. Over the 1975–1999 period, AOSTRA invested about \$2 billion (split equally between industry and government) in the development of technologies such as CSS and SAGD. While this is an excellent example of leveraging capital resources, it is an even better example of how to leverage the knowledge (or brainpower) of multiple organizations.

Today, AOSTRA has been re-invented and is now a separate provincial corporation known as Alberta Innovates – Energy and Environment Solutions, with a mandate that extends beyond the oil sands to include all sources of energy and the environmental challenges associated with them. In this way, Alberta can continue to leverage its knowledge base across various companies and industries, who share common challenges and opportunities.

The Oil Sands Handbook Lays the Foundation for the Path Forward

Quite simply, it has been technology that has allowed oil sands development to reach the point it is at today, and it will be technology that takes the oil sands industry where it needs to go in the future. The *Handbook on Theory and Practice of Bitumen Recovery from Athabasca Oil Sands* defines the current state of oil sands science and technology. However, there are many other technical innovations and breakthroughs under development and, perhaps most significantly, germinating in the minds of future oil sands scientists and developers.

This handbook is made up of two volumes. Volume I provides a comprehensive description of the science behind the key technologies, while Volume II is a consolidation of the best industrial practice across all of the major aspects of oil sands planning and production. Including both volumes recognizes that technological breakthroughs will not only occur in research laboratories and pilot plant demonstrations, but also by developing the technology “knowhow” that exists among the workforce of commercial field operations.

History has shown how oil sands development has progressed by building on existing technology platforms. As such, this handbook is a consolidation of the current technological foundation. It is intended to be a living document that is updated and augmented over time with ongoing technological and operational advancements. It is meant to engage the minds of professors, students, researchers, engineers, and technical operating staff. It will provide them with the technology foundation that will serve as the springboard for the future enhancements required for the sustainable development of our vast oil sands resource. It is their bright ideas and innovations that will be so vitally important if we, as Canadians, are to realize the huge socio-economic potential of this strategic global resource.

The lead authors and the many others who have contributed to this handbook deserve our gratitude. It is a monumental undertaking that will have immediate application and impact.

Dr. Eric P. Newell, O.C., AOE, FCAE, P.Eng

List of Commonly-used Abbreviations

AAS: atomic absorption spectrophotometer
AER: Alberta Energy Regulator
AEUB: Alberta Energy and Utilities Board
AOSP: Athabasca Oil Sands Project
APCI: atmospheric pressure chemical ionization
APPI: atmospheric pressure photo ionization
bbl: barrel
CCC: critical coagulation concentration
CEC: cation exchange capacity
CHP: combined heat and power
CHWE: Clark Hot Water Extraction
CMC: critical micellization concentration
CNAC: critical nano-aggregate concentration
CNRL: Canadian Natural Resources Limited
CO₂e: carbon dioxide equivalent
CT: consolidated or composite tailings
DRU: diluent recovery unit DRU
DSPW: doped simulated process water
ERCB: Energy Resources Conservation Board
ESI: electrospray ionization
FCF: flocculation-coagulation-flocculation
FFT: fluid fine tailings
FGD: flue gas desulphurization
FIMS: electric field ionization
FTFC: Fine Tailings Fundamentals Consortium
FTIR: Fourier transform infrared spectroscopy
GCOS: Great Canadian Oil Sands
GPC: gel permeation chromatography
HHV: higher heating value
HLB: hydrophilic lipophilic balance
HRTEM: high-resolution transmission electron microscopy

IFN: instream flow needs

IFT: interfacial tension

IPS: inclined plate settler

LCA: life cycle analysis

LDMS: laser desorption

LHES: laboratory hydrotransport extraction system

MIBC: methyl isobutyl carbinol

MFT: mature fine tailings

MS: mass spectrometry

NEB: National Energy Board

OHWE: OSLO Hot Water Extraction

OSA: oil sands area

PSC: primary separation cell

PSD: particle size distribution

PSV: primary separation vessel

PZC: point of zero charge

SAGD: steam-assisted gravity drainage

SARA: saturates, asphaltenes, resins, and aromatics

SCO: synthetic crude oil

SFR: sand-to-fines ratio

SG: specific gravity

SPW: simulated process water

SRF: specific resistance to filtration

STP: standard temperature and pressure

TAN: total acid number

TDS: total dissolved solids

TRFD: time-resolved fluorescence depolarization

TT: thickened tailings

TTW: tank-to-wheels

VDU: vacuum distillation unit

VPO: vapour pressure osmometry

WTT: well-to-tank

WTW: well-to-wheels

Chapter 1

Introduction to the Athabasca Oil Sands

As one of the world's leading sources of non-conventional petroleum, Canada has a vast crude bitumen resource.¹ Crude bitumen is a type of heavy crude oil, characterized by very high viscosities, high densities, relatively high heavy metal concentrations, and a low hydrogen-to-carbon ratio in comparison with conventional crude oil.² Crude bitumen is highly viscous and does not flow easily under gravity; at room temperature, its viscosity is generally over 500 Pa·s and its behaviour similar to that of cold molasses. Its density ranges from 970 kg/m³ to 1015 kg/m³ (8° API to 14° API). Crude bitumen must be treated before it can be converted into synthetic crude oil (SCO), which is then fractionated in traditional refineries to produce gasoline, heating oils, and jet and diesel fuels.

The crude bitumen and the rock matrix in which it is found, along with other associated mineral material (with the exception of natural gas), are called *oil sands*. Sometimes referred to as *tar sands* or *bituminous sands*,³ oil sands are sedimentary deposits that are impregnated with viscous petroleum of a high molar mass. Oil sands deposits are found throughout the world, usually in the same geographical location as conventional petroleum. Other types of heavy oil are also deemed to be oil sands if they are located within an oil sands area.

1 Venezuela's Orinoco Belt is another leading source of non conventional oil, estimated to contain 300 10⁹ m³ (1.9 trillion bbl) of oil in place, 43.2 10⁹ m³ (272 billion bbl) of ultimate recoverable reserves, and 12.3 10⁹ m³ (77.4 billion bbl) of proven reserves. The deposits found in Venezuela are referred to as heavy and extra heavy crude oil.

2 According to ERCB, in Alberta, crude oil is considered to be "oil produced outside the Oil Sands Areas, or if within the Oil Sands Areas (AER) from formations other than the Mannville or Woodbend" (2009, p. 3 1). ERCB further classifies crude oils with a density of less than 900 kg/m³ as light medium, and those with densities of 900 kg/m³ or more as heavy. Table 1.2 provides details on Alberta crude oil reserves.

3 The use of the word tar to refer to oil sands deposits is incorrect, since tar is a man-made substance and not a naturally occurring hydrocarbon. Tar, by definition, is produced through the destructive distillation of organic material.

Canada's crude bitumen resource is present mainly in the northeastern part of the province of Alberta, within three core oil sands areas (OSAs): Athabasca Wabiskaw-McMurray, Cold Lake Clearwater, and Peace River Bluesky-Gething (Figure 1.1). Together, these three OSAs occupy an area of approximately 142 000 km² (Energy Resources Conservation Board [ERCB] 2009, p. 2-4). The Athabasca Wabiskaw-McMurray OSA, known commonly as the Athabasca oil sands, is the largest of the three oil sands areas in Alberta.

Other crude bitumen reserves are present within the Devonian and Mississippian carbonate deposits that unconformably underlie the Athabasca and Peace River unconsolidated sands. The deposits at Peace River, referred to as *carbonate bitumen* deposits, have not been commercially produced.

Within the three OSAs, there are 15 separate oil sands deposits across different geological zones (Hein, Marsh, and Boddy 2008). Figure 1.2 shows the locations of bitumen-in-clastic sands and bitumen-in-carbonate rocks that form the main deposits in Alberta.

Collectively, Alberta's oil sands contain one of the largest known hydrocarbon deposits in the world. With initial established reserves estimated at 28.092 10⁹ m³ (176.7 billion bbl),⁴ the province was ranked second in the world in terms of oil reserves, after Saudi Arabia (Radler 2003).

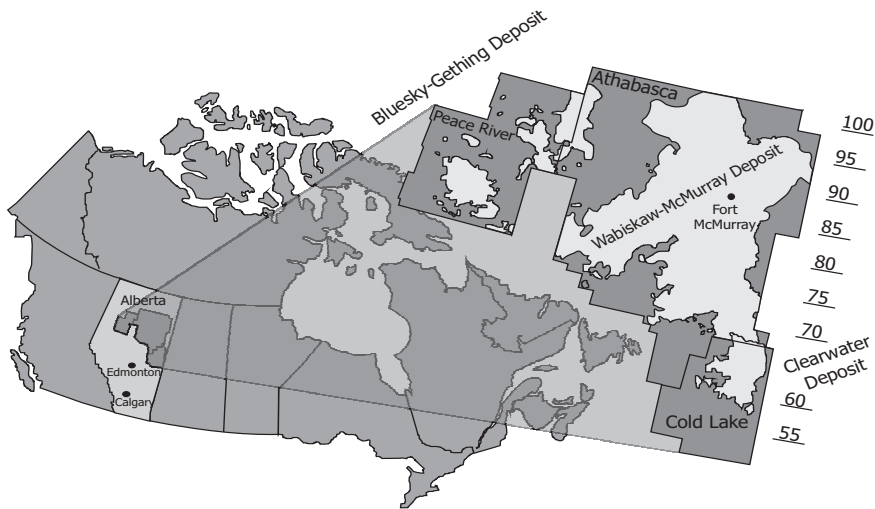


Figure 1.1 Alberta oil sands regions: Athabasca, Peace River, and Cold Lake. Township markers of 50 km spacing are shown on the right for scale.

Adapted from ERCB (2009).

⁴ Conversion to barrels is rounded off in agreement to cited references. One cubic metre is equivalent to 6.29 barrels. A barrel is 42 US gallons.

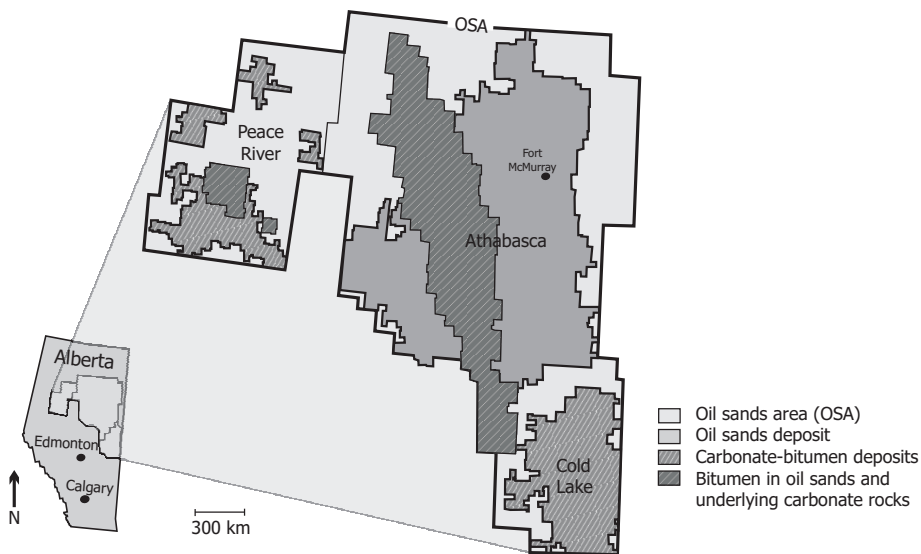


Figure 1.2 Map showing locations of main bitumen deposits in Alberta.

Source: Hein, Marsh, and Boddy (2008).

1.1 Geology

1.1.1 Origins of Oil Sands

There are two main theories regarding the origin of oil: organic (biogenic) and inorganic (abiogenic). The inorganic theory was propagated, in part, by the father of the periodic table of elements, Dmitri Mendeleev, who reasoned that acetylene (C_2H_2) was formed through a reaction of carbides with water, and that it, in turn, formed the petroleum. This theory is now discredited.

The widely accepted organic theory assumes that:

1. Marine life, mainly plankton and other marine animals, die and sink to the ocean bottom and are embedded by sedimentary minerals. Major alteration is caused via aerobic bacterial action (in the presence of oxygen), followed by anaerobic bacterial action (in the absence of oxygen).
2. With temperatures rising to $\sim 150^\circ C$, and with rising pressure due to increasing burial depths (300 to 1500 atm), the proteins, carbohydrates, and other materials are destroyed and converted to kerogen (a process known as diagenesis). Eventually, the kerogen decomposes to produce liquid petroleum. At the same time, the organically rich sediments are converted into rocks, which, after more geologic time, are deformed, buckled, and uplifted.

- The liquid petroleum flows through the pores of the rock in which it was formed until it becomes trapped and cannot flow any further, thereby forming an oil reservoir.

According to Adams, Rostron, and Mendoza (2004, p. 1080), who refer to studies by Garven (1989), the “tectonic uplift of the western part of the Alberta basin caused a topography-driven flow system to develop shortly after the maximum burial [of the formed liquid petroleum]. Topographic relief drove basal fluids [i.e., water] through the petroleum source rocks. . . . This flow system acted as the main conduit for hydrocarbon-charged water to the Athabasca oil sands area.” Other geologists suggest that water flow is not necessary as a driving force for petroleum migration, but rather that the light liquid petroleum simply migrates through displacement or diffusion as a single- or multiphase fluid. In either case, as the crude migrated up-dip, its path became progressively restricted, and as a result, a large quantity of petroleum was trapped in the permeable sands of the McMurray Formation, between the Devonian carbonate below and the overlying/capping Cretaceous Clearwater Formation shale, as shown in Figures 1.3 and 1.4 (Cuddy 2004).

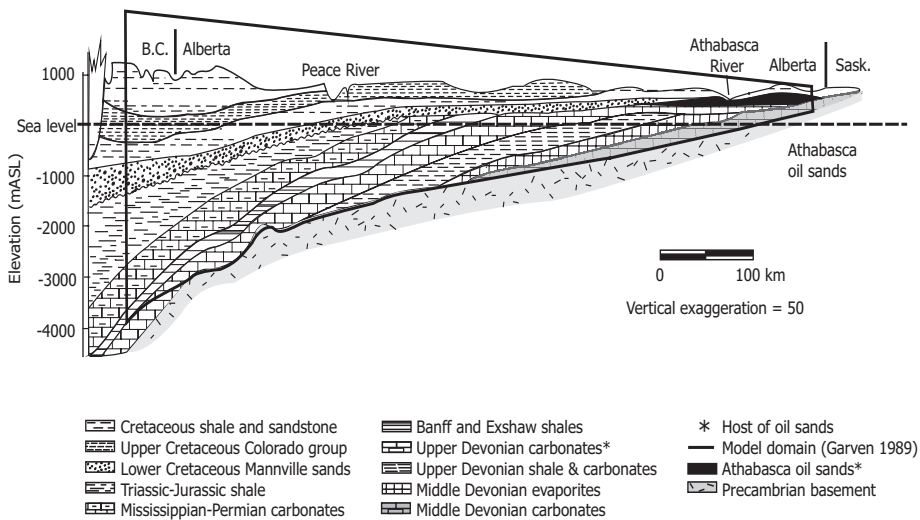


Figure 1.3 Geological formation and migration of crude oil.

Source: Adams, Rostron, and Mendoza (2004)

The main point of uncertainty is whether the source rocks are from the Mississippian or the Jurassic period, or some combination of the two. It is now widely accepted that light oil was sourced in the deeper portions of the pre-Cretaceous formations of the Western Canada Sedimentary Basin (WCSB) and migrated long distances before becoming trapped in its present location. The McMurray and other corresponding formations were the primary collectors of the generated oil and provided the main conduit for west-to-east migration. It is estimated that the migration path was at least

360 km for the Athabasca deposit and at least 80 km for the Peace River deposit. These lighter oils were then subjected to aerobic biodegradation and transformed into bitumen.

Bacterial degradation of the trapped liquid petroleum over millions of years led to the formation of a heavier oil, i.e., crude bitumen. It resulted in the absence of straight-chain hydrocarbons (such as pentanes) and led to an increase in hydrocarbon species of higher molecular weight. As a result, the oil-specific gravity and sulphur content of residual material, i.e., bitumen, increased. As well, the concentration of heavy minerals, such as vanadium, nickel, magnetite, gold, and silver, also increased. To that end, crude bitumen at room temperature has a density higher than that of water and a viscosity of $\sim 500 \text{ Pa}\cdot\text{s}$. It has a sulphur content of $\sim 4.5 \%$, a nitrogen content of $\sim 0.5 \%$, and a heavy metal (vanadium and nickel) content of $\sim 300 \text{ ppm}$. The bacteria may also have modified some of the simpler sulphur molecules, leaving behind the more complex ones. Subsequently, there are more “heavy” hydrocarbons, complex sulphur and nitrogen compounds, and metals in bitumen than there are in conventional crude oil.

It has been estimated that prior to biodegradation, the original volume of oil in the oil sands was two to three times that of today’s. The characteristics of the bitumen and the reservoir properties of the oil sands are in large part a function of the degree of biodegradation that took place (Canadian Centre for Energy Information [CCEI] 2004; Cuddy 2004; Adams, Rostron, and Mendoza 2004; Garven 1989).

1.1.2 The Athabasca Wabiskaw-McMurray Deposit

As mentioned earlier, the Athabasca oil sands deposit area is the largest of the three oil sands areas in Alberta. It is also the only one that is accessible to open-pit mining. Most of the Athabasca reserves are contained within the Lower Cretaceous McMurray Formation, where the bitumen is contained within unconsolidated (uncemented) clastic sand. The entire Mannville Group is exposed in river sections in the vicinity of Fort McMurray. However, the McMurray Formation is the only one within the Mannville Group that is oil-saturated. The McMurray Formation overlies the Devonian rocks and the Devonian strata that unconformably overlie the Precambrian rocks. The Devonian rocks consist of limestone, dolomite, shale, anhydrite, and salt.

The McMurray Formation was deposited directly onto the pre-Cretaceous erosional surface in a major north-to-south trending depression. This depression was initiated by the salt solution removal of the Middle Devonian evaporates and the consequent collapse of the overlying formations. A fluvial drainage system occupied the depression in the early Cretaceous period. This carved the exposed limestone into a landscape of highly variable relief. The locations of highs and lows on the weathered Devonian surface are critical to the distribution of oil sands reserves in the Athabasca deposit, because the bulk of the reserves in the deposit is contained in the sands of the lower and middle members of the McMurray Formation (Cuddy 2004).

The Clearwater Formation overlies the McMurray Formation. Above it lies the sandstone of the Grand Rapids Formation. A distinct contact point for these two formations is sometimes difficult to determine due to their interfingering nature. The

Clearwater and Grand Rapids Formations are barren in the Athabasca OSA, but are bitumen-bearing in the Wabiskaw and Cold Lake OSAs.

The McMurray Formation is informally divided into three subsections that reflect the environments of sediment deposition: Lower (continental fluvial), Middle (tidal estuary), and Upper (tidal marine) (Cuddy 2004). Although the Lower McMurray is normally highly saturated with bitumen and has coarser sand, in some regions of the Athabasca deposit, it contains water-bearing sands that have little or no bitumen saturation. Such sands are referred to as *basal water sands* (BWS).

Figure 1.4 shows the geological strata for the McMurray Formation on Lease 18 of CNRL's Horizon Project. In this lease, the Upper McMurray is relatively shallow and most of the oil sands resources are found within the Lower and Middle McMurray Formations. The Clearwater Formation that overlies the Upper McMurray comprises marine clay, fine sand, and siltstone. The deposition of these sediments occurred in a marine environment during the rise of the boreal Clearwater Sea.

EON	ERA	PERIOD	STRATIGRAPHY			LITHOLOGY	Unit	
			GROUP	FORMATION	MEMBER			
Phanerozoic	Ceno- zoic	Pleistocene and recent deposits				Till, sand, silt, gravel, and muskeg	Aquifer - Aquitard	
		Erosional unconformity						
	Mesozoic	Cretaceous	Upper	Colorado	LaBiche (Klb)	1ws	Shale	Aquitard
						2ws		
						BFSc		
				Viking (Kv)	Sandstone		Aquifer	
				Joli Fou (Kj)	Shale		Aquitard	
				Grand Rapids (Kg)	Lithic sand and sandstone		Aquifer	
		Lower	Mannville	Clearwater (Kc)	Shale and sandstone		Aquitard	
					Wabiskaw	Glauconitic sand and silt	Minor aquifer	
			McMurray	Upper	Nearshore marine sands and black clays		Aquitard where oil-saturated/ Aquifer where water-saturated	
				Middle	Estuarine fine sands and grey clay with oil impregnation			
				Lower	Continental clays			
					Medium to coarse sands			
			Devonian	Upper	Beaverhill Lake	Waterways	Moberly	Argillaceous limestone
	Christina	Calcareous shale and						
	Calumet	Clastic limestone						
	Firebag							
	Paraconformity							
							Aquifer: Water-permeable Aquitard: Non-permeable	

Figure 1.4 Geological strata for the McMurray Formation.

Source: CNRL (2002a).

1.2 Alberta's Crude Bitumen Resource

1.2.1 Oil Sands Ore Characterization

Among several other important factors, the quality of an oil sands deposit depends primarily on the weight percentage (wt. %) of bitumen in the deposit and the thickness of the saturated bitumen zone. The weight percentage of bitumen content, also referred to as the *bitumen grade*, varies significantly within a deposit, both laterally and with depth. It decreases as the reservoir shale or clay content increases or as the porosity decreases. As both bitumen and water occupy the pore space of the rock or sand formation, increasing the water volume (or weight) within the pore space also decreases the weight percentage of bitumen in the reservoir.

Table 1.1 Initial in-place volumes of crude bitumen and characteristics in various OSAs

Source: ERCB (2009, p. 2-11).

Oil Sand Area (OSA)	Initial in-place volume (10 ⁹ m ³)	Area (km ²)	Average pay thickness (m)	Average bitumen saturation		Average porosity (%)
				Weight (%)	Pore volume (%)	
Athabasca						
Grand Rapids	8.678	6890	7.2	6.3	56	30
Wabiskaw-McMurray (mineable)	20.728	3740	25.8	10.1	76	28
Wabiskaw-McMurray (in situ)	132.319	47 010	13.1	10.2	73	29
Nisku	10.330	4990	8.0	5.7	63	21
Grosmont	50.500	41 670	10.4	4.7	68	16
Subtotal	222.555	104 300				
Cold Lake						
Grand Rapids	17.304	17 090	5.9	9.5	66	31
Clearwater	9.422	4330	11.8	8.9	59	31
Wabiskaw-McMurray	4.287	4850	5.4	7.3	59	27
Subtotal	31.013	26 270				
Peace River						
Bluesky-Gething	10.968	10 160	6.1	8.1	68	26
Belloy	0.282	260	8.0	7.8	64	27
Debolt	7.800	3020	23.7	5.1	65	18
Shunda	2.510	1430	14.0	5.3	52	23
Subtotal	21.560	14 870				
Total	275.128	145 440				

In Table 1.1, the terms pore volume, porosity, and bitumen saturation are used to characterize an oil sands ore. Pore volume refers to the ratio of the total space of the voids in an oil sands ore to its total undisturbed volume. This is an important property when dealing with an in situ production operation, where bitumen is able to flow within the pore space of the oil sands matrix. The porosity of an oil sands ore is defined as the ratio of pore volume to sand volume. The bitumen saturation of an oil sands ore can be expressed in one of two ways: as the weight percentage of bitumen relative to the total weight of the oil sands ore, including all bitumen, water, and mineral solids (sand, shale, and clay); or as the percentage of pore volume that is occupied by bitumen.

Figure 1.5 shows a bitumen pay thickness map for the Athabasca Wabiskaw-McMurray OSA, with cutoffs of 6 % wt. bitumen and 1.5 m pay thickness. The map construction considers the deposit to be a single bitumen zone and the pay zone to have accumulated over the entire geological interval (ERCB 2008).⁵ The figure also indicates the designated surface-mineable area. This area is restricted to the vicinity of Athabasca River and is a relatively small fraction of the Athabasca Wabiskaw-McMurray deposit. This is the only surface-mineable deposit within the three OSAs.

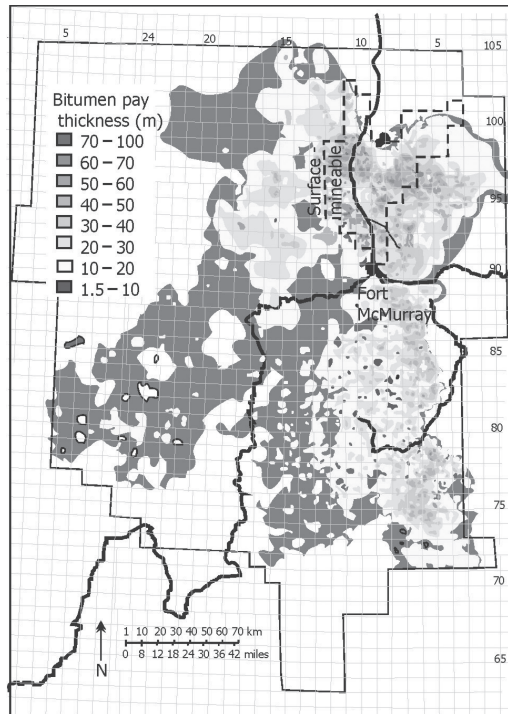


Figure 1.5 Bitumen pay thickness of the Athabasca Wabiskaw-McMurray OSA.

Adapted from ERCB (2009).

⁵ ERCB provides these types of contour maps on a regular basis in its ST-98 statistical survey reports.

1.2.2 Recovery Methods

To date, there are two main methods used for the recovery of bitumen from the Athabasca oil sands: open-pit mining and in situ. Mining operations are applied in relatively shallow oil sands formations. Vegetation and surface cover, i.e., muskeg and overburden, are first removed using shovels, exposing the oil sands formation. Presently, the truck-and-shovel method and at-face mining equipment are used to mine the oil sands ore. The mined oil sands are treated with hot water to liberate the bitumen from the sand grains for subsequent recovery and cleaning.

In situ bitumen recovery is used when the overburden is too deep for economical mining operation. Steam-assisted gravity drainage (SAGD) is currently used in commercial operations. In this approach, two horizontal wells, parallel to each other, are drilled into the lower part of the oil sands formation. Steam is introduced into the upper well, heating the surrounding formation and reducing the bitumen's viscosity. The bitumen, together with condensed steam, flows to the lower well, from which it is pumped to the surface.

The division between surface mining and in situ areas is based on the thickness of the overburden, with mining operations generally limited to areas where the overburden thickness is less than ~ 75 m (ERCB 2008).

Table 1.2 Alberta reserves and production of crude bitumen and crude oil

Sources: ERCB (2009); NEB (2004).

	Crude bitumen		Crude oil	
	Billion cubic metres (10 ⁹ m ³)	Billion barrels ^a	Billion cubic metres (10 ⁹ m ³)	Billion barrels ^a
Ultimate in-place volume	400	2500		
Initial in-place volume	275.128	1731	10.782	67.8
Ultimate potential recoverable reserves	50.0	314.5	3.13	67.8
Initial established reserves	28.092	177	2,773	17.50
Remaining established reserves, as of end of 2008	27.072	170	0.233	1.5
Annual production, 2008	0.076	0.477	0.0293	0.184
Cumulative production volume as of end of 2008	1.02	6.42	2.540	16.0

Note: A volume of one cubic metre is equivalent to approximately 6.29 barrels. One barrel is equivalent to approximately 159 L or 0.159 m³.

^a The numbers quoted in cubic metres are used to convert to barrels.

1.2.3 Crude Bitumen Reserves: Definitions and Values

A specific terminology has developed within the industry and both the provincial and federal governments to describe crude bitumen volumes and reserves. In this section, we explore these terms in more detail and present the established numbers for crude bitumen production in Alberta. Note that the numbers can vary slightly according to the criteria used in defining them and are updated as new core data are acquired. The data presented in the following section are shown in Tables 1.1 to 1.4.

Table 1.3 In-place and established mineable and in situ reserves and cumulative production of crude bitumen
Sources: ERCB (2009); NEB (2004).

Crude bitumen	Recovery method billion cubic metres (10 ⁹ m ³)		Billion cubic metres (10 ⁹ m ³)
	Minable	In Situ	Total
Ultimate in place volume	22	378	400
Initial in-place volume	20.7	254.4	275.1
Ultimate potential recoverable reserves	11.0	39.0	50.0
Initial established reserves	6.16	21.94	28.09
Cumulative production as of end of 2008	0.670	0.350	1.020
Remaining established reserves as of end of 2008	5.487	21.585	27.072
Remaining established reserves under active development as of end of 2008	3.74	0.56	4.30

Table 1.4 Mineable crude bitumen reserves in some reported areas *under active development* as of the end of 2008
Source: ERCB (2009, p. 2-12). Note: 1 km² = 100 ha.

Develop- ment project	Project area (km ²)	Initial mineable in-place volume (10 ⁹ m ³)	Initial established reserves (10 ⁹ m ³)	Cumulative production (10 ⁹ m ³)	Remaining established reserves (10 ⁹ m ³)
Albian Sands	135.81	0.672	0.419	0.049	0.371
Fort Hills	189.76	0.699	0.364	0	0.364
Horizon	284.82	0.834	0.537	0	0.537
Jackpine	79.58	0.361	0.222	0	0.222
Suncor	191.55	0.990	0.687	0.250	0.437
Syncrude	440.37	2.071	1.306	0.371	0.935
Kearl	196.74	1.324	0.872	0	0.872
Sum total	1518.63	6.951	4.407	0.670	3.738

Initial In-Place Volume of Crude Bitumen

This term refers to the volume of crude bitumen estimated, calculated, or interpreted to be initially contained in a deposit “before any volume has been produced and without regard for the extent to which such volumes will be recovered” (NEB 2004, p. 119). This value is established using specific drillhole data, including geophysical logs and core analyses.

In ERCB’s 2008 and 2009 ST-98 documents, for Cretaceous sands, the initial in-place volume of crude bitumen was determined “using a minimum saturation cutoff of 3 mass per cent crude bitumen and a minimum saturated zone thickness of 1.5 m for in situ areas.” For surface-mineable areas, “cutoffs were increased to 6 mass per cent and 3.0 m” in 1999. For carbonate deposits, the crude bitumen “was determined using a minimum bitumen saturation of 30 per cent of pore volume and a minimum porosity value of 5 per cent” (ERCB, 2008, p. 2-4). The ERCB suggests that the 1999-era change in the oil sands quality cutoff “more accurately reflects the volumes from which bitumen can be reasonably expected to be recovered.” This change decreases the initial in-place volume estimation of the crude bitumen resources (ERCB 2008, p. 2-5).

Table 1.1 provides the initial in-place volume of crude bitumen in the various OSAs. The initial in-place volume of crude bitumen, as shown in Table 1.2, is estimated at $275.128 \times 10^9 \text{ m}^3$ (1731 billion barrels) (ERCB 2009).

Ultimate In-Place Volume of Crude Bitumen

This term refers to the estimated ultimate volume of crude bitumen expected to be found by the time “all exploratory and development activity has ceased” (NEB 2004, p. 4), and “without regard for the extent to which such volumes will be recovered” (p. 119). We can, therefore, regard the ultimate in-place volume of crude bitumen as representative of the uppermost crude bitumen estimate.

The ultimate in-place volume of crude bitumen is estimated at $400 \times 10^9 \text{ m}^3$ (2.5 trillion barrels) (NEB 2004, p. 4). Of this amount, NEB categorizes $22 \times 10^9 \text{ m}^3$ (140 billion barrels) as amenable to surface mining (in-pit mining) and the remaining $378 \times 10^9 \text{ m}^3$ (2.4 trillion barrels) as amenable to in situ recovery or underground mining methods. The volume of crude bitumen within the carbonate rocks of Devonian and Mississippian origin is estimated at $60.8 \times 10^9 \text{ m}^3$ (ERCB 2009, p. 2-9).

Ultimate Potential Recoverable Reserves of Crude Bitumen

ERCB defines *ultimate potential* as “an estimate of the initial established reserves that will have been developed in an area by the time all exploratory and development activity has ceased, having regard for the geological prospects of that area and anticipated technology and economic conditions.” ERCB further includes “cumulative production, remaining established reserves, and future additions through extensions and revisions to existing pools and the discovery of new pools” in its definition, and expresses ultimate potential using the equation: “Ultimate potential = initial established reserves + additions to existing pools + future discoveries” (ERCB 2009, p. A7).

Of the ultimate in-place volume of crude bitumen, 12 % to 13 %, or ~ 50 10^9 m³ (314.5 billion barrels), are estimated to be potentially recoverable reserves. The ultimate potential reserves of crude bitumen recoverable by in situ methods is estimated to be 33 10^9 m³ from Cretaceous sediments and 6 10^9 m³ from Paleozoic carbonate sediments. Nearly 11 10^9 m³ is expected from within the surface-mineable boundary. ERCB's current estimate of total ultimate potential crude bitumen reserves (50 10^9 m³) is unchanged from previous estimates and can be considered optimistic (ERCB 2009).

Established Reserves of Crude Bitumen

ERCB defines established reserves as “reserves recoverable under current technology and present and anticipated economic conditions specifically proved by drilling, testing, or production, plus the portion of contiguous recoverable reserves that are interpreted to exist from geological, geophysical, or similar information with reasonable certainty” (2009, p. A2).

Initial Established Reserves of Crude Bitumen

This term refers to the “established reserves [of crude bitumen] prior to the deduction of any production” (ERCB 2009, p. A4). The initial established reserves of crude bitumen are estimated at 28.092 10^9 m³ (176.7 billion barrels). Of this amount, ~ 80 % (21.94 10^9 m³) is amenable to in situ production, and ~ 20 % (6.16 10^9 m³) is amenable to surface mining (ERCB 2009, p. 2-3). The initial established reserves of crude bitumen are considered a reasonable estimate of recoverable crude bitumen in the next several decades.

According to ERCB, when determining initial established reserves in surface-mineable areas, reduction factors must be applied to account for “bitumen ore sterilized due to environmental protection corridors along major rivers, small isolated ore bodies, and the location of surface facilities (plant sites, tailings ponds, and waste dumps)” (ERCB 2009, p. 2-11). ERCB estimates these reduction factors at 0.9 and assumes an average recovery efficiency factor of 0.82 for combined mining/extraction and bitumen cleaning.

For those areas considered amenable to in situ production, ERCB applied bitumen zone thickness cutoffs based on the “type of development and [on] deposit characteristics.” A cutoff of 10 m to 15 m was used for deposits amenable to thermal recovery, and a minimum cutoff of 3 m or lower was used for primary development. ERCB used “a minimum saturation cutoff of 3 mass per cent,” but notes that “future reserves estimates will likely be based on values higher [than this].”⁶ For areas meeting cutoff criteria, recovery factors of 20 % for thermal recovery and 5 % for primary development were applied (ERCB 2008, p. 2-12).

⁶ As noted in ERCB's ST98 report, “the selection of appropriate saturation and thickness cutoff varies, depending on the purpose the resource evaluation and other factors, such as changes in technology and economic conditions”(p. 2-4, 2008).

At the end of 2008, the ratios of initial established reserves to initial in-place volume were 0.298 and 0.086 for mineable and in situ productions, respectively. The very low ratio for in situ production is reflected, to a large extent, by the low recovery of crude bitumen and the criteria used in estimating the reserves (Table 1.3). Details for the initial in-place volume and deposit characteristics of each OSA are provided in Table 1.1. As noted, the Athabasca oil sands area is the largest in terms of surface area and crude oil deposits.

Remaining Established Reserves of Crude Bitumen

This term refers to the volume of “initial established reserves of crude bitumen, less cumulative production” (ERCB 2008, p. A6).

As can be seen in Table 1.3, at the end of 2008, only ~ 3.3 % of the initial established reserves (equivalent to $1.020 \cdot 10^9 \text{ m}^3$) had been produced since 1967, when production on a commercial scale began. The cumulative production was $0.670 \cdot 10^9 \text{ m}^3$ for surface mining and $0.350 \cdot 10^9 \text{ m}^3$ for in situ. The total remaining established reserves of crude bitumen were $27.072 \cdot 10^9 \text{ m}^3$ (~ 170.3 billion barrels), of which ~ 80 % (or $21.585 \cdot 10^9 \text{ m}^3$) is considered to be recoverable by in situ methods and ~ 20 % ($5.487 \cdot 10^9 \text{ m}^3$) by surface mining methods. Of the remaining established reserves, $0.5607 \cdot 10^9 \text{ m}^3$ of the in situ-recoverable and $3.738 \cdot 10^9 \text{ m}^3$ of the mineable reserves are within the active development areas (ERCB 2009). At a daily production of 5 million barrels, the remaining established crude bitumen reserves would be depleted after about one century of production. ERCB estimates that bitumen production by 2018 will be double that of 2008 (ERCB 2009, p. 5).

As can be seen from Table 1.2, the remaining established reserves of crude oil are less than ~ 1 % of that of crude bitumen.

Synthetic Crude Oil Production

We have referred to *crude bitumen* to indicate non-upgraded bitumen. During upgrading operations, there is a 10 % to 20 % reduction in bitumen volume due to coke rejection in the upgrading process or as a result of asphaltene precipitation and rejection during bitumen froth treatment. We refer to upgraded bitumen as *synthetic crude oil* (SCO). In 2008, ~ 59 % of crude bitumen produced in Alberta was upgraded to SCO in the province. This percentage is expected to increase to ~ 61 % by 2018 (ERCB 2009, p. 3). Up-to-date estimates and data can be obtained from AER ST-98 publications.

Table 1.5 In situ crude bitumen reserves^a in areas under active development as of end of 2008

Source: ERCB (2009, p. 2-14).

Development project	Initial in-place (10⁹ m³)	Recovery factor (%)	Initial established reserves (10⁹ m³)	Cumulative production^b (10⁹ m³)	Re-maining established reserves (10⁹ m³)
Peace River Oil Sands Area					
Thermal commercial projects	0.0558	40	0.0223	0.01	0.0123
Primary recovery schemes	0.1608	5	0.008	0.0061	0.0019
Subtotal	0.2166		0.0304	0.0161	0.0143
Athabasca OSA					
Thermal commercial projects	0.3137	50	0.1569	0.0369	0.1200
Primary recovery schemes	1.0262	5	0.0513	0.0204	0.0309
Enhanced recovery schemes ^c	0.289 ^d	10	0.0289	0.0103	0.0186
Subtotal	1.3399		0.2371	0.0676	0.1695
Cold Lake Oil Sands Area					
Thermal commercial (CSS) ^e	1.2128	25	0.3032	0.1848	0.1184
Thermal commercial (SAGD) ^f	0.0338	50	0.0169	0.001	0.0159
Primary production within projects	0.6011	5	0.0301	0.0137	0.0164
Primary recovery schemes	4.3471	5	0.2174	0.0527	0.1647
Lindbergh primary production	1.3093	5	0.0655	0.0073	0.0582
Subtotal	7.5041		0.633	0.2595	0.3735
Experimental schemes (all areas)					
Active	0.0081	15 ^g	0.0012	0.0011 ^h	0.0001
Terminated	0.0874	10 ^g	0.0091	0.0058	0.0033
Subtotal	0.0955		0.0103	0.0069	0.0035
Total	9.116		0.9087	0.3501	0.5607

^a Thermal reserves for this table are assigned only for lands approved for thermal recovery and having completed drilling development.

^b Cumulative production to December 31, 2007, includes amendments to production reports.

^c Schemes currently on polymer or waterflood in the Brintnell-Pelican area. Previous primary production is included under primary schemes.

^d The in-place number is that part of the primary number above that will see incremental production due to polymer or waterflooding

^e Cyclic steam simulation projects.

^f Steam-assisted gravity drainage projects.

^g Averaged values.

^h Production from the Athabasca OSA is 0.86 10⁶ m³ and from the Cold Lake OSA is 0.2 10⁶ m³.

1.2.4 Crude Bitumen and Synthetic Crude Oil Under Active Development

Table 1.4 lists current and approved surface-mineable projects as of December 2008. Up to the end of November 2008, Suncor Energy Inc., Syncrude Canada Ltd., and Shell Albian Sands (formerly known as Albian Sands Energy Inc.)⁷ were the only producers in the surface-mineable area. The cumulative crude bitumen production for the three producers, starting from 1967, is $0.670 \times 10^9 \text{ m}^3$ (4.21 billion barrels). Considering that the total remaining mineable established reserves are $5.487 \times 10^9 \text{ m}^3$, the mineable established reserves under active development are substantial.

The total crude bitumen production in Alberta during 2007 was $76.6 \times 10^6 \text{ m}^3$, with $31.1 \times 10^6 \text{ m}^3$ coming from in situ operations and $45.5 \times 10^6 \text{ m}^3$ from surface mining. Surface mining accounted for ~ 59 % of total production in 2007 and in situ for ~ 41 %. The corresponding production values for 2008 are $33.9 \times 10^6 \text{ m}^3$ from in situ and $42.0 \times 10^6 \text{ m}^3$ from surface mining, where surface mining accounts for ~ 55 % of total production.

ERCB has determined the initial established reserves for in situ production. The cumulative production under active development within the in situ-designated areas presently totals $0.3501 \times 10^9 \text{ m}^3$, of which $0.2595 \times 10^9 \text{ m}^3$ is from the Cold Lake OSA, where major in situ activities take place (Table 1.5). The remaining active established reserves for in situ are estimated at $0.5607 \times 10^9 \text{ m}^3$, which accounts for only 2.6 % of the initial established reserves (ERCB 2009). Thermal recovery accounts for a major portion of the total in situ production.

A historical daily production of surface-mineable crude bitumen and synthetic crude oil within the Athabasca OSA for the 1967–2007 period is given in Figure 1.6. In 1967, the first integrated surface mining and bitumen upgrading operation was initiated with the establishment of Great Canadian Oil Sands (GCOS), the precursor to present-day Suncor. This was followed by Syncrude in 1978 and by Albian and the Scotford Upgrader in the Edmonton area in 2003. In 2009, CNRL started its integrated operation with the Horizon Project north of Fort McMurray.

The daily in situ crude bitumen production of the three OSAs is shown in Figure 1.7. The Cold Lake OSA was steady for the period 1997–2002, with increased production starting in 2002. Although the Cold Lake OSA is a major source of crude bitumen production, there has been a significant production increase within the Athabasca OSA since 2002 due to the development of thermal production through SAGD. The more recent in situ production increase in the Peace River OSA is mainly due to primary crude bitumen production in the Seal area (ERCB 2009).

⁷ As of January 2009, Shell Canada Energy became the operator of the Muskeg River Mine and the Jackpine Mine, located north of Fort McMurray. These operations, formerly known under the name “Albian Sands Energy” became “Shell Albian Sands.” Here, we will use the term “Albian” to indicate Shell Albian Sands. The Athabasca Oil Sands Project (AOSP) comprises both the above-mentioned mines and the Scotford Upgrader located outside of Edmonton. Production at AOSP began in 2003.

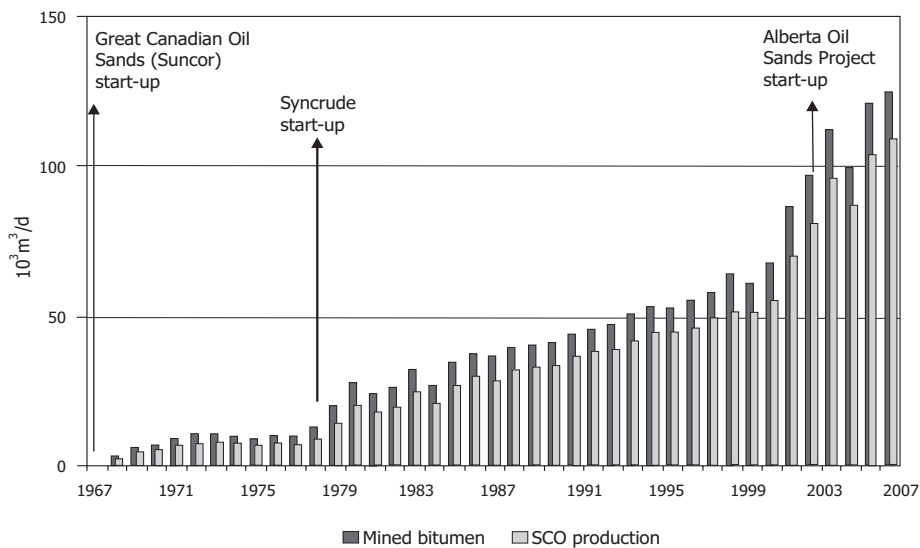


Figure 1.6 Mined crude bitumen and synthetic crude oil production in Alberta. Based on data from ERCB (2009).

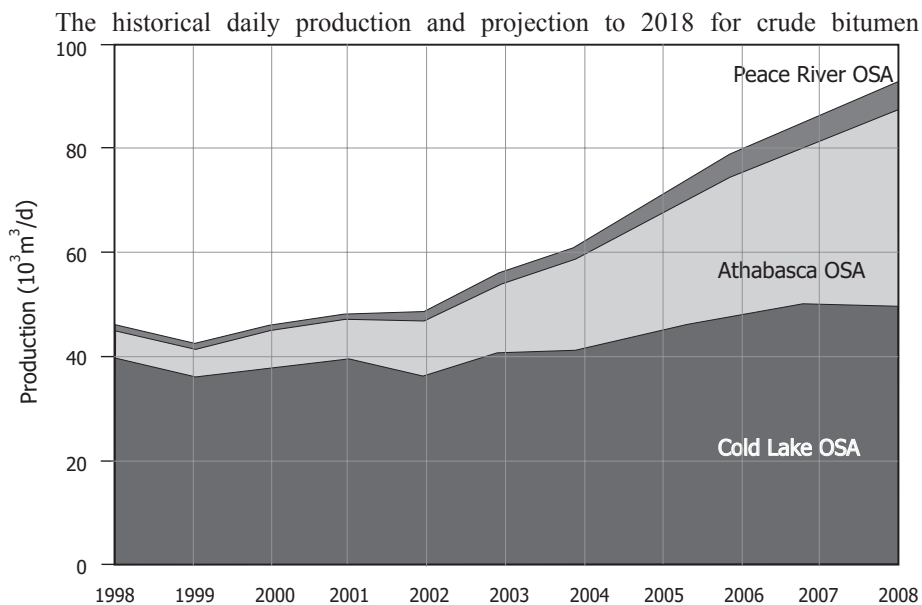


Figure 1.7 Crude bitumen production by oil sands area (OSA). Based on data from ERCB (2009).

production from surface mining and in situ are shown in Figure 1.8. In 2008, the daily in situ production was 92 900 m³/d, while daily surface mining production was 114 700 m³/d. By 2018, these figures are expected to increase to 221 000 m³/d and 249 000 m³/d, respectively, to a total equivalent of well over 3 million barrels per day (bbl/d) (ERCB 2009).

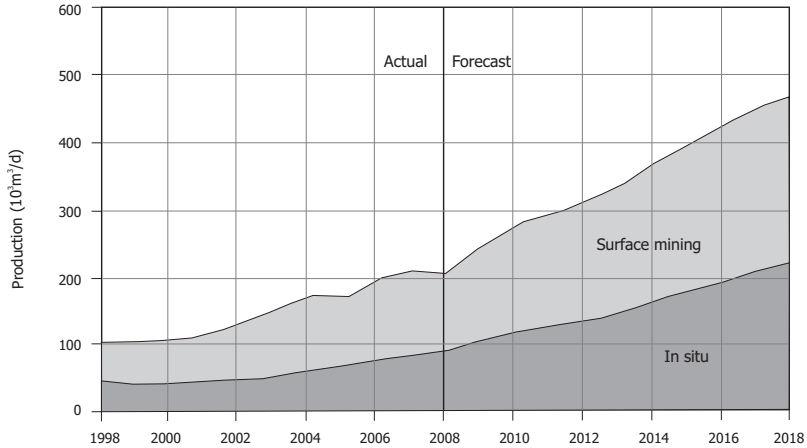


Figure 1.8 Alberta crude bitumen production from surface mining and in-situ.

Based on data from ERCB (2009).

Up to 2008, all of the surface-mined production and a small portion of in situ production in Alberta were upgraded to SCO. The average daily production of the Shell, Suncor, and Syncrude upgraders is given in Table 1.6. The three upgraders produce different varieties of refined products. Shell produces intermediate refinery feedstock for the Shell Scotford Refinery, as well as sweet and heavy SCO.

Table 1.6 Production of synthetic crude oil (SCO) in 2008

Based on data from ERCB (2009) and other oil sands annual and sustainability publications.

Producer	Annual production of SCO (10 ⁶ m ³ /y)	Daily production of SCO (m ³ /d)	Daily production of SCO (kbbbl/d)
Scotford Upgrader (Shell)	7.48	20 500	129
Suncor Energy Inc.	13.43	36 800	231
Syncrude Canada Ltd.	17.01	46 600	293
Total	37.92	103 900	653

Note: Data in the table above differ slightly from those given in other sources.

Suncor produces light sweet and light sour crudes and diesel fuel. In 2007, for example, Suncor produced 43 % light sweet crude oil, 11 % diesel, 43 % light sour crude oil, and ~ 3 % bitumen (Suncor 2007a). The Syncrude upgrader produces light sweet synthetic crude.

In 2008, the total daily SCO production was 103 900 m³/d, and ERCB expects it to increase to 245 000 m³/d by 2018 (2009). There was a decrease of ~ 5 % in 2008. The historical daily production of SCO is provided in Figure 1.9. It is clear that the daily synthetic crude oil production has been on a relatively steep slope of increase for both Suncor and Syncrude.

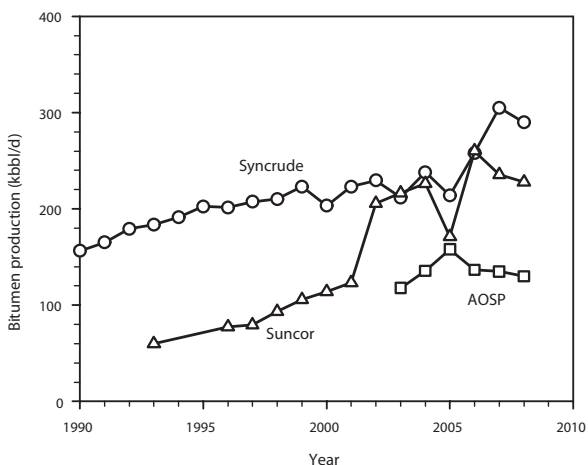


Figure 1.9 Historical production of synthetic crude oil in Alberta by the major bitumen producers.

Based on data from Shell, Syncrude, and Suncor annual and sustainability reports.

1.3 Bitumen Production From the Athabasca Oil Sands: Historical Background

In 1778, fur trader and founding member of the North West Company, Peter Pond, became the first European to examine the Athabasca oil sands. Ten years later, explorer Alexander Mackenzie wrote in his diary:

About twenty-four miles from the Fork are some bituminous fountains into which a pole of twenty feet long may be inserted without the least resistance. The bitumen is in a fluid state and when mixed with gum, or the resinous substance collected from the spruce fir, serves to gum the canoes. In its

heated state it emits a smell like that of sea coal. The banks of the river, which are there very elevated, discover veins of the same bitumenous quality (Mackenzie 1801, p. lxxxvii).

Positive assessments of the region's resource potential were presented in the early 1870s and 1880s by John Macoun and Robert Bell of the Geological Survey of Canada (Ferguson 1985), and again in 1889 by Charles Mair, a secretary for the Treaty 8 Métis Scrip Commission. Mair, chronicling his travels across the Treaty 8 area, echoed Mackenzie's observations:

In the neighbourhood of McMurray there are several tar-wells, so called, and there, if a hole is scraped in the bank, it slowly fills in with tar mingled with sand. This is separated by boiling, and is used, in its native state, for gumming canoes and boats. . . . Farther up are immense towering banks . . . everywhere streaked with oozing tar, and smelling like an old ship. . . . That this region is stored with a substance of great economic value is beyond all doubt, and, when the hour of development comes, it will, I believe, prove to be one of the wonders of northern Canada. We were deeply impressed by this scene of Nature's chemistry, and realized what a vast storehouse of not only hidden but exposed resources we possess in this enormous country (Mair 1908, p. 121).

According to Barry Glen Ferguson in his detailed historical overview of the oil sands, "in 1894, an initial \$7,000 was voted by Parliament for experimental drilling," which was carried out at three separate locations: Athabasca Landing, Pelican River, and Victoria Settlement. However, none of the three locations ultimately yielded the desirable result of "petroleum proper," and "after 1898, no further drilling work was carried out" (Ferguson 1985, p. 20–21). For the next decade, government and industry interest in the oil sands waned, with the exception of some speculative activity. As further explained by Ferguson,

Federal involvement recurred after 1912 in the context of British pressures on the Canadian government to devise a policy on oil exploration. In 1913, the federal government placed the oil sands region under a reserve, halting the speculative activity which had gone on in the previous half-dozen years. This policy decision occurred at a time when the Dominion was awakening to the importance of petroleum as a fuel (1985, p. 21–22).

In 1913, Sidney Ells, then a geologist working with the Mines Branch,

surveyed some 185 miles of river frontage and used a hand-auger to take two hundred core samples. . . . Ells argued that there was a resource of considerable extent which had great potential as a road-surfacing material; [and that] these asphalt reserves would constitute an immediately useful resource (Ferguson 1985, p. 23).

In 1921, the Scientific and Industrial Research Council of Alberta (SIRCA; presently Alberta Research Council, or ARC) was formed to assist the province in achieving economic development and growth. In the 1920s, under the auspices of SIRCA, Dr. Karl Clark (originally of Ontario) began conducting experimental work on the separation of bitumen from oil sands at the University of Alberta. Clark's background in mineral processing and physical chemistry was very much suited to research in bitumen separation. In 1924, together with Sidney Blair and David Pasternack, he constructed a bench-scale separation unit in the basement of the University of Alberta's Power Plant and developed a hot water flotation process to separate bitumen from sand. In 1924, they built a larger bitumen separation unit in northern Edmonton's Dunvegan railway yards, which was redesigned, dismantled, and rebuilt in 1929 on a field scale in Fort McMurray. In Clark's studies, hot water with caustic addition was used in bitumen flotation and separation. It was Clark's pioneering work that installed the scientific basis behind bitumen extraction and positioned Alberta's oil sands as a commercially viable future energy resource.

In the late 1960s, GCOS developed a surface mining operation comprised of three parts: an open-pit mine, a hot water extraction plant to recover bitumen from the oil sands, and an upgrading complex to upgrade the extracted bitumen to a light synthetic crude (Morgan 2001). The GCOS commercial operation was followed by Syncrude Canada's open-pit mine at Mildred Lake in the late 1970s. There have been many expansions at both Suncor and Syncrude since these initial operations.

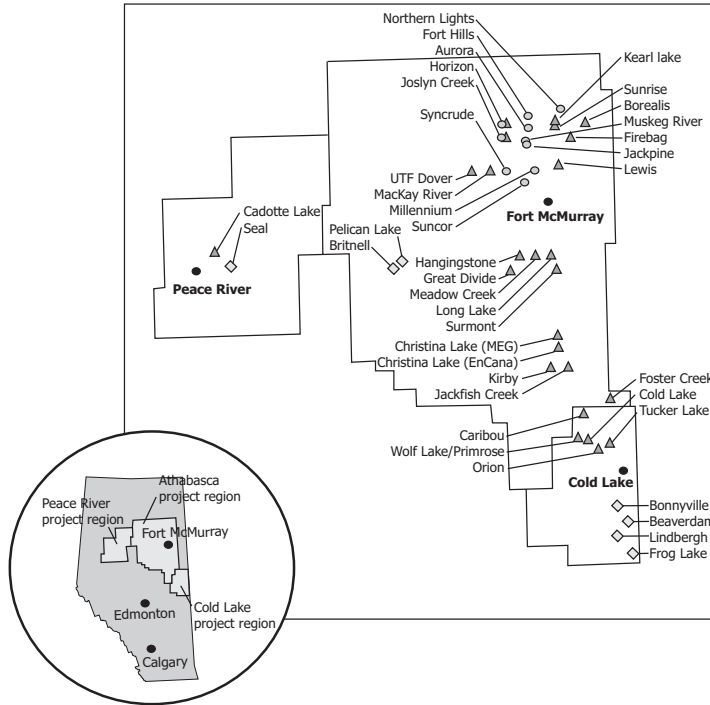
In early 2003, Albion Sands Energy Inc. (presently Shell Albion Sands) started its open-pit mining operation to recover bitumen from oil sands. All three commercial oil sands operations use hot or warm water processes to float and recover the bitumen, demonstrating the major role of Clark's initial studies in the development of commercial plants. In late 2008, CNRL began its Horizon Project operation.

Research into bitumen extraction from oil sands and the associated processing is ongoing at the Alberta Research Council, the federal government's CanmetENERGY (previously known as CANMET Energy Technology Centre), and more recently, the University of Alberta under the sponsorship of the Industrial Research Chairs of Natural Sciences and Engineering Research Council of Canada (NSERC) and various industrial partners.

In the 1960s, concurrent with the efforts devoted to developing open-pit commercial operations, the industry began to devote efforts to the deeper-buried oil sands ore deposits that could not be economically mined. The first commercially viable method of producing bitumen from the deeper formations was developed by Imperial Oil at its Cold Lake leases in the 1980s, using cyclic steam stimulation (CSS), also known as the 'huff and puff' technique. Imperial's cyclic steam commercial project proved to be the most successful large-scale Canadian application of in situ bitumen production. With the introduction of horizontal wells, a second generation of in situ technology evolved (Morgan 2001), and was adopted by many commercial operators, including Alberta Energy Company Ltd. (at Foster Creek) and Suncor (at Firebag) (Gray, Xu, and Masliyah 2009).

Initially, producing synthetic crude from mineable oil sands was very difficult and expensive. The commercial operations were stymied by high costs and little financial returns on investment. However, improvements in construction materials, materials

handling, and in situ production technology; the introduction of the truck-and-shovel method and hydrotransport pipelines to the mining operation; and a better understanding of the science of bitumen extraction and upgrading have all successfully reduced the high cost of bitumen recovery and upgrading to a level that is presently competitive on a global scale (Mathieson et al. 2001).



Legend

In Situ Projects Δ

- Orion
- Kirby
- Wolf Lake/Primrose
- Surmont
- Great Divide
- UTF (Dover)
- Jackfish Creek
- Borealis
- Christina Lake
- Foster Creek
- Caribou
- Sunrise
- Tucker Lake
- Cold Lake
- Hangingsone
- Christina Lake
- Long Lake
- Lewis
- Mackay River
- Meadow Creek
- Cadotte Lake
- Firebag
- Joslyn Creek

Operator

- Black Rock Ventures
- Canadian Natural Resources
- Canadian Natural Resources
- ConocoPhillips/Total
- Connacher Oil and Gas
- Devon Energy
- Devon Energy
- EnCana
- EnCana
- EnCana
- Husky Energy
- Husky Energy
- Husky Energy
- Imperial Oil
- Japan Canada Oil Sands (JACOBS)
- MEG
- OPTI/Nexen
- Petro-Canada
- Petro-Canada
- Petro-Canada/Nexen
- Shell Canada
- Suncor Energy
- Total E&P Canada

Mining Projects \circ

- Muskeg River
- Jackpine Mine
- Horizon*
- Kearl Lake
- Suncor Base Mine
- Millennium
- Syncrude Base Mine
- Aurora
- Northern Lights
- Fort Hills
- Joslyn Creek

Operator

- Albian Sands (Shell/Chevron/Western Oil Sands)
- Albian Sands (Shell/Chevron/Western Oil Sands)
- Canadian Natural Resources
- Imperial Oil
- Suncor Energy
- Suncor Energy
- Syncrude Joint Venture
- Syncrude Joint Venture
- Synenco
- Petro-Canada/UTS Energy/Teck Cominco
- Total E&P Canada

Major Primary Production Areas \diamond

- SEAL
- Pelican Lake
- Lindbergh
- Frog Lake
- Brintnell
- Bonnyville
- Beaverdam

* Includes plans for in situ and mining

Figure 1.10 Alberta oil sands regions and oil sands operators: mining and in situ operating, under construction, and planned.

Source: Adapted from NEB (2006). See also NEB (2008).

As we stated earlier, commercial bitumen production is achieved either through in situ production (for oil sands deposits normally buried more than 100 m)⁸ or open-pit mining (for shallower deposits). In practice, most in situ bitumen and heavy oil production normally comes from deposits buried more than 200 m, and most open-pit mining from deposits buried less than 75 m. Figure 1.10 shows the three oil sands regions in Alberta, together with the presently associated and future oil sands operators, for both mining and in situ operations. It should be noted that, at present, there is no proven commercial technology to recover bitumen from the intermediate depths between the surface-mineable and in situ zones.

Figure 1.11 depicts the leases held by Suncor, Syncrude, Shell Canada, CNRL, and others for their present and future oil sands operations.

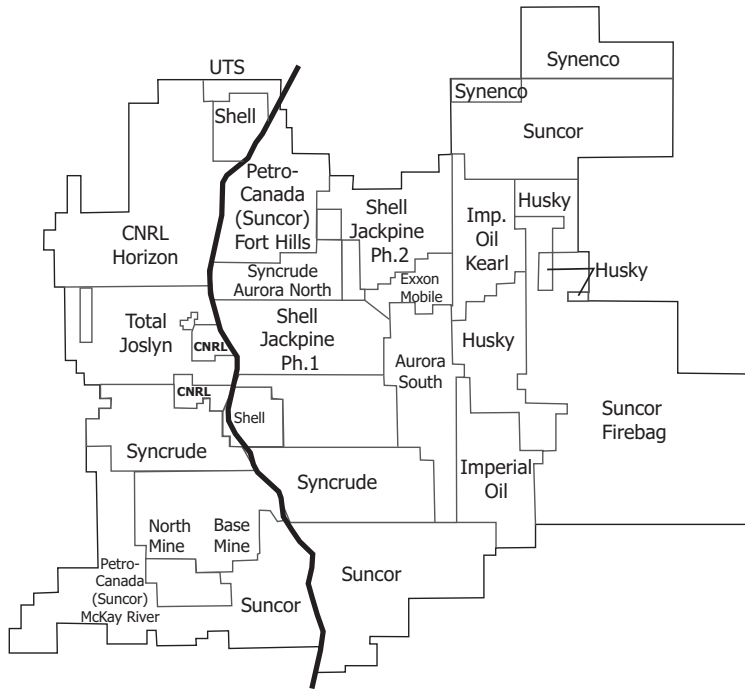


Figure 1.11 Oil sands leases, 2007.

Source: Canadian Oil Sands Trust website (2007).

Excellent historical background on the oil sands is given by Carrigy and Kramers (1973), Ferguson (1985), Sheppard (1989), the National Energy Board (2000, 2004, 2008), and the Alberta Chamber of Resources (2004). More on the social background of Fort McMurray and the history of oil sands development in the Athabasca area can be found in Huberman (2001).

8 ERCB's cutoff for in situ production is 75 m.

1.4 Driving Forces in Oil Sands Development

Growth in the world's oil demand indicates that there will be a market for more bitumen production. Before we can accommodate this increased production, there are significant challenges that must be overcome, stemming from a number of major factors that will influence the degree and pace of future oil sands development. These factors, illustrated in Figure 1.12, are outlined below.

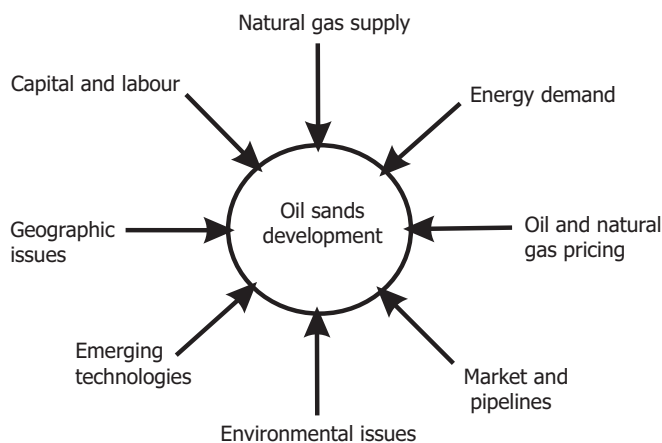


Figure 1.12 Driving forces in oil sands development.

Source: NEB (2004).

Natural Gas

This commodity is required for heating water in the extraction step (250 scf/bbl), for steam generation in SAGD (1100 scf/bbl; SOR = 2.5)⁹, and for the upgrading process (400 scf). By 2015, the overall gas intensity for both in situ and mining/upgrading combined will average 700 scf/bbl (NEB 2004).

Energy Demand

Investment incentive in oil sands projects decreases with lower energy demand.

Oil and Gas Pricing

The effect of natural gas price is very acute for in situ production using classical SAGD operation. According to NEB, “gas costs can comprise up to 50 percent or more of the total costs in thermal in situ project . . . companies are developing new technologies designed to reduce or eliminate the need for natural gas in oil sands operations.” NEB further cites the “bitumen gasification process in the proposed Nexen/OPTI Long Lake project and fuel switching capabilities at Suncor’s Firebag project” as fine examples of natural gas–reduced usage (2004, p. xiv).

9 SOR: Steam-to-oil ratio.

Market and Pipelines

Produced bitumen needs to be transported to markets via pipelines. Their availability is very important, as otherwise, diluted crude bitumen and synthetic crude oil cannot reach markets south of Fort McMurray and Edmonton or the rest of Canada and the midwestern United States.

Managing Environmental Issues

Water use and carbon dioxide emissions are major issues in oil sands sustainability. Public concerns related to river water withdrawal, ever-increasing volumes of tailings pond water and mature fine tailings, and Kyoto targets are in the forefront of future developments of oil sands.

Technology Innovation

Innovations tend to improve bitumen recovery, reduce production costs, and reduce water use and emissions.

Geographic Issues

Green (new) fields are now further away from Fort McMurray. Transportation and accommodation have become an issue for those in construction camps and personnel working on site.

Rising Capital and Labour Costs

With the great demand for steel and concrete, building commodities are less available. With spikes in the economy and with simultaneous ongoing projects, there is a shortage of skilled labour, operators, and engineers.

Another vital contributing factor that is not shown in Figure 1.12 is the *people* component—workers who have devoted tremendous energy and team effort to the design, construction, and operation of the oil sands plants and who have led to the success of recovering this resource. They have the potential to significantly affect the degree and pace of future oil sands development.

Costs of crude bitumen production and upgrading are a major variable in the oil sands industry. In 2004, Syncrude reported a total operating cost of \$18.61/bbl of Syncrude Sweet Blend (SSB). The overburden removal was \$2.10/bbl for mining, \$10.51/bbl for extraction and upgrading, \$0.71/bbl for catalyst cost, \$4.24/bbl for energy purchase, and \$1.05/bbl for administrative and research costs. Syncrude's 2007 operating costs were \$25.26/bbl (that is, the costs associated with the mining of oil sands ore, extraction and upgrading of the bitumen into Syncrude Sweet Blend, maintenance of facilities, administration costs, start-up costs, research, and purchased energy) (Syncrude 2004, 2007). This cost number jumped to \$35.26/bbl in 2008 due to operational upset, higher volumes of overburden removal, and higher natural gas prices and consumption (Canadian Oil Sands Trust 2008, p. 8). Similarly, at Suncor,

the total operating costs for SCO production from mining operations jumped from \$26.15 in 2006 to \$34.15 in 2007 and \$45.85 in 2008 (Suncor Energy Inc. 2006, 2007b, 2008).¹⁰

1.5 Bitumen Extraction and Upgrading Schemes

1.5.1 Extraction

A typical bitumen extraction scheme is shown in Figure 1.13. Oil sands are mined and crushed (a). Water and additives are added into the slurry preparation equipment to reduce the size of the crushed oil sands lumps using rotary breakers, cyclofeeders, or mixing boxes with vibration screens (b). The slurry, which contains oil sands lumps of a suitably reduced size, is fed into hydrotransport pipelines along with its associated liberated bitumen and solids (c), whereby further reduction of lump size takes place and the bitumen becomes fully liberated from the sand grains. In the hydrotransport pipeline, the liberated bitumen droplets attach to air bubbles that were entrained during the slurry preparation step. The slurry at the exit of the hydrotransport pipeline is diluted with water and fed into gravity separation vessels within the extraction plant (d). Flotation cells are used to recover bitumen from the middlings stream of the gravity separation vessels. The aerated bitumen froth rises to the top of the separation vessel to form a bitumen froth that, on average, contains 60 wt. % bitumen, 30 wt. % water, and 10 wt. % solids. The solids in the bitumen froth have a much smaller particle distribution than the vessel's feed stream, and most of the entrained water in the bitumen froth is in a free form. The bitumen froth is first deaerated and fed to the bitumen froth treatment plant (e) to remove its solids and water. In the froth treatment plant, solvents are used to reduce the bitumen viscosity and density in order to facilitate solids and water removal.

The operations that take place between steps (a) and (d) are, to a large extent, fairly standard among the various oil sands operators. In the bitumen froth treatment operation, there are two main variants. *Naphthenic froth treatment* involves the addition of naphtha as the diluent (solvent) of choice. The diluent reduces the viscosity and density of the bitumen, thereby enhancing the separation of the solids and emulsified water from the diluted bitumen. In this approach, asphaltenes, which are a constituent of bitumen, do not precipitate. Inclined plates settlers, hydrocyclones, and centrifuges are employed for the solids and water separation. Naphthenic froth treatment is employed by Suncor, Syncrude and CNRL, and leaves ~ 1.5 wt. % to 2.5 wt. % water and ~ 0.4 wt. % to 0.8 wt. % solids in the diluted bitumen product. *Paraffinic froth treatment* involves the addition of a paraffinic diluent (solvent) for bitumen viscosity and density reduction. With the addition of an appropriate amount of diluent, about 1/3 to 1/2 of the asphaltenes is precipitated. The precipitated asphaltenes act as a

10 The figures quoted are in Canadian dollars.

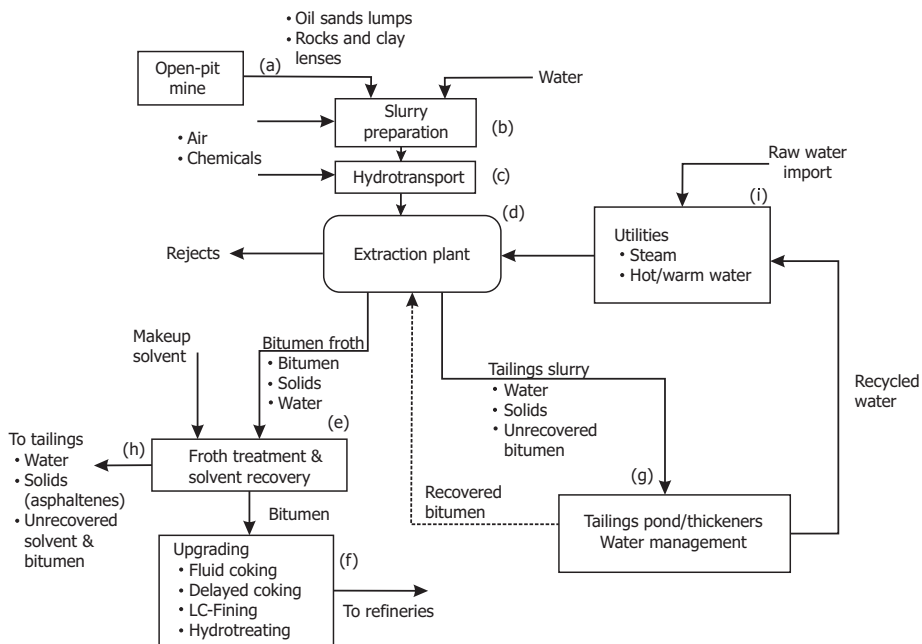


Figure 1.13 Schematic of bitumen production for surface mining.

collector for the fine solids and emulsified water in the diluted bitumen. The resulting diluted bitumen product contains ~ 500 ppmw to 800 ppmw solids and ~ 100 ppmw to 300 ppmw water. Settling vessels are employed in the paraffinic froth treatment process. Initially, at Albion, where this process is employed, bitumen froth treatment was carried out at ~ 35 °C to avoid boiling of the diluent, as C₅ and C₆ alkanes are used. However, recent improvements have introduced operations at 70 °C to 90 °C where pressure vessels are employed. Future paraffinic froth treatment will utilize the higher-temperature approach.

In both naphthenic and paraffinic bitumen froth treatment, the diluent is removed prior to bitumen upgrading (f). On average, two tonnes of oil sands are required to produce one upgraded barrel of bitumen.

The upgrading of crude bitumen is dependent on the state of the bitumen, whether it is whole bitumen or deasphalted. Cokers (delayed or fluid cokers) with coke rejection are employed for whole bitumen upgrading, whereas LC-Fining is normally employed for deasphalted bitumen upgrading.

Within the extraction plant, the tailings slurry from the gravity separation vessels and secondary flotation cells is treated in thickeners or simply diverted to tailings ponds (g). When thickeners are employed, warm recycle water can be made available, and a thickened tailings paste is produced from the thickeners that is either disposed of in specially dedicated tailings ponds or mixed with the coarse solids of the extraction tailings within the same pond. In the absence of thickeners, the tailings are introduced

to the tailings pond. Upon settling of the coarse solids and some of the fine solids, water from the tailings ponds is recycled and used in the bitumen extraction process. Over several years, the fine solids and clays consolidate in the tailings ponds to create a sludge, known as *mature fine tailings* (MFT), which has a solids concentration of ~ 30 wt. %.

The rejected solids and water, fugitive bitumen and solvent, and any precipitated asphaltenes from the bitumen froth treatment plant are led to a tailings pond for disposal (h). Steam and hot water are produced in the utilities plant (i).

1.5.2 Upgrading

As we pointed out earlier, crude bitumen must be upgraded to a product that can be fractionated in a refinery. Prior to upgrading, the crude bitumen is a viscous, hydrogen-deficient hydrocarbon with high levels of sulphur and heavy metals. During the upgrading process, it is transformed into a high-quality upgraded crude oil (i.e., synthetic crude oil, or SCO) that has density and viscosity characteristics quite similar to those of conventional light sweet crude oil, but with a very low sulphur content of 0.1 % to 0.2 % (NEB 2004).

Figure 1.14 shows an upgrading scheme that uses delayed coking technology suitable for naphthenic froth treatment, where no asphaltenes rejection takes place.

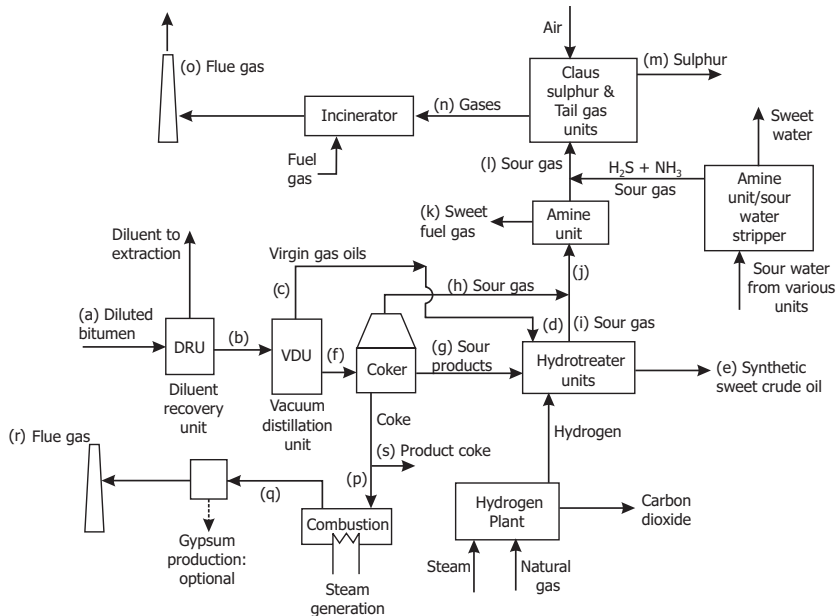


Figure 1.14 Schematic of bitumen upgrading using coking technology.

The diluted bitumen (a), which contains naphtha diluent from the bitumen froth treatment plant, is fed into the diluent recovery unit (DRU) to remove the diluent (naphtha) for reuse in the froth bitumen treatment plant. The bitumen is heated and subsequently fed to a vacuum distillation unit (VDU) (b), where some of the lighter end products are removed (c). This light end product stream can be fed into the hydrotreater units (d) or simply mixed with the final finished hydrocarbon oil product (e). The bottoms of the VDU are heated and fed to delayed cokers (f). During the coking process, the large bitumen molecules are thermally cracked. This leads to the formation of a coke product that is ultimately rejected. The coke product has a slightly higher carbon content than the crude bitumen; however, it has a higher sulphur and heavy metals content. A sour liquid distillate stream (g) is produced from the cokers. The sour liquid distillate is forwarded to hydrotreater units, where hydrogen is added. Within the hydrotreater units, the hydrogen reacts with the hydrocarbon vapours at high pressures and temperatures in the presence of a catalyst, thereby eliminating the heteroatoms (i.e., sulphur, nitrogen, and oxygen) from the coker's sour liquid products and increasing the hydrogen-to-carbon ratio of the hydrocarbon inlet stream. A synthetic crude oil is produced (e).

During the coking (h) and hydrotreating (i) processes, a sour gas containing hydrogen sulphide (H_2S) and some ammonia (NH_3) is produced (j) and treated in amine units to produce sweet fuel gas (k) and sour gas (l) streams. The latter stream, together with sour gas from the amine sour water stripper, is treated in Claus sulphur and tail gas units, where elementary sulphur blocks (m) are produced. The remaining H_2S in the gases (n), upon leaving the tail gas units, are incinerated to produce sulphur dioxide that is vented to the atmosphere (o).

Using the Claus sulphur and tail gas units, one can expect to capture more than 99 % of the hydrogen sulphide in the sour gases. In the case of the delayed coker (as used by Suncor), part of the rejected coke (p) is used as a fuel to produce steam and other heat requirements in the extraction plant. The sulphur dioxide in the generated flue gases (q) produces the calcium sulphate (gypsum) that is needed in the consolidated tailings (CT) process for the treatment of mature fines tailings contained in the tailings ponds. The sulphur dioxide in the flue gas (r) accounts for most of SO_2 emissions. The excess coke (s) is stockpiled or sold for use in ammonia plants or in other thermal applications. The delayed coker process is a batch operation, where the coker drum is emptied once it is filled with coke.

To process bitumen in fluid coker units (as practiced at Syncrude using fluid cokers), the coke is circulated between the coker drum and the burner, where it is burned. The liberated thermal energy is used for steam production, thereby integrating with the extraction plant, where hot water and steam are required. Excess coke is rejected and stockpiled. The fluid coker operation is continuous. However, the coker drum needs to be emptied on a regular basis. The flue gases from the fluid coker units, if not treated while being vented to the atmosphere, would carry large amounts of sulphur dioxide. Traditionally, the flue gases are treated with ammonia, where ammonium sulphate salt is produced and used as fertilizer. Sulphur dioxide in the untreated flue gases from the fluid coker units accounts for the majority of SO_2 emission at Syncrude.

The hydrogen gas needed in the hydrotreater units is obtained from natural gas using stream reforming. Several operators are considering coke and asphaltenes gasification to produce the required hydrogen.

For the purposes of gaining some appreciation of the SCO yield and sulphur balance, Figure 1.15 shows the Sturgeon Upgrader, an upgrading scheme using delayed cokers proposed prior to Suncor's acquisition of Petro-Canada (Petro-Canada Inc., UTS Energy Corporation, and Teck Cominco Ltd. 2007). Naphtha-diluted bitumen was to be pipelined from the Fort Hills project near Fort McMurray, where the extraction plant is located, to the Edmonton-area upgrader. Let us consider the hydrocarbon balance in this proposed design. We assume a processing capacity of 165 000 bbl/d, equivalent to a daily bitumen rate of 26 232 m³/d or 26 626 t/d, where the bitumen specific gravity is taken as 1.015 10³ kg/m³. The produced coke is 5465 t/d. This is equivalent to a coke rejection of 20.5 wt. % of the original crude bitumen. Due to the upgrading process, where hydrogen is added, the synthetic crude oil is 18 407 t/d or 22 272 m³/d. This corresponds to a volume yield of 84.9 %, typical of a coker yield obtained through hydrotreating.

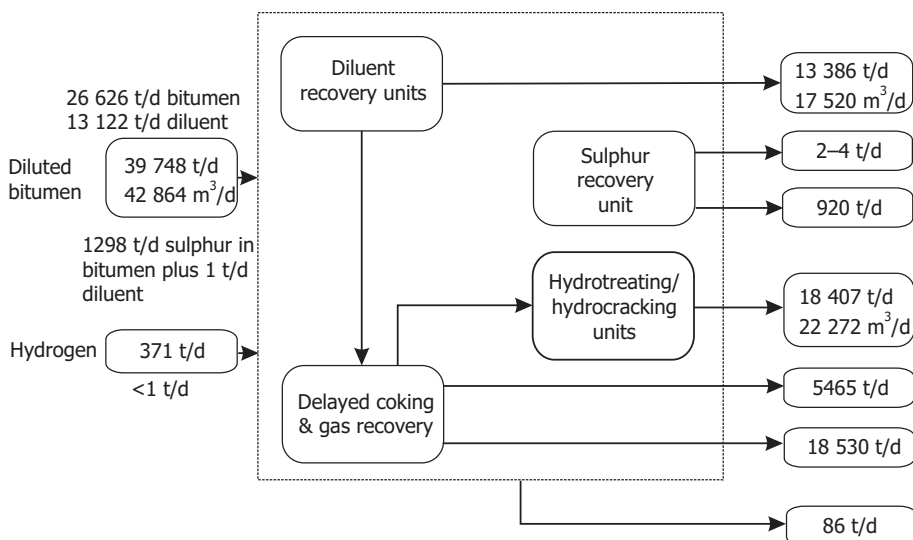


Figure 1.15 Schematic of bitumen upgrading at proposed Sturgeon Upgrader.

Source: Petro-Canada Inc., UTS Energy Corporation, and Teck Cominco Ltd. (2007).

For the sulphur balance, the sulphur in the bitumen is 1298 t/d, which constitutes 4.875 wt. % sulphur in the crude bitumen stream. The coke's sulphur rate is assumed to be 369 t/d, leading to 6.752 wt. % sulphur in the rejected coke. The two sulphur weight percent values would indicate a higher sulphur concentration in the coke stream, where the increase in the sulphur coke concentration is expected from a coker unit. The sulphur recovery unit and its associated other recovery units recover the bulk of the sulphur from the crude bitumen. According to the process flow sheet (Figure 1.15), sulphur emission is expected to be 2 t/d to 4 t/d, which would correspond to 4 t/d to 8 t/d of SO₂. The upper value gives an emission of 0.057 kg of SO₂ per barrel of SCO. In comparing existing SO₂ emission values from Suncor, we note that the suggested SO₂ emission is quite low and can likely be achieved using very efficient sulphur recovery processes and very aggressive flue gas desulphurization.

The processing stage in which bitumen is thermally cracked (as in a coker unit) is referred to as *primary upgrading*. The processing stage in which sulphur and nitrogen are removed using hydrogen in the presence of a catalyst, and under high pressure and temperature, is referred to as *secondary upgrading*.

In operations where partial deasphalting of crude bitumen takes place during bitumen froth treatment, a coke rejection-type operation would not necessarily be advantageous, as most of the larger molecules in the bitumen are excluded in the deasphalting operation. When the bitumen feed is partially deasphalted during bitumen froth treatment (with ~ 9 wt. % rejection or 50 % of C₅ asphaltenes), it is possible to use hydroprocessing in place of delayed or fluid cokers; this is the case at the Athabasca Oil Sands Project (AOSP), comprised of the Muskeg River Mine, Jackpine Mine, and the Scotford Upgrader. The latter, which processes Shell Albion's partially deasphalted bitumen, is based on the ebullated bed LC-Fining process. In this case, there is no coke produced, although there is a small hydroprocessing bottoms (residue) stream at the refining stage that requires further processing. By using this hydrogen-addition technology, not accounting for asphaltenes rejection in the bitumen extraction step, the upgrading scheme would achieve close to 100 % volume yield. Compared to coke rejection processes, there are less SO₂ and CO₂ emissions, as there is no coke combustion.

Figure 1.16 is a simplified flow sheet of the Scotford Upgrader process. Atmospheric distillation is used to remove the low boiling point diluent (C₄-C₅) from the partially deasphalted bitumen, followed by vacuum distillation to remove the light-end hydrocarbons from the bitumen. Sulphur recovery units are employed to reject sulphur. Hydrogen is produced in a similar approach as mentioned above. The liquid products from the hydrotreater units are further processed at Shell's Scotford Refinery.

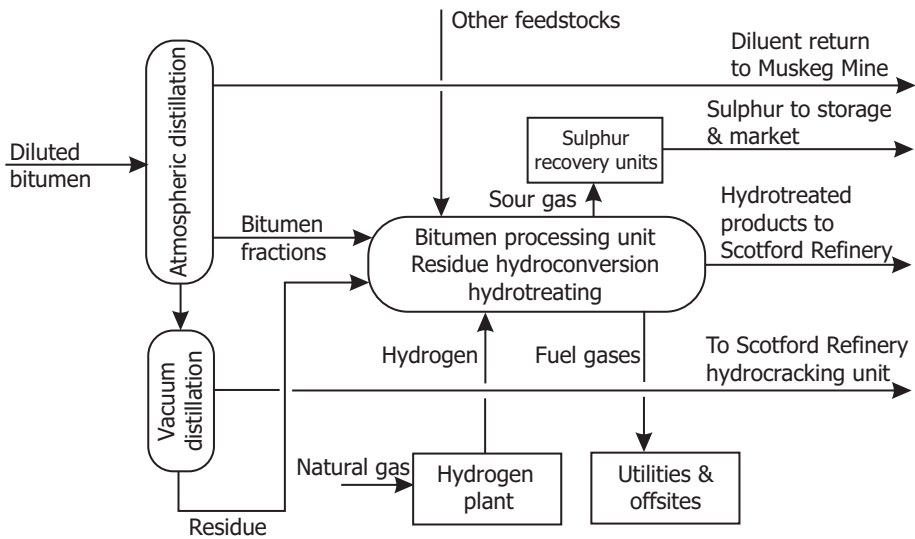


Figure 1.16 Schematic of Scotford Upgrader.

Source: Shell Canada Ltd. (2005).

1.5.3 Sulphur and Sulphur Dioxide Production

ERCB estimates that in 2008, the elemental sulphur produced due to crude bitumen upgrading was 1.4×10^9 kg, and that $\sim 222.4 \times 10^9$ kg of elemental sulphur will be recoverable from the 5.49×10^9 m³ of remaining established crude bitumen reserves in the surface-mineable OSAs (2009, p. 7-2). This estimate assumes current and expected use of high-conversion, hydrogen-addition upgrading technologies. If in situ-produced crude bitumen were upgraded in Alberta, a higher elemental sulphur reserve would be expected. In the period 1967–2008, a total of 21.2×10^9 kg of elemental sulphur has been produced from oil sands mining operators (2009, p. 7-4). It should be noted that although elemental sulphur production due to crude bitumen upgrading is quite large, it represents about one third of that produced from natural gas due to hydrogen sulphide removal.

Sulphur dioxide (SO₂) is formed mainly during the burning of coke produced either in delayed coker units (as is the case at Suncor) or in fluid coker units (as is the case at Syncrude). Sulphur dioxide is present in the flue gases of the gas stacks. Emissions of SO₂ gas in combination with water result in acid rain that leads to acidification of soils and water bodies. In recent years, the topsoil around the Fort McMurray area has shown lower pH values than it showed ten years ago. Emissions of sulphur compounds and hydrocarbons can also contribute to smog and affect local air quality (Government of Alberta 2006).

Figure 1.17 gives the historical sulphur dioxide (SO₂) intensity for the AOSP, Suncor, and Syncrude operations. The intensity is based on the emission mass per one barrel of synthetic crude oil. The lower SO₂ emission intensity at Suncor is due to flue gas desulphurization (FGD), which produces calcium sulphate (gypsum) for use in tailings pond remediation. In 2006, Syncrude initiated FGD to eliminate nearly all sulphur dioxide emissions from one of the newer fluid cokers. Ammonia is used for that purpose to produce ammonium sulphate that can be used as a fertilizer. The FGD unit (which became fully operational in 2009) was necessary, as increased bitumen production would not be permitted if the associated SO₂ emissions surpassed the total allowable value of 250 t/d (91.3 kt/y). In 2004, SO₂ emissions were close to the maximum yearly allowable value.

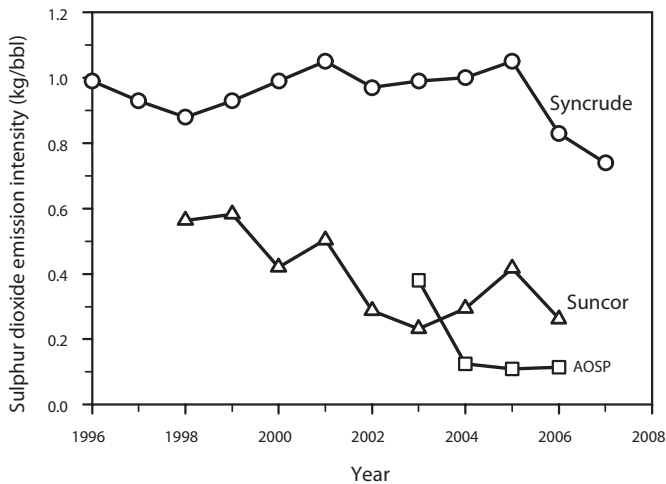


Figure 1.17 Sulphur dioxide emission intensity for AOSP, Suncor, and Syncrude operations.

Based on data from Shell, Syncrude, and Suncor annual and sustainability reports.

As can be noted from Figure 1.17, SO₂ emission intensity for the years 2004–2006 was much lower at AOSP than at the other two operations—a result of intensive sulphur dioxide capture in the flue gases. The higher level of emissions for AOSP in 2003 reflects start-up operations at the Scotford Upgrader.

Figure 1.18 shows the historical total sulphur dioxide emissions at AOSP, Suncor, and Syncrude. Although there has been a slight decline in SO₂ intensity over the last decade, the total SO₂ emission has steadily increased with time due to increased synthetic crude oil production. It should be noted that all oil sands operators work within the upper limit of emission allowances given by the appropriate government agencies.

For the period of 2002–2007, nitrogen oxides emission intensities were ~ 0.18 and ~ 0.24 kg NO_x/bbl at Suncor and Syncrude, respectively.

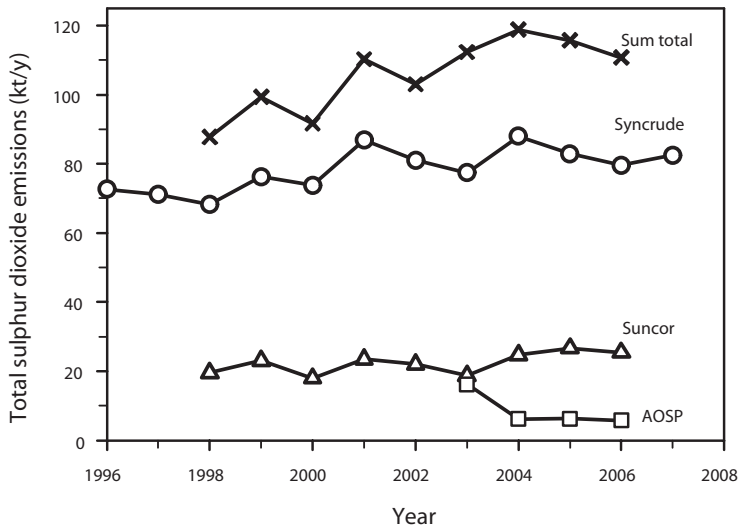


Figure 1.18 Sulphur dioxide annual emission oil sands operations at AOSP, Suncor, and Syncrude.

Based on data from Shell, Syncrude, and Suncor annual and sustainability reports.

1.5.4 Greenhouse Gases (GHGs) and Energy Intensity

With new emission regulations and growing concern over global warming, it has become increasingly important to reduce greenhouse gas (GHG) emissions, including carbon dioxide and methane (denoted by *equivalent carbon dioxide*, or CO₂e). Carbon dioxide emission intensities are shown in Figure 1.19. Current data from AOSP, Syncrude, and Suncor show a steady reduction in CO₂e per barrel of bitumen produced (Shell 2006; Syncrude 2007; Suncor 2007a). Currently, ~ 130 kg of CO₂e is produced for each barrel of sweet synthetic blend (SSB), based on Syncrude data. The emission intensity is slightly lower for Suncor. Yearly CO₂e emissions at AOSP operations between 2004 and 2006 were much lower than those at Syncrude and Suncor. This is partially due to the use of thickeners in warm water recycling at the extraction plant. It is worth noting here that a 0.4 kg/bbl to 0.5 kg/bbl reduction in CO₂e emissions is achieved for every degree Celsius where no natural gas is used for heating the process water. The CO₂e reduction is also reflected in the type of upgrading process employed at the Scotford Upgrader. The high AOSP 2003 CO₂e emissions seen in Figure 1.19 reflect start-up operations. The reader is urged to exercise prudence in comparing the various operators, as the final SCO quality is not the same.

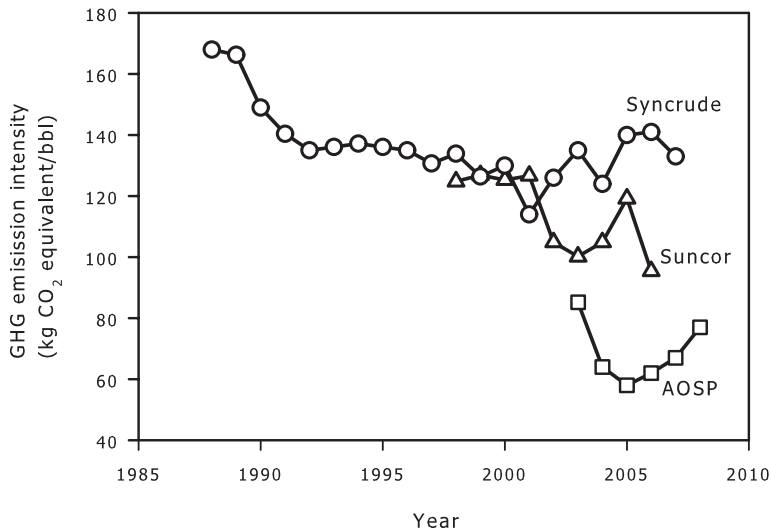


Figure 1.19 Carbon dioxide equivalent emission intensity for AOSP, Suncor, and Syncrude operations.

Based on data from Shell, Syncrude, and Suncor annual and sustainability reports.

Note: For Suncor, as of 2004, the data include in situ operations at Firebag. Suncor GHG emissions are evaluated using American Petroleum Institute methodology, with adjustments made to account for the uniqueness of oil sands (Suncor 2007a). For Syncrude, CO₂e emissions include combustion of clear diesel and gasoline, biomass combustion, aerobic decomposition, and industrial processes. As of 2007, Syncrude has revised and improved their CO₂e reporting (Syncrude 2007). Data from prior to 2001 have been adjusted by a multiplier of 1.08 using data from Syncrude sustainability reports from prior to 2007.

Although there has been a steady reduction of mass of CO₂e produced per unit volume of upgraded bitumen, with increased crude bitumen production, the amount of CO₂e emitted into the atmosphere is climbing, as indicated by Figure 1.20. It should be noted that Syncrude produces a higher-grade synthetic crude oil than Suncor; while Suncor produces light sweet, light sour, and diesel synthetic crudes. For this reason, rather than comparing CO₂e production between the two producers, it is more appropriate to concentrate on the historical trends in CO₂e intensity and on the total production for each.

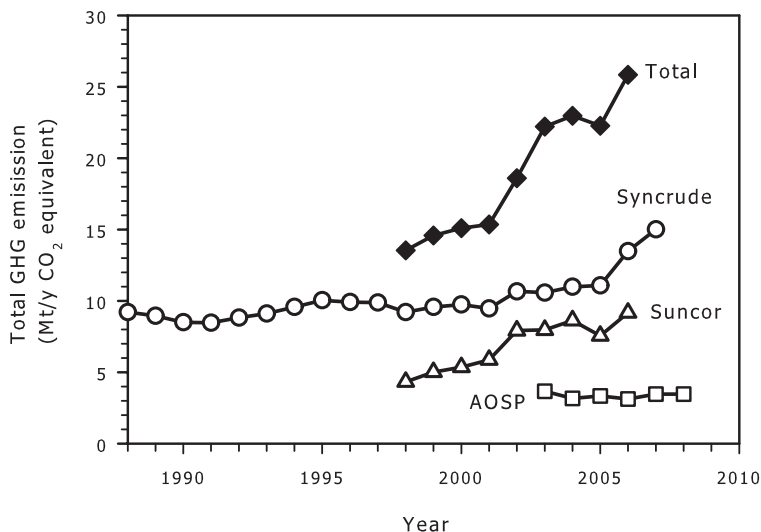


Figure 1.20 Total carbon dioxide equivalent emission for AOSP, Suncor, and Syncrude operations.

Based on data from Shell, Syncrude, and Suncor annual and sustainability reports.

The energy intensity required to produce upgraded bitumen at AOSP, Suncor, and Syncrude is shown in Figure 1.21. The Suncor and Syncrude operations require an energy intensity of ~ 1.3 GJ/bbl, which can be obtained from just over 0.22 bbl of upgraded bitumen. This translates to ~ 78 % energy gain through the production of one barrel of upgraded bitumen. The energy gain for the AOSP operation is close to 85 %.

Let us define ‘percent energy input’ as the percentage of thermal energy required to produce one barrel of upgraded bitumen to the thermal energy contained in one barrel of upgraded bitumen. In these terms, the average energy input is ~ 22 % for Suncor and Syncrude and 15 % for AOSP. Figure 1.22 shows the variation of carbon dioxide equivalent intensity emission (kg CO₂e/bbl SCO) with percent energy input. There is a clear correlation between CO₂e emission and percent energy input. In other words, higher bitumen production efficiency would translate to lower CO₂e emissions.

There is much discussion related to greenhouse gas emissions resulting from the production of crude bitumen and its upgrading to synthetic crude oil and refining to transportation fuel. In order to determine the carbon emission intensity of a fossil fuel, it becomes essential to conduct a life cycle analysis (LCA) that incorporates, among other things, crude production, upgrading, refining, transportation, blending, storage, and dispensing. This is termed a *well-to-tank* (WTT) LCA, and it includes the collective carbon imprint needed to produce a liquid product suitable as a transportation fuel. To

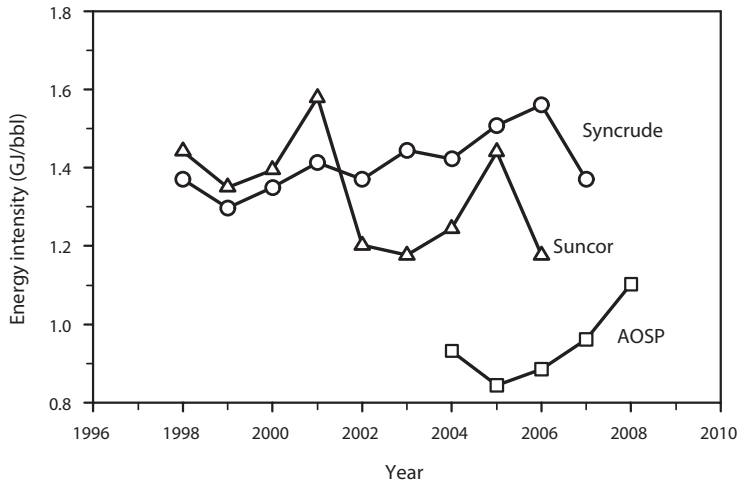


Figure 1.21 Energy intensity to produce upgraded bitumen for AOSP, Suncor, and Syncrude operations.

Based on data from Shell, Syncrude, and Suncor annual and sustainability reports.

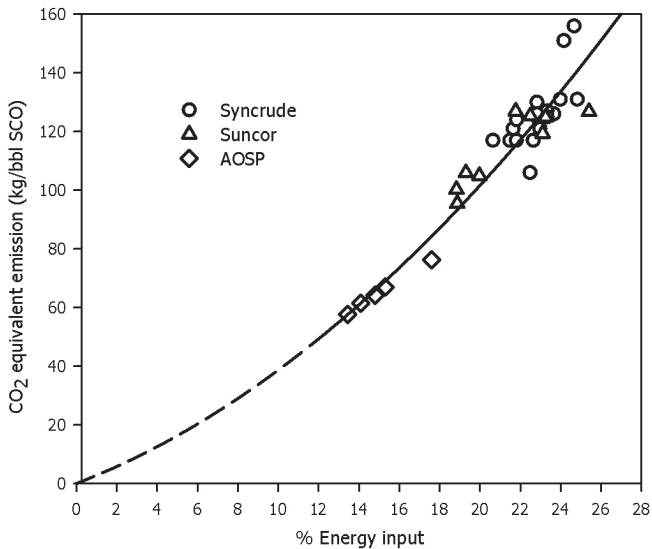


Figure 1.22 Relationship between equivalent carbon dioxide emission and percent energy input for Syncrude, Suncor, and AOSP operations.

complete the analysis, one should also include carbon emissions resulting from the use of the fuel, say, in an internal combustion engine, i.e., *tank-to-wheels* (TTW). A complete life cycle analysis, *well-to-wheels* (WTW), would include both WTT and TTW, that is, greenhouse gas emissions from the production stage through to the vehicle tailpipe. Here, $WTW = WTT + TTW$.

Results from the California Air Resources Board (2009) for ultra-low sulphur diesel (ULSD) for average crude refined in California showed that WTW is about 94.7 CO₂e/MJ of refined product. About 80 % of the CO₂e emissions is from fuel consumption in vehicles (TTW), and only 20 % of the emissions results from crude production and refining (WTT).

Through the Alberta Energy Research Institute (AERI), two well-to-wheels life cycle studies for direct emissions were conducted to establish the impact of crudes processed in US refineries (TiAx LLC and MathPro Inc. 2009; Jacobs Consultancy Life Cycle Associates 2009).

Figure 1.23 shows the WTW life cycle emissions for different crudes and modes of production (Jacobs Consultancy Life Cycle Associates 2009). The data are given in CO₂e g/MJ of gasoline. For identical vehicles, the GHG emission intensities are the same in terms of CO₂e emission per kilometre. The crudes are placed into three categories: conventional, thermal, and mining. In the conventional crudes category, six crudes were considered. In the thermal category, one California thermal-enhanced oil recovery crude was considered, together with four bitumen crudes obtained from SAGD operations. Two different scenarios were considered for bitumen crude from mining operations. The WTW CO₂e emission intensity for the conventional crude ranged from ~ 98 CO₂e g/MJ to 106 CO₂e g/MJ. The WTW for the case of refined fuel obtained from crudes via thermal operations showed the highest CO₂e intensity. The higher level of CO₂e emission for thermal (in situ) operations is due to the energy required to heat the underground formation in order to recover the bitumen or heavy oil. For the case of California heavy oil, the WTW emission intensity is about 114 CO₂e/MJ compared to about 119 CO₂e/MJ for SAGD SCO–eb. bed (a case that is not commercially favoured) and 106 CO₂e/MJ for SAGD dilbit. The WTW CO₂e emission intensities for refined fuel derived from crude bitumen obtained from mining operations were approximately 105 CO₂e g/MJ to 108 CO₂e g/MJ. Comparing the WTW emission intensities for conventional crudes for cases covered by the Jacobs Consultancy study with crude bitumen from mining operations, the emissions for refined fuel derived from oil sands mining operations are about 5 % higher. The results from the TIAX LLC study are similar to those in the Jacobs Consultancy study for the commonly considered crudes.

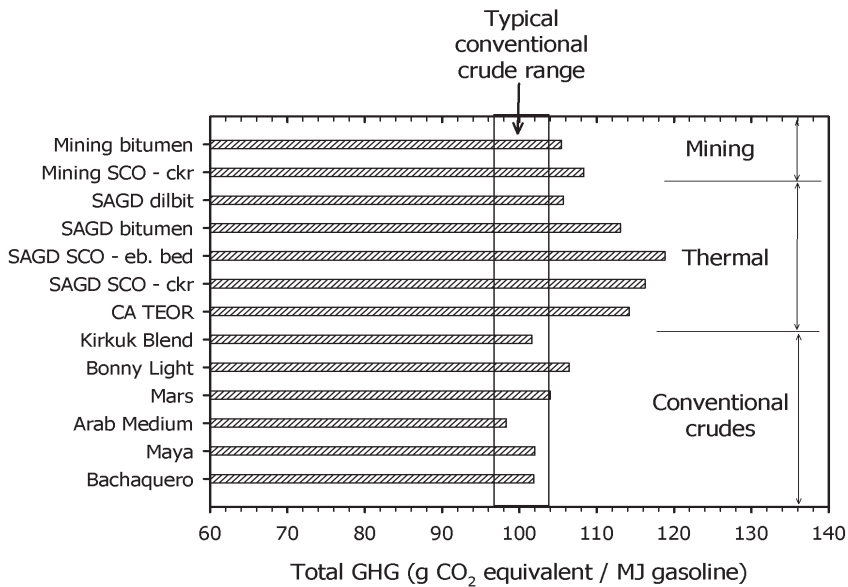


Figure 1.23 Life cycle emission intensity represented for well-to-wheels (WTW). See below the key aspects of the crudes that were evaluated in the study and the legend for the various crudes.

Source: Jacobs Consultancy Life Cycle Associates (2009).

Legend:

Mining bitumen: Bitumen produced in Alberta by surface mining. The bitumen is shipped to a PADD2* refinery as dilbit**. The diluent is returned. This example is not extensively practiced because of the high sediment, chloride, and water content of mined bitumen. However, with technological improvement, this practice may become more prevalent in the future.

Mining SCO–ckr: Bitumen produced by surface mining is upgraded to SCO in a delayed coking–based upgrader, shipped to a PADD2 refinery, and converted primarily to gasoline and diesel fuel.

SAGD SCO–ckr: Bitumen produced in Alberta with a 3 SOR (steam-to-oil ratio), upgraded in delayed coking based upgrader to produce primarily gasoline and diesel fuel. Bitumen in this study has 8.4 API and 4.8 wt% sulphur.

SAGD SCO–eb. bed: Similar to the prior case, except that the SCO is produced in an upgrader based on an ebullating bed resid hydrocracking unit. The SCO contains unconverted oil.

SAGD bitumen: Bitumen produced in Alberta using a 2 SOR (steam-to-oil ratio) is transported to a US PADD2 refinery as dilbit (naphtha diluent and bitumen); naphtha diluent is returned to Alberta.

SAGD dilbit: Similar to the previous case, except that the diluent is not returned to Alberta and is instead converted to gasoline.

CA TEOR: California thermal enhanced oil recovery using cyclic steam injection in the San Joaquin Valley of California (Kern River). This heavy oil (13.4 API, 1 wt. % sulphur crude) is refined in a high conversion refinery in California. Diesel and gasoline are used in California.

Conventional crudes: Kirkuk (Iraq), Bonny Light (Nigeria), Mars (US Gulf Coast), Arab Medium (Saudi Arabia), Maya (Mexico), and Bachaquero (Venezuela) crude oils, produced and transported to a high conversion refinery in PADD2 of the US, where the crude is converted to mainly gasoline and diesel fuel used in PADD2. **Kirkuk Blend** is a 36.6 API and 1.94 wt. % sulphur crude. **Bonny Light** is a 32.9 API and 0.16 wt. % sulphur crude. **Mars** is a US domestic sour crude produced offshore, in the deepwater of the Gulf of Mexico. The crude is 31.5 API and 1.8 wt. % sulphur. **Arab Medium** is a nominal 31.2 API and 2.5 wt. % sulphur crude. **Maya** is a 22.1 API, 3.3 wt. % sulphur crude. For this work, Jacobs selected the heaviest of the **Bachaquero** blends at 10.7 API and 2.8 wt. % sulphur.

*PADD refers to *Petroleum Administration for Defense District*. PADD2 is located in the US Midwest.

**Dilbit is assumed to be a 25/75 volume blend of diluent (natural gas condensate) and bitumen.

Cogeneration, also known as combined heat and power (CHP), is the use of a power plant to simultaneously generate both electricity and useful heat rather than producing each utility separately. It is a thermodynamically efficient use of fuel. The impact of cogeneration can be considerable in bitumen production from oil sands, where hot water, steam, and electricity are required. In bitumen production, natural gas is normally used to generate steam and electric power, and accordingly, the impact of carbon dioxide emission due to burning of natural gas can be reduced through cogeneration. The Jacobs Consultancy study showed through the life cycle analysis that the impact of cogeneration can be quite significant. A credit of, say, 50 % for cogeneration power export in bitumen production would lead to lower emission intensities to the extent that fuel produced from bitumen derived from mining operations would have a CO₂e emission intensity comparable to that from conventional crude.

It is of interest to note that the use of refined fuel derived from coal (coal-to-liquid, CTL) leads to a CO₂e emission intensity nearly double that derived from conventional crude. CTL technology to produce gasoline has been used in South Africa since 1955 and is being developed in China and contemplated in the US.

1.5.5 Water Use

Bitumen extraction from oil sands in mineable operations is based on the use of water in the extraction process. This is because, by and large, oil sands mineral solids are hydrophilic, and bitumen separation can be achieved quite easily using water

as the extraction medium. Figure 1.24 shows simplified input and output water streams, which are linked with utilities, extraction, and upgrading. The precipitation and evaporation in the Athabasca region are nearly equal. Most of the water is imported from the Athabasca River. This water is used in utilities to generate steam, in upgraders for hydrogen generation, and in cooling towers. Although the general rule is that no water can be returned to the Athabasca River, Suncor has a special license for some water return to the river. The discharged water is mainly limited to ‘once-through’ cooling water, discharge of process effluent created in the upgrading operations, and surface runoff waters from mining leases. Prior to discharge, all water has to be treated to ensure that it meets effluent quality standards (Suncor 2007a). No water that has been in direct contact with oil sands can be returned to the Athabasca River.

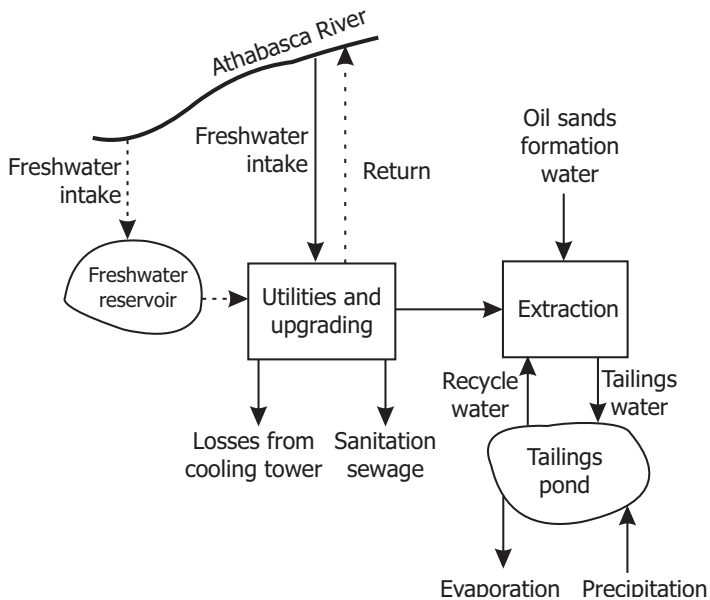


Figure 1.24 Water input and output streams for a water-based bitumen extraction plant with on-site bitumen upgrading.

During the summer months, when the river flow is high, freshwater intake is carried to freshwater reservoirs. This additional water capacity is essential during the winter months, when the river flow is low and river water withdrawal is limited. At CNRL, Suncor, and Syncrude, the extraction plant receives its water from the clarified tailings ponds; this water is referred to as *recycle plant water*. At Albian, thickener-clarified warm water is recycled back to the extraction plant, together with cold makeup recycle water from the tailings pond.

An overall water mass balance around the water streams in Figure 1.24 would clearly show an accumulation of water within the plant, where the magnitude of the return water flow rate is either nil or much smaller than the freshwater intake. Such accumulation takes place in the tailings pond itself. With no water discharge from

the tailings pond, the tailings pond water inventory increases with time. Indeed, most of the water in the ponds is not ‘free’ water, but is trapped within fine mineral solids (mainly clays), forming a sludge toward the bottom of the tailings pond. The sludge is normally referred to as *mature fine tailings* (MFT) and has a solids concentration of ~ 30 wt. %. It is estimated that about two barrels of sludge are formed for every barrel of synthetic crude oil produced, and that the volume of solids to water in the MFT is 1:6.

Without sufficient water of acceptable quality (in terms of suspended solids, salt content, and pH), development of the oil sands resource would not be feasible with today’s technology. Water is a precious commodity, and the difficult fact is that the current freshwater withdrawal is mainly centered on the Athabasca River. With increasing bitumen production, the demand on the Athabasca River increases. Water withdrawal becomes more complicated due to the large variance in river flow during the winter and summer months: flows well exceed 1200 m³/s during June and July, but are slightly less than 100 m³/s between January and March. Figure 1.25 shows the Athabasca River flow in 2002. In that year, the river flows were quite low.

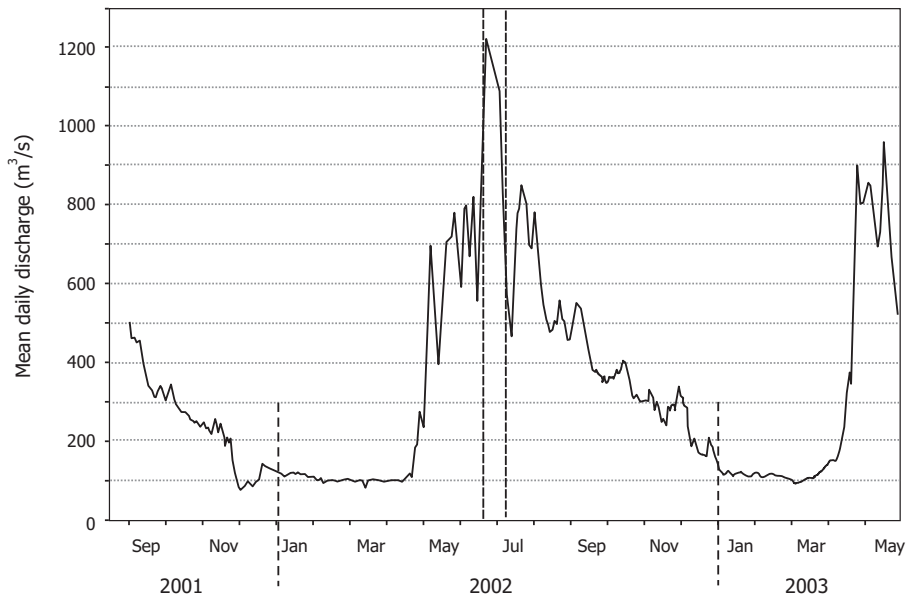


Figure 1.25 Athabasca River monthly flows, 2001–2003.

Source: McEachern and Marriott (2007).

The water balance in the Athabasca Region is very complex, as it includes precipitation, evaporation, run-off, muskeg, major rivers and creeks, shallow and deep aquifers, and basal water sands that are present in the Lower McMurray. Except for the latter, all of these sources vary by year, season, and location (Government of Alberta Fish and Wildlife Division 2007a, 2007b). As stated in the

Water Management Framework, established by Alberta Environment and Fisheries and Oceans Canada:

Preserving seasonal cycles is important, as a river and the ecosystem it supports is a product of the energetic forces dissipated over the natural range of variability. The life histories of fish and other aquatic species are adapted to high and low flows at appropriate times of year. For example, high flows are required in spring for fish that spawn at this time while fish that spawn in the fall do best with typical low flows in fall. Preserving year-to-year fluctuations is important for maintaining the diversity of species in the aquatic ecosystem. Some species do best in wet years. To maintain these species in their natural proportions, fluctuations in flow from year to year need to be preserved. . . . As long as the percent withdrawal is not too severe the IFN will mimic the natural hydrograph, providing wet and dry seasons and wet and dry years at the appropriate time (2007, p. 32).

The term IFN refers to ‘instream flow needs’ or ‘instream needs.’ The Water Management Framework defines it as “the amount of water, the flow rate, the water level, and/or the water quality that is required in a river or other body of water to sustain a healthy aquatic ecosystem” (2007, p. 22). Instream flow needs are specified for a given segment of a river and for a given time period.

The Water Management Framework divides the Athabasca River flow zones into three categories: green, yellow, and red (2007). The environmental implications for each are outlined below.

Green Zone: Water Availability is Sufficient

The river flow is sufficient and control withdrawal should have no negative impact on the ecosystem. This zone occurs mainly during summer weeks. In this zone, it is not likely for water withdrawals to affect fish habitats, and a *Fisheries Act* Authorization is usually not required. The maximum cumulative withdrawal rate is 15 % of *instantaneous* flow.

Yellow Zone: Cautionary Threshold (CT)

This threshold is defined by flows corresponding to 80 % habitat exceedence (HDA80 flow) for a given week. Such a measure means that habitat values (e.g. wetted area) below this level occur 20 % of the time. This is a measure of the decline in a wetted area. The maximum flow withdrawal has been determined as 10 % of the average of HDA80 and Q95. Here, Q95 is defined by 95 % flow exceedence, i.e., water flows below this value occur 5 % of the time. However, the total cumulative withdrawal rate is limited to a maximum of 15 m³/s during winter weeks and 34 m³/s during summer weeks. In this zone, it is not likely that water withdrawal would result in impact on fish habitat. However, a *Fisheries Act* Authorization may be required.

Red Zone: Potential Sustainability Threshold (PST)

In the red zone, it is likely that water withdrawal would result in impact on fish habitat and may require a *Fisheries Act* Authorization. This zone restriction applies to all licenses. The total cumulative water withdrawal rate is set at 5.2 % of historical *median* flow in each week. This corresponds to historical Q95. However, the total cumulative water withdrawal rate is limited to a maximum 15 m³/s during winter and 34 m³/s during summer weeks (Alberta Environment and Fisheries and Oceans Canada 2007).

In order to secure freshwater availability during yellow and red zones, freshwater reservoirs are used in areas where they are replenished during summer months, when water flow in the Athabasca River is high. Water is withdrawn from the freshwater reservoirs during winter months or when required. Such reservoirs have the capacity to hold as much as a six-month supply of freshwater.

The net freshwater intake from the Athabasca River by the major oil sands operators since 1998 is shown in Figure 1.26. The intake of freshwater by Syncrude has been quite steady, although synthetic crude oil production has increased significantly over the last decade. However, there is a slight increase in water withdrawal over 2005 due to higher year-over-year production and start-up demand associated with Stage 3 expansion (Syncrude 2006). Syncrude's annual freshwater withdrawal license from Athabasca River is 61.6 10⁶ m³/y (Syncrude 2002).

Suncor shows a significant increase in the net water intake during 2000 and 2002 to support production expansion (as seen in Figure 1.9), where bitumen production increased from 123.2 kbbbl/d in 2000 to 205.8 kbbbl/d in 2002 and 216.5 kbbbl/d in 2003. Suncor is licensed to withdraw 59.8 10⁶ m³/y of freshwater from the Athabasca River on an annual basis (Suncor 2005).

In 2006, the freshwater withdrawal from Athabasca River at Albion's Muskeg River Mine was fairly low due to the high supply of recycled water from the tailings ponds, where the freshwater intake was reduced to 8.4 10⁶ m³ during that period. In 2008, freshwater intake from the Athabasca River was ~ 13.6 10⁶ m³/y. The average water intake required by the Scotford Upgrader between 2004 and 2006 was 3.5 10⁶ m³/y; this was withdrawn from the North Saskatchewan River.

The total water withdrawal from Athabasca River of 120 Mm³/y by the four present oil sands operators (Albian, CNRL, Suncor, and Syncrude) represents less than 4 % of the Athabasca River flows during the winter months (100 m³/s), and only 1 % of the average river flow, estimated at 400 m³/s. As compared to the other rivers in Alberta, such as the North and South Saskatchewan Rivers, water withdrawal from the Athabasca River is quite low. The issue at hand is not river water withdrawal, but rather the accumulation of water in the tailings ponds.

The intensity of freshwater intake, i.e., the volume of water per unit volume of produced synthetic crude oil, is shown in Figure 1.27. At Syncrude, it is clear that there was a steady decrease in the freshwater intensity over the 2000–2008 period, leading to a usage of approximately two barrels of freshwater intake for one barrel of SCO in 2008.

A similar case can be made for Suncor in terms of decreasing freshwater intensity. It should be noted that freshwater intake intensity for the case of Suncor includes

crude bitumen production from Firebag. As Firebag in situ operations require less net water intake, freshwater intensity based on water intake from Athabasca River and upgraded bitumen derived from the mining operation alone would give higher values (5 % to 15 %) than those shown for Suncor in Figure 1.27 for 2004–2008. Firebag production started in 2004 at a rate of 10 900 bbl/d, increasing to 36 900 bbl/d in 2007 and 37 400 bbl/d in 2008. In contrast to mining operations, at Suncor’s Firebag in situ project, ~ 90 % of the water is recovered, treated, and recycled back into the steam generators. The initial water volume and the bulk of make-up water are taken from the oil sands wastewater systems (Suncor 2007a).

At Albian, except for the 2004–2005 period, the freshwater intake intensity has been less than two barrels of water per barrel of deasphalted bitumen (Figure 1.27). In addition to the freshwater withdrawn by Albian from the Athabasca River, ~ 0.4 barrels of freshwater intake per barrel of synthetic crude oil production is drawn from the North Saskatchewan River for the Scotford Upgrader, where the deasphalted bitumen is upgraded. Freshwater intake at Albian and its Scotford Upgrader is reflected in the AOSP curve in Figure 1.27.

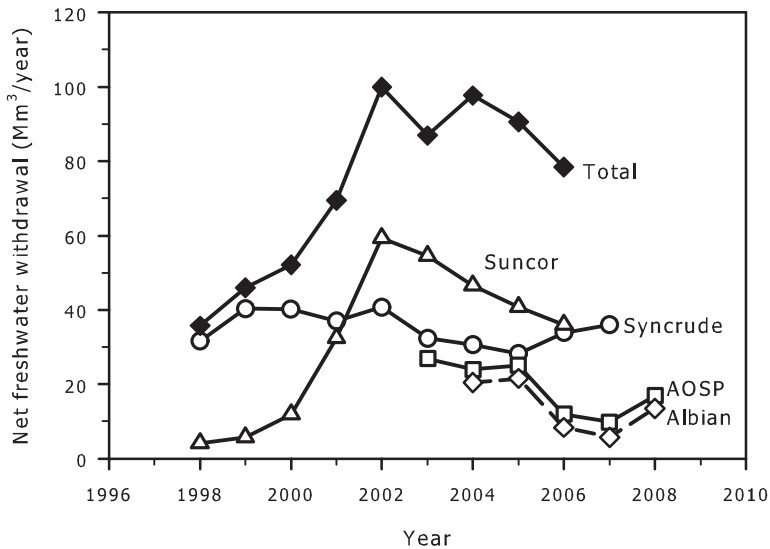


Figure 1.26 Net freshwater intake by Albian, AOSP, Suncor, and Syncrude from Athabasca River. The AOSP intake data refer to both extraction and upgrading, where for upgrading, withdrawal is from North Saskatchewan River.

Based on data from Syncrude and Suncor annual and sustainability reports and from Shell Canada Ltd. (2010, p. 14).

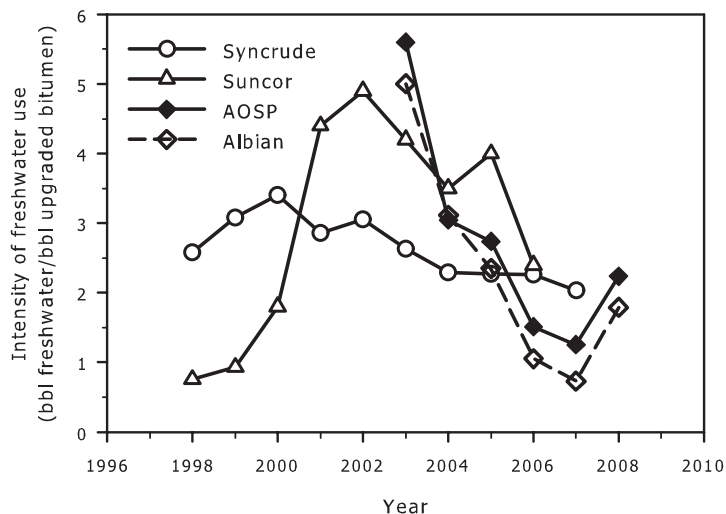


Figure 1.27 Net freshwater intake intensity for Suncor and Syncrude for both extraction and upgrading. Albian intensity data are for extraction alone. Suncor intensity data include Firebag in situ production and withdrawal from the Athabasca River and wells. The latter is 0 %–0.8 % of the river intake. Data for AOSP include freshwater intake from North Saskatchewan River and Athabasca River for upgrading needs.

Based on data from Shell, Syncrude, and Suncor annual and sustainability reports.

Syncrude water usage, in terms of freshwater intake from the Athabasca River, recycle clarified pond water, and total water used in the bitumen production, is shown in Figure 1.28. Clearly, a very large amount of water is needed for SCO production. Nearly 85 % of the water used is from recycle tailings pond water, while the freshwater intake constitutes a smaller fraction of ~ 15 %. There are several projects underway at the Mildred Lake site at Syncrude to recover condensate and cooling water, which is expected to reduce freshwater intake by ~ 2.1×10^6 m³/y. At the Aurora site, water diversion projects to prevent entry of freshwater into the mine pit and settling basins are expected to preserve the integrity of around 6.5×10^6 m³/y (Syncrude 2006).

Water intensities in terms of water volume used per unit volume of Syncrude Sweet Blend (SSB) are provided in Figure 1.29. About 17 barrels of water are needed to process one barrel of SSB. However, on average, only 2 to 3 barrels of freshwater are needed. Water intake intensity was reduced to 2.03 barrels in 2007.

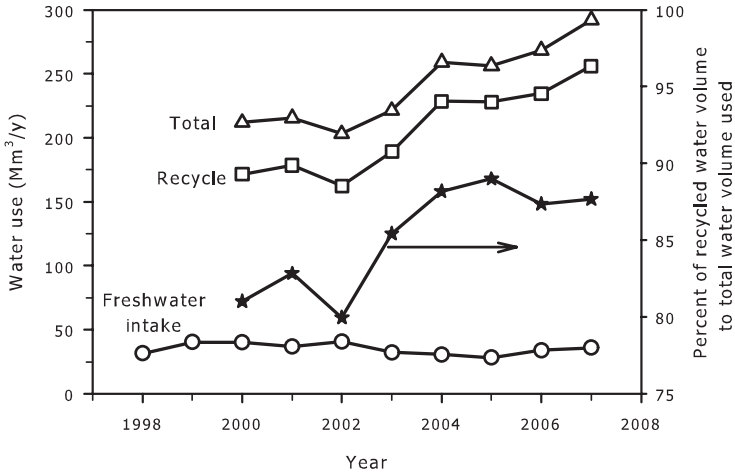


Figure 1.28 Water use by Syncrude for extraction and upgrading. “Total” refers to the sum of fresh and recycle water.

Based on data from Syncrude annual and sustainability reports.

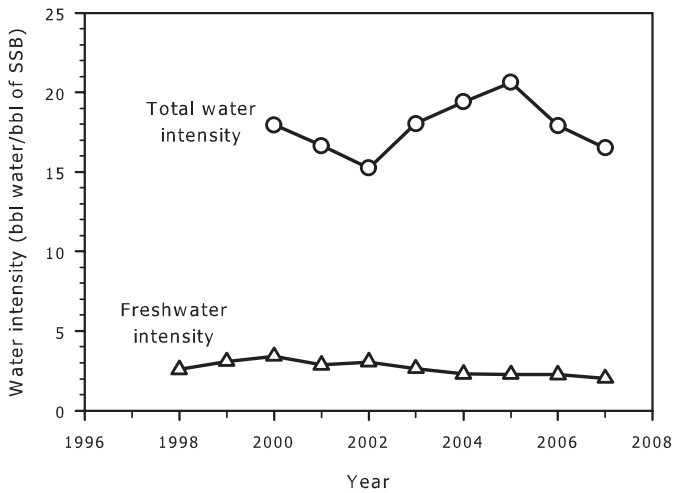


Figure 1.29 Syncrude water use intensity for freshwater intake and total use.

Based on data from Syncrude annual and sustainability reports.

1.6 References

- Adams, J.J., B.J. Rostron, and C.A. Mendoza. 2004. Coupled fluid flow, heat and mass transfer, and erosion in the Alberta Basin: Implications for the origin of the Athabasca oil sands. *Canadian Journal of Earth Sciences* 41 (9): 1077–1095.
- Alberta Chamber of Resources. 2004. *Oil sands technology roadmap: Unlocking the potential*. Edmonton: Alberta Chamber of Resources.
- Alberta Environment, and Fisheries and Oceans Canada. 2007. *Water management framework: Instream flow needs and water management system for the Lower Athabasca River*. Edmonton: Alberta Environment and Fisheries and Oceans Canada.
- California Air Resources Board (CARB). 2009. *Detailed California-modified GREET pathway for ultra low sulfur diesel (ULSD) from average crude refined in California*: California Environmental Protection Agency.
- Canadian Centre for Energy Information (CCEI), and R.D. Bott. 2004. *Our petroleum challenge: Sustainability into the 21st century*. 7th ed. Calgary: Canadian Centre for Energy Information.
- Canadian Natural Resources Limited (CNRL). 2002a. *Horizon Oil Sands Project application for approval. Submitted to Alberta Energy and Utilities Board and Alberta Environment*: Canadian Natural Resources Limited.
- Canadian Oil Sands Trust. 2007. *Oil Sands Lease Map*. <http://www.cos-trust.com> (accessed 2007)
- . 2008. *Annual Report: We are the definitive investment in the oil sands*. Calgary: Canadian Oil Sands Limited.
- Carrigy, M.A., and J.W. Kramers. 1973. *Guide to the Athabasca Oil Sands Area*. Edmonton: Alberta Research Council.
- Cuddy, G. 2004. Oil sands geology. Guest lecture notes for Chemical Engineering 534, Fundamentals of Oil Sands Extraction, January 7–9, at University of Alberta, Edmonton.
- Energy Resources Conservation Board (ERCB). 2008. *ST98: Alberta's energy reserves 2007 and supply/demand outlook 2008–2017*. Calgary.
- . 2009. *Alberta's energy reserves 2008 and supply/demand outlook 2009–2018*. Calgary: ERCB (Energy Resources Conservation Board).
- Ferguson, B.G. 1985. Athabasca Oil Sands: Northern Resource Exploration, 1875–1951. Regina: Canadian Plains Research Centre and Alberta Culture.
- . 1985. *Athabasca oil sands: Northern resource exploration, 1875–1951*. Regina: Alberta Culture/Canadian Plains Research Centre.
- Garven, G. 1989. A hydrogeologic model for the formation of the giant oil sands deposits of the Western Canada Sedimentary Basin. *American Journal of Science* 289 (2): 105–166.

- Government of Alberta. 2006. *Acidification of sensitive soils*. http://www3.gov.ab.ca/env/soe/land_indicators/44_soil_acidification.html (accessed July 11, 2008).
- Government of Alberta Fish and Wildlife Division. 2007a. *Instream Flow Needs for Alberta*. <http://www.srd.gov.ab.ca/fishwildlife/fishingalberta/pdf/Instream%20Flow%20Needs%20October%202007.pdf>
- . 2007b. *The Instream Flow Needs Program*. <http://www.srd.gov.ab.ca/fishwildlife/fishingalberta/instreamflowneedsprogram.aspx>
- Gray, M., Z. Xu, and J. Masliyah. 2009. Physics in the oil sands of Alberta. *Physics Today*, March, 31–35. See also Timblin, L.O. Jr., G. Stiles, E. Wood, M. Gray, Z. Xu, and J. Masliyah. 2009. Efficiency and environmental effects in the oil sands of Alberta. *Physics Today*, December, 8–9.
- Hein, F.J., R.A. Marsh, and M.J. Boddy. 2008. Overview of the oil sands and carbonate bitumen of Alberta: Regional geologic framework and influence of salt-dissolution effects. *Search and Discovery, American Association of Petroleum Geologists*.
- Huberman, I. 2001. *The place we call home: A history of Fort McMurray, as its people remember, 1778–1980*. Fort McMurray: Fort McMurray Historical Society.
- Jacobs Consultancy Life Cycle Associates. 2009. *Life cycle assessment comparison of North American and imported crudes. Prepared for Alberta Energy Research Institute. File no. AERI 1747*. Chicago.
- Mackenzie, A. 1801. *Voyages from Montreal, on the River St. Laurence, through the continent of North America, to the Frozen and Pacific oceans; in the years 1789 to 1793. With a preliminary account of the rise, progress, and present state of the fur trade of that country*. London: Cadell and Davies.
- Mair, C. 1908. *Through the Mackenzie Basin: A narrative of the Athabasca and Peace River Treaty Expedition of 1899*. Toronto: William Briggs.
- Mathieson, D., D. Stenason, B. Betanski, and A. Taylor. 2001. Investing in oil sands: Investment opportunities in Canada's energy future. *The Drill Bit*.
- McEachern, P., and P. Marriott. 2007. Paper read at CONRAD Water Management Seminar, November 21-22, at Calgary.
- Morgan, G. 2001. An Energy renaissance in oil sands development. *World Energy*, 46–53.
- National Energy Board (NEB). 2000. *Canada's oil sands: A supply and market outlook to 2015: An energy market assessment (October 2000)*. Calgary: National Energy Board.
- . 2004. *Canada's oil sands: Opportunities and challenges to 2015: An energy market assessment (May 2004)*. Calgary: National Energy Board.
- . 2006. *Canada's oil sands: Opportunities and challenges to 2015: An update: An energy market assessment (June 2006)*. Calgary: National Energy Board.
- . 2008. *Canadian energy overview 2007: An energy market assessment (May 2008)*. Calgary: National Energy Board.

- Petro-Canada Inc., UTS Energy Corporation, and Teck Cominco Ltd. 2007. *Application for approval of the Sturgeon Upgrader, submitted to Alberta Energy and Utilities Board and Alberta Environment*. Calgary.
- Radler, M. 2003. Worldwide reserves grow; oil production climbs in 2002. *Oil & Gas Journal* 101 (49).
- Shell Canada Ltd. 2005. *AEUB application for the approval of the Scotford Upgrader Expansion Project, Volume I*. Calgary.
- . 2006. *Sustainable development report*. Calgary: Shell Canada Limited.
- . 2010. *Canada's oil sands: Issues and opportunities*. http://www.shell.ca/home/content/can-en/aboutshell/our_business/oil_sands/unique_resource/water/
- Sheppard, M.C. 1989. *Oil sands scientist: The letters of Karl A. Clark, 1920–1949*. Edmonton: University of Alberta Press in association with Alberta Culture and Multiculturalism.
- Suncor Energy Inc. 2005. *Report on sustainability*. Calgary: Suncor Energy Inc.
- . 2006. *Annual report*. Calgary: Suncor Energy Inc.
- . 2007a. *Report on sustainability: A closer look at our journey toward sustainable development*. Calgary: Suncor Energy Inc.
- . 2007b. *Annual report*. Calgary: Suncor Energy Inc.,
- . 2008. *Annual report*. Calgary: Suncor Energy Inc.
- Synchrude Canada Ltd. 2002. *Sustainability report*. Fort McMurray: Synchrude Canada Ltd.
- . 2004. *Sustainability report*. Fort McMurray: Synchrude Canada Ltd.
- . 2006. *Sustainability report*. Fort McMurray: Synchrude Canada Ltd.
- . 2007. *Sustainability report*. Fort McMurray: Synchrude Canada Ltd.
- Tiax LLC, and MathPro Inc. 2009. Comparison of North American and imported crude oil lifecycle GHG emissions. Prepared for Alberta Energy Research Institute. Cupertino, CA.

Chapter 2

Basic Scientific Background

2.1 Surface and Colloid Science

Colloid science deals with dispersed multiphase systems. When the dispersed phase consists of relatively large-sized particles, the bulk properties of both the continuous and disperse phases determine the behaviour of the whole system. If we make the particles smaller, the interfacial area increases with decreasing particle size,¹ as does the contribution of surface forces and other surface phenomena to the overall properties of the system. Ultimately, in systems containing sufficiently small particles, surface phenomena control the properties of the overall system.

Why is a large surface or interfacial area so important? The main issue that we should keep in mind is that it takes a lot of energy to bring an atom or a molecule to the surface. We will discuss this in more detail in the section on surface tension. For now, let us note that, because bringing a molecule to the surface requires work to be performed against intermolecular forces, the energetic state of a molecule at the surface is different from that of one in the bulk. As a consequence, properties of molecules sitting at the surface are different from those in the bulk.

As the interfacial (or surface) area increases with decreasing particle size, it eventually begins to control the properties of the whole system. Such systems are called *colloids*. As we will see later in this chapter, the presence of electric charges on particle surfaces is one of the sources of surface forces. Because of this, and because surface phenomena control properties of colloidal systems, colloid science, interface science, and some aspects of electrochemistry must be approached as integrated concepts. In this chapter, we will give a basic overview of the scientific background of surface and colloid science as it relates to oil sands processing.

So, what is a colloidal system? Traditional definitions are usually based on dispersed particle size and define a colloid as a dispersion of particles smaller than a set unit, for example, 1 μm . There is no sharp distinction between colloidal and

¹ If we start with a single cube with side a and cut it N times parallel to each of the three perpendicular sides, we will get $(N+1)^3$ small cubes of a total surface area $N + 1$ times larger than the starting cube area.

non-colloidal dispersions. A large soap bubble can easily be a few centimeters in size, yet its very existence is a result of the stabilizing electrical interactions between both sides of the thin liquid film forming the bubble. Therefore, a soap bubble is a colloidal system. Similarly, foams and emulsions are usually treated as colloids, despite the fact that their individual particle or droplet dimensions are often well above 1 μm .

As we said above, colloids are dispersions of at least two different phases. One of them forms a continuous medium in which small particles of the second phase are dispersed. Based on the physical nature of these phases, colloidal dispersions can be classified as shown in Table 2.1. Because all gases mix well with each other, there are no gas-in-gas dispersions. Liquid dispersions in a continuous gas phase (e.g., air) are quite common—clouds and fogs are dispersions of small water droplets in air. When the water droplets coalesce and grow bigger, water eventually falls down as rain. Solid particles dispersed in air form aerosols. Smoke is an example from the aerosol group of colloidal systems.

There are three types of colloidal dispersions in a liquid continuous phase: *foams*, *sols*, and *emulsions*. *Foams* are dispersions of a gas in a liquid continuous phase. Many types of foams have important industrial applications; two examples are firefighting foams and flotation foams or froths. Foaming may be detrimental, e.g., in industrial boilers or fermenters.

Suspensions of small solid particles in a liquid are called sols. Examples of such systems are middlings and fine tails in oil sands extraction (these are mostly suspensions of small clay particles in water). Toothpaste or murky river water after heavy rains are also examples of sols.

Dispersions of a liquid in another immiscible liquid are called emulsions. Milk, mayonnaise, and many cosmetics are dispersions of oil in water. In the petroleum industry, we often encounter both water-in-oil and oil-in-water emulsions. We will discuss water-in-oil emulsions in detail in Chapter 7, which is devoted to the fundamentals of froth treatment.

There are also interesting systems in which a solid forms a continuous phase. *Solid foams* are gas dispersions in a solid (e.g., pumice or Styrofoam). Liquid droplets dispersed in a solid continuous phase are called *solid emulsions*, of which opal and pearls are just two examples. Finally, solid dispersions in a solid continuous phase are called *solid suspensions*, with numerous examples in rocks, including ores of metals like copper, zinc, or gold; some coloured glass; and polycrystalline metal alloys.

As we will see in the following section, there is an excess energy associated with any phase boundary. Dispersed systems with a large interfacial area have higher internal energy than that of a system of the same composition but with a smaller interfacial area (or coarser particles). At the same composition, the smaller the particles, the larger the interfacial area, and consequently, the larger the particles' internal energy. Fine dispersions, like colloids, are thus intrinsically unstable, as all systems evolve to lower their internal energy. Therefore, stabilization mechanisms must be involved for a colloid to exist for an extended period of time. In the rest of this chapter, we will discuss the factors that contribute to the stability of colloidal systems.

Manipulation of these factors allows for such everyday applications as controlling the shelf time of mayonnaise or the dewatering efficiency of crude oil fed to a refinery.

Table 2.1 Types of colloidal dispersions

		Dispersed phase		
		Gas	Liquid	Solid
Continuous phase	Gas		Liquid aerosol (fog, mist, sprays)	Aerosol (smoke, dust)
	Liquid	Foam (soap foams; firefighting foams; flotation froth is a foam also containing other particles)	Emulsion (milk, mayonnaise, petroleum water-in-oil and oil-in-water emulsions)	Sol (clay suspension, oil sands middlings, toothpaste, murky water)
	Solid	Solid foam (styrofoam, pumice)	Solid emulsion (opal, pearls)	Solid suspension (mineral dispersions: many rocks, including some metal ores)

2.2 Surface and Interfacial Tension

2.2.1 Introduction

When we consider a two-phase system, e.g., a liquid in equilibrium with its vapour, the densities of these two neighbouring phases are usually quite different. The lower the density, the larger the mean distance between the molecules. Let us consider water in equilibrium with its vapour at 25 °C and 101.3 kPa (1 atm or 14.7 psi). Intermolecular forces acting on the water molecules in the bulk of both phases balance each other, such that the net force acting on any single molecule in a bulk phase, i.e., far from the interface, is zero. This is not the case when a molecule sits at the boundary between the liquid and vapour phases. The density of liquid water is 1000 kg/m³, while the density of water vapour at 25 °C and 101.3 kPa is about a thousand times smaller at 804·10⁻³ kg/m³. There are about a thousand times less water molecules in the same volume of vapour than in the liquid, meaning that the mean distances between the water molecules in the vapour phase are about ten times larger than those in the liquid. The interaction energy between two atoms or molecules $E_{m/m}$ always decays with the sixth power of the distance r between them: $E_{m/m} = \beta r^{-6}$ (β is a constant dependent on the nature of the interacting molecules). Therefore, a force acting on a water molecule sitting at the liquid-vapour interface, directed towards the denser phase (in our case,

liquid water), is a million (10^6) times stronger than the one directed towards the vapour phase. The net force acting on all molecules at the interface is balanced by the compressibility of the liquid phase and is the source of so-called internal phase pressure.

Another consequence of the difference between intermolecular forces acting on molecules at interfaces and in the bulk is what we call *surface tension*. If we bring a liquid molecule to the liquid-vapour interface, we must perform work against this above mentioned net force. To be more specific, let us suppose that we have a spherical droplet of liquid with a radius of r . If we add a very small amount of the liquid to the droplet, such that the droplet radius increases by dr , the droplet's surface area and its volume increase by $2\pi r dr$ and $4\pi r^2 dr$, respectively. By increasing the droplet surface area, we bring more liquid molecules to the surface, and by doing so, we perform work dW against the intermolecular forces mentioned above. From the energy conservation principle, it follows that this work must be equal to the increase in the energy of the droplet due to the increase of the droplet surface area. This work or excess energy must be proportional to the increase in surface area S

$$dW = \gamma dS = \gamma 2\pi r dr \quad (2.1)$$

where γ is a proportionality factor with a dimension of energy per unit area, and $S = \pi r^2$ is the surface area. This proportionality factor γ is called *surface tension* when referring to a gas-liquid interface or *interfacial tension* (IFT) when referring to a liquid-liquid or solid-liquid system.

It is worth noting that the dimension of surface or interfacial tension is given in unit of energy per unit of area (J/m^2), which is the same as unit of force per unit of length (N/m). This is why γ is referred to as tension. However, it should be remembered that this is just a consequence of a simple mathematical operation: $\text{J}/\text{m}^2 = \text{N} \cdot \text{m}/\text{m}^2 = \text{N}/\text{m}$. The physical meaning of surface tension is an excess energy associated with the existence of the interfacial boundary, and there is no tangent force actually acting on the interface itself. There are only forces acting on individual molecules as a result of intermolecular interactions, with the net force perpendicular to the surface and balanced by the liquid compressibility. A net force tangent to the surface can only be observed at a boundary of three different phases (often referred to as a three-phase contact line), as will be discussed later.

2.2.2 Young-Laplace Equation

We have shown above that an increase in a droplet's size results in an increase in its total energy. For a spherical droplet, this energy increase can also be expressed as the work performed against a pressure difference inside and outside of the droplet:

$$\Delta p = p_{\text{inside}} - p_{\text{outside}}$$

This work can be written as

$$dW = dpdV,$$

where dV is an increase in the droplet's volume. Substituting $dV = 4\pi r^2 dr$ yields

$$dW = \Delta p 4\pi r^2 dr \quad (2.2)$$

Comparing Eqs. 2.1 and 2.2 we obtain

$$\gamma 2\pi r dr = \Delta p 4\pi r^2 dr,$$

or

$$\Delta p = 2\gamma / r \quad (2.3)$$

The above equation, valid for a spherical droplet, bubble, or particle, is known as the Young-Laplace equation. It gives the pressure difference across a curved interface of spherical geometry. In general, the pressure difference across any element of a curved interface is given by the general form of the Young-Laplace equation

$$\Delta p = \gamma(1/r_1 + 1/r_2) \quad (2.4)$$

where r_1 and r_2 are the two principal radii of curvature of the element. The Young-Laplace equation has profound consequences. We will explore some of them in more detail below.

2.2.3 Superheating, Supercooling, and Ostwald Ripening

One of the consequences of the pressure difference across a curved interface is that the increased pressure inside a drop or a solid particle increases the chemical potential and activities of all components forming the dispersed phase, causing a number of interesting phenomena. We will describe some of them below.

Superheating

Let us consider the simple process of boiling water. As we heat the water, its temperature increases, causing water activity to increase, and, consequently, saturated water vapour pressure to increase with it. When the water vapour pressure equals the atmospheric pressure, vapour bubbles form in the bulk of the water, and the

water boils. However, formation of the bubble nucleus is difficult. As an example, let us consider a bubble 1 μm in diameter. Substituting a water surface tension of $\gamma = 72 \text{ mJ/m}^2$ and $r = 0.5 \cdot 10^{-6} \text{ m}$ into the Young-Laplace equation $\Delta p = 2\gamma/r$, we obtain $\Delta p = 2.9 \cdot 10^5 \text{ Pa}$ (2.9 atm or 42 psi). Saturated water pressure at 100 $^\circ\text{C}$ is only $1.01 \cdot 10^5 \text{ Pa}$ (1 atm or 14.7 psi). A bubble nucleus 1 μm in diameter cannot be formed at 100 $^\circ\text{C}$. Formation of a 1 μm bubble would require a water temperature of above 157 $^\circ\text{C}$ (315 $^\circ\text{F}$), where the saturated water vapour pressure reaches $2.9 \cdot 10^5 \text{ Pa}$. Yet, the nucleus bubble, when it is formed, is even smaller, containing ~ 10 to 100 water molecules, which would correspond to a diameter of about 10 nm, yielding an even higher temperature than is necessary to form the nucleus.

In real life, boiling starts at the heated surface, where local roughness promotes vapour nucleation. However, if we heat any homogeneous liquid, free from any suspended solids, in a vessel with smooth walls, the nucleation of vapour bubbles is to a large extent retarded. The liquid can be heated to a temperature substantially higher than its boiling temperature without really boiling. When this happens, we say that the liquid is *superheated*. Generally, this creates a dangerous situation, as any random event yielding bubble nuclei will result in the extremely vigorous or even explosive onset of boiling, with obvious negative consequences.

Similarly, the evolution of gas bubbles from an open pop bottle or a beer can, for example, depends on the formation of CO_2 gas bubble nuclei. Normally, the nuclei are formed only along the container walls, but if we shake the container vigorously before opening, many gas nuclei are formed in the bulk of the liquid as well, such that when the container is eventually opened, the instantaneous gas evolution causes the liquid to spill.

Supercooling

A similar mechanism is involved in supercooling, or in a liquid-to-solid phase transition such as water freezing or salt crystallization from a saturated solution. Here, again, the formation of a new solid phase nuclei is retarded by the increased pressure inside the nucleus due to its small radius of curvature. This effect can be observed on a large scale in a lake or a pond, which can cool below the freezing point of water under very calm atmospheric conditions, until a disturbance, such as a landing bird, a gust of wind, or a thrown stone, causes instantaneous formation of an ice layer. On a pond or lake, supercooling is a very rare event, as it is very difficult to avoid any nuclei on a large scale. However, it is very easy to cool a small water droplet below its freezing temperature. Freezing rain is caused by droplets of supercooled water freezing at impact on any surface, such as a road, power line, or tree branch.

Ostwald Ripening

Yet another phenomenon associated with Young-Laplace pressure is *Ostwald ripening*. To illustrate this process, let us imagine a cloud (a suspension of small water droplets in air). Most clouds do not produce any rain, as the drops are too small to fall down. They can grow bigger through several mechanisms, such as collisions that occur due to shear induced by wind or due to Brownian movements. In addition, any differences in their sizes are amplified by the fact that the smaller the drop, the higher the vapour pressure in equilibrium with it. Thus, smaller drops evaporate and larger drops grow bigger by condensation of the water vapour. The fog grows coarser as the initial droplet size distribution shifts towards larger sizes. This is an example of Ostwald ripening, which shifts the size distribution towards larger sizes in emulsions, crystalline precipitates, and in any other fine dispersion. Whether Ostwald ripening causes any significant changes depends on the kinetics of the process, which are very case-sensitive—they may be either fast or slow, depending on the system. Even in cases where the kinetics is slow, the thermodynamic driving force for Ostwald ripening is always present.

Oily coating on fog droplets due to urban pollution drastically slows water evaporation from coated drops and consequently slows the kinetics of Ostwald ripening. This was a major contributing factor to the infamous London smog, which was known to last for many hours, and on occasion, even days.

2.2.4 Three-Phase Contact and Contact Angle

When three different phases are present in a system, e.g., a gas, a liquid, and a solid, a number of interesting phenomena can be observed at the line where the three phases meet, called the three-phase boundary. Such systems are of great practical importance. It is sufficient to mention that the attachment of a mineral grain or bitumen droplet to an air bubble in water, which is at the very foundation of mineral beneficiation by flotation, involves the formation of a three-phase boundary, resulting in several phenomena which we will briefly describe in this section.

When a bubble and a mineral grain are immersed in water without contacting each other, we only have to deal with a two-phase boundary, which we can describe with excess surface energy or surface tension, as discussed above. However, when the mineral grain is permanently attached to the bubble, a three-phase contact line is established. It is convenient to introduce the subject using the example of a drop of a liquid placed on a slab of a solid, as shown in Figure 2.1. As will be discussed later, the exact shape of the drop is the result of the system minimizing the surface and potential energies. For now, let us focus on the conditions at the contact line. Each of the three boundaries (solid-liquid, solid-gas, and liquid-gas) has their own surface tension. One can consider the force balance at the three-phase contact line. At equilibrium, the net force acting on the contact line must be zero, otherwise the contact line would move. We can thus write,

$$\gamma_{s/g} = \gamma_{s/l} + \gamma_{g/l} \cos \theta \quad (2.5)$$

where $\gamma_{s/g}$, $\gamma_{s/l}$ and $\gamma_{g/l}$ are surface tensions of solid-gas, solid-liquid, and liquid-gas interfaces, respectively, and θ is the contact angle. Eq. (2.5) is known as Young's equation, after Thomas Young, who first introduced it in 1805.²

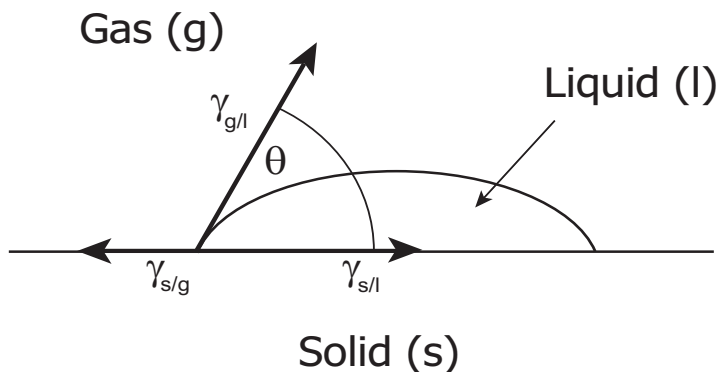


Figure 2.1 Contact angle (θ) of a liquid drop (l) on a solid substrate (s) in air (g). $\gamma_{s/g}$, $\gamma_{s/l}$ and $\gamma_{g/l}$ are surface (or interfacial) tensions of solid-gas, solid-liquid, and gas-liquid interfaces, respectively.

Contact angle is a measure of the ability of the liquid to wet the solid. The contact angle is zero if the liquid wets the solid perfectly. We may think of a droplet of water placed on perfectly clean glass. The water will spread over the glass, forming a contact angle of zero. However, if we place a water drop on glass that is not so clean, the drop will assume a contact angle with a finite value. The contact angle of water on Teflon is close to 180° .

Materials or surfaces that are easily wetted by water, i.e., those with a contact angle close to zero, are called *hydrophilic* (Greek for ‘water-loving’). The substances or surfaces that form a contact angle of close to 180° with water are called *hydrophobic* (‘water-hating’). In the petroleum industry, the scientifically correct terms ‘hydrophilic’ and ‘hydrophobic’ are often replaced with ‘*water-wet*’ and ‘*oil-wet*,’ respectively. One has to be careful using these common terms, as it is difficult to distinguish between

² Thomas Young (1773–1829) was an English scientist and physician who made significant contributions to diverse fields of science and medicine, including physiology, mechanics, thermodynamics, optics, languages, musical theory, and Egyptology. He was the first to introduce the wave theory of light and the notion of Young’s modulus characterizing elasticity. While working on capillarity in 1804, Young proposed an expression for pressure difference across a curved surface (Eq. (2.4)), which was independently developed by Laplace a year later (this is the previously-discussed Young–Laplace equation). He also introduced the above equation (Eq. (2.5)), describing contact angle. Trying to decipher Egyptian hieroglyphs, he became the first to translate the Egyptian Demotic text on the Rosetta Stone. A truly remarkable man.

a property (hydrophilic or ‘water-wet’) and a state (immersed in water or wet with water). For instance, a piece of hydrophobic Teflon can be totally immersed in water. The Teflon’s properties have not changed, only its status has. It still remains hydrophobic (or ‘oil-wet’), despite the fact that when immersed in water, it is in fact wetted with water. So, when immersed in water, Teflon becomes an oil-wet, yet water-wetted, material.

Contact angle is a quantity that can be measured from direct observations of three-phase contact profiles, as well as by other methods, which will be described later.

Contact Angle Hysteresis

If we place a liquid drop on a tilted plate, it will assume the shape shown in Figure 2.2. The drop has a tendency to slide down on the plate under gravity. We see that the contact angle on the advancing edge of the drop is substantially larger than the one on the receding edge. The difference between the advancing and receding contact angles is due to contact angle hysteresis, which has considerable impact on a number of phenomena in which contact angle plays a role.

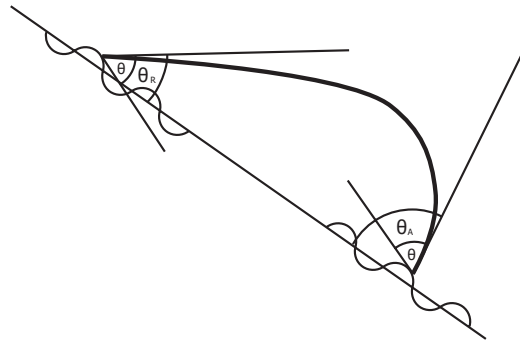


Figure 2.2 A drop on a tilted plate; an example of contact angle hysteresis.

Contact angle hysteresis may result from a number of different causes, and in a practical system, is likely due to a combination of factors. One of the most important reasons for contact angle hysteresis is surface roughness, as shown in Figure 2.2. Surface roughness can be visualized as local valleys and hills. Even when local microscopic advancing and receding contact angles are the same (θ), macroscopically observable advancing (θ_A) and receding (θ_R) contact angles will differ from each other, resulting in contact angle hysteresis, as seen in Figure 2.2. Contact angle hysteresis can also be caused by non-uniform values of local microscopic contact angles, which in turn may result from differences in local chemical composition of the solid plate—a common feature of natural materials such as minerals and rocks. It can also be caused by non-uniform adsorption of chemicals, which alters the surface properties of the solid.

2.2.5 Spreading

Adhesion and Cohesion Energies

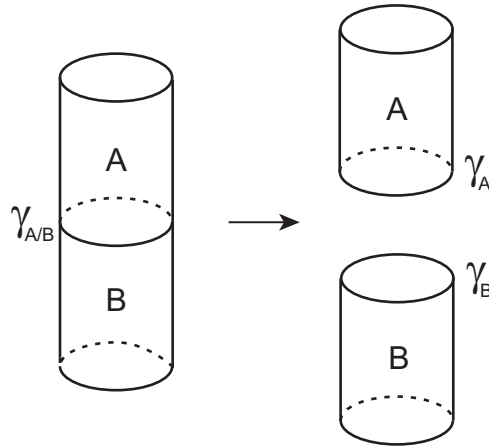


Figure 2.3 Definition of adhesion energy, as described in the text.

To introduce the notion of adhesion and cohesion energies, let us consider a cylinder made of two bodies (which can be immiscible liquids) A and B in contact with each other, as shown on the left side of Figure 2.3. When we separate the bodies, their mutual interface, which is characterized by interfacial tension $\gamma_{A/B}$, disappears and is replaced with two corresponding surfaces of body-air contact, characterized by surface tensions of the corresponding bodies, γ_A and γ_B . The work required to separate a unit area of the body A–body B interface and to form two separate body-air interfaces is called the work (or energy) of adhesion, W_{ad} , and is given by the Dupré equation:

$$W_{ad} = \gamma_A + \gamma_B - \gamma_{A/B} \quad (2.6)$$

When both bodies are the same, $\gamma_A = \gamma_B$ and $\gamma_{A/B} = 0$. The work required to separate a cylinder made of body A and to form two body A–air interfaces, each a unit in area, is called the work (or energy) of cohesion, W_{co} , and is given by

$$W_{co} = 2\gamma_A \quad (2.7)$$

Adhesion and cohesion energies are convenient for analyzing the spreading of one liquid over another or for soldering, welding, or choosing a proper glue. They also govern the attachment of bitumen to air bubbles in water during bitumen extraction.

Spreading Coefficient

When a drop of insoluble oil is placed on a water surface, it can either spread out as a liquid film with two distinct boundaries (with the water below and the air above) or it can form a lens, which usually further spreads out as a monomolecular layer in equilibrium with excess oil in the lens. A vegetable oil poured over water forms lenses. A mineral oil may spread into a liquid film with distinct boundaries, such that the light reflected from the top and bottom interfaces interferes, forming rainbow like colours, as often seen on puddles of water in parking lots after a rain. Higher alcohols, like octanol, spread and form monomolecular layers in equilibrium with lenses.

The spreading behaviour depends on the so-called spreading coefficient, defined as

$$S = \gamma_{W/A} - (\gamma_{O/A} + \gamma_{O/W}) \quad (2.8)$$

where $\gamma_{W/A}$ is the surface tension of water against air, $\gamma_{O/A}$ is the surface tension of oil against air, and $\gamma_{O/W}$ is the interfacial tension of oil against water. Spontaneous spreading of oil on water occurs when $S \geq 0$. Substituting the above formula for spreading coefficient into the Dupré equation above, we find a connection between spreading coefficient and the energies of cohesion and adhesion:

$$S = W_{ad(O/W)} - 2\gamma_{O/W} = W_{ad(O/W)} - W_{co(O/O)} \quad (2.9)$$

Spreading occurs for positive values of S or for $W_{ad(O/W)} > W_{co(O/O)}$. This means that spreading of oil on water occurs when adhesion of the oil to water is stronger than cohesion of the oil to itself.

Bitumen spreads on water. As we can see in Table 2.2, at about 80 °C, surface tensions of water and bitumen (against air) are ~ 72 mJ/m² and 27 mJ/m², respectively, and bitumen interfacial tension against water is 14 mJ/m² to 15 mJ/m². Thus, $S = 70 - (27 + 15) = 28$. This is a positive value that implies spontaneous spreading. Indeed, under conditions of hot water extraction, at temperatures of ~ 80 °C, bitumen spreads over air bubbles. One may think of the bitumen spreading on the water surrounding the bubble. It results in very strong bonding between air bubbles and bitumen, which is beneficial for bitumen flotation. Surface tensions of liquids do not strongly depend on temperature. Bitumen spreading would also occur at, say, 25 °C or 40 °C, but the viscosity of bitumen is too high for this process to be observed on a relevant time scale of seconds or minutes. At temperatures below, say, 40 °C or 50 °C, bitumen droplets or specks attach to air bubbles, forming a three-phase contact line, but without visible spreading. Obviously, in such a case, bitumen-to-air bonding is weaker than it is at higher temperatures, where spreading does take place.

Table 2.2 Selected surface and interfacial tensions (against water)

Liquid	Surface tension (mJ/m ²) ^a	Interfacial tension (against water) (mJ/m ²) ^b
n-Pentane	15.49	
n-Hexane	17.89	51.1
n-Heptane	19.65	50.2
n-Octane	21.14	50.8
n-Decane	22.38	51.2
Toluene	27.93	36.1
Benzene	28.22	35.0
Oleic acid		15.7
Octanoic acid		8.5
1-Butanol	26.28	1.8
1-Pentanol	26.67	4.4
1-Octanol	28.30	8.5
Water	71.99	n/a
Mercury	485.48	
Athabasca bitumen	27 ^c	14 ^c , 15 ^d

^a Source: CRC Handbook of Chemistry and Physics (2008–2009).

^b Source: Morrison and Ross (2002).

^c Source: Takamura and Isaacs (1989). Ring method at 80 °C. Interfacial tension against heavy water D₂O.

^d Source: Moran et al. (2000). Micropipette method at room temperature and pH = 8.

2.3 Measurements of Surface and Interfacial Tension

Many methods of surface and interfacial tension measurements take advantage of the Young-Laplace equation for spherical symmetry (Eq. (2.3)). Below, we will explain the most commonly used methods of surface tension measurements and provide brief descriptions of their advantages and disadvantages.

2.3.1 Capillary Rise Method

Imagine a circular cross-section glass capillary with one end immersed in a liquid that is in a beaker (Figure 2.4). If the liquid perfectly wets the capillary walls (forming a contact angle of zero), the liquid forms a concave, hemispherical meniscus inside the capillary. The radius of the meniscus curvature is the same as the capillary radius. Thus, the pressure in the liquid just below the meniscus is lower than that under the

flat surface in the beaker. The pressure difference is given by Eq. (2.3): $\Delta p = 2 \gamma / r$. This pressure difference will induce flowing of the liquid from the beaker into the capillary, causing the meniscus to rise until the hydrostatic pressure ρgh (where ρ is the liquid density, g is acceleration due to gravity, and h is the capillary rise) becomes equal to the capillary pressure due to the concave meniscus. By comparing the two formulas, one can express surface tension γ as a function of all other parameters:

$$\gamma = \frac{1}{2} \rho gh r.$$

Now, knowing the liquid density ρ and the gravity constant g , the measuring capillary inner radius r , and the capillary rise h , one can calculate the surface tension of the investigated liquid. In practice, instead of measuring the capillary diameter under a microscope, which is both tedious and not very accurate, the capillary rise of a standard liquid with well-known surface tension γ_{st} is measured first. The capillary rise for the investigated liquid is then measured using the same capillary. It is easy to show that $\gamma = \gamma_{st} \rho h / (\rho_{st} h_{st})$.

The capillary rise method is very simple, and if one uses a standard liquid instead of measuring the capillary radius, the method does not require any sophisticated equipment and can be done easily in the field or in a classroom. Because this method is sensitive to impurities in the capillary (which could affect the required perfect wettability of the capillary walls), the same capillary cannot be used many times. If capillary rise is measured with a simple ruler, the accuracy of the method is low.

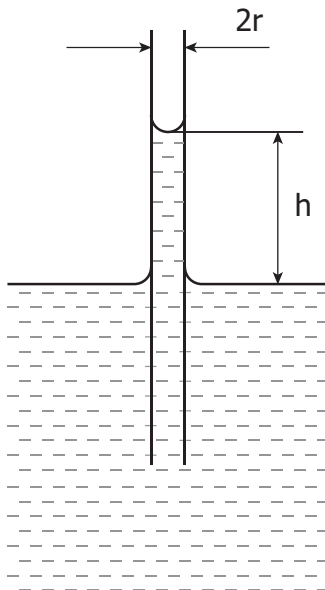


Figure 2.4 Capillary rise method.

2.3.2 Maximum Bubble Pressure Method

When a gas is blown down a capillary immersed in a liquid, initially, a flat gas-liquid interface is formed (see **a**, Figure 2.5). Since the interface is flat, there is no pressure difference across it, and the gas pressure inside the capillary p is equal to the sum of the atmospheric pressure p_o and the hydrostatic pressure at the tip of the capillary ($p = p_o + hgp$). As the gas pressure is increased, a convex interface is formed. The incremental pressure, related to the formation of the curved interface, is balanced by the pressure difference across the curved interface as given by the Young-Laplace equation. Thus, we have:

$$p = p_o + hgp + 2\gamma / r_{curv} \quad \text{or} \quad \Delta p = hgp + 2\gamma / r_{curv}$$

r_{curv} is the curvature radius of the bubble formed on the tip of the capillary. As the pressure p is increased further, the curvature radius r_{curv} decreases until it reaches the smallest possible value, at which it is equal to the capillary radius (**b**, Figure 2.5). At this point, the pressure inside the bubble reaches the maximum value. Up to this point, the system is stable, as any incremental increase in pressure is balanced by an increased Young-Laplace pressure drop across the curved interface. However, if we keep inflating the bubble, it will grow bigger, and its curvature radius r_{curv} will increase above its minimum value (corresponding to the maximum pressure). The Young-Laplace pressure resulting from the bubble curvature becomes smaller than the pressure inside the bubble. The bubble spontaneously grows larger and detaches from the capillary (**c**, Figure 2.5), and the cycle repeats. The maximum pressure in the capillary is achieved when the bubble radius is the smallest, at which point it is equal to the capillary radius. Since all variables in the above equation can be directly measured, maximum bubble pressure can be used to calculate the liquid surface tension. (Capillary radius can either be measured under a microscope or evaluated by measuring the maximum bubble pressure for a liquid with known surface tension.)

There are several advantages of the maximum bubble pressure method: first of all, it is very simple and can be set up without using any sophisticated instruments. For instance, gas pressure can be measured with a simple glass U-tube filled with water, making it an inexpensive but relatively accurate method of measuring surface tension. By making measurements at different bubbling rates (e.g., ranging from forming a single bubble every few minutes to, say one bubble per second), one can get some information on the dependence of surface tension on time (sometimes referred to as *dynamic surface tension*). Since every consecutive bubble creates a new gas-liquid interface, the method is not sensitive to small amounts of impurities in the liquid studied.

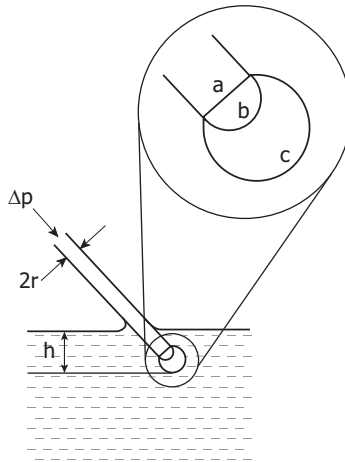


Figure 2.5 Maximum bubble pressure. Inset a: Flat interface, no pressure difference across the meniscus. Inset b: Hemispherical meniscus; radius of meniscus equals capillary radius (the smallest possible), resulting in maximum bubble pressure. Inset c: Unstable, spontaneously growing bubble; the pressure inside the bubble is lower than maximum because the radius of the meniscus is larger than the capillary radius.

2.3.3 Wilhelmy Plate Method

In this method, shown in Figure 2.6, a vertical plate of known perimeter is hooked up to a balance, and its weight is measured first in the air and then partially immersed in the liquid studied. The force registered by the balance f , corrected for the dry plate weight and its buoyancy, can be used to determine the liquid-gas tension or the contact angle from $f = 2l\gamma_{lg} \cos \theta$ (assuming the plate thickness is negligibly small compared to the plate width). If the contact angle θ of the liquid on the plate is zero (i.e., the plate is perfectly wettable by the liquid), the method yields the liquid surface tension. It can also be used to determine the contact angle θ for systems where the liquid surface tension is known.

This method is well suited for studying long-term changes of either contact angle or surface tension, as the plate can be suspended from an automatic recording balance and the measurements can be easily performed over a time scale of hours or days.

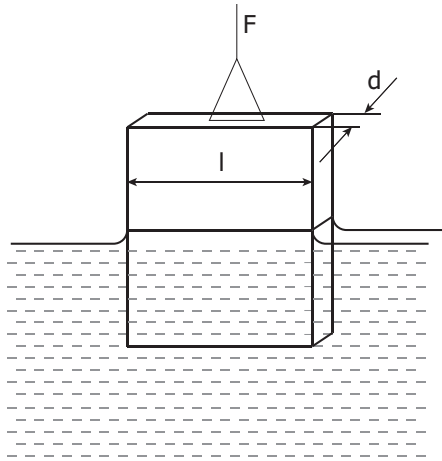


Figure 2.6 Wilhelmy plate method.

2.3.4 Du Noüy Ring Method

The Du Noüy ring method (Figure 2.7) is very similar to the Wilhelmy plate method. Instead of a vertical plate, a thin horizontal ring is suspended from a balance. The wetting properties of the ring have little impact on the results obtained using the ring method, in which a total pull f is measured. Surface tension is calculated from $f = 4\pi r \gamma_{l/g}$, where $2r$ is the ring diameter. It is assumed here that the diameter of the wire forming the ring is negligibly small compared to the ring diameter. The factor of 4 in the formula comes from the fact that we have to account for the pull by surface tension inside and outside of the ring (of $2\pi r$ perimeter). The ring method is often used for measuring interfacial tension (IFT) between two immiscible liquids. In this case, the ring is placed on the liquid-liquid interface and the pull required to break it from the liquid-liquid boundary is measured (corrected of course for its dry weight and buoyancy).

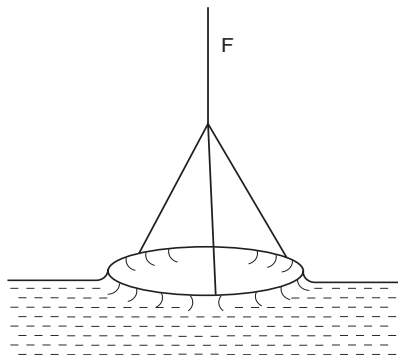


Figure 2.7 Du Noüy ring method.

2.3.5 Drop Shape Methods

A sessile drop on a plane surface assumes a shape that minimizes the sum of its potential energy due to gravity and the surface excess energy due to surface tension. The minimum surface energy corresponds to a spherical shape, while to attain a minimum of potential energy due to gravity, the drop needs to spread into a very thin layer on the substrate, which increases the surface energy of the drop. Obviously, there is an optimum shape between these two extrema that minimizes the total drop energy. Similarly, there is a shape that minimizes the total energy of a pendent drop. These shapes can be precisely calculated by numerically solving corresponding systems of partial differential equations (the Laplace problem). The droplet profile can be obtained by taking a photograph of the drop. Then, surface tension can be evaluated by fitting the recorded drop shape to the solution of the Laplace problem. There are several commercial apparatuses for making these types of measurements. They all acquire an image of the drop profile with a charge-coupled device (CCD) camera and fit the acquired shape to the Laplace shape using proprietary algorithms to yield surface or interfacial tension and contact angle information.

Both sessile and pendent drop methods are absolute (i.e., they do not require any calibration), and both use small amounts of liquid of known density, allow for easy temperature control, do not rely on detachment force measurements, and do not depend on contact angle. They are often used for studying aging effects and can be used for systems involving highly viscous liquids, such as crude oils and bitumen. The main and often-overlooked disadvantage of these methods is that for many systems, the droplet shape may not be Laplacian. This is almost always the case if the studied liquid contains solid particles such as clays. The solid fines can cover the drop surface and form a rigid skin, which makes attaining a Laplacian shape impossible.

2.3.6 Spinning Drop (or Spinning Bubble) Method

A gas bubble or a droplet of liquid is placed in a liquid of higher density in a tubular cell that can be rotated along its axis at up to 20 000 rpm. The centrifugal force pushes the denser fluid to the cell wall such that the inner drop becomes elongated. The lower the interfacial tension (IFT) between the two liquids, the greater the elongation of the inner droplet. Calculation of IFT from the droplet elongation involves solving the Laplace problem, similar to the procedure used in drop shape methods.

This method is especially useful for measuring very low IFTs. There are two restrictions: (i) the outer liquid must be transparent, such that the inner drop can be observed, and (ii) the inner drop of liquid must be of a lesser density than the outer, transparent one.

2.3.7 Drop Weight (or Volume) Method

When a liquid drains slowly from a tube, a drop is first formed at the end of the tube and grows steadily larger until its weight overcomes the surface tension forces, at which point it falls off. The drop weight at detachment can be written as $mg = V\rho g = 2\pi r\gamma f$, where m is the drop mass, g the acceleration due to gravity, V the drop volume, ρ the liquid density, and f a correction factor. The correction factor f is due to the fact that the drop, before falling, forms a neck with a diameter slightly smaller than the diameter of the tube. The correction factors were calculated for various experimental conditions (Harkins and Brown 1919). The drop weight can be estimated by weighing several drops or by counting the number of drops formed from a given volume of the liquid and its density. Both can be estimated with accuracy much better than 1 %, yielding highly precise surface or interfacial tension values. The equipment necessary for the drop weight method is simple and experiments are easy to perform. This method is not suitable for studying long-term aging effects and cannot be used for high-viscosity liquids.

2.3.8 Micropipette Methods

All of the methods of IFT measurement described above depend on the existence of a density difference between the two neighbouring liquids. However, the density difference between bitumen and water is very low within the temperature range of importance for the oil sands industry (0 °C to 100 °C) and vanishes to zero at about 45 °C (Takamura and Isaacs 1989). Therefore, to estimate bitumen-water IFT, a series of IFT measurements were performed for bitumen diluted with a light hydrocarbon solvent, and the data obtained were then extrapolated to zero dilution (Takamura and Isaacs 1989). Obviously, such a procedure introduces uncertainty that is inherently associated with extrapolation outside the data set range.

Recently, new methods were developed for IFT measurements on micron-sized emulsion droplets using suction micropipettes (Yeung, Dabros, and Masliyah 1998; Moran et al. 2000; Moran, Yeung, and Masliyah 1999). One of the methods is similar to the maximum bubble pressure method. However, instead of measuring the pressure required to form a bubble, the minimum pressure necessary to suck a droplet into the micron sized capillary is measured and converted to IFT using the Young-Laplace equation (Yeung, Dabros, and Masliyah 1998). The method can be used for density-matched systems. The limitation is that both liquids (i.e., the liquids forming the drop and the medium) have to be of relatively low viscosity, so that the pressure needed to cause the fluid to flow (when the droplet is sucked into a capillary) can be neglected in comparison with the Young-Laplace pressure.

In the second micropipette-based method (Moran, Yeung, and Masliyah 1999; Moran et al. 2000), an emulsion droplet is captured between two suction capillaries and elongated by pulling with one of the capillaries mounted on a micromanipulator. The second capillary is bent to form a cantilever, such that the force required to elongate

the droplet can be measured directly from the cantilever deflection. The droplet IFT is then calculated from force-drop deformation analysis, similar in principle to the analysis of the sessile or pendent drop shape in the gravity field.

The cantilever micropipette method of IFT measurement is the only one that allows for studies of systems with no density difference and involving high-viscosity liquids. As such, it is the only method capable of direct measurements of bitumen-water IFT (Moran et al. 2000). However, the method requires a relatively complicated experimental set-up that is not commercially available.

2.4 Methods of Measuring Contact Angle

2.4.1 On Flat Surfaces

Contact angle on flat surfaces can be determined from an image of a sessile drop taken with a camera or by using a contact angle goniometer. The latter is a device on which a drop is observed by a lunette equipped with a crosshair that can be aligned with the substrate and then with the drop profile line at the point of contact, allowing direct measurements of the angle between the two lines. As mentioned above, observations of sessile drop silhouette can be used for both contact angle and surface tension measurements.

2.4.2 On Powders

When the solid of interest is only available as powder, contact angle can be measured on a pellet pressed out of the powdered material. Although this approach is frequently used, the results are affected by the pellet porosity and inevitable substrate roughness. The contact angle can also be calculated from the pressure required to remove the liquid from a plug formed from the powder and saturated with investigated liquid using the Young-Laplace equation for capillary pressure (Bartell and Whitney 1932). The average pore size of the plug, which is necessary for calculations, can be estimated using commercial mercury porosimeters or from the flow rate–pressure relationship for a liquid perfectly wetting the porous plug. When the contact angle has a finite value and the solid particles are small, the powder will float on the surface of the liquid the same way water striders do. Knowing the particle size, density, and centrifugal force required to sink the particle, we can calculate the contact angle from the force balance (Huethorst and Leenaars 1990).

2.5 Adsorption

In Section 2.2, we determined that surface tension is a direct result of intermolecular interactions. The stronger the attractive forces acting between liquid molecules, the higher the surface tension of the liquid. If the liquid contains different molecules, or

in other words, if it is a mixture, some of the molecules will preferentially go to the interface such that there will be more of them at the interface than in the liquid bulk phase. This partition process, or preferential enrichment of the interfacial region as compared with the bulk, is called *adsorption*. Obviously, the molecules adsorbing at the interface must lower surface tension, and by doing so, lower the total internal energy of the system. In the next subsection, we will analyze the process of adsorption from a thermodynamic point of view. The important thing to remember is that the molecules that have the ability to lower surface tension spontaneously adsorb at interfaces. The driving force for adsorption is a decrease in the surface tension, which results in a decrease in the total energy of the system.

2.5.1 Thermodynamics of Adsorption

Rigorous thermodynamic description of the adsorption process was first provided by Gibbs.³ In the following section, we will briefly outline the main concepts of Gibbs' approach.

At the foundation of Gibbs' adsorption analysis are the concepts of dividing plane and surface excess. To better understand the problem, let us remember that in the three-dimensional bulk of any phase, we can easily define the concentration of any component (this being the number of moles of that component contained in a unit of volume). This is not so at the boundary between two phases, because such a boundary is, by its very nature, two-dimensional. The two-dimensional character of interfaces, combined with finite dimensions of atoms and molecules, does not allow us to apply the three-dimensional notion of concentration at the two-dimensional interface. The phase composition (concentrations of all components) and the density, which do not change from place to place in the bulk of neighbouring phases, *do* change across the phase boundary.

Although, say, a surface of water in a glass is clearly visible as a sharp boundary between the liquid and air, it is not easy to say where this boundary is located exactly if we consider it to be a plane in a mathematical sense, i.e., having a thickness equal to zero. As we cross the water-air interface, the density of the liquid water below the surface must change to the much lower density of air somewhere above the visible water surface. This change is sharp, occurring over a very small distance, but it has to be continuous, as Nature does not tolerate discontinuities well.

There are two ways of dealing with the problem. One is to define a surface region, or *surface phase*, of finite thickness, which is unknown, and apply the standard notion of concentration to the liquid below, the air above, and the interfacial region in-between. In the surface region, we can define, for instance, the surface concentration

³ J. Willard Gibbs (1839–1903) was one the greatest American scientists of all time. Gibbs, a professor of mathematical physics at Yale University, laid the theoretical foundation for chemical thermodynamics. Between 1876 and 1878, he published a series of papers on the analysis of multiphase systems, including a thermodynamic description of adsorption. In 1901, Gibbs was awarded the highest possible scientific honour of his day: the Copley Medal of the Royal Society of London. (The Nobel Prize, first awarded in 1901, gained its current distinction later.)

of component i as the number of moles of the component i in the surface region divided by the volume of the surface region. This is equivalent to taking an average value (within the surface region) of the parameter we want to define. The problem with this approach is that if we assume the surface region thickness to be too small, we may not totally encompass the region within which physical properties such as density or concentrations change. If we take it to be too large, we lose specifics related to the existence of the phase boundary. Therefore, we will still have problems with where exactly the boundaries of our surface phase should be located.

The second way of dealing with the problem was proposed by Gibbs and is described in more details below.

Gibbs' Surface Excess and Diving Plane Concepts

Let us put a mathematical plane, called Gibbs' dividing plane, somewhere near the visible boundary between phases α and β . At the moment, we are not concerned about the exact location of this plane, as long as it is close to the visible phase boundary (we will return to the dividing plane position a bit later). Let us, for instance, consider number bulk concentrations (number of moles of component i per unit of volume) in the two phases α and β (n_i^α and n_i^β), as shown in Figure 2.8.

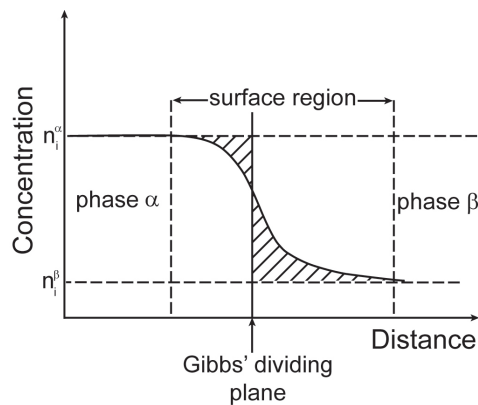


Figure 2.8 The concept of Gibbs' dividing plane.

The total number of moles of component i in the system can be calculated by integrating, over the distance, the continuous line depicting the continuously changing concentration. This is the true number of moles of component i in the system. The other way of calculating the total number of moles of the i -component is to multiply its bulk concentration in phase α by the volume of this phase (as specified by the position of the dividing plane), do the same for the phase β , and then add the two values together. The difference between the latter value and the true number of moles of component i in the system is called *surface excess*. It can be positive, negative, or zero, depending on how we place the hypothetical dividing plane. Looking at Figure 2.8, if the shaded area

left of the dividing plane is much smaller than the one on the right, surface excess of this particular component would be negative. This is because, by counting the number of moles based on bulk concentrations, we overestimate the true value by an amount proportional to the shaded area to the left of the dividing plane, and underestimate it by an amount proportional to the shaded area to the right of the dividing plane. For a single-component system, the placing of the dividing plane should be simple; there is no adsorption in a single-component system and we wish to calculate a true value, so we place the dividing plane such that surface excess is zero, or both shaded fields have the same areas. For a multi-component system, it is not so simple. Usually, we can easily single out one component of the system as the solvent in which the other components are dissolved. We can now place the dividing surface such that the surface excess for the solvent (usually water) is zero, and calculate surface excesses of all other components *relative* to the dividing surface placed in this unique way. This is the genius of Gibbs' approach. Now, without any ambiguity, we can strictly apply a rigorous thermodynamic analysis to describe the adsorption process.

Gibbs' Adsorption Equation

A general thermodynamics equation for the change in internal energy U of a system that allows an exchange of mass with the surroundings is

$$dU = TdS + \bar{d}W + \sum_i \mu_i dn_i \quad (2.10)$$

where T is absolute temperature, S is entropy, W is any type of work performed on the system, and μ_i and n_i are chemical potential and number of moles of the i^{th} component of the system, respectively. The bar over differential symbol $\bar{d}W$ denotes that the term is not a complete differential. This is a mathematical consequence of the fact that the performed work may depend on the path along which the system evolves from its initial to its final state, and not only on the difference between the initial and final states of the system.

Without dwelling on this mathematical nicety for too long, the types of work we need to consider are the volumetric work $-pdV$, the surface expansion work γdA , and the electrical work involved in charging of the interface $\psi_o dq$, where ψ_o is the surface electric potential and q the surface electric charge (we will discuss electric surface phenomena in the following sections). Eq. (2.10) thus becomes

$$dU = TdS - pdV + \gamma dA + \sum_i \mu_i dn_i \quad (2.11)$$

U , S , V , A , q , and n_i are known as extensive parameters, that is, their values depend on the size of the system. If we double the system size, the values of all extensive parameters will double as well. The overall change in the system energy dU is the sum

of the energy changes for phases α and β , and for the interface between them denoted with superscript s :

$$dU = dU^\alpha + dU^\beta + dU^s$$

For the neighbouring phases α and β , one can write

$$dU^\alpha = TdS^\alpha - pdV^\alpha + \sum_i \mu_i dn_i^\alpha$$

and

$$dU^\beta = TdS^\beta - pdV^\beta + \sum_i \mu_i dn_i^\beta$$

The energy change for the surface is

$$dU^s = TdS^s + \gamma dA + \psi dq + \sum_i \mu_i dn_i^s \quad (2.12)$$

In the above, all superscripted extensive parameters are defined following Gibbs' approach as described above. As such, the extensive parameters U^s , S^s , and n_i^s in Eq. (2.12) are *surface excess* in the Gibbs sense, which means that their numerical values depend on the location of the Gibbs dividing plane.

If one allows all extensive parameters (energy, entropy, area, surface charge, and number of moles) to increase from zero to any finite values, keeping intensive parameters (temperature, pressure, surface tension, surface potential, and chemical potentials) constant, Eq. (2.12) becomes

$$U^s = TS^s + \gamma A + \psi q + \sum_i \mu_i n_i^s,$$

which can be differentiated in the usual way, yielding

$$dU^s = TdS^s + S^s dT + \gamma dA + Ad\gamma + \psi dq + qd\psi + \sum_i \mu_i dn_i^s + \sum_i n_i^s d\mu_i \quad (2.13)$$

Comparison of Eqs. (2.12) and (2.13) gives

$$S^s dT + Ad\gamma + qd\psi + \sum_i n_i^s d\mu_i = 0 \quad (2.14)$$

For constant temperature and dividing both sides of Eq. (2.14) by surface area A , we finally obtain:

$$d\gamma = -\sigma d\psi - \sum_i \Gamma_i d\mu_i = -\sigma d\psi - RT \sum_i \Gamma_i d \ln a_i \quad (2.15)$$

where Γ_i is called Gibbs' surface excess of component i , σ is the surface charge density (charge per unit of area), and a_i is the activity of component i .

Eq. (2.15) is a general form of Gibb's adsorption equation, in which we included electric work connected with charging of the interface. When there is no electric work involved, or $d\psi = 0$, Eq. (2.15) takes the familiar form of

$$d\gamma = -RT \sum_i \Gamma_i d \ln a_i \quad (2.16)$$

As mentioned in the previous section, we can place Gibbs' dividing plane anywhere in the vicinity of the visible surface. In particular, we can place it in a position where, for a selected component i , $\Gamma_i = 0$. For a two-component system, composed of a diluted solution of a solute in a solvent, we can place Gibbs' dividing surface such that the solvent surface excess is zero. Then, substituting solute concentration for its activity, Eq. (2.16) takes the form

$$\Gamma = -\frac{1}{RT} \frac{d\gamma}{d \ln c} = -\frac{c}{RT} \frac{d\gamma}{dc} \quad (2.17)$$

For example, if we consider a diluted solution of ethyl alcohol (EtOH) in water, we will have

$$d\gamma = -RT(\Gamma_{\text{water}} d \ln a_{\text{water}} + \Gamma_{\text{EtOH}} d \ln a_{\text{EtOH}}).$$

Then, placing the dividing plane such that $\Gamma_{\text{water}} = 0$, we will have

$$\Gamma_{\text{EtOH}} = -\frac{1}{RT} \frac{d\gamma}{d \ln a_{\text{EtOH}}} \quad (2.18)$$

In this example, the value of the surface excess of ethanol, given by the above equation, has a strict and rigorous thermodynamic meaning. It is the surface excess of ethanol relative to such a position of the Gibbs dividing plane at which the surface excess of water is zero. This is the most common way of defining surface excess. For diluted ethanol solutions, ethanol activity a_{EtOH} can be replaced with its concentration c_{EtOH} yielding:

$$\Gamma_{EtOH} = -\frac{1}{RT} \frac{d\gamma}{d \ln c_{EtOH}} = -\frac{c_{EtOH}}{RT} \frac{d\gamma}{dc_{EtOH}}$$

In the latter, all variables on the right side of the equation can be determined experimentally, and the surface excess can be evaluated from the experimental data on surface tension dependence on concentration.

2.5.2 Adsorption Isotherms

Eq. (2.18) provides a relationship between four intensive variables needed to describe adsorption: surface excess (Γ), surface tension (γ), bulk activity of the adsorbing species (a), and temperature (T). Therefore, for a constant temperature, only two of these variables are independent and required in order to univocally describe adsorption. Depending on our choice, we may use

- a surface tension equation: $\gamma = \gamma(a)$,
- an adsorption isotherm: $\Gamma = \Gamma(a)$, or
- a surface equation of state: $\gamma = \gamma(\Gamma)$.

Each of the three relationships above describes adsorption in a binary system. Usually, we select the equation that provides a relationship between variables that can be easily measured under given experimental conditions. For instance, when dealing with adsorption on fluid interfaces, surface tension and concentration (or activity) are easily measurable. In the case of gas adsorption on a porous solid with a large surface area, such as activated carbon, gas pressure (which is related to gas activity) and surface excess are experimentally measurable. For Langmuir trough experiments with insoluble monolayers, both surface excess and surface tension are directly accessible.

For adsorption on liquid interfaces, we use the experimentally determined surface tension and, applying Gibbs' adsorption equation, we can calculate surface excess. Obviously, surface excess (which is a measure of the amount of the substance adsorbed) depends on the concentration of the substance of interest in the solution. The amount adsorbed increases with increasing concentration. The function linking the two quantities is called the adsorption isotherm. Below, we will discuss a few common adsorption isotherms.

Langmuir's Adsorption Isotherm

Derivation of the Langmuir adsorption is based on the assumption that individual molecules adsorb on distinct adsorption sites at the interface, and that all of these sites are identical in all aspects; in particular, they all have the same adsorption energy.

Since the number of the adsorption sites is finite, there is also a maximum value for the surface excess, or the maximum possible amount of adsorbed material, Γ_{∞} .

The rate of adsorption, v_{ads} , is proportional to the concentration of adsorbing molecules, c , and to the area of the surface not yet covered with adsorbing molecules. It can be written as:

$$v_{ads} = k_{ads}(\Gamma_{\infty} - \Gamma)c$$

while the rate of desorption, v_{des} , is proportional to

$$v_{des} = k_{des}\Gamma$$

In the equilibrium, adsorption and desorption rates must be equal ($v_{ads} = v_{des}$), yielding the following formula for the Langmuir isotherm:

$$\Gamma = \Gamma_{\infty} \frac{Kc}{1 + Kc} \quad (2.19)$$

where the equilibrium constant K is given by the ratio of adsorption to desorption rate constants, $K = k_{ads}/k_{des}$

Figure 2.9 shows the plot of Langmuir's adsorption isotherm (Eq. 2.19) in the form of surface coverage $\theta = \Gamma/\Gamma_{\infty}$ as a function of concentration normalized to $1/K$. The saturating character of Langmuir adsorption is clearly visible.

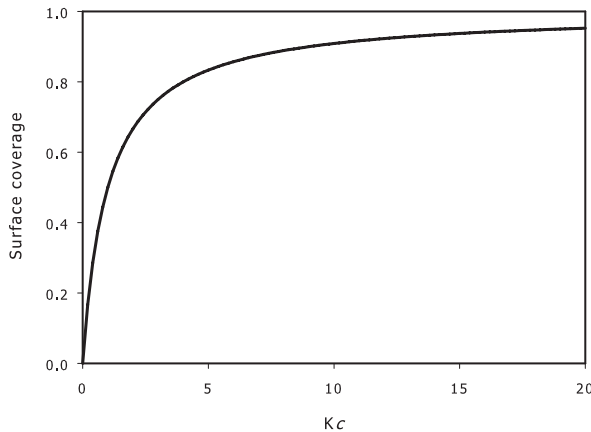


Figure 2.9 Plot of Langmuir adsorption isotherm.

The BET Isotherm

In the case of a gas adsorbing on a porous solid of a high surface area, it is quite common for the adsorbing gas to form multilayered coverage on the solid. Often, the adsorbing gas fills the pores with condensed liquid. Adsorption of gases on solids is important for heterogeneous catalysis, among other applications. In these relatively common cases, the Langmuir isotherm, which assumes monolayer adsorption, is obviously not valid. In 1938, S. Brunauer, P. Emmett, and E. Teller derived a model isotherm allowing for multilayered adsorption.⁴ This is known as the BET isotherm, after the first letters of the inventors' names. The key assumption for the BET isotherm is that the first layer of adsorbed molecules follows the Langmuir model. It is further assumed that the adsorption energy for every layer except the first is the same and equal to the heat of condensation of the adsorbing gas into a liquid. In other words, it is assumed that the gas adsorbs in the first layer following the Langmuir model, and the consecutive layers condensate on the first layer formed as if it were a bulk. Since the BET isotherm describes the adsorption of gases, it is often written in the following form:

$$\frac{V}{V_m} = \frac{k\varphi}{(1-\varphi)[1+(k-1)\varphi]} \quad (2.20)$$

In the above equation, V is the volume of gas adsorbed per unit mass of solid, V_m is the volume of gas needed to form a complete monolayer on the solid, k is a constant, and φ is equal to p/p_s , where p is the gas partial pressure and p_s is the equilibrium vapour pressure at the experimental temperature. The shape of the BET isotherm is shown in Figure 2.10 (indicated in the figure by a solid line). Note that Langmuir's isotherm (dashed line) would eventually approach the value of 1. With this in mind, we see that for low partial pressure of the gas, the adsorption initially follows Langmuir's isotherm, implying the formation of a monolayer. Then, at higher gas pressures, multilayered adsorption takes place, accounting for the deviation of the BET from Langmuir's isotherm.

⁴ Stephen Brunauer, born in Hungary and educated in the US, received his PhD at Johns Hopkins University in 1933 for his work on nitrogen adsorption on an iron ammonia catalyst. This work was the starting point for the derivation of the BET isotherm with Paul Emmett and Edward Teller. Brunauer was the first director of the famous Clarkson Institute of Colloid and Surface Chemistry at Clarkson University in Potsdam, N.Y. Paul Emmett was the Chair of Chemical Engineering at Johns Hopkins and a member of the Manhattan Project, where he contributed significantly to the uranium enrichment technique. Edward Teller, another Hungarian émigré, became famous as the father of the US hydrogen bomb. He was a co-founder of the Lawrence Livermore National Laboratory. He was also known for his support of controversial military and civilian applications of nuclear energy.

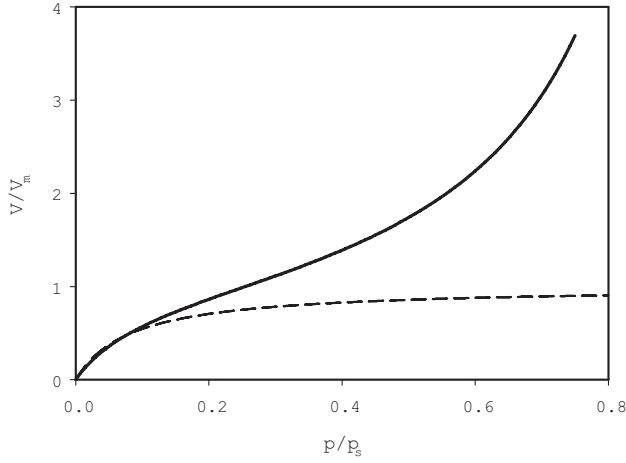


Figure 2.10 BET adsorption isotherm, indicated by the solid line (dashed line represents Langmuir's isotherm).

The BET isotherm is frequently used for measuring specific surface area of catalysts, powders, and porous adsorbents. For that purpose, Eq. (2.20) is rearranged to the form

$$\frac{\varphi}{V(1-\varphi)} = \frac{1}{kV_m} + \frac{(k-1)\varphi}{kV_m}$$

Plotting experimental data as $\varphi/[V(1-\varphi)]$ against φ , the values of constants k and V_m can be evaluated from the slope and intercept of the plot obtained. Since V_m is the volume of gas needed to form a monolayer, knowing the molecular cross-section area of the gas, we can calculate the solid surface area. This is the reason for the importance of the BET isotherm, as it is the most frequently used procedure for measuring the surface area of solids. Numerous commercial instruments are available for this purpose.

Henry's Isotherm

For very small values of c , the term Kc in Eq. (2.19) can be neglected in comparison with 1, yielding

$$\Gamma = \Gamma_{\infty} Kc = k_H c \quad (2.21)$$

and indicating a linear relationship between surface excess and bulk concentration. k_H in the above equation is Henry's constant, equal to the limiting slope of the plot

of adsorption versus concentration at a concentration approaching zero. This type of isotherm is called Henry's isotherm, and is always applicable in very diluted systems.

2.6 Electric Surface Phenomena

All surfaces between phases are electrically charged. This has numerous important consequences that will be discussed in more detail in this section. Let us start with the origin of surface charge and some basic concepts. This will be followed by a review of electrokinetic phenomena and measurements of the so-called *zeta potential* (ζ).

2.6.1 Origins of Surface Charge

There are several mechanisms contributing to the formation of electrical charges on boundaries between various phases. Although the mechanisms described below can be involved at boundaries between any phases, let us, for the sake of simplicity, consider a boundary between a solid and an aqueous phase containing dissolved substances. One common source of surface charge is the adsorption of ions from a neighbouring solution on an initially uncharged solid surface. Another common mechanism is the dissociation of surface groups. Orientation of adsorbed molecules with a permanent dipole moment can also contribute to surface charge. Here, we are mostly interested in bitumen extraction from oil sands, where most, if not all, processes of interest are occurring at boundaries between water and oil; various solid phases and water or oil; or air bubbles and the phases mentioned before. In most cases, water is one of the phases of interest, so we will begin with a water-solid interface to analyze the origin of the surface charge on the solid.

Let us take a silica sand grain immersed in water. In the following chemical equation, the symbol $(\text{SiO}_2)_s$ indicates that the following chemical species is either adsorbed at the solid surface or is an integral part of the solid surface:



The equation above indicates that silica at the sand grain surface reacts with water, forming silicic acid, which in turn dissociates, forming a silicic anion at the surface and a hydrogen ion that diffuses off into the solution. This chain of events negatively charges the solid surface, as the diffusing H^+ ion carries away a positive charge and leaves the negative charge behind. Since all of these steps are reversible, and since the last step produces hydrogen ions in the bulk of the solution, the surface charge is sensitive to the bulk pH value. At high pH, i.e., at low concentration of H^+ ions, the equilibrium is shifted to the right, resulting in a higher negative charge of the silica surface. At low pH, the opposite is true, and the surface is positively charged.

Obviously, somewhere in between, there is a point (at a certain pH value) at which the net surface charge is zero. This point is called the *point of zero charge* (PZC).

The above mechanism is a simplified picture of the physics involved. In reality, silicon dioxide and water form a large family of chemical compounds. The simplest of them, shown in the example above, is metasilicic acid, H_2SiO_3 . Attaching one more water molecule to it yields orthosilicic acid, H_4SiO_4 . Attaching another SiO_2 molecule to metasilicic acid produces disilicic acid, $\text{H}_2\text{Si}_2\text{O}_5$; adding two waters to the latter yields pyrosilicic acid, $\text{H}_6\text{Si}_2\text{O}_7$; and so on. The general formula for silica-water compounds is $[\text{SiO}_x(\text{OH})_{4-2x}]_n$. The simplest forms of these compounds can be identified in dilute aqueous solutions. However, in the solid state, they are all likely condensed into a form of an inorganic polymer of a complex chemical structure. One may think of a sand grain in water as being covered with a mixture of polymeric silicic acids at various hydration levels. Complete removal of these hydrating water molecules is very difficult. Water can still be detected on silica by IR spectroscopy, even after prolonged heating. Regardless of the exact chemical composition of the surface layer, our sand grain is able to exchange hydrogen and hydroxyl ions with the water phase, resulting in a net surface charge that is a function of pH, as discussed above.

Similar mechanisms are involved in the charging of all oxide-type minerals, e.g., clays, alumina, and many others. Some oxides may not be capable of forming inorganic polymers, but all are able to exchange either hydroxyl or hydrogen ions with the aqueous phase, making their surface charge a function of pH.

The dependence of the surface charge on pH makes it possible to experimentally determine not only PZC, but also the total surface charge and, if the total surface area is known, surface charge density. The procedure is relatively simple: Let us suppose that we want to determine the surface charge on clay particles suspended in water. First, we take a volume of deionized (DI) water, (for example, 100 ml). DI water should have pH close to 7. Next, we add a certain volume of an acid, for example, 0.001 M HCl, and measure pH again. As we add acid to the water, its pH decreases, as seen in Figure 2.11 (dashed line). Starting from a new DI water sample, we can repeat the titration process with a base such as NaOH. Adding caustic will increase the pH of the water. By following this process, we receive a titration curve for water, showing a pH of the water as a function of the amount of added acid or base (dashed line in the figure). We can now disperse our clay in the DI water (for example, 10 g of clay in 100 ml of DI water) and titrate the clay suspension with both acid and base. The titration curve for the clay suspension is indicated in Figure 2.11 by a solid line. We can now look at the differences between the amounts of acid (or base) required to bring the clay suspension to the same pH value as the clean DI water. In Figure 2.11, an arrow shows this difference at pH = 5. This difference corresponds to the amount of the hydrogen ions (from the added acid) consumed by the clay. Those ions are removed from water and do not contribute to lowering its pH. Instead, they make the clay surface more positively charged. We can thus calculate the clay surface charge from the amount of hydrogen ions consumed by the clay. If we also know the total

surface area of the clay, for instance from BET adsorption method, we can calculate surface charge density. We can also see that, at a pH of about 8.5, the two curves intersect. At this pH, there is no excess base or acid required to bring the pH of the suspension to the same value as that of water;⁵ therefore, the clay surface charge at this point is zero (Kosmulski 2001).

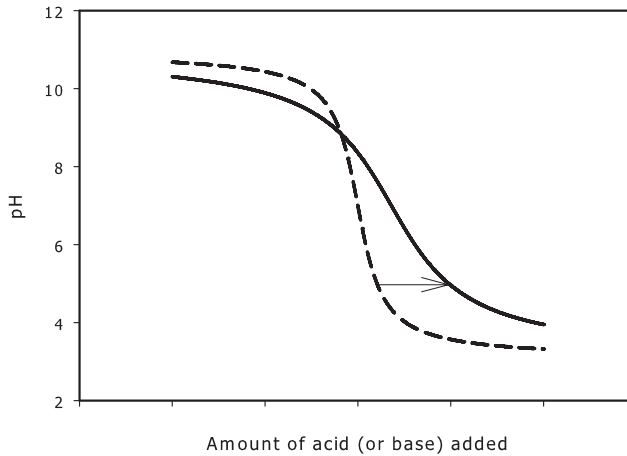


Figure 2.11 Determination of point of zero charge (PZC) by titration of a colloidal suspension.

2.6.2 Electrical Double Layer

Regardless the origin of surface charge on a solid surface, the system of the solid and the solution in contact with the solid must remain electrically neutral. Therefore, not only is a solid particle immersed in water charged, but the water itself also carries an electric charge, equal in value and opposite in sign to the charge on the solid particle. In essence, we have a charge separation, with the system as a whole remaining electrically neutral. When the solid is negatively charged, as most solid particles in water under moderate conditions are, the aqueous phase is charged positively, and the absolute values of both charges are the same. A negatively charged solid attracts positive ions in the solution and repels negative ions, such that in the vicinity of a negatively charged solid, there is a net excess of positive charge.

⁵ The suspended solids may alter the water pH a little, as most oxides exhibit either acidic (e.g., silica) or basic (e.g., alumina) characteristics. To correct for this, the suspension is titrated in a solution of an inert electrolyte (e.g., NaClO_4) instead of water. Titrations at different concentrations of added inert electrolyte yield a family of curves all intersecting at PZC.

The charge on the surface and the charge in the solution form a system of charges called the *electric double layer*. This layer is similar to a capacitor, where one plate is charged negatively and the other positively. Indeed, one of the first theoretical models of a double layer (developed by Helmholtz in late nineteenth century) assumed a condenser-like structure, consisting of a rigid layer of positive ions (cations) adsorbed on a negatively charged solid surface. The Helmholtz model explained some experimental observations, but it was too simplistic. Obviously, since ions can move in a solution, thermal movements of water molecules would disturb a rigid ionic layer on the solid surface. Indeed, we have to consider two competing forces: one is the electric attraction of counter-ions and repulsion of co-ions by the charged interface, and the other is the force that results from thermal molecular motions that tends to disarray any ordering caused by electric forces. At equilibrium, the layer of ions in the solution is diffuse in nature, and the probability of finding a counter-ion near the surface is larger than the probability of finding a co-ion. Both probabilities converge to the same value at a large distance from the charged surface, where the net ionic charge is zero. Figure 2.12 shows the distribution of charge-carrying ions in the vicinity of a charged interface.

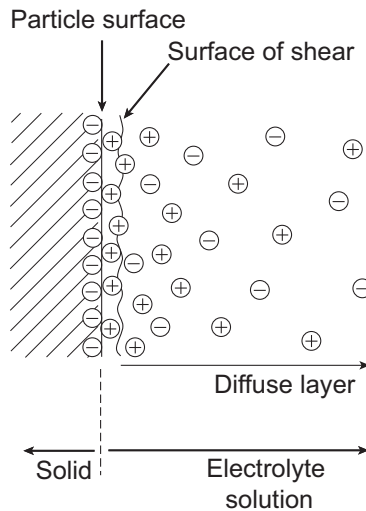


Figure 2.12 Electrical double layer.

For our following discussion of electrokinetic phenomena, it is important to note that the ions form a diffuse layer in the vicinity of a charged interface. This layer carries a net charge equal in value and opposite in sign to the charge of the solid surface, such that the system as a whole is electrically neutral. The diffuse layer is mobile in the sense that the ions contained in it can be carried away with the liquid if there is a liquid flow parallel to the solid surface. This carrying away of ions from the electric double layer results in charge separation on a macroscopic length scale, which is the source of the important and interesting electrokinetic phenomena that we will discuss below.

We mentioned above that electric double layer is similar to a capacitor. The capacity of the electric double layer can be measured experimentally, and such measurements are one of the important tools used in studying the structure of the electrical double layer.

2.6.3 Theory of Electrical Double Layer Structure

As mentioned above, the electric double layer consists of the electric charge on the solid surface and the charged ions in the solution. Additionally, some of these ions can be adsorbed on the solid surface, altering the effective surface charge. Ions in the solution, forming the so-called diffuse part of the double layer, are influenced by electric interaction with the charged surface and by random thermal movements (Masliyah and Bhattacharjee 2006).

Let us first consider the structure of the diffuse part of the electric double layer. The simplest theoretical description of the diffuse double layer was given by Gouy and Chapman at the beginning of the twentieth century. It was based on several simplifying assumptions. First, the solid surface was assumed to be flat, infinite, and uniformly charged. Second, the ions in the solution were assumed to be point charges (the finite dimensions of ions were neglected), and it was assumed that the spatial distribution of ions could be described by Boltzmann's statistical theory. Third, it was assumed that the liquid is a continuous medium, characterized by the dielectric constant ϵ (i.e., the discrete molecular structure of the liquid was neglected). Let us briefly review the thought process involved in solving this problem.

We will attempt to calculate the electric potential ψ in the solution as a function of a distance x from the solid surface. For a positively charged solid, cations will be repelled from the surface and anions will be attracted. Applying Boltzmann's statistics, ion concentration at any point at a distance x will be given by $n_i = n_i^o \exp(z_i e \psi(x)/kT)$. Here, n_i^o is the bulk concentration of i -type ions, z_i is their valency, e is the elementary charge, k is the Boltzmann constant, and T is the absolute temperature. The net free charge density ρ at any point is:

$$\rho = \sum_i z_i e n_i = \sum_i z_i e n_i^o \exp\left(-\frac{z_i e \psi}{kT}\right) \quad (2.22)$$

The above equation links the charge density ρ with potential ψ at any point in the vicinity of a charged surface. Both ρ and ψ are a priori unknown functions of the distance x . We thus have one equation with two unknown functions. In order to solve the Boltzmann equation (Eq. 2.22), we have to find another formula linking ρ and ψ . They are related to each other by Poisson's equation, which, for a flat surface, takes the form

$$\frac{\partial^2 \Psi}{\partial x^2} = -\frac{\rho}{\epsilon} \quad (2.23)$$

In the previous equation, ε is the permittivity of the medium ($\varepsilon = \varepsilon_r \cdot \varepsilon_o$, where ε_r is a dimensionless relative dielectric constant of the medium, and ε_o is the electric permittivity of free space or a vacuum equal to $8.854 \cdot 10^{-12}$ F/m, also known in the SI system as electric constant). Combining Boltzmann and Poisson's equations yields

$$\frac{\partial^2 \psi}{\partial x^2} = -\frac{e}{\varepsilon} \sum_i z_i n_i^o \exp\left(-\frac{z_i e \psi_i}{kT}\right) \quad (2.24)$$

The above partial differential equation can be solved with boundary conditions of

$$\begin{aligned} \psi &= \psi_o & \text{at } x &= 0 \\ \psi &= 0 \text{ and } d\psi/dx = 0 & \text{at } x &= \infty, \end{aligned}$$

yielding electric potential in the solution as a function of the distance from the charged solid surface. The solution, which is a lengthy expression, can be markedly simplified for low values of surface potential ψ_o , i.e., for $ze\psi_o/kT \ll 1$. Under this condition, the exponential function in the Boltzmann equation can be expanded into a power series, and after neglecting higher expansion elements, the solution to such a linearized Poisson-Boltzmann equation is

$$\psi = \psi_o \exp(-\kappa x) \quad (2.25)$$

where κ is a constant which depends on the electrolyte composition and temperature:

$$\kappa = \sqrt{\left(\frac{e^2}{\varepsilon kT}\right) \sum_i z_i^2 n_i^o} = \sqrt{\left(\frac{e^2}{\varepsilon kT}\right) \sum_i z_i^2 c_i N_A} \quad (2.26)$$

In Eq. (2.26), N_A is the Avogadro number and c_i is the molar concentration of an i -type ion.

κ , called the Debye parameter, is a very important quantity. Forces between colloidal particles, resulting from their electric charge, can only be important when the potential ψ , given by Eq. (2.25), has a significant value. As follows from the equation, this potential decays exponentially with the distance from the charged surface, with a characteristic scale of $1/\kappa$, which has a dimension of length. The value of $1/\kappa$ is often called electric double layer thickness. It gives a rough estimation of the distance at which electric interactions have to be considered. We will return to this point later, in Section 2.7, while discussing surface forces and DLVO theory of colloid stability.

Figure 2.13 shows the plots of electric potential (normalized to surface potential ψ_o) in the double layer as calculated according to Eq. (2.25). When the distance from the charged surface is equal to $1/\kappa$, then, according to Eq. (2.25), the potential in

the double layer drops to the value of $\psi_0/2.72$ (2.72 being the approximate value of the natural logarithm base, equal to 2.71828...). A solid horizontal line is drawn at $\psi/\psi_0 = 1/2.72 \approx 0.368$; it intersects the potential vs. distance curves at points with abscissae at the corresponding $1/\kappa$ (or double layer thickness) values. One can compare these abscissae with the values listed in Table 2.1. It is easily seen that the double layer thickness strongly depends on the electrolyte concentration. It can also be observed that the term *double layer thickness* is perhaps a misnomer, as the double layer extends well beyond this point. However, as we will see in a moment, there is some justification for the use of this term (besides simply for the sake of tradition).

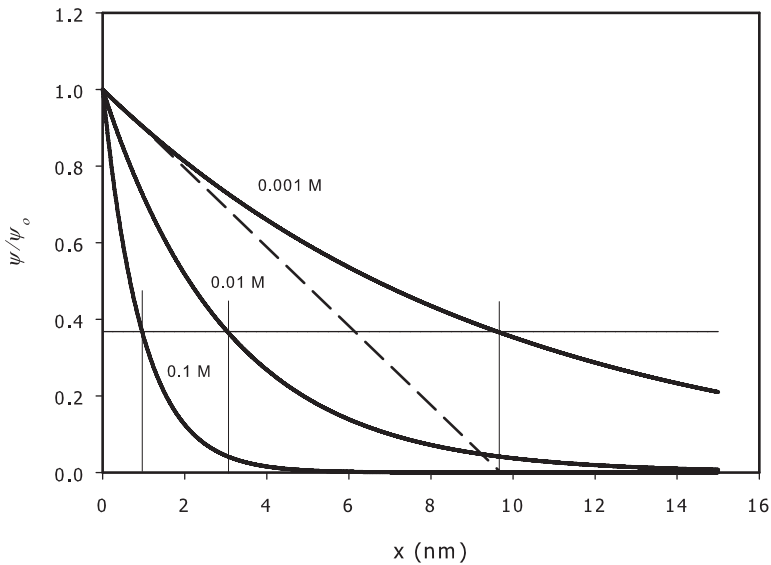


Figure 2.13 Electric potential in the double layer as function of distance from charged interface for different 1:1 electrolyte concentrations.

Surface potential ψ_0 can be related to the surface charge density σ_0 at the solid surface. From the electroneutrality condition, the total charge of the double layer is equal in value (and opposite in sign) to the charge at the surface: $\sigma_0 = -\int_0^{\infty} \rho dx$. Again, applying the Boltzmann distribution, and at low surface potential values, the resulting approximate formula is quite simple:

$$\sigma_0 = \epsilon \kappa \psi_0 \quad (2.27)$$

The above formula (Eq. 2.27) implies that the surface potential ψ_0 depends on both surface charge density σ_0 and, through κ , on the electrolyte composition. If electrolyte concentration is increased, κ increases according to Eq. (2.26). At constant

surface charge, the surface potential ψ_0 must therefore decrease, or, at constant surface potential, the surface charge σ_0 must increase. In most real systems, both surface charge and surface potential change when the electrolyte concentration is altered.

If the double layer is considered to be a simple plane capacitor, then, from Eq. (2.27), it follows that its capacitance (capacity for unit plate area) is equal to $\epsilon\kappa$, or that the distance between the capacitor plates is $1/\kappa$. The dashed line in Figure 2.13 shows the electrical potential inside such a capacitor for the case of a double layer in 0.001 M 1:1 electrolyte. Note an interesting feature of this line. It is tangent to the electric potential in a diffuse double layer, as described by Eq. (2.25), at $x = 0$. Indeed, from Eq. (2.25) we have

$$(d\psi/dx)_{x=0} = (d(\psi_0 \exp(-\kappa x))/dx)_{x=0} = -\psi_0\kappa$$

Obviously, this tangent line intersects the x-axis at $x = 1/\kappa$. In summary, the capacity of the diffuse double layer is equal to the capacity of a plane capacitor with the distance between the plates equal to $1/\kappa$. This is another reason why $1/\kappa$ can be considered to be the ‘thickness’ of the electric double layer.

Numerical values of the Debye parameter κ and double layer thickness $1/\kappa$ are listed in Table 2.3 for symmetrical electrolytes of different valencies and concentrations. We see that double layer thickness decreases as the concentration or electrolyte valency increases. The capacity of the double layer capacitor increases as the double layer thickness decreases, attaining a high electric charge storage capacity for high electrolyte concentrations. This is the physical basis for the so-called super capacitors, one of the devices proposed for storage of electric energy in ‘green’ vehicles.

Table 2.3 Values of electric double layer thickness $1/\kappa$ for aqueous solutions at 25 °C

Molarity[mole/L]	Valency	Debye parameter κ [m ⁻¹]	Double layer thickness $1/\kappa$ [m]
0.001	1:1	$1.0 \cdot 10^8$	$9.7 \cdot 10^{-9}$
	2:2	$2.1 \cdot 10^8$	$4.9 \cdot 10^{-9}$
	3:3	$3.1 \cdot 10^8$	$3.2 \cdot 10^{-9}$
0.01	1:1	$3.3 \cdot 10^8$	$3.1 \cdot 10^{-9}$
	2:2	$6.5 \cdot 10^8$	$1.5 \cdot 10^{-9}$
	3:3	$9.9 \cdot 10^8$	$1.0 \cdot 10^{-9}$
0.1	1:1	$9.8 \cdot 10^8$	$9.7 \cdot 10^{-10}$
	2:2	$2.1 \cdot 10^9$	$4.9 \cdot 10^{-10}$
	3:3	$3.1 \cdot 10^9$	$3.2 \cdot 10^{-10}$

2.6.4 Electrokinetic Phenomena

One of the consequences of the existence of the electric double layer discussed in the previous section is a family of four events known as *electrokinetic phenomena*. The ions forming the diffuse part of the double layer can freely move with the liquid phase.

A liquid flowing relative to a solid surface, like a liquid flowing through a capillary, shears away the ions forming the double layer, causing charge separation and a rise of electric potential. Similarly, the application of an electric field to a dispersed system will cause movements of ions. The moving ions drag the liquid with them, causing the flow of a liquid relative to solid surfaces. The four different electrokinetic phenomena are listed and briefly described in Table 2.4.

Table 2.4 Types of electrokinetic phenomena

Phenomenon	Stationary phase	Mobile phase	Description	Applications
Electrophoresis	Liquid	Solid	Movement of solid particles in a liquid medium is induced by an externally applied electric field.	Determination of ‘zeta potential’ and surface charge. Separation of proteins, with numerous applications in biology, medicine, clinical chemistry, and molecular biology.
Sedimentation potential	Liquid	Solid	Sedimenting solid particles under the influence of gravity results in the creation of a vertical potential gradient.	Since the velocities of falling particles are low, the resulting potential differences are very small and difficult to measure. There are no important applications of this effect.
Streaming potential	Solid	Liquid	An electric potential difference is created when an applied pressure causes liquid to flow through a plug of a porous solid.	Determination of ‘zeta potential’ and surface charge. This phenomenon is responsible for the charge separation that occurs when a hydrocarbon fuel is pumped through a hose. Since hydrocarbons have low electric conductance, the resulting potential may reach high values up to a spark discharge, a potential source of fuel ignition.
Electro-osmosis	Solid	Liquid	A flow of a liquid through a porous plug is induced by an externally applied electric field.	Electro-osmosis has been used for decades to dewater soil under architectural monuments for foundation stabilization. Modern applications include pumps in microfluidic devices, capable of delivering high pressure and large volumetric flows.

Electrophoresis

Electrophoresis is the most important of the electrokinetic phenomena, having the greatest practical applicability. It is the movement of solid particles suspended in a liquid under the influence of an applied electric field. Usually, electrophoresis is observed in a thin, rectangular, horizontal glass cell with two electrodes at each end, as shown in Figure 2.14. After connecting the electrodes to an electric power supply, the movements of suspended particles can be observed and their velocities measured under a microscope.

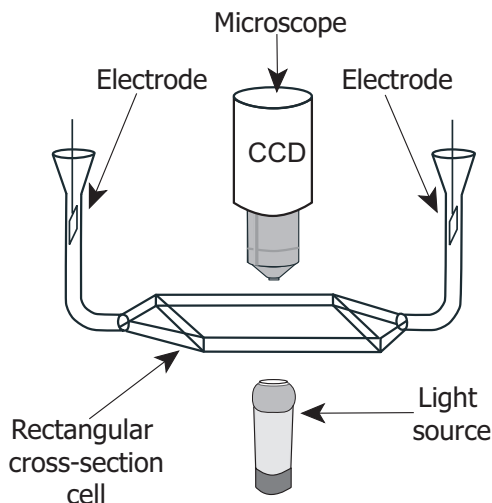


Figure 2.14 Electrophoresis cell.

Particle velocity is proportional to the applied electric field strength $v = \mu_e E$, where μ_e is the particle electrophoretic mobility (or particle velocity in a field of unit strength). The most well-known theory of electrophoresis was developed by Polish physicist Marian Smoluchowski in 1903. According to Smoluchowski's theory, valid for $\kappa a \gg 1$ (where κ is the Debye parameter defined by Eq. (2.26) and a is the particle radius), the electrophoretic mobility can be written as:

$$\mu_e = \frac{\varepsilon \zeta}{\eta} \quad (2.28)$$

where ε is the electric permittivity of the medium, η is the liquid dynamic viscosity, and ζ is an electric potential at a plane where the liquid starts moving relative to the solid particle (the plane of shear or slip plane). It is generally referred to as zeta potential. The physical meaning of zeta potential will be discussed briefly below. For the time being, let us note that it is the closest measurable approximation of the surface potential ψ_o , which itself cannot be measured.

The validity condition of Smoluchowski's theory, $\kappa a \gg 1$, simply implies that the particle size is much larger than the double layer thickness $1/\kappa$. In practical terms,

the Smoluchowski theory is valid for particles larger than, say, 0.1 μm suspended in water, where double layer thickness is of an order of several nanometres. For nanometre-sized particles in water-based media, i.e., for $\kappa a < 1$, the corresponding expression for electrophoretic mobility was developed by Hückel in 1924:

$$\mu_e = \frac{2\varepsilon\zeta}{3\eta} \quad (2.29)$$

Electrophoresis is probably the most commonly used method for zeta potential determination, as will be discussed in Section 2.6.5.

Streaming Potential

Streaming potential is a phenomenon where an electric potential difference is created as a result of the flow of a liquid through a porous plug or a channel. The liquid flow is usually induced by applying a pressure difference across the plug. The flowing liquid carries away the diffuse part of the electric double layer outside the slip plane, resulting in electric charge separation. This charge separation gives rise to the potential difference across the plug. In well-defined geometries, streaming potential is a convenient way of measuring the zeta potential of various solids, an important quantity in colloid and interface science as well as in mineral processing.

The buildup of potential difference across an orifice (or a porous plug) induces a flow of electric current, compensating the charge separation and, under most conditions, preventing the streaming potential from reaching high values. However, when the liquid has very low electric conductivity, as is the case of liquid hydrocarbons, the streaming potential may reach a value high enough to cause a spark discharge. Needless to say, this can be a source of ignition. This mechanism has been the cause of a number of industrial fires that took place during the pumping of hydrocarbon fuels like gasoline. Short-circuiting the fueling hose nozzle with the receiving tank or grounding both prevents the charge buildup and alleviates the associated danger.

Electro-osmosis

Electro-osmosis is the flow of a liquid through a channel, porous plug, or membrane, caused by the application of an electric field. Early applications of this phenomenon were in dewatering of soil and in the stabilization of foundations of architectural monuments. In recent times, there has been a great deal of interest in using electro-osmosis to create liquid flow in microfluidic devices, where a flow of several millilitres per second, and pressures of up to hundreds of atmospheres, can be achieved. Electro-osmosis is involved in ion transport through membranes in fuel cells. It is also likely involved in plant biology as one of the mechanisms of water transport through phloem, the innermost layer of tree bark.

Sedimentation Potential

In the last of the electrokinetic phenomena, solid particles, sedimenting through a liquid under the influence of gravity, give rise to an electric potential in the sedimentation column, called *sedimentation potential*. Since small particles sediment slowly, the absolute values of sedimentation potential are very low. So far, there have been no practical applications of this effect.

2.6.5 Zeta Potential

Figure 2.15 shows a typical electric potential distribution near the surface of a large, charged solid particle immersed in an aqueous electrolyte solution. The plot in the figure is reproduced from Figure 2.13 for the case of 0.001 M 1:1 electrolyte. According to Eq. (2.25), the potential decays exponentially with distance x with a characteristic length of $1/\kappa$. As discussed before, the initial slope of the $\psi(x)$ curve, i.e., $(d\psi/dx)_{x=0}$ is equal to $-\psi_0\kappa$; thus, the line tangent to the $\psi(x)$ curve at $x=0$ (dotted line in the figure) intersects the x -axis at a distance of $1/\kappa$ or at the double layer thickness. The problem is that surface potential ψ_0 cannot be measured experimentally, nor calculated from other measurable data. This is because we can only measure potential differences between points *within a single phase*. Let us consider the following example: we would like to estimate the surface potential of a solid immersed in a solution. We connect the solid to a voltmeter with an electric lead. Any attempt to measure the potential difference between the solid and the solution would inevitably require inserting into the solution another lead, to be connected to the second terminal of the measuring device. This introduces a new interface to the system, namely that between the lead and the solution with its own surface potential. Therefore, neglecting all other interface boundaries in our system, we would only be able to measure the sum of the surface potentials mentioned above.

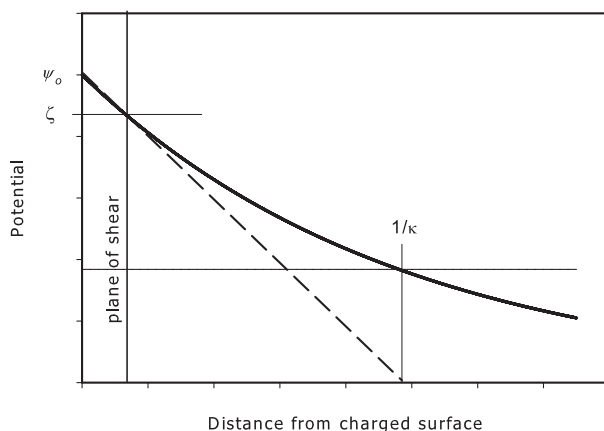


Figure 2.15 Zeta potential.

In the previous section, we saw that measurement of electrokinetic phenomena yields zeta potential (ζ), i.e., a potential on a slip plane, which is located very close to the solid particle surface. Therefore, zeta potential (which we can measure) has a value close to that of surface potential (ψ_0) (which cannot be measured experimentally). Because of this, zeta potential is a very important characteristic of colloidal particles, and is used in place of the immeasurable surface potential. As we have discussed, electrokinetic phenomena are often used to experimentally determine the value of zeta potential. For dilute colloidal dispersions, the most convenient way to evaluate zeta potential is to measure electrophoretic mobility of suspended particles or droplets. When the dispersed particles are coarse, such that they sediment off the suspension quickly, electrophoretic mobility measurements are impossible. In such situations, one can measure streaming potential across a plug made of the dispersed phase while forcing the liquid to flow through the plug under known pressure. Both approaches are used frequently.

Many commercial instruments to measure potential zeta are available. Most of them use automatic measurements of electrophoretic mobility. Particle velocities are calculated by illuminating the particles with a monochromatic laser light and measuring the Doppler shift of the reflected light. Other electrophoretic instruments use image analysis. The channel with the investigated sample is observed with a charge-coupled device (CCD) camera, and a particular particle or a cluster of particles is followed for a certain time, such that the particle velocity can be evaluated from the particle displacement. Some modern instruments measure the mobilities of a large number of suspended particles, providing a histogram of zeta potential values instead of its average. These are especially useful for studies of such phenomena as slime coating formation on bitumen droplets, which will be described in detail in Chapter 6.

2.7 Surface Forces

Surface forces act at boundaries of different phases. They are of a very short range, somewhat larger than molecular dimensions, and are the source of many important phenomena characteristic to colloidal systems, with many practical implications in mineral processing (including bitumen recovery), stability of emulsions (with implications for froth treatment), and stability of mineral suspensions (with obvious implications for tailings management), among others. Because of this, we will briefly discuss the nature and origin of surface forces. There are several kinds of surface forces; we will start our review with van der Waals forces. We will then examine electrical double layer forces, introduce the DLVO theory of colloid stability and extensions to the DLVO theory, and then briefly discuss steric and structural surface forces.

2.7.1 Van der Waals Forces

To understand the physics of van der Waals surface forces, we have to first recall that all single atoms and molecules in a vacuum attract each other. This intermolecular attraction was first noticed as a deviation in the behaviour of a real gas from that of an ideal gas. For an ideal gas, its pressure p , volume V , and temperature T are linked by the well-known equation of state $pV = nRT$, where n is the number of moles and R is the gas constant equal to $8.31 \text{ J/(K}\cdot\text{mole)}$. Dutch physicist Johannes van der Waals (1837–1923) attributed the above deviation to the finite dimensions of molecules and accounted for intermolecular attraction in his equation of state:

$$p + \frac{a}{b} \left(p + n^2 \frac{a}{V^2} \right) (V - nb) = nRT \quad (2.30)$$

where a is a measure of intermolecular attraction, and b is the volume excluded from V due to the finite volume of molecules. It is important to keep in mind that van der Waals derived his equation in 1873, when the existence of atoms was still vigorously disputed. He assumed not only that they exist, but that they are of a finite size and that they attract each other. For this work, he was awarded the Nobel Prize in Physics in 1910. Since he was the first to postulate the existence of intermolecular forces, we apply his name to a broad range of interactions resulting from the simple fact that individual atoms or molecules attract each other.

Dipole-Dipole Interaction

Intermolecular attraction stems from three types of interactions. The first case, and the easiest to analyze, is one in which both molecules have permanent electric dipole moments. Two electric dipoles can repel or attract each other, depending on their mutual orientation: in a parallel orientation, they repel each other; in an anti-parallel orientation, they attract each other. Averaging the dipole-dipole interaction energy over all possible orientations results in the net dipole-dipole attraction energy V_{d-d} given by $V_{d-d} = -\beta_{d-d} r^{-6}$, where β_{d-d} is a characteristic constant that depends on the dipole strength, and r is the separation between the dipole centres. Note that this attraction energy decays with the sixth power of separation. The net attraction force is given by the derivative of energy over separation, such that the force decays with the seventh power of dipole-dipole separation.

Dipole-Induced Dipole Interaction

Let us now consider a second type of interaction, where one of the molecules has a permanent dipole moment, but the second does not. If the second molecule is in the proximity of the first (i.e., the one with a permanent dipole moment), the electric field originating from the dipole will cause a polarization (a small shift in electric charge distribution) in the second molecule, making it an induced dipole. This induced

dipole will be attracted by the permanent dipole. Again, if we analyze the physics of this dipole-induced dipole interaction, we will find that the overall attraction energy is V_{d-id} equal to $-\beta_{d-id}r^{-6}$. The constant β_{d-id} depends on the first molecule's dipole strength and the second molecule's polarizability (i.e., its ability to be polarized). Let us note that, as in the dipole-dipole case, the attraction energy in the dipole-induced dipole case also decays with the sixth power of the separation distance, and the attraction force decays with the seventh.

Dispersive Interaction

The third type of intermolecular interaction is the most important and most prevalent kind. In this case, both interacting molecules lack permanent dipole moments, but both are polarizable. In fact, all molecules can be polarized in an electric field, although their polarizabilities differ in different kinds of molecules. Imagine that, due to random fluctuations of electron positions in the first molecule, a transient dipole moment is formed. This, of course, creates a transient electric field in its vicinity, which in turn induces a transient dipole moment in the second molecule, resulting in both molecules attracting each other. The lifetime of such fluctuations is very short, and on average, no overall dipole moment is formed. Those short-lived, transient dipoles create induced dipoles in neighbouring molecules, resulting in an overall attraction. This is called dispersive interaction and it also decays with the sixth power of the separation.

Regardless of the origin of the interaction, whether it is due to a permanent or induced dipole or to random charge fluctuations, the average energy is always decaying with the sixth power of the distance $V = -\beta r^{-6}$, where β is a constant accounting for all types of molecular interactions. This allows for the calculation of the interaction energy between colloidal particles using a relatively simple pairwise summation. In principle, this summation says that the interaction energy between colloidal particles is the sum of interaction energies between all pairs of atoms in both interacting particles.

Looking at Figure 2.16, we will do this summation in two steps. First, we select an atom (1) in particle A and an atom (2) in particle B. Keeping the first atom fixed, we add the energies of the interactions between the selected atom 1 in particle A and all of the atoms in particle B. When done, we have the interaction energy of the atom (1) in particle A with all of the atoms in particle B. In the second step, we repeat the summation over all the atoms in particle A to obtain the interaction energy between particles A and B (V_{A-B}). In practice, the summation is replaced by integration, such that the final interaction energy V_{A-B} is expressed as a six-fold integral over the particles' volumes. For simple geometries of particles A and B, the integration can be performed analytically to yield the exact formulas, some of which are listed in Table 2.5.

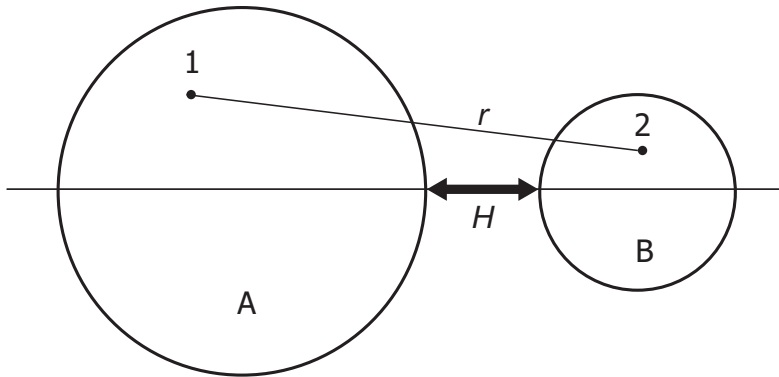


Figure 2.16 Pairwise summation for a sphere-sphere geometry.

Table 2.5 Expressions for van der Waals Energy for simple geometries*

Geometry	Energy	Assumptions/Comments
Sphere-sphere (unequal radii)	$V_{s-s} = -\frac{A}{6H} \frac{a_1 a_2}{(a_1 + a_2)}$	a_1 and $a_2 \gg H$
Sphere-sphere (equal radii)	$V_{s-s} = -\frac{A}{12H} a$	$a = a_1 = a_2 \gg H$
Sphere-flat block of infinite thickness (half space)	$V_{s-fb} = -\frac{A}{6H} a$	$a = a_1$; $a_2 \rightarrow \infty$; $a \gg H$
Identical flat blocks of infinite thickness (half space–half space)	$V_{fb-fb} = -\frac{A}{12\pi H^2}$	van der Waals energy per unit area
Crossed, infinitely long cylinders	$V_{cr.cyl.} = -\frac{A}{6H} \sqrt{a_1 a_2}$	a_1 and $a_2 \gg H$

* A is the Hamaker constant (see Table 2.6), H is surface-surface separation, and a , a_1 , and a_2 are the particles' radii.

Table 2.6 Hamaker constant values for selected materials ($A \cdot 10^{20}$ Joule)

Material (M)	M-Air-M	M-Water-M	Material (M)	M-Air-M	M-Water-M
Air or vacuum	0.0	3.7	Pentane	3.8	0.34
Water	3.7	0	Hexane	4.1	0.36
Quartz (fused)	6.5	0.83	Heptane	4.3	0.39
Quartz (crystalline)	8.8	1.7	Octane	4.5	0.41
Calcite	10.1	2.2	Nonane	4.7	0.44
Mica	10.1	2.0	Decane	4.8	0.46
Sapphire	15.6	5.3	Dodecane	5.0	0.5
Graphite	47.0		Tetradecane	5.1	0.51
			Hexadecane	5.2	0.54
			Benzene	5.0	
			Toluene	5.4	
			Acetone	4.2	
			Teflon	3.8	0.3
			Bitumen		0.3

The numerical values of the Hamaker constant are listed in Table 2.6 for the interactions of two bodies of the same material in air and in water. In mineral processing, including oil sands operations, we do not often deal with material-air-material situations. We are mostly interested in interactions between particles suspended in a liquid medium (usually water). If particles of the same material interact with each other through a medium, the Hamaker constant in the equations listed in Table 2.5 must be replaced with an effective Hamaker constant, which can be calculated from the following formula:

$$A_{121} = \left(\sqrt{A_1} - \sqrt{A_2} \right)^2 \quad (2.31)$$

where A_{121} is the effective Hamaker constant and A_1 and A_2 are the constants for the particles and the medium, respectively. It is important to note that, because of the square on the right side of Eq. (2.31), A_{121} is always positive, regardless of the values of A_1 and A_2 . This means that particles of the same material always attract each other, regardless of the medium in which they are suspended. However, as can be seen in Table 2.6, the attraction energy between particles through a medium such as water will usually be substantially reduced compared to that of particles in a vacuum or in air.

If the interacting particles are not of the same material, e.g., in the case of the interaction of a bitumen droplet with an air bubble through water, the expression for an effective Hamaker constant takes the form

$$A_{123} = (\sqrt{A_1} - \sqrt{A_2})(\sqrt{A_3} - \sqrt{A_2}) \quad (2.32)$$

where A_1 and A_3 are Hamaker constants for materials 1 and 3 (bitumen and air in our example), and A_2 is the Hamaker constant for the medium (here, water).

If the Hamaker constant of the medium has a value between the values for the two particles' material, the effective Hamaker constant is negative. In such a case, the particles will repel each other. Because of the relatively low value of the Hamaker constant for water ($3.7 \cdot 10^{-20}$ J) in practically all cases important to air flotation, when mineral particles interact with air bubbles through water, the Hamaker constant is negative, and van der Waals forces repel the mineral particles from the bubbles. This effect has no practical consequences for large mineral particles (say, larger than $\sim 20 \mu\text{m}$), where the particle collides with the bubble predominantly under the influence of inertial forces, but it becomes important for very small mineral particles. For particles smaller than $\sim 5 \mu\text{m}$ or $10 \mu\text{m}$, inertial effects are negligibly small. Mineral particles and air bubbles are likely to have negative charges in water under most conditions. As a result, they repel each other due negative Hamaker constant and to their double layer interactions, discussed in the following section. Without any attractive forces and practically no inertial effects, it is almost impossible for a small particle to attach itself to an air bubble, making air flotation of micron-sized particles practically impossible.

Hamaker constants are either evaluated from direct measurements or calculated from the materials' spectral data. In both cases, the results are subject to errors resulting from insufficient experimental accuracy or assumptions made in the theory. Hamaker constants are listed in Table 2.6 to illustrate general trends, e.g., to indicate that the Hamaker constant increases with molecular weight in a homologous series of alkanes, or that the Hamaker constant of graphite is high as compared with that of most other materials (this is due to the high electric conductivity of graphite). The values given in Table 2.6 are accurate to the order of magnitude. They can also be used to make approximate estimations of the interaction energies and forces in many real systems.

We would like to make one more closing comment: as seen from the expressions listed in Table 2.5, van der Waals interaction energy decays with the inverse of the separation distance. The interaction force decays even faster (with the inverse of the square of the separation). Both become insignificant at distances of more than $\sim 100 \text{ nm}$. At such short distances, an error introduced with uncertainty in the separation distance is usually greater than that due to inaccuracies in the Hamaker constant values.

2.7.2 Double Layer Overlapping Forces

When two charged colloidal particles approach each other, they interact with each other due to their surface charges. However, contrary to charged particles in a vacuum, it is not a simple electrostatic problem. The particles are immersed in a medium containing

ions, and at small separations, their double layers overlap, complicating calculation of the interaction energy and force. To simplify our analysis, let us assume that both particles are made of the same material and are of the same size. Furthermore, let us assume that the particle radii are large compared with the distance between them. This would allow us to consider two flat double layers separated by a distance H . Let us also assume that the particles are immersed in a solution of a symmetrical electrolyte.

The force between the surfaces is the sum of two contributions. The first is Maxwell's stress due to electric potential:

$$F_E = -\frac{\varepsilon}{2} \left(\frac{d\psi}{dx} \right)^2$$

The second is the osmotic pressure term due to increased counter-ion concentration in the gap:

$$F_O = (n_+ + n_-)kT - 2n_0kT$$

In the above equations, ε is the electric permittivity of the solutions, ψ is the electric potential, x is the distance from the charged surface, n_+ and n_- are cation and anion number concentrations, n_0 is the bulk electrolyte number concentration, k is the Boltzmann constant, and T is temperature. Since the local ion concentrations depend on the local potential values, both osmotic and Maxwell terms can be written as functions of electric potential ψ and then integrated. Without going into details of the derivation, in the symmetric case of two infinitely thick flat slabs (half spaces) considered, the potential energy of interactions (per unit area) resulting from double layer overlapping is

$$E_{DL} = \frac{64n_0kT}{\kappa} \tanh^2 \left(\frac{ze\psi_0}{4kT} \right) \exp(-\kappa H) \quad (2.33)$$

In the above equation, ψ_0 is the surface potential and z is the valency of the counterion. For two identical spherical particles, the double layer interaction energy is

$$V_{DL} = \frac{64n_0kTa}{\kappa^2} \tanh^2 \left(\frac{ze\psi_0}{4kT} \right) \exp(-\kappa H) \quad (2.34)$$

For small surface potentials, i.e., for $e\psi_0 < kT$ (implying $\psi_0 < 25 \text{ mV}$) and using Eq. (2.27) to substitute surface charge density σ for surface potential ψ_0 , Eqs. (2.33) and (2.34) simplify to

$$V_{DL} = \frac{2\sigma^2}{\kappa\varepsilon} \exp(-\kappa H) \quad (2.35)$$

(per unit area of two flat bodies separated by a distance H), and to

$$V_{DL} = \frac{2\pi\sigma^2 a}{\kappa^2 \epsilon} \exp(-\kappa H) \quad (2.36)$$

for two spheres of radius a .

Interaction force can be derived from the above formula by differentiation against the separation H . It is important to notice that the interaction energy will decrease with increasing κ or increasing electrolyte concentration, as in Eq. (2.26).

2.7.3 DLVO Theory of Colloid Stability

As mentioned in Section 2.2.1, molecules at interfaces have higher energy than those in the interior of any of the neighboring phases. With increasing interfacial area, the total energy of the system increases. Thus, highly dispersed systems, such as colloids, are inherently unstable. Colloids should spontaneously evolve so that the dispersed particles grow bigger and the total interfacial area—and thus, the system energy—decreases. A question arises: Why do some colloids appear stable for an extended period of time? There must be stabilization mechanisms that prevent dispersed particles from joining together and growing bigger.

The first successful theory of colloid stability became known as the *DLVO theory*, after the scientists who proposed it. Russian physicists Derjaguin and Landau published their fundamental papers in 1941, in Russian. Because the papers were published during the Second World War, they were not immediately known in the West. Dutch scientists Verwey and Overbeek published *their* monograph seven years later (1948). It was later agreed by the international scientific community that the theory of colloid stability was developed by the two groups independently, and all four researchers' names were incorporated to give the theory its current name.

The basic assumption of the DLVO theory is that the energy of a colloidal system E is treated as the sum of attractive van der Waals energy V_{vdW} and the repulsive double layer overlapping energy V_{DL} :

$$E = E_{vdW} + E_{DL} \quad (2.37)$$

Van der Waals and electrical double layer terms were discussed in detail in the preceding sections. We mentioned there that the van der Waals term is usually, but not always, attractive, and that the double layer overlapping term is usually, but not always, repulsive. We will return to this point later. For now, let us substitute the terms on the right-hand side of Eq. (2.37) with appropriate expressions for sphere-sphere interaction. The expression for V_{vdW} is listed in the second row of Table 2.5 and V_{DL} is given by Eq. (2.36). We will have

$$V = -\frac{A}{12H} a + \frac{64kTn_0a}{\kappa^2} \tanh^2\left(\frac{ze\psi_0}{4kT}\right) \exp(-\kappa H) \quad (2.38)$$

Figure 2.17 shows the van der Waals attraction, the double layer repulsion, and the total interaction energy as given by Eq. (2.38) for two spherical particles in 0.001 M KCl solution at 25 °C. Particle surface potential was assumed to be 15 mV and the Hamaker constant for the particle material was taken to be $8 \cdot 10^{-21}$ J. The figure presents a typical plot of interaction energies of colloidal particles as a function of the distance between them (surface-to-surface separation).

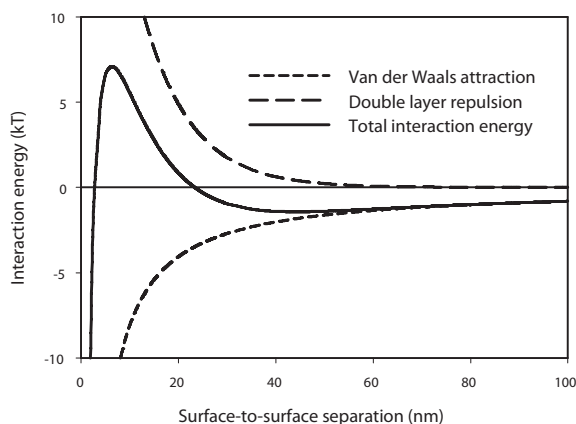


Figure 2.17 Van der Waals attraction, double layer repulsion, and total interaction energies for two 1 μm spherical particles in 0.001 M KCl at 25 °C. Particle surface potential was assumed to be 15 mV and Hamaker constant was taken to be $8 \cdot 10^{-21}$ J.

The total particle-particle interaction energy is indicated in Figure 2.17 by a solid line. The dashed lines represent contributions of van der Waals attraction and double layer repulsion to the total energy. The abscissa on the plot shows particles' surface-to-surface separation. The ordinate shows particles' interaction energy expressed in kT units.

It is worth remembering the physical sense of these units: In physical chemistry, the Boltzmann distribution is a probability measure for distribution of energy between atoms, molecules, or particles forming a system. The term $\exp(-E/kT)$ gives the probability that a molecule or particle has a thermal energy E greater than kT . In the above, k is the Boltzmann constant, equal to $1.38 \cdot 10^{-23}$ J/K, and T is absolute temperature (in K).⁶

⁶ The product of the Boltzmann constant and the Avogadro number is the gas constant R .

We can see in Figure 2.17 that at large distance, the total particle-particle interaction energy is small and negative. This means that the particles are weakly attracting each other. When the particles approach each other, this attraction becomes stronger as the total interaction energy decreases, eventually reaching a minimum of about -1.5 kT units at ~ 45 nm surface-to-surface separation. The physical meaning of this minimum is that the particles form a weak doublet when they are separated by ~ 45 nm. The doublet is weak because the energy that is keeping the particles together, or the depth of this minimum, is relatively small (only -1.5 kT units). Since $\exp(-1.5) = 0.223$, approximately one out of five such doublets will have sufficient thermal energy to break apart at any given time. Of course, the doublets form and break apart all the time, such that their total number does not change.

As the particles approach each other further, their energy rises to a positive value of ~ 7 kT units at 6 nm. The energy difference between the minimum and maximum is thus 8.5. This corresponds to an energetic barrier of 8.5 kT units. The probability of a doublet jumping across this barrier is $\exp(-8.5) = 2 \cdot 10^{-4}$, meaning that only one in about 20 000 doublets will have sufficient energy to cross the barrier to form a permanent doublet in the very deep energy minimum at contact.

A system is considered unstable if collisions between particles result in the formation of aggregates. The process of aggregate formation is called *coagulation* or *flocculation*. The terms are often used interchangeably. However, some prefer to use the term *flocculation* to describe only aggregation that is induced by polymer bridging (described below in the section on steric interactions) and *coagulation* in reference to aggregation caused by changes in water chemistry, i.e., changes in pH or resulting from the addition of electrolytes. In this section, we focus on the latter, and will use the term coagulation.

The shape of the curves in Figure 2.17 is very sensitive to the values of surface potential ψ_o , and, through κ , to the electrolyte concentration. Below, we will discuss both effects separately.

Impact of Surface Potential

Figure 2.18 shows the total interaction energy as a function of surface-to-surface separation for various surface potential values ψ_o . The solid line, corresponding to $\psi_o = 15$ mV, is redrawn from Figure 2.17. We see from the figure that as the surface potential increases, the energy barrier discussed above increases. There is no barrier for surface potentials of 5 mV and 10 mV. For a surface potential of 15 mV, the barrier is ~ 7 kT high and increases to ~ 24 kT and 50 kT units for surface potentials of 20 mV and 25 mV, respectively. To put it in perspective, the barrier of 7 kT corresponded to a relatively stable system, as only one of the 20 000 particle-particle doublets had sufficient energy to cross the barrier to coagulate. For 50 kT, only one out of $5 \cdot 10^{21}$ particles would have sufficient energy to coagulate. For all practical purposes, such a system will be infinitely stable.

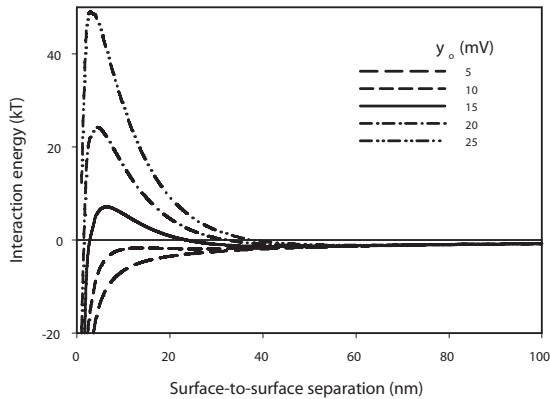


Figure 2.18 Figure 2.18 Interaction energy for two spherical particles as a function of surface-to-surface separation for different surface potentials ψ_o . Electrolyte concentration $C = 0.001$ M; Hamaker constant $A = 8 \cdot 10^{-21}$ J.

It should be noted that, for the selected values of Hamaker constant and electrolyte concentration, the system is very sensitive to surface potential. The difference between an infinitely stable system at $\psi_o = 25$ mV and an unstable one at $\psi_o = 10$ mV is small (only 15 mV). Such a small change can easily occur through the adsorption of counter-ions. In a suspension of clay particles in water, such a change can be easily induced by changing the pH of the suspension or by adsorption of positively charged ions, e.g., calcium ions. In fact, this is the basis for the consolidated tailings (CT) technology discussed in Volume 2.

Impact of Electrolyte Concentration

Figure 2.19 shows the total interaction energy as a function of surface-to-surface separation for various electrolyte concentrations for the same particles as shown in Figure 2.17. The top solid line is redrawn from Figure 2.17. The other lines represent the energy of the same particles with increasing electrolyte concentration. We see from the figure that, as the electrolyte concentration increases, the energy barrier decreases from a positive value (0.001 M electrolytes) to a negative value (0.01 M). Somewhere in between, there will be a concentration value for which the barrier height is equal to zero. With no energy barrier for coagulation, the system is unstable and will coagulate. This electrolyte concentration is called *critical coagulation concentration* (CCC).

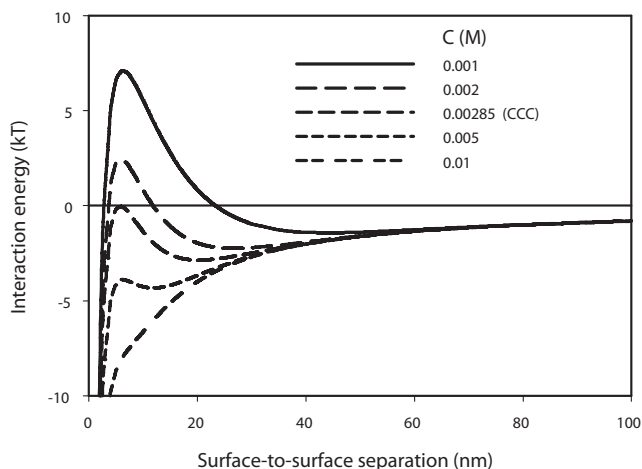


Figure 2.19 Interaction energy of two spherical particles as a function of surface-to-surface separation for different electrolyte concentrations. Particles' surface potential $\psi_o = 15$ mV; Hamaker constant $A = 8 \cdot 10^{-21}$ J.

Critical Coagulation Concentration (CCC)

Critical coagulation concentration (CCC) can be calculated from Eq. (2.38) using $dV/dH = 0$ (condition for a maximum on $V = V(H)$ curve) and $V = 0$ (condition of no energy barrier). By performing the necessary calculations for the particles shown in Figure 2.19, we obtain $CCC = 0.00285$ M. The corresponding curve is shown in the figure. In calculating the CCC, we assumed that the surface potential ψ_o is not affected by the changing electrolyte concentration, which is not realistic. However, it is convenient to make this assumption in order to separate the two effects so that the only effect under consideration is the effect of electrolyte composition on double layer thickness ($1/\kappa$). Double layer thickness determines the range of repulsive forces resulting from surface charge. As salt concentration increases, the diffuse electric double layer shrinks, and the particles can approach each other at a smaller distance, so that eventually, van der Waals attraction starts to dominate and the particles form an aggregate.

But $1/\kappa$ depends not only on electrolyte concentration, but also on ion valency. It can be shown that for a symmetric electrolyte, CCC is proportional (\propto) to

$$CCC \propto z^{-6} A^{-6} \tanh(ze\psi_o/4kT) \quad (2.39)$$

For high values of surface potential ψ_o (say, greater than ~ 100 mV; i.e., where $ze\psi_o > 4kT$ and $\tanh(ze\psi_o/4kT) \rightarrow 1$), CCC is proportional to z^{-6} . In other words,

the CCC of NaCl, CaSO₄, and AlPO₄ ions, for example, would decrease in the ratio of 1 : 0.016 : 0.0014. Even for non-symmetrical electrolytes, the impact of multivalent ions is so big that the CCC for, say, NaCl, CaCl₂, and AlCl₃ decreases in a similar manner. Putting it in different words, an aluminum ion, Al³⁺, is about a thousand times more effective as a coagulant than sodium. The above is a theoretical justification of experimental observations known as the Schulze-Hardy rule, which says that the valency of a counter-ion has a dominant effect on colloid stability, and the effectiveness of an ion is proportional to the sixth power of its valency.

The Schulze-Hardy empirical rule was based on observations of the stability of gold sol (a suspension of colloidal gold particles in water), where common ions do not affect the gold's surface charge and potential. In reality, the Schulze-Hardy rule is rarely followed. There are several reasons for this. First, Eq. (2.39) is only valid for *inert* electrolytes, i.e., where changes in electrolyte concentration do not affect the surface potential ψ_o . This is almost never the case, as the condition excludes all cases where counter-ions adsorb on solid particle surfaces. Second, in Eq. (2.39), ion valency is also part of the argument of the tanh function and for low values of ψ_o , the tanh term has to be included. Coagulation rarely happens at surface potentials high enough to satisfy the $ze\psi_o > 4kT$ condition. It usually takes place for surface (or zeta) potentials of less than ~ 30 mV. For low surface potentials, CCC is proportional to z^{-2} rather than to z^{-6} .

Impact of Specific Ion Adsorption

There are many important instances in which ions specifically adsorb on a particle surface. Such adsorption is often the source of surface charge (and thus surface potential), as discussed in Section 2.6.1 on the origin of surface charge. A suspension of clay particles in water is a good example of such a system. The clay surface charge depends on pH, as hydroxyl ions are potential controlling ions for oxide-type minerals. Also, multivalent ions, such as calcium or aluminum ions, specifically adsorb on clays, making them less negatively charged. By doing so, they make the suspension less stable, and as discussed above, the impact of surface potential on colloid stability is much stronger than that of electrolyte concentration.

Alum or aluminum potassium sulphate (KAl(SO₄)₂·12H₂O) is an effective coagulant in water treatment, not because it decreases the double layer thickness, but because adsorbing aluminum ions are very effective at lowering clay surface potential. A clay particle-calcium ion system, important for both bitumen extraction and tailings management in the oil sands industry, should not be analyzed based on the Schulze-Hardy rule, but rather by considering specific adsorption of calcium ions on clays resulting in lowering clay surface potential.

From the above discussion, it is clear that small changes in surface potential and/or electrolyte concentration have a tremendous impact on the stability of a colloidal system. From an oil sands extraction point of view, this is a very significant thing to know, as it points to the importance of water chemistry in a process' performance. It is possible to manipulate water chemistry to within a range that, for instance, can

change bitumen recovery from poor to good. In the same manner, by manipulating water chemistry, we may stop tailings from separating into coarse sand and fines and change them into the non-segregating mixture required for CT technology. These issues are covered in more depth in Chapter 6, which is devoted to bitumen recovery.

2.8 Non-DLVO Interactions

2.8.1 Steric Repulsion

Adsorbed layers, especially of polymers, can have a significant impact on colloid stability, which obviously is of great interest to us. An added polymer can adsorb at particle surfaces, forming loops, trains, and tails, as shown in Figure 2.20. As the particles approach each other, the adsorbed layers come into contact. If the particles come any closer, the adsorbed polymer layers penetrate each other. Since the polymer chains forming loops and tails are hydrophilic and thus hydrated, such penetration or overlapping requires at least partial dehydration of the polymer chains dangling in the water phase. This increases the total energy of the system and therefore results in a repulsive surface force. Quite often, such steric interactions are approximated with a hard sphere model. It is assumed that the interaction energy (and force) is zero at large separations and becomes infinite at the distance where the adsorbed layers start to overlap. Despite its simplicity, the hard sphere model is quite useful for most practical applications.

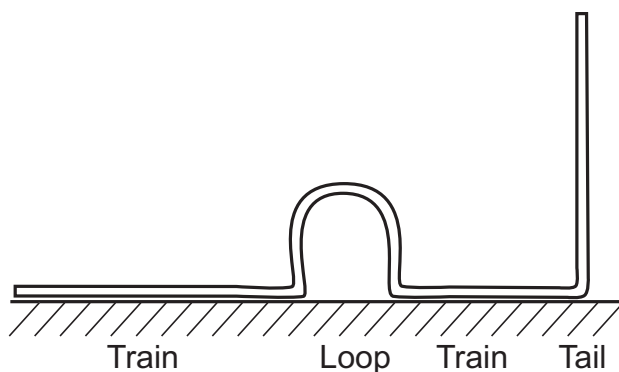


Figure 2.20 Possible configurations of an adsorbed polymer on a solid surface: loop, train, and tail.

The adsorbed polymer layer has a low Hamaker constant, in large extent due to hydration of the polymer chains. Thus, there is little van der Waals attraction between the adsorbed polymer layers. If their thickness is large enough, van der Waals attraction between the particle cores is also low, as the van der Waals energy decays fast with distance. Thus, polymer steric stabilization is mostly a result of keeping particles apart at distances large enough to prevent strong attraction between their cores. The most

important factor in steric stabilization is the thickness of the adsorbed polymer layer relative to the particle size. As shown in Table 2.5, van der Waals attraction energy is proportional to the particle size. Thus, larger particles require a thicker polymer coating to achieve the same degree of steric stabilization as small particles.

The degree of steric polymer stabilization can be manipulated by changing the solvency of the polymer in the medium. For instance, with polyethylene oxide/polypropylene oxide copolymers, steric stability would decrease with increasing temperature due to dehydration of the polymer chains. Polymer solvency can also be manipulated with water chemistry.

Steric stabilization of emulsions can also result from solid particles anchored at the surface of an emulsified liquid droplet. Again, the hard sphere model can be successfully applied to explain most of the phenomena encountered in practical systems. In solid-stabilized emulsions, one can manipulate the stabilization by changing the contact angle on the stabilizing solid particles. Increasing the wettability of these solids by liquid-forming emulsion droplets would cause the solids to immerse themselves deeper into the droplets, resulting in a thinner steric layer, and thus, lower stability. The contact angle can be manipulated by the addition of suitable surfactants.

2.8.2 Polymer Bridging

The addition of a polymer can also destabilize a colloid. A single polymer molecule adsorbing at more than one particle forms bridges between them, resulting in flocculation. The increased size of the aggregates would then cause them to sediment at an accelerated pace as compared with an untreated system. This is the basis for the so-called paste technology used in tailings management. In froth treatment operations, dewatering of diluted bitumen is facilitated by bridging flocculation of water droplets induced by the addition of demulsifiers.

For the bridging mechanism to be effective, the polymer must adsorb on more than one particle. The polymer should therefore have a large molecular weight, often of several million daltons, so that it can form long loops and tails, increasing the probability of attachment to other particles. Bridging requires relatively low dosages of the polymer, as there must be bare places on other particles for the polymer to adsorb and form a bridge. Too little polymer may result in insufficient bridging between particles. Too much is also detrimental, as at higher-than-optimum dosage, there will be too little or no polymer-free surfaces that are necessary for bridging to occur. Overdosing with a polymer is thus detrimental in both tailings flocculation and, as will be discussed later, in froth treatment. This is important to keep in mind, as it is very human to think that if something is good (polymer addition), then more of it is even better. It is not so here, as in addition to increasing costs, overdosing is detrimental to polymer performance.

2.8.3 Hydration Effects

Water molecules close to the surface of hydrophilic particles, such as clays or other oxides, are under the influence of particle surface charge, which promotes water molecule orientation and formation of hydrogen bonds with oxygen atoms at the oxide surface. When two particles with hydrated surfaces approach each other, they will generally experience a repulsion force *in addition* to the double layer overlapping forces. This additional force stems from the need to remove hydrating water in order to make it possible for the particles to get closer. In a sense, it is similar to steric repulsion, but the origins of this repulsion are water molecules rather than polymers. Removal of the hydrating water requires work. This results in an increase in the system energy and gives rise to a hydration-repulsive force. Since water molecules at the surface influence the orientation of neighbouring water molecules, the range of hydration forces may be of several molecular dimensions ($\sim 1\text{--}2$ nm). The impact of hydration effects on colloid stability may be important for systems with high electrolyte concentrations, where they may account for some apparent deviations from DLVO predictions.

2.8.4 Hydrophobic Interactions

When there are no polar groups or hydrogen bonding atoms (oxygen or nitrogen) on a particle surface, there is no affinity between water and the surface. The particle will be hydrophobic. The nature of the water in contact with such a surface will be different from that of the bulk water. In bulk, water molecules form hydrogen bonds with surrounding molecules, with no preferred direction. Hydrogen bonding results in the formation of multi-molecular water clusters with a crystal-like structure. Liquid water is, in fact, a collection of small chunks of ice, constantly forming and falling apart. This association of water molecules into ice-like aggregates makes water (hydrogen oxide or H_2O) a liquid at room temperature, while its heavier homolog, hydrogen sulphide (H_2S), is a gas under the same conditions. This iceberg water structure, as it is called, is responsible for a number of anomalous water properties, including its liquidity, the dependence of its density on temperature (with a maximum density at 4°C), and the high equivalent electric conductivities of hydrogen and hydroxyl ions, just to mention a few.

As mentioned above, a water molecule in the bulk forms hydrogen bonds with its neighbours with no preferred direction. Close to a hydrophobic surface, this symmetry of hydrogen bonding is broken because water molecules cannot form hydrogen bonds with a hydrophobic surface. Also, water in a gap between two hydrophobic surfaces cannot form clusters larger than the gap width. In small gaps, this is a serious limitation that results in an attractive force with an entropic origin. The range of these 'hydrophobic forces' may be quite large, of some tens of nanometres. Some direct measurements of surface forces seem to indicate that hydrophobic forces can be stronger and farther-ranging than the van der Waals attraction.

The nature of hydrophobic forces is far from clear, and there is no theory that would link hydrophobic forces to basic electromagnetic interactions, as is the case for all DLVO forces. Some question the very existence of hydrophobic interactions, attributing observable effects to other causes, e.g., the presence of very small gas bubbles on hydrophobic surfaces. Others use the concept of hydrophobic forces to explain many important effects, such as the attachment of air bubbles to hydrophobic mineral surfaces in flotation.

2.9 Coagulation Kinetics

In the introduction to this chapter, we wrote that dispersed systems with a large interfacial area have high internal energy and are thus intrinsically unstable. Stability is therefore one of the most important characteristics of colloidal dispersions. In the previous section on surface forces, we discussed the various phenomena that give rise to attractive or repulsive interactions between particles and that control overall system stability.

Under favourable conditions, when a colloidal dispersion is unstable, some collisions between particles result in the formation of aggregates. As mentioned before, the terms *coagulation* and *flocculation* are often used interchangeably. Sometimes, the term *flocculation* is used to describe aggregation induced by the addition of polymers and *coagulation* to refer to aggregation caused by decreasing double layer repulsion. Following the previously adopted style, we will continue using the term *coagulation* to describe the formation of aggregates regardless the mechanism responsible for destabilization.

2.9.1 Stability Ratio

Before going any further, let us introduce the concept of the *stability ratio*, W , defined as the ratio of the number of all collisions between particles to the number of effective collisions, i.e., the collisions that result in the formation of an aggregate:

$$W = \frac{\text{number of all collisions}}{\text{number of effective collisions}} \quad (2.40)$$

When there is no potential barrier for aggregation, the coagulation rate depends only on the rate of particle collisions, since each collision results in the formation of an aggregate. We call this the *rapid coagulation* case. In the presence of a stabilization barrier, only some collisions are effective, meaning that only some of the colliding particles form aggregates. We call this the *slow coagulation* case (Masliyah and Bhattacharjee 2006).

2.9.2 Theory of Rapid Coagulation

Smoluchowski's Theory

In the simplest case—when all particles are initially of the same size; collisions between the particles are due to their Brownian movements; all collisions are effective (i.e., all lead to coagulation); and no particle breakup takes place—the kinetics of the coagulation process can be described using the Smoluchowski approach for rapid coagulation.⁷ In this approach, we neglect all interaction between the particles. In spherical symmetry, the flux J of particles to a selected central particle is given by Fick's law:

$$J = 4\pi r^2 D \frac{dn}{dt} \quad (2.41)$$

where r is the particles' centre-to-centre separation, n is the number concentration of the particles, and D is their diffusion coefficient. This equation can be integrated to yield

$$n = n_0 - \frac{J}{4\pi Dr} \quad (2.42)$$

Here, n_0 is the particles' concentration far from the central particle. It is assumed that the particles coagulate at contact, i.e., when $r = 2a$. The concentration of incoming particles at contact with the central particle is zero (as they vanish while coagulating with the central particle), so we can write $n = 0$ at $r = 2a$. We can thus write

$$J = 8\pi Dan_0 \quad (2.43)$$

The particle that we selected to be central is undergoing Brownian movements as well, such that the diffusion coefficient in Eq. (2.43) is the double of individual particle diffusion coefficients. The initial coagulation rate is equal to the sum of the fluxes given by Eq. (2.43) for all particles in the system. We can thus write:

$$-\frac{dn}{dt} = \frac{1}{2} Jn_0 = 8\pi Dan_0^2 \quad (2.44)$$

⁷ Polish physicist Marian Smoluchowski (1872–1917) made fundamental contributions to the kinetic theory of matter. In 1908, he was the first to attribute light scattering to density fluctuations in gases, a problem related to the blue colour of the sky. In 1906, independently of Albert Einstein, Smoluchowski derived a relation between particle diffusion coefficient, particle size, and temperature, known as the Einstein Smoluchowski relation, an important basis for the theory of stochastic processes.

The factor of 1/2 in the above equation is written to avoid counting the collisions between the same two particles twice. Rapid coagulation is often characterized by the time by which the initial number of particles is reduced by half. We can estimate this time by integrating Eq. (2.44) for all particles in the system.

$$-\int_{n_0}^{\frac{n_0}{2}} \frac{dn}{n^2} = 8\pi Da \int_0^{t_{1/2}} dt$$

yielding

$$t_{1/2} = \frac{1}{8\pi Da n_0} \quad (2.45)$$

If we substitute $D = \frac{kT}{6\pi\eta a}$ (Einstein's formula), we finally obtain

$$t_{1/2} = \frac{3\eta}{4kTn_0} \quad (2.46)$$

An interesting feature of this result is that the coagulation time $t_{1/2}$ is inversely proportional to the initial particle concentration. In concentrated suspensions (say, ~ 5 vol. %) and particles with a radius of 1 μm , initial particle concentration n_0 is approximately 10^{16} particles per metre cubed. Thus, in water at room temperature, $t_{1/2}$ is ~ 0.02 s. For diluted suspensions, the coagulation times are much longer (Masliyah and Bhattacharjee 2006).

Smoluchowski's Continuity Equation

Smoluchowski expanded his treatment of rapid coagulation past the initial stage of the process, into longer times at which collisions between various sized particles have to be considered. Assuming that initially, all particles were of the same size, all particles present in the system at any time are multiples of the monomers present at time zero. In other words, all particles present at any time are monomers, doublets, triplets, and so on, such that we can consider the system as being composed of discrete-sized particles. We will consider the formation of a class containing k monomers by writing:

$$\frac{dn_k}{dt} = \frac{1}{2} \sum_{j=1}^{k-1} \beta_{j(k-j)} n_j n_{k-j} - \sum_{j=1}^{\infty} \beta_{kj} n_j n_k \quad (2.47)$$

Eq. (2.47) gives the change in the number concentration of k -sized particle ation of k^{th} particles due to coagulation of smaller particles. The factor of 1/2 is introduced to avoid counting the same collision twice. The second term reflects the loss of k^{th} particles due their coagulation with any other particle, as such coagulation makes them bigger, moving them from the class k . β_{jk} is the collision frequency kernel for particles

with diameters of a_j and a_k . The kernel depends on the hydrodynamic conditions prevailing when particles collide.

For Brownian coagulation, also known as *perikinetic coagulation*, where particles collisions are due to their Brownian movements, the kernel β_{jk} can be written as:

$$\beta_{ij}(\text{Brownian}) = \frac{2kT}{3\mu} \frac{(a_i + a_j)^2}{a_i a_j} \quad (2.48)$$

where k is the Boltzmann constant, T the absolute temperature, a_i the particle radius, and μ the viscosity of the fluid. Brownian coagulation is relatively slow.

In real situations, we rarely deal with purely Brownian coagulation. Collisions between particles usually occur when the suspension is subjected to some kind of agitation, such as that resulting from stirring or fluid flow. Coagulation in a flowing medium is called *orthokinetic coagulation*. Fluid motion enormously increases the number of collisions compared with the Brownian coagulation, given the same particle concentration, size, and fluid viscosity. This is due to the fact that neighbouring layers of fluid have different velocities, and a particle in a given layer is outrun by faster-moving particles and passes slower-moving particles. The first treatment of orthokinetic coagulation was also done by Smoluchowski (1917). He considered the simplest case of orthokinetic coagulation in simple shear flow, obtaining the following kernel for the case:

$$\beta_{ij}(\text{shear}) = \frac{4}{3}(a_i + a_j)^3 G \quad (2.49)$$

where G is the shear rate. Under most conditions, shear-induced coagulation is much faster than that due to Brownian diffusion. Comparing Eqs. (2.48) and (2.49), we can obtain the ratio of coagulation rates under ortho- and perikinetic conditions:

$$\frac{\beta_{ij}(\text{shear})}{\beta_{ij}(\text{Brownian})} = \frac{4G\mu a^3}{kT} \quad (2.50)$$

For 1- μm particles in water at room temperature and under a moderate shear rate of about 10 s^{-1} , the rates of ortho- and perikinetic coagulation are about the same. With higher shear rates and, especially for larger particles, the shear coagulation is much faster.

Another important practical case is when particles collide due to sedimentation in a gravity field, and particles of different sizes move with different velocities. In this case, the kernel in the continuity equation is

$$\beta_{ij}(\text{sedimentation}) = \frac{2\pi g}{9\mu} (\rho - \rho_s)(a_i - a_j)(a_i + a_j)^3 \quad (2.51)$$

where g is acceleration due to gravity, ρ and ρ_p are densities of the fluid and particle, respectively, and μ is the fluid viscosity. This type of coagulation is especially important for large and dense particles. The sedimentation coagulation rate becomes equal to that of shear-induced for particles of $\sim 10 \mu\text{m}$. For larger particles, it is the dominant mechanism. In the oil sands industry, sedimentation coagulation is of importance in dealing with flocculation of tailings (by addition of polymer or gypsum) and in the paraffinic froth treatment process.

The change in the total number of particles in the system n_{tot} can be calculated as the sum over all sizes of particles:

$$\frac{dn_{\text{tot}}}{dt} = \frac{d \sum_{k=1}^{\infty} n_k}{dt} = \frac{1}{2} \sum_{j=1}^{\infty} \beta_{kj} n_j^2 + \sum_{j=1}^{k-1} \beta_{kj} n_j n_{k-j} - \sum_{k=1}^{\infty} \sum_{j=1}^{\infty} \beta_{kj} n_k n_j = -\frac{1}{2} \beta_{ij} \left(\sum_{j=1}^{\infty} n_j \right)^2 \quad (2.52)$$

For Brownian coagulation,

$$\beta_{ij} = 4\pi D_{ij} R_{ij} = 4\pi (D_i + D_j) R_{ij} \quad (2.53)$$

Here, D_{ij} is the mutual diffusion coefficient for i and j particles, equal to the sum of diffusion coefficients for individual particles; R_{ij} is the radius of interaction equal to the sum of individual particles radii $R_{ij} = a_i + a_j$. Since the diffusion coefficient is inversely proportional to the particle radius, we can therefore write

$$D_{ij} R_{ij} = (D_i + D_j)(a_i + a_j) = D_i a \left[\left(\frac{1}{a_i} + \frac{1}{a_j} \right) (a_i + a_j) \right] \quad (2.54)$$

Smoluchowski reasoned that, if the particle sizes are relatively close to each other, the term in the square bracket in Eq. (2.54) is approximately equal to 4 (Smoluchowski 1917). We can thus rewrite Eq. (2.52) as

$$\frac{dn_{\text{tot}}}{dt} = -8\pi D_1 a n_{\text{tot}}^2 = k_r n_{\text{tot}}^2 \quad (2.55)$$

reproducin the result already presented by Eq. (2.44) valid for the initial time of the coagulation process. But this time, the result is valid for any time. It shows that coagulation rate is proportional to the square of the total number of particles (of any size) present in the system. k_r is the rapid coagulation rate constant. Integrating Eq. (2.55), we can estimate coagulation half-time, again obtaining the value given by Eq. (2.46). Using this result, we can now solve Eq. (2.47) for any particle class to get the time evolution of different aggregate sizes:

$$n_i = n_{\text{tot}} \frac{(t/t_{1/2})^{i-1}}{(1+t/t_{1/2})^{i+1}} \quad (2.56)$$

Figure 2.21 shows the time evolution for monomers, dimers, and trimers calculated from Eq.(2.56). It is seen that as the monomer particle concentrations (normalized to the initial monomer concentration) decrease rapidly with time, the concentration of higher class aggregates increases from zero to a maximum and then decays as the coagulation process proceeds to form even larger aggregates. The total number of particles in the system decreases with time, as given by

$$n_{tot} = \frac{n_0}{1 + \frac{1}{2} \beta_{ij} n_0 t} \quad (2.57)$$

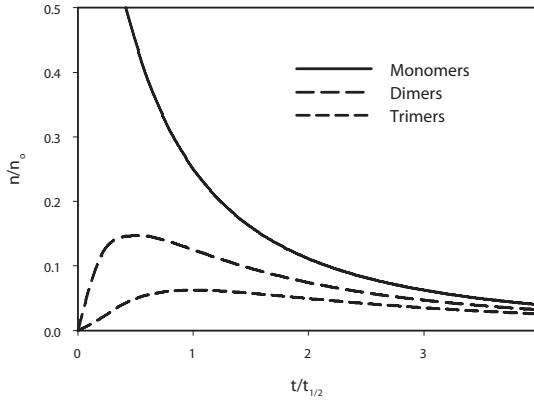


Figure 2.21 Time evolution of different aggregate sizes calculated from Eq. (2.56).

2.9.3 Slow Coagulation

The kinetic expressions in Eqs. (2.41) to apply to such cases where there is no energy barrier for collisions and all collisions are effective. Now we have to consider cases where an energy barrier exists, leading to a repulsion force that opposes the approach of the particles. An overall effect of energy barrier is that it decreases the coagulation rate by a factor known as stability ratio W , which we introduced in Eq. (2.40). A theoretical expression for the stability ratio has been developed by Fuchs by integrating the energy barrier V over the distance r (1934). If all particles are of the same size, the stability ratio can be thus written as:

$$W = 2a \int_{2a}^{\infty} \exp\left(\frac{V(r)}{kT}\right) \frac{dr}{r^2} \quad (2.58)$$

where a is the radius of the particles. When the stabilization energy barrier is described by the DLVO theory, we can use Eq. (2.38) to express energy barrier as function of distance. After integration and with a few approximations, we finally obtain:

$$W \approx \frac{1}{2\kappa a} \exp\left(\frac{E_{\max}}{kT}\right) \quad (2.59)$$

Eq. (2.59) is a convenient expression for approximate estimation of stability ratio for systems where particle size a , double layer thickness $1/\kappa$, and the height of the energy barrier E_{\max} are known.

2.10 Surfactants

The term *surfactant* is derived from the words **surface active agent**, and refers to a class of chemicals that are active at water-air or water-oil interfaces. Surfactants are organic compounds with a characteristic molecular structure. Their molecules are composed of two distinctly different parts: a hydrophilic (water-loving) polar head, and a hydrophobic (water-hating) hydrocarbon tail. Such molecules are called *amphiphilic* because they have an affinity for both water and oil, and therefore are at least partly soluble in both water and organic solvents.

Surfactants adsorb at water-air and water-oil interfaces, reducing the surface and interfacial tensions of their solutions. Most surfactants at higher concentration in their aqueous solutions undergo *spontaneous aggregation*, a process in which individual surfactant molecules aggregate, forming *micelles*. Micelles are colloidal particles containing several tens of individual surfactant molecules. In micelles, the surfactant molecules are oriented in such a way that the polar, hydrophilic heads are facing water, while the hydrophobic tails form the micelle interior. The process of micelle formation is the simplest form of molecular self-organization, a process at the very essence of life and the basis of many biological phenomena. Therefore, surfactants are of great scientific interest, as they are on the border between organized and disorganized states of matter. They are also of great practical importance, playing a key role in such processes as wetting, detergency, washing, foaming, and many others.

2.10.1 Common Surfactant Types

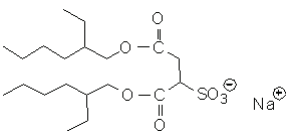
As mentioned above, surfactants are molecules with a hydrophilic polar head and a hydrophobic hydrocarbon tail. Depending on the nature of the polar group, surfactants are classified as anionic, cationic, and non-ionic, depending on the charge carried by the active part of the molecules. For instance, soap is a sodium salt of long-chain carboxylic acids (fatty acids). As such, it dissociates in water into a sodium cation and a carboxylate anion. It is therefore an anionic surfactant. Table 2.7 shows examples of anionic, cationic, and non-ionic surfactants.

There is also a large group of natural or biological surfactants. The most important are derivatives of fats (e.g., phospholipids, the main building block of cell membranes) and derivatives of cholesterol (e.g., components of animal bile). Many plants contain

saponins, amphiphilic glycosides that are capable of forming soap-like foams in aqueous solutions. Many saponins are toxic and probably evolved as part of the plant's natural defence against plant-eating insects or higher animals.

Molecules of all synthetic and natural surfactants contain parts of distinctly different properties: a hydrophilic polar 'head,' and a fatty hydrocarbon 'tail,' as shown in Figure 2.22.

Table 2.7 Examples of common surfactant types

Anionic	Formula	Comments
Sodium stearate	$\text{CH}_3(\text{CH}_2)_{16}\text{COO}^-\text{Na}^+$	Conventional soaps, easily biodegradable if made of natural fats
Sodium oleate	$\text{CH}_3(\text{CH}_2)_7\text{CH}=\text{CH}(\text{CH}_2)_7\text{COO}^-\text{Na}^+$	
Sodium dodecyl benzyl sulphonate	$\text{CH}_3(\text{CH}_2)_{11}\text{C}_6\text{H}_5\text{SO}_3^-\text{Na}^+$	
Sodium alkyl (R) sulphate or phosphate, e.g., sodium dodecyl sulphate (SDS)	R- SO_4^-Na^+ or R- $\text{OPO}_3^-\text{Na}^+$ e.g., $\text{CH}_3(\text{CH}_2)_{11}\text{SO}_4^-\text{Na}^+$	SDS is the most commonly manufactured surfactant
Sodium bis(2-ethylhexyl) sulfosuccinate (Aerosol OT, AOT)		Wetting agent, commonly used in paints, printing inks, glass cleaning (including windshield washing fluids), and in agricultural formulations. Easily biodegradable.
Cationic		
Alkyl amine hydrochloride, e.g., dodecyl amine hydrochloride	R- NH_3^+Cl^- $\text{CH}_3(\text{CH}_2)_{11}\text{NH}_3^+\text{Cl}^-$	
Alkyl trimethyl ammonium salts, e.g., Dodecyl trimethyl ammonium bromide (DTAB)	$\text{CH}_3(\text{CH}_2)_{11}\text{N}(\text{CH}_3)_3^+\text{Cl}^-$	
Non-ionic		
Polyethylene oxides, e.g., Sorbitan alkanolate (Span)	R-(OCH_2CH_2) _n OH	Common active ingredient in washing powders
Ethoxylated sorbitan alkanolate (Tween)		A family of ICI commercial wetting agents and emulsifiers used in the food, cosmetics, and drug industries.

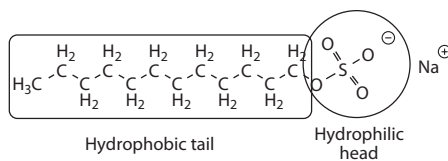


Figure 2.22 Typical structure of surfactant molecule containing hydrophobic tail and hydrophilic head. Sodium dodecyl sulphate (SDS) molecule is used as an example.

2.10.2 LHB scale

As mentioned above, all surfactant molecules exhibit amphiphilic properties. Their polar heads are hydrophilic and their tails are hydrophobic. The amphiphilic nature of surfactants can be expressed in terms of an empirical scale of hydrophilic-lipophilic⁸ balance (HLB), introduced by Griffin in 1949 for cosmetic formulations (1949). Thus, HLB is an experimental measure of the balance between the contradictory ‘preferences’ of two parts of surfactant molecules. High HLB values indicate that the polar head prevails, while low HLB characterizes molecules where the balance is shifted towards the fatty tail.

HLB can be evaluated from the ratio of the surfactant solubility in water and oil (partition coefficient) or calculated from the relation

$$\text{HLB} = 7 + \Sigma(\text{hydrophilic group numbers}) + \Sigma(\text{lipophilic group numbers}),$$

using hydrophilic and lipophilic (hydrophobic) group numbers, some of which are listed in Table 2.8.

The agreement between measured and calculated HLB numbers is surprisingly good, such that, for most practical applications, quick and easy calculation is more than sufficient.

Table 2.8 HLB group numbers

Hydrophilic group	HLB number	Hydrophobic group	HLB number
-OSO ₃ Na	38.7	-CH ₂ -	-0.475
-COONa	19.1	-CH ₃	
-N(tertiary amine)	9.4	-CH=	
Ester (sorbitan ring)	6.8	=C=	
Ester free	2.4		
-COOH	2.1		
-OH	1.9	Ethylene/propylene oxide	
-O-	1.3	-(CH ₂ -CH ₂ -O)-	0.33
-OH (in sorbitan ring)	0.5	-(CH ₂ -CH ₂ -CH ₂ -O)-	-0.15

8 Lipophilic, or ‘liking fat,’ is another term for hydrophobic.

Table 2.9 HLB values and typical applications

HLB range	Application	Solubility in water	Example
1–4		Insoluble	Fatty alcohols
3–6	W/O emulsifiers	Poor solubility	Fatty acids
7–9	Hydrotropes Demulsifiers	Milky, unstable dispersion	Span 20 (sorbitan monolaurate)
8–18	O/W emulsifiers	Stable, translucent dispersion	Tween 60 (polyoxyethylene sorbitan oleate)
> 15	Wetting agents Detergents Solubilizers	Clear solution, increasing light scattering above CMC	Soaps (HLB ~ 20) SDS (HLB = 40)

For example, let us calculate HLB values for dodecyl alcohol, lauric acid and its corresponding sodium salt (a soap), and sodium dodecyl sulphate (one of the most common surfactants). For dodecyl alcohol, we would have $HLB(C_{12}H_{25}OH) = 7 + 1.9 - 0.475 \cdot 12 = 3.2$. For the corresponding lauric acid, $HLB(C_{11}H_{23}COOH) = 7 + 2.1 - 0.475 \cdot 11 = 3.9$. Note that the carboxylic group is counted as a whole unit, including the twelfth carbon atom of the molecule. Similarly, HLB for sodium salt of the lauric acid, or sodium laurate, a common component of commercial soaps $HLB(C_{11}H_{23}COONa) = 7 + 19.1 - 0.475 \cdot 11 = 20.9$. Finally, for SDS, $HLB(C_{12}H_{25}SO_4Na) = 7 + 38.7 - 0.475 \cdot 12 = 40$.

Let us note that, because HLB for ethylene oxide group (EO) is 0.33 and for propylene oxide (PO) is -0.15 , by varying the EO-to-PO ratio in the polymer, one can produce a surfactant with a desired HLB value. Most of the commercial demulsifiers used in the petroleum industry, including oil sands froth treatment, are EO/PO copolymers often linked to a central sorbitol group. By changing the molecular weight of the polymer and the EO/PO ratio, one can produce a chemical with finely tuned properties for a particular field application. There will be more on this subject in Volume 2 in the chapter devoted to chemical aids.

2.10.3 Micellization and Critical Micelle Concentration (CMC)

Micelle Formation

As mentioned in the introduction to this section, surfactants adsorb at water-air and water-oil interfaces, reducing surface and interfacial tensions. Solutions of surfactant in water exhibit unusual physical properties. At low concentrations, they behave like any other solution, but at a rather well-defined concentration, the physical properties of a surfactant solution undergo an abrupt change. This change is due to the formation of micelles, i.e., aggregates of 50 to 100 individual surface-active molecules into colloidal-sized particles called *micelles*. The concentration at which

the process of micelle formation starts is called *critical micellization concentration* (CMC). Figure 2.23 shows the typical changes in a number of physical properties of a surfactant solution around its CMC. Any of these properties can be measured as a function of the surfactant concentration to determine its CMC value. Surface tension and turbidity are probably the most commonly used methods for CMC determination. The solubilization method (see below) does not require any instrumentation and can be used for quick and rough estimation of the CMC.

Krafft Point

Another important property of surfactants is the dependence of their solubility on temperature. As the temperature is increased, the solubility also slowly increases, until a certain temperature is reached at which a sudden increase in the solubility occurs. This increased solubility is due to micelle formation; in other words, micelles are only formed above a certain temperature. This is called the *Krafft temperature* or Krafft point, and is characteristic for each surfactant. If we plot the solubility and CMC as functions of temperature on the same plot, the two curves merge at the Krafft point, as shown in Figure 2.24.

At Krafft point, the surfactant solubility is equal to its CMC. It is also the lowest temperature at which micelles can exist. Below Krafft temperature, surfactants form normal solutions without forming micelles. The picture shown in Figure 2.24 is just a small fragment of the surfactant phase diagram. At higher surfactant concentrations, new phases can be formed (e.g., liquid crystals). There will be more on phase diagrams in Chapter 7, which is devoted to the fundamentals of froth treatment.

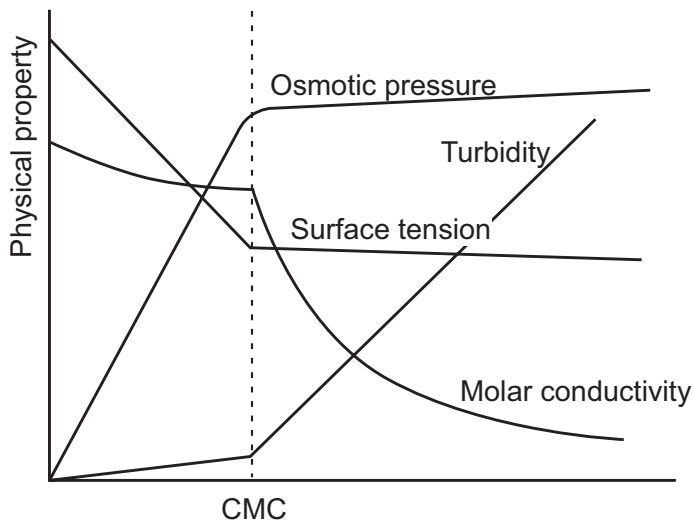


Figure 2.23 Change of selected solution properties at critical micelle concentration (CMC).

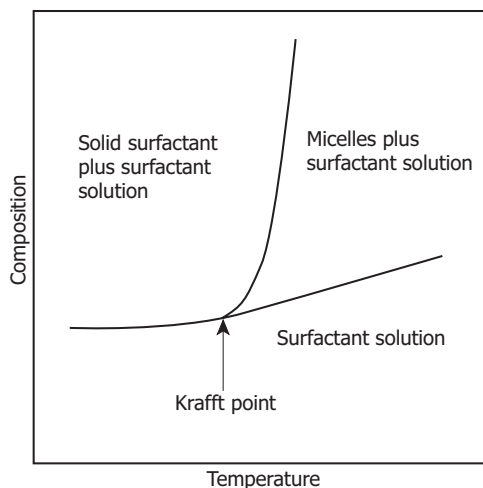


Figure 2.24 Krafft point: Dependence of surfactant solubility on temperature.

It is generally accepted that micelles, at moderate surfactant concentrations, have an approximately spherical shape, with the hydrophilic polar heads facing the water, and the hydrophobic hydrocarbon tails forming the micelle interior. Micelle formation is a characteristic phenomenon in surfactant solutions and is, in a sense, the intermediate stage between phase separation and a true solution. It is interesting to ask why this phenomenon takes place, and why it is limited to molecules with rather long hydrocarbon tails and at the same time, strongly hydrophilic heads, resulting in high LHB values typically greater than 20.

The driving force for micelle formation is a change in water entropy. Normally, water molecules form short-term, crystalline-like associations with their neighbours through hydrogen bonds. These associations are formed on a distance scale of several water molecules, and are like mini icebergs floating in water. The iceberg-like structure of water is responsible for the many extraordinary properties of water. One of them is the very fact that water, or hydrogen oxide (H_2O), is a liquid under normal conditions, while the much heavier analogue, hydrogen sulphide (H_2S), is a gas. Immersion of a hydrocarbon molecule in water disrupts this hydrogen bonding, as water cannot form hydrogen bonds with hydrogen atoms in a hydrocarbon. As a result, the entropy of the system increases. When a hydrocarbon chain forming the tail of a surfactant molecule is removed from water to form a micelle, the hydrogen bonding of water is restored. The corresponding decrease in the system entropy is the main driving factor behind micellization. The head groups remain in contact with water; thus, the thermal effects of micelle formation are small.

Because micellization is driven mostly by entropic effects connected to the removal of the hydrocarbon part of a surfactant molecule from water, the CMC values of surfactants with the same number of carbon atoms in their tails are relatively close to each other. For instance, CMC of surfactants with 12 carbon atoms are of about 10 mmol/L, regardless the nature of the hydrophilic polar head (see Table 2.10).

Table 2.10 CMC values of selected surfactants

Surfactant	CMC (mole/m ³)
Anionic:	
Sodium dodecyl sulphate (SDS)	0.0081
Sodium dodecyl sulphonate	0.0098
Sodium laurate	0.023
Cationic:	
Dodecyl trimethyl ammonium bromide (DTAB)	0.015
Dodecylamine hydrochloride	0.013
Non-ionic:	
Dodecyl (oxyethylene) ₁₂ alcohol	0.0065

Factors Affecting the CMC

For surfactants with a single, straight hydrocarbon tail, the logarithm of CMC decreases linearly with the number of carbon atoms in the tail (n), as shown in the following formula:

$$\log(\text{CMC}) = a - bn,$$

where a and b are constants. The values of b are usually about 0.3, meaning that an increase in the hydrocarbon tail by one CH₂ group is equivalent to a decrease in CMC by a factor of about 2. The nature of the head group controls the value of the constant a and slightly affects the value of b .

Pressure and temperature have little effect on CMC. This is a surprising observation if we keep in mind that micellization is an association process. However, micellization results from a subtle balance of changes in a number of molecular characteristics, including heat capacity, hydrogen bonding, molecular ordering, etc.

Added salt screens the repulsive interaction between the polar, ionic heads of surfactant molecules. It has a strong impact on CMC values. It is not surprising that the impact of added salt is different for ionic and non-ionic surfactants. For ionic surfactants, the impact is double logarithmic:

$$\log(\text{CMC}) = c + d\log(C_s),$$

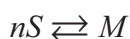
where c and d are constants and C_s is the concentration of the added salt. For non-ionic surfactants, the impact of added salt is much weaker. Salt addition affects the CMC of non-ionic surfactants mostly through slight changes in activities of both the monomer

and micelle species of the surfactant in water. We will not discuss this issue in greater detail, but it is perhaps worth noting that non-ionic detergents would perform relatively well in seawater, while some ionic detergents, like conventional soaps, fail in that environment.

Added organics have a strong effect on CMC. This effect will be discussed in more detail in the following section devoted to solubilization.

Thermodynamics of Micellization

Micellization is usually described using a chemical equilibrium approach known as the *mass action model*. In this model, micellization is formally treated as a chemical reaction



where S and M represent a single surfactant molecule and a micelle, respectively, and n is the aggregation number, i.e., the number of single molecules forming a micelle. The equilibrium constant for the above reaction can be written as

$$K_{micellization} = \frac{a_M}{a_S^n} = \frac{c_M}{c_S^n}$$

Here, a_M and a_S are activities of micelles and monomer surfactant species. Since CMC is relatively low, the activities can be safely replaced with corresponding concentrations c_M and c_S . Aggregation numbers n are relatively high, usually in the range of 50 to 100. As a result, there are practically no micelles in the system at low surfactant concentrations. After crossing the critical micelle concentration, practically all added surfactant ends up forming the micelles. The transition is sharp. The higher the aggregation number, the sharper the transition. This explains the abrupt change in all physical properties of surfactant solutions around CMC. For instance, solutions' turbidity (or ability to scatter light) increases slowly with increasing solute concentration. That is true for any solute. For surfactants, the solution turbidity follows this general trend until CMC. Above CMC, the solution turbidity increases sharply. This is perhaps the best indication of micelle formation, as each micelle becomes a centre for light scattering. Therefore, one would expect almost linear increase in turbidity with increasing concentration, starting at CMC. Such linear increase in turbidity is indeed observed above CMC, as shown in Figure 2.23.

We should add perhaps one more note here, concerning the application of Gibbs' adsorption equation to calculate the surface excess of surfactants. Initially, the surface tension of a surfactant solution decreases with increasing slope, indicating increased adsorption and rising surfactant surface excess, as predicted by Gibbs' equation. Above the CMC, the surface tension of the solution becomes practically constant.

Applying Gibbs's equation to the entire surface tension vs. concentration curve would imply that the surface excess drops to practically zero above CMC—an obviously false conclusion. To avoid any such conclusions, one has to remember that, above CMC, almost all added surfactant contributes to the increased number of micelles, rather than increasing the monomer surfactant concentration. Thus, it is the *monomer* surfactant concentration that does not change above CMC. The surfactant surface excess above CMC remains the same as it was at the CMC.

2.10.4 Solubilization

As mentioned in the previous section, surfactant micelles at moderate surfactant concentrations have an approximately spherical shape, with the polar heads facing the water and the hydrocarbon tails forming the micelle interior. As a result, micelles' interior is almost exclusively composed of hydrocarbons, and as such, is capable of dissolving materials insoluble in water but soluble in organic solvents. As a consequence, aqueous surfactant solutions at concentrations above CMC are capable of dissolving significant amounts of water-insoluble species, all of them ending up in the micelles. This process is called *solubilization*.

The solubilized material causes the micelles to swell and grow bigger. Eventually, if sufficient quantities of the surfactant are present, the swollen micelles may grow so large (up to and above a few micrometres) that they become indistinguishable from typical emulsion droplets. In other words, the boundary between thermodynamically stable, swollen micelles and conventional, thermodynamically unstable emulsions is fuzzy, and a continuous transition from one type of a system to another is possible.

It is worth adding that solubilization can be used for approximate CMC determination. For example, if the solubilized substance is a dye soluble in oil as a neutral molecule, dissociating and forming an organic ion in water, and if the ionic and neutral forms of the dye have different colours, solubilization can be used for very simple determination of the CMC by dilution or titration with water. This process does not call for any of the costly instrumentation required by more precise methods, such as the light-scattering method.

2.10.5 Emulsification

Emulsions are dispersions of a liquid in another immiscible liquid. All highly dispersed colloidal systems, including emulsions, are thermodynamically unstable. When the droplets of emulsified liquid coalesce, the free energy of the system as a whole decreases. Therefore, emulsions should spontaneously separate into two liquid phases. Yet, we know well that many emulsions (like those in many foods and cosmetics) are very stable, lasting for months if not years. Some emulsions are very difficult to break (including those in the petroleum industry). This persistence of emulsions implies the existence of stabilization mechanisms that slow down inevitable phase separation.

There are several emulsion stabilization mechanisms that we should mention. All involve alternation to the surface of emulsified liquid droplets. A dispersion of one clean liquid in another clean liquid, without any additives, will quickly separate into two phases. However, as discussed above, a swollen micelle with solubilized oil in its interior is thermodynamically stable. Between the two extreme systems, there is a whole spectrum of emulsions stabilized with adsorbed surfactant molecules, as in a very large swollen micelle.

Thus, one type of emulsion stabilization mechanism is due to the adsorption of ionic surfactants on the oil-water interface. For oil-in-water (O/W) emulsions, the surfactant adsorbs with its hydrophobic tail immersed in the oil droplet, while the hydrophobic head faces the continuous water phase. In W/O emulsions, the surfactant molecule orientation is reversed. Adsorbed surfactant ions charge the emulsion droplet and electrostatic repulsion resulting from the charged surfaces is responsible for the stabilization, as discussed in details in the section on DLVO theory.

Stabilization may also be due to the physical barrier formed by the adsorption of neutral molecules, often polymers, which prevent the emulsified liquid droplets from approaching each other at a distance small enough for them to coalesce. We call this *steric stabilization*. Often, steric stabilization is not due to the adsorption of individual molecules but to the presence of small solid particles that can get attached to the liquid-liquid interface. Attachment of small solid particles requires that the particles are not completely wettable by any of the liquids. They cannot be completely hydrophilic or hydrophobic. If they were, they would end up completely immersed in the liquid they have affinity to. Steric stabilization by solids requires the contact angle on solid particles to be in the vicinity of 90° .

Emulsions are usually made by vigorous mixing of two liquids in the presence of stabilizers. For instance, mayonnaise (an oil-in-water emulsion) is made by adding a vegetable oil into a small amount of vinegar or lemon juice and an egg yolk. Lecithin, a natural surfactant present in egg yolk, acts as an emulsifier and contributes to the electrostatic repulsion between the oil droplets. Often, small amounts of prepared mustard are also added; the solids from the ground mustard seeds provide additional steric stabilization. Denatured egg proteins also form the steric stabilizing layer.

In the petroleum industry, we often deal with both oil-in-water and water-in-oil emulsions. We will discuss these in more detail in Chapter 7.

2.10.6 Detergency and Flotation

Both detergency and flotation are important industrial processes, and each depends on the manipulation of surface wettability to achieve the desired industrial outcome. The two processes cover a wide variety of phenomena from all areas of colloid and surface chemistry.

Because detergency and flotation are so complex, it would be impossible to describe them in full in the following paragraphs. Thus, we will discuss them here briefly as a conclusion to this chapter on the basics of colloid and surface science.

Detergency

The term ‘detergency’ is used to describe a wide range of phenomena involved in the removal of foreign material from solid surfaces using surface active chemicals. It covers the removal of impurities from fabric, metal surfaces, kitchenware, and glass through the use of surface-active agents (surfactants). It does not cover cleansing purely through mechanical means, such as abrasion or dissolution. Detergency is involved in a variety of practical applications, both everyday and industrial. It is used in personal hygiene; in doing laundry; in washing cars, windows, or dishes; in cleaning laboratory glass; and in washing the trucks used in oil sands mining operations, among many other applications.

Garment fabrics become dirty because oils from skin secretions and hydrocarbons adsorbed from the air act as a binder for dust, soot, etc. Thus, the dirt that accumulates on fabrics and other surfaces has a hydrophobic, oily character. It adheres to the fabric, as the lower the surface energy of the liquid (in this case, the dirt), the more easily it spreads onto a solid of higher surface energy. In oil sands applications, bitumen, an oily liquid, spreads easily on steel, the main material of a truck. It can then capture particles of sand, dust, and other substances. Eventually, thick deposits of dirt (mostly oil sand) accumulate, increasing the vehicle weight and lowering the box capacity.

The removal of a dirt particle in the form of a solid or a very viscous liquid, depicted in Figure 2.25, is governed by the thermodynamics of spreading, discussed in Section 2.2.5. For instance, to analyze a case of dirt removal from a fabric by washing with water, we would use Eq. (2.8), in the form

$$S = \gamma_{F/W} - (\gamma_{F/D} + \gamma_{D/W})$$

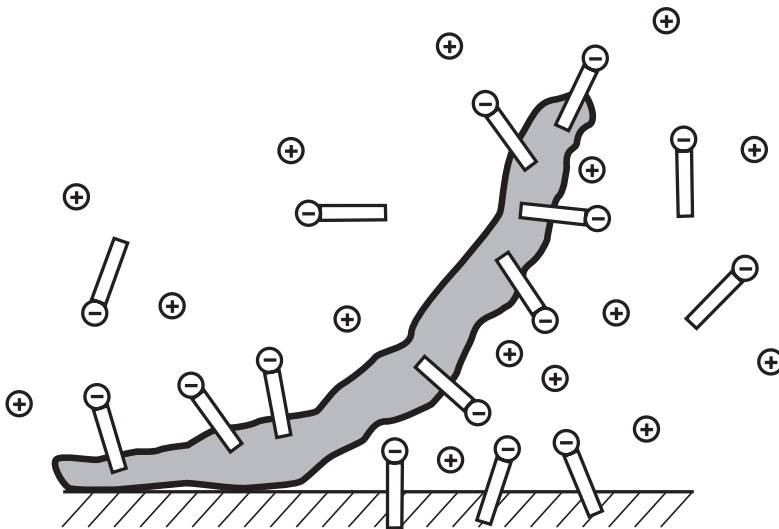


Figure 2.25 Detergency.

If the spreading coefficient of dirt on fibre in water is positive ($S \geq 0$), the dirt will stick to the fibre surface. To remove the dirt from the fibre, we must make the spreading coefficient negative. This can be achieved by lowering the value of the interfacial tension between the fibre and water ($\gamma_{F/W}$). Surfactants adsorb on the fibre, lowering its interfacial tension with water. Thus, the addition of a surfactant will help to 'roll' the dirt off the fibre. We should note that the process of immersing the soiled fabric in water itself makes dirt removal easier, because the fibre-water interfacial tension is lower than that of fibre-air. The addition of a surfactant or a wetting agent makes the surface of the fibre even more favourable to dirt removal. Removal of bitumen from steel (as in washing trucks and other mining equipment) is governed by the same mechanism as the removal of dirt from soiled fabric.

Temperature has a great influence on dirt removal. As the temperature increases, the viscosity of oily dirt (or bitumen) decreases, making its removal easier. Perhaps we should note here that bitumen liberation from sand is, in principle, a washing process: the goal is to wash bitumen off the sand so that it forms individual bitumen droplets. All wetting and spreading science applies as much to washing clothes as to bitumen liberation.

One should also remember that van der Waals forces involved in keeping the dirt at the soiled surface are lower in a water medium than in air (compare the values of the Hamaker constants in air and in water given in Table 2.6). The same mechanism also helps the removal of a sticky label from a glass or a plastic container when the container with the label is immersed in warm water.

Water chemistry has a big impact on washing in general and bitumen recovery in particular. Multivalent cations like calcium and magnesium ions form insoluble precipitates with carboxylic ions (soaps) as well with sulphate-type surfactants. Thus, in hard water, a substantial portion of added soap or synthetic surfactants is used up to bind calcium and magnesium ions from the water. Laundry detergent formulations usually contain sodium metaphosphate (also known as Calgon), a water-softening agent. The role of water chemistry in the oil sands industry will be covered in more depth in Chapter 6.

Flotation

Flotation is the recovery of a valuable mineral by utilizing the differences in wettability between the mineral surface and the gangue rock particles. The process is ages old. In ancient Greek mythology, Jason and his Argonauts went on a quest for the Golden Fleece. Today, there are many interpretations of what the Golden Fleece actually was. A plausible explanation relates to a method of recovering gold from gold-laden streams that was used as early as the fifth century BC. Sheep fleece on a wooden frame was immersed in the stream. The process utilized the natural fats present in the fleece to make the gold particles hydrophobic and to adhere to the fat-covered hairs. The fleece was then dried and the gold shaken out.

Many non-ferrous metals are recovered from their ores by flotation. The ore is first ground to liberate valuable mineral particles from other ore components, called *gangue*. Grinding is usually performed in water, yielding a water-mineral slurry or pulp. A chemical is then added to make the valuable mineral hydrophobic. In flotation,

this chemical is called a *collector*. Another chemical, called a *frother*, is added to facilitate the subsequent dispersion of air into the slurry. Flotation pulp is pumped to flotation cells, where air is introduced and dispersed by mechanically driven rotors. Hydrophobic mineral particles preferentially attach themselves to air bubbles, and having positive buoyancy, form a mineralized froth at the top of the flotation cell, leaving the hydrophilic gangue particles behind. Without going into many details of flotation science and engineering (some of which will be discussed in Chapter 6), we would like to stress that the very basis of the process is the manipulation of mineral wetting character by proper use of chemicals. In this sense, flotation and detergency are just two of many important industrial processes that depend on our ability to control the wetting character of materials.

2.11 Physical Constants and Basic SI Units

Table 2.11 Selected, commonly used physical constants
Source: Masliyah and Bhattacharjee (2006).

Quantity	Symbol	Value and units
Elementary charge	e	$1.602 \cdot 10^{-19}$ [C]
Electric constant (vacuum permittivity)	ϵ_0	$8.854 \cdot 10^{-12}$ [F/m = C/V = C ² /N·m ²]
Avogadro number	N_A	$6.022 \cdot 10^{23}$ [1/mol]
Boltzmann constant	k	$1.381 \cdot 10^{-23}$ [J/K]
Gas constant	$R = k \cdot N_A$	8.314 [J/K·mol]
Faraday constant	F	$9.649 \cdot 10^4$ [C/mol]
Gravity constant	g	9.807 [m/s ²]
Speed of light in vacuum	C	$2.998 \cdot 10^8$ [m/s]
Standard atmosphere	p_0	$1.013 \cdot 10^5$ [Pa]
Zero of Kelvin scale		-273.2 °C or -459.7 °F

Table 2.12 Selected SI units

Quantity	Name	Symbol	Definition
Basic units:			
Mass	Kilogram	kg	
Length	Metre	m	
Time	Second	s	
Temperature	Kelvin	K	
Amount of substance	Mole	mol	
Electric current	Ampere	A	
Luminous intensity	Candela	cd	
Derived units:			
Force	Newton	N	$\text{kg} \cdot \text{m}/\text{s}^2$
Pressure	Pascal	Pa	$\text{N}/\text{m}^2 = \text{kg}/\text{m} \cdot \text{s}^2$
Energy	Joule	J	$\text{N} \cdot \text{m} = \text{kg} \cdot \text{m}^2/\text{s}^2$
Power	Watt	W	$\text{J}/\text{s} = \text{kg} \cdot \text{m}^2/\text{s}^3$
Electric charge	Coulomb	C	$\text{A} \cdot \text{s}$
Electric potential	Volt	V	$\text{J}/\text{C} = \text{kg} \cdot \text{m}^2/\text{s}^3\text{A}$
Electric conductance	Siemens	S	$\text{A}/\text{V} = \text{s}^3 \cdot \text{A}^2/\text{kg} \cdot \text{m}^2$
Electric resistance	Ohm	Ω	$\text{V}/\text{A} = \text{kg} \cdot \text{m}^2/\text{s}^3\text{A}^2$
Electric capacitance	Farad	F	$\text{C}/\text{V} = \text{s}^4 \cdot \text{A}^2/\text{kg} \cdot \text{m}^2$
Frequency	Hertz	Hz	$1/\text{s}$

2.12 References

- Bartell, F.E., and C.E. Whitney. 1932. Adhesion tension. III. *Journal of Physical Chemistry* 36 (12): 3115–3126.
- CRC Press. 2008–2009. *CRC Handbook of Chemistry and Physics*. 82nd ed. Boca Raton: CRC Press.
- Derjaguin, B.V., and L.D. Landau. 1941. Theory of the stability of strongly charged lyophobic sols and of the adhesion of strongly charged particles in solutions of electrolytes. *Acta Physicochem USSR* 14 (6): 633–662.
- Fuchs, N. 1934. Über die Stabilität und Aufladung der Aerosole. *Z. Phys* 89 (11–12): 736–743.
- Griffin, W.C. 1949. Classification of surface-active agents by HLB. *Journal of the Society of Cosmetic Chemists* 1 (5): 311–326.

- Harkins, W.D., and F.E. Brown. 1919. The determination of surface tension (free surface energy), and the weight of falling drops: The surface tension of water and benzene by the capillary height method. *J. Am. Chem. Soc.* 41: 499–524.
- Huethorst, J.A.M., and A.F.M. Leenaars. 1990. A new method for determining the contact angle of a liquid against solid spherical particles. *Colloids and Surfaces* 50: 101–111.
- Kosmulski, M. 2001. *Chemical properties of material surfaces*. Vol. 102, Surfactant science series. New York: Marcel Dekker.
- Masliyah, J.H., and S. Bhattacharjee. 2006. *Electrokinetic and Colloid Transport Phenomena*. New York: John Wiley and Sons.
- Moran, K.L., A. Yeung, J. Czarnecki, and J.H. Masliyah. 2000. Micron-scale tensiometry for studying density-matched and highly viscous fluids: with application to bitumen-in-water emulsions. *Colloids and Surfaces A: Physicochemical and Engineering Aspects* 174 (1–2): 147–157.
- Moran, K.L., A. Yeung, and J. Masliyah. 1999. Measuring interfacial tensions of micrometer-sized droplets: A novel micromechanical technique. *Langmuir* 15 (24): 8497–8504.
- Morrison, I.D., and S. Ross. 2002. *Colloidal dispersions: Suspensions, emulsions, and foams*. New York: Wiley-Interscience.
- Smoluchowski, M. 1917. Versuch einer mathematischen Theorie der Koagulationskinetik kolloider Lösungen. *Z Phys. Chem* 92: 129–168.
- Takamura, K., and E.E. Isaacs. 1989. Interfacial properties. In *AOSTRA technical handbook on oil sands, bitumens and heavy oils, AOSTRA technical publication series no. 6*, AOSTRA Technical Publication Series No. 6, ed. L. E. Hepler and C. Hsi. Edmonton: Alberta Oil Sands Technology and Research Authority (AOSTRA).
- Verwey, E.J.W., and J.T.G. Overbeek. 1948. *Theory of stability of lyophobic colloids*. Amsterdam: Elsevier.
- Yeung, A., T. Dabros, and J.H. Masliyah. 1998. Does equilibrium interfacial tension depend on method of measurement? *Journal of Colloid and Interface Science* 208 (1): 241–247.

Chapter 3

Fluid Particle Dynamics as Applied to Oil Sands Operations

3.1. Multiphase Flow and Applications

The transport of particles in a fluid depends on the force exerted by the fluid on the particles (here, we use the term *fluid* to refer to both liquids and gases). Our discussion will focus mainly on liquid suspensions in a Newtonian carrier liquid. The flow of suspensions of solids and aerated bitumen of varying sizes occurs in a number of oil sands processes, including slurry flow (in hydrotransport and tailings pipelines) and vertical and inclined plate settlers.

Flows are broadly classified as either vertical or horizontal. *Vertical flows* occur in slurries flowing through vertical standpipes and during particle settling in vertical vessels. *Horizontal flows* occur in tailings slurries flowing through horizontal pipelines. The vertical/horizontal classification is based on the nature of the forces acting on the particles in the slurry. In a vertical flow, fluid drag force plays a major role in the movement of the particles within the pipe or vessel. In a horizontal flow, lift forces suspend the particles in the flowing slurry, while fluid drag force allows them to move along with the fluid.

In this chapter, we will focus on vertical flows. We will examine settling in a closed container, vertical flows in standpipes, and separation of particulate matter of different densities and sizes in gravity separation vessels.

The simplest case of fluid particle interaction is that of a steady, slow motion of a solid spherical particle in an infinite expanse of an incompressible Newtonian fluid. We think of the surrounding fluid as infinite to eliminate the effects of the container's walls and the presence of other particles. Here, the analysis of a single particle forms the basis for the analysis of systems containing many particles.

In the following section, we will provide the expressions to deal with a rigid particle of an immobile surface (as opposed to a liquid drop, whose surface can be mobile). We will only formulate the hydrodynamic forces experienced by the particles in which other forces are not present. The influence of other forces (e.g., colloidal surface forces, which are significant for particles of micron and submicron size) will be formulated through empirical parameters.

In describing suspensions of solid particulates, we refer to a system as being *ideal* when the hydrodynamic forces are dominant and *non-ideal* when there are significant colloidal surface forces in addition to the hydrodynamic forces. In non-ideal systems, solids flocculation, repulsion between solids, and clay swelling can take place. Non-ideal systems are typical of suspensions of micron and submicron-sized particles.

3.2. Drag on a Single Rigid Sphere

Consider a rigid (solid) spherical particle of diameter D_p , falling with a velocity $V_{p\infty}$ in a stagnant fluid of a large expanse having a density ρ_f and viscosity μ_f . The forces acting on the spherical particle are:

gravity, F_g :

$$F_g = \rho_p \frac{\pi}{6} D_p^3 g \quad (3.1)$$

buoyancy, F_b :

$$F_b = \rho_f \frac{\pi}{6} D_p^3 g \quad (3.2)$$

and fluid drag, F_d :

$$F_d = \frac{\pi}{8} \rho_f |V_{p\infty}| V_{p\infty} D_p^2 C_D \quad (3.3)$$

where g is the acceleration due to gravity and ρ_p is the particle density. The terminal velocity of the particle in an infinite medium, $V_{p\infty}$, is taken as positive in the same direction as gravity. The drag coefficient, C_D , is defined as

$$C_D = \frac{\text{Drag force } (= F_d)}{(\text{Particle projected area}) \left(\frac{1}{2} \rho_f |V_{p\infty}| V_{p\infty} \right)} \quad (3.4)$$

For a spherical particle, the projected area is $(\pi/4)D_p^2$. The term for the terminal velocity $V_{p\infty}^2$ is written as $|V_{p\infty}| V_{p\infty}$ to account for the fact that both the velocity and force are vector quantities and, by definition, the drag coefficient is a scalar positive quantity.

As seen in Figure 3.1, a force balance on the spherical particle, at steady motion (i.e., in the absence of acceleration), gives

$$F_g = F_d + F_b,$$

leading to

$$\rho_p \frac{\pi D_p^3 g}{6} = \frac{\pi}{8} \rho_f |V_{p\infty}| V_{p\infty} D_p^2 C_D + \rho_f \frac{\pi D_p^3 g}{6} \quad (3.5)$$

and

$$|V_{p\infty}| V_{p\infty} = \frac{4 D_p g}{3 \rho_f C_D} (\rho_p - \rho_f) \quad (3.6)$$

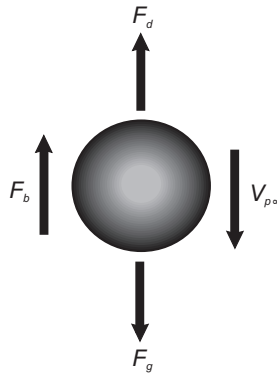


Figure 3.1 Forces on a spherical particle translating in a large expanse of a fluid.

Eq. (3.6) is a general expression for the terminal velocity of a spherical particle in a stagnant fluid. However, in order to determine the terminal velocity, $V_{p\infty}$, we must know the drag coefficient, C_D . The drag coefficient is a function of the Reynolds number (Re), which is defined as

$$\text{Re}_{p\infty} = \frac{D_p |V_{p\infty}| \rho_f}{\mu_f}$$

It is traditionally accepted that a positive value for velocity is used in the Reynolds number expression and that it is not necessary to include the absolute value notation in the Reynolds number term. The Reynolds number is a dimensionless positive number. We can thus write

$$\text{Re}_{p\infty} = \frac{D_p V_{p\infty} \rho_f}{\mu_f} \quad (3.7)$$

The drag coefficient for a solid (rigid) spherical particle is given as

$$C_D = \frac{24}{\text{Re}_{p\infty}} \quad \text{Re}_{p\infty} \rightarrow 0 \quad (3.8a)$$

Stokes' regime

$$C_D = \frac{24 \left[1 + 0.15 \text{Re}_{p\infty}^{0.687} \right]}{\text{Re}_{p\infty}} \quad \text{Re}_{p\infty} < 10^3 \quad (3.8b)$$

Intermediate range, Shiller and Nauman (1933)

$$C_D \sim 0.44 \quad 10^3 \leq \text{Re}_{p\infty} \leq 2 \cdot 10^5 \quad (3.8c)$$

Newton regime

A more general expression for the drag coefficient that covers a wider range of Reynolds numbers for a rigid spherical particle is given by Turton and Levenspiel (1986):

$$C_D = \frac{24}{\text{Re}_{p\infty}} \left[1 + 0.173 \text{Re}_{p\infty}^{0.657} \right] + \frac{0.413}{1 + 16300 \text{Re}_{p\infty}^{-1.09}} \quad \text{Re}_{p\infty} < 2 \cdot 10^5 \quad (3.9)$$

Note that in the Stokes regime, i.e., $\text{Re}_{p\infty} \rightarrow 0$, the expressions for C_D presented by Eqs. (3.8b) and (3.9) become that of Eq. (3.8a) (Stokes 1851).

Figure 3.2 shows the variation of C_D with $\text{Re}_{p\infty}$ for a solid particle.

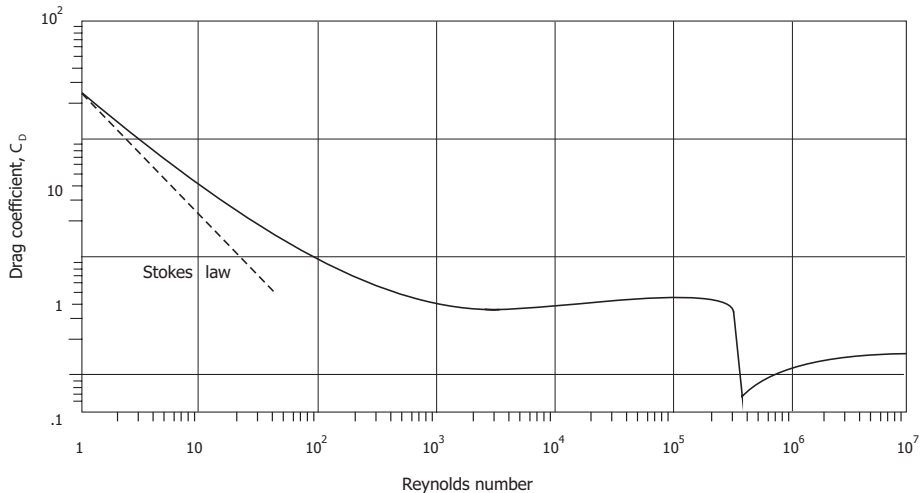


Figure 3.2 Drag coefficient of a spherical particle as a function of Reynolds number (standard drag curve).

Using Eqs. (3.6) and (3.8a), we find that, in a Stokes regime where the particle Reynolds number is very small, the Stokes terminal velocity ($[V_{p^\infty}]_{Stokes}$) of a spherical particle in a stagnant fluid (Stokes 1851) is given by:

$$[V_{p^\infty}]_{Stokes} = \frac{gD_p^2(\rho_p - \rho_f)}{18\mu_f} \quad \begin{array}{l} \text{Re}_{p^\infty} \rightarrow 0, \text{ say, } \text{Re}_{p^\infty} < 0.1 \\ \text{Stokes regime} \end{array} \quad (3.10)$$

Making use of Eq. (3.8b) for $\text{Re}_{p^\infty} < 10^3$, we can write

$$V_{p^\infty} = \frac{gD_p^2(\rho_p - \rho_f)}{18\mu_f [1 + 0.15 \text{Re}_{p^\infty}^{0.687}]} \quad \text{Re}_{p^\infty} < 10^3 \quad (3.11)$$

Making use of Eq. (3.10), we obtain

$$V_{p^\infty} = \frac{[V_{p^\infty}]_{Stokes}}{[1 + 0.15 \text{Re}_{p^\infty}^{0.687}]} \quad \text{Re}_{p^\infty} < 10^3 \quad (3.12)$$

Eq. (3.12) indicates that, at a higher Reynolds number, the terminal velocity of a rigid spherical particle can be substantially lower than its Stokes velocity. Due to the presence of the velocity term in the Reynolds number, Eq. (3.11) indicates that an iterative procedure would be required to evaluate the terminal velocity V_{p^∞} .

For a given particle diameter and density difference, the terminal velocity of a rigid spherical particle in the Stokes regime becomes inversely proportional to the liquid viscosity. However, in the Newton regime, $10^3 < \text{Re}_{p^\infty} < 10^5$, $C_D \sim 0.44$, and the terminal velocity becomes

$$V_{p^\infty} = [3.03D_p g(\rho_p - \rho_f)/\rho_f]^{1/2} \quad (3.13)$$

Eq. (3.13) indicates that the terminal velocity of a rigid spherical particle is *independent* of the fluid viscosity. If we apply the drag coefficient expression of Eq. (3.9) to higher Reynolds numbers, the fluid viscosity has little effect on the particle terminal velocity. From above, it can be seen that the dependence of the particle terminal velocity, V_{p^∞} , on the fluid viscosity is highest when Re_{p^∞} is small, say, $\text{Re}_{p^\infty} < 1$. Consequently, in any viscometry measurement, when the terminal velocity of the particle is used to evaluate the fluid viscosity, it is best to work within the Stokes regime and avoid high Re_{p^∞} situations.

As mentioned earlier, it is clear from Eqs. (3.11) and (3.12) that the Reynolds number contains a velocity term, and therefore, the equations are not explicit in velocity. One can avoid the iterative procedure by a rather elegant approach that was recognized several decades ago. It is based on the fact that the product of C_D and $\text{Re}_{p^\infty}^2$ does not contain a velocity term. Making use of Eq. (3.6) and the definition of Reynolds number, we have

$$C_D \text{Re}_{p\infty}^2 = \frac{4gD_p^3 \rho_f (\rho_p - \rho_f)}{3\mu_f^2} \quad (3.14)$$

It is clear that the term on the right-hand side of Eq. (3.14) contains physical properties only and that it does not contain the particle terminal velocity. The term

$$\frac{gD_p^3 \rho_f (\rho_p - \rho_f)}{\mu_f^2}$$

is known as the Galilei number (Ga) or Archimedes number (Ar). Curve fitting of $C_D \text{Re}_{p\infty}^2$ (i.e., Ga) against $\text{Re}_{p\infty}$ would provide a convenient equation for predicting $\text{Re}_{p\infty}$ and subsequently, $V_{p\infty}$. For our purposes, let us write

$$\text{Ga} = \frac{gD_p^3 \rho_f |(\rho_p - \rho_f)|}{\mu_f^2} \quad (3.15)$$

Traditionally, the absolute notation is not used, based on the assumption that the Galilei number is positive. For Reynolds number evaluation, Hartman et al. (1989) give:

$$\begin{aligned} \log_{10}(\text{Re}_{p\infty}) &= P(A) + \log_{10}(R(A)) \quad \text{for } 1 < \text{Ga} < 10^7 \\ P(A) &= \left[(0.0017795A - 0.0573)A + 1.0315 \right] A - 1.26222 \\ R(A) &= 0.99947 + 0.01853 \sin(1.847A - 3.14) \end{aligned} \quad (3.16)$$

where $A = \log_{10}(\text{Ga})$.

Another useful, frequently used relationship for Reynolds number evaluation, based on Eq. (3.9), is provided by Turton and Clark (1987). It applies for $\text{Re}_{p\infty} < 260\,000$:

$$\text{Re}_{p\infty} = \frac{D_p V_{p\infty} \rho_f}{\mu_f} = \text{Ga}^{1/3} \left[\left(\frac{18}{\text{Ga}^{2/3}} \right)^{0.824} + \left(\frac{0.321}{\text{Ga}^{1/3}} \right)^{0.412} \right]^{-1.214} \quad (3.17a)$$

$$\text{Re}_{p\infty} < 260\,000$$

Once the particle Reynolds number is evaluated, the terminal velocity can be calculated from the Reynolds number given by Eq. (3.7). Both of the above correlations are for subcritical flow over a rigid sphere, where there is no shift in the flow boundary layers, i.e., no discontinuity in the C_D vs. $\text{Re}_{p\infty}$ curve. Figure 3.2 shows an abrupt change in C_D near the critical region.

For non-spherical particles, the concept of sphericity, ϕ , (defined as the ratio of the surface of a sphere having the same volume as the particle to the actual surface

area of the particle) is used to account for the particle's shape in predicting the drag coefficients (Haider and Levenspiel 1989). For $0.5 \leq \phi \leq 1$ and $Re_{p\infty} < 25000$, the following correlation is given:

$$Re_{p\infty} = \frac{D_p V_{p\infty} \rho_f}{\mu_f} = Ga^{1/3} \left[\left(\frac{18}{Ga^{2/3}} \right) + \left(\frac{2.335 - 1.744\phi}{Ga^{1/6}} \right) \right]^{-1} \quad (3.17b)$$

For a non-spherical particle, D_p becomes the diameter of a sphere that has the same volume as the particle. For $\phi = 1$, the case of a perfect sphere, Eq. (3.17b) gives slightly different values for the Reynolds number as compared with Eq. (3.17a). It is recommended that Eq. (3.17a) be used for spherical particles. Bowen and Masliyah (1973) provide a correlation for the drag coefficient for various non-spherical shapes in the Stokes regime.

Example 3.1 Terminal Velocity of a Solid Spherical Particle

We wish to evaluate the terminal settling velocity of a grain of sand in water. The grain has a density of 2650 kg/m^3 and an equivalent diameter of 0.5 mm . Assume that water has a viscosity of $0.001 \text{ Pa}\cdot\text{s}$ and a density of 998 kg/m^3 . There are several methods of approaching this problem.

Method 1

In the first method, we will use an iterative approach to evaluate the terminal velocity. The best initial estimate is made using Eq. (3.10), which gives the Stokes terminal velocity of a spherical particle in a fluid:

$$[V_{p\infty}]_{Stokes} = \frac{gD_p^2(\rho_p - \rho_f)}{18\mu_f}$$

$$V_{p\infty} = \frac{9.81 \times (0.0005)^2 (2650 - 998)}{18 \times 0.001} = 0.225 \text{ m/s}$$

leading to

$$Re_{p\infty} = \frac{D_p V_{p\infty} \rho_f}{\mu_f} = \frac{0.0005 \times 0.225 \times 998}{0.001} = 112.3$$

The improved estimate of the terminal velocity value is obtained from Eq. (3.11),

$$V_{p\infty} = \frac{gD_p^2(\rho_p - \rho_f)}{18\mu_f \left[1 + 0.15 \text{Re}_{p\infty}^{0.687}\right]}$$

giving 0.0465 m/s.

Using the latest velocity estimation, the new Reynolds number is 23.2. Repeating the iterative procedure, we obtain a terminal velocity of 0.0785 m/s. This value is quite different from that given by the Stokes equation due to the higher Reynolds number of the particle, evaluated as 39.2.

Method 2

In the second approach, we employ our own correlation. Let us fit a curve for the term $C_D \text{Re}_{p\infty}^2$ using Eq. (3.8b) for the drag coefficient. Let $x = C_D \text{Re}_{p\infty}^2$ and $y = \text{Re}_{p\infty}$. In the interval of $\text{Re}_{p\infty} = 0 - 100$, we obtain

$$y = 0.0257x - 7.9034 \times 10^{-6}x^2 + 2.023 \times 10^{-9}x^3 - 2.862 \times 10^{-13}x^4 \\ + 2.034 \times 10^{-17}x^5 - 5.680 \times 10^{-22}x^6.$$

From Eq. (3.14), we can evaluate the x value, which is $C_D \text{Re}_{p\infty}^2$:

$$x = \frac{4gD_p^3\rho_f(\rho_p - \rho_f)}{3\mu_f^2} = \frac{4\text{Ga}}{3}$$

$$\frac{4 \times 9.81 \times (0.0005)^3 \times 998 \times (2650 - 998)}{3 \times (0.001)^2} = 2695.6$$

From the curve-fitting equation above, we obtain $y = \text{Re}_{p\infty} = 39.0$.
Since

$$\text{Re}_{p\infty} = \frac{D_p V_{p\infty} \rho_f}{\mu_f}$$

then

$$39.0 = \frac{0.0005 \times V_{p\infty} \times 998}{0.001}$$

leading to $V_{p\infty} = 0.0782$ m/s, which, for all purposes, is identical to the value obtained using the iterative method.

Method 3

Let us now use the correlation given by Eqs. (3.16) and (3.17a):

$$\begin{aligned} \text{Ga} &= \frac{gD_p^3\rho_f(\rho_p - \rho_f)}{\mu_f^2} \\ &= \frac{9.81 \times (0.0005)^3 \times 998 \times (2650 - 998)}{(0.001)^2} = 2021.7 \end{aligned}$$

Eq. (3.16) gives a value of 0.0772 m/s for $V_{p\infty}$, while Eq. (3.17a) gives 0.0806 m/s. These terminal velocity values are considered to be close to each other and to the value obtained by trial and error.

3.3. Bubbles and Drops

An excellent review on single bubbles and liquid drops is given by Clift, Grace, and Weber (1978). Drops and bubbles are different from rigid particles, which are inherently assumed to have an immobile surface. The outer surface of a drop or bubble may not be rigid. Both have some fluid circulating inside them. Moreover, due to their non-rigid outer surface, drops and bubbles are subject to deformation.

The drag coefficient in cases where the bubble or drop Reynolds number is higher than the limiting case of zero, coupled with a large Eötvös number (Eo), becomes a function of several physical parameters.

The drag coefficient of a fluid drop or bubble in the Stokes regime in the absence of surface-active agents is given by Hadamard (1911) as where K is the viscosity ratio of the fluid outside of the drop or bubble (continuous phase) to that inside it (dispersed phase):

$$C_D = \frac{24}{\text{Re}_\infty} \left(\frac{(2/3)K + 1}{1 + K} \right) \quad \text{Re}_\infty \rightarrow 0, \text{ say } \text{Re}_\infty < 0.1 \quad (3.18)$$

$$\begin{aligned} K &= \mu_f / \mu_{\text{inner}}; \\ \mu_f &= \text{viscosity of continuous phase;} \\ \mu_{\text{inner}} &= \text{viscosity of dispersed phase.} \end{aligned}$$

For rigid spheres, $K \rightarrow 0$. For gas spheres, $K \rightarrow \infty$; i.e.,

$$C_D = \frac{24}{\text{Re}_\infty} \quad K \rightarrow 0 \text{ (rigid sphere)} \quad (3.19a)$$

$$C_D = \frac{16}{\text{Re}_\infty} \quad (3.19b)$$

According to Eq. (3.19b), in a perfectly clean system where no surface-active materials (surfactants) are present, the drag coefficient for an air bubble is less than that for a rigid sphere. However, in practice, the presence of surfactants makes the outer surface of a gas bubble or a liquid drop immobile, and we can apply the drag coefficient for the rigid sphere. As oil sands slurries contain surface-active components, in the case of very small Reynolds numbers, a single gas bubble or a drop behaves as a rigid spherical particle.

Let us now consider the case of higher Reynolds numbers. Bubbles and drops in free rise or fall in an infinite media, under the influence of gravity, are grouped under the categories spherical, ellipsoidal, and spherical cap. These shapes occur depending on the bubble Reynolds number (Re_∞) and the Eötvös number. Figure 3.3 shows the various regimes for a single bubble or drop.

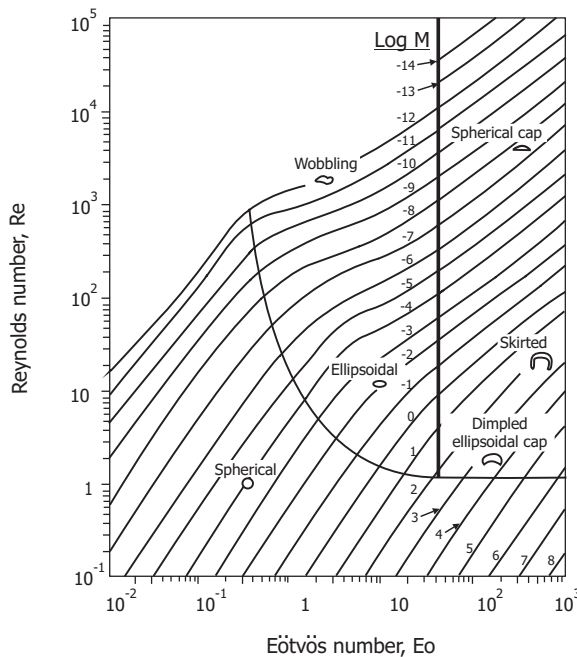


Figure 3.3 Shape regimes of bubbles and drops in unhindered gravitational motion through liquids.

Source: Clift, Grace, and Weber (1978).

For bubbles and drops, we have the Reynolds number,

$$\text{Re}_\infty = \rho_f De V_\infty / \mu_f = \frac{\text{Inertial force}}{\text{Viscous force}}$$

the Morton number,

$$\text{Mo} = g \mu_f^4 \Delta\rho / \rho_f^2 \sigma^3$$

and the Eötvös number,

$$\text{Eo} = g \Delta\rho D_e^2 / \sigma = \frac{\text{Buoyancy force}}{\text{Interfacial tension force}}$$

where

- ρ_f = density of continuous phase, in $\text{kg}\cdot\text{m}^{-3}$;
- μ_f = viscosity of continuous phase, in $\text{Pa}\cdot\text{s}$;
- σ = interfacial tension, in $\text{N}\cdot\text{m}^{-1}$;
- $\Delta\rho$ = absolute value of density difference between particle and continuous phase, in $\text{kg}\cdot\text{m}^{-3}$;
- V_∞ = fall or terminal rise velocity of a drop or bubble, in $\text{m}\cdot\text{s}^{-1}$;
- De = diameter of volume equivalent $De = (6V_o / \pi)^{1/3}$, in m;
- V_o = volume of bubble or drop, in m^3 ; and
- g = gravitational acceleration, in $\text{m}\cdot\text{s}^{-2}$.

Experimentally measured terminal rise velocities of an air bubble in pure water and in water contaminated with surface-active components are given in Figure 3.4. For air bubbles of an intermediate diameter (0.8 mm to 10 mm), the plot shows a significant difference in air rise velocity between pure and contaminated water. With increasing size, the bubble changes its shape and, consequently, its rise velocity becomes quite different from that of a rigid spherical particle.

The terminal velocity (V_∞) of a drop or bubble in an infinite media is correlated by Clift, Grace, and Weber (1978) as

$$V_\infty = \frac{\mu_f}{\rho_f De} \text{Mo}^{-0.149} (J - 0.857) \quad (3.20)$$

where

$$H = (4/3) Eo Mo^{-0.149} (\mu_f / \mu_w)^{-0.14};$$

$$Eo = g \Delta\rho D e^2 / \sigma \text{ (Eötvös number);}$$

$$Mo = g \mu_f^4 \Delta\rho / \rho_f^2 \sigma^3 \text{ (Morton number);}$$

$$J = 0.94 H^{0.757} \quad (2 < H \leq 59.3);$$

$$J = 3.42 H^{0.441} \quad (H > 59.3); \text{ and}$$

$$\mu_w = 0.0009 \text{ Pa}\cdot\text{s (reference viscosity).}$$

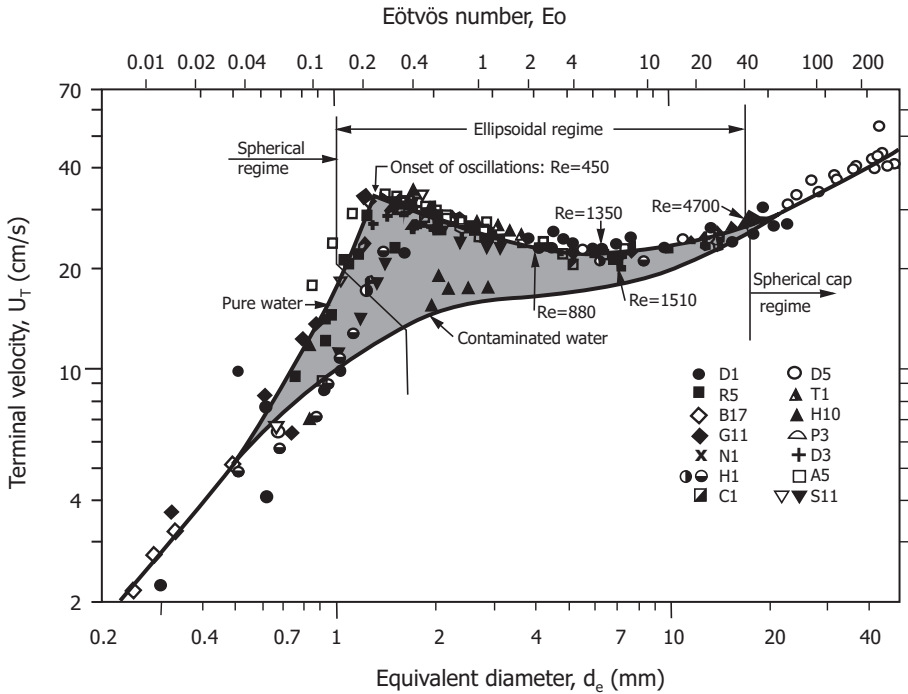


Figure 3.4 Terminal velocity of air bubbles in pure and contaminated water as a function of bubble equivalent diameter. Shaded area is where most of the rise velocity data would fall depending on the type and concentration of the surface-active agents in the water.

Source: Clift, Grace, and Weber (1978).

Example 3.2 Terminal Velocity of a Light Oil Drop

In this example, we wish to evaluate the terminal rise velocity of a light oil in water. The oil has a density of 850 kg/m³ and an equivalent diameter of 5.5 mm. Assume that the oil has a viscosity of 0.0007 Pa·s, while the water has a viscosity of 0.001 Pa·s and a density of 998 kg/m³. The interfacial tension is 0.045 N/m. Let us evaluate each pertinent term:

$$E_o = g \Delta\rho D e^2 / \sigma ;$$

$$E_o = 9.81 \times (998 - 850) \times (0.0055)^2 / 0.045 = 0.976;$$

$$M_o = g \mu_f^4 \Delta\rho / \rho_f^2 \sigma^3 ;$$

$$M_o = 9.81 \times (0.001)^4 \times (998 - 850) / [(998)^2 \times (0.045)^3];$$

$$M_o = 1.6 \times 10^{-11};$$

$$H = (4/3) E_o M_o^{-0.149} (\mu_f / \mu_w)^{-0.14};$$

$$H = (4/3) \times 0.976 \times (1.6 \times 10^{-11})^{-0.149} (0.001/0.0009)^{-0.14} = 52.07;$$

$$J = 0.94 H^{0.757} = 0.94 \times (52.07)^{0.757} = 18.73;$$

$$V_\infty = \frac{\mu_f}{\rho_f D e} M_o^{-0.149} (J - 0.857);$$

$$V_\infty = \frac{0.001}{0.0055} (1.6 \times 10^{-11})^{-0.149} (18.73 - 0.857) = 0.132 \text{ m/s}$$

The Reynolds number of the drop is

$$Re = \frac{D e V_\infty \rho_f}{\mu_f} = \frac{0.0055 \times 0.132 \times 998}{0.001} = 725$$

With an Eötvös number of close to unity and a Reynolds number of 725, the oil drop would fit in the wobbling category indicated in Figure 3.3. The terminal velocity of air bubbles in pure and contaminated water is given in Figure 3.4.

3.4. Ideal System: Multi-Particle System of the Same Species

In the previous section, we implicitly assumed that the fluid itself is stagnant and that we are dealing with a single particle, with no other particles close to it, and in the absence of any walls containing the particle and the surrounding fluid. In this section, we will concern ourselves with a suspension of solid particles of the same density and diameter. The presence of other particles in a suspension influences the drag experienced by a given particle in the system.

Escudie et al. (2006) give a good summary on solids-liquid settling systems. For a generalized problem, the relative velocity between a particle's velocity in a suspension and the fluid velocity, denoted as $V_p - V_f$, is given in Wallis (1969) as

$$V_p - V_f = V_{p\infty} \alpha_f F(\alpha_f, \text{Re}_{p\infty}) \quad (3.21)$$

The velocities are relative to a stationary frame of reference, such as a pipe through which a suspension flows. In terms of the terminal velocity expression provided by Eq. (3.17a), Eq. (3.21) becomes

$$V_p - V_f = \left[X \frac{\mu_f}{D_p \rho_f} \right] \alpha_f F(\alpha_f, \text{Re}_{p\infty}) \quad (3.22)$$

where X represents the right-hand side of Eq. (3.17a). What is important here is that the term $[o]$ represents the particle terminal velocity in an infinite stagnant medium, irrespective of the expression or method used in its evaluation.

To simplify the analysis, let us use the expression given for $V_{p\infty}$ by Eq. (3.11), even though it is restricted to $\text{Re}_{p\infty} < 10^3$. Eq. (3.21) becomes

$$V_p - V_f = \left[\frac{g D_p^2 (\rho_p - \rho_f)}{18 \mu_f (1 + 0.15 \text{Re}_{p\infty}^{0.687})} \right] \alpha_f F(\alpha_f, \text{Re}_{p\infty}) \quad (3.23)$$

for $\text{Re}_{p\infty} < 10^3$

One can also write

$$V_p - V_f = \left[\frac{[V_{p\infty}]_{Stokes}}{(1 + 0.15 \text{Re}_{p\infty}^{0.687})} \right] \alpha_f F(\alpha_f, \text{Re}_{p\infty}) \text{ for } \text{Re}_{p\infty} < 10^3 \quad (3.24a)$$

In the Stokes regime, we have

$$V_p - V_f = \left[\frac{g D_p^2 (\rho_p - \rho_f)}{18 \mu_f} \right] \alpha_f F(\alpha_f) \quad (3.24b)$$

where $\frac{gD_p^2(\rho_p - \rho_f)}{18\mu_f}$ is the Stokes terminal velocity, $[V_{p\infty}]_{\text{Stokes}}$.

The following definitions apply:

V_p = particle velocity in a suspension relative to a stationary observer, in $\text{m}\cdot\text{s}^{-1}$;

$V_{p\infty}$ = particle terminal velocity in a stagnant fluid at infinite dilution, in $\text{m}\cdot\text{s}^{-1}$;

V_f = fluid velocity relative to a stationary observer, in $\text{m}\cdot\text{s}^{-1}$;

μ_f = fluid viscosity, in $\text{Pa}\cdot\text{s}$;

ρ_p = particle density, in $\text{kg}\cdot\text{m}^{-3}$;

ρ_f = fluid density, in $\text{kg}\cdot\text{m}^{-3}$;

g = gravitational acceleration, in $\text{m}\cdot\text{s}^{-2}$;

α_f = fluid volume fraction (porosity); and

$F(\alpha_f, \text{Re}_{p\infty})$ = function of fluid volume fraction and Reynolds number to account for the presence of particles. It is a hindered settling function.

As the velocities are vector quantities, we need to be concerned with direction as well as with their scalar values. In this chapter, we denote a downward direction as being positive.

The hindered settling function, $F(\alpha_f, \text{Re}_{p\infty})$, is given by various researchers. The best known expression for $F(\alpha_f, \text{Re}_{p\infty})$ is that of Richardson and Zaki, for rigid spherical particles (1954). They give

$$F(\alpha_f, \text{Re}_{p\infty}) = \alpha_f^{n-2} \quad (3.25)$$

The Richardson-Zaki index, n , is a function of the particle Reynolds number, $\text{Re}_{p\infty}$. Eq. (3.21) becomes

$$V_p - V_f = V_{p\infty} \alpha_f^{n-1} \quad (3.26a)$$

When the Richardson and Zaki hindered settling function is used together with the $V_{p\infty}$ expression given in Eq. (3.11), Eq. (3.26a) becomes

$$V_p - V_f = \left[\frac{gD_p^2 (\rho_p - \rho_f)}{18\mu_f (1 + 0.15 \text{Re}_{p\infty}^{0.687})} \right] \alpha_f^{n-1} \quad \text{for } \text{Re}_{i\infty} < 10^3 \quad (3.26b)$$

In the absence of colloidal forces and particle flocculation, the index n becomes only a function of the Reynolds number and is given by Wallis (1969) in terms of the Reynolds number as

$$n = 4.7 \frac{1 + 0.15 \text{Re}_{p\infty}^{0.687}}{1 + 0.253 \text{Re}_{p\infty}^{0.687}} \quad \text{for } \text{Re}_{p\infty} < 10 \quad (3.27a)$$

In the Rowe correlation (1987), the index n is given in terms of the Reynolds number as

$$n = 4.7 \frac{1 + 0.0874 \text{Re}_{p\infty}^{0.75}}{1 + 0.175 \text{Re}_{p\infty}^{0.75}} \quad \text{for } \text{Re}_{p\infty} < 10^5 \quad (3.27b)$$

In the Khan and Richardson (1989) correlation, the index n is given in terms of the Galilei number as

$$n = 4.8 \frac{1 + 0.0215 \text{Ga}^{0.57}}{1 + 0.043 \text{Ga}^{0.57}} \quad \text{for } \text{Re}_{p\infty} < 10^5 \quad (3.27c)$$

The particle Reynolds number can be evaluated from Eqs. (3.16) or (3.17a) to be used in Eq. (3.27) for n -index evaluation. The Galilei number is defined by Eq. (3.15) and contains only the physical properties of the system. Accordingly, index n can be directly evaluated from Eq. (3.27c) using the physical properties of the system.

A comparison of the various equations for the n index are shown in Figure 3.5. The correlations by Khan and Richardson (1989) and Rowe (1987) are quite similar. The Wallis correlation (1969) deviates sharply from the others at higher Reynolds numbers.

For a system with large spherical particles, say, $D_p > 100 \mu\text{m}$, in the absence of surface colloidal forces (i.e., surface charges), the value of n is 4.7 for $\text{Re}_{p\infty} \rightarrow 0$. For systems with colloidal flocculating particles, n can be much larger than 4.7—as high as 20, if not higher. In an ideal system, for the Stokes regime, we have $n = 4.7$, and Eq. (3.26b) becomes

$$V_p - V_f = \left[\frac{gD_p^2 (\rho_p - \rho_f)}{18\mu_f} \right] \alpha_f^{3.7} \quad (3.28)$$

The general relative (slip) velocity ($V_p - V_f$) relationship of Eq. (3.21) and the more specific relative velocity of Eqs. (3.22), (3.26b), and (3.28) can be used quite effectively in solving many problems involving moving particles in a suspension. Note that the derived relative velocity equations are valid for only *one* particle species in the suspension, i.e., all particles present in the suspension have the same density and diameter.

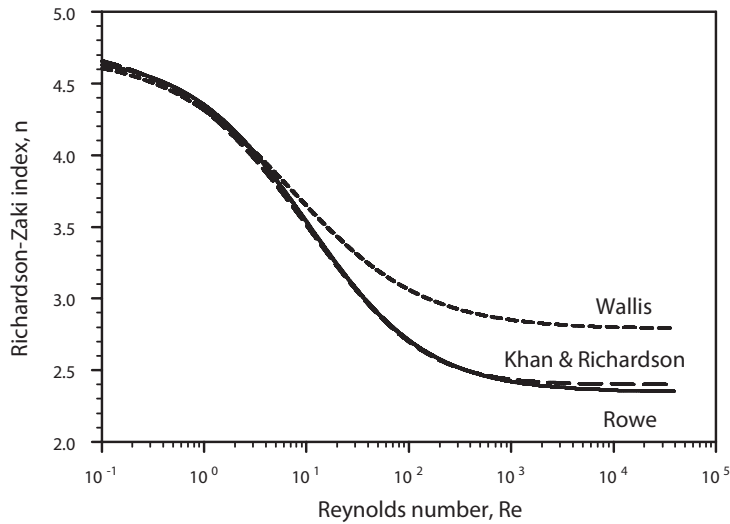


Figure 3.5 Comparison between various correlations for the variation of Richardson-Zaki index, n , with Reynolds number, Re .

Sources: Wallis (1969), Khan and Richardson (1989), and Rowe (1987).

Example 3.3 Batch Settling of a Suspension in a Closed Vertical Container

Consider a suspension of rigid spherical particles, such as sand, in water that is contained inside a vertical graduated cylinder, as shown in Figure 3.6.

Assume that the particles are of diameter D_p and of density ρ_p . The density of the liquid (water) is ρ_f and its viscosity is μ_f . The volume fraction of the particles is α_p and that of the liquid is α_f . Our task is to evaluate the suspension settling velocity, V_p . Only hydrodynamic forces are present. The applicable expression for the relative velocity is given by Eq. (3.26a), where it is assumed that colloidal forces are absent. We have:

$$V_p - V_f = V_{p\infty} \alpha_f^{n-1} \quad (3.29)$$

The velocity given by V_p is the settling velocity of the suspension. We need more information in order to eliminate V_f from Eq. (3.29). At the interface of the falling suspension and across a horizontal surface drawn through the suspension, the volumetric rate of the particles settling (downward direction) is equal to the volumetric rate of the rising liquid (upward direction). This is true because the volumetric rate

of the settling particles must be replaced by the liquid. This kinematic volumetric relationship is given as

$$A\alpha_p V_p + A\alpha_f V_f = 0 \quad (3.30)$$

Eq. (3.30) states that there is no net volumetric flow across a horizontal plane within the suspension. Here, α_p is the volume fraction of the particles and A is the cross-sectional area of the graduated cylinder. Eq. (3.30) leads to

$$V_f = \frac{-(1-\alpha_f)V_p}{\alpha_f} \quad (3.31)$$

where

$$\alpha_p + \alpha_f = 1 \quad (3.32)$$

and where α_p is the volume fraction of the particles. Using Eq. (3.31) to eliminate V_f from Eq. (3.29) yields

$$V_p + \frac{(1-\alpha_f)V_p}{\alpha_f} = V_{p\infty}\alpha_f^{n-1} \quad (3.33)$$

Eq. (3.33) reduces to

$$\frac{V_p}{V_{p\infty}} = \alpha_f^n \quad (3.34a)$$

Since $\alpha_p + \alpha_f = 1$, Eq. (3.34a) becomes

$$\frac{V_p}{V_{p\infty}} = (1-\alpha_p)^n \quad (3.34b)$$

In the Stokes regime, $n = 4.7$, so for Eq. (3.34), we can write

$$\left[\frac{V_p}{V_{p\infty}} \right]_{Stokes} = \alpha_f^{4.7} = (1-\alpha_p)^{4.7} \quad (3.35)$$

Eq. (3.35) is the Richardson-Zaki batch settling equation of a suspension of rigid spheres in the Stokes regime. It gives the settling rate of the suspension as compared to the settling rate of a single particle in an infinite medium. Eq. (3.35) shows a strong dependence of the settling velocity on the suspension volume fraction, as shown in Table 3.1. In the literature related to solids thickening, the fluid concentration, α_p , is simply the suspension porosity, ε .

The reason for including the term α_f on the right-hand side of Eq. (3.21) is to ensure that the derived form of Eq. (3.34) conforms to the historical batch settling equation format of Richardson and Zaki.

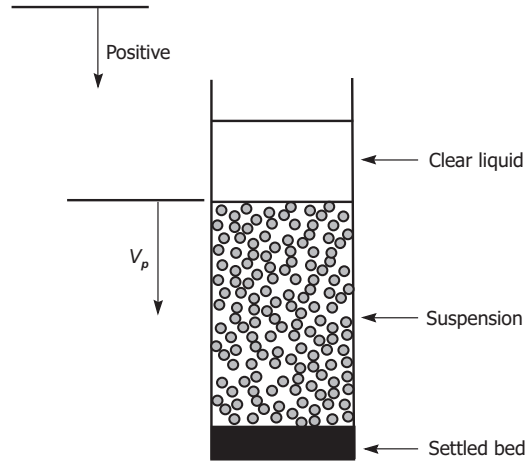


Figure 3.6 Settling of a suspension in a graduated cylinder.

Table 3.1 Effect of solids volume fraction on normalized suspension settling velocity

Volumetric solids concentration (α_p)	$V_p / [V_{p\infty}]_{\text{Stokes}}$
0	1.00
0.1	0.61
0.2	0.35
0.3	0.19
0.4	0.09

Example 3.4 Liquid Fluidization of Particles Assumed to be Spherical

Here, we deal with liquid (e.g., water) fluidization of sand. The liquid enters at the bottom of a cylinder containing the sand. At a sufficiently high water flow rate, the sand particles are fluidized and the sand bed expands with increasing water flow rate (Figure 3.7). Using the same assumptions as in Example 3.3, the governing relative velocity expression is provided by Eq. (3.26a):

$$V_p - V_f = V_{p\infty} \alpha_f^{n-1} \quad (3.36)$$

At any given horizontal plane within the fluidized bed, there is no net flow of solids. This is evident by the fact that no solids leave the cylinder. Hence, $V_p = 0$, and, from Eq. (3.36), we obtain

$$V_f = [-V_{p\infty}] \alpha_f^{n-1} \quad (3.37)$$

The negative sign in Eq. (3.37) is due to the upward direction of the liquid velocity (a positive sign is ascribed to a downward velocity). The terminal sand particle velocity, $V_{p\infty}$, is positive.

If the volumetric liquid flow rate is Q_f within the fluidized bed, we obtain

$$Q_f = A[-V_f] \alpha_f \quad (3.38)$$

where A is the cross-sectional area of the empty bed. Combining Eqs. (3.37) and (3.38) yields

$$Q_f = AV_{p\infty} \alpha_f^n = AV_{p\infty} (1 - \alpha_p)^n \quad (3.39)$$

This is the liquid volumetric flow rate required to fluidize the particles at a fluidized bed solids volume fraction of α_p . In the Stokes regime, we have

$$Q_f = A[V_{p\infty}]_{Stokes} \alpha_f^{4.7} = A[V_{p\infty}]_{Stokes} (1 - \alpha_p)^{4.7}$$

We can write

$$\alpha_p = 1 - \left[\frac{[Q_f/A]}{[V_{p\infty}]_{Stokes}} \right]^{1/4.7} \quad (3.40)$$

Figure 3.8 shows the sand bed expansion as a function of $[Q_f/A]/[V_{Stokes}]$. Clearly, we cannot have a negative solids volume fraction, which occurs when $[Q_f/A]/[V_{Stokes}]$ is greater than unity. This is because the liquid flow velocity in the cylinder exceeds the terminal velocity of the solid particles (single sand grains) and there are no remaining solids in the cylinder.

Due to physical restriction, spherical solids packing cannot exceed that of dense packing (about 0.75). Therefore, introducing physical constraints, the curve within BC of Figure 3.8 is the only valid part of Eq. (3.40). One can easily generalize the examples for solids settling and fluidization to other flow systems.

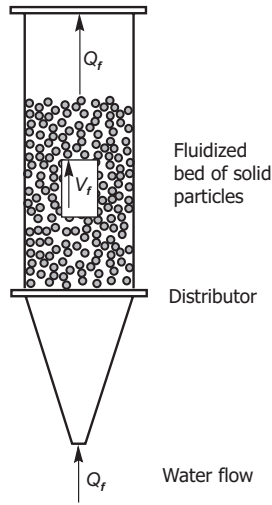


Figure 3.7 Liquid fluidization of spherical solid particles.

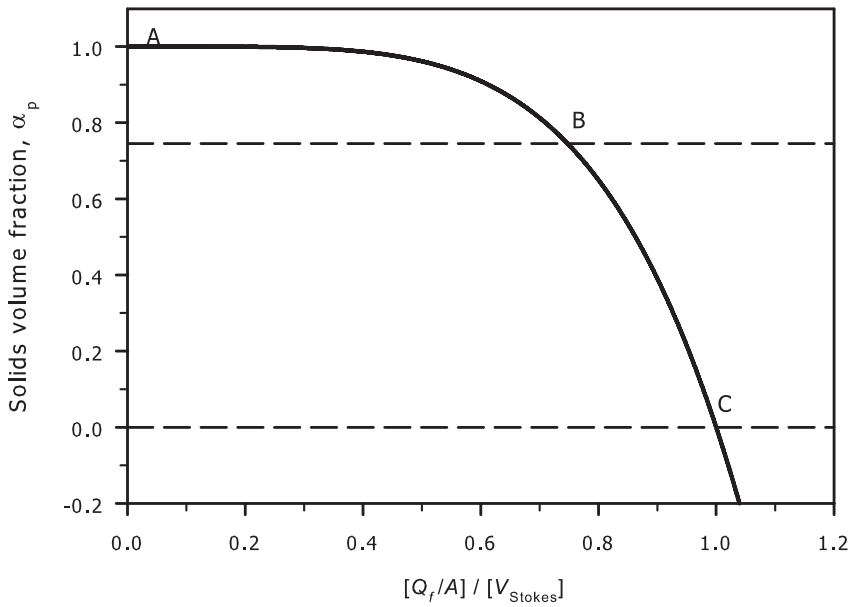


Figure 3.8 Solids bed expansion in liquid fluidization.

Example 3.5 Downward Vertical Flow of a Slurry (Suspension) in a Standpipe

Let us consider a dilute slurry (suspension) entering a vertical pipe with a vertically downward flow (Figure 3.9). Let us assume that the solids are spherical particles with a diameter of 2 mm and a density of 2650 kg/m³. At the inlet, the solids' mass flow rate is 50 kg/s. Water is mixed with the solids at a rate of 150 kg/s. The pipe's inner diameter is 0.7 m. Assume that the density of the water is 998 kg/m³ and its viscosity is 0.001 Pa·s. We wish to determine the following:

- What is the solids volume fraction of the suspension entering the pipeline?
- What is the solids in situ volume fraction?
- What is the solids in situ weight percent?

Let mass flow rate be presented by M (kg/s). Let density be represented by ρ (kg/m³) and the water viscosity by μ_f (Pa·s).

(a) Let the volume fraction of the solids at the pipe inlet be α_p . Then,

$$(\alpha_p)_{Inlet} = \frac{\frac{M_p}{\rho_p}}{\frac{M_p}{\rho_p} + \frac{M_f}{\rho_f}} = \frac{\frac{50}{2650}}{\frac{50}{2650} + \frac{150}{998}} = 0.1115$$

If we were to collect the suspension in a vessel, its solids volume fraction would be 0.1115 and its solids weight percent would be 25 wt. %.

(b) The relative velocity equation $V_p - V_f = V_{p\infty} \alpha_f^{n-1}$ is given by Eq. (3.26a). The term α_f represents the in situ water volume fraction in the pipe. We can write $M_p = AV_p \alpha_p \rho_p$ for the solids mass flow rate and $M_f = AV_f \alpha_f \rho_f$ for the water mass flow rate, where A is the pipe inner cross-section flow area, and α is volume fraction (where $\alpha_f + \alpha_p = 1$). The subscripts f and p refer to water and particles, respectively.

$$\frac{M_p}{A\rho_p\alpha_p} - \frac{M_f}{A\rho_f\alpha_f} = V_{p\infty}\alpha_f^{n-1} \quad (3.41)$$

Making use of the mass flow rates, we obtain the relative velocity equation. We can evaluate the Reynolds number of the particles, $Re_{p\infty}$, using Eq. (3.17a), and the coefficient n using Eq. (3.27c). The Galilei number is now given as

$$Ga = \frac{gD_p^3\rho_f(\rho_p - \rho_f)}{\mu_f^2} = \frac{9.81 \times (0.002)^3 \times 998 \times (2650 - 998)}{(0.001)^2} = 129390$$

From Eq. (3.17a), we have

$$\text{Re}_{p\infty} = (129390)^{1/3} \left[\left(\frac{18}{(129390)^{2/3}} \right)^{0.824} + \left(\frac{0.321}{(129390)^{1/3}} \right)^{0.412} \right]^{-1.214}$$

This gives us $\text{Re}_{p\infty} = 544.7$, which leads to

$$V_{p\infty} = \frac{\text{Re}_{p\infty} \mu_f}{D_p \rho_f} = \frac{544.7 \times 0.001}{0.002 \times 998} = 0.273 \text{ m/s}$$

From Eq. (3.27c),

$$n = 4.8 \frac{1 + 0.0215 \text{Ga}^{0.57}}{1 + 0.043 \text{Ga}^{0.57}}$$

we have

$$n = 4.8 \frac{1 + 0.0215 \times (129400)^{0.57}}{1 + 0.043 \times (129400)^{0.57}} = 2.47$$

Finally, Eq. (3.41) gives

$$\frac{50}{0.385 \times 2650 \times (1 - \alpha_f)} - \frac{150}{0.385 \times 998 \times \alpha_f} = 0.273 \alpha_f^{2.47-1}$$

where the pipe flow area A is 0.385 m^2 .

When we solve the above non-linear equation, we obtain a water volume fraction of $\alpha_f = 0.9263$ and a solids volume fraction of $\alpha_p = 0.0737$. We recall that the inlet particle volume fraction, (α_p), is 0.1115, as evaluated under case (a). The reason for the difference between the inlet volume fraction and the in situ value within the vertical pipe is that the particles move faster than the water due to their settling within the pipeline.

From $M_p = A V_p \alpha_p \rho_p$, we obtain

$$V_p = \frac{M_p}{A \alpha_p \rho_p} = \frac{50}{0.385 \times 0.0737 \times 2650} = 0.665 \text{ m/s}$$

for the particle velocity, which is relative to a stationary observer—the pipe itself.

From $M_f = A V_f \alpha_f \rho_f$ we obtain the fluid velocity,

$$V_f = \frac{M_f}{A \alpha_f \rho_f} = \frac{150}{0.385 \times 0.9263 \times 998} = 0.421$$

which is also relative to the pipe itself.

(c) The in situ solids weight percent, W_p , is given as

$$W_p = \frac{100\alpha_p\rho_p}{\alpha_p\rho_p + \alpha_f\rho_f} = \frac{100 \times 0.0737 \times 2650}{0.0737 \times 2650 + 0.9263 \times 998} = 17.4 \text{ wt. \%}$$

If we were to measure the solids volume fraction inside the pipe using, say, a gamma ray sensor, then 0.0737 would be the measured solids volume fraction value with a solid weight percent of 17.4. In the next example, we will consider an upward flow of a suspension in a vertical pipeline.

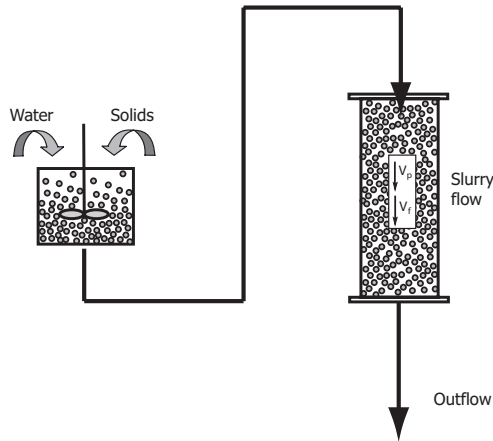


Figure 3.9 Downflow of a suspension.

Example 3.6 Upward Vertical Flow of a Slurry (Suspension) in a Standpipe

In this example, we have an upward flow in a vertical pipe (Figure 3.10). The inlet volume fraction of the particle solids and water are the same, including the particles' Galilei number and n value. The difference arises in the mass balance equations. We now have

$$M_p = -AV_p\alpha_p\rho_p$$

for the particle mass balance and

$$M_f = -AV_f\alpha_f\rho_f$$

for the water mass balance.

In our analysis, a negative sign denotes an upward direction, which is the case here for both the particles and the water (conversely, a positive sign denotes a downward direction). Since the mass flow rate is composed of scalar and positive numbers, it becomes necessary to include the negative sign in the mass balance equations. The relative velocity equation becomes

$$-\frac{M_p}{A\alpha_p\rho_p} + \frac{M_f}{A\alpha_f\rho_f} = [V_{p^\infty}] \alpha_f^{n-1} \quad (3.42)$$

leading to

$$-\frac{50}{0.385 \times (1 - \alpha_f) \times 2650} + \frac{150}{0.385 \times \alpha_f \times 998} = 0.273 \alpha_f^{2.47-1} \quad (3.43)$$

Solving for α_p , we obtain $\alpha_f = 0.8200$ and $\alpha_p = 0.1800$. Clearly, the particles' in situ volume fraction in the vertical pipe is much higher than that in the inlet mixture, which is 0.1115.

Using the mass balance equations for the particles' velocity in the pipe, we have:

$$V_p = \frac{-M_p}{A\alpha_p\rho_p} = \frac{-50}{0.385 \times 0.18 \times 2650} = -0.272 \text{ m/s}$$

with respect to a stationary observer. For the fluid velocity in the pipe, we have:

$$V_f = \frac{-M_f}{A\alpha_f\rho_f} = \frac{-150}{0.385 \times 0.82 \times 998} = -0.476 \text{ m/s}$$

also with respect to a stationary observer. The negative sign indicates that the velocities are upward.

The in situ weight percent of the particles is given as

$$W_p = \frac{100\alpha_p\rho_p}{\alpha_p\rho_p + \alpha_f\rho_f} = \frac{100 \times 0.18 \times 2650}{0.18 \times 2650 + 0.82 \times 998} = 36.8 \text{ wt. \%}$$

At 36.8 wt. %, the in situ solids concentration is much higher than the inlet concentration (25 wt. %). The results of this example suggest that, at high coarse solids loading, it is quite possible for a pipe to become "choked" during upward slurry flow as a result of increased solids concentration in the pipe. This is particularly important in the transportation of tailings slurry and oil sands lumps using vertical upward flows.

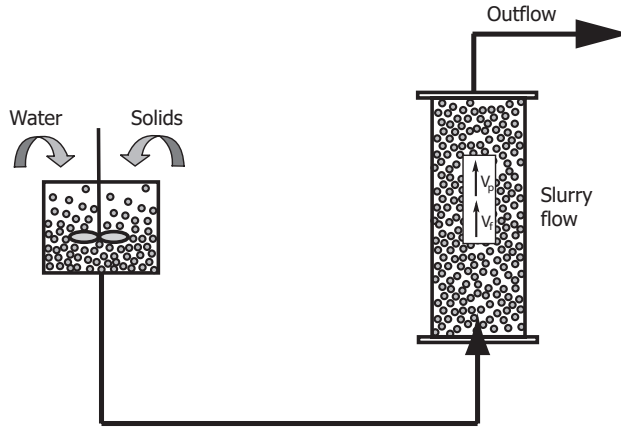


Figure 3.10 Upflow of a suspension.

3.5. Ideal system: Multi-Particle System Containing Different Species

We will now generalize the relative (slip) velocity established for a species of monosized and monodensity particles. The relative velocity equation is necessary for dealing with suspensions of particles of different sizes and densities. For example, it is applied in the modelling of gravity separation vessels (employed in bitumen extraction), where the sand grains and bitumen droplets vary in size and density.

Generalized relative velocity equations and batch settling have been proposed, among others, by Lockett and Bassoon (1979); Masliyah (1979); Batchelor and Wen (1982); Patwardhan and Tien (1985); Davis and Gecol (1994); Bhattacharya and Dutta (2002); Xue and Sun (2003); and Berres, Bürger, and Tory (2005a, 2005b). The Masliyah-Lockett-Bassoon (MLB) derivation will be employed where it was extensively tested for its numerical stability by Bürger's group (Basson, Berres, and Bürger 2009). The Masliyah approach (1979) will also be used in our discussion.

The relative velocity equation was derived for the Stokes regime to give

$$V_i - V_f = \left[\frac{gD_i^2 (\rho_i - \rho_{susp})}{18\mu_f} \right] F(\alpha_f) \quad (3.44)$$

The suspension density is given simply by

$$\rho_{susp} = \rho_f \alpha_f + \sum_{i=1}^N \rho_i \alpha_i \quad (3.45)$$

Here, N is the number of particle species. The term $(\rho_p - \rho_{susp})$ for particles of the same density is given by

$$\begin{aligned}\rho_p - \rho_{susp} &= \rho_p - \left[\rho_f \alpha_f + \rho_p \sum_{i=1}^N \alpha_i \right] \\ &= \rho_p - \left[\rho_f \alpha_f + \rho_p (1 - \alpha_f) \right] = \alpha_f (\rho_p - \rho_f)\end{aligned}\quad (3.46)$$

For particles of the same density and size, Eq. (3.44) becomes identical to the relative velocity equation [Eq. (3.24b)]. A difficulty arises in generalizing the relative velocity equation for higher Reynolds numbers. To do this, we use a heuristic argument, so that the relative velocity equation for higher Reynolds numbers can be given as

$$V_i - V_f = \left[\frac{gD_i^2 (\rho_i - \rho_{susp})}{18\mu_f [1 + 0.15 \text{Re}_{i\infty}^{0.687}]} \right] F(\alpha_f, \text{Re}_{i\infty}) \quad \text{for } \text{Re}_{i\infty} < 10^3 \quad (3.47)$$

Here,

- V_i = velocity of the i^{th} particle species in the suspension with respect to a stationary observer;
- $V_{i\infty}$ = terminal velocity of the i^{th} particle species in an infinite medium;
- D_i = diameter of the i^{th} particle species;
- $\text{Re}_{i\infty}$ = Reynolds number of the i^{th} particle species
($\text{Re} = V_{i\infty} D_i \rho_f / \mu_f$);
- α_i = volume fraction of the i^{th} particle species;
- α_f = fluid volume fraction in the suspension;
- ρ_i = density of the i^{th} particle species;
- ρ_f = density of the fluid;
- ρ_{susp} = density of suspension; and
- μ_f = viscosity of carrier fluid (e.g., pure water).

For an ideal mixture of spherical particles, where we deal only with hydrodynamic effects, the hindered settling function can be given as $\alpha_f^{n_i-2}$. This leads to the following relative velocity expression for a polydisperse system:

$$V_i - V_f = \left[\frac{gD_i^2 (\rho_i - \rho_{susp})}{18\mu_f [1 + 0.15 \text{Re}_{i\infty}^{0.687}]} \right] \alpha_f^{n_i-2} \quad \text{for } \text{Re}_{i\infty} < 10^3 \quad (3.48)$$

For a monodisperse system, Eq. (3.48) becomes equivalent to Eq. (3.26b). The i th particle Reynolds number can be evaluated using Eq. (3.17a), and the Richardson-Zaki index, n_p , can be evaluated using Eq. (3.27b) or (3.27c).

3.6. Non-Ideal System: Multi-Particle System of the Same Species

The effect of colloidal forces on sedimentation of monodisperse systems is a very complex research area, and has been researched extensively (see Buscall et al. 1982; Buscall and White 1987; Auzeais, Jackson, and Russel 1988; Russel, Saville, and Schowalter 1989; Barker and Grimson 1990; Al Naafa and Sami Selim 1993; Eckert et al. 1996; and Vesaratchanon, Nikolov, and Wasan 2007).

For our purposes, we will expand on previous studies of ideal systems. So far, we have considered only ideal suspensions, where colloidal forces have little effect on the solid particulates. The hindered settling function, $F(\alpha_f, \text{Re}_{p\infty})$, is taken as α_f^{n-2} , which takes into account the hydrodynamic effect of the particles' assemblage in a suspension. We need to generalize the hindered settling function, $F(\alpha_f, \text{Re}_{p\infty})$, to include non-ideal systems, in which fine solids are present and colloidal forces are of significance. The colloidal forces control particle aggregation (or flocculation) and inter-particle interaction in terms of attractive or repulsive forces. Rather than dwelling on modeling the colloidal forces, researchers have *empirically* adjusted the hindered settling function to account for the colloidal forces (Tadros 1987). We will follow this approach.

We have discussed the generalized relative (slip) velocity equation, as given by Eq. (3.21):

$$V_p - V_f = V_{p\infty} \alpha_f F(\alpha_f, \text{Re}_{p\infty})$$

For the special case of the Stokes regime, one can write

$$V_p - V_f = \frac{gD_p^2(\rho_p - \rho_f)}{18\mu_f} \alpha_f F(\alpha_f) \quad (3.49)$$

For batch settling (see Example 3.3), Eq. (3.49) reduces to

$$\left[\frac{V_p}{V_{p\infty}} \right]_{\text{Stokes}} = \alpha_f^2 F(\alpha_f) \quad (3.50)$$

For non-flocculated large spherical particles in the absence of surface forces, the function $F(\alpha_f)$ is given simply by $F(\alpha_f) = \alpha_f^{2.7}$. For batch settling, this function leads to

$$\left[\frac{V_p}{V_{p^\infty}} \right]_{Stokes} = \alpha_f^{4.7} = (1 - \alpha_p)^{4.7} \quad (3.51)$$

The index value of 4.7 is known as the Richardson and Zaki power. Several experimental studies (Jottrand 1952; Whitmore 1957; Richardson and Meikle 1961; Epstein 1979; and Vesaratchanon, Nikolov, and Wasan 2007, 2008) have shown that, for batch settling tests of flocculating suspensions,

$$F(\alpha_f) = \alpha_f^{2.7+r} \quad (3.52)$$

where r is a non-zero positive number. For example, in the case of alumina powder of a mean diameter of 5.5 μm , the value of r was found to be 8.5. It was also found that the value of r increases as the particle diameter decreases. The presence of the electric double layers becomes more significant as the particle concentration increases and as the particle size decreases (to, say, less than 1 μm).

In order to accommodate the Richardson and Zaki power of 4.7 in a Stokes regime that is normally associated with batch settling of non-colloidal solid spheres, several researchers (Whitmore 1957; Richardson and Meikle 1961; Steinour 1944a, 1944b; and Fouda and Capes 1977, 1979) introduced the following modified hindered settling equation:

$$\left[\frac{V_p}{V_{p^\infty}} \right]_{Stokes} = (1 - K\alpha_p)^{4.7} \quad (3.53)$$

where K is the hydrodynamic volume factor and α_p is the particles' volume fraction. This modification assumes the presence of an immobile liquid surrounding the particles or aggregates. The presence of this 'liquid film' increases the effective concentration of the particles and thereby decreases the settling velocity of the suspension in a batch settling tube.

For smooth large spheres ($> 100 \mu\text{m}$), K has a value of unity, and Eqs. (3.51) and (3.53) become identical. For colloidal particles, the value of K can be as high as 3, such as in flat mica particles (Fouda and Capes 1977). Unfortunately, no uniquely definable relationship has yet emerged between the hydrodynamic volume factor and the particle shape or surface electric properties. Empirical modeling is required to estimate K .

Comparing Eqs. (3.50) and (3.53), the hindered settling function can be estimated as

$$F(\alpha_f) = (1 - K\alpha_p)^{4.7} / \alpha_f^2 \quad (3.54)$$

For higher Reynolds numbers, Eq. (3.54) is generalized to

$$F(\alpha_f, \text{Re}_{p^\infty}) = (1 - K\alpha_p)^n / \alpha_f^2 \quad (3.55)$$

We recall that K is unity for large particles ($> 100 \mu\text{m}$), and that $K > 1$ for small mineral solids. In other words, fine clay particles behave as if they have an apparent volume fraction that is several times their true size. The coefficient K is a function of the system chemistry, the solids' surface properties, and the solids' size.

In summary, the generalized relative velocity equation for colloidal particles, using the Richardson-Zaki hindered settling function, becomes

$$V_p - V_f = V_{p\infty} \frac{(1 - K\alpha_p)^n}{\alpha_f} \quad (3.56)$$

In terms of an explicit expression for the terminal velocity (i.e., for $\text{Re}_{p\infty} < 10^3$), Eq. (3.56) becomes

$$V_p - V_f = \left[\frac{gD_p^2(\rho_p - \rho_f)}{18\mu_f [1 + 0.15 \text{Re}_{p\infty}^{0.687}]} \right] \frac{(1 - K\alpha_p)^n}{\alpha_f} \quad \text{for } \text{Re}_{i\infty} < 10^3 \quad (3.57)$$

where the index n is given by Eqs. (3.27b) and (3.27c). Clearly, when K is unity, Eq. (3.56) becomes Eq. (3.26a), and Eq. (3.57) becomes Eq. (3.26b).

3.7. Non-Ideal System: Multi-Particle System Containing Different Species

In the previous section, we dealt with a single-species non-ideal system, where all the solids have the same diameter and density. Due to a lack of available literature on non-ideal multi-species systems, we will employ an analogy to Eq. (3.55), which considers a non-ideal single-species system, in order to arrive at the hindered settling function for a non-ideal multi-species system. Thus, for the hindered settling function for the i^{th} species, we write:

$$F(\alpha_f, \text{Re}_{i\infty}) = \left[1 - \sum_{i=1}^N K_i \alpha_i \right]^{n_i} / \alpha_f^2 \quad (3.58)$$

where K_i is the hydrodynamic volume factor belonging to particle species i , whose volume fraction in the suspension is α_i . Although Eqs. (3.27b) and (3.27c), used to evaluate index n , are strictly valid for ideal systems, they are nevertheless used here to evaluate the Richardson-Zaki index, n_i . This is justified by the fact that the non-ideality is accommodated for by the K_i coefficient in Eq. (3.58). The relative velocity for a non-ideal multi-species system becomes

$$V_i - V_f = \left[\frac{gD_i^2(\rho_i - \rho_{susp})}{18\mu_f [1 + 0.15 \text{Re}_{i\infty}^{0.687}]} \right] \left[1 - \sum_{i=1}^N K_i \alpha_i \right]^{n_i} / \alpha_f^2 \quad (3.59)$$

for $\text{Re}_{i\infty} < 10^3$

In the limiting case of an ideal monodisperse system where all solids are of the same density and diameter, Eq. (3.59) becomes Eq. (3.26b).

3.8. Modelling of a Gravity Separation Vessel

3.8.1 Modelling of a Bidisperse Suspension Separation

Gravity separation vessels are used in the oil sands industry to separate aerated bitumen from the slurry at the exit of the hydrotransport pipeline, as shown in Figure 3.11. Gravity separation vessels have several streams, including a slurry feed stream from which the aerated bitumen needs to be recovered; a tailings stream that carries nearly all the coarse sand and fugitive bitumen and exits at the bottom of the vessel; and a bitumen froth stream that carries the bulk of the recovered bitumen. In addition, there is a middlings stream located near the middle of the vessel that withdraws a slurry stream into flotation cells. There are also input streams to the vessel for froth underwash and middlings displacement.

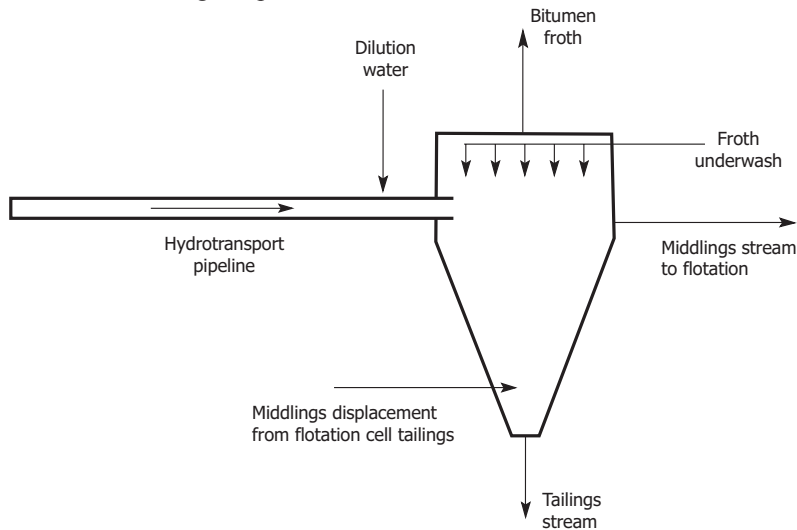


Figure 3.11 Gravity separation vessel with its various input and output streams.

The modelling of a laboratory-scale gravity separation vessel was conducted using the concepts put forward in the previous sections. Masliyah, Kwong, and Seyer (1981) worked with a pilot-type arrangement that separated two solids species, one light and the other heavy. Nasr-El-Din et al. (1988) also used a laboratory set-up for two particle species. The details of the experimental set-up, tests, and modelling of both groups can be found in their respective papers, referenced at the end of this chapter.

Masliyah, Kwong, and Seyer (1981) assumed a gravity separation vessel to consist of a source zone, located where the feed is discharged into the separation vessel, as shown in Figure 3.12. This zone supplies the solids to the underflow and overflow streams. The composition of this zone is not necessarily the same as that of the feed stream. The concentration of the heavy and light particles within this zone is assumed to be uniform. If the downward fluid velocity is higher than the rise velocity of the light particles, the fluid can carry the light particles across the lower boundary of the source zone to report to the underflow stream. Light particles can also cross the upper boundary of the source zone to report to the overflow stream. No light particles can cross the lower boundary to enter into the source zone. A similar constraint applies to the heavy particles (in this case, mineral solids) at the upper boundary of the source zone, in that no heavy particles enter the source zone from the upper boundary.

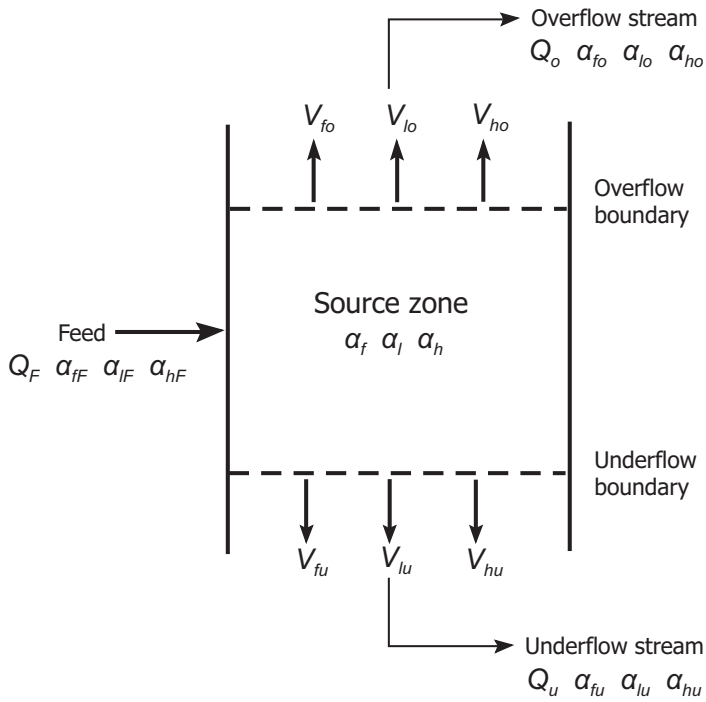


Figure 3.12 Schematic of a vertical settler for the mathematical model showing the source zone.

In order to simplify our analysis below, we are assuming that we have ideal spherical particles and that the Stokes regime applies (i.e., $F(\alpha_p) = \alpha_j^{2.7}$). We also assume that hard pull takes place in the overflow stream, and that there is no middlings stream. As well, only two species of particles are assumed to coexist in the present analysis: heavy particles, which represent the mineral solids, and light particles, which represent the aerated bitumen. In an actual gravity separation vessel model, several species of mineral solids and aerated bitumen droplets are present.

Now let us go back to the simplified gravity separation vessel model. The volumetric balances over the source zone are given by the following equations:

for fluid:

$$Q_F \alpha_{fF} = A \alpha_f (V_{fu} - V_{fo}) \quad (3.60)$$

for light particle species:

$$Q_F \alpha_{lF} = A \alpha_l (V_{lu} - V_{lo}) \quad (3.61)$$

and for heavy particle species:

$$Q_F \alpha_{hF} = A \alpha_h (V_{hu} - V_{ho}) \quad (3.62)$$

where Q_f is the volumetric flow rate of a slurry feed of light and heavy particle volume fractions of α_{lF} and α_{hF} , respectively; V_{lu} and V_{ho} are the velocities of the light and heavy particles at the underflow and overflow boundaries of the source zone, respectively; α_f , α_l and α_h are the source zone volume fractions of the fluid, light particle species, and heavy particle species, respectively; and A is the cross-sectional area of the vessel. *The downward direction is taken as positive.*

The vertical velocity of a particle species at the *overflow* boundary of the source zone is given by the following equations:

for light particles:

$$V_{lo} = V_{fo} + \frac{gD_l^2 (\rho_l - \rho_{susp}) \alpha_f^{2.7}}{18\mu_f} \quad (3.63)$$

for heavy particles:

$$V_{ho} = V_{fo} + \frac{gD_h^2 (\rho_h - \rho_{susp}) \alpha_f^{2.7}}{18\mu_f} \quad (3.64)$$

Similarly, the vertical velocity of a particle species at the *underflow* stream boundary of the source zone is given by the following equations:

for light particles:

$$V_{lu} = V_{fu} + \frac{gD_l^2 (\rho_l - \rho_{susp}) \alpha_f^{2.7}}{18\mu_f} \quad (3.65)$$

for heavy particles:

$$V_{hu} = V_{fu} + \frac{gD_h^2 (\rho_h - \rho_{susp}) \alpha_f^{2.7}}{18\mu_f} \quad (3.66)$$

where D_l and D_h are the diameter of the light and heavy particles species, respectively; ρ_l , ρ_h , and ρ_{susp} are the density of the light particles, heavy particles, and the suspension, respectively; and μ_f is the viscosity of the working fluid (i.e., pure water). The suspension density is given by

$$\rho_{susp} = \alpha_f \rho_f + \alpha_l \rho_l + \alpha_h \rho_h \quad (3.67)$$

where ρ_f is the fluid (water) density. In the absence of a middlings zone and the presence of a “hard pull” in the overflow stream, one must specify the withdrawal rate of either the underflow or overflow stream. The overflow stream flow rate, Q_o , must be specified. It is given by

$$Q_o = -A \left[V_{lo} \alpha_l + V_{ho} \alpha_h + V_{fo} \alpha_f \right] \quad (3.68)$$

An additional constraint for the source zone is

$$\alpha_f + \alpha_l + \alpha_h = 1 \quad (3.69)$$

Eqs. (3.60) to (3.69) provide a simple one-dimensional model for the continuous separation of a bidisperse suspension in a vertical settler, in the Stokes regime, in the absence of any lateral concentration gradients. The unknowns to be evaluated are α_f , α_l , α_h , V_{lo} , V_{ho} , V_{fo} , V_{lu} , V_{hu} and V_{fu} . The feed stream flow rate and composition are specified together with the overflow (or underflow) stream flow rate.

Model Verification

Experimental work was conducted with an idealized system using an experimental set-up, as shown in Figure 3.13 (Nasr-El-Din et al. 1988). The modelling was carried out using a non-Stokes regime. The bidisperse suspensions used were made up of monosized spherical particles of light polystyrene beads ($D_l = 0.265 \times 10^{-3}$ m and $\rho_l = 1050$ kg/m³) and heavy polymethyl methacrylate beads ($D_h = 0.261 \times 10^{-3}$ m and $\rho_h = 1186$ kg/m³) in a salt solution ($\mu_f = 1.41 \times 10^{-3}$ Pa·s and $\rho_f = 1120$ kg/m³). The cross-sectional settler dimensions are 8 cm × 0.53 cm, and its height is 40 cm.

Figure 3.14 shows the concentration of heavy particles in the underflow and overflow streams at a feed flow rate of $1.41 \text{ cm}^3/\text{s}$. The feed stream has equal volume fractions of heavy and light particles where $\alpha_{lF} = \alpha_{hF} = 0.06$. Because of the symmetrical properties of the system and the operating conditions, the variation of the heavy particles' concentration as a function of the split ratio, Q_U/Q_F , is a mirror image of that of the light particles (Q_U is the underflow stream flow rate and Q_F is the feed volumetric flow rate). At split ratios greater than 0.7, the upward water velocity is not sufficient to carry any of the heavy particles to the overflow; hence, its concentration (α_{ho}) approaches zero. Over this range of split ratios, one can observe a bidisperse zone below the feed and a monodisperse zone of light particles above the feed. A mirror image behaviour was also observed with symmetrical feeds at all other feed flow rates studied. This behaviour is to be expected, as both the light and heavy particles have the same relative velocities due to their equal size, feed concentration, and density difference with respect to the fluid.

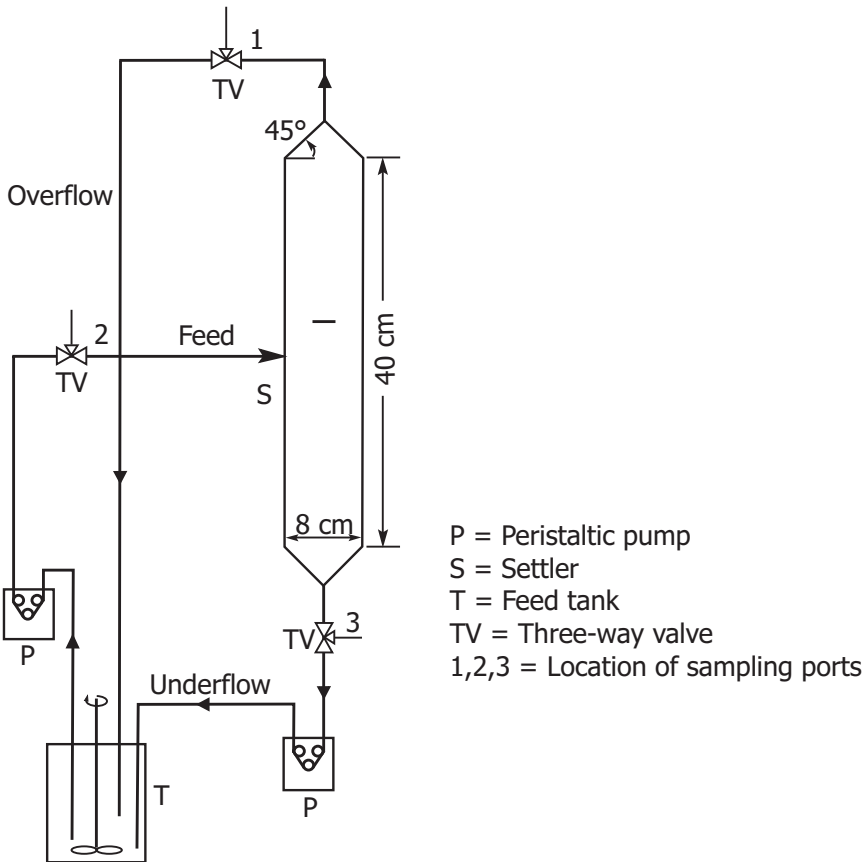


Figure 3.13 Experimental set-up of bidisperse separation in a vertical gravity separation vessel.

Source: Nasr-El-Din et al. (1988).

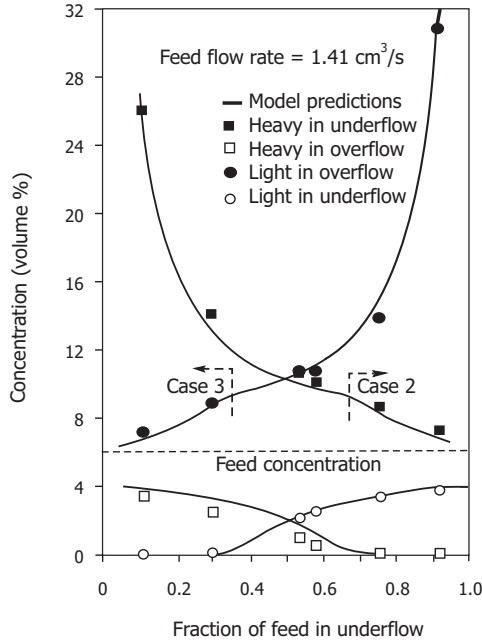


Figure 3.14 Figure 3.14 Variation of light and heavy particle concentrations in the overflow and underflow streams as a function of the split ratio Q_U/Q_F , for $\alpha_{lF} = 0.06$ and $\alpha_{hF} = 0.06$.

Source: Nasr-El-Din et al. (1988).

While the exit concentrations presented here are a useful measure for designs based on purity specifications, the variation of recovery under the operating conditions is an alternate measure of the performance of a settler. *Recovery* is defined as the fraction of light (or heavy) particles in the feed that has been collected in a product stream. Figure 3.15 shows the recovery of light particles in the overflow stream and heavy particles in the underflow stream as a function of Q_U/Q_F and Q_O/Q_F , respectively, at $Q_F = 1.41 \text{ cm}^3/\text{s}$ and $\alpha_{lF} = \alpha_{hF} = 0.06$. At low split ratios (≤ 0.3), the recovery of light particles in the overflow is 100%. At higher split ratios (≥ 0.3), the recovery decreases linearly with increasing split ratio.

Agreement with the model's predictions, as well as the mirror image behavior, is evident in Figure 3.15. Note that a 100% recovery of light particles in the overflow only implies that all the light particles in the feed have reported to the overflow. In particular, it does not exclude the presence of heavy particles in the overflow stream; consequently, a different performance measure should be used. The concentration variation, shown in Figure 3.14, provides this necessary information. Although the system is symmetrical, one has to operate the settler at a split ratio of 0.85 to obtain an even distribution of light particles in the product streams, as shown by the dotted lines of Figure 3.15.

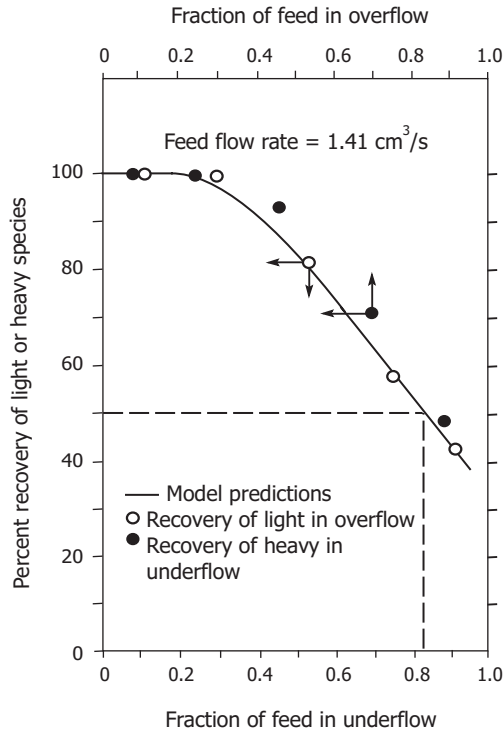


Figure 3.15 Figure 3.15 Recovery of light and heavy particles as a function of the split ratio Q_U/Q_F , for $\alpha_{IF} = 0.06$ and $\alpha_{hF} = 0.06$.

Source: Nasr-El-Din et al. (1988).

3.9. Inclined Plate Settlers (IPS)

The removal of particulate solids from process streams is usually required in many industrial processes. In particular, it is desirable to separate heavy solid particles and light bitumen droplets from slurry streams, such as gravity separation vessel feed streams or diluted bitumen froth streams. Normally, vertical gravity separation vessels, cyclones, and centrifuges are employed for the separation of the heavy and light species. However, there is another class of gravity separators known as *inclined plate settlers*. In order to gain an appreciation for this technology, we shall first consider heavy solids separation, followed by heavy and light species separation.

3.9.1 Settling of Heavy Particles in an Inclined Plate Settler

The curious phenomenon of settling in inclined plate settlers was first reported by Boycott (1920). Boycott observed that when “oxalated or defibrinated blood is put to stand in narrow tubes, the corpuscles sediment a good deal faster if the tube is inclined than when it is vertical.” This phenomenon is referred to as the *Boycott effect*. Acrivos and Herbolzheimer (1979, p. 437) give an excellent account of Boycott effect:

To begin we note that, [in an inclined tube], if the particles just settled vertically, particle-free fluid would appear above the suspension, both at the top of the vessel and directly under the downward-facing surface, and that every point on the interface separating the clear liquid region from the suspension would fall vertically with a velocity v_o , the particle settling velocity of the same suspension as measured in a container with vertical walls. Experimental observations of the inclined settling process show, however, a markedly different [settling-flow] behaviour. First of all, although a clear-fluid layer does form under the downward-facing plate [see Figure 3.16], its thickness remains small and is essentially independent of time. Also, although a sharp, effectively horizontal interface between the suspension and the clear liquid does exist on top (as in a vertical settling), this interface falls with an enhanced vertical velocity that is typically several times greater than v_o [where v_o is the particle settling velocity of the same suspension in a container with vertical walls].

Indeed, as can be seen from Figure 3.16, clarified liquid crosses the B-C boundary from the suspension into the clear liquid layer and flows upwards along the upper inclined container’s wall.

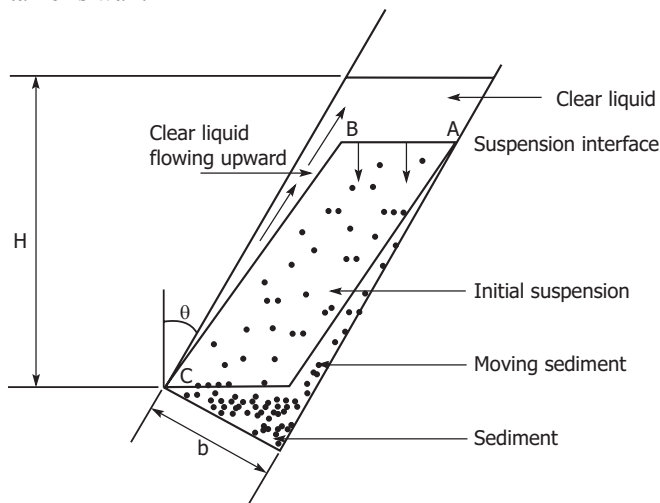


Figure 3.16 Effect of feed flow rate on the recovery enhancement factor.

Ponder (1925) and Nakamura and Kuroda (1937) developed a kinematic model to explain the enhanced vertical velocity of the suspension, referred to as the PNK theory. They argued that the volumetric flow rate of the clarified liquid crossing the inclined interface (B-C) is added to the clear liquid above the horizontal interface (A-B) (Figure 3.16). According to the PNK theory, the volumetric liquid flow rate across B-C represents the enhanced vertical velocity of interface A-B. The volumetric rate (S), at which clarified liquid is formed above the suspension, is given by the particles' velocity (v_o ; as in a vertical settler) multiplied by the area normal to flow and the particle concentration in the suspension:

$$S = \left(\frac{H}{\cos \theta} \right) \times (v_o \sin \theta) \alpha_p + \left(\frac{b}{\cos \theta} \right) v_o \alpha_p \quad (3.70)$$

Here, v_o is the vertical fall velocity of particles in the same suspension in a vertical container, and α_p is the volume fraction of the solids in the suspension. The overall volumetric rate of the clarified water is the same as the product of the observed fall velocity of interface A-B, v , times its area and solids concentration:

$$S = \frac{b}{\cos \theta} v \alpha_p \quad (3.71)$$

Equating equations (3.70) and (3.71) leads to

$$v = v_o \left(1 + \frac{H}{b} \sin \theta \right) \quad (3.72)$$

where v is the observed fall velocity of interface A-B. As the term in the brackets of Eq. (3.72) is greater than unity, there is an enhancement in solids settling. This enhancement is simply due to an increase in the settling surface area, as represented by $H \sin \theta / b$.

Acrivos and Herbolzheimer were the first to identify the conditions for which Eq. (3.72) is valid. According to their argument, Eq. (3.72) can be used to predict the settling rate in inclined channels provided that “(i) the suspension is monodisperse, (ii) the particle Reynolds number is small, (iii) the initial concentration distribution is uniform, (iv) Λ [the ratio of the sedimentation Grashof number and the sedimentation Reynolds number] is large, and (v) the interface between the clear fluid and the suspension remains stable” (Acrivos and Herbolzheimer 1979). Λ and Re are defined as follows:

$$\Lambda = \frac{H^2 g (\rho_p - \rho_f) \alpha_p}{V_o \mu_f} \quad \text{and} \quad Re = \frac{\rho_f H v_o}{\mu_f} \quad (3.73)$$

where ρ_p and ρ_f are the densities of the solids (particulates) and fluid, respectively; μ_f is the fluid viscosity; H is the suspension height; g is the gravitational acceleration; and α_p is the suspension solids volume fraction.

Modelling for polydisperse suspensions was carried out by Davis and Gecol (1994) using Batchelor's coefficient (Batchelor and Wen 1982; Batchelor and Janse van Rensburg 1986).

3.9.2 Separation of Particles in an Inclined Plate Settler

Batch separation of bidisperse suspensions of light and heavy particles has been examined by Law, Masliyah, and Nandakumar (1987) and Law et al. (1988). In the absence of lateral concentration heterogeneities (fingers), it was found that the PNK model predicts the settling rates of light and heavy particles fairly well. The theoretical model developed for the case of an inclined settler (Masliyah, Nasr-El-Din, and Nandakumar 1989) very closely follows that developed for a vertical settler (Masliyah, Kwong, and Seyer 1981; Nasr-El-Din et al. 1988).

Figure 3.17 shows the recovery enhancement factor as a function of the feed flow rate at a split ratio $Q_U/Q_F = 0.5$, with the angle of inclination as a parameter. The recovery enhancement factor is defined as the ratio of recovery at an angle θ to that at angle $\theta = 0^\circ$ (i.e., a vertical column) at the same conditions. For a given angle θ , the recovery enhancement factor curve exhibits a maximum, and both the location and the value of the maximum depend on the angle of the inclination. Figure 3.17 suggests that the optimal use of an inclined plate settler is dependent on the feed flow rate employed (Masliyah, Nasr-El-Din, and Nandakumar 1989).

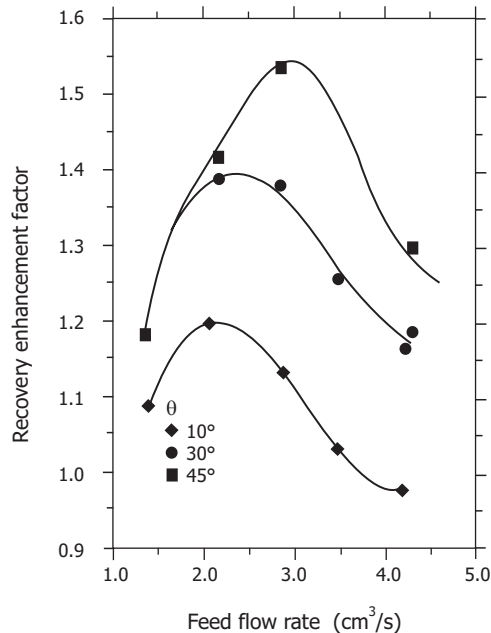


Figure 3.17 Effect of feed flow rate on recovery enhancement factor. Cross-sectional area is 4.24 cm^2 ; all other physical properties are similar to those in source study.

Source: Nasr-El-Din et al. (1988).

3.10. Concluding Remarks

The analysis presented above is very powerful for the study of the rise and fall of multi-species particulates in essentially vertical flows. For horizontal slurry flows, the analysis is not as straightforward and would require substantial experimental input. There is much need for theoretical and experimental studies of settling of particulate systems where both colloidal forces and hydrodynamic forces are present.

3.11. References

- Acrivos, A., and E. Herbolzheimer. 1979. Enhanced sedimentation in settling tanks with inclined walls. *Journal of Fluid Mechanics* 92 (3): 435–457.
- Al Naafa, M.A., and M. Sami Selim. 1993. Sedimentation and Brownian diffusion coefficients of interacting hard spheres. *Fluid Phase Equilibria* 88: 227–238.
- Auzerais, F.M., R. Jackson, and W.B. Russel. 1988. The resolution of shocks and the effects of compressible sediments in transient settling. *Journal of Fluid Mechanics* 195: 437–462.
- Barker, G.C., and M.J. Grimson. 1990. Theory of sedimentation in colloidal suspensions. *Colloids and Surfaces* 43 (1): 55–66.
- Basson, D.K., S. Berres, and R. Bürger. 2009. On models of polydisperse sedimentation with particle-size-specific hindered-settling factors. *Applied Mathematical Modelling* 33 (4): 1815–1835.
- Batchelor, G.K., and R.W. Janse van Rensburg. 1986. Structure formation in bidisperse sedimentation. *Journal of Fluid Mechanics* 166: 379–407
- Batchelor, G.K., and C.-S. Wen. 1982. Sedimentation in a dilute polydisperse system of interacting spheres. Part 2. Numerical results. *Journal of Fluid Mechanics* 124: 495–528 (with corrigendum in *Journal of Fluid Mechanics* 137: 467–469).
- Berres, S., R. Bürger, and E.M. Tory. 2005a. On mathematical models and numerical simulation of the fluidization of polydisperse suspensions. *Applied Mathematical Modelling* 29 (2): 159–193.
- . 2005b. Applications of polydisperse sedimentation models. *Chemical Engineering Journal* 111 (2–3): 105–117.
- Bhattacharya, S., and B.K. Dutta. 2002. Effective voidage model of a binary solid-liquid fluidized bed: Application to solid layer inversion. *Industrial & Engineering Chemistry Research* 41 (20): 5098–5108.
- Bowen, B.D., and J.H. Masliyah. 1973. Drag force on isolated axisymmetric particles in Stokes flow. *Canadian Journal of Chemical Engineering* 51: 8–15.
- Boycott, A.E. 1920. Sedimentation of blood corpuscles. *Nature* 104 (2621): 532.

- Buscall, R., J.W. Goodwin, R.H. Ottewill, and T.F. Tadros. 1982. The settling of particles through Newtonian and non-Newtonian media. *Journal of Colloid and Interface Science* 85 (1): 78–86.
- Buscall, R., and L.R. White. 1987. The consolidation of concentrated suspensions. Part 1 – The theory of sedimentation. *Journal of the Chemical Society. Faraday Transactions I: Physical Chemistry in Condensed Phases* 83: 873–891.
- Clift, R., J.R. Grace, and M.E. Weber. 1978. *Bubbles, drops, and particles*. New York: Academic Press.
- Davis, R.H., and H. Gecol. 1994. Hindered settling function with no empirical parameters for polydisperse suspensions. *AIChE Journal* 40 (3): 570–575.
- Eckert, W.F., J.H. Masliyah, M.R. Gray, and P.M. Fedorak. 1996. Prediction of sedimentation and consolidation of fine tails. *AIChE Journal* 42 (4): 960–972.
- Epstein, N. 1979. Letter to the Editor: Hydrodynamic particle volume factor and settled bed volume. *Canadian Journal of Chemical Engineering* 57: 383.
- Escudié, R., N. Epstein, J.R. Grace, and H.T. Bi. 2006. Layer inversion phenomenon in binary-solid liquid-fluidized beds: prediction of the inversion velocity *Chemical Engineering Science* 61 (20): 6667–6690.
- Fouda, A.E., and E. Capes. 1977. Hydrodynamic particle volume and fluidized bed expansion. *Canadian Journal of Chemical Engineering* 55: 386.
- . 1979. Hydrodynamic particle volume and fluidized bed expansion. *Canadian Journal of Chemical Engineering* 57: 120.
- Hadamard, J.S. 1911. Slow permanent motion of a viscous liquid sphere in a viscous fluid. *Comptes Rendus de l'Académie des sciences* 152: 1735–1738.
- Haider, A., and O. Levenspiel. 1989. Drag coefficient and terminal velocity of spherical and nonspherical particles. *Powder Technology* 58 (1): 63–70.
- Hartman, M., V. Havlin, O. Trnka, and M. Carsky. 1989. Predicting the free-fall velocities of spheres. *Chemical Engineering Science* 44 (8): 1743–1745.
- Jottrand, R. 1952. An experimental study of the mechanism of fluidisation. *Journal of Applied Chemistry* 2 (Suppl. 1): S17–S26.
- Khan, A.R., and J.F. Richardson. 1989. Fluid-particle interactions and flow characteristics of fluidized beds and settling suspensions of spherical particles. *Chemical Engineering Communications* 78 (1): 111–130.
- Law, D.H.-S., R.S. MacTaggart, K. Nandakumar, and J.H. Masliyah. 1988. Settling behaviour of heavy and buoyant particles from a suspension in an inclined channel. *Journal of Fluid Mechanics* 187: 301–318
- Law, D.H.-S., J.H. Masliyah, and K. Nandakumar. 1987. Ablation of frozen oil sands under the influence of turbulent axisymmetric jets. *AOSTRA Journal of Research* 3: 177–182
- Lockett, M.J., and K.S. Bassoon. 1979. Sedimentation of binary particle mixtures. *Powder Technology* 24 (1): 1–7.

- Masliyah, J.H. 1979. Hindered settling in a multi-species particle system. *Chemical Engineering Science* 34 (9): 1166–1168.
- Masliyah, J.H., T. Kwong, and F.A. Seyer. 1981. Theoretical and experimental studies of a gravity separation vessel. *Industrial & Engineering Chemistry Process Design and Development* 20 (1): 154–160.
- Masliyah, J.H., H. Nasr-El-Din, and K. Nandakumar. 1989. Continuous separation of bidisperse suspensions in an inclined channel. *International Journal of Multiphase Flow* 15 (5): 815–829.
- Nakamura, H., and K. Kuroda. 1937. La cause de l'accélération de la vitesse de sédimentation des suspensions dans les récipients inclinés. *Keizyo Journal of Medicine* 8: 256–296.
- Nasr-El-Din, H., J. Masliyah, K. Nandakumar. 1990. Continuous gravity separation of bidisperse suspension in a vertical column. *Chemical Engineering Science* 43 (12): 3225–3234.
- Patwardhan, V.S., and C. Tien. 1985. Sedimentation and liquid fluidization of solid particles of different sizes and densities. *Chemical Engineering Science* 40 (7): 1051–1060.
- Ponder, E. 1925. On sedimentation and rouleaux formation: I. *Experimental Physiology* 15: 235–252
- Richardson, J.F., and R. Meikle. 1961. Sedimentation and fluidization, part IV: Drag force on individual particles in an assemblage. *Transactions of the Institution of Chemical Engineers* 39: 357–362.
- Richardson, J.F., and W.N. Zaki. 1954. Sedimentation and fluidization. *Transactions of the Institution of Chemical Engineers* 32: 35–53.
- Rowe, P.N. 1987. A convenient empirical equation for estimation of the Richardson-Zaki exponent. *Chemical Engineering Science* 42 (11): 2795–2796.
- Russel, W.B., D.A. Saville, and W.R. Schowalter. 1989. *Colloidal dispersions*. Cambridge: Cambridge University Press.
- Schiller, L., and A. Naumann. 1933. Über die grundlegenden Berechnungen bei der Schwerkraftaufbereitung. *Zeitschrift des Vereines deutscher Ingenieure* 77: 318–320.
- Steinour, H.H. 1944a. Rate of sedimentation: nonfloculated suspensions of uniform spheres. *Industrial & Engineering Chemistry* 36 (7): 618–624.
- . 1944b. Rate of sedimentation: suspensions of uniform-size angular particles. *Industrial & Engineering Chemistry* 36 (9): 840–847.
- Stokes, G.G. 1851. On the effect of the internal friction of fluids on the motion of pendulums. *Transactions of the Cambridge Philosophical Society* 9: 8.
- Tadros, T.F. 1987. Settling of suspensions and prevention of formation of dilatant sediments. In *Solid/liquid dispersions*, ed. T. F. Tadros. New York: Academic Press.

- Turton, R., and N.N. Clark. 1987. An explicit relationship to predict spherical particle terminal velocity. *Powder Technology* 53 (2): 127–129 (with corrigendum in *Powder Technology* 54 (1): 75).
- Turton, R., and O. Levenspiel. 1986. A short note on the drag correlation for spheres. *Powder Technology* 47 (1): 83–86.
- Vesaratchanon, J.S., A. Nikolov, and D.T. Wasan. 2007. Sedimentation in nano-colloidal dispersions: Effects of collective interactions and particle charge. *Advances in Colloid and Interface Science* 134–135.
- . 2008. Sedimentation of concentrated monodisperse colloidal suspensions: Role of collective particle interaction forces. *Journal of Colloid and Interface Science* 322 (1): 180–189.
- Wallis, G.B. 1969. *One-dimensional two-phase flow*. New York: McGraw-Hill.
- Whitmore, R.L. 1957. The relationship of the viscosity to the settling rate of slurries. *Journal of the Institute of Fuel* 30: 238–242.
- Xue, B., and Y. Sun. 2003. Modeling of sedimentation of polydisperse spherical beads with a broad size distribution. *Chemical Engineering Science* 58 (8): 1531–1543.

Chapter 4

Physical and Chemical Properties of Oil Sands

In this chapter, we will discuss the physical properties of oil sands constituents and the chemical properties of bitumen that are relevant to the recovery of bitumen from the Athabasca oil sands.

Typical oil sands consist of a mixture of coarse sand grains, fine mineral solids, clays, formation water, electrolytes, and bitumen. Clay minerals are assumed to be suspended mainly in the water phase (Takamura 1982). A schematic illustration of the oil sands matrix is shown in Figure 4.1. The bitumen content (saturation or grade) can vary widely, from zero to as high as 16 % by weight. Low bitumen saturation is of less commercial value in present commercial open-pit mining operations, where the cutoff for mining is 7 % by weight. Mineral solids constitute the most mass in oil sands ores. Water content can vary from nearly zero in dehydrated (weathered) oil sands ores to as high as 7 % by weight. The indigenous formation water present in oil sands contains a variety of electrolytes, including sodium, calcium, magnesium, chloride, potassium, sulphate, and bicarbonate ions. The concentrations of these electrolytes vary widely, from high values (marine-type ores) to low values (fluvial ores). In marine-type ores, the sodium concentration is similar to that of seawater.

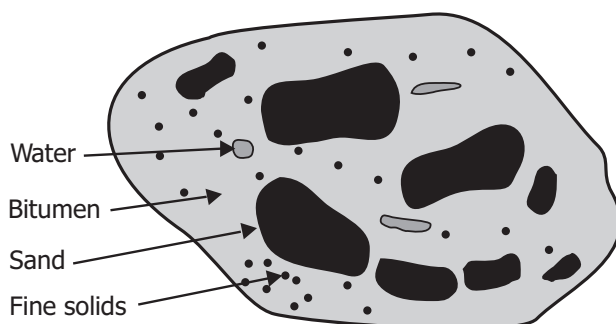


Figure 4.1 Oil sands matrix.

The properties of oil sands constituents play a major role in determining the processability of oil sands ores. The nature of the bitumen and its components; the bitumen's physical and interfacial properties; the mineral solids size distribution; the percent fine solids and clays in the ore and their mineralogy and surface characteristics; the pH of the formation water; and the electrolyte type and concentration all play an important role in the efficiency of bitumen liberation, flotation, and recovery. These properties also dictate the choice of operational conditions and the type of equipment used in oil sands extraction processes.

The physical and interfacial properties of an oil sands ore are influenced by the processing temperature, the properties of the processing water chemistry, and the type of diluent used in bitumen froth treatment.

The successful application of water-based technology in the recovery of bitumen from the Athabasca oil sands lies in the key fact that the sand grains are hydrophilic. There is a notion that a thin layer of water surrounds individual sand grains, separating them from the bitumen. As noted by Mossop (1980):

Perhaps the single most characteristic feature of the Alberta oil sands, and almost certainly the most fortunate, is that the grains are water-wet or hydrophilic. The oil in the pores is not in direct contact with mineral grains. Rather, each grain is surrounded by a thin film of water beyond which, in the center of the pore, is the oil. This hydrophilic tendency of the sands is fortunate because the hot water extraction process would not work if the grains were other than water-wet.¹

The presence of a water film around the sand grains of the Athabasca oil sands deposit has been postulated from the early stage of oil sands development (Clark and Pasternack 1932; Ball 1935; Clark 1944). It was hypothesized that, were it not for the intervention of the water layer, the process of bitumen separation from the oil sands would not only be difficult, but also economically unfeasible (Fitzgerald 1978).

The water film is assumed to be stabilized by electrostatic forces between the electrical double layers created at the oil-water and sand-water interfaces (Takamura 1982; Hall, Collins, and Melrose 1983; Anderson 1986). The thickness of the thin water film sandwiched between a sand grain and bitumen is predicted to be about 10 nm (Takamura 1982; Hall, Collins, and Melrose 1983). However, the existence of this water film remains to be experimentally verified.

The hydrophobic character of sand grains in the Utah oil sands, as opposed to the hydrophilic nature of those in the Athabasca oil sands, may partially explain why the Utah oil sands cannot be effectively processed using conventional water-based extraction processes (Sepulveda and Miller 1978; Miller and Misra 1982; Misra and Miller 1991). Czarnecki et al. (2005) give a detailed discussion on the possibility of the presence of a water film on the Athabasca sand grains. For our purposes, it is sufficient to designate a surface as being *hydrophilic* or *hydrophobic* when referring to solids.

¹ In this quotation, Mossop uses the terms 'hydrophilic' and 'water-wet' as synonyms, which may not be necessarily correct, as discussed in more detail in Chapter 2 of this volume.

Clay minerals are assumed to be suspended mainly in the water phase (Cottrell 1963; Cameron Engineers 1978; Takamura 1982). A schematic illustration of this structural model, normally referred to as Cottrell's model, is shown in Figure 4.2. Dusseault and Morgenstern (1978) and Mossop (1980) suggested alternative models. Another model, clearly showing a thin water layer on a sand grain, is shown in Figure 4.3 (Takamura 1982).

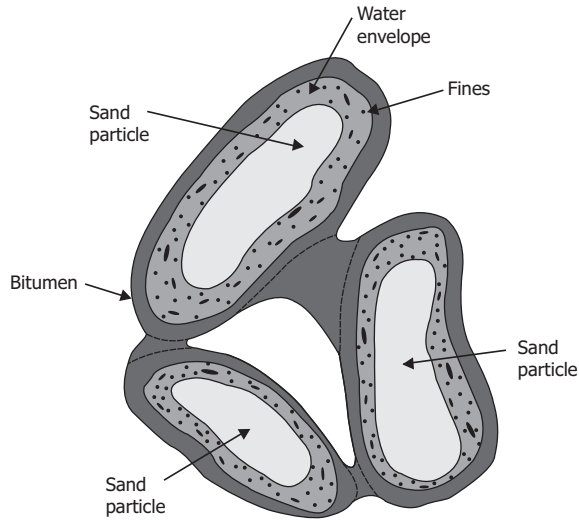


Figure 4.2 A schematic model structure of Athabasca oil sands.

Source: Cottrell (1963).

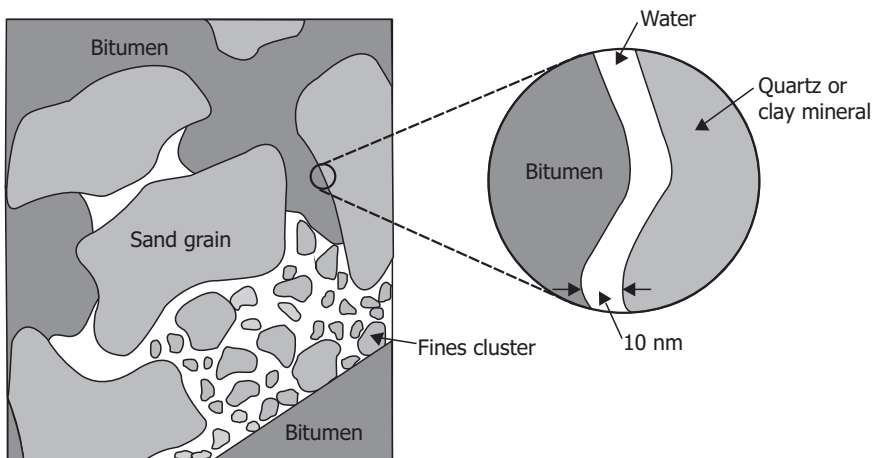


Figure 4.3 A refined model for the structure of Athabasca oil sand.

Source: Takamura (1982).

In order for bitumen embedded in the unconsolidated coarse sand and clays to be separated out, it must be 1) liberated (i.e., taken out) from the sand grains, 2) become aerated, and 3) float to the top of the pulp, where it is collected as bitumen froth. This is achieved by mixing the oil sands with hot water and any entrained air. The efficiency and kinetics of bitumen separation are linked to the properties of the ore constituents and the physicochemical properties (temperature and chemistry) of the processing water.

For convenience, the physical properties of oil sands are divided into two broad categories. The first includes *bulk properties*, such as density, viscosity, reflective index, specific heat, and heat of combustion. The characterization of oil sands ores, in terms of mineral particle size distribution and electrolyte type and concentration in the formation water, is also grouped into this category. Bulk properties are easily appreciated in many cases. For example, the viscosity of bitumen, as affected by temperature and diluent (solvent) addition, is known to affect bitumen flow in a pipeline; while the solids particle size distribution and the presence of clays have been proven to affect slurry flow in a hydrotransport or tailings pipeline (in terms of pumping power requirements and pipe sanding prevention). The second category deals with *interfacial properties*, including surface properties such as wettability (contact angle), surface tension, interfacial tension, and surface charge. The slurry that results from the processing of oil sands is made up of coarse and fine solids, clays, bitumen droplets, and air bubbles. The interaction among these entities is highly influenced by their surface characteristics. For example, the attachment of a clay particle to a bitumen droplet surface, or the liberation of bitumen from a sand grain, is directly affected by the surface properties of the clays, bitumen, and sand grains. The surface properties of mineral solids, air bubbles, and bitumen are influenced by water temperature and chemistry. For our purposes, it suffices to say that the presence of ions (such as sodium, calcium, magnesium, chlorides, or/and bicarbonates), the water alkalinity, and surfactants (surface-active agents) individually and collectively determine the nature of the water chemistry.

The surface properties of sand grains and bitumen also have a marked effect on the separation of bitumen from the sand grains. Since the liberated bitumen needs to be floated, the air-bitumen attachment process (i.e., bitumen aeration) is vital for bitumen recovery. Clearly, it is necessary to understand the surface properties that affect the air attachment process.

The chemical properties (composition) of bitumen are also of key importance in bitumen upgrading; these will be discussed briefly for completeness in Section 4.8.

4.1 Oil Sands Composition: Bitumen, Mineral Solids, and Inorganic Ions

4.1.1 Bitumen Grade Distribution

The amount of bitumen in Athabasca oil sands ores ranges from ~ 0 % to 16 % by weight. An ore with a bitumen content of 7 wt. % to 8 wt. % is considered to be low-grade; 8 wt. % to 10.5 wt. %, average-grade; and 11 wt. % or more, high-grade. Typically, the oil sands ore mined by the four commercial open-pit mining operators (Suncor, Syncrude, Albion, and CNRL) is about 9 wt. % to 13 wt. % bitumen, with a minimum grade cutoff of 7 wt. %. Figure 4.4 shows the bitumen grade distribution for the Jackpine Mine Lease for a TV:BIP (total volume-to-bitumen-in-place) ratio of < 12. In mining operations, there is a cutoff in the bitumen grade distribution at 7 wt. % grade and at a minimum ore thickness of 3 m.

Figure 4.5 shows the bitumen grade distributions for different leases on CNRL's Horizon Project. The volume-weighted average ore grade for the Horizon-area deposit is ~ 10.8 wt. % bitumen. However, the ore grade within the lease varies depending on the stratigraphical location, from low bitumen grades in the upper part (Upper McMurray) to higher bitumen grade in the middle and lower regions (Middle and Lower McMurray). From Figures 4.4 and 4.5, it is clear that there is no uniformity in the bitumen grade across a lease, and certainly not across the entire Athabasca oil sands area.

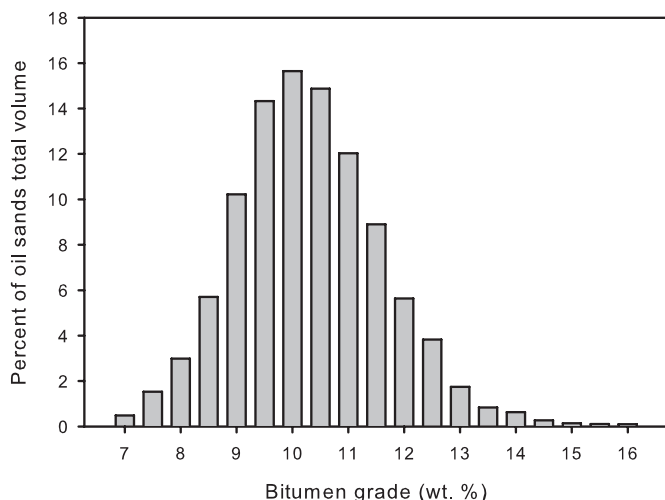


Figure 4.4 Bitumen grade distribution in Jackpine Lease.

Source: Shell Canada Ltd. (2007, p. 4.14).

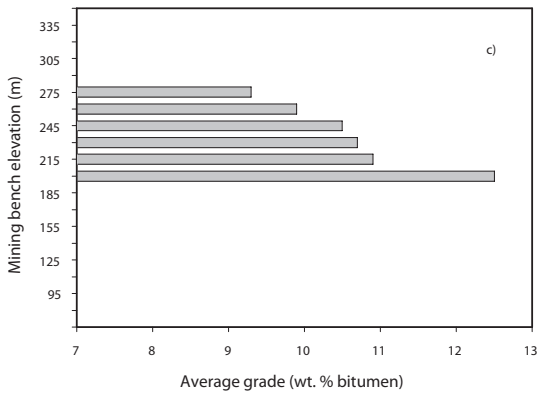
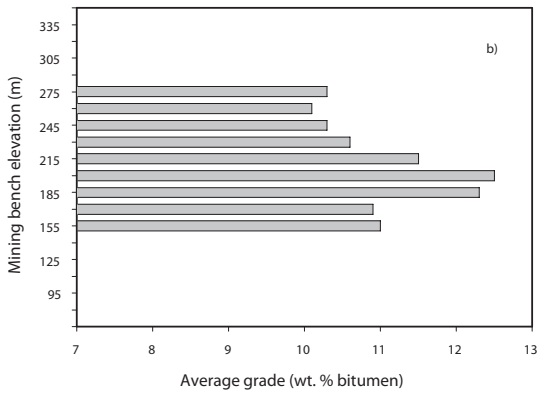
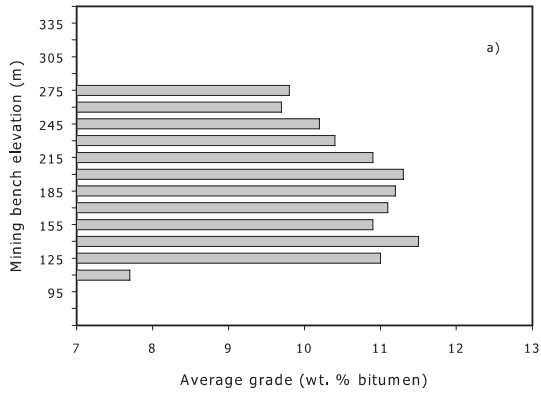


Figure 4.5 Bitumen grade variation with depth for CNRL Horizon Project (a) Lease 18, (b) Lease 10, and (c) Lease 25, by mining bench.

Source: Canadian Natural Resources Limited (2002a, p. 2-47).

4.1.2 Mineral Solids

The particle size distribution (PSD) of mineral solids in an oil sands ore can vary quite substantially from one ore body to another, from submicron-size to nearly over 1 mm (1000 μm). The PSD of mineral solids is a very important parameter in designing tailings and hydrotransport pipelines. The minimum velocity required to move the solids within a hydrotransport or tailings pipeline is a function of both the fine and coarse mineral solids content. To minimize pipeline erosion, slurry pipelines are normally operated at the lowest possible velocity, i.e., the lowest velocity at which no stationary solids bed is formed. Accordingly, the PSD of mineral solids is needed for the design and operation of tailings and hydrotransport pipelines. In addition, because the content of fine solids and clays play such a major role in bitumen flotation, knowledge of the PSD of solids in an ore body becomes one of the first steps in oil sands ore characterization.

Fines is the term adopted by the oil sands industry to describe the portion, by weight, of mineral solids that are smaller than 44 μm . *Clays* refers to mineral solids smaller than 2 μm , while *clay minerals* can refer to clays of any size, as the term describes their chemical, rather than physical, nature. Figure 4.6 shows the size distribution of mineral solids in an oil sands ore with a fines content of 30 % and a mean size (D_{50}) of 72 μm (i.e., 50 % of the mineral solids have a size of less than 72 μm). The actual particle size distributions of ores of different percent fines in the Athabasca formation are shown in Figure 4.7. Within a given lease, the particle size distribution can vary over quite a large range. The percent fines shown in Figure 4.7 ranges from approximately 8 % to 30 %, with a corresponding D_{50} of 300 μm and 85 μm , respectively.

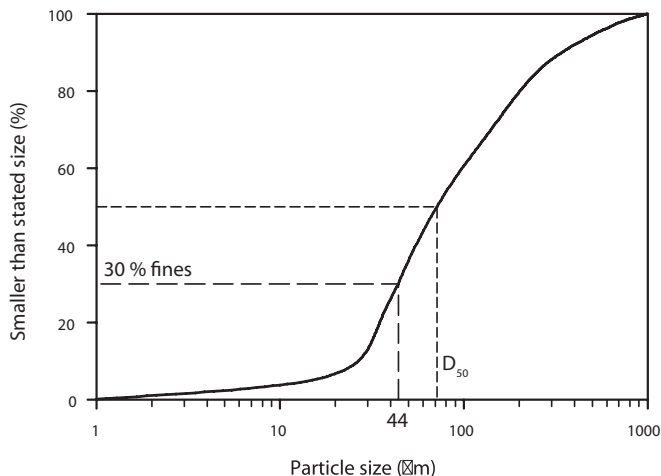


Figure 4.6 Particle size distribution of mineral solids in oil sands

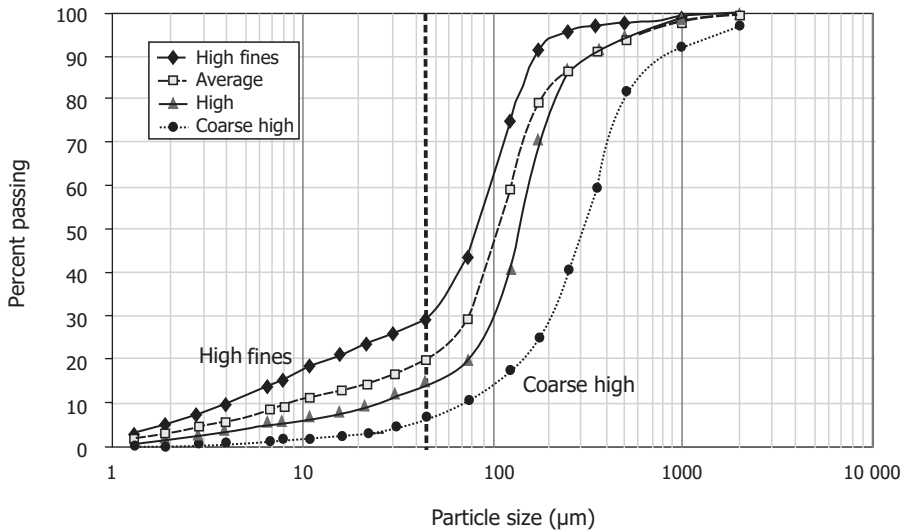


Figure 4.7 Particle size distribution of the mineral solids in oil sands.

Source: Tipman and Sharp (2004).

The *percent fines* (weight percentage of mineral solids smaller than 44 µm) in an oil sands ore is an important parameter for ore characterization. First, by and large, the percent fines can be correlated with bitumen recovery. Other parameters being equal, a high-fines ore leads to a lower bitumen recovery. Percent fines is referred to in the industry in a variety of ways, such as in fine solids capture during the beaching of tailings streams into a tailings pond; during the reprocessing of mature fine tailings; in designing gravity separation vessels; and in defining government regulations in terms of fine tailings capture and storage. Moreover, bitumen grade (saturation) is, to some extent, correlated to percent fines.

One would expect solids much smaller than 44 µm (e.g., 1 µm) to affect bitumen recovery through their interaction with bitumen. Indeed, there is a reasonable correlation between percent fines and smaller-size minerals, as seen in Figure 4.8. It is likely that this positive correlation led to the industry's use of 44 µm as a cutoff marker for fines solids. It is worth noting that wet sieving, using standard procedures, leads to reproducible sieving results down to 44 µm. Solids characterization for particles smaller than this can be equipment-dependent. It is therefore more difficult to compare bitumen recovery data for smaller solids (e.g., 1 µm) across different testing equipment. Nevertheless, it may be preferable to use a given measuring technique and available PSD data for solids smaller than 44 µm to correlate solids of, say, 1 µm, with oil sands processability. Figure 4.9 shows that it is possible to correlate cuts of 1.9 µm and 44 µm with D_{50} .

The results of a typical x-ray diffraction analysis of oil sands solids, including both the coarse and fines solids fractions, were combined to characterize oil sands solids (Hepler and Smith 1994). A typical mineral composition of the total solids is given

in Table 4.1. Heavy minerals, such as titanium, are found in the fraction representing smaller-size mineral solids.

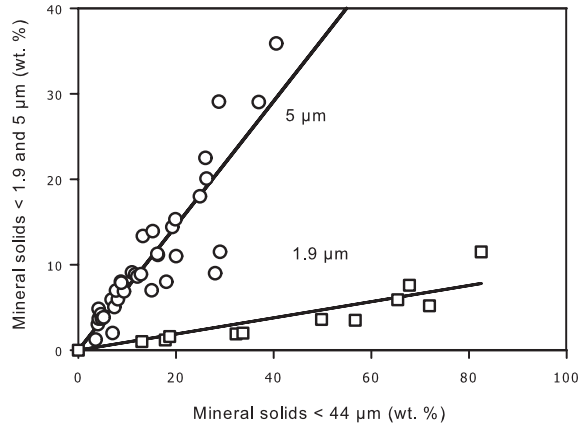


Figure 4.8 Relationship between < 44- μm size fraction and the < 5- μm size fraction of solids in Athabasca oil sands.

Source: Sanford (1983). Data for 1.9 μm are taken from Imperial Oil (2005 p. 4-12). See also Shaw, Schramm, and Czarnecki (1996).

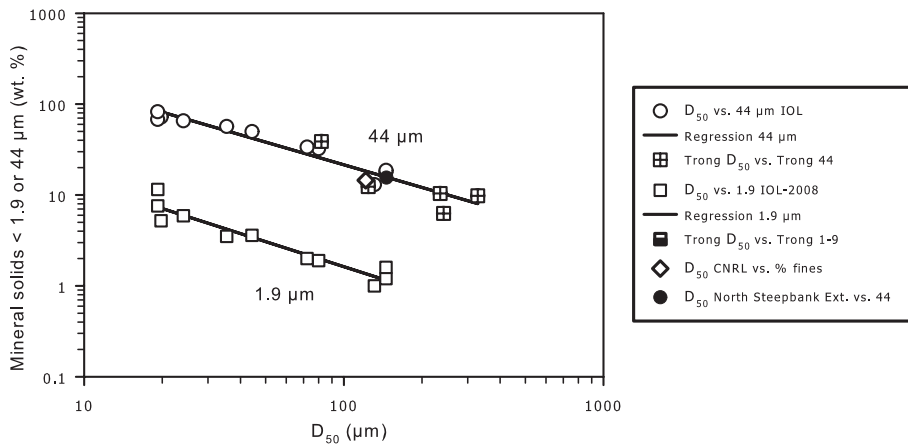


Figure 4.9 Variation of percent fines (44 μm and 1.9 μm) with D_{50} for various ores.

Sources: Open circles and squares from Imperial Oil (2005, p. 4-12); diamonds from CNRL (2002a, p. 2-45); solid circles from Suncor Energy Inc. (2005, p. 4-42); crossed squares based on University of Alberta data.

Table 4.1 Mineral components in total oil sand solids

Source: Hepler and Smith (1994).

Component	Weight percent
Quartz	82
K-feldspar	5
Calcite	Trace
Dolomite	Nil
Siderite	Trace
Pyrite	Nil
Kaolinite	4
Illite	7
Chlorite	1
Smectite	Trace
Mixed layer clays	1
Anhydrite	Trace

Clays

Various types of clays are a major contributor to the fines content of oil sands ores. The type and amount of clay play a critical role, not only in bitumen recovery and froth treatment, but also in tailings management and process-affected warm water recycling. In bitumen recovery, the presence of clays can cause slime coating on bitumen droplets and hinder bitumen aeration. Clay fines can also induce slurry gelation in primary separation vessels (cells), which can hinder the flotation of aerated bitumen. In bitumen froth treatment, the presence of clays can contribute to the stabilization of emulsions of water in diluted bitumen, creating challenges in producing a bitumen product of required specifications for downstream upgrading. In tailings management, the formation of mature fine tailings or fluid fine tailings in tailings ponds is mainly attributed to clays. The challenges presented by the presence of clay minerals in oil sands processing are largely related to the high specific surface areas and anisotropic surface characteristics of small-sized platy clay particles. Understanding the properties of clays is, therefore, of great importance, as they affect the entire process chain of bitumen recovery and tailings management.

The typical composition of clays commonly encountered in the Athabasca oil sands is shown in Figure 4.10 and Table 4.1. The dominant clay minerals are kaolinite and illite.² Trace amounts of montmorillonite and smectite clays may be present in the fines fraction.

² The ratio of kaolinite to illite shown in Table 4.1 is different from the pie chart value in Figure 4.10. This difference is due to different ore samples being used in the analysis and the fact that the ore body is not uniform across the Athabasca oil sands area. By and large, kaolinite is the dominant clay fraction.

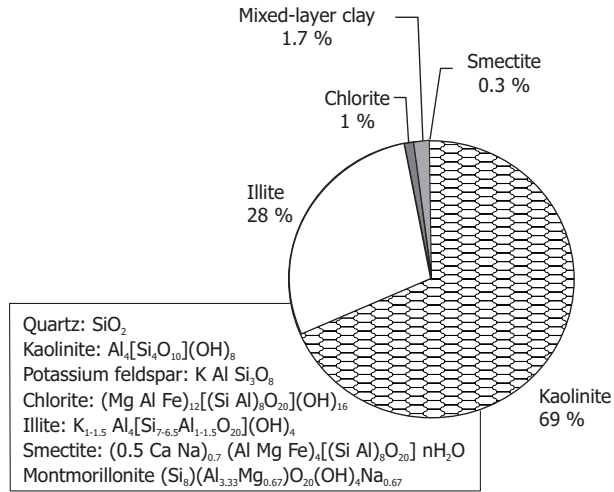


Figure 4.10 Relative amounts of clay minerals in an oil sands sample.

Source: Cuddy (2004).

As shown in Figures 4.11 and 4.12, clay minerals are composed of two basic layers: a silicon-oxygen tetrahedron sheet (T) and an aluminum-oxygen-hydroxyl octahedron sheet (O, known as *gibbsite*). When the octahedron sheet is made of magnesium hydroxide, it is called *brucite*. Different arrangements of tetrahedron and octahedron basic sheets result in various types of clay minerals, such as two-layer structured kaolinite (1:1 or –TO–TO–), and three-layer structured illite and smectite (2:1 or –TOT–TOT–), where – represents binding between two-sheet (TO) or three-sheet (TOT) unit layers, known as building blocks. The tetrahedron and octahedron sheets are covalently bound through sharing of the apex oxygen atoms of the tetrahedron sheet. The structures of four typical clay minerals encountered in the oil sands are shown in Table 4.2. The schematic structures of these four clay minerals are shown in Figure 4.13.

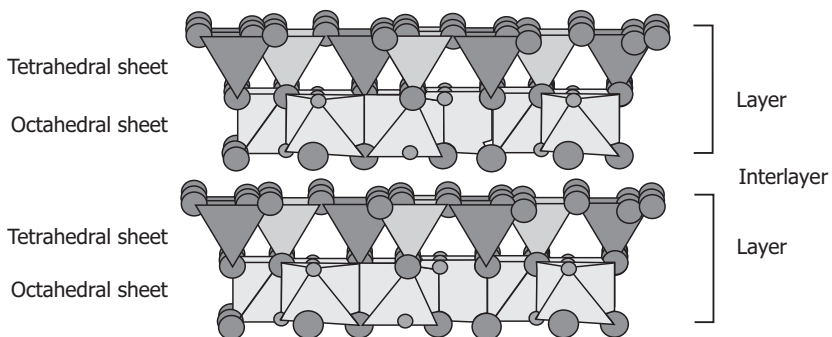


Figure 4.11 Two unit layers of kaolinite, with an interlayer between them. Each layer is composed of a siliceous tetrahedral and a dioctahedral aluminous sheet.

Source: Konan et al. (2007).

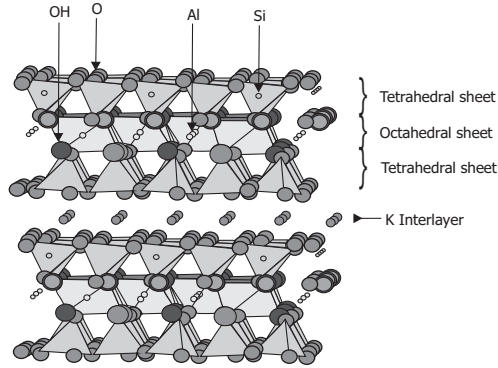


Figure 4.12 Two unit layers of illite with potassium ions in the interlayer between them. Each layer is composed of one dioctahedral aluminous sheet sandwiched between two siliceous tetrahedral sheets.

Source: Konan et al. (2007).

Table 4.2 Characteristics of clays commonly encountered in oil sands formations

Mineral	Kaolinite	Illite	Montmorillonite	Chlorite
Abundance (wt. %)	69	28	0.3	1
Composition*	$Al_2Si_2O_5(OH)_4$	$K(Al,Fe,Mg)_5(Al,Si)_8O_{20}(OH)_4$	$(Na,Ca,H_3O)_x[Al_{4-x}(Fe,Mg)Si_8O_{20}(OH)_4]$	$(Mg,Fe,Al)_6(Al,Si)_4O_{10}(OH)_8$
Type of structure	Two-Layer (TO)	Three-Layer (TOT)		
Cleavage (Basal) planes	SiOSi siloxane	SiOSi siloxane		SiOSi siloxane
	Al-OH hydroxyl			MgOH hydroxyl
Isomorphic substitution	Low in T	High in T	Both in T and O	
Compensating ions	K^+	K^+	Na^+, Ca^{2+}	O-brucite
Specific surface area (m ² /g)*	10–20	65–100	50–120 (external) 700–840 (total)	42
Cation exchange capacity* (meq/100g)	3–5	10–40	80–150	10–40

*Mitchell (1976).

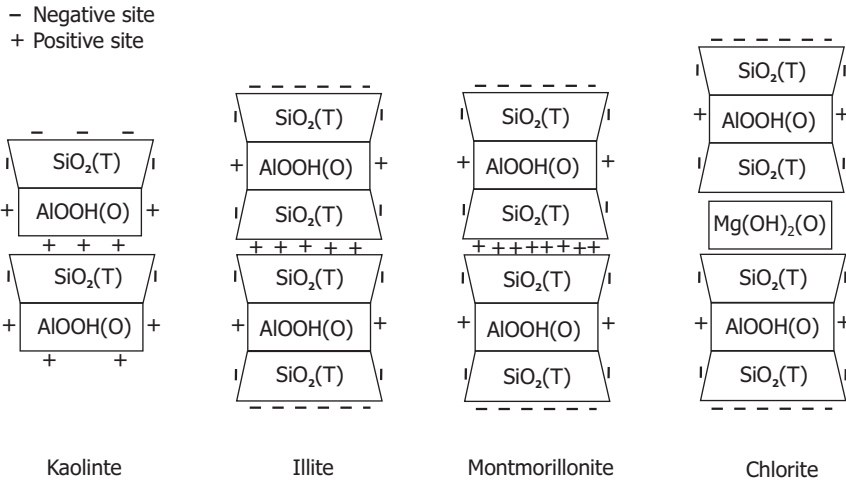


Figure 4.13 Schematic structure of four clay minerals typically encountered in oil sands.

Both kaolinite and illite clays are not expandable, i.e., they do not easily swell in water. Smectite clays, however, are known to do so, and can have a marked influence on the viscosity of the conditioning slurry. The presence of smectite clays can cause gelling in a gravity separation vessel, as mentioned above. Smectite is also characterized by a large specific surface area and high cation exchange capacity. Current literature recognizes smectite as a group and montmorillonite as a mineral belonging to the smectite group (van Olphen 1963; Giese and van Oss 2002).

Two-Layer Kaolinite Clays

Kaolinite is a Si:Al 1:1-type clay (Figure 4.11). Each unit layer is made up of a siliceous tetrahedral and a dioctahedral aluminous sheet. The 1:1 layer has basal oxygen on the tetrahedral surface sheet and hydroxyls on the octahedral aluminous sheet. The bonding between the unit layers occurs via a hydrogen bond between one hydroxyl group in the octahedral surface and the adjacent oxygen in the tetrahedral surface. As there is an abundance of these bonds, the binding between the layers is strong. In other words, kaolinite clays do not delaminate easily. The layers do not swell when placed in water or in an electrolyte solution.

In nature, water can intercalate with kaolinite clay to form $\text{Al}_2\text{Si}_2\text{O}_5(\text{OH})_2 \cdot 2\text{H}_2\text{O}$ clays, thereby increasing the layer thickness from 0.7 nm to ~ 1 nm. There is very little ionic penetration into the interlayer by ions present in the electrolyte solution. The cationic exchange of kaolinite clay (i.e., the ability to exchange, say, sodium within the layer with calcium in an external electrolyte solution) is considered to be low. Cationic exchange occurs mainly at the edges of the layers.

The ion exchange offered by the clays is of great importance. The clays act as a sink or a scavenger for calcium present in the processing water, where high levels of calcium ions can be detrimental to bitumen recovery. For each atom of calcium taken up by kaolinite clay, two atoms of sodium are released from its outer surface (Stumm and Morgan 1996; Essington 2004).

The perfect tetrahedron and octahedron sheets are electrically neutral. However, *isomorphic substitution* of higher valence cations by lower valence cations of similar sizes, such as silicon (Si^{4+}) by aluminum (Al^{3+}) in the tetrahedron sheet and/or aluminum (Al^{3+}) by magnesium (Mg^{2+}) in the octahedron sheet, results in a net charge deficiency, causing the building blocks to carry a permanent negative charge. The charge deficiency is balanced by interstitial compensating cations (such as sodium, potassium, calcium, magnesium, and ferrous ions), which make the clay minerals electrically neutral. When kaolinite clay is placed in an aqueous solution, a surface charge appears on the external basal surfaces and near the layer edges due to the departure of the compensating cations. These charges are pH-insensitive at the siliceous faces, slightly pH-sensitive at the aluminous faces, and pH-sensitive at the edges. In other parts of this chapter, we will detail the electric surface properties of the clays as they are affected by pH and electrolytes.

For two-layer kaolinite (1:1), the degree of isomorphic substitution, mainly in the tetrahedron sheets, is relatively small, leading to a relatively low permanent charge. The compensating ions sit in the hexagonal holes created by six oxygen atoms on the tetrahedron surface (Bergaya, Theng, and Lagaly 2006), holding the building blocks together tightly, as shown in Figure 4.13. As a result, two-layer kaolinite is non-swelling, and the compensating ions are not available for exchange with other cations in the solution. Under mechanical delamination, the cleavage of TO–TO linkage leads to two different surfaces, a tetrahedron siloxane surface (SiOSi) and an aluminum hydroxyl surface (Al-OH), known as basal planes (Bergaya, Theng, and Lagaly 2006). Although the aluminum hydroxyl surface is hydrophilic, the neutral siloxane surface is normally of moderate hydrophobicity, with a water contact angle of around 40° to 45° (Gee, Healy, and White 1990; Kanta, Sedev, and Ralston 2005). It is possible to hydrolyze the siloxane bonds to silanol groups, making the siloxane surface hydrophilic. However, the hydrolysis of siloxane bonds is generally relatively slow unless it occurs in extremely high pH solutions. This is one of the reasons why high pH is beneficial for bitumen liberation, as it can quickly and effectively hydrolyze the silica surface so that it becomes hydrophilic.

The isomorphic substitution of silicon by aluminum creates a negative charge on the surface that is compensated by interstitial cations. When placed in an aqueous solution, the compensating ions on the exposed basal planes leave the surface as a result of their strong hydration characteristics, leading to net negative charges on the basal plane, which is pH-insensitive. This surface charge is known as *permanent surface charge* (Tombácz and Szekeres 2006). The presence of this charge makes the basal plane surface hydrophilic.

The exposed aluminum hydroxyl surface (Al-OH) can be protonated at low pH and deprotonated at high pH by following hydrolysis reactions similar to those in the silanol groups shown in Figure 4.14 (reactions II and III, respectively), causing the

surface to carry a pH-dependent surface charge that is positive at low pH and negative at high pH (Tombácz and Szekeres 2006).

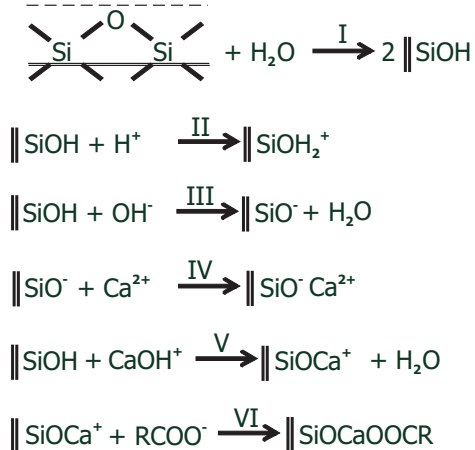


Figure 4.14 Surface reactions on silica basal planes of clays that make the surfaces amenable for surfactant contamination and hydrophobization. I: Hydrolysis of siloxane bonds or broken SiO⁻ bonds. II: Protonation of silanol group to carry positive charge at low pH. III: Deprotonation of hydrolyzed surfaces to make them negatively charged at high pH. IV: Divalent calcium adsorption under electrostatic attraction. V: Specific surface condensation reaction of hydrolyzed calcium monohydroxyl groups (CaOH⁺) with surface silanol groups (SiOH) to form a covalent bond (SiOCa⁺). VI: Adsorption of anionic natural surfactant on activated clay silica basal plane surfaces, which makes them hydrophobic, hindering bitumen liberation and inducing clay flotation, resulting in lower bitumen recovery and/or poorer froth quality.

In addition to these two different basal plane surfaces, clay particles also have edge surfaces with broken Si-O and Al-O bonds. When immersed in water, these broken bonds undergo a hydrolysis process similar to that of silica and alumina. The hydrolyzed sites experience different degrees of dissociation, depending on the characteristics of the metal oxide surfaces and the solution pH. An acidic silica surface, for example, exhibits a point of zero charge (PZC) at a pH of around 2, where PZC is defined as the minus log of potential determining ion (pdi) concentration (-log [pdi]) or pH at which a surface carries a net zero charge. In metal oxide systems, hydrogen ions are potential determining ions. The PZC is an important parameter in characterizing the electric characteristics of solids. Above the PZC, particles carry a net negative charge, while below the PZC, they carry a positive surface charge. For alumina of basic characteristics, the PZC is around pH 9. Based on the Si:Al ratio, the PZC of kaolinite edge surfaces varies between 6 and 6.5 for kaolinite clays (Tombácz and Szekeres 2006). For two-layer kaolinite particles, the overall charge is a result of all three types of surfaces (two basal planes and an edge) and depends on pH, as shown by the results in Figure 4.15. The zeta potential of kaolinite is shown to be strongly

pH-dependent, indicating a weak permanent charge on the kaolinite basal planes and a high ratio of edges-to-basal plane surface area, such that the edges become a dominant contributor to overall surface charge. In this particular case, an isoelectric point (IEP), where zeta potential is zero, is observed at pH 3.2. It is important to note that, although the kaolinite particles are electrically neutral at their IEP, the surface remains charged, with the T-basal plane being negatively charged and the O-basal plane and edges being positively charged. Such complex charge characteristics lead to various important practical issues, such as the formation of card-house structure and the gelation of clays (van Olphen 1963).

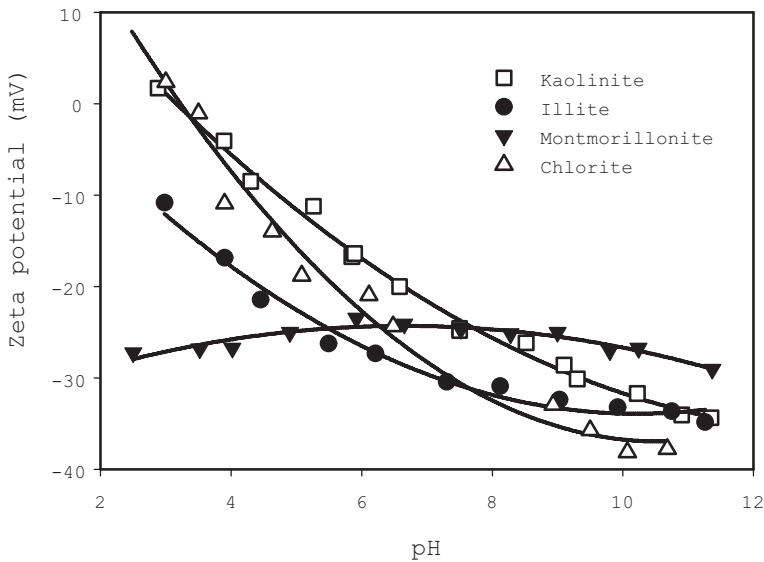


Figure 4.15 Zeta potential of clay particles as a function of pH in 1 mM KCl aqueous solutions.

Replotted based on the results by Liu, Xu, and Masliyah (2004). The results for chlorite (Wu 2009, pers. comm.) have not been published. The minerals were purchased from Ward's Natural Sciences (Rochester, NY).

Three-Layer Clays

The main differences among various three-layer clay minerals (such as illite and smectite) are in the degree and location of isomorphic substitution and the type of compensating ions. Illite clay, for example (Figure 4.12), is a dioctahedral 2:1 phyllosilicate that occurs in abundance in oil sands, soils, and sedimentary rocks. Its chemical composition can vary widely.

The isomorphic substitution of illite occurs mainly in the tetrahedron sheet, where a quarter of silicon atoms are substituted by aluminum atoms with compensating ions (mainly potassium) sitting in the hexagonal holes. Such an arrangement makes the

binding of the basic building units very strong. As the layers do not easily part, the interlayer potassium cations are not available for cation exchange. However, cation exchange does occur, mainly at the edges of the layers (as in kaolinite). The ion exchange offered by the illite clays is significant, as the clays act as a sink to the divalent cations in the processing water. Again, the electric surface properties of illite clays are dependent on the solution's pH, electrolyte type, and concentration. Apart from its chemical composition, illite clay is distinguished from smectites (or montmorillonites) mainly by the absence of interlayer swelling with water or hydrocarbon compounds.

In smectite clays such as montmorillonite, the isomorphic substitution occurs in both the tetrahedron and octahedron sheets. The substitution in the tetrahedron sheet of smectite is similar to that of kaolinite and illite. However, the isomorphic substitution in the octahedron sheet is sandwiched between two tetrahedron sheets, making the permanent charge in the O-sheet delocalized. In this case, the compensating ions are separated from the octahedron sheet and sit on the tetrahedron sheet. The presence of such compensating ions between the layers of the building blocks weakens the interlayer binding, such that the compensating ions become available for ion exchange, displaying the well-known swelling characteristics of smectite clay minerals. As a result, smectite clays exhibit a high cation exchange capacity (CEC).

When three-layer clay minerals undergo shear forces, their interlayer binding is broken and they become delaminated, exposing their basal plane surfaces. Unlike in two-layer kaolinite, a common feature of three-layer clay minerals is that both basal planes produced from the cleavage have identical siloxane surfaces. The siloxane basal planes are less sensitive to the aqueous pH than the aluminum hydroxyl basal planes of 1:1 kaolinite. Because illite and smectite undergo a greater isomorphic substitution of the tetrahedron sheet than kaolinite, their basal planes feature a more negative surface charge than kaolinite when placed in water. As well, the aluminum-to-silicon ratio on the edge surfaces of three-layer (2:1) clay minerals is lower than that on the two-layer (1:1) kaolinite edge surfaces. Since the PZC for broken aluminum oxide and silica surfaces are pH_{PZC} 9 and 2, respectively, at a given pH, one would expect lower positive or more-negative edge surfaces in three-layer clay minerals than in two-layer clay minerals. Overall, three-layer clay minerals for a given solution condition should exhibit a more negative (or less positive) zeta potential, as shown in Figure 4.15.

It is interesting to note major differences in the zeta potential profiles of kaolinite (1:1) and illite (2:1) and of illite and montmorillonite (2:1). Illite has a more negative zeta potential profile than kaolinite, attributed to a greater isomorphic substitution and a higher Si:Al ratio on its edge surfaces. There is no IEP for illite over the pH range studied, indicating a dominant contribution of permanent charge on the basal plane to the overall charge of illite, which is pH-independent. However, at very high pH (above 11), the zeta potential profiles of illite and kaolinite converge to the same curve, suggesting a similar saturation charge density on the edge surfaces and basal planes of both illite and kaolinite surfaces.

For montmorillonite, a flat zeta potential profile with only a slight decrease (i.e., a slightly more negative zeta potential) with increasing pH above 10 is observed. This zeta potential profile is in great contrast to that for illite, although both are 2:1 clay minerals. The fact that the zeta potential of montmorillonite clays is insensitive to pH is attributed to the significant contributions of the basal planes in comparison to

those of the edge surfaces, a unique feature of swelling clays. Such an observation is anticipated by considering typical edge surface areas of kaolinite and montmorillonite (around 20 % and less than 1 %, respectively) and corresponding plate thicknesses (40 nm and 1 nm) (Wan and Tokunaga 2002). It should be noted that due to the complex nature and contamination of clay minerals, there is a wide range of points of zero charge reported in literature for illite and montmorillonite clays. The clays shown in Figure 4.15, with their specific electrokinetic characteristics, are just one example.

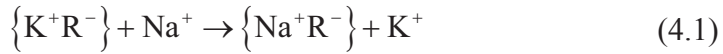
Chlorite

Another type of clay encountered in the oil sands, although only in small amounts, is three-layer chlorite. The isomorphous substitution in chlorite occurs in both the tetrahedron and octahedron sheets. In contrast to illite and montmorillonite, charge compensation due to isomorphous substitution in three-layer chlorite occurs through the positively charged brucite layer, in which some magnesium ions are substituted by aluminum ions. For this reason, chlorite is sometimes considered a four-layer (1:2:1) clay mineral. When chlorite is cleaved along the basal planes, two distinct basal planes are produced: a tetrahedron siloxane basal plane and an octahedron magnesium hydroxide basal plane. The permanent charges on the siloxane basal plane are pH-independent and the charges on the magnesium hydroxide basal plane are highly pH-dependent following protonation and deprotonation of magnesium hydroxides. On the edge surfaces, chlorite contains a similar aluminum-to-silicon molar ratio as on the edge surfaces of three-layer illite or montmorillonite clay minerals. However, chlorite also contains magnesium ions from the compensating brucite layers. Considering pH_{pzc} values of 9.1 for aluminum oxide (hydroxide) and 11.8 for magnesium oxide (hydroxide) (King 1982), one would expect chlorite to have more positive zeta potential values above PZC, or less negative zeta potential values below PZC, than illite. Indeed, the zeta potential profile of chlorite in Figure 4.15 shows these characteristics. It is also interesting to note that chlorite has a more pH-dependent zeta potential profile than illite, but is similar to kaolinite in this respect. This trait is not unexpected, and clearly illustrates the major contribution of charge from the edges to the overall surface charge in both chlorite and kaolinite, a unique feature of non-swelling clays.

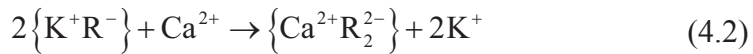
Cation Exchange Capacity of Clays

The above discussion established that isomorphous substitution and the location of compensating ions determine, to a large extent, the electric surface properties of clay minerals. The net charge due to isomorphous substitution in basal planes is balanced by the interstitial compensating ions that can be exchanged by other cations available in the solution. The amount of compensating ions that can be exchanged, known as the

cation exchange capacity (CEC), is therefore a good measure of isomorphic substitution and of clay characteristics in general. The CEC is expressed in milliequivalents per 100 grams of clays. Common cations capable of ion exchange with compensating ions include H^+ , Na^+ , NH_4^+ , Ba^{2+} , and Ca^{2+} . Cation exchange is driven by high concentration (and hence, high chemical potential in a solution for cation exchange), and, as outlined in Stumm and Morgan (1996), is expressed by



and



Typical CEC values of various types of clays are given in Table 4.2. For kaolinite, cation exchange occurs mainly on the external basal planes and on edge surfaces. Because kaolinite has a low degree of isomorphic substitution, its CEC is generally very low (3–5 meq/100 g). An increased degree of isomorphic substitution in illite makes its CEC slightly higher (10–40 meq/100 g). Degradation or weathering of illite can cause its CEC to increase slightly. In contrast, montmorillonite has a much higher CEC (around 100 meq/100 g), not only due to its higher isomorphic substitution, but also to delocalized compensating ions that result from a high degree of isomorphic substitution in the octahedron layer. The delocalization of compensating ions in montmorillonite makes the clay swell and the compensating ions accessible for cation exchange. The cation exchange capacity of chlorite is extremely low due to its unique, tightly bound octahedron brucite layer structure, which compensates the permanent structural charges of isomorphic substitution.

It is important to note that divalent cations have a higher affinity to clay surfaces than monovalent cations, depending on the type of clay and the concentration of exchanging cations in the solution. The competitive cation exchange of monovalent and divalent cations on various types of clay surfaces is shown by the experimental results in Table 4.3. It is evident that the lower the exchanging cation concentration in the solution, the higher the selectivity of cation exchange towards the higher-valence cations. Also interesting to note is that the selectivity is higher for smectite than for non-swelling clays, indicating a stronger affinity of divalent cations than monovalent cations to swelling clays. The results in Table 4.3 suggest that, to accurately determine the CEC value for a given clay, the presence of excess exchanging cations is necessary in a solution in order to ensure a complete exchange.

Table 4.3 Selectivity of cation exchange on three major clay minerals encountered in oil sands formations
Source: Stumm and Morgan (1996).

Clays	Ca ²⁺ /K ⁺ molar ratio on clay surfaces in solutions of 2[Ca ²⁺]+[K ⁺] (meq/L)			
	100	10	1	0.1
Kaolinite	—	1.8	5.0	11.1
Illite	1.1	3.4	8.1	12.3
Montmorillonite	1.5	—	22.1	38.8

Mineral Solids and Bitumen Grade

A characteristic of the oil sands is that the particle size distribution (PSD) of their mineral solids is, by and large, a function of the bitumen content of the oil sands ore. Finer mineral solids are present in low-grade ores, whereas coarser solids are present in high-grade ores. Cameron Engineers offered one of the first representations of the relationship between percent fines and bitumen grade (alternatively, bitumen saturation or content), shown in Figure 4.16 (1978). Despite the high degree of scatter in the plot, there is a clear trend: high-grade oil sands ores are associated with low percent fines. More recent core analysis data, showing the relationship between bitumen grade and percent fines, are given in Figures 4.17, 4.18, and 4.19 for mines in operation at Syncrude, Suncor, and Imperial Oil, respectively. Again, there is much scatter in the data, but this is to be expected from a natural formation. Figure 4.20 depicts an averaged estimate for bitumen grade and percent fines.

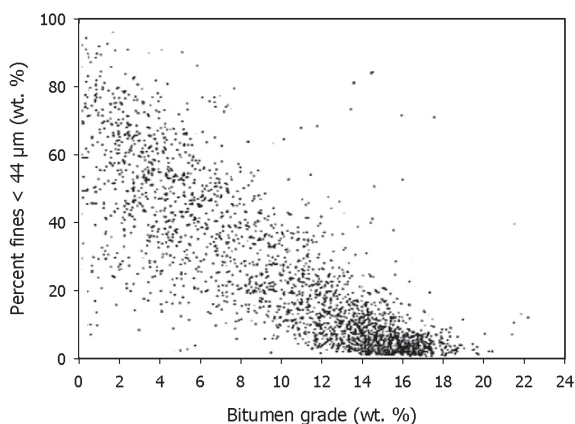


Figure 4.16 Core analysis data: relationship between percent fines and bitumen grade.

Source: Cameron Engineers (1978).

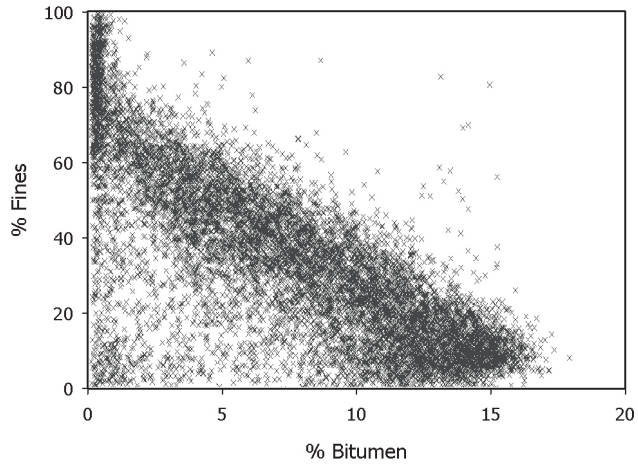


Figure 4.17 Core analysis data: relationship between percent fines and bitumen grade, Syncrude.

Source: Cuddy (2004).

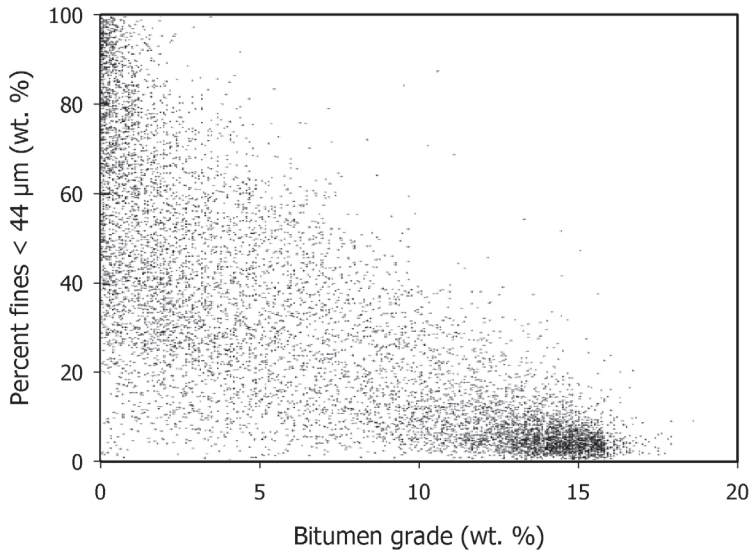


Figure 4.18 Core analysis data: relationship between percent fines and bitumen grade, Suncor.

Courtesy Mr. Wayne Hill, Suncor Energy Inc.

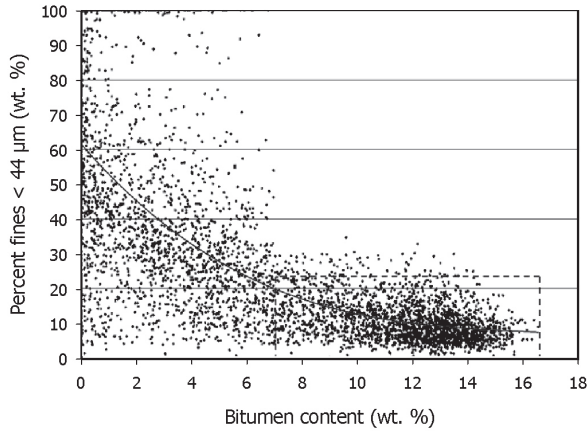


Figure 4.19 Core analysis data: relationship between percent fines and bitumen grade, Kearl Oil Sands Project, Imperial Oil.
 Source: Imperial Oil Ltd. (2005, Figure 4-5).

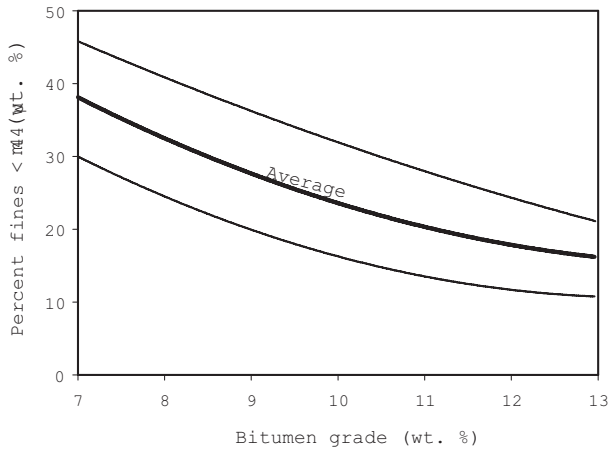


Figure 4.20 Estimate of average bitumen grade with percent fines.

A relationship between percent fines and water content in oil sands samples is shown in Figure 4.21. There is a trend of increasing percent fines with percent water in the oil sands.

Although in most literature, data for percent fines are correlated in terms of percent bitumen content in oil sands, there is a reasonable correlation between much smaller mineral solids and oil sands bitumen grade. Figure 4.22 shows the variation of mineral solids smaller than 2 μm with bitumen weight percentage—i.e., the oil sands grade; the expected positive correlation can be seen in the figure.

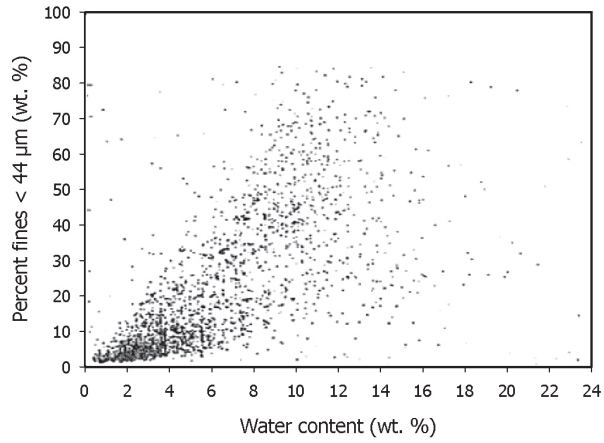


Figure 4.21 Core analysis data: relationship between percent fines and water weight percent.

Source: Cameron Engineers (1978).

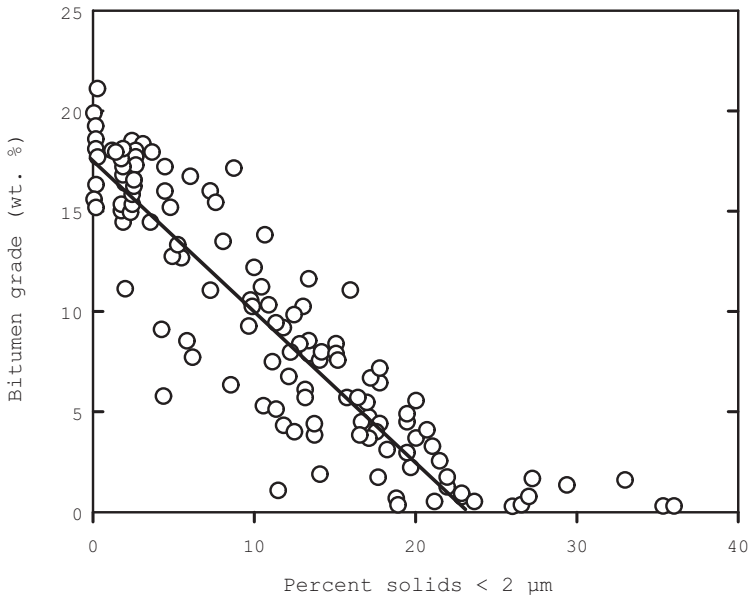


Figure 4.22 Relationship of bitumen percent to mineral solids smaller than 2 μm .

Source: Czarnecki et al. (2005).

4.1.3 Electrolytes in Oil Sands

As discussed earlier, crude oil migrated into sedimentary formations that had indigenous water in them. As well, for millions of years, underground water flowed through the oil formations as a result of hydrologic gradients (albeit at an exceedingly slow pace). The resulting electrolyte content and type, i.e., the presence of ions such as sodium, calcium, chloride, bicarbonate, and sulphate in the formation water, is the result of a very complex process. The electrolyte content and type vary with depth and lateral location from one ore formation to another and within a given formation. As the electrolyte type and concentration tend to have a marked effect on bitumen recovery, tailings water management, and bitumen froth treatment, much effort has been devoted to studying the ionic content of the Athabasca formation. To that end, the gathering of core data on leases, the bitumen grade; the percent fines and D_{50} ; and the ionic strength of chloride, sodium, bicarbonate, sulphate, calcium, and magnesium have all become an essential part of lease characterization.

Measuring the composition and concentration of the electrolytes present in an oil sands ore sample may seem like a straightforward task, as analytical techniques to measure ion type and concentration in a water sample are widely available. However, the complexity arises from the fact that the water (when it contains the majority of the ions) is not present in the oil sands matrix as a distinct layer that can easily be separated out. The logical approach is to mix an oil sands sample with hot water to remove the bitumen from the sand grains, centrifuge the sand-water-bitumen slurry, and analyze the ionic type and composition of the supernatant water layer. Knowing the mass of added water and the water content of the original oil sands sample, one then evaluates the ionic type and content of the oil sands sample. The former can be easily measured using the Dean-Stark analytical method.

Herein lies the difficulty. Once water is added to the oil sands sample, clays will exchange ions from the water in the slurry. The equilibrium ionic strength of the water in the slurry will depend on the amount and the temperature of the added water, as well as the percentage and type of clays in the oil sands sample. In reality, one is not measuring the *true* electrolyte strength of the formation water itself. For that reason, a protocol must be followed in assigning a *relative* value to the concentration of a given ionic species in an oil sands sample. This value is noted in mg/kg or mmol/kg (milligrams or millimoles of ionic species per kilogram of oil sands ore).

The normal protocol is to add boiling distilled water at 100 °C in amounts equal in weight to the oil sands sample and to measure the ionic concentration in the water after bitumen removal and centrifugation.³ The results can then be recorded in milligrams of a given ion per kilogram of oil sands (mg/kg). We will refer to concentrations as being in “kilograms of oil sands” with the knowledge that they are measured in the collected water after mixing distilled water with an equal mass of oil sands. Electric conductivity and pH are measured in the final collected test water. It is best to avoid the units mg/L and mmol/L, as it may be potentially unclear whether they refer to the volume of the formation water or the collected test water.

³ Unfortunately, in some literature, the water collected during ionic determination tests is described using the term *connate water*. This can be rather confusing, as this term refers to water trapped in a sediment or rock at the time of deposition (literally, existing at birth or from the beginning).

There are very large variations in the ionic concentrations of the different ionic species in oil sands ores from one location to another. Therefore, there are no representative plots of ionic concentrations. Here, we will refer to some open literature to illustrate variations within a core or within an oil sands lease from which different core samples are used.

The concentrations of sodium and chloride ions tend to vary substantially within the Athabasca oil sands area. The variations between these two ions within one ore body (in this case, from the Horizon Project) can be seen in Table 4.4. As can be noted from the table, the arithmetic average of the measured chlorides values is 117 mg/kg (milligrams of chloride per kilogram of oil sands ore), while the corresponding value for sodium is 109 mg/kg. These values are consistent with the upper range values reported at other oil sands operations located near the Horizon Project leases. It is interesting to note the wide variation in the sodium and chloride concentrations, as given by their maximum and minimum values in Table 4.4.

Table 4.4 Chloride and sodium ions, CNRL's Horizon Oil Sands Project
Source: CNRL (2002a, p. 2-49).

Statistics	Ionic concentration (mg/kg of oil sands)	
	Chloride, Cl	Sodium, Na
Arithmetic average	117	109
Minimum value	0	4
Maximum value	552	453
Standard deviation	99	79
Number of essays	293	293

Table 4.5 Soluble ionic concentrations for 348 core samples from the 2003–2004 core hole program, Kearn project
Source: Imperial Oil Ltd. (2005, Table 4-4, p. 4-16).

Statistics	Bitumen grade (wt. %)	pH	Anions (mg/L)				Cations (mg/L)				
			Electric conductance (mS/cm)	Bicarbonates	Carbonates	Chlorides	Sulphates	Calcium	Magnesium	Sodium	Potassium
Arithmetic average	12.0	7.7	0.4	48.9	7.5	16.4	113.1	22.1	7.2	21.7	15.3
Minimum value	0.8	4.0	—*	3.3	1.6	1.5	22.2	1.5	0.7	3.0	1.4
Maximum value	16.0	9.3	1.2	145.0	15.9	68.4	603.0	115.0	28.0	104.0	59.7
Standard deviation	2.1	0.8	0.2	29.1	3.3	12.2	77.7	15.9	4.8	14.1	9.5

* Tabulated as zero in the original reference.

For comparison, the corresponding data for the Kearl Project are given in Table 4.5. The mean values reported for sodium and chloride concentrations are lower than those reported for the Horizon Project.

Figures 4.23 and 4.24 show the variation, with depth, of the concentrations of calcium and magnesium, respectively, in oil sands core samples. In this particular lateral location within the oil sands formation, the difference between the marine and estuarine sediments is quite substantial. The ore from the marine sediment, which is located in the Upper McMurray layer, has a much higher calcium and magnesium content than that from the deeper estuarine sediment of the Middle and Lower McMurray layers. This is due to the ionic strength of the formation water prior to oil migration and the history of water migration through the formation. The very high spike in calcium and magnesium concentrations at the highest depth is due to the presence of basal water sands.

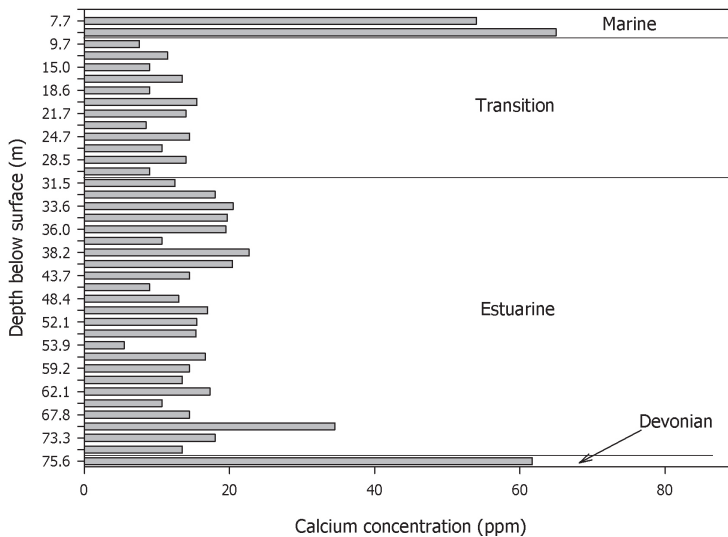


Figure 4.23 Variation of calcium with depth for marine and estuarine ores in an oil sand core at the same lateral location.

Source: Cuddy (2004).

Core analysis data from different core samples for calcium plus magnesium are provided in Figure 4.25. Here, there is a clear trend in the variation of calcium plus magnesium with depth, where the marine ore-type deposit carries higher concentrations in divalent cations as compared to the estuarine ore deposit. The ratio of calcium to magnesium (wt./wt.) from different core samples is given in Figure 4.26. There is a tendency of the Ca:Mg ratio to increase with depth; however, it remains, by and large, less than 3.

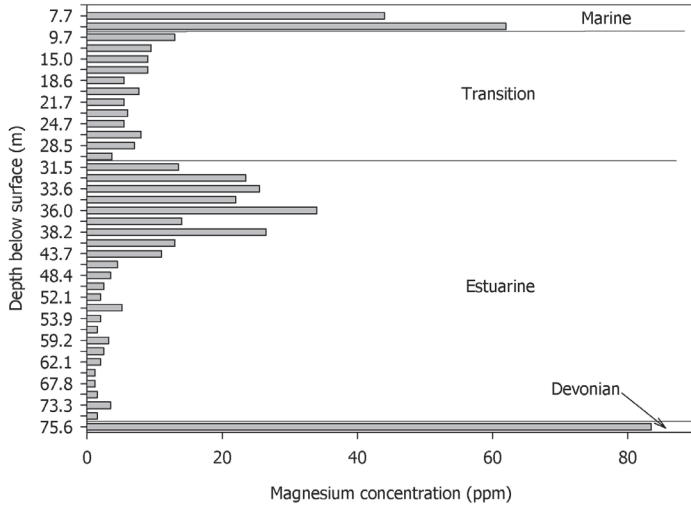


Figure 4.24 Variation of magnesium with depth for marine and estuarine ores in an oil sand core at the same lateral location.

Source: Cuddy (2004).

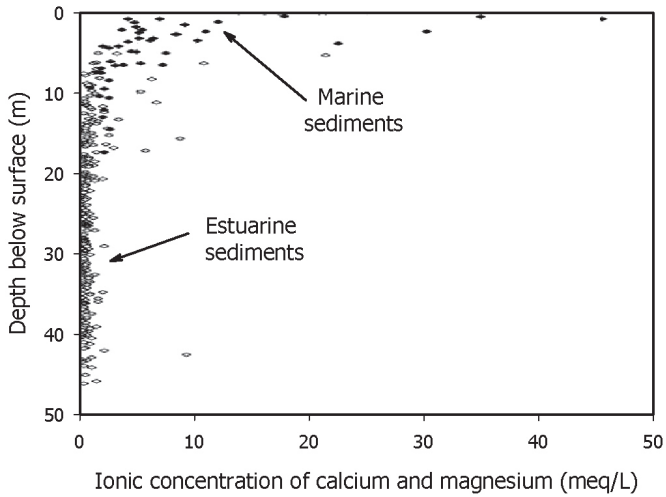


Figure 4.25 Variation of calcium plus magnesium with depth for marine and estuarine ores in oil sand cores.

Source: Cuddy (2004).

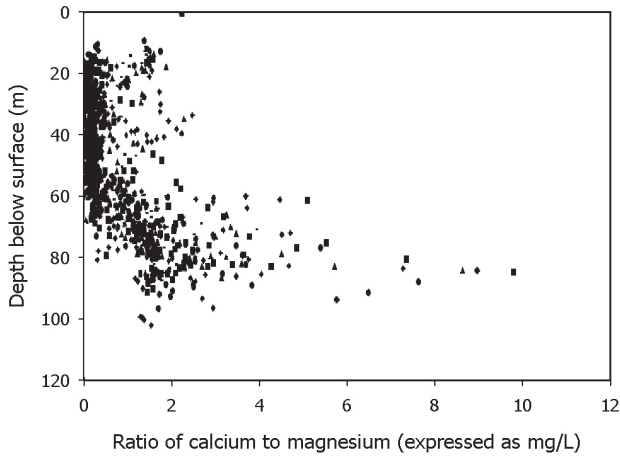


Figure 4.26 Variation of the ratio of Ca:Mg, expressed by mass ratio as a function of depth.

Source: Cuddy (2004).

In general, the concentration of sulphate ions (SO_4^{2-}) tends to be less than 100 mg per kilogram of ore, as shown in Figure 4.27 for the estuarine sediment. On this particular lease, the sulphate concentration is very high in the marine sediment. However, one should not assume that all marine sediments have very high sulphate concentrations and that they are acidic due to the sulphate presence.

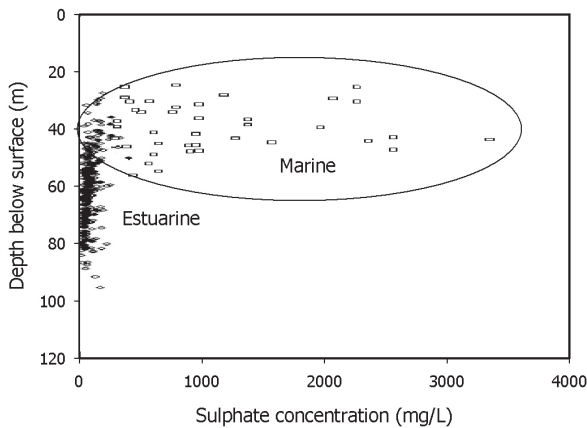


Figure 4.27 Relationship of sulphate in oil sands with depth for marine and estuarine ores.

Source: Cuddy (2004).

The pH of an aqueous solution is a measure of its hydrogen ion concentration, which is influenced by the presence of ionic species such as sulphates and bicarbonates. As sulphates comprise the main negative divalent ions in the aqueous solution, an increased number of sulphate ions would lead to lower pH values. From Figure 4.28, there appears to be a fair correlation between ore sulphate concentration and pH. By and large, the pH of the oil sands ore from the tested lease ranges between 7 and 9. Data from the Kearn project give a sulphate range of 22.2 mg/L to 603 mg/L, with a mean value of 113.1 mg/L; and a corresponding pH of 9.3 to 4.0, with a mean value of 7.7 (Table 4.5). These data fit in quite well with those presented in Figure 4.28. The variation of sulphate ion concentration with depth is shown in Figure 4.29 for a Syncrude lease (Cuddy 2004). The pH values are close to 8. Towards higher depths, the pH drops to as low as ~ 3 due to the oxidation of iron sulphide and organic matter. The sulphide oxidation is:

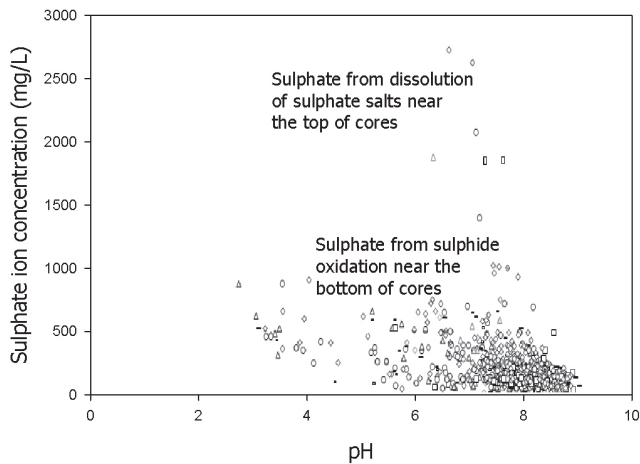
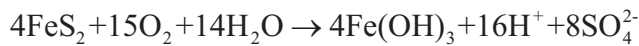


Figure 4.28 Variation of test water pH as a function of sulphate concentration.

Source: Cuddy (2004).

It is of interest to note that the Athabasca River contains relatively low levels of various ions, whose concentrations vary with location and season. Annual averages are provided in Table 4.6. The calcium concentration is shown to be ~ 33 mg/L, which is comparable to that in tailings ponds, while the sodium concentration, at ~ 8.8 mg/L, is much lower than that in tailings ponds. The Athabasca River water has a pH of around 7.9, which is slightly alkaline, and its value of total dissolved solids (TDS) is about 170 mg/L. In contrast, basal water sands can have very high total dissolved

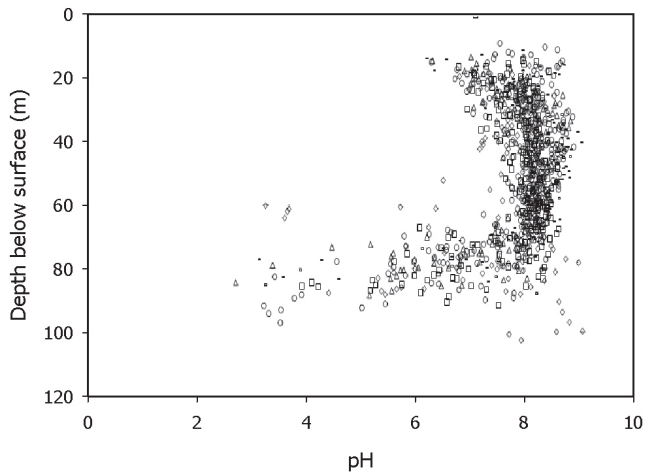


Figure 4.29 Variation of test water pH as a function of depth.

Source: Cuddy (2004)

solids. For example, at Total's Joslyn North Mine Project, the total dissolved solids range from ~ 10 000 mg/L to as high as 58 000 mg/L (in the northwestern part of the lease) (Deer Creek Energy Ltd. 2006).

Normally, electric conductance is measured for water bodies. It provides a measure of the ionic strength of the various electrolytes in the water. The symbol S represents the unit *siemens*, which is equal to ampere/volt. For reference, 2 mM (116.9 mg/L) of NaCl in water would have an electric conductance of 245 $\mu\text{S}/\text{cm}$, and 1 mM (142 mg/L) of Na_2SO_4 would have an electric conductance of 248 $\mu\text{S}/\text{cm}$ (Masliyeh and Battacharjee 2006).

Table 4.6 Water quality of Athabasca River

Sources:

^a CNRL (2002b, p. C7-23).^b Petro-Canada Inc. (2001, p. 6–7).

Data are based on measurements at mid-river, October 3, 2000.

Parameter	Unit	Downstream of Fort McMurray ^a (October 3, 2000)	Upstream of Fort Creek ^b (Annual observed median values)
Conventional parameters			
pH			7.9
Electric conductance	µS/cm		280
Total alkalinity	mg/L		99
Total dissolved solids	mg/L	170	170
Total suspended solids	mg/L		25
Dissolved organic carbon	mg/L	8.35	8
Total organic carbon	mg/L		10
Biochemical oxygen demand	mg/L		< 2.0
Major ions			
Bicarbonate	mg/L		121
Calcium	mg/L	33.5	31
Chloride	mg/L	2.7	11
Magnesium	mg/L	8.7	9
Potassium	mg/L		1
Sodium	mg/L	8.75	13
Sulphate	mg/L	25.15	25
Sulphide	µg/L		3
Organics			
Naphthenic acids	mg/L		2
Total phenolics	µg/L	2	2
Total metals			
Aluminum	µg/L	510	870
Antimony	µg/L	0.08	< 5.0
Arsenic	µg/L	0.6	< 1.0

4.2 Bitumen Density

The density of a material is defined as its mass per unit volume, given by

$$\text{Density} = \text{Mass/Volume.}$$

The unit of density is normally given as kg/m³. For example, at room temperature, water has a density of about 998 kg/m³. This is equivalent to 0.998 tons/m³. For convenience, the term *specific gravity* (SG) is used; this is defined as the ratio of the density of a material of interest relative to a reference density. The reference density normally used is that of water at 3.98 °C, which is 1000 kg/m³. Specific gravity has no units, as it is the ratio of two quantities of the same units.

Gas density is a strong function of temperature and pressure. Liquid and solids densities are very weak functions of pressure, but they vary with temperature. Within the range of operating temperatures of bitumen extraction, the density of sand and clays is normally given as 2650 kg/m³.

We are accustomed to thinking of light oil crude as having a lower density than that of water (e.g., 900 kg/m³, versus 998 kg/m³ for water). This is precisely why oils of a density of ~920 kg/m³ (e.g., olive oil) float on top of water or vinegar. In this context, “lighter” materials have a lower density than “heavier” materials.

In the petroleum industry, a different density scale is used. It is referred to as the *American Petroleum Institute gravity scale*, or *API gravity* for short. API gravity is a measure of how heavy or light a petroleum liquid is compared to water. It is given in degrees, and is defined as:

$$^{\circ}\text{API} = \frac{141.5}{\text{Liquid SG at } 15.6^{\circ}\text{C}} - 131.5 \quad (4.3)$$

Since water has a specific gravity of unity, the above equation yields a value of 10° API for water. Thus, a hydrocarbon with of more than 10° API will float in water, whereas a hydrocarbon having an API smaller than 10° will sink in water.

4.2.1 Classifications of Oil Crude

In general, oils with higher API gravity values are of greater commercial value. Conversely, oils of a lower API have a lower commercial value. Based on its measured API gravity, crude oil is classified as light, medium, or heavy:

Light crude oil is defined as an oil with an API gravity greater than 31.1° API.

Medium crude oil is defined as an oil with an API gravity between 22.3° API and 31.1° API.

Heavy crude oil is defined as an oil with an API gravity below 22.3° API.

Bitumen is a heavy oil that does not flow at room temperature without dilution, i.e., solvent addition. It has an API gravity of less than 10°. At Syncrude it is upgraded as Syncrude Sweet Blend to an API gravity of 31° to 33°. Upgraded bitumen is known as synthetic crude oil (SCO). West Texas Intermediate has an API gravity of 39.6°; oil between 40° API and 45° API would command high prices.

A density-temperature plot is reproduced in Figure 4.30. As shown by the figure, within the extraction temperature range, the density of bitumen is very close to that of water. As indicated by Figure 4.31, bitumen has a high density compared to heavy oils. Certainly, it has a much higher density than solvents such as toluene, heptane, and naphtha. Due to the very small density difference between water and bitumen, air attachment to bitumen becomes very important in bitumen recovery processes that depend on a density difference.

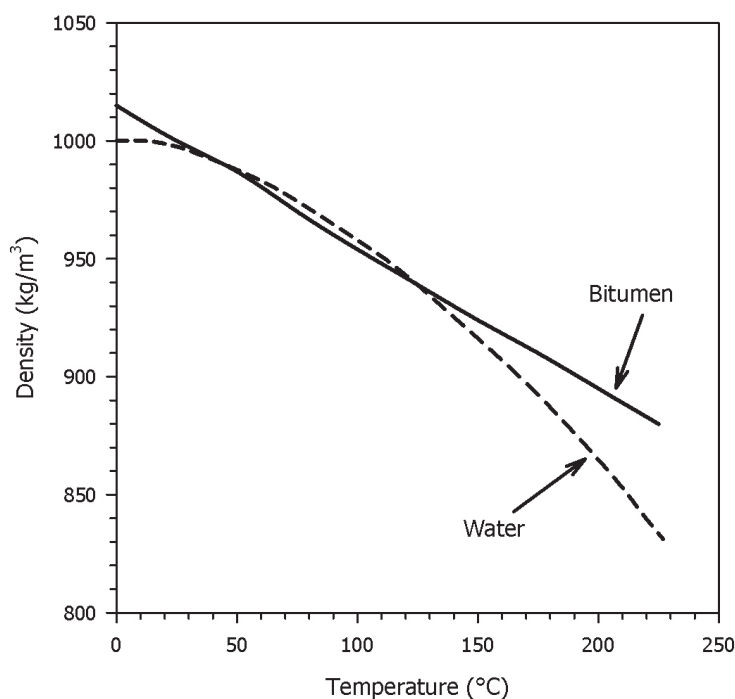


Figure 4.30 Bitumen density compared with water density.

Sources: Cameron Engineers (1978) and Komery, O'Rourke, and Chambers (1993).

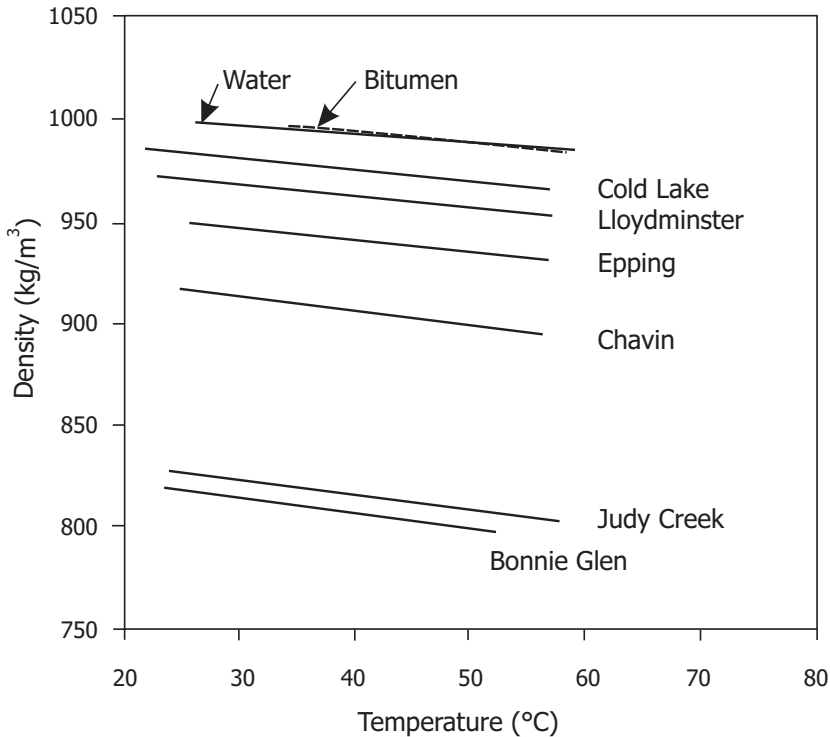


Figure 4.31 The effect of temperature on the density of some Western Canadian crudes.

Source: Takamura and Isaacs (1989).

Table 4.7 provides some numerical values for water and crude bitumen densities. It should be noted that the density of bitumen is not as precisely measured or universal as that of water. This is due to the fact that bitumen density depends on its source and the method used in its measurement. Therefore, the two intersection points between water and bitumen density curves, seen in Figure 4.30, should not be taken as representative. At higher temperatures, e.g., greater than 200 °C, bitumen density becomes sufficiently higher than that of water, and gravity separation between the two becomes feasible.

$$\text{Bitumen density} = 1015 - 0.615T + 5.45 \times 10^{-5}T^2 \text{ (kg/m}^3\text{)} \quad (4.4)$$

A curve-fitting correlation for the bitumen density, for $T < 200$ °C, is given by: where T is in degrees Celsius.

Table 4.7 Table Density variation of water and bitumen with temperature

Temperature (°C)	Water density (kg/m ³)	Temperature (°C)	Bitumen density (kg/m ³)
10	999.7	25	1000
20	998.2	50	987
30	995.7	100	954
40	992.2	125	939
50	988.1	150	924
60	983.2	175	910
70	977.8	200	895
80	971.8	225	880

4.3 Bitumen Dynamic Viscosity

The *dynamic viscosity* (or simply, viscosity) of a fluid reflects its resistance to flow. By and large, for a given temperature and pressure, bitumen behaves as a Newtonian fluid, where the applied force is proportional to the induced shear rate. An excellent compilation on the dynamic viscosity of bitumen is given by Seyer and Gyte (1989). The SI unit of dynamic viscosity is the pascal-second (Pa·s), which is equivalent to kg/m·s. Normally, viscosity is given in mPa·s, equivalent to the less-commonly used centipoise (cP) unit. *Kinematic viscosity* is defined as the ratio of dynamic viscosity to fluid density, and is given in units of m²/s. Examples of the dynamic viscosities and densities of different hydrocarbons are given in Table 4.8.

Table 4.8 Viscosity of some organic solvents and oil at 20 °C

Source: Shaughnessy, Katz, and Schaffer (2005).

Liquid at 20 °C	Density (kg/m ³)	Dynamic viscosity (Pa·s = kg/m·s)
Benzene	881	6.51·10 ⁻⁴
Ethanol	789	1.2·10 ⁻³
Gasoline	680	2.92·10 ⁻⁴
Kerosene	804	1.91·10 ⁻³
SAE 10W oil	870	1.04·10 ⁻¹
Water	998	1.00·10 ⁻³

Due to the very high viscosity of bitumen, great care must be taken in order to obtain reliable viscosity data. This is due to viscous heating during the viscosity measurements. Typical rheological devices used in viscosity measurements are the bob and cup viscometer and the cone and plate viscometer (Figure 4.32). In the case of the bob and cup device, bitumen is placed in the gap between the bob (inner cylinder)

and the cup (outer cylinder), and the inner cylinder is rotated. From the measurement of the torque needed to rotate the cylinder, it is possible to calculate the bitumen viscosity. The cup is usually jacketed, and water is circulated to maintain a constant temperature of the test liquid within the gap.

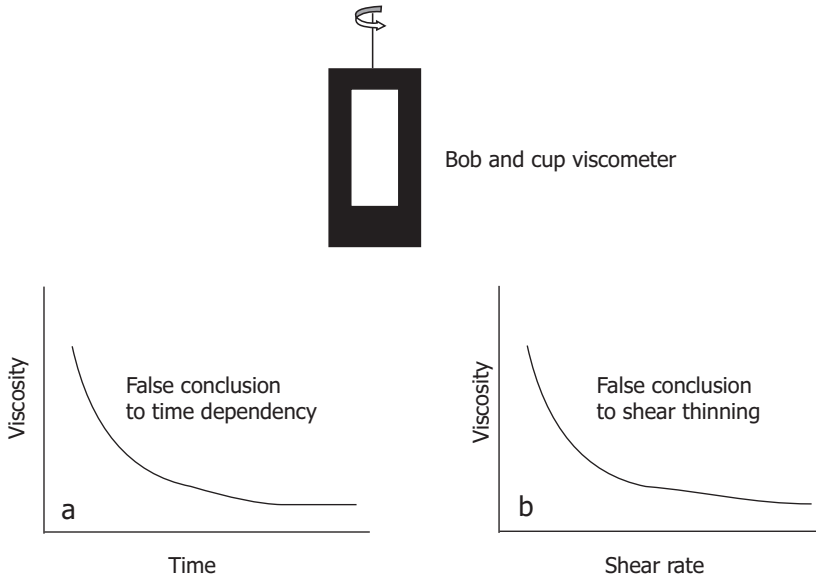


Figure 4.32 False viscosity measurements are easily made for very viscous fluids due to viscous heating effects.

The difficulty is that, due to rotation of the inner cylinder (bob), heat is generated within the bitumen sample due to viscous dissipation. The generated thermal energy is related to $\mu\dot{\gamma}^2$, where μ is the bitumen viscosity and $\dot{\gamma}$ is an average shear rate within the bitumen sample in the gap. Although the outer surface of the cup is within circulating water of a constant temperature, the temperature of the bitumen within the gap is higher than that of the circulating water due to viscous heating. As viscous heating is proportional to $\mu\dot{\gamma}^2$, the bitumen's steady-state temperature depends on the magnitude of the applied rate of shear and on the bitumen viscosity itself. As well, the bitumen steady-state temperature is dependent on the viscometer geometry. As bitumen viscosity is sensitive to temperature, erroneous viscosity data can be generated when careful attention is not paid to bitumen heating while performing viscosity measurements (Sukanek and Laurence 1974).

For example, Figure 4.32 shows the *apparent* bitumen viscosity variation with time and shear rate. In Figure 4.32a, a bitumen sample is sheared. At time zero, the bitumen is at temperature T_i . As the bitumen is sheared at a given shear rate, its temperature rises due to viscous dissipation and it eventually reaches a steady-state value. A plot based on Figure 4.32a would appear to indicate that bitumen viscosity is time-dependent. However, the change of bitumen viscosity with time is simply due to bitumen heating with time, leading to a lower viscosity.

Figure 4.32b shows different *apparent* viscosity behaviour. Here, a bitumen sample is subjected to different levels of shear rate. A corresponding plot would appear to indicate that bitumen is a shear-thinning liquid, as bitumen viscosity decreases with shear rate. However, the decrease in viscosity is simply due to the fact that the bitumen's steady-state temperature due to viscous dissipation increases as the shear rate is increased. Consequently, the curve of Figure 4.32b is a result of a bitumen viscosity being temperature-dependent. If the bitumen under the testing conditions is kept exactly at a constant temperature, there would be no viscosity variation with time or with shear rate.

The dynamic viscosity of bitumen at room temperature (Figure 4.33) is very high compared to that of water. It is similar to the viscosity of refrigerated honey. The viscosity of bitumen is very dependent on the source of the bitumen and on the methods used in separating it from the oil sands ore. Bitumen will hardly flow at room temperature and it is a strong function of temperature. Bitumen from the Cold Lake region is normally considered to be less viscous and to have a higher API gravity value than Athabasca bitumen.

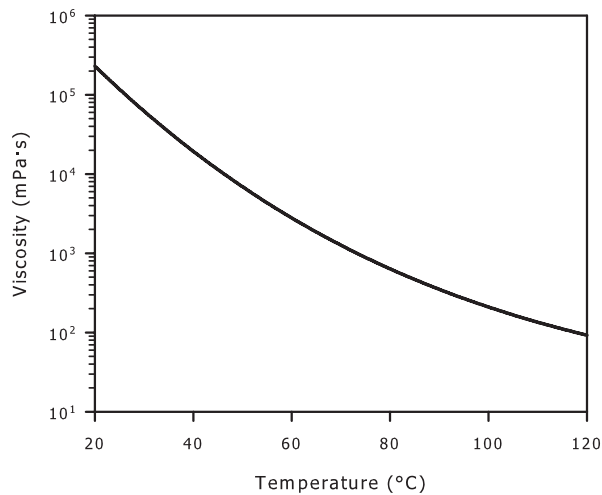


Figure 4.33 Mean viscosity of Athabasca bitumen.

Source: Seyer and Gyte (1989).

Bitumen viscosity varies nearly five orders of magnitude over a temperature range of 20 °C to 200 °C. Hepler and Smith (1994) gave the following generic equation for bitumen viscosity (μ_B):

$$\mu_B = 4 \times 10^{-10} \exp[10100 / T] \quad 300 < T < 375 \text{ K} \quad (4.5)$$

where T is in degrees Kelvin⁴ and μ_B is in mPa·s. The constant 4×10^{-10} can vary from 1×10^{-10} to 7×10^{-10} .

Note that water viscosity also decreases with temperature. This temperature dependence is typical of liquids. For gases, the gas dynamic viscosity increases with temperature.

Athabasca bitumen viscosity data for a temperature range of -10°C to 50°C is shown in Figure 4.34. Figure 4.35 shows Athabasca bitumen viscosities measured from samples taken from different locations. The “standard” viscosity-temperature curve of Figure 4.33 is also included. Clearly, there is no unique viscosity-temperature curve for bitumen, as viscosity is location-dependent.

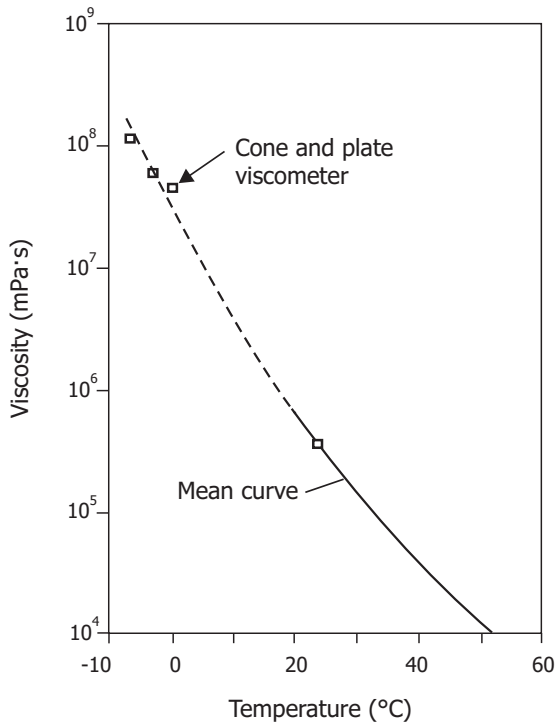


Figure 4.34 Mean viscosity of Athabasca bitumen (cold temperature data, $< 20^\circ\text{C}$).

Source: Seyer and Gyte (1989).

4 Absolute zero is given as -273.15°C . To convert degrees Celsius to Kelvin, add 273.15.

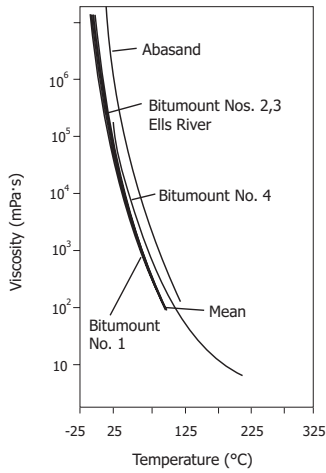


Figure 4.35 Variation of Athabasca bitumen viscosity with location.

Source: Seyer and Gyte (1989).

A comparison between Cold Lake heavy oil viscosity and bitumen is shown in Figure 4.36. The heavy oil viscosity (Esso Cold Lake) is about one order of magnitude less than that of bitumen. Another way of comparing the viscosity of the two hydrocarbons is that it is necessary to heat bitumen by about 40 °C above the temperature required for heavy oil in order to obtain the same viscosity value.

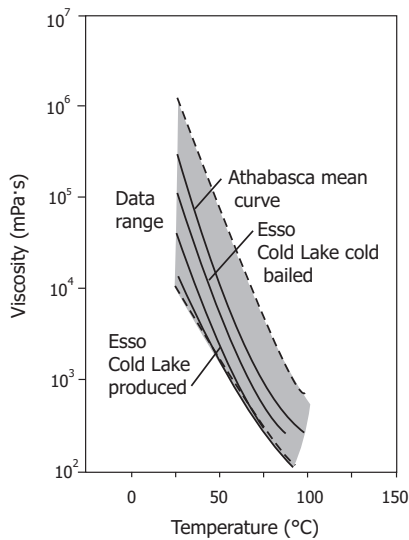


Figure 4.36 Cold Lake and Athabasca comparison.

Source: Seyer and Gyte (1989).

Pumping of cold bitumen in pipes or in open channels is not practical. In the case of closed-pipe flow, a high pressure gradient would be required in order to pump bitumen. For open-channel flow, the channel needs to be quite steep for a meaningful flow to occur.

Let us consider an example of bitumen flow in a pipeline. For laminar flow in circular closed pipes, the pressure gradient is proportional to the viscosity of the flowing liquid, where

$$\text{Pressure gradient} = \frac{8\mu Q}{\pi R^4}$$

for a Reynolds number (Re) less than 2000, where

Re	=	$2RU\rho / \mu$;
Q	=	volumetric flow rate, in m ³ /s;
R	=	inner pipe radius, in m;
U	=	average velocity of liquid, in m/s;
μ	=	liquid viscosity, in Pa·s; and
ρ	=	liquid density, in kg/m ³ ;

for

R	=	0.15 m;
U	=	1.5 m/s;
μ	=	10 Pa·s; and
ρ	=	1000 kg/m ³ .

Using the pumping system characteristics provided, the calculated Reynolds number is 45—well within the laminar flow regime—allowing for the use of the pressure gradient equation above. An excessive pressure gradient of 5.3 kPa/m is required for the pumping operation. From the example, it becomes essential to lower the bitumen viscosity in order to economically and practically transport bitumen in a pipeline.

As an alternative to bitumen heating, reduction in the crude bitumen viscosity can also be achieved with the addition of dissolved gases or solvents to the bitumen. Figure 4.37 shows the viscosity reduction of Athabasca bitumen with the inclusion of CH₄, C₂H₆, CO₂, and toluene. On a weight percent basis, materials with lower molecular weights are the most effective viscosity-reduction agents (Seyer and Gyte, 1989). Bitumen viscosity reduction using various solvents is also shown in Figures 4.38 and 4.39. As indicated by Figure 4.38, benzene and toluene yield nearly the same viscosity reduction at the same weight percentage of solvent added. For the aliphatic solvents, Figure 4.39 shows that a lower-molecular-weight alkane gives a higher viscosity reduction at the same solvent concentration.

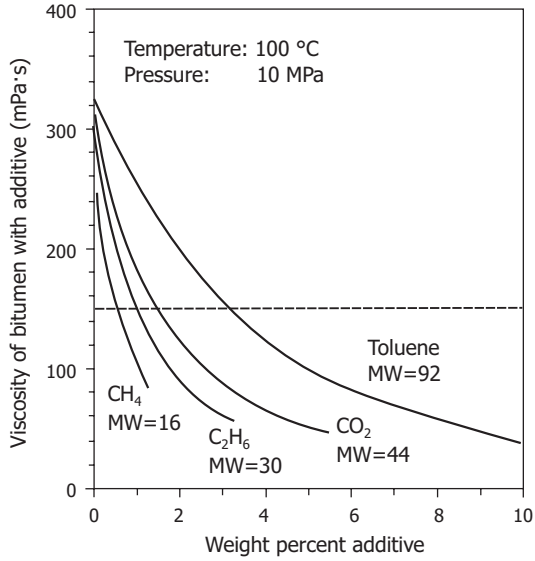


Figure 4.37 Effect of various additives on the viscosity of Athabasca bitumen.

Source: Seyer and Gyte (1989).

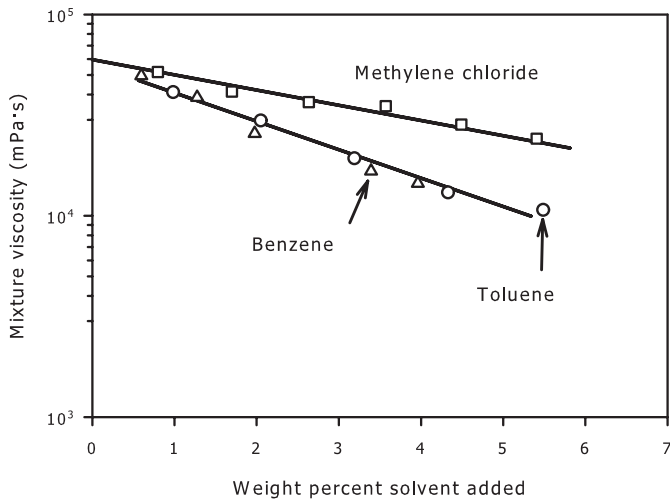


Figure 4.38 Reduction of bitumen viscosity by different solvents at 38 °C for Cold Lake bitumen.

Source: Seyer and Gyte (1989).

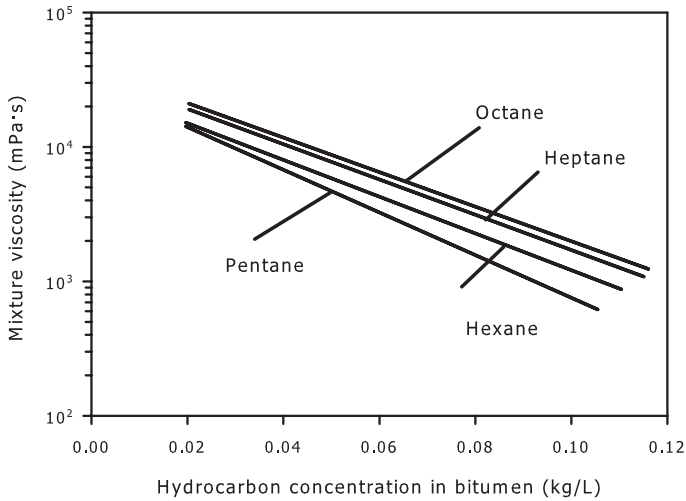


Figure 4.39 Reduction of bitumen viscosity by addition of various alkane solvents at 25 °C for Athabasca bitumen.

Source: Seyer and Gyte (1989).

As naphtha is commercially used as a diluent (solvent) for reducing bitumen froth viscosity, data on the viscosity of bitumen-naphtha mixtures is more readily available. Figure 4.40 gives a comprehensive set of viscosity data for bitumen-naphtha mixtures. As bitumen viscosity is dependent on the origin of the bitumen, the viscosity plot of Figure 4.40 should be used relative to a bitumen-naphtha-free case. Clearly, a mixture with a naphtha-to-bitumen ratio of ~ 0.18 leads to two orders of magnitude reduction in the bitumen viscosity for a temperature of 10 °C. Making use of the pipe flow example above, the flow Reynolds number becomes 4500, whereby the flow in the pipe is in the turbulent regime. With the reduction in bitumen viscosity, the pressure gradient is much lower.

It is of interest to note that at higher temperatures, the effectiveness of solvent addition on bitumen viscosity decreases. An N:B ratio of 0.6 (wt./wt.) is typically used in naphthenic bitumen froth treatment at an operating temperature of ~ 85 °C.

The effect of the addition of naphtha to bitumen froth is shown in Figure 4.41. Once again, we note that the addition of naphtha can reduce bitumen froth viscosity quite dramatically. Presently, naphthenic froth treatment is employed at Suncor, Syncrude, and CNRL to reduce bitumen density and viscosity to enhance solids and water separation from the bitumen froth.

The kinematic viscosities (defined as the ratio of dynamic viscosity to density) for bitumen, as compared to upgraded products, are shown in Figure 4.42. From the plot, we note that bitumen has a much higher kinematic viscosity than upgraded products. The figure also shows parallel temperature dependence when a semi-log plot is used (Seyer and Gyte 1989).

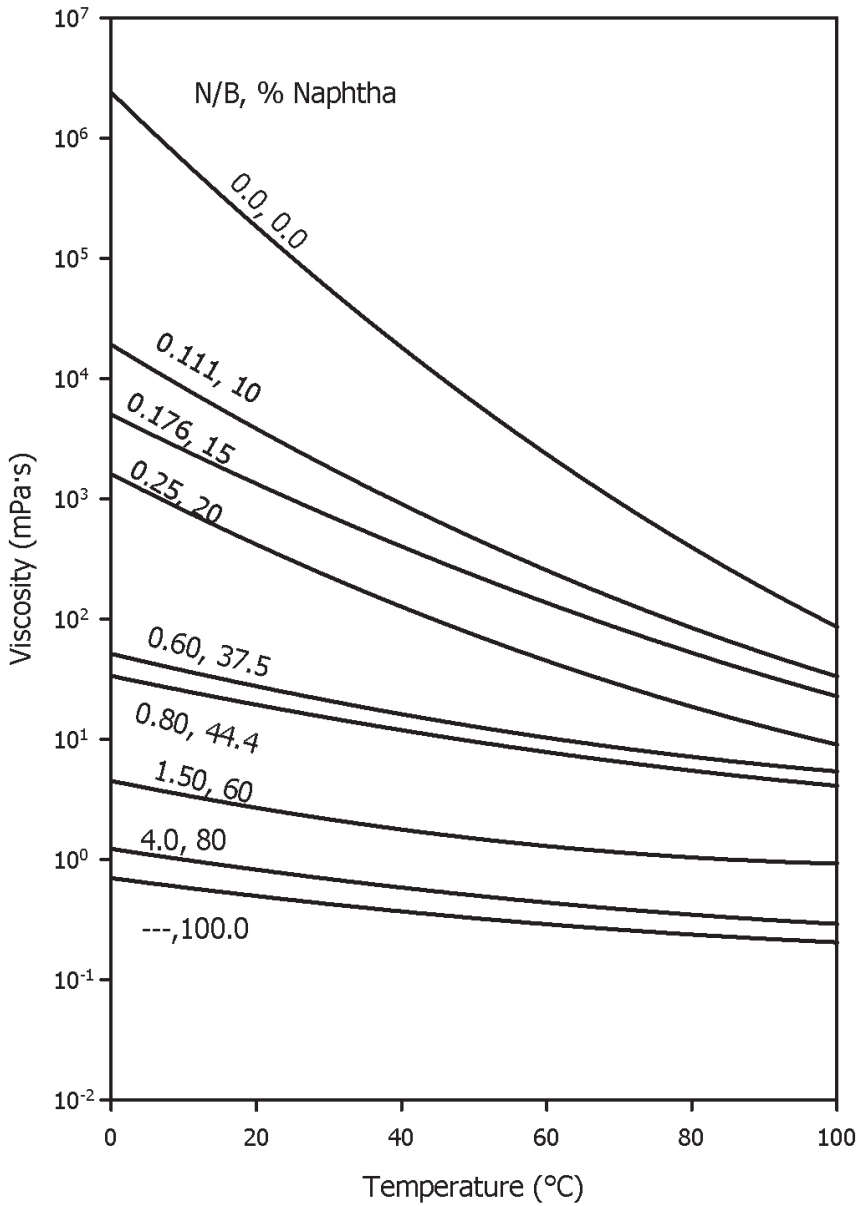


Figure 4.40 Athabasca bitumen viscosity reduction by naphtha on a weight basis.

Source: Seyer and Gyte (1989).

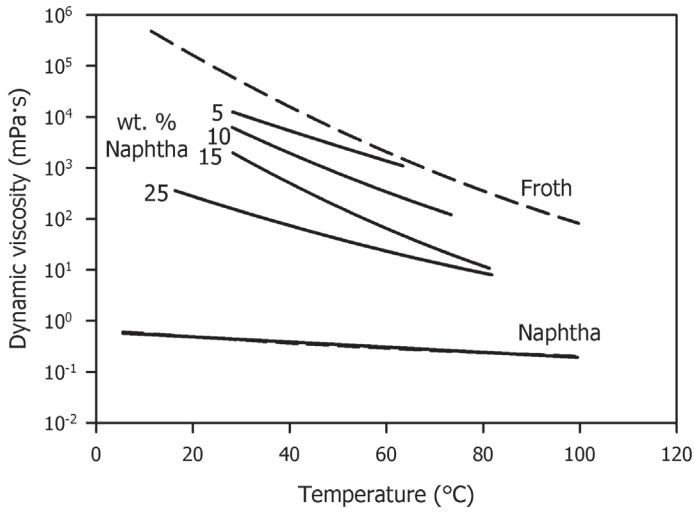


Figure 4.41 Viscosity of bitumen froth samples diluted with naphtha.

Sources: Seyer and Gyte (1989); Schramm and Kwak (1988).

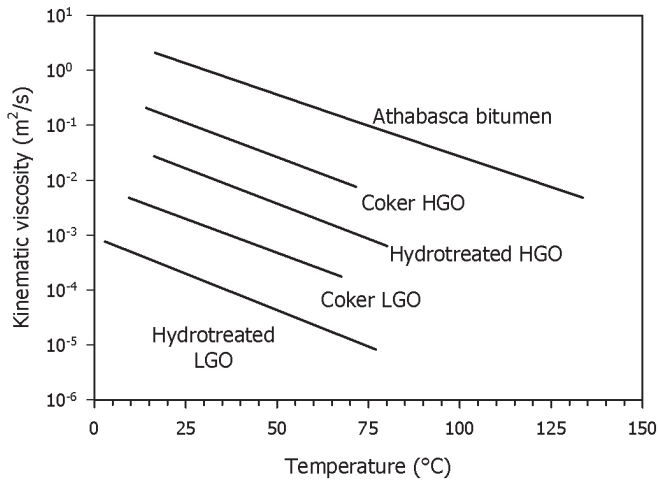


Figure 4.42 Variation of the kinematic viscosity of different upgraded bitumen streams with temperature.

Sources: Seyer and Gyte (1989).

Based on plots relating to viscosity, it becomes clear that bitumen viscosity can be reduced dramatically through heating, solvent addition, and upgrading. Publications

on viscosity prediction for hydrocarbons (and more specifically, for bitumen) are provided by Mehrotra (1991, 1992a, 1992b); Puttagunta, Miadonye, and Singh (1992); and Mehrotra, Monnery, and Svrcek (1996). The correlations provide a means of predicting the viscosity of bitumen diluted with liquid hydrocarbons and/or diluents (solvents) over a wide range of conditions.

4.4 Refractive Index of Bitumen

Refractive index measurements for diluted bitumen and deasphalted bitumen are provided by Buckley (1996, 1999); Buckley et al. (1998), and Taylor, Czarnecki, and Masliyah (2001). Refractive index data for Athabasca bitumen and for heptane deasphalted bitumen from the latter researchers are shown in Figures 4.43 and 4.44, respectively. Due to the opaque nature of the bitumen, data were collected for a bitumen volume fraction of less than 0.5. Extrapolated values were obtained by plotting $(n^2 - 1)/(n^2 + 2)$ versus the bitumen volume fraction. Here, n is the refractive index of the bitumen solution. Refractive index measurements can be used for a quick estimation of the solvent volume fraction in bitumen. The refractive index of bitumen can be taken as 1.58, while that of deasphalted bitumen can be taken as 1.57.

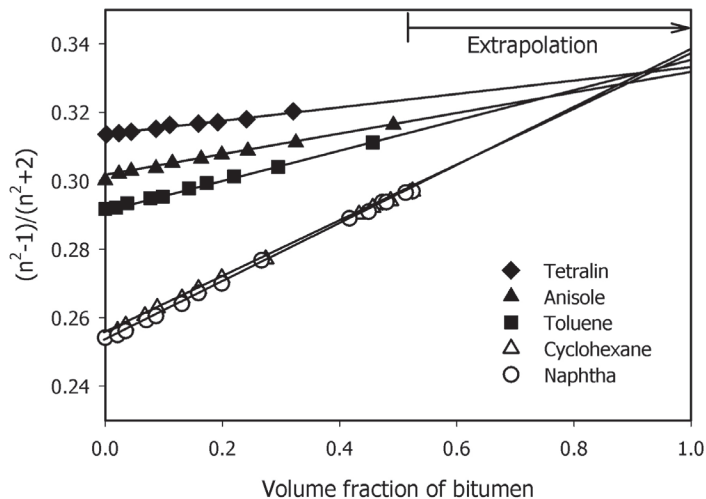


Figure 4.43 Refractive index measurements on mixtures of bitumen with various solvents.

Source: Taylor, Czarnecki, and Masliyah (2001).

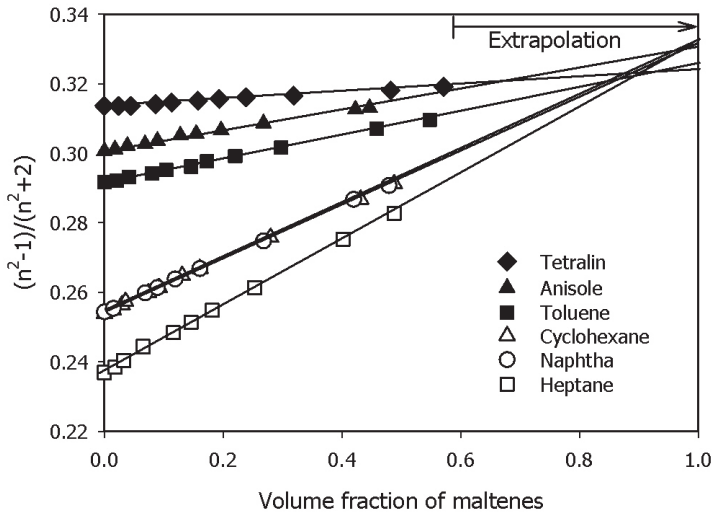


Figure 4.44 Refractive index measurements on mixtures of deasphalted bitumen with various solvents.

Source: Taylor, Czarnecki, and Masliyah (2001).

4.5 Specific Heat

Specific heat is defined as the thermal energy needed to raise the temperature of one kilogram of a material by one degree Celsius at constant pressure. For our purposes, we will assume a condition of constant pressure. The units for specific heat are J/kg °C, and the symbol used is C_p . The specific heat of a material is a function of temperature. Where it is possible, an average value is used in the calculations. Water has a high specific heat compared to sand or bitumen. The specific heat of water is shown in Figure 4.45. It has a minimum value at ~32 °C. However, it is within 1 % of the range of 0 °C to 100 °C. Table 4.9 gives the specific heat values of some materials of interest.

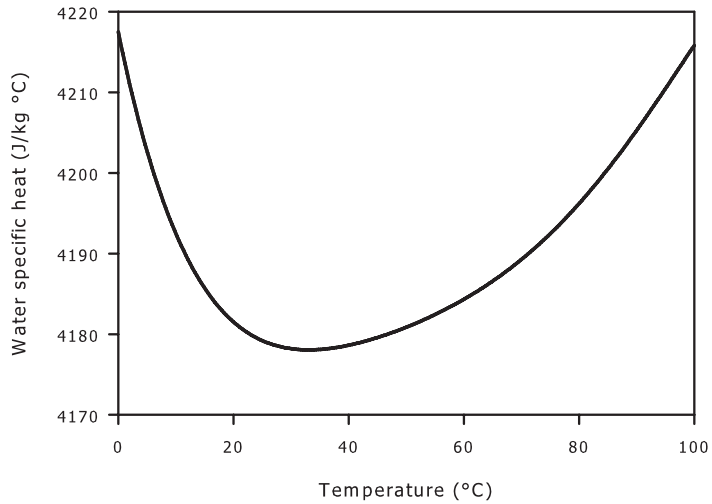


Figure 4.45 Variation of specific heat of water with temperature.

Table 4.9 Specific heat values of some materials of interest

Source: Incropera and DeWitt (1985).

Material	Specific heat at 27 °C(J/kg °C)
Engine oil	1909
Paraffin	2890
Sand	800
Cement mortar	780
Water	4178

The specific heat values of coarse solids from the Athabasca oil sands, mostly SiO_2 and > 325 mesh (or $> 44 \mu\text{m}$), are expressed in $\text{J/kg}\cdot\text{K}$ as follows:

$$C_p = 168 + 2442 \times 10^{-3}T - 1611 \times 10^{-6}T^2 \quad (4.6)$$

or

$$C_p = 914 + 331 \times 10^{-3}T - 2415 \times 10^4 T^{-2} \quad (4.7)$$

for $300 < T < 700 \text{ K}$.

For Athabasca fine solids < 325 mesh (or < 44 μm), the specific heat is given as:

$$C_p = 342 + 1873 \times 10^{-3} T - 926 \times 10^{-6} T^2 \quad (4.8)$$

or

$$C_p = 787 + 644 \times 10^{-3} T - 1559 \times 10^{-4} T^{-2} \quad (4.9)$$

for

$$320 < T < 680 \text{ K.}$$

Specific heats for bitumen and related oil sands constituents are given below for bitumen, asphaltenes, and Syncrude coke (Cassis et al. 1985):

Bitumen:

$$C_p = 55 + 6818 \times 10^{-3} T - 4464 \times 10^{-6} T^2 \quad (4.10)$$

or

$$C_p = 1763 + 1542 \times 10^{-3} T - 4884 \times 10^{-4} T^{-2} \quad (4.11)$$

for

$$300 < T < 600 \text{ K.}$$

Asphaltenes:

$$C_p = -593 + 8079 \times 10^{-3} T - 5353 \times 10^{-6} T^2 \quad (4.12)$$

or

$$C_p = 1444 + 1748 \times 10^{-3} T - 5609 \times 10^{-4} T^{-2} \quad (4.13)$$

for

$$280 < T < 620 \text{ K.}$$

Syncrude coke:

$$C_p = -141 + 3928 \times 10^{-3} T - 2108 \times 10^{-6} T^2 \quad (4.14)$$

or

$$C_p = 778 + 1239 \times 10^{-3} T - 2739 \times 10^{-4} T^{-2} \quad (4.15)$$

for

$$280 < T < 720 \text{ K.}$$

T is in degrees Kelvin (K). The equations expressed in terms of T^2 are generally best suited for extrapolating at lower temperatures, while equations expressed in terms of T^{-2} are generally best suited for extrapolation at higher temperatures (Smith-Magowan, Skauge, and Hepler 1982; Hepler and Smith 1994).

Figure 4.46 gives a plot of the variation of specific heats of different oil sands components with temperature, based on Eqs. (4.6) to (4.15). Typical specific heat values are 1800 J/kg·K for bitumen and 820 J/kg·K for sand (Smith-Magowan, Skauge, and Hepler 1982). The specific heats of some minerals are given in Table 4.10.

In the above equations, the specific heats are provided for a given temperature. The average specific heat between temperatures T_1 and T_2 can be obtained from Eqs. (4.6) to (4.15) through integration, where:

$$[C_p]_{Average} = \frac{1}{T_2 - T_1} \int_{T_1}^{T_2} C_p dT \quad (4.16)$$

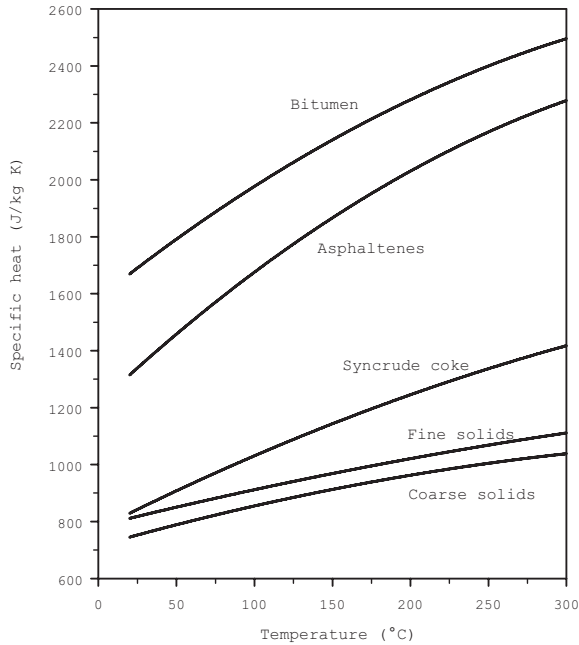


Figure 4.46 Variation of specific heat of different oil sands components with temperature.

Table 4.10 Specific heats of some minerals

Source: Hepler and Smith (1994).

Mineral	Specific heat, C_p (J/kg·K)		
	300 K	400 K	500 K
SiO ₂ (quartz)	743	889	990
CaCO ₃ (calcite)	835	969	1044
CaMgCO ₃ (dolomite)	855	995	1095
MgCO ₃ (magnesite)	904	1074	1185
Kaolinite	962	1151	1270
Illite	808	955	1046
Montmorillonite	811	996	1084

In oil sands processing, the ore is normally mixed with water at a given ratio to produce a slurry of desired density and temperature. Normally, the process requirements dictate the ratio of oil sands to water and the final slurry temperature. For example,

the tumblers formerly used at Suncor and Syncrude required an ore-to-water ratio as high as 1:0.3 by weight (resulting in a slurry density of $\sim 1700 \text{ kg/m}^3$) and a desired slurry temperature of, say, $75 \text{ }^\circ\text{C}$; whereas, in a hydrotransport pipeline operation, the desired ratio is approximately 1:0.6 by weight (producing a slurry density of $\sim 1500 \text{ kg/m}^3$) and the exit slurry temperature is $40 \text{ }^\circ\text{C}$ to $55 \text{ }^\circ\text{C}$. With a ‘back of the envelope’ calculation, it is possible to use the specific heat data to construct a plot showing the water temperature needed to produce an oil sands slurry of a given final (exit) temperature. The thermal energy balance is given below:

$$\int_{T_W}^{T_{exit}} C_{pW} M_W dT + \int_{T_{O/S}}^{T_{exit}} C_{pO/S} M_{O/S} dT = 0 \quad (4.17)$$

To simplify the calculations, temperature-averaged specific heat values are used in the calculations. For constant specific heats, we can write

$$M_W C_{pW} T_W + M_{O/S} C_{pO/S} T_{O/S} = [M_W C_{pW} + M_{O/S} C_{pO/S}] T_{exit}$$

where:

- C_{pW} = Average specific heat of water (J/kg $^\circ\text{C}$);
- $C_{pO/S}$ = Average specific heat of oil sands (J/kg $^\circ\text{C}$);
- M_W = Mass flow rate of water (kg/s);
- $M_{O/S}$ = Mass flow rate of oil sands (kg/s);
- T_W = Water inlet temperature ($^\circ\text{C}$);
- $T_{O/S}$ = Oil sands inlet temperature ($^\circ\text{C}$); and
- T_{exit} = Slurry exit temperature ($^\circ\text{C}$).

Figure 4.47 shows the exit slurry temperature as a function of water temperature and ore-to-water ratio. To produce an oil sands slurry with an ore-to-water ratio of 1:0.3 by weight at $55 \text{ }^\circ\text{C}$, the addition of water at $\sim 100 \text{ }^\circ\text{C}$ is required. Consequently, at this specified ratio, steam is needed to produce a slurry with a temperature higher than $55 \text{ }^\circ\text{C}$. Indeed, a 1:0.3 ratio was formerly employed at Suncor and Syncrude in a tumbler operation, and steam was added to produce an exit tumbler slurry temperature of $70 \text{ }^\circ\text{C}$ to $80 \text{ }^\circ\text{C}$.

For a hydrotransport pipeline operating at a slurry density of 1500 kg/m³ to 1600 kg/m³ and an exit temperature of 55 °C, no steam is required.

It is clear from Figure 4.47 that the process-water temperature required to produce a slurry of a given temperature very much depends on the oil sands ore-to-water ratio and on the final oil sands slurry temperature.

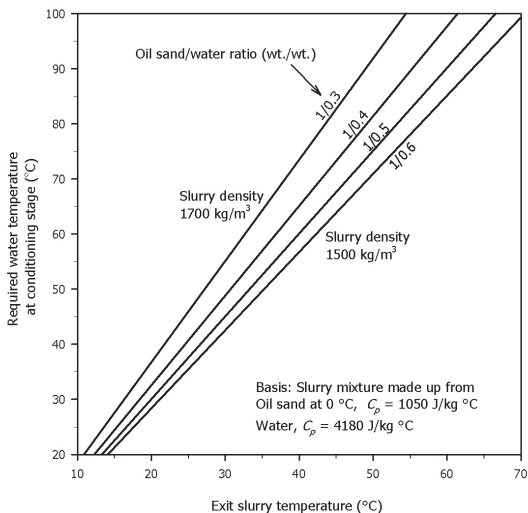


Figure 4.47 Water temperature required to produce given final slurry temperature.

4.6 Heat of Combustion

The *heat of combustion* is defined as the thermal energy obtained by burning one kilogram of fuel under controlled conditions; it is given in units of kJ/kg or J/kg. It can also be referred to as higher heating value (HHV), gross calorific value, or gross energy. The HHV of a fuel is defined as the amount of heat released by a specified mass (initially at 25 °C) once it is combusted and the combustion products, including water, have returned to a temperature of 25 °C. The HHVs for some fuels of interest are given in Table 4.11. The HHV of natural gas varies according to its composition. For Canadian natural gas, it is ~ 38 300 kJ/m³ (1082×10³ kJ/1000 ft³) at standard temperature and pressure.

Heats of combustion for different substances related to Athabasca oil sands are also given in Table 4.11. The heat of combustion is 41 500 kJ/kg for crude bitumen and 45 700 kJ/kg for Syncrude Sweet Blend (SSB). In comparison, methane, which is the main constituent of natural gas, has a heat of combustion value of 55 500 kJ/kg.

Table 4.11 Heats of combustion, higher heating value (HHV)

Source: Hepler and Smith (1994).

Note: Latent heat of vaporization of water is 2256.9 kJ/kg at 100 °C.

Substance	Heat of combustion (exothermic) kJ/kg
Anthracite	33 000–37 000
Bituminous coal	25 000–35 000
Sub-bituminous coal	18 000–28 000
Lignite	13 000–18 000
Charcoal	29 000
Gasoline	46 000–48 000
Kerosene	44 000–48 000
Bitumen from Athabasca	41 500
Syncrude gas oil	44 500
Syncrude synthetic crude	45 700
Syncrude naphtha	44 600–46 400
Syncrude H-oil pitch	38 600
Asphaltenes from Athabasca	36 900
Maltenes from Athabasca	42 200
Syncrude coke	28 900–29 700
Methane, CH ₄	55 500

Clearly, the values of heat of combustion for fossil fuel are quite large. Let us illustrate just *how* large using an example. Let us find the approximate volume of water that can be heated from 10 °C to 70 °C by burning one barrel of SSB at 70 % efficiency. Let us assume that the specific heat of water is 4180 J/kg °C and that one barrel of SSB has a mass of ~ 138 kg (one barrel is equivalent to 0.159 m³). The approximate water mass is given by

$$\text{Mass of water} = \frac{45\,700\,000 \times 138 \times 0.7}{4180 \times (70 - 10)}$$

Thus,

$$\text{Mass of water} = 17\,600 \text{ kg (or } \sim 17\,000 \text{ L of hot water).}$$

If we assume that a person uses 100 litres of hot water (plus additional cold water) per one shower, in this case, the amount of water required for the production of one barrel of Syncrude Sweet Blend would be enough for at least 170 showers, or nearly one year's supply of hot water for bathing! This example demonstrates the very high thermal energy concentration in one barrel of oil.

4.7 Thermal Conductivity

The thermal conductivity of oil sands is an important physical property, as it controls the effectiveness of heating cold oil sands lumps in tumblers, rotary breakers, or hydrotransport pipelines. It ultimately defines the residence time required for an oil sands lump to be heated. Thermal conductivity measurements for oil sands were done by Clark and Pasternak (1932), Clark (1944), and Karim and Hanafi (1981). A large degree of scatter exists in the data. For convenience, the correlation is given as

$$k = 1.415 - 0.0108(T - 0.0033T^2) \quad (4.19)$$

where k is the thermal conductivity of the oil sand (W/m °C) and T is in degrees Celsius.

For a temperature of 45 °C, the thermal conductivity of an average oil sands ore sample, according to Karim and Hanafi (1981), can be taken as 1 W/m °C. However, more recent data, based on the thermal conductivity of twelve different oil sands samples, shows that k values vary widely, depending on the ore type (Mohamad and Masliyah, pers. comm. 2009). No general trends could be found in terms of the ore composition. The margin of error in the measurements that were repeated five times for a given ore sample was fairly small in comparison to the margin of error for ore type. A transient measurement technique was employed. The results are given in Figure 4.48.

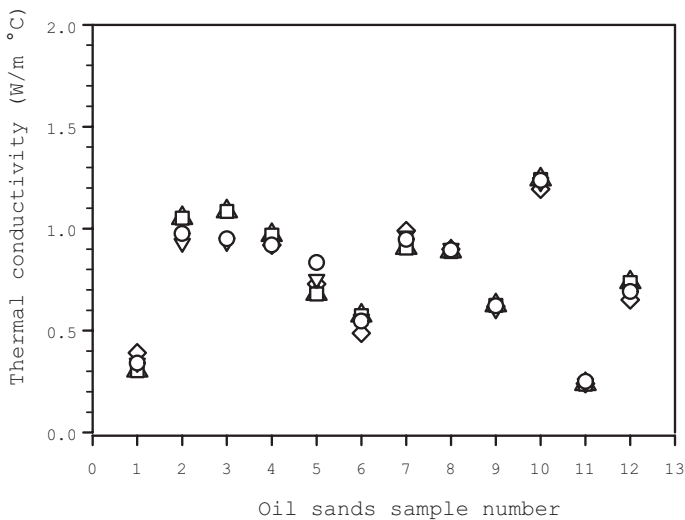


Figure 4.48 Specific heat of twelve different oil sands ore samples at room temperature.

4.8 Chemical Aspects of Bitumen

The composition of bitumen is a consequence of its history—its formation in its source rock, migration to the present-day sedimentary formation, and biodegradation by bacteria on its journey. Bacteria used the light-end, hydrogen-rich components of the petroleum crude as a food source, leaving behind the heavier components (those of a higher molecular weight and boiling point). The degradation process also left behind higher amounts of sulphur, nitrogen, oxygen, vanadium, and nickel elements, which form part of the heavier organic components of the bitumen. The sulphur, nitrogen, and oxygen atoms are referred to as heteroatoms.

Bitumen is a natural mixture of semi-solid and solid hydrocarbons. It is composed mainly of carbon and hydrogen. It also contains sulphur, nitrogen, oxygen, nickel, and vanadium. Isolation of the individual compounds is a frustrating task. Due to the complexity of bitumen, it is nearly impossible to identify all of the species present within it. The chemical and structural identification of some of the major bitumen components can lead to a better understanding of the location of the heteroatoms present in the complex bitumen molecules. This can lead to improvements in processes used for their elimination and in upgrading technologies.

We have limited our discussion of bitumen density to its API gravity. Although petroleum products are classified by this value, other properties are also important in their characterization. Along with API gravity, sulphur content and octane or cetene numbers would, by and large, determine the value and price of the petroleum commodity.

For our purposes, a sour crude has a fairly high sulphur content, in the range of 0.5 wt. % to 2 wt. %. When bitumen undergoes primary treatment in, say, a delayed coker, the product stream is that of a sour product from which the sulphur has not yet been removed. During hydrotreating, a thermal catalytic upgrading process during which hydrogen is added, sulphur and nitrogen are removed, rendering a sour crude oil into a sweet crude oil with a low sulphur and nitrogen content ($S < 0.5$ wt. %). For light crudes, nitrogen is nearly absent.

Gray (2002) showed that the density of Alberta heavy oils and bitumens can be correlated with the elemental composition of the petroleum. The oil density is given by

$$\text{Density} = 1033 - 13.7 H + 13.8 S + 115.7 N; \text{ kg/m}^3$$

Here, H refers to hydrogen, S refers to sulphur, and N refers to nitrogen, and all of the components are in weight percent. Figure 4.49 shows a plot of the above equation.

An interesting observation for this density correlation is that the sign for the hydrogen term is negative. This means that the more hydrogen present, the lower the bitumen density or the higher the API gravity. On the other hand, the presence of both sulphur and nitrogen contributes to a higher density. Removal of these two chemical elements would decrease the bitumen density, leading to a higher API gravity and a higher price.

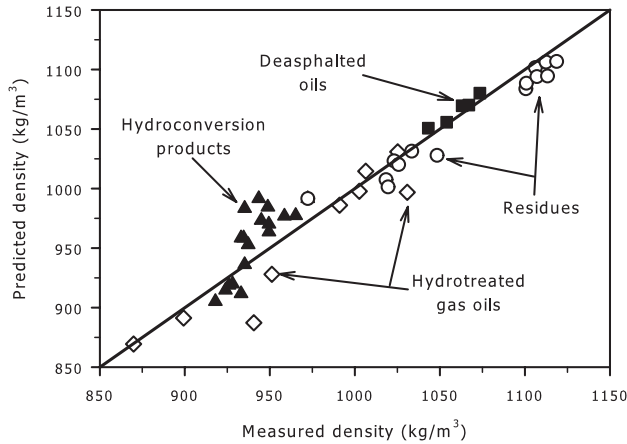


Figure 4.49 Density of oil dependence on various elements.

Source: Gray (2002).

Let us assume that, for typical Athabasca bitumen, $H = 10$, $S = 5$, and $N = 0.4$. The density would then be given as

$$\text{Density} = 1033 - 13.7 \times 10 + 13.8 \times 5 + 115.7 \times 0.4 = 1011 \text{ kg/m}^3$$

4.8.1 Bitumen Characterization

Due to the complexity of bitumen and different end-use requirements, there are several approaches to bitumen chemical characterization. We will deal very briefly with just three of these approaches.

The *elemental composition* approach deals with the different elements that make up the bitumen as a whole or with the composition of some fractionated parts of the bitumen. For example, if we heat bitumen under a vacuum and recover the condensed vapours at different intervals, then we can carry out elemental analysis on each of the collected bitumen fractions. Here, we are mainly interested in the carbon, hydrogen, oxygen, and nitrogen elements that make up the bitumen.

The *solubility and adsorption* class deals with the fractionation of bitumen according to its solubility in solvents and its adsorption on solids. For example, the addition of large quantities of n-heptane to bitumen leads to precipitation. The precipitate is referred to as *asphaltenes*. It is made up of a very large number of different molecules. If one would allow the filtrate to flow through a column filled with silica gel, there would be some adsorption on the silica gel. The elutriate and the adsorbed species will be different in their chemical composition.

Chemical structure studies of bitumen components are very complex and labour-intensive. One must isolate pure compounds prior to structure identification. Both of these processes require strong analytical chemistry skills.

Elemental Composition

The elemental chemical composition of pure compounds is essential for understanding their chemical structures. The value of a hydrocarbon fuel is linked to its atomic hydrogen-to-carbon ratio, or $(\text{H:C})_a$. This is the ratio of the number of hydrogen atoms to the number of carbon atoms in the hydrocarbon molecule. It is an important property of the hydrocarbon. The higher the $(\text{H:C})_a$, the more valuable the petroleum crude. Table 4.12 provides the $(\text{H:C})_a$ for some compounds of interest. Methane has the highest ratio. In petroleum crude, the $(\text{H:C})_a$ can vary considerably. It can be as high as 2.0 to 2.4 for a very light oil crude; between ~ 1.5 and 1.55 for bitumen; and ~ 1.15 for asphaltenes.

Table 4.12 Hydrogen-to-carbon atomic ratio for some hydrocarbons
Source: Strausz and Lown (2003)

Compound	$(\text{H:C})_a$
Methane, CH_4	4
Propane, $\text{CH}_3\text{CH}_2\text{CH}_3$	2.67
Higher paraffins	> 2
Naphthenes	1-2
Aromatics	< 1
Gasoline	1.9–1.95
Bitumen	< 1.55

Pure hydrocarbons are made up of carbon and hydrogen. Knowing the elemental chemical composition of bitumen does not provide the chemical structure of the multitude of different bitumen components, but it can shed some light on the possible hydrocarbon groups in the bitumen. For example, if a hydrocarbon compound has a hydrogen-to-carbon ratio of 3, then this compound cannot be an aromatic, unsaturated hydrocarbon ring, whose hydrogen-to-carbon ratio would be much lower. A bitumen sample with a $(\text{H:C})_a$ of ~ 1.55 would indicate that it must be rich in naphthenes and aromatics, as shown in Table 4.12.

In general, bitumen is composed of five main chemical elements: carbon and hydrogen (which together make up over 93 wt. %); and nitrogen, oxygen, and sulphur (collectively called NOS). These five chemical elements amount to ~ 99.4 wt. % to 99.9 wt. %. There is no free nitrogen, oxygen, or sulphur in bitumen. The remainder (~ 0.1 wt. % to 0.6 wt. %) is made up of metals in the form of organometallics (metals that are an integral part of the hydrocarbon molecule). These

include vanadium and nickel porphyrins, carboxylic salts (e.g., surfactants), submicron silicates and clay particles, clay organics, and heavy metals (Strausz and Lown 2003). The weight percent elemental composition is given in Table 4.13.

Table 4.13 Athabasca bitumen constituents by weight
Source: Strausz and Lown (2003).

Compound	Weight percent
Carbon	83.1±0.5
Hydrogen	10.3±0.3
Nitrogen	0.4±0.1
Oxygen	1.1±0.3
Sulphur	4.6±0.5
Nickel (ppm)	80
Vanadium (ppm)	220

Solubility and Adsorption

‘Solubility class’ is a peculiar classification. It does not relate to molecular structure or composition. It simply relates to a hydrocarbon fraction or a hydrocarbon class that is not soluble in a given solvent. Accordingly, such an insoluble class of hydrocarbon can have a wide range of distribution in terms of chemical structure, composition, and molar mass. At best, it is an ad hoc classification. However, it is widely used in the petroleum industry.

The ‘adsorption class’ is also used in hydrocarbon classification. Here, a mixture of a hydrocarbon in a solvent is allowed to flow in a column filled with ‘absorbing’ solids, such as clays or silica gel. While the flow is taking place, certain species become adsorbed at the absorbent surface. Subsequently, a different solvent is allowed to flow in the column to desorb the already adsorbed chemical species. Using appropriate solvents and absorbing media, it is possible to fractionate the hydrocarbons into aromatics and saturates. Again, the fractionated portions contain a multitude of different chemical species.

The acronym SARA denotes a technique designed to separate the main bitumen fractions into saturates, aromatics, resins, and asphaltenes. It combines selective solvent extraction (precipitation) with sorption on silica gel and clays.

The SARA method, illustrated in Figure 4.50, can be summarized as follows: A large amount of a paraffinic solvent e.g., n-pentane, is added at a solvent-to-bitumen ratio of 40:1 (vol./vol.), leading to the precipitation of the higher molar fraction of bitumen (this precipitate is referred to as asphaltenes). Following solvent removal, the supernatant is referred to as *maltenes* or deasphalted bitumen. The maltenes can be fractionated by column chromatography into resins or oils. The resins are sorbed from the n-pentane solution by silica gel or clay and subsequently elutriated by pyridine. The oils, which are not sorbed (i.e., taken up and held due to adsorption), can be

further separated into aromatics (which are sorbed from the solution in n-pentane by $\text{SiO}_2/\text{Al}_2\text{O}_3$ and elutriated by benzene) or saturates (which are not sorbed and remain dissolved in n-pentane).

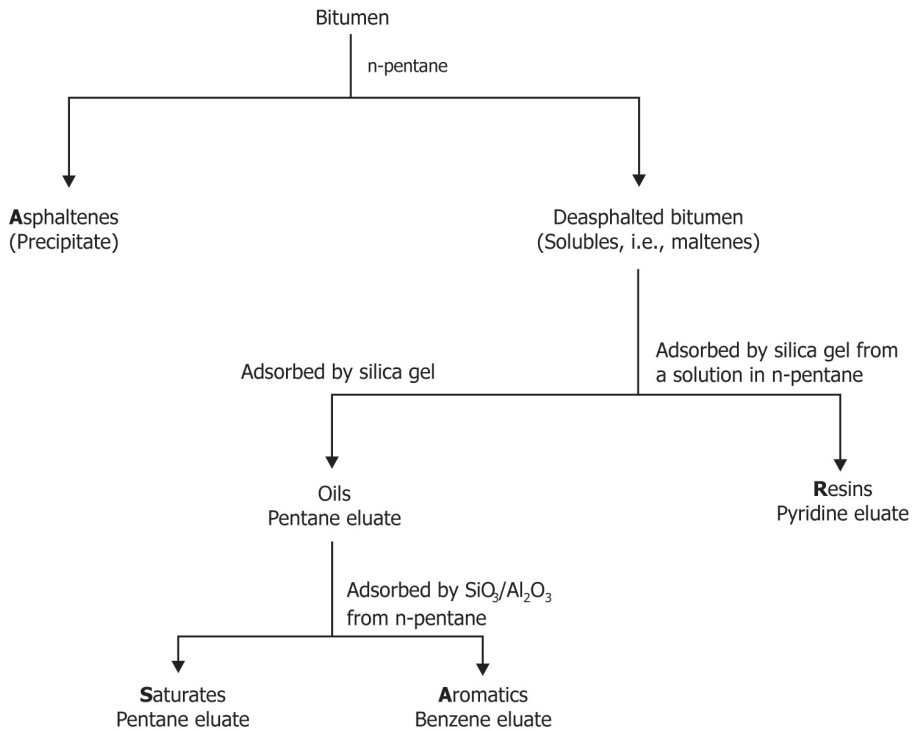


Figure 4.50 SARA (saturates, asphaltenes, resins, and aromatics) fractionation.

Adapted from Berkowitz (1998).

Asphaltenes that are soluble in benzene but insoluble in n-pentane can be further fractionated into soluble carbenes and insoluble carboids by extraction with carbon disulphide (CS_2) (Berkowitz 1998).

There is much variation in SARA analysis, and it is operator-dependent. At times, the total composition percentage does not add up to 100 due to experimental error. Much is dependent on the exact experimental procedure and the type of sorbent being used. In the case of asphaltenes, their composition very much depends on how well the precipitate is washed by the precipitating solvent (Alboudwarej et al. 2003; Zhang et al. 2005).

The saturate fraction contains one- to six-ring hydrocarbons. The different available procedures allow for clean saturates separation, where the levels of aromatics and heteroatom contamination are low. The aromatic fraction contains the heteroatom compounds, mainly sulphur (in the form of cyclic sulphides) and thiophenes. The

resin fraction consists of acidic, basic, amphoteric (exhibiting both acidic and basic properties), and neutral constituents. According to Strausz and Lown (2003), the following ranges, by weight, are suggested:

- Saturates: 15 % to 21 %
- Aromatics: 18 % to 19 %
- Resins: 44 % to 48 %
- Asphaltenes: 14 % to 20 %.

The molar masses of the various bitumen fractions, according to SARA fractionation, are shown in Figure 4.51. The molar masses were measured in toluene using vapour pressure osmometry. Because asphaltenes self-associate (i.e., the asphaltene molecules form aggregates), their molar mass is dependent on their temperature and their concentration in toluene (or whichever solvent is used in the molar mass determination). For that reason, the molar mass values obtained by different investigators can vary widely. The data reported for asphaltenes are at infinite dilution, where it is expected that self-association is minimal. The asphaltenes were precipitated using n-pentane, and are therefore referred to as C₅ asphaltenes. The use of a different paraffinic solvent would result in the formation of a different type of precipitate in terms of composition and molecular weight. As the bitumen fractions of aromatics, resins, and asphaltenes are nearly all polynuclear aromatics, the following correlation, relating the molar mass to mass density, was identified by Alboudwarej et al. (2003):

$$\text{Density} = 670 [\text{Molar mass}]^{0.0639} \text{ kg/m}^3$$

Here, the molar mass is in g/mol.

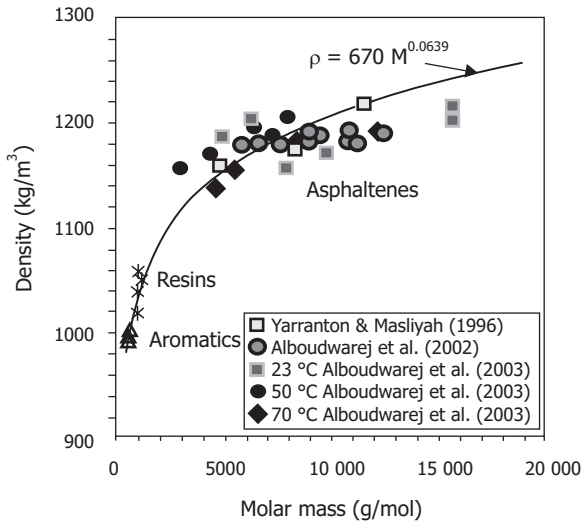


Figure 4.51 Bitumen density variation with molar mass.

Sources: Yarranton and Masliyah (1996); Alboudwarej et al. (2002); Alboudwarej et al. (2003).

The amount of asphaltenes precipitating in an n-alkane, e.g. methane and n-pentane, depends on the carbon number of the n-alkane solvent. As the nature of the precipitate changes with the type of solvent used in the precipitation, the precipitated asphaltenes take on the solvent's name. For example, asphaltenes precipitated with n-heptane are referred to as C₇ asphaltenes.

Figure 4.52 shows that the percent bitumen that would precipitate varies according to the carbon number within the n-alkane series. At high values of solvent-to-bitumen ratio, the weight percent of the precipitate increases with decreasing carbon number (n-heptane to n-pentane). An asymptote in the asphaltene yield occurs at a solvent-to-bitumen mass ratio of ~ 15.

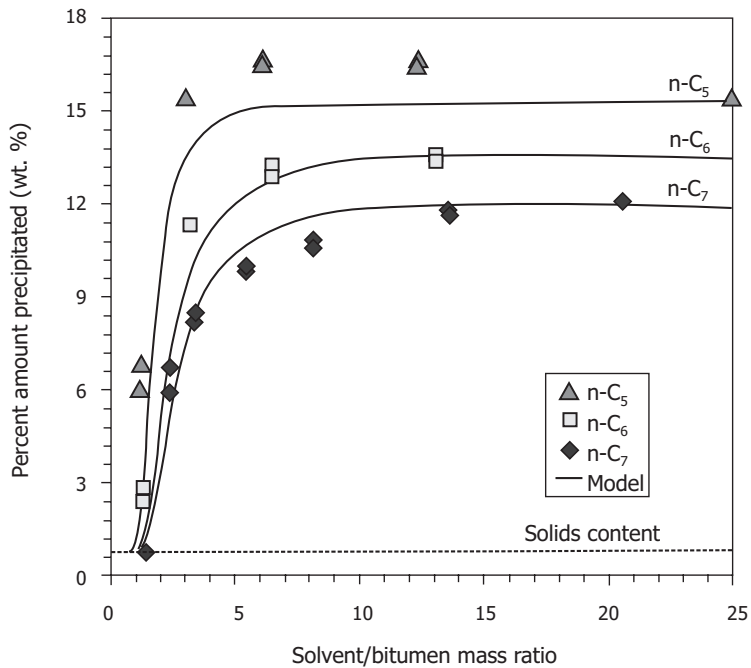


Figure 4.52 Fractional asphaltenes yield from Athabasca bitumen diluted with various n-alkanes.

Source: Alboudwarej et al. (2003).

For a given solvent, there is a critical ratio of solvent to bitumen for the onset of asphaltene precipitation. This critical ratio varies with the solvent used for the precipitation. The onset of precipitation is not easy to observe, and it takes place at a ratio of ~ 1.3 (wt./wt.) for n-heptane. Once precipitation takes place, there is sharp initial increase in the amount of asphaltene precipitation with an increasing ratio of solvent to bitumen. For the case of n-heptane, about half of the total asphaltenes would precipitate at a n-heptane-to-bitumen ratio of 2.5 (Figure 4.52). Since n-alkanes (mixed isomers of alkanes) are used as the solvents of choice in bitumen paraffinic froth treatment and only a fraction of the available asphaltenes is precipitated, good control

of the solvent-to-bitumen ratio is required. Below a temperature of about 100 °C, for a given n-alkane, and at given solvent-to-bitumen ratio, the percent of asphaltenes precipitation decreases with increasing temperature. For example, at a mass ratio of 2.9 of n-heptane to bitumen, 6.6 wt. % is precipitated at 25 °C, as opposed to 4.0 wt. % at 65 °C (Dabros et al. 2004).

We mentioned earlier that n-alkane is a poor solvent for bitumen and above a critical alkane solvent-to-bitumen ratio, asphaltenes begin to precipitate. On the other hand, toluene is a good solvent, and no asphaltenes precipitation takes place at any toluene-to-bitumen ratios. It thus stands to reason that if a mixture of n-heptane and toluene is used for asphaltenes precipitation, asphaltenes precipitation would take place at a critical fraction of n-heptane in the solvent mixture.

Figure 4.53 shows the fraction of the total asphaltenes that would precipitate while increasing the weight fraction of n-heptane in a mixture of n-heptane and toluene. The x-axis can be thought of as being a scale for the aromaticity of the solvent or its asphaltene solvency power. For this case of n-heptane and toluene, the onset of precipitation is at about 0.35 n-heptane volume fraction in the mixture.

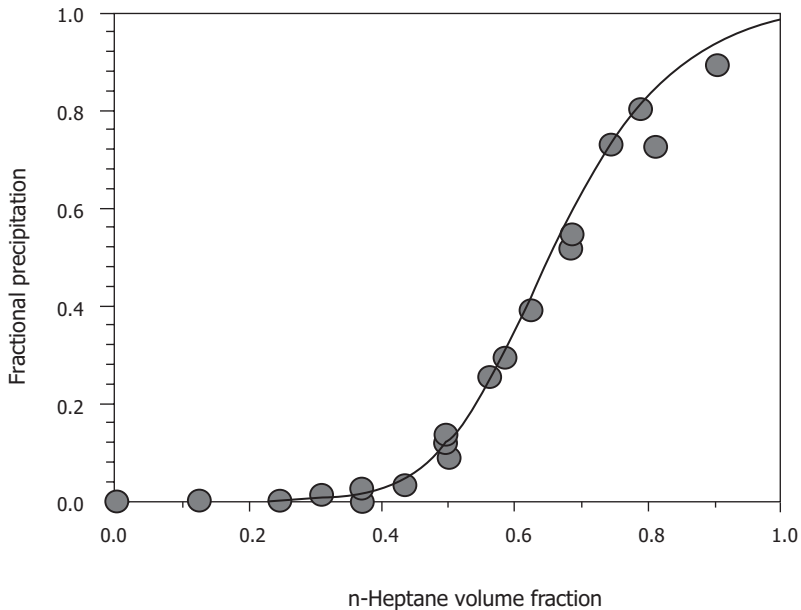


Figure 4.53 Asphaltenes precipitation in solutions of n-heptane and toluene at a high ratio of solvent to bitumen.

Source: Alboudwarej et al. (2003)

Naphtha is used by CNRL, Suncor, and Syncrude in bitumen froth treatment. As naphtha is a distillation cut, its composition varies from one operator to another. Nevertheless, asphaltenes can be precipitated by naphtha at a naphtha-to-bitumen ratio of 4:1 (wt./wt.). Naphtha is roughly equivalent to a n-heptane-to-toluene solvent mixture at 80:20 (vol./vol.) ratio.

Chemical Structure

By and large, bitumen contains a combination of paraffinic, aromatic, and naphthenic groups. The aromatic fractions of bitumen and heavy oils contain a multitude of aromatic compounds, which range from alkylbenzene to large condensed polyaromatic (benzene rings attached to each other) and heteroaromatic (benzene rings with embedded nitrogen, oxygen, or sulphur atoms) together with nickel or vanadium atoms. It should be remembered that the aromatic benzene ring is not saturated, and that double bonds exist between the carbon atoms within an aromatic ring. Chromatography is employed in the identification of the molecular species.

Athabasca bitumen and heavy oil, in general, do not contain a high concentration of non-cyclic (acyclic) saturates. This is simply because bitumen is the residue of a crude oil following microbiological degradation. Indeed, bitumen does not contain any n-alkanes such as n-pentane or n-heptane. Normal alkanes tend to be a favourite food for bacteria. According to Strausz and Lown (2003), once normal alkanes (n-alkanes) are consumed, the branched alkanes are consumed, and there is decreasing preference for degradation with increasing number of branches. As well, simple cyclic saturates can also be degraded through the action of bacteria. Due to microbial degradation within the saturates, only highly branched alkanes and naphthenics are present in bitumen.

Asphaltenes are the precipitate resulting from the addition of large amounts of an n-alkane (paraffinic) solvent. They are made up of a multitude of molecules of different composition and structure. The main structure of the molecule is made up of polyaromatic rings that are attached to aliphatic chains. The molecule also has nitrogen, oxygen, and sulphur heteroatoms that are associated with a chemical group. Asphaltene molecules also contain nickel and vanadium.

There is debate regarding the experimental values of the molar mass of asphaltenes. As asphaltenes self-associate, it is difficult to measure their exact average molar mass and their molar mass distribution. The reported molecular weight of asphaltenes can vary from over 1000 to several thousands Dalton. Asphaltenes are presumed to be the precursors to coke, and they are stabilizing agents for water-in-oil emulsions. The composition of asphaltenes by weight is: C = 80.5 ± 3.5 , H = 8.1 ± 0.4 , N = 1.1 ± 0.3 , O = 2.5 ± 1.2 , and S = 7.9 ± 1.1 (Strausz and Lown 2003).

4.9 Interfacial Properties in Bitumen Recovery

As discussed in previous sections, the physical properties of oil sands components, such as the density and viscosity of bitumen, and the particle size and density of sands grains and fines, play a critical role in bitumen recovery and tailings management. However, the *surface* properties of oil sands components, such as wettability and surface charge, govern almost all aspects of bitumen production from mined oil

sands using water-based extraction processes. For example, the wettability of solids determines how easily bitumen can be separated from sands grains, an essential step for bitumen recovery. As shown in Figure 4.54a, the shape of the bitumen sitting on a sand grain in water determines the level of difficulty of separating the bitumen from the sand grain i.e., bitumen liberation. It is clear that the smaller the contact angle (θ), measured through the aqueous phase, as shown in the right of Figure 4.54a, the more easily the bitumen detaches from the sand grain. On the other hand, in bitumen aeration, i.e., bitumen attachment to air bubbles (Figure 4.54b), a larger contact angle (as in the left of Figure 4.54b) represents a stronger attachment, and hence is more beneficial.

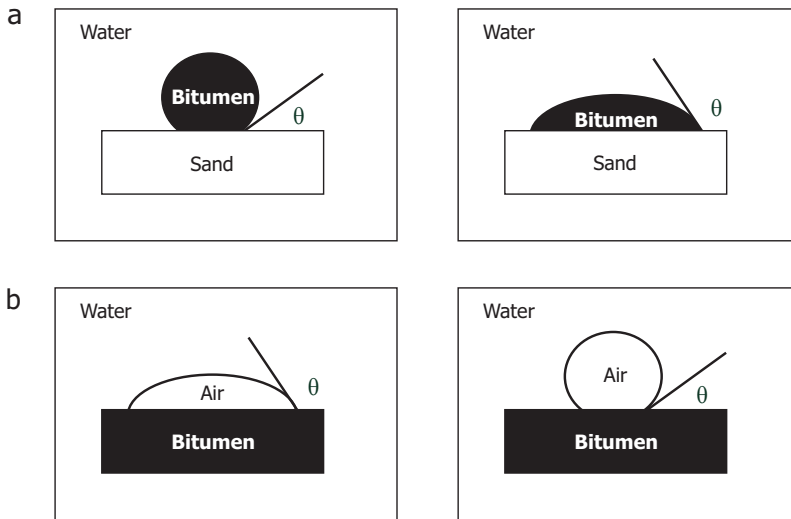


Figure 4.54 The shape of a bitumen droplet on a solid surface (a) and of an air bubble on bitumen (b) in water determines the difficulty of bitumen liberation and aeration, respectively. In (a), bitumen would be more easily liberated from the solid surface in the left plate than in the right plate; in (b), bitumen would much more easily attach to an air bubble in the left plate than in the right plate.

There is an apparent conflict with regard to the value of the contact angle, as liberation calls for low contact angle values, while aeration calls for high contact angle values. It is therefore important to know what determines the contact angle and which parameters in a bitumen extraction system can be manipulated to control the contact angle to maximize the overall benefits of both bitumen liberation and aeration. The value of contact angle reflects the affinity of surfaces (solid or bitumen) to a liquid (water) medium, also referred to as *wettability*. As discussed earlier, a water-wettable solid has an affinity to water, and can be called *hydrophilic*. On the contrary, if a solid repels water from its surface, it is referred to as being *hydrophobic*. The hydrophobicity of solids, often measured by their contact angle values, plays a critical role in water-based oil sands extraction.

The surface charge and wettability of fines determine not only particle aggregation, which is desirable for tailings management, but also the interaction of particles with bitumen, which has a profound effect on bitumen recovery, froth quality, and bitumen froth cleaning. In bitumen aeration, for example, the coating of bitumen by fine clays, known as *slime coating*, can change the surface properties of bitumen to clay-like, as shown in Figure 4.55. When an air bubble approaches a liberated bitumen droplet, as shown in Figure 4.55a, the bubble will attach to the bitumen droplet, provided that the bitumen is hydrophobic, as in Figure 4.54b (left). Together, they will float to the top of the slurry, where the bitumen can be recovered as bitumen froth, resulting in a clean bitumen product. However, when an air bubble approaches a bitumen droplet fully covered by hydrophilic fines, the bubble will not be able to attach to the slime-coated bitumen (Figure 4.55b). As a result, the bitumen droplet will remain in the slurry due to its similar density to the processing fluid (pulp), or drop to tailings due to increased density of the clay-coated bitumen droplet, reducing bitumen recovery. When an air bubble approaches a liberated bitumen droplet that is partially covered by hydrophilic fines (Figure 4.55c) or fully covered by hydrophobic fines (Figure 4.55d), the bubble will be able to attach to the bitumen droplet and lift it to the top of slurry, forming bitumen froth. In this case, the quality of the bitumen froth will be decreased drastically,

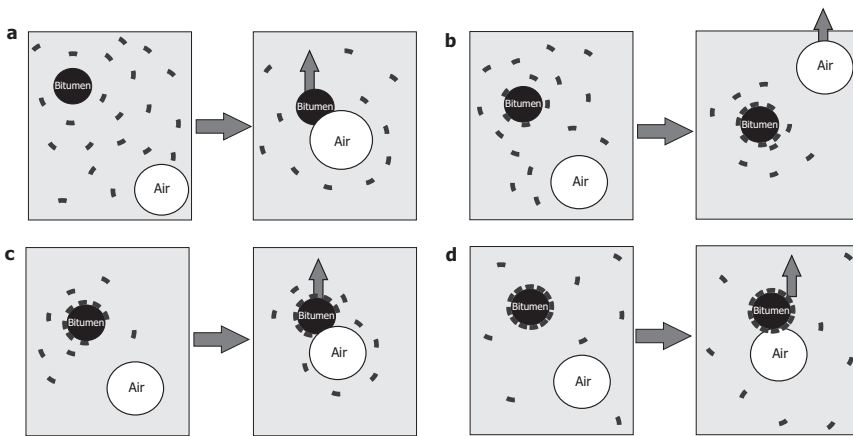


Figure 4.55 Role of fines characteristics and their interaction with bitumen in bitumen aeration, assuming bitumen is hydrophobic: (a) fines are well dispersed and an air bubble easily attaches to a clean liberated bitumen surface for high bitumen recovery and good froth quality; (b) an air bubble is unable to attach to a bitumen droplet fully covered by hydrophilic fines, leading to low bitumen recovery; (c) an air bubble finds and attaches to an uncovered area of a bitumen droplet that is partially covered by hydrophilic fines, a case of both low bitumen recovery and poor froth quality; and (d) an air bubble attaches to a bitumen droplet through the hydrophobic fines fully or partially covering the bitumen, leading to poor froth quality but without sacrificing bitumen recovery.

depending on the degree of slime coating. Clearly, understanding the mechanisms of fine particle attachment to bitumen surfaces is crucial for controlling the slime coating phenomenon.

It is extremely important to note that the wettability and surface charge of oil sands components are highly coupled with the chemistry of the processing water, such as the pH of the slurry and the presence and concentration of organic and inorganic ions. Controlling the surface properties to optimize all aspects of bitumen production (bitumen recovery, bitumen froth cleaning, and tailings management) requires an in-depth understanding of these surface parameters.

4.9.1 Surface Tension

The shape of a bitumen droplet on a sand grain or of an air bubble on a bitumen surface in process water (and hence the contact angle of water) is largely determined by interfacial tension (γ), as given by the well-known Young equation (Eq. [2.5]), where the subscripts represent the appropriate interfaces. To understand the wettability of a surface by a liquid, it is therefore important to know the origin of the surface energy and surface tension. The former is defined as the free energy required to create a unit area of surface (or interface) under the condition of constant temperature, pressure, and chemical composition; the latter as the tension force applied to a unit length of three-phase contact line acting in a direction that would reduce the total surface energy. Surface tension force is illustrated in Figure 4.56 from an atomic or molecular interaction viewpoint. Figure 4.56a shows a two-dimensional array of atoms or molecules, constituting a single-component liquid such as water, exposed to a vapour environment. For the simplicity of illustration, the number of molecules in the vapour above the surface can be considered negligible as compared to the number of liquid molecules in the bulk liquid. Let us take a water molecule *A* in the bulk liquid as a reference. It interacts with all of the other water molecules surrounding it (the direction and strength of the force are represented in the figure by arrows). Clearly, the forces in each direction are balanced by the intermolecular forces from the opposite directions. As a result, the net force on molecule *A* is zero. However, if one examines a molecule *B* sitting at the liquid-vapour interface, there exists a net downward force pulling the molecule into the liquid, as shown by the bold arrow, although the net force in horizontal directions is zero. The net pulling force on the surface molecules towards the bulk liquid phase is due to a lack of molecular forces from the vapour phase. Such a downward force into the liquid signifies the tendency of molecule *B* to move into the bulk liquid. A force manifested as surface tension force retains this molecule at the liquid-vapour interface. On the other hand, work is required to move the molecules from the bulk to the surface by overcoming the pulling force acting on molecule *B* to create new surfaces, where the molecules experience tension.

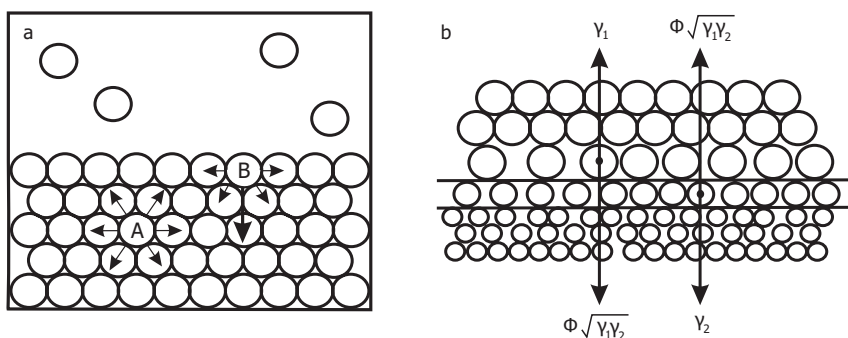


Figure 4.56 Molecular mechanism of (a) surface and (b) interfacial tensions.

Based on the above analysis, it is clear that the stronger the intermolecular forces of a liquid, the higher the liquid's surface tension. This conclusion is remarkably well supported by the surface tension values of common liquids given in Table 4.14. For a paraffinic liquid such as n-hexane, for example, the molecules interact mainly through van der Waals forces, which are relatively weak compared to other specific interactions. As a result, the surface tension of n-hexane appears to be the lowest of the liquids given in Table 4.14. On the other hand, the hydrogen bonding among water molecules contributes significantly to intermolecular forces, leading to a much higher surface tension value of water. It is not surprising that the surface tension values of other organic molecules with various weak molecular forces in addition to van der Waals forces lie in-between the surface tension values of n-hexane (18.4 mN/m) and water (72.8 mN/m). The surface tension of liquid mercury is much greater than that of any other liquid listed in Table 4.14, a result of strong metallic bonds among mercury atoms. Based on this molecular theory of surface tension, the surface tension can be estimated from the density of the liquid and the interaction energy of the molecules in bulk, which is linked with the free energy of liquid evaporation (Butt, Graf, and Kappel 2003).

Table 4.14 Surface tension (γ) and temperature coefficient ($d\gamma/dT$) of common liquids at 20 °C

Sources: Fowkes (1965); van Oss (2006); Hiemenz and Rajagopalan (1997).

Type of liquids	Organic					Water	Mercury
	n-Hexane	Cyclohexane	Methanol	Toluene	Naphtha*		
γ (mN/m)	18.4	25.5	25.5	28.5	21.5–29.4	72.8	484
$d\gamma/dT$ (mN/m·K)	-0.105		-0.086	-0.081		-0.152	-0.220

*Values for naphtha and heavy naphtha, respectively, measured using Du-Noüy ring method (X.H. Feng, pers. comm., 2009).

Example 4.1

The pair molecular interaction energy, $W_{AA}(r)$, defined as the energy required to separate two molecules from a separation distance r to an infinite separation distance, is given for cyclohexane (C_6H_{12}) at 20 °C as -1.69×10^{-20} J, which is estimated from the energy of cyclohexane vaporization by considering an average of six nearest neighbouring molecules (Butt, Graf, and Kappl 2003). The density (ρ) of cyclohexane at 20 °C is 778 kg/m³ and its molar mass (M) is 84.16 g/mole. Calculate the surface tension of liquid cyclohexane.

Solution:

First, let us assign the energy per molecule as E , and the number of the nearest neighbour molecules in the bulk and on the surface as Z_b and Z_s , respectively. Clearly, $Z_b > Z_s$. We can further assume that the distance between the nearest neighbour molecules in the bulk (r_b) and at the surface (r_s) is the same, i.e., $r_b = r_s$. The energy of molecules in the bulk (E_b) and that on the surface (E_s) on a per-molecule basis are given, respectively, by

$$E_b = \frac{Z_b}{2} W_{AA}(r_b)$$

and

$$E_s = \frac{Z_s}{2} W_{AA}(r_s)$$

The energy required to move a molecule from the bulk to the surface is, therefore, given by

$$\Delta\tilde{G} = E_s - E_b = \frac{1}{2} [Z_s W_{AA}(r_s) - Z_b W_{AA}(r_b)]$$

Since $r_b = r_s$ and thus, $W_{AA}(r_b) = W_{AA}(r_s)$, then

$$\Delta\tilde{G} = \frac{W_{AA}(r)}{2} (Z_s - Z_b)$$

Knowing that $Z_b > Z_s$ and that $W_{AA}(r) < 0$, it is evident that $\Delta\tilde{G} > 0$, i.e., energy is required to move the molecules from the bulk to the surface. For a surface of area A with N molecules on the surface, $\Delta G = N\Delta\tilde{G}$, and the surface tension is therefore given by

$$\gamma = \frac{\Delta G}{A} = \frac{N\Delta\tilde{G}}{A} = \frac{W_{AA}(r)}{2(A/N)} (Z_s - Z_b)$$

Here, A/N is the area per molecule (σ), which can be estimated from the density of the liquid by

$$\sigma = \frac{A}{N} = \left[\frac{M}{\rho N_A} \right]^{2/3} = 3.18 \times 10^{-19} \text{ m}^2$$

where N_A is the Avogadro number. If we take a small cube of liquid as a reference and compare, we would have six faces of the cube in the bulk and only five faces of the cube on the surface, which are surrounded by the nearest neighbour molecules. Therefore, we can simply consider Z_b to equal 6 and Z_s to equal 5. Inserting all of the known values, we can calculate the surface energy (tension) as:

$$\gamma = \frac{W_{AA}(r)}{2(A/N)} (Z_s - Z_b) = \frac{-1.69 \times 10^{-20}}{2 \times 3.18 \times 10^{-19}} (5 - 6) = 0.026 \text{ J/m}^2$$

Considering all of the assumptions, this calculated value is considered to be in excellent agreement with the measured value of 25.5 mJ/m² given in Table 4.14. It is evident that the surface tension or the surface energy is directly related to the strength of molecular interactions, given by $W_{AA}(r)$ and the distance (r) between the neighbouring molecules in liquids.

The above molecular mechanism of surface tension also accounts for the observed dependence of liquid surface tension on temperature. As we know, increasing the temperature imparts more kinetic energy to liquid molecules. As a result, the distance between molecules increases, while the strength of intermolecular forces decreases as a result of the increased thermal motion of molecules. Therefore, a reduction of surface tension with increasing temperature, i.e., a negative temperature coefficient of surface tension, is expected. The measured temperature coefficients of a few common liquids are listed in Table 4.14. A negative temperature coefficient of surface tension indicates that less energy is required to move molecules from the bulk liquid to the surface with increasing temperature.

The surface tension of bitumen centrifuged directly from the Athabasca oil sands has been measured at around 32 mJ/m² at 40 °C and 28.2 mJ/m² at 90 °C, with a temperature coefficient of -0.076 mJ/m² K (Potoczny et al. 1984). It is well established that the surface tension of bitumen varies, depending on the method used in isolating the bitumen from the oil sands ore and on the source of the ore. Details on the temperature dependence of the surface tension of bitumen from oil sands ores of various sources and prepared using various methods are given in Isaacs and Morrison (1985) and Hepler and Smith (1994). Overall, the range of surface tension given above falls within the range of typical hydrocarbons, e.g., 24 mN/m and 29 mN/m for liquid cyclohexane and benzene, respectively (Fowkes 1965). This is not unexpected, as bitumen consists mainly of hydrocarbons containing aromatic rings, although it is a mixture of many types of complex molecules, including saturates, aromatics, resins, and asphaltenes (SARA).

4.9.2 Interfacial Tension

Because interfaces (bitumen-water, bitumen-solid, and solid-water) are so often encountered in oil sands processing (bitumen liberation and aeration), it is important to understand interfacial phenomena and their governing principles. It is not difficult to extend the molecular mechanism of the surface tension of liquids (Figure 4.56a) to interfaces (Figure 4.56b), where molecules from a second liquid, such as liquid hydrocarbon (upper phase), exert a pulling force on the immiscible liquid molecules on the surface of the lower phase. This force weakens the overall force that pulls the molecules from the interface into the bulk. The magnitude of this force from the opposite phase is determined by the intermolecular forces across the interface and is conventionally described by the geometric mean of the surface tension of the individual phases in contact, corrected by the phenomenological Good and Girifalco parameter (Φ), as $\Phi\sqrt{\gamma_1\gamma_2}$. The correction is necessary to account for the complex nature of molecular interactions across an interface (van Oss 2006). An equal force in the opposite direction exists from the lower phase towards the molecules on the surface of the upper phase. To simplify the formulation, the interfacial tension, $\gamma_{1/2}$, defined as the tension force on a unit length of interface, can be considered to be the summation of surface tension forces of each phase in contact, i.e.,

$$\gamma_{1/2} = (\gamma_1 - \Phi\sqrt{\gamma_1\gamma_2}) + (\gamma_2 - \Phi\sqrt{\gamma_1\gamma_2}) = \gamma_1 + \gamma_2 - 2\Phi\sqrt{\gamma_1\gamma_2} \quad (4.20)$$

For molecules interacting across the interface by van der Waals forces only, Φ becomes 1, and only the van der Waals components of surface tension (γ^{vdW}) need to be considered, i.e.,

$$\gamma_{1/2} = \gamma_1 + \gamma_2 - 2\sqrt{\gamma_1^{vdW}\gamma_2^{vdW}} \quad (4.21)$$

This simple relation, known as the Fowkes equation, provides an excellent estimate of the interfacial tension of hydrocarbon liquids in contact with water (Fowkes 1965), but caution should be exercised when applying it to other liquids, as will be illustrated in Example 4.2. The Fowkes equation can be extended by considering and formulating other specific interactions. One such formulation is proposed for acid-base interactions, including hydrogen bonding, by van Oss, Chaudhury, and Good (1987) and has been widely used in literature. Readers interested in this subject are referred to a review article by Lee (1996).

Example 4.2

Table 4.15 gives the surface tensions and van der Waals components of n-hexane, toluene, and water, along with the measured interfacial tension values. Calculate the interfacial tension of water in contact with n-hexane and toluene using Fowkes' equation and compare the results with the measured values.

Table 4.15 Surface tensions and van der Waals components of surface tension and interfacial tension of selected liquids
Source: van Oss (2006).

Surface/interfacial tension (mN/m)	n-hexane	Toluene	Water
γ	18.4	28.5	72.8
γ^{vdW}	18.4	28.5	21.8
γ_{12} (measured)	51.1	36.1	0*

**A note to the reader: Why do you think the surface/interfacial tension of water is listed as 0?*

Solutions:

Inserting the numbers given in Table 4.15 into the Fowkes equation (Eq. [4.21]), we obtain

$$\gamma_{12}(\text{water-hexane}) = 72.8 + 18.4 - 2\sqrt{21.8 \times 18.4} = 51.1 \text{ mN/m}$$

and

$$\gamma_{12}(\text{water-toluene}) = 72.8 + 28.5 - 2\sqrt{21.8 \times 28.5} = 51.4 \text{ mN/m}$$

Clearly, the calculated interfacial tension for water-hexane agrees well with the measured value of 51.1 mN/m, indicating that the van der Waals forces are the only forces operating between water molecules and n-heptane across the interface, even though there is strong hydrogen bonding among the water molecules. In contrast, the measured interfacial tension of 36.1 mN/m for water-toluene is much lower than the value calculated using Fowkes' equation. The overestimate of interfacial tension using Fowkes' equation indicates that the interaction between water and toluene is stronger than the van der Waals forces, most likely due to water highly polarizing the conjugated (delocalized) π -electrons of toluene and inducing additional attraction. This observation further confirms the limitation of applying Fowkes' equation to systems where van der Waals forces are the only forces operating across the interface.

Figure 4.57a shows the interfacial tension of bitumen in contact with water, determined using microtensiometry (Moran et al. 2000) and drop-shape recovery methods (Moran 2001), as a function of pH. For comparison, the surface tensions of water alone and water in contact with bitumen as a function of pH are shown in Figure 4.57b. The interfacial tension of bitumen in contact with simulated process water (SPW) and simulated process water doped with divalent cations (DSPW), in this case, 0.3 mM calcium and 0.3 mM magnesium, respectively (Figure 4.57a), is significantly lower than the typical interfacial tension of simple organic liquids

(such as hexadecane and toluene) in contact with water (49 mN/m and 36.1 mN/m, respectively). Although the interfacial tension of bitumen-water is not sensitive to cation addition at the 0.3 mM level, it decreases steadily with increasing solution pH, from 23 mN/m at pH 4 to less than 0.1 mN/m at pH above 12. This is in great contrast to the observed pH-independence of the surface tension of water and the interfacial tension of hexadecane (or other simple hydrocarbon liquids) in contact with water (Wang et al. 2004).

To account for the observed change in the bitumen-water interfacial tension with the pH of the aqueous phase when no change has been made to the surface tension of the water, we assume that the chemistry of the bitumen-water interface must have undergone a change. Bitumen is known to contain various types of surface-active components, collectively known as natural surfactants (described in Section 2.10 of Chapter 2). Surfactants have an amphiphilic nature, exhibiting two distinct characteristics: affinity to water at one end (hydrophilic head) and aversion to water at the other end (hydrophobic or lyophilic tail). Moving an amphiphilic molecule (as opposed to a water or non-amphiphilic organic molecule) from the bulk aqueous or organic phase to the interface would lead to a reduction in the system energy. For example, moving an amphiphilic molecule from the bulk aqueous phase to an oil-water interface in such a way that the organic part of the amphiphilic molecule resides in the organic phase would eliminate unfavourable contact of the organic moiety with water, lowering the energy of the system by $n \times 2.5$ kJ/mole, where n is the number of carbons in the amphiphilic molecule (Fuerstenau 1982). Similarly, transferring an amphiphilic molecule from a bulk organic phase to an oil-water interface in such a way that the hydrophilic head resides in the aqueous phase would lead to a reduction in the system energy by the difference between the hydration energy and the solvation energy of the hydrophilic head group.

When bitumen makes contact with water, the surface-active components migrate from the bulk bitumen to the bitumen-water interface in such a way that their hydrophilic head group moves into the aqueous phase, while their hydrophobic tails remain in the bitumen. Depending on the type of surfactant and the pH of the aqueous phase, the head group can be protonated or deprotonated to carry positive (cationic) or negative (anionic) charges. Charging the surfactant molecules will change their hydrophilic-lyophilic balance (HLB), and thus, their solubility and surface activity. The presence of a surfactant containing a carboxylic acid in bitumen is well documented (Bowman 1967; Schramm 1984; Schramm and Smith 1987). Increasing pH is known to ionize the carboxylic group ($-\text{COOH}$) of surface-active molecules to carboxylate ($-\text{COO}^-$), increasing its HLB number (shown in Table 2.8) and solubility in water. As a result, increasing the aqueous pH facilitates the accumulation of natural surfactant molecules from the bulk bitumen onto the interface and their consequent migration into the aqueous phase. This is confirmed in Figure 4.57b by the sharp reduction of surface tension of water from 72 mN/m to around 63 mN/m after its contact with bitumen at pH 11.5.

The degree of surfactant accumulation at the bitumen-water interface is determined by surfactant concentration in bulk aqueous solutions, which is governed by Gibbs' equation (Eq. [2.15]). A reduction in the surface tension of water after its contact with

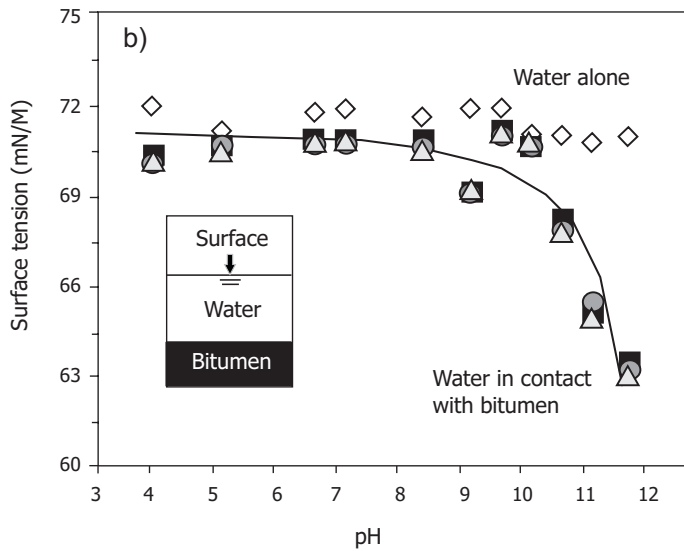
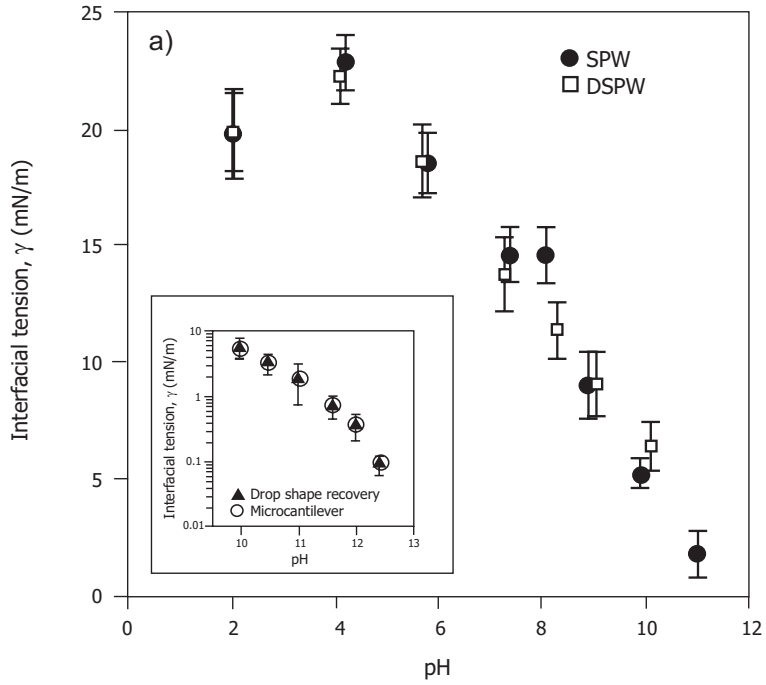


Figure 4.57 Bitumen-water interfacial tension as a function of aqueous pH (a), in comparison with surface tension of water alone and in contact with bitumen (b).

Source: Wang et al. (2010).

bitumen and with increasing aqueous pH, shown in Figure 4.57b, indicates an increase in the concentration of natural surfactant released from bitumen into the aqueous phase, as predicted from applying Gibbs' equation to the surface of the aqueous phase. Such an increase in surfactant concentration in the bulk aqueous phase reflects an accumulation of surfactant at the bitumen-water interface, causing a corresponding decrease in bitumen-water interfacial tension, as seen in Figure 4.57a.

From the viewpoint of oil sands processing, a significant reduction in bitumen-water interfacial tension with increasing aqueous pH would aid in bitumen liberation, as will be discussed later. However, an excessively low bitumen-water interfacial tension indicates the potential for spontaneous bitumen emulsification when the oil sands ores are processed in highly alkaline slurry. The highly charged bitumen emulsion droplets are stable in highly alkaline slurry and are not easily aerated due to their small sizes, leading to low bitumen recovery. The entrainment of alkaline water in bitumen froth also leads to difficulties in bitumen froth cleaning due to the stabilization of highly emulsified, alkaline water droplets in diluted bitumen. Increasing pH will also increase the wettability of bitumen, leading to difficulties in bitumen aeration and hence reducing bitumen recovery, as will be discussed later.

4.9.3 Surfactant Chemistry

Although non-ionic surfactants are less sensitive to solution pH, the characteristics of ionic surfactants (and hence their hydrophilic nature) change with pH. This can affect the interfacial tension and impact bitumen recovery and froth cleaning. It is therefore important to understand the ionization characteristics of surfactants and the effect of water chemistry on interfacial properties. Based on the nature of their ionization, three major types of ionic surfactants are present in bitumen: strong-acid, weak-acid, and weak-base surfactants. Sulphonate ($-\text{SO}_3^-$) and sulphate ($-\text{OSO}_3^-$) are typical polar groups of strong-acid surfactants. When dissolved in aqueous solutions, strong-acid surfactants ionize, and hence carry a negative charge over almost the entire pH range. The carboxylic acid group ($-\text{COOH}$) is a common type of weak-acid surfactant, while various types of amines ($-\text{NH}_2$) are weak-base surfactants. A common feature of weak-acid and weak-base surfactants is their pH-dependent ionization. The pH-dependent protonation of amine-type surfactants makes them positively charged, while the pH-dependent dissociation of carboxylic-acid type surfactants makes them negatively charged. Table 4.16 gives the pertinent equilibrium reactions and corresponding equilibrium constants for dodecyl amine (RNH_2) and stearic acid (RCOOH), where R is $\text{CH}_3(\text{CH}_2)_{11}-$ and $\text{CH}_3(\text{CH}_2)_{16}-$, respectively.

From the equilibrium reactions given in Table 4.16, it is evident that when a surfactant is dissolved in an aqueous solution, it distributes among various species. Added surfactant in solid form contributes little to the desired functions. In most cases, only charged species perform the desired functions of surfactants. To understand the effect of pH on bitumen-water interfacial tension and its role in bitumen liberation and

eration, it is instructive to determine the surfactant species distribution as a function of solution pH. We will use stearic acid to illustrate the principle of constructing a surfactant speciation diagram.

Table 4.16 Equilibrium reactions and corresponding equilibrium constants for dodecyl amine and stearic acid at 25 °C

Reaction no.	Reaction type	Reaction	Equilibrium constant
Dodecyl amine			
(R-1)	Dissolution	$\text{RNH}_2(s) \rightleftharpoons \text{RNH}_2(aq)$	$2 \cdot 10^{-5}$
(R-2)	Protonation	$\text{RNH}_2(aq) + \text{H}_2\text{O} \rightleftharpoons \text{RNH}_3^+ + \text{OH}^-$	$4.3 \cdot 10^{-4}$
Stearic acid			
(R-3)	Dissolution	$\text{RCOOH}(s) \rightleftharpoons \text{RCOOH}(aq)$	$3 \cdot 10^{-7}$
(R-4)	Dissociation	$\text{RCOOH}(aq) \rightleftharpoons \text{RCOO}^- + \text{H}^+$	$1 \cdot 10^{-5}$

Example 4.3

Using the equilibrium constants provided in Table 4.16 for an aqueous solution containing 1×10^{-4} mole/L stearic acid, determine the critical precipitation pH above which the added stearic acid is completely soluble and the pH at which the concentration of soluble stearic acid equals that of the ionized stearic acid. Construct a speciation diagram for a pH range of 2 to 10.

Solutions

The total amount of stearic acid ($[\text{RCOOH}]_T = 1 \times 10^{-4}$ mole/L) placed in water distributes among $\text{RCOOH}(s)$, $\text{RCOOH}(aq)$, and RCOO^- . From the definition of critical precipitation pH (pH_{cp}), we know that the concentrations of $\text{RCOOH}(s)$ and $\text{RCOOH}(aq)$ are nil and 3×10^{-7} mole/L, respectively, at the pH_{cp} . Considering the materials balance at critical precipitation pH, we have:

$$[\text{RCOOH}]_T = [\text{RCOOH}(aq)] + [\text{RCOO}^-] \quad (4.22)$$

Inserting the known values for $[\text{RCOOH}]_T$ and $[\text{RCOOH}(aq)]$ into Eq. (4.22) and rearranging leads to:

$$[\text{RCOO}^-] = 1 \times 10^{-4} - 3 \times 10^{-7} = 9.97 \times 10^{-5} \text{ mole/L} \quad (4.23)$$

Applying the mass action law to (R-4) in Table 4.16 leads to:

$$K_4 = \frac{[\text{RCOO}^-][\text{H}^+]}{[\text{RCOOH}(\text{aq})]} \quad (4.24)$$

Inserting the known values of K_4 , $[\text{RCOO}^-]$, and $[\text{RCOOH}(\text{aq})]$ into Eq. (4.24) and rearranging leads to:

$$[\text{H}^+]_{\text{cp}} = \frac{K_4[\text{RCOOH}(\text{aq})]}{[\text{RCOO}^-]} = \frac{1 \times 10^{-5} \times 3 \times 10^{-7}}{9.97 \times 10^{-5}} = 3.009 \times 10^{-8} \text{ mole/L}$$

Therefore, $\text{pH}_{\text{cp}} = -\log[\text{H}^+] = -\log 3.009 \times 10^{-8} = 7.52$

When $[\text{RCOOH}(\text{aq})] = [\text{RCOO}^-]$, Eq. (4.24) gives $[\text{H}^+] = K_4$, i.e., $\text{pH} = \text{p}K_4 = 5$.

It is important to note that below the critical precipitation pH, the system is in equilibrium with solid stearic acids, $\text{RCOOH}(\text{s})$, such that $\text{RCOOH}(\text{aq})$ is constant at 3×10^{-7} mole/L, the solubility limit of stearic acid (C_s). From Eq. (4.24), we can then readily calculate the concentration of ionized stearic acid as a function of pH using

$$[\text{RCOO}^-] = \frac{K_4[\text{RCOOH}(\text{aq})]}{[\text{H}^+]} \quad (4.25)$$

where $[\text{RCOOH}(\text{aq})] = C_s$. In logarithm form, Eq. (4.25) becomes

$$\begin{aligned} \log[\text{RCOO}^-] &= \log C_s - \text{p}K_4 + \text{pH} \\ &= \log(3 \times 10^{-7}) + \log(1 \times 10^{-5}) + \text{pH} = -11.52 + \text{pH} \end{aligned} \quad (4.26)$$

The concentration of solids is then given by

$$[\text{RCOOH}(\text{s})] = [\text{RCOOH}]_{\text{T}} - [\text{RCOO}^-] - C_s \quad (4.27)$$

Above the critical precipitation pH, on the other hand, $[\text{RCOOH}(\text{s})] = 0$. In this case, Eq. (4.22) is valid. Rearranging Eq. (4.25) to replace $[\text{RCOOH}(\text{aq})]$ in Eq. (4.22) leads to

$$[\text{RCOOH}]_{\text{T}} = \frac{[\text{RCOO}^-][\text{H}^+]}{K_4} + [\text{RCOO}^-] = [\text{RCOO}^-] \left(\frac{[\text{H}^+]}{K_4} + 1 \right) \quad (4.28)$$

We can then obtain:

$$[\text{RCOO}^-] = \frac{[\text{RCOOH}]_T}{\left(\frac{[\text{H}^+]}{K_4} + 1\right)} = \frac{[\text{RCOOH}]_T K_4}{[\text{H}^+] + K_4} \quad (4.29)$$

and

$$\begin{aligned} [\text{RCOOH}(\text{aq})] &= [\text{RCOOH}]_T - [\text{RCOO}^-] \\ &= [\text{RCOOH}]_T \left(1 - \frac{K_4}{([\text{H}^+] + K_4)}\right) \end{aligned} \quad (4.30)$$

At pH below $\text{pH}_{\text{cp}} = 7.52$, Eqs. (4.26) and (4.27), along with $[\text{RCOOH}(\text{aq})] = C_s$, can be plotted as a function of pH, while at pH above pH_{cp} , Eqs. (4.29) and (4.30) can be plotted to complete the stearic acid speciation diagram, as shown in Figure 4.58.

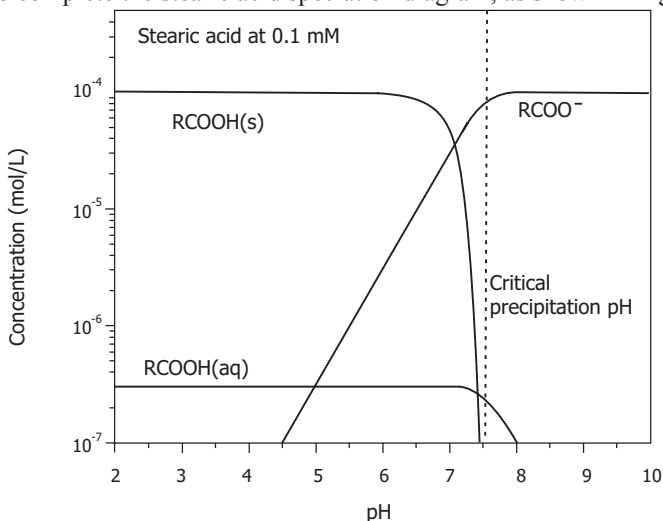


Figure 4.58 Speciation diagram of 0.1 mM stearic acid in an aqueous solution.

The speciation diagram of stearic acid in Figure 4.58 shows that the ionized species become dominant only when the pH is above pK_a (or more precisely, above critical precipitation). The ionic form is more soluble in water and, due to its high HLB value,⁵ becomes more surface-active than the undissociated acid. This supports the measured reduction in bitumen-water interfacial tension with increasing aqueous pH seen in Figure 4.57a. The dominant species of stearic acid at a pH value that is above its critical precipitation pH carries a negative charge. Its adsorption at the bitumen-water interface would impart hydrophilic characteristics to bitumen, enhancing bitumen liberation but hindering bitumen aeration, as will be discussed later.

5 See HLB group number of $-\text{COOH}$ and $-\text{COONa}$ in Table 2.8 of Chapter 2.

The results in Figure 4.58 also suggest that adding more surfactant into a system below the surfactant's critical precipitation pH has no benefit, as the additional surfactant exists mainly in solid form of little surface activity. For a weak-acid surfactant to be effective, the process must operate at pH levels above the surfactant's critical precipitation pH. A similar analysis applies to cationic surfactants such as amines.

Although it is instructive to understand surfactant chemistry, oil sands processing is a far more complex system than discussed here. It contains many other types of surfactant and inorganic ions, such as calcium and magnesium ions. Calcium ions are known to react with stearic acid to form calcium salts of extremely low solubility. The calcium salt of stearic acid in water undergoes various equilibrium reactions, which are affected by the presence of carbonate or bicarbonate (Table 4.17). Example 4.4 illustrates the role of water chemistry on free surfactant concentration of desired surface activity.

Table 4.17 Equilibrium reactions and corresponding equilibrium constants of bicarbonate in the presence of calcium and stearic acid, where calcium hydrolysis is not considered

Reaction number	Equilibrium reaction	Equilibrium constant
(R-5)	$\text{Ca}(\text{RCOO}^-)(\text{s}) \rightleftharpoons \text{Ca}^{2+} + 2\text{RCOO}^-$	$K_{\text{sp}(\text{R-5})} = [\text{Ca}^{2+}][2\text{RCOO}^-] = 10^{-15.8}$
(R-6)	$\text{CaCO}_3(\text{s}) \rightleftharpoons \text{Ca}^{2+} + \text{CO}_3^{2-}$	$K_{\text{sp}(\text{R-6})} = [\text{Ca}^{2+}][\text{CO}_3^{2-}] = 10^{-8.47}$
(R-7)	$\text{H}_2\text{CO}_3(\text{aq}) \rightleftharpoons \text{H}^+ + \text{HCO}_3^-$	$K_{(\text{R-7})} = \frac{[\text{H}^+][\text{HCO}_3^-]}{[\text{H}_2\text{CO}_3(\text{aq})]} = 10^{-6.35}$
(R-8)	$\text{HCO}_3^- \rightleftharpoons \text{H}^+ + \text{CO}_3^{2-}$	$K_{(\text{R-8})} = \frac{[\text{H}^+][\text{CO}_3^{2-}]}{[\text{HCO}_3^-]} = 10^{-10.33}$

Example 4.4

To illustrate the impact of water chemistry on free surfactant concentration, let us look at process water containing 0.1 mM stearic acid and 40 ppm (1 mM) calcium ions with and without 1000 ppm carbonate (CO_3^{2-}) in a closed system at pH 8.5. The calcium hydrolysis to form CaOH^+ and precipitation of $\text{Ca}(\text{OH})_2(\text{s})$ can be considered negligible at this pH.

Solutions:

Case A: Without Bicarbonate

From Figure 4.58, we see that pH 8.5 is well above the critical precipitation pH of stearic acid, and hence, stearic acid is mainly in the ionic form, with a negligible amount in the acidic form. Therefore, both $\text{RCOOH}(\text{aq})$ and $\text{RCOOH}(\text{s})$ are essentially zero, and the stearic acid balance can be written as

$$[\text{RCOOH}]_T = [\text{RCOO}^-] + 2[\text{Ca}(\text{RCOO}^-)_2(\text{s})] \quad (4.31)$$

where RCOO^- is given from the solubility equilibrium of (R-5) by

$$[\text{RCOO}^-] = \sqrt{\frac{K_{\text{sp(R-5)}}}{[\text{Ca}^{2+}]}} \quad (4.32)$$

Since CaOH^+ and $\text{Ca}(\text{OH})_2(\text{s})$ are not considered at this pH, the calcium will be mainly in the form of Ca^{2+} or $\text{Ca}(\text{RCOO}^-)_2(\text{s})$ in the absence of carbonate and bicarbonate. The calcium balance is therefore given by:

$$[\text{Ca}]_T = [\text{Ca}^{2+}] + [\text{Ca}(\text{RCOO}^-)_2(\text{s})] \quad (4.33)$$

Rearranging Eq. (4.33) leads to

$$[\text{Ca}^{2+}] = [\text{Ca}]_T - [\text{Ca}(\text{RCOO}^-)_2(\text{s})] \quad (4.34)$$

Inserting Eq. (4.34) into Eq. (4.32) and the resultant equation into Eq. (4.31) leads to

$$[\text{RCOOH}]_T = \sqrt{\frac{K_{\text{sp(R-5)}}}{[\text{Ca}]_T - [\text{Ca}(\text{RCOO}^-)_2(\text{s})]}} + 2[\text{Ca}(\text{RCOO}^-)_2(\text{s})] \quad (4.35)$$

Since $[\text{RCOOH}]_T = 10^{-4}$ M and $[\text{Ca}]_T = 10^{-3}$ M, while $K_{\text{sp(R-5)}} = 10^{-15.8}$, as given, the only unknown in Eq. (4.35) is $[\text{Ca}(\text{RCOO}^-)_2(\text{s})]$, which is solved numerically (using the “Solver” tool in Microsoft Office Excel, for example) to be 4.98×10^{-5} mole/L. With this value, RCOO^- in Eq. (4.31) is calculated to be 4×10^{-7} mole/L. Clearly, almost all the added stearic acid molecules are in the form of solid calcium salt, with very little left to be effective. The precipitation of calcium salt of stearic acid reduces the calcium ion concentration from 1 mM to 0.5 mM, representing a 50 % reduction.

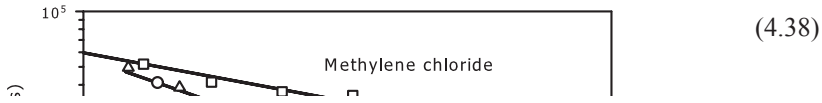
Case B: With 1000 ppm (0.016 M) Carbonates (CO_3^{2-})

Material balances can be set for $[\text{CO}_3^{2-}]_T$, $[\text{Ca}^{2+}]_T$, and $[\text{RCOOH}]_T$ (Eq. (4.36), Eq. (4.37) and Eq. (4.31), respectively):

$$[\text{CO}_3^{2-}]_T = [\text{CO}_3^{2-}] + [\text{HCO}_3^-] + [\text{H}_2\text{CO}_3(\text{aq})] + [\text{CaCO}_3(\text{s})] \quad (4.36)$$

$$[\text{Ca}]_T = [\text{Ca}^{2+}] + [\text{CaCO}_3(\text{s})] + [\text{Ca}(\text{RCOO}^-)_2(\text{s})] \quad (4.37)$$

Inserting Eq. (4.31) into Eq. (4.32) and rearranging leads to



From (R-6), we have

$$[\text{Ca}^{2+}] = \frac{K_{\text{sp(R-6)}}}{[\text{CO}_3^{2-}]} \quad (4.38)$$

Inserting Eq. (4.39) into Eq. (4.38) and then Eq. (4.37) and rearranging the resulting equation leads to

$$[\text{CaCO}_3(\text{s})] = [\text{Ca}]_{\text{T}} - \frac{K_{\text{sp(R-6)}}}{[\text{CO}_3^{2-}]} - \frac{1}{2} \left([\text{RCOOH}]_{\text{T}} - \left(\frac{K_{\text{sp(R-5)}}}{K_{\text{sp(R-6)}}} [\text{CO}_3^{2-}] \right)^{\frac{1}{2}} \right) \quad (4.40)$$

In Eq. (4.36), the component concentration of $[\text{HCO}_3^-]$ and $[\text{H}_2\text{CO}_3(\text{aq})]$ can be expressed in terms of the soluble carbonate concentration, $[\text{CO}_3^{2-}]$, and the equilibrium constants of reactions (R-7) and (R-8), which leads to

$$[\text{CO}_3^{2-}]_{\text{T}} = [\text{CO}_3^{2-}] \left(1 + \frac{[\text{H}^+]}{K_{\text{(R-8)}}} + \frac{[\text{H}^+]^2}{K_{\text{(R-7)}}K_{\text{(R-8)}}} \right) + [\text{Ca}]_{\text{T}} - \frac{K_{\text{sp(R-6)}}}{[\text{CO}_3^{2-}]} - \frac{1}{2} \left([\text{RCOOH}]_{\text{T}} - \left(\frac{K_{\text{sp(R-5)}}}{K_{\text{sp(R-6)}}} [\text{CO}_3^{2-}] \right)^{\frac{1}{2}} \right) \quad (4.41)$$

For a given pH (8.5) and total concentrations of calcium (1 mM), carbonate (16 mM), and stearic acid (0.1 mM) with all of the known equilibrium constants in Table 4.17, Eq. (4.41) can be solved numerically to obtain the soluble carbonate concentration, which can then be used to calculate the concentration of soluble calcium, and hence, the surfactant concentration. The species concentration is given in Table 4.18.

Table 4.16 Species distribution of 0.0001 M stearic acids in 0.001 M calcium and 0.016 M carbonate solutions at pH 8.5 and 10

Species	CO_3^{2-}	HCO_3^-	$\text{H}_2\text{CO}_3(\text{aq})$	Ca^{2+}	$\text{CaCO}_3(\text{aq})$	RCOO^-	$\text{Ca}(\text{RCOO})_2(\text{s})$
Concentration (milimole/L)							
pH = 8.5	0.218	14.74	0.104	$15.5 \cdot 10^{-3}$	0.936	$3.19 \cdot 10^{-6}$	$48.4 \cdot 10^{-3}$
pH = 10.5	8.97	6.07	$0.43 \cdot 10^{-3}$	$0.38 \cdot 10^{-3}$	0.960	$20.5 \cdot 10^{-6}$	$39.8 \cdot 10^{-3}$

In the above example, it is interesting to note that without carbonate (or bicarbonate) in the system, almost all of the stearic acid is in the form of precipitates as $\text{Ca}(\text{RCOO}^-)_2(\text{s})$, and a very small fraction, less than 0.4 %, is in soluble ionized form. As a result, very little stearic acid is left in the form of a surface-active component available for bitumen liberation, hindering bitumen recovery. Significant reduction of stearic acid by calcium also implies a strong binding of calcium to stearic acid. Such a characteristic of calcium would allow it to attach to the bitumen surface, where the deprotonated carboxylic group was found to prevail in zeta potential distribution measurements (Liu, Zhou, and Xu 2002). The adsorption of divalent calcium cations would make the bitumen surface locally positively charged, attracting negatively charged fine solids (as shown in Figure 4.55b or Figure 4.55c), and lead to low bitumen recovery or poor froth quality (Gu et al. 2003). Despite the negative impact of calcium on bitumen recovery, strong binding of calcium with stearic acid allows for the removal of potentially toxic surfactants by calcium ion addition, which is followed by flocculation or precipitates flotation to clean up the surface-active organics (such as naphthenic acids) from the process water for safe discharge.

Since calcium negatively affects bitumen recovery by reducing the active ingredients of surface-active components in bitumen, oil sands processing is often operated at alkaline pH, not only to produce and ionize the natural surfactants needed for bitumen liberation (discussed later), but also to introduce carbonates to minimize the detrimental effect of calcium ions. The calculation above for the closed system containing 1000 ppm carbonate showed an almost sevenfold increase in the concentration of soluble stearic acid, from 4×10^{-7} mole/L without carbonate to 3.19×10^{-6} mole/L with carbonate. This is attributed to a significant reduction of soluble calcium ions, from 1 mM to 0.016 mM, by the formation of 0.936 mM calcium carbonate precipitates in the presence of 1000 ppm carbonate. Clearly, increasing the concentration of soluble stearic acid (RCOO^-) by scavenging soluble calcium ions using carbonate or bicarbonate is effective.

It is interesting to see the effect of pH on soluble stearic acid anion concentration by recalculating species distribution at higher pH (e.g., 10.5). Table 4.18 shows a further increase in soluble stearic acid anion concentration, from 3.19×10^{-6} mole/L to 20.5×10^{-6} mole/L, which results simply from increasing pH at the fixed total carbonate concentration of 1000 ppm. Such an increase in soluble stearic acid anion concentration is attributed to the increase of carbonate (CO_3^{2-}) concentration with pH (from 0.218 mM to 8.97 mM), leading to increased precipitation of calcium carbonate at 0.96 mM and a corresponding decrease in soluble calcium ion concentration from 15.5×10^{-3} mM to 0.38×10^{-3} mM. It is evident that high pH is favourable for maintaining a high concentration of soluble stearic acid anions when bicarbonate is co-present with calcium.

In view of the importance of bicarbonate in controlling soluble calcium concentration, it is instructive to calculate speciation distribution. For a given total carbonate concentration ($[\text{CO}_3^{2-}]_T$) below its solubility limit, and without considering calcium, Eq. (4.36) can be applied by setting $[\text{CaCO}_3(\text{s})]$ to equal zero. Applying dilute solution approximation, the concentration of various carbonate species can be

expressed in terms of equilibrium constants in (R-6) and (R-7) as a function of pH (hydrogen ion concentration) using the mass action principle. The materials balance equation of carbonates (Eq. [4.36]) then becomes

$$[\text{CO}_3^{2-}] = \frac{[\text{HCO}_3^-]_T}{\left(1 + \frac{[\text{H}^+]}{K_{\text{R-8}}} + \frac{[\text{H}^+]^2}{K_{\text{R-7}}K_{\text{R-8}}}\right)} \quad (4.42)$$

For a given pH, Eq. (4.42) allows us to calculate the carbonate anion concentration, from which the concentration of other species can readily be calculated. The speciation diagram in Figure 4.59 shows the results obtained for $[\text{HCO}_3^-]_T = 16 \text{ mM}$. It is evident that, over a pH range of 6 to 10.5, bicarbonate anions (HCO_3^-) dominate. Below pH 6, the neutral molecular carbonic acid, $\text{H}_2\text{CO}_3(\text{aq})$, dominates, while at pH above 10.5, divalent anionic carbonate, CO_3^{2-} , begins to dominate. It is therefore anticipated that, for an open system, the amount of dissolved CO_2 increases significantly at pH levels above 10.5, increasing the concentration of carbonate ions, which effectively remove calcium ions by forming calcium carbonate precipitate. Clearly, the presence (addition) of CO_3^{2-} is highly beneficial for controlling the calcium level, and hence, the optimized performance of bitumen recovery.

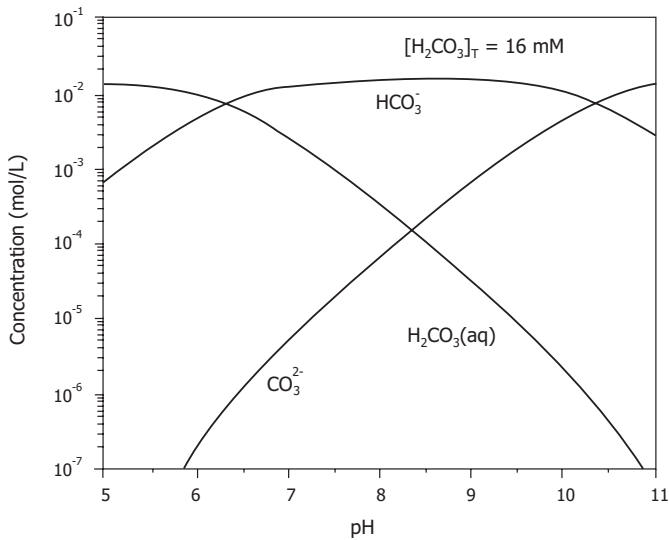


Figure 4.59 Speciation diagram of carbonate for a closed system of $[\text{HCO}_3^-]_T = 16 \text{ mM}$.

It should be noted that the above approach for calculating soluble calcium, carbonate, and surfactant concentrations is limited to closed systems only, such as those encountered inside hydrotransport slurry pipelines, where bitumen liberation

and aeration occur. In oil sands extraction, many unit operations (such as flotation cells and tailings ponds) are open to the atmosphere, where mass transfer occurs between CO₂ in the atmosphere and in the pulp/suspension. Thermodynamically, the amount of CO₂ dissolved in the aqueous phase is determined by Henry's law for a low concentration regime of CO₂:

$$[\text{CO}_2(\text{aq})] = [\text{H}_2\text{CO}_3(\text{aq})] = K_{\text{H}}P_{\text{CO}_2} \quad (4.43)$$

where K_{H} is Henry's constant and P_{CO_2} is the partial pressure of CO₂ in the atmosphere. At ambient conditions (i.e., $P = 1 \text{ atm}$ and $T = 298 \text{ K}$), $K_{\text{H}} = 10^{-1.48} \text{ mole/bar}\cdot\text{L}$ and $P_{\text{CO}_2} = 3.5 \cdot 10^{-4} \text{ bar}$. In an open system, the concentration of H₂CO₃(aq) is governed by Henry's law, which allows for the calculation of other carbonate species as a function of pH using equilibrium reactions and the corresponding equilibrium constants given in Table 4.17. The procedures outlined in Example 4.4 could easily be modified to calculate species distributions. A detailed analysis of water chemistry for calcium precipitation using bicarbonate is provided in Chapter 6.

4.9.4 Natural Surfactants in Bitumen

The presence of natural surfactants in bitumen is well established, although their role in bitumen recovery remains controversial (Hepler and Smith 1994). Due to their amphiphilic nature, surfactant molecules accumulate at air-water or oil-(bitumen)-water interfaces, as shown in Figure 4.60. By eliminating unfavourable contact between hydrocarbon (or fluorocarbon) tails and water and between polar heads and the organic phase, the accumulation of surfactant at the oil-water or air-water interface reduces the interfacial energy, as moving a surfactant molecule from the bulk solution to the interface requires much less energy than moving a water molecule to the interface.

Depending on caustic addition (or more specifically, on the pH), some surfactant molecules can be made water-soluble and transfer from bitumen to the aqueous phase. Bichard (1987) reported that the lowest solubility (extraction) of natural surfactant from bitumen to the aqueous phase was at neutral pH, indicating the presence of both weak-acid (carboxylic acid-type, -COOH) and weak-base (amine-type, -NH₂) surface-active molecules in bitumen. Although carboxylic acid-types of surfactants have been considered by many to be the major surface-active components in bitumen following caustic addition, emphasizing the importance of caustics in bitumen recovery, others have reported the presence of sulphonate, sulphate, or sulphoxide surfactants (Ali 1978; Moschopedis et al. 1980; Schramm and Smith 1987).

In his early studies, Bichard suggested the bridging of natural surfactant molecules and bitumen by polyvalent cations (1987). This hypothesis was later experimentally confirmed by zeta potential distribution measurements (Liu et al. 2002). The use of chelating agents to scavenge polyvalent cations or high caustic addition to produce a sufficient amount of surface-active components from bitumen have been proposed as

methods of improving bitumen recovery and froth quality. Increasing pH, in addition to producing more natural surfactants from bitumen, also dissociates carboxylic acids, thus rendering bitumen-water and oil-water interfaces progressively more negative while accelerating the hydrolysis of siloxane bonds (Si-O-Si) and the dissociation of silanol (-SiOH) groups on solids. As a result, solids become more hydrophilic, leading to better bitumen-solids separation. However, the loading of negatively charged surfactants at the bitumen-water and air-water interfaces makes bitumen-air attachment more difficult, reducing bitumen recovery. Decreasing the bitumen-water interfacial tension to extremely low values at high pH also emulsifies bitumen, making the recovery of ultrafine bitumen droplets even more challenging.

The detrimental effect of excessive caustic addition on bitumen recovery is well documented by Misra, Aguilar, and Miller (1981), Hupka and Miller (1991), and Schramm and Smith (1984), leading to the concept of critical surfactant concentration for optimal bitumen recovery. A critical surfactant concentration of 0.1 mM (Schramm, Smith, and Stone 1984) occurs at a pH of around 9 (Bichard 1987). The demand for caustic addition to achieve this level of natural surfactant release depends on the characteristics of the ore. More caustic is required for high-fines and weathered ores.

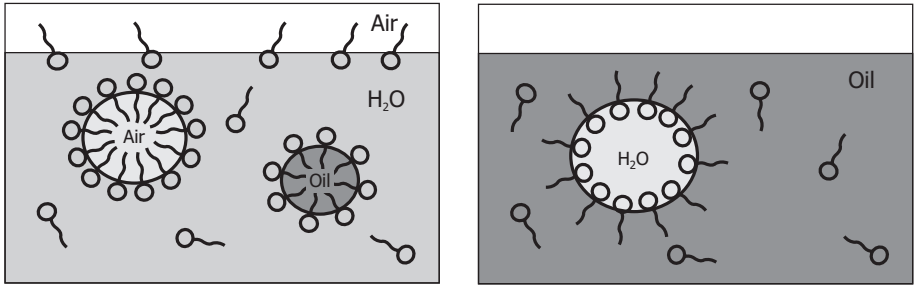


Figure 4.60 Schematic illustration of surfactant adsorption at air-water and oil-water interfaces.

Zeta Potential

As mentioned earlier, the amphiphilic nature of the natural surfactants from bitumen causes them to migrate from bitumen to the bitumen-water interface, transfer into water, and then migrate to the air-water interface. The extent of surfactant transfer depends on caustic addition. As discussed in Section 4.9.3 on surfactant chemistry, a pH-dependent ionization of the weak acid- or base-types of surfactants (Table 4.16) creates a pH-dependent surface charge at oil-(bitumen)-water and air-water interfaces. As we can see, measurement of interfacial charge characteristics (zeta potential) is a powerful method for determining the type and concentration of natural surfactant present at the bitumen-water and air-water interfaces and released into the aqueous phase during oil sands extraction.

Following early work by Takamura and Chow (1983, 1985), Schramm and Smith (1984), and Hupka and Miller (1991), a systematic study was conducted by Liu, Zhou, and Xu (2002) to determine the type of natural surfactant released into industrial process water and accumulated at the bitumen-water interface. As shown in Figure 4.61, the zeta potential profile of hexane droplets in oil sands industrial CT (consolidated or composite tailings) process water can only be matched by the zeta potential profile of hexane droplets in 1 mM KCl and 1 mM CaCl₂ electrolyte solutions containing all three types of surfactants: sodium dodecyl sulphate (SDS), dodecyl amine hydrochloride (DAH), and sodium salt of palmitic acids (NaPa) at 1:1:X molar ratios (where X is variable). An attempt to match the measured zeta potential profiles of hexane droplets in 1 mM KCl solutions containing either a single or binary surfactant of SDS, DAH, or NaPa with the profile of hexane droplets in oil sands process water was not successful (Liu, Zhou, and Xu 2002). These results indicate not only the presence of these three types of surfactants, but also their relative concentrations. It is interesting to note that the measured zeta potential value of hexane droplets in an aqueous solution is less sensitive to the change of NaPa concentration ratio (with X varying from 0.5 to 2) than to the change of SDS and DAH concentration ratio. Furthermore, the measured zeta potential of hexane droplets in tailings pond water was found to be more negative than that in CT process water, which was attributed to a higher concentration of calcium ions in the CT process water than in the tailings pond water. The zeta potential profiles of hexane droplets in tailings pond water and CT process water can be well matched by the measured zeta potentials of hexane droplets in aqueous solutions that contain not only the same level of inorganic ions, but also SDS:DAH:NaPa surfactants at 1:1:1 molar ratios.

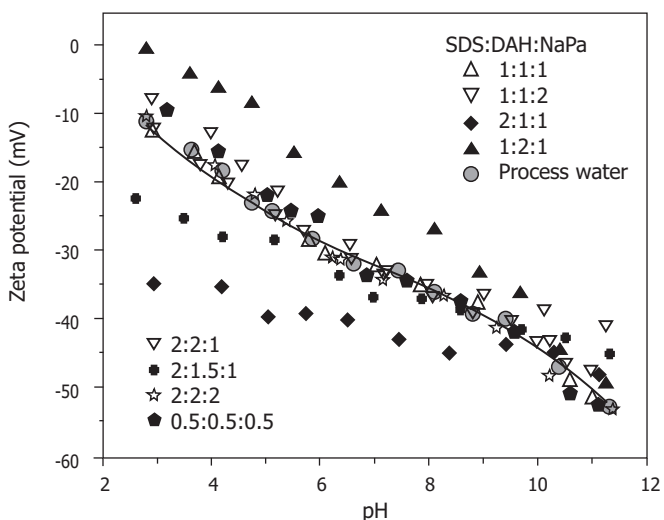


Figure 4.61 Zeta potentials of hexane droplets as a function of pH in 1 mM KCl and 1 mM CaCl₂ solutions containing mixed surfactants (symbols) in CT process water (curve). The surfactant concentration is indexed as 0.5 = 0.005 mM, 1 = 0.01 mM, and 2 = 0.02 mM.

More interestingly, the measured zeta potential profile of bitumen in 1 mM KCl solutions can be well matched by the zeta potentials of hexane droplets in 1 mM KCl solutions containing a 1:1:1 molar ratio of SDS:DAH:NaPa, each at 0.01 mM, as shown in Figure 4.62. The measured zeta potential profiles of hexane droplets in a binary surfactant solution do not provide a satisfactory matching. This finding is particularly important, as it indicates the presence of all three types of natural surfactants on bitumen surfaces in aqueous solutions. Clearly, the electric charge on the bitumen surface is complex and by no means uniformly distributed.

It should be noted that the adsorption of natural surfactants at the air-water interface will also lead to similar pH-dependent charge characteristics. The only difference is that the amount of natural surfactant adsorbed at the air-water interface (adsorption density) may well be different from that at the bitumen-water interface, leading to differences in the absolute value of surface charge density and hence, in the zeta potential. The adsorption of natural surfactants not only makes air bubbles more stable and less amenable to attachment to bitumen surfaces, but also induces electrostatic double layer repulsive forces that prevent bubbles from approaching the bitumen surface, leading to poor bitumen aeration. The impact of surfactant adsorption on bubble generation and stabilization will be discussed in later chapters.

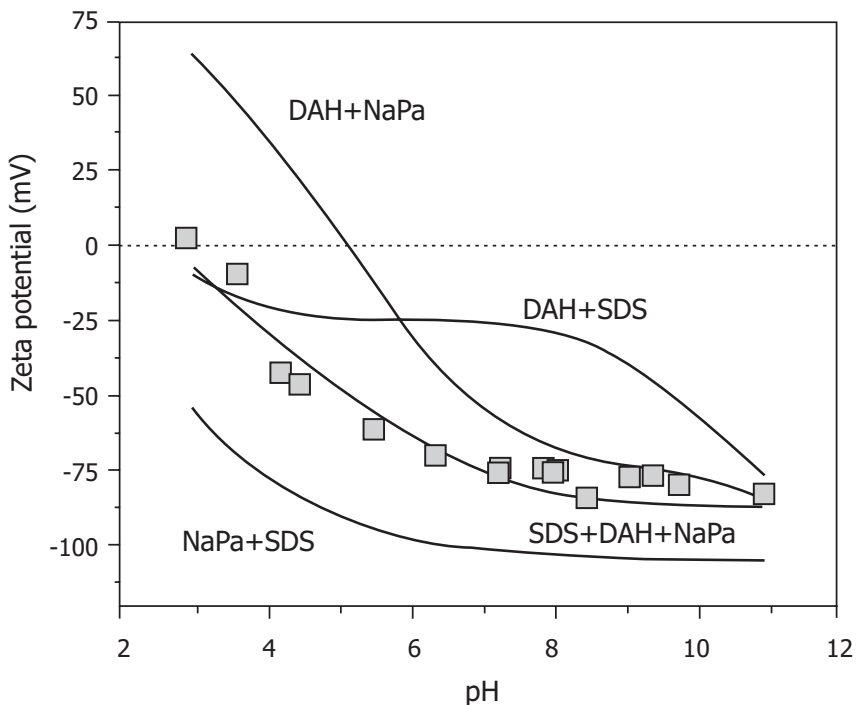


Figure 4.62 Zeta potentials of hexane droplets in surfactant containing solutions at a 1:1:1 molar ratio, each at the 0.01 mM level (solid lines), and of bitumen in 1 mM KCl supporting electrolyte solution (symbols).

Efforts have been made to better understand the surface charge characteristics at bitumen-water interfaces by applying the ionizable surface group model (Healy and White 1978) to the ionization of surfactant molecules adsorbed at bitumen-water interfaces (Takamura and Chow 1985). In this model, surface charge develops as a result of the ionization (dissociation or protonation) of surface groups. At the bitumen-water interface, it is the dissociation of carboxylic groups and the protonation of amine groups of natural surfactants adsorbed at the interface that contribute to the total surface charge. An early attempt by Takamura and Chow (1985) considered only the carboxylic surfactants at the bitumen-water interface. Although the predicted zeta potentials from this model show a reasonable agreement with the measured zeta potential, the presence of mixed surfactants of different ionization characteristics poses challenges in accurately modelling electrical properties of bitumen-water or air-water interfaces, as reported by Liu et al (2008). A main difficulty lies in accurately determining the adsorption density of each type of surfactant at the bitumen-water interface, which can change with changing solution pH. Considering the important role of surfactants in bitumen liberation and aeration and their application in bitumen recovery, continuing research in this direction would be fruitful.

4.10 References

- Alboudwarej, H., K. Akbarzadeh, J. Beck, W.Y. Svrcek, and H.W. Yarranton. 2003. Regular solution model for asphaltene precipitation from bitumens and solvents. *AIChE Journal* 49 (11): 2948–2956.
- Alboudwarej, H., J. Beck, W.Y. Svrcek, and H.W. Yarranton. 2002. Sensitivity of asphaltene properties to separation techniques. *Energy Fuels* 16 (2): 462–469.
- Ali, L.H. 1978. Surface active agents in the aqueous phase of the hot water flotation process for oil sands. *Fuel* 57 (6): 357–360.
- Anderson, W.G. 1986. Wettability literature survey, part 1: Rock/oil/brine interactions and the effects of core handling on wettability. *Journal of Petroleum Technology* 38 (10): 1125–1144.
- Ball, M.W. 1935. Athabaska oil sands: Apparent example of local origin of oil. *AAPG Bulletin* 19: 153–171.
- Bergaya, F., B.K.G. Theng, and G. Lagaly, eds. 2006. *Handbook of clay science*. Oxford: Elsevier.
- Berkowitz, N. 1998. *Fossil hydrocarbons: Chemistry and technology*. San Diego: Academic Press.
- Bichard, J.A. 1987. *Oil sands composition and behaviour research: The research papers of John A. Bichard, 1957–1965*, AOSTRA Technical Publication Series No. 4. Edmonton: Alberta Oil Sands Technology and Research Authority (AOSTRA).

- Bowman, C.W. 1967. Molecular and interfacial properties of Athabasca tar sands. In *Proceedings of the 7th World Petroleum Congress*. Mexico City, Mexico.
- Buckley, J.S. 1996. Microscopic investigation of the onset of asphaltene precipitation. *Fuel Science and Technology International* 14 (1–2): 55–74.
- . 1999. Predicting the onset of asphaltene precipitation from refractive index measurements. *Energy & Fuels* 13 (2): 328–332.
- Buckley, J.S., G.J. Hirasaki, Y. Liu, S.V. Drasek, J.-X. Wang, and B.S. Gill. 1998. Asphaltene precipitation and solvent properties of crude oils. *Petroleum Science and Technology* 16 (3): 251–285.
- Butt, H.J., K. Graf, and M. Kappl. 2003. *Physics and chemistry of interfaces*. Weinheim, Germany: Wiley-VCH.
- Cameron Engineers. 1978. Oil sands. In *Synthetic fuels data handbook: U.S. oil shale, U.S. coal, oil sands*, ed. G. L. Baughman. Denver: Cameron Engineers.
- Canadian Natural Resources Limited (CNRL). 2002a. *Horizon Oil Sands Project application for approval. Submitted to Alberta Energy and Utilities Board and Alberta Environment. Volume 1, Section 2. Geology and Resource Base*: Canadian Natural Resources Limited.
- Canadian Natural Resources Limited (CNRL). 2002b. *Horizon Oil Sands Project application for approval. Submitted to Alberta Energy and Utilities Board and Alberta Environment. Vol. 5, Attachment C7*: Canadian Natural Resources Limited.
- Cassisi, R., N. Fuller, L.G. Hepler, R.J.C. Mclean, A. Skauge, N.S. Srinivasan, and H.-K. Yan. 1985. Specific heat capacities of bitumens and heavy oils, reservoir minerals, clays, dehydrated clays, asphaltenes and coke. *AOSTRA Journal of Research* 1: 163–173.
- Clark, K.A. 1944. Some physical properties of Alberta bituminous sands. *Canadian Journal of Research* F22: 174–180.
- Clark, K.A., and D.S. Pasternack. 1932. Hot water separation of bitumen from Alberta bituminous sand. *Industrial and Engineering Chemistry Research* 24 (12): 1410–1416.
- Cottrell, J.H. 1963. Development of an anhydrous process for oil sand extraction. In *The K.A. Clark volume: A collection of papers on the Athabasca oil sands presented to K.A. Clark on the 75th anniversary of his birthday*, ed. M. A. Carrigy, 196–206. Edmonton: Alberta Research Council.
- Cuddy, G. 2004. Oil sands geology. Guest lecture notes for Chemical Engineering 534, Fundamentals of Oil Sands Extraction, January 7–9, at University of Alberta, Edmonton.
- Czarnecki, J., B. Radoev, L.L. Schramm, and R. Slavchev. 2005. On the nature of Athabasca oil sands. *Advances in Colloid Interface Science* 114–115: 53–60.
- Dabros, T., X. Yang, Y. Long, and H.A. Hamza. 2004. Settling properties of paraffinic solvent-diluted bitumen emulsions. Paper read at 5th International Conference on Petroleum Phase Behaviour and Fouling, June 13–17, at Banff, Alberta.

- Deer Creek Energy Ltd. 2006. *Joslyn north mine project: AEUB application. CR-11, appendix A1, version 1. Aquatic resources report.*
- Dusseault, M.B., and N.R. Morgenstern. 1978. Shear strength of Athabasca oil sands. *Canadian Geotechnical Journal* 15 (2): 216–238.
- Essington, M.E. 2004. *Soil and water chemistry: An integrative approach.* Boca Raton: CRC Press.
- Fitzgerald, J.J. 1978. *Black gold with grit: The Alberta oil sands.* Sidney: Gray's Publishing.
- Fowkes, F.M. 1965. Attractive forces at interfaces. In *Chemistry and physics of interfaces.* Washington, D.C.: ACS.
- Fuerstenau, D.W. 1982. Thermodynamics of surfaces, adsorption and wetting. In *Principles of Flotation*, ed. R. P. King. Johannesburg: South African IMM.
- Gee, M., T. Healy, and L. White. 1990. Hydrophobicity effects in the condensation of water films on quartz,. *Journal of Colloid and Interface Science* 140 (2): 450–465.
- Giese, R.F., and C.J. van Oss. 2002. *Colloid and surface properties of clays and related minerals.* New York: Marcel Dekker.
- Gray, M.R. 2002. New technique defines the limits of upgrading heavy oil, bitumens. *Oil & Gas Journal* 100 (1): 50–54
- Gu, G., Z. Xu, K. Nandakumar, and J.H. Masliyah. 2003. Effects of physical environment on induction time of air-bitumen attachment. *International Journal of Mineral Processing* 69 (1–4): 235–250
- Hall, A.C., S.H. Collins, and J.C. Melrose. 1983. Stability of aqueous wetting films in Athabasca tar sands. *Society of Petroleum Engineers of AIME* 23 (2): 249–258.
- Healy, T.W., and L.R. White. 1978. Ionizable surface group models of aqueous interfaces. *Advances in Colloid Interface Science* 9 (4): 303–345.
- Hepler, L.G., and R.G. Smith, eds. 1994. *The Alberta oil sands: Industrial procedures for extraction and some recent fundamental research.* AOSTRA technical publication series no. 14. Edmonton: Alberta Oil Sands Technology and Research Authority (AOSTRA).
- Hiemenz, P.C., and R. Rajagopalan. 1997. *Principles of colloid and surface chemistry.* 3rd ed. New York: Marcel Dekker.
- Hupka, J., and J.D. Miller. 1991. Electrophoretic characterization and processing of Asphalt Ridge and Sunnyside tar sands. *International Journal of Mineral Processing* 31: 217–231.
- Imperial Oil Ltd. 2005. Alberta Energy and Utilities Board (AEUB) *Application for Approval for Kearn Oil Sands Project. Vol. 1.* Calgary: Imperial Oil Ltd.
- Incropera, F.P., and D.P. DeWitt. 1985. *Fundamentals of heat and mass transfer.* New York: Wiley.
- Isaacs, E.E., and D.N. Morrison. 1985. Interfacial films at the Athabasca bitumen/water interface. *AOSTRA Journal of Research* 2: 113–119.

- Kanta, A., R. Sedev, and J. Ralston. 2005. Thermally- and photoinduced changes in the water wettability of low-surface-area silica and titania. *Langmuir* 21 (6): 2400–2407.
- Karim, G.A., and A. Hanafi. 1981. The thermal conductivity of oil sands. *Canadian Journal of Chemical Engineering* 59 (4): 461–464.
- King, R.P., ed. 1982. *Principles of flotation*. Johannesburg: South African IMM.
- Komery, D.P., J.C. O'Rourke, and J.I. Chambers. 1993. AOSTRA underground test facility UTF phase B: Implications for commercialization. Paper read at Oil Sands: Our Petroleum Future Conference, April 4–7, at Edmonton, Alberta, Canada.
- Konan, K.L., C. Peyratout, J.-P. Bonnet, A. Smith, A. Jacquet, P. Magnoux, and P. Ayrault. 2007. Surface properties of kaolin and illite suspensions in concentrated calcium hydroxide medium. *Journal of Colloid and Interface Science* 307 (1): 101–108.
- Lee, L.H. 1996. Correlation between Lewis acid-base surface interaction components and linear solvation energy relationship solcatochromic α and β parameters. *Langmuir* 12 (6): 1681–1687.
- Liu, J., Z. Xu, and J. Masliyah. 2004. Role of fine clays in bitumen extraction from oil sands. *AIChE Journal* 50 (8): 1917–1927.
- Liu, J., L. Zhang, P. Breen, Z. Xu, and J. Masliyah. 2008. Application of site-binding modeling to oil droplets in aqueous solutions. In *Internationaal Mineral Processing Congress*, edited by Z. Wang, Y. Sun, F. Wang, L. Zhang and L. Han. Beijing: Science Press.
- Liu, J., Z. Zhou, and Z. Xu. 2002. Electrokinetic study of hexane droplets in surfactant solutions and process water of situmen extraction systems. *Industrial and Engineering Chemistry Research* 41 (1): 52–57.
- Liu, J., Z. Zhou, Z. Xu, and J.H. Masliyah. 2002. Bitumen-clay interactions in aqueous media studied by zeta potential distribution measurement. *Journal of Colloid and Interface Science* 252 (2): 409–418.
- Masliyah, J.H., and S. Battacharjee. 2006. *Electrokinetic and colloid transport phenomena*. Hoboken: Wiley-Interscience.
- Mehrotra, A.K. 1991. A generalized viscosity equation for pure heavy hydrocarbons. *Industrial & Engineering Chemistry Research* 30 (2): 420–427.
- . 1992a. Mixing rules for predicting the viscosity of bitumens saturated with pure gases *Canadian Journal of Chemical Engineering* 70 (1): 165–172.
- . 1992b. A generalized viscosity equation for liquid hydrocarbons: Application to oil-sand bitumens. *Fluid Phase Equilibria* 75: 257–268.
- Mehrotra, A.K., W.D. Monnery, and W.Y. Svrcak. 1996. A review of practical calculation methods for the viscosity of hydrocarbons and their mixtures. *Fluid Phase Equilibria* 117 (1–2): 344–355.

- Miller, J.D., and M. Misra. 1982. Hot water process development for Utah tar sands. *Fuel Processing Technology* 6 (1): 27–59.
- Mishra S.K.. 1988. Anionic collectors in nonsulfide mineral flotation. In *Reagents in Mineral Technology*, eds P. Somasundaran and B.M. Moudgil: 195-217, New York: Marcell Decker.
- Misra, M., R. Aguilar, and J.D. Miller. 1981. Surface chemistry features in the hot water processing of Utah tar sand. *Separation Science Technology* 16 (10): 1523–1544.
- Misra, M., and J.D. Miller. 1991. Comparison of water-based physical separation processes for U.S. tar sands. *Fuel Processing Technology* 27 (1): 3–20.
- Mitchell, J.K. 1976. *Fundamentals of soil behavior*. New York: Wiley.
- Moran, K.L. 2001. Micro-mechanics of emulsion drops. PhD diss., Department of Chemical and Materials Engineering, University of Alberta, Edmonton.
- Moran, K.L., A. Yeung, J. Czarnecki, and J.H. Masliyah. 2000. Micron-scale tensiometry for studying density-matched and highly viscous fluids: with application to bitumen-in-water emulsions. *Colloids and Surfaces A: Physicochemical and Engineering Aspects* 174 (1–2): 147–157.
- Moschopedis, S.E., K.F. Schulz, J.G. Speight, and D.N. Morrison. 1980. Surface-active materials from Athabasca oil sands. *Fuel Processing Technology* 3 (1): 55–61.
- Mossop, G.D. 1980. Geology of the Athabasca oil sands. *Science* 207: 145–152.
- Petro-Canada Inc. 2001. *Application for approval, Fort Hills Oil Sands Project. Submitted to AEUB*.
- Potoczny, Z.M., E.I. Vargha-Butler, T.K. Zubovits, and A.W. Neumann. 1984. Surface tension of bitumen. *AOSTRA Journal of Research* 1: 107–115.
- Puttagunta, V.R., A. Miadonye, and B. Singh. 1992. Viscosity temperature correlation for prediction of kinematic viscosity of conventional crude. *Chemical Engineering Research and Design: Transactions of the Institution of Chemical Engineers* 70 (6): 627–631.
- Sanford, E.C. 1983. Processability of Athabasca oil sand: Interrelationship between oil sand fine solids, process aids, mechanical energy and oil sand age after mining. *Canadian Journal of Chemical Engineering* 61 (4): 554–567.
- Schramm, L.L., and Smith, R.G., inventors, and Petro-Canada Exploration Inc., owner. 1984. Control of process aid used in hot water process for extraction of bitumen from tar sand. US Patent 4,462,892, filed Mar. 17, 1983, and issued Jul. 31, 1984.
- Schramm, L.L., and J.C.T. Kwak. 1988. The rheological properties of an Athabasca bitumen and some bituminous mixtures and dispersions. *Journal of Canadian Petroleum Technology* 27 (1): 26–35.
- Schramm, L.L., and R.G. Smith. 1987. Two classes of anionic surfactant and their significance in hot water processing of oil sands. *Canadian Journal of Chemical Engineering* 65 (5): 799–811.

- Schramm, L.L., R.G. Smith, and J.A. Stone. 1984. A surface-tension method for the determination of anionic surfactants in hot water processing of Athabasca oil sands. *Colloids and Surfaces A: Physicochemical and Engineering Aspects* 11: 247–263.
- Sepulveda, J.E., and J.D. Miller. 1978. Separation of bitumen from Utah tar sands by a hot water digestion-flotation technique. *Mining Engineering* 30: 1311–1320.
- Seyer, F.A., and G.W. Gyte. 1989. Viscosity. In *AOSTRA technical handbook on oil sands, bitumens and heavy oils, AOSTRA technical publication series no. 6*, ed. L. E. Hepler and C. Hsi. Edmonton: Alberta Oil Sands Technology and Research Authority (AOSTRA).
- Shaughnessy, E.J., I.M. Katz, and J.P. Schaffer. 2005. *Introduction to fluid mechanics*. New York: Oxford University Press.
- Shaw, R.C., L.L. Schramm, and J. Czarnecki. 1996. Suspensions in the hot water flotation process for Canadian oil sands. In *Suspensions: Fundamentals and applications in the petroleum industry*, ACS Advances in Chemistry Series 251, ed. L. L. Schramm, 639–675. Washington: American Chemical Society.
- Shell Canada Ltd. 2007. Jackpine Mine application. Submitted to Alberta Energy and Utility Board.
- Smith-Magowan, D., A. Skauge, and L.G. Hepler. 1982. Specific heats of Athabasca oil sands and components. *Journal of Canadian Petroleum Technology* 21 (3): 28–32.
- Strausz, O.P., and E.M. Lown. 2003. *The chemistry of the Alberta oil sands bitumens and heavy oils*. Calgary: Alberta Energy Research Institute.
- Stumm, W., and J.J. Morgan. 1996. *Aquatic chemistry*. 3rd ed. New York: Wiley.
- Sukanek, P.C., and R.L. Laurence. 1974. An experimental investigation of viscous heating in some simple shear flows. *AIChE Journal* 20 (3): 474–484
- Suncor Energy Inc. 2005. *North Steepbank Extension Project Application. Submitted to AEUB. Vol. 1A: Geology*.
- Takamura, K. 1982. Microscopic structure of Athabasca oil sand. *Canadian Journal of Chemical Engineering* 60: 538–545.
- Takamura, K., and R.S. Chow. 1983. A mechanism for initiation of bitumen displacement from oil sands. *Journal of Canadian Petroleum Technology* 22 (6): 1–9.
- . 1985. The electric properties of the bitumen/water interface. Part II: Application of the ionizable surface-group model. *Colloids and Surfaces A: Physicochemical and Engineering Aspects* 15: 35.
- Takamura, K., and E.E. Isaacs. 1989. Interfacial properties. In *AOSTRA technical handbook on oil sands, bitumens and heavy oils, AOSTRA technical publication series no. 6*, AOSTRA Technical Publication Series No. 6, ed. L. E. Hepler and C. Hsi. Edmonton: Alberta Oil Sands Technology and Research Authority (AOSTRA).

- Taylor, S.D., J. Czarnecki, and J.H. Masliyah. 2001. Refractive index measurements of diluted bitumen solutions. *Fuel* 80 (14): 2013–2018.
- Tipman, R.N., and J. Sharp. 2004. Oil sands mining and processing. Paper presented to the Canadian Heavy Oil Association
- Tombácz, E., and M. Szekeres. 2006. Surface charge heterogeneity of kaolinite in aqueous suspension in comparison with montmorillonite. *Applied Clay Science* 34 (1–4): 105–124.
- van Olphen, H. 1963. *An introduction to clay colloid chemistry for clay technologists, geologists, and soil scientists*. New York: Interscience.
- van Oss, C.J. 2006. *Interfacial forces in aqueous media*. Boca Raton: Taylor & Francis (CRC Press).
- van Oss, C.J., M.K. Chaudhury, and R.J. Good. 1987. Monopolar surfaces. *Advances in Colloid and Interface Science* 28 (1): 35–64.
- Wan, J., and T.K. Tokunaga. 2002. Partitioning of clay colloids at air-water interface. *Journal of Colloid and Interface Science* 247 (1): 54–61.
- Wang, L., T. Dang-Vu, Z. Xu, and J. Masliyah. 2010. Use of short-chain amine in processing of weathered/oxidized oil sands ores. *Energy & Fuels* (In press).
- Wang, W., Z. Zhou, K. Nandakumar, and Z. Xu. 2004. Effect of charged colloidal particles on adsorption of surfactants at oil-water interface. *Journal of Colloid and Interface Science* 274: 625–630.
- Yarranton, H.W., and J.H. Masliyah. 1996. Molar mass distribution and solubility modeling of asphaltenes. *AIChE Journal* 42 (12): 3533–3543.
- Zhang, L.Y., R. Lopetinsky, Z. Xu, and J.H. Masliyah. 2005. Asphaltene monolayers at a toluene/water interface. *Energy & Fuels* 19 (4): 1330–1336.

Chapter 5

Slurry Preparation and Conditioning

When Suncor and Syncrude first began bitumen extraction operations (the former in 1967 and the latter in 1978), both initially employed the Clark Hot Water Extraction (CHWE) process with the addition of caustic at operating temperatures of 70 °C to 80 °C.¹ Today, there is an increasing shift towards operating at lower temperatures (and to some extent, towards lowering or eliminating the use of caustic). The shift in temperature reduction is evident in the design of Suncor's 1998 Steepbank Mine and 2001 Millennium project; Syncrude's North Mine and Aurora Mine Trains 1 and 2 (2000–2003); and Albion's Muskeg River Mine (2003). The operating temperature plays a major role in the design of a bitumen extraction plant, and is based on a number of different factors, including the residence time of oil sands lumps in the extraction unit, unit operations within the extraction plant, the available thermal energy (which is normally dependent on the presence or absence of upgrading facilities nearby), heat integration, and the use of recycle water. A brief review of some alternative bitumen extraction processes is given by Fuhr et al. (1993) and the Fine Tailings Fundamentals Consortium (FTFC) (1995). In the last decade, plant experience and laboratory tests have indicated the significance of the extraction operating temperature. The general rule is to avoid operating at temperatures below 40 °C (Long, Xu, and Masliyah 2005).

The basic steps of bitumen recovery are outlined below.

1. Mining of oil sands

Oil sands are mined using shovels, and the mined dry ore is transported to the extraction plant by trucks (this is referred to as the truck-and-shovel method). More recently, Suncor introduced mobile mining technology as an alternative to the traditional truck-and-shovel operation. The mined oil sands are crushed and mixed with water at the mine face and transported to the processing facility by pipeline, thereby eliminating the use of trucks.

¹ *Operating temperature* refers to the temperature of the exit slurry in a bitumen digestion unit, i.e., tumbler or hydrotransport pipeline.

2. Oil sands ore preparation

Oil sand lumps are crushed and then mixed with recycle process water in mixing boxes, cyclofeeders, or rotary breakers. At this stage, chemical additives can be included. Air entrainment takes place.

3. Digestion of oil sand lumps with subsequent bitumen liberation and aeration

This step involves lump size reduction, bitumen liberation from sand grains, bitumen-bitumen coalescence, and aeration. In early oil sands development, rotating drums (tumblers) were used. At present, slurry hydrotransport pipelines are used in this step. Air, at low doses, can be added to the hydrotransport pipeline to allow for more bitumen aeration.

4. Separation of the liberated and aerated bitumen aggregates from the water-solids slurry

The flotation of the aerated bitumen and settling of the solids are achieved using large gravity separation vessels, which are referred to as *primary separation vessels* (PSVs); *sep cells*, or *primary separation cells* (PSCs).

5. Bitumen flotation

Further recovery of small bitumen aggregates (usually unaerated bitumen) is achieved using induced air flotation in flotation cells or columns, tails oil recovery vessels, cycloseparator, or hydrocyclones.

6. Froth treatment

Bitumen froths that are recovered from gravity separation vessels or flotation cells are first deaerated. At Syncrude, Suncor, and more recently, CNRL's Horizon Project, naphtha is used as a solvent (diluent) to reduce the bitumen density and viscosity. The solids and water are then removed from the bitumen froth using inclined plate settlers, cyclones, and centrifuges. At Albion's froth treatment plant, rather than a naphthenic diluent, a paraffinic diluent is used. As the use of paraffinic diluent leads to asphaltene precipitation, the paraffinic froth treatment process has changed the nature of water and solids removal, leading to new technological challenges. The paraffinic froth treatment process produces fairly clean, partially deasphalted bitumen with very small amounts of residual mineral solids and emulsified water.

7. Fine tailings management

At Suncor and Syncrude, the whole tailings are fed to tailings ponds. To reduce the accumulated mature fine tailings, they employ the consolidated (composite) tailings process, whereby gypsum, together with mature fine tails, is used to consolidate the fines and capture the coarse sand, thereby releasing recycle water for further use in the extraction process. At Albion, coarse sand is separated from the tailings slurry using hydrocyclones, and the fine solids are treated in thickeners to produce thickened tailings (TT) and warm water for recycling.

A generic flow diagram of the bitumen production process, from oil sands mining to bitumen upgrading, is shown in Figure 5.1. Each box in the figure identifies a unit plant operation that is well-integrated within the whole oil sands extraction operation and with upgrading when it is available in proximity of the extraction plant. The basic units of a bitumen extraction plant, as shown in the figure, include the mine face, utilities, extraction, froth treatment, upgrading, and water management (tailings pond/thickeners).

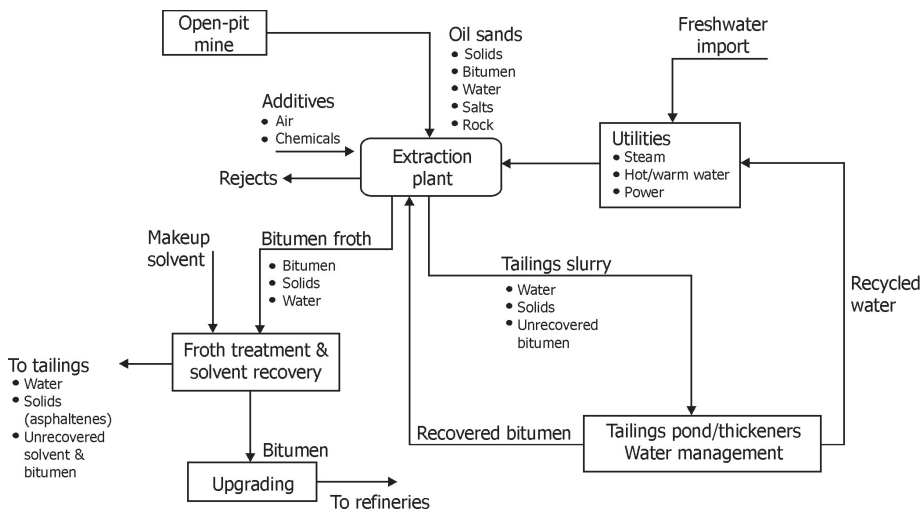


Figure 5.1 Schematic of various units for bitumen production.

Adapted from Fine Tailings Fundamentals Consortium (FTFC) (1995).

It is clear that all the units are inter-related. The mining operation affects extraction, and in turn, the extraction operation affects the upgrading operation. One should not think of mining, extraction, and upgrading as three independent operations. Only through proper integration and through meeting the specifications and goals of each operation can bitumen be efficiently recovered with minimum adverse environmental impact. In such a massive operation, the maximization of bitumen recovery should always guide the three basic operations: mining, extraction, and upgrading. With new oil sands operations under consideration, the impact of bitumen recovery from oil sands should seriously address the environmental issues that accompany such operations. Land disturbance and reclamation, greenhouse gas emission, freshwater use, and human resources need always play a major role in the design and operation of commercial oil sand plants.

In this chapter, we will deal with the theory of lump size reduction (i.e., lump ablation) and with the fundamentals involved in bitumen liberation from a solid surface.

5.1 Modelling of Lump Digestion in a Hydrotransport Pipeline

The purpose of this section is to illustrate oil sands lump digestion in a hydrotransport pipeline using a phenomenological approach.

5.1.1 Conceptual Model

An oil sands slurry in a pipeline is envisioned to flow as shown schematically in Figure 5.2. The larger material (i.e., lumps and coarse sand) forms a bed that moves along the bottom of the pipeline. Rocks that are similar in density to clay lumps, but higher in density than oil sand lumps, travel along the pipeline with the coarse sand bed. Finer material is suspended by fluid motion, forming a mixture that fills the region above the moving bed and the interstices between the lumps in the bed.

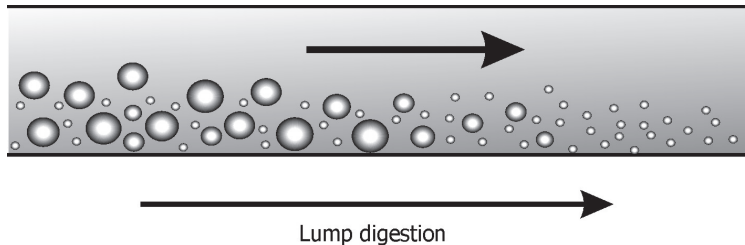


Figure 5.2 Conceptual model of oil sand flow in a pipeline.

Relative motion between lumps travelling in the moving bed results in shear stresses being applied to the surface of a lump. In addition, the slurry provides a heating medium to heat the oil sands lumps and reduce the bitumen viscosity. More precisely, the bitumen viscosity is lowered at the outer layer of an oil sands lump. The effect of shear stress being applied to an oil sands lump is that the outer layer of the lump is removed or ablated away. As the outer layer of an oil sands lump is sheared away, it exposes a lower temperature surface. The newly exposed outer layer of the lump becomes heated, its viscosity is then lowered, and it is subsequently sheared away. The cycle repeats itself until the entire oil sands lump is digested. Aerated bitumen, the recoverable product, is ultimately produced as bitumen is liberated from the sand grains and attaches itself to air bubbles.

The ability of a lump to resist digestion depends on the lump type (i.e., rock, clay, or oil sand). A rock will not lose any mass given the distances that this material is being pipelined. However, oil sands lumps would be expected to lose mass. The resistance of a clay lump to digestion is not a strong function of temperature, whereas the digestion of oil sands lumps is very dependent on lump temperature (Law, Masliyah, and Nandakumar 1987; Gilles and Small 1996).

An oil sands lump can only be digested if energy is imparted to it. In the case of an oil sands lump flowing in a pipeline, it is the mechanical energy from the surface shear stresses and the thermal energy as a result of heat transferred from the conveying slurry that are the energy inputs. Therefore, two key elements in developing a model for oil sands lump digestion are the determination of surface shear stress on the lump and the evaluation of the mass lost from the lump, taking into consideration the temperature profile of the lump.

5.1.2 Model Development

The starting point for developing the digestion model is the conservation of mass and energy. The governing equations can be derived by considering a differential segment of pipe of length Δz , as noted in Figure 5.3. At a given axial location within the pipeline, the flow medium is assumed to be composed of lumps (that include oil sand rocks and clay) and digested slurry (made up of mineral solids, bitumen, and water). It is assumed that the material ablated from the outer layer of a lump becomes part of the slurry.

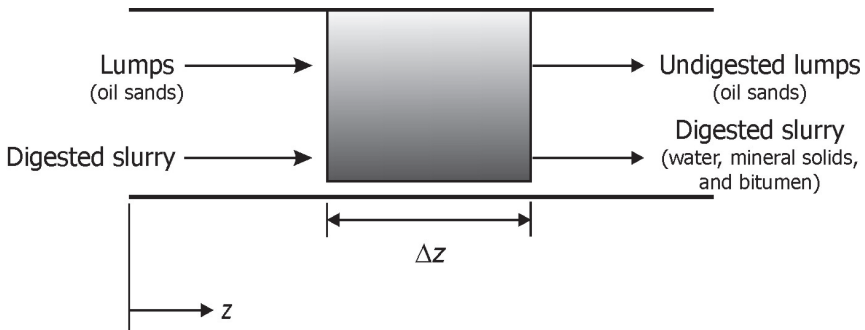


Figure 5.3 Differential segment of pipeline showing flow of slurry and lumps.

Conservation of Mass

At any given axial location within the pipeline, lump digestion takes place and transfer of mass occurs between the lumps and the slurry. The total mass flow rate, \dot{m}_z at any given axial location in the pipeline is given as

$$\dot{m}_z = \dot{m}_s + \sum_{i=1}^N \dot{m}_i \quad (5.1)$$

where \dot{m}_s is the mass flow rate of slurry, \dot{m}_i is the mass flow rate of the i^{th} lump species, and N is the total number of lump species.

Assuming that the flow is steady-state (i.e., \dot{m}_z is constant for all axial locations), Eq. (5.1) can be differentiated to obtain the mass balance for an infinitesimal element of pipe length $\Delta z \rightarrow 0$. The resulting expression is

$$\frac{d\dot{m}_s}{dz} = -\sum_{i=1}^N \frac{d\dot{m}_i}{dz} \quad (5.2)$$

An expression for the change of mass flow rate with distance for an i^{th} lump species (i.e., $d\dot{m}_i/dz$) can be developed by considering the concept presented by the schematic shown in Figure 5.4.

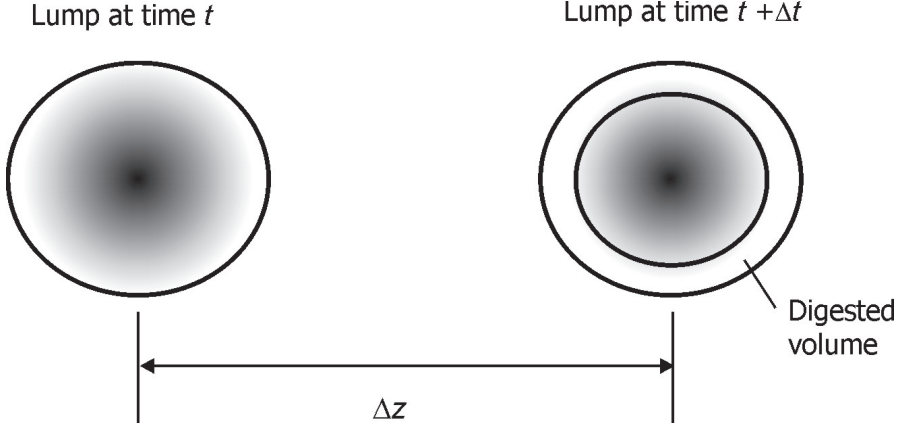


Figure 5.4 Ablated lump volume ΔV after a travel distance of Δz .

If the volume of a lump at time t is V_i , the fractional reduction in volume after the lump has travelled a distance Δz is $\Delta V_i/V_i$. Assuming that the density, ρ_i , of the i^{th} lump species is constant, the differential change in mass flow rate for the i^{th} lump species is simply

$$\Delta\dot{m}_i = \frac{\Delta V_i}{V_i} \dot{m}_i \quad (5.3)$$

Dividing Eq. (5.3) by Δz and taking the limit as $\Delta z \rightarrow 0$ results in

$$\frac{d\dot{m}_i}{dz} = \frac{1}{V_i} \frac{dV_i}{dz} \dot{m}_i \quad (5.4)$$

If we let the volumetric rate of a material that is being ablated from a lump be Q_i , the rate of volume reduction of a lump is then simply given by

$$\frac{dV_i}{dt} = -Q_i \quad (5.5)$$

Introducing variation with respect to axial distance, z , to the right-hand side of Eq. (5.5) and noting that $v = dz/dt$ (where v is the velocity of the lump in the pipeline), we obtain

$$\frac{dV_i}{dt} = \frac{dV_i}{dz} \frac{dz}{dt} = -Q_i \Rightarrow \frac{dV_i}{dz} = \frac{-Q_i}{v_i} \quad (5.6)$$

Given that the slurry is comprised of mineral solids, bitumen, and water, the mass flow rate of the slurry at any axial location along the pipeline can be expressed as

$$\dot{m}_s = \dot{m}_m + \dot{m}_b + \dot{m}_w \quad (5.7)$$

The ablated components of the oil sands lumps leave the lumps and become part of the slurry. In other words, the loss of a component due to lump ablation is a gain by the slurry. Each component of the slurry can then be expressed as below:

Mineral solids:

$$\frac{d\dot{m}_m}{dz} = -\sum_{i=1}^N \gamma_{mi} \frac{d\dot{m}_i}{dz} \quad (5.8)$$

Bitumen:

$$\frac{d\dot{m}_b}{dz} = -\sum_{i=1}^N \gamma_{bi} \frac{d\dot{m}_i}{dz} \quad (5.9)$$

Water:

$$\frac{d\dot{m}_w}{dz} = -\sum_{i=1}^N \gamma_{wi} \frac{d\dot{m}_i}{dz} \quad (5.10)$$

It follows from Eqs. (5.4), (5.6), and (5.8) to (5.10) that a mass balance for each individual component of the slurry (i.e., mineral solids, bitumen, and water) on a pipeline segment of infinitesimal length (i.e., $\Delta z \rightarrow 0$) is given for each component by the following equations.

Mineral solids:

$$\frac{d\dot{m}_m}{dz} = \sum_{i=1}^N \frac{\gamma_{mi}}{V_i} \frac{Q_i}{v_i} \dot{m}_i \quad (5.11)$$

Bitumen:

$$\frac{d\dot{m}_b}{dz} = \sum_{i=1}^N \frac{\gamma_{bi}}{V_i} \frac{Q_i}{v_i} \dot{m}_i \quad (5.12)$$

Water:

$$\frac{d\dot{m}_w}{dz} = \sum_{i=1}^N \frac{\gamma_{wi}}{V_i} \frac{Q_i}{v_i} \dot{m}_i \quad (5.13)$$

Here, \dot{m}_m , \dot{m}_b and \dot{m}_w are the mass flow rates for mineral solids, bitumen, and water in the slurry stream, respectively. The quantities γ_{mi} , γ_{bi} , and γ_{wi} are the mass fractions of the mineral solids, bitumen, and water in an i^{th} lump species, respectively. For a given lump, they are constant along the pipeline.

For a given i^{th} lump species, the conservation of mass fractions dictates that for $i = 1$ to N , where N is the number of lump species.

$$\gamma_{mi} + \gamma_{bi} + \gamma_{wi} = 1 \quad (5.14)$$

At the pipeline inlet, $z = 0$, and the initial lump mass flow rate as well as lump size and component mass fractions (i.e., γ_{mi} , γ_{bi} , and γ_{wi}) must be known. Eqs. (5.11) to (5.13) can be integrated along the pipeline to evaluate the mass flow rate of each slurry component at a given pipeline location. However, the quantity Q_i is not known, and a model for the lump ablation rate Q_i must be developed. Clearly, any model for the prediction of Q_i should take into account the temperature profile inside a lump and the shear stress acting on the lump's surface.

Conservation of Thermal Energy

At any given axial location, neglecting heat transfer to the surroundings or internal heat addition due to friction losses, there is a transfer of thermal energy between the lumps and the slurry. Assuming that the flow is steady-state, a thermal energy balance on a differential element of pipe segment of length Δz , if we let $\Delta z \rightarrow 0$, gives

$$\frac{d}{dz} (\dot{m}_s c_{ps} T_s(z)) = - \sum_{i=1}^N \frac{d}{dz} (\dot{m}_i c_{pi} \bar{T}_i(z)) \quad (5.15)$$

where \dot{m}_s and \dot{m}_i are the mass flow rates of the slurry and i^{th} lump species at axial location z , respectively. Here c_{ps} and c_{pi} are the specific heats of the slurry and i^{th} lump species, respectively. T_s is the temperature of the slurry, which is assumed to be uniform across the cross-sectional area of the pipeline, and \bar{T}_i is the volume average temperature of the i^{th} lump species.

The initial condition for Eq. (5.15) is that the slurry temperature, T_s , is the temperature of the added water at the pipeline inlet, and T_i is the dry oil sand feed temperature of the i^{th} lump species. The volume average temperature of the i^{th} lump species, \bar{T}_i , at an axial distance z , is defined as

$$\bar{T}_i(z) = \frac{\int T_i(r, z) dV_i}{\int dV_i} \quad (5.16)$$

where T_i is the temperature of each infinitesimal volume element at a position r within the lump for a given axial location z . If the lumps are assumed to be spherical, Eq. (5.16) results in

$$\bar{T}_i(z) = \frac{\int_0^{R_i} 4\pi T_i(r, z) r^2 dr}{\int_0^{R_i} 4\pi r^2 dr} = \int_0^{R_i} \frac{3T_i(r, z) r^2}{R_i^3} dr \quad (5.17)$$

where R_i is the radius of the i^{th} lump species and $T_i(r, z)$ is the lump temperature at radial location r for a given axial location z .

The temperature profile of a lump is governed by the heat conduction equation. For a lump that is spherical in shape, the heat conduction equation, in spherical coordinates, is

$$\frac{\partial T_i}{\partial t} = \frac{k_i}{\rho_i c_{pi}} \frac{1}{r^2} \left[\frac{\partial}{\partial r} \left(r^2 \frac{\partial T_i}{\partial r} \right) \right] \quad (5.18)$$

where T_i is the lump temperature, which is a function of both radial position r and axial location z (i.e., $T_i = T_i(r, z)$). The term $(k_i/\rho_i c_{pi})$ is the thermal diffusivity of the i^{th} lump species. Here, k_i is the thermal conductivity, ρ_i is the density, and c_{pi} is the specific heat (at constant pressure). As time and distance are related to the velocity of a lump (v_i), by $v_i = dz/dt$, Eq. (5.18) can be transformed to

$$\frac{\partial T_i}{\partial z} = \frac{1}{v_i} \frac{k_i}{\rho_i c_{pi}} \frac{1}{r^2} \left[\frac{\partial}{\partial r} \left(r^2 \frac{\partial T_i}{\partial r} \right) \right] \quad (5.19)$$

The *initial conditions* are:

At $z = 0$ for $0 \leq r \leq R_i$, $T_i =$ oil sand feed temperature for $i = 1$ to N .

The *boundary conditions* are:

For all axial locations z , at $r = 0$, $\partial T_i/\partial r = 0$ for $i = 1$ to N .

A *convective boundary condition* is applied at the surface of the lump, given by

$$h_i (T_{i, \text{surface}} - T_s) = -k_i \left. \frac{\partial T_i}{\partial r} \right|_{r=R_i}$$

there ($T_{i, surface} - T_s$) is the temperature difference between an i^{th} lump species surface and slurry, and h_i is the heat transfer coefficient for the i^{th} lump and can be evaluated from Hines and Maddox (1985, p. 194).

Model for Lump Ablation

In modelling an oil sands lump, it is assumed that the bitumen is the ‘glue’ that holds the lump together. Under an applied shear stress, the bitumen will flow, resulting in material being removed from the lump. The rate at which the bitumen *ablates* or becomes ‘extruded’ from the lump depends on the magnitude of the shear stress applied at the surface of the lump as well as the viscosity of the bitumen. For a sphere, the shear stress is assumed to be applied over an equatorial line. Given that a velocity profile develops over the circular cross-section bordered by the equatorial line, an ablation rate of material from the lump, Q_i , can be obtained if the velocity profile is integrated over the circular area. This results in the following expression for the i^{th} lump:

$$Q_i = 2\pi \int_0^{R_i} u_i(r) r dr$$

where $u_i(r)$ is the extrusion or ablation velocity within a lump as a function of radial position r , and R_i is the radius of the i^{th} lump. Both R_i and $u_i(r)$ are functions of travel distance along the pipeline, Z , since the lump reduces in size as it travels down the pipeline.

The ablation of material from a lump can be visualized as shown in Figure 5.5. Under the applied shear stress, material can be visualized as being extruded from the lump (i.e., ablated off at the rate given by Eq. [5.20]). This extruded material continually breaks off and becomes part of the slurry.

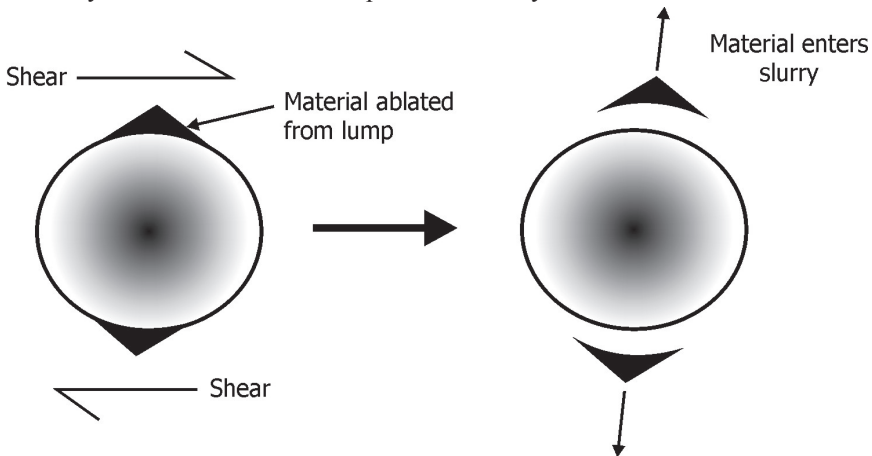


Figure 5.5 Schematic representation of lump losing material to slurry.

For a given axial location along the pipeline, it is assumed that the velocity profile that develops within an oil sands lump obeys Newton's law of viscosity, given by

$$\tau_{bed} = \tau_{lump} = \mu_{bitumen} \frac{du}{dr} \quad (5.21)$$

where τ_{bed} is the shear stress in the moving bed, τ_{lump} is the shear stress that the lump experiences (i.e., the bed shear stress, τ_{bed}), $\mu_{bitumen}$ is the viscosity of the bitumen, and du/dr is the velocity gradient of the flowing bitumen within a lump. The velocity profile of the flowing bitumen in the oil sand lump can be obtained by integrating Eq. (5.21) to yield the following expression:

$$u(r) = \tau_{lump} \int_0^r \frac{dr}{\mu_{bitumen}} \quad (5.22)$$

A temperature gradient can exist within the lump. Therefore, the bitumen viscosity, $\mu_{bitumen}$, is a function of the radial position r , as well as travel distance, and remains inside the integral. Combining Eqs. (5.20) and (5.22) results in the following final expression for Q_i :

$$Q_i = 2\pi\tau_{lump} \int_0^{R_i} \int_0^r \frac{dr}{\mu_{bitumen}} r dr \quad (5.23)$$

From Eq. (5.23), it can be observed that the shear stress acting on a lump, τ_{lump} , is the only quantity left to be determined in order to complete the pipeline lump digestion model. It was evaluated using the Wilson-Shook two-layer model (Gilles, Shook, and Wilson 1991).

Lump Shear Stress

The shear stress that a lump is subjected to is calculated using the concept of a suspension viscosity for the moving bed, where the shear stress is equal to the suspension viscosity multiplied by a shear rate (i.e., Newton's law of viscosity). Using the expression developed by Barnea and Mizrahi (1973) for the viscosity of a concentrated suspension, the shear stress within a bed of material moving along the bottom of a pipe can be expressed as

$$\tau_{bed} = \frac{dw}{dy} \underbrace{\mu_1 \exp \left[\frac{2.66C_{lim}}{1 - C_{lim}} \right]}_{\text{suspension viscosity}} \quad (5.24)$$

where dw/dy is the velocity gradient in the moving bed, μ_1 is the viscosity of water at the prevailing slurry temperature, and C_{lim} is the volume fraction of solids in the moving bed.

The shear rate, dw/dy , and the volumetric fraction of solids in the moving bed, C_{lim} , can be obtained by employing the two-layer model developed by Gilles, Shook, and Wilson (1991). In the two-layer model, pipeline slurry flow is assumed to be composed of two layers. The top layer has a volume fraction of C_1 , while the bottom layer has a volume fraction of $C_1 + C_2$. The volume fraction of the bottom layer or moving bed, C_{lim} (i.e., $C_1 + C_2$), is assumed to be 0.6 (Gilles, Shook, and Wilson 1991). The two-layer model provides an average velocity for each of the upper and lower layers in the pipeline. The lower layer, which contains the larger particles, moves at a slower average velocity than the upper layer.

5.1.3 Comparison of Model to Experimental Measurements

The validity of the pipeline digestion model was tested by comparing predictions of lump digestion to experimental measurements. The measurements were obtained from a study of oil sands slurry flow in a pipeline conducted at the Saskatchewan Research Council's pipeline loop facility (Gilles and Small 1996). Lump digestion experiments consisted of adding a known mass of lumps into the pipeline loop, then straining the lumps out of the system at a specified time and measuring the remaining undigested mass of the lumps. From these tests, it was possible to construct data sets of mass lost from the lumps against time.

Predictions of lump digestion at three slurry temperatures were compared to experimental measurements. Only the plot for a slurry temperature of 30 °C is shown here (Figure 5.6). As can be noted from the figure, the simulation of lump digestion is a fair prediction of the measured data. The comparison provides an indication of the model's overall ability to predict oil sands lump digestion in a pipeline.

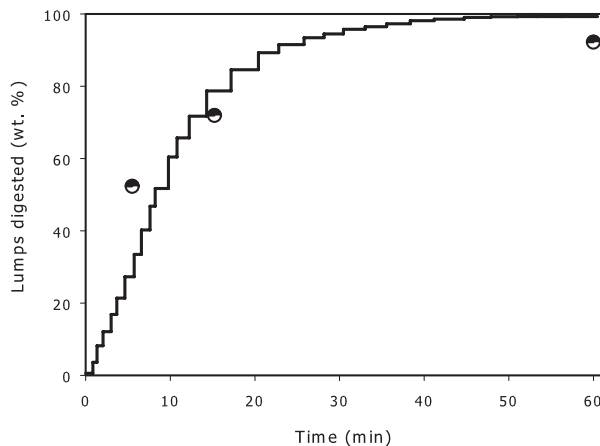


Figure 5.6 Predictions of lump digestion compared to measurements.

5.1.4 Model Parametric Study Predictions

The main objective in developing a model for oil sands lump digestion in a hydrotransport pipeline was to investigate lump digestion (size reduction) in a warm-temperature extraction scenario. Rather than inputting a range of lump sizes, only one size was used in the simulation. In all of the test runs, unless specifically mentioned, the ratio of oil sand feed flow rate to that of water was kept at 2000 kg/950 kg. For fully digested lumps, the discharge density was 1548 kg/m³. The pipeline inner diameter was 71 cm (28 in). At the inlet to the hydrotransport pipeline, the initial temperature of the lumps was 0 °C.

Figure 5.7 is a plot showing the variation in lump digestion with distance travelled along a pipeline (up to 4 km) for a lump of an initial size of 10 cm (4 in) for different slurry delivery temperatures in the range of 20 °C to 50 °C. The slurry water temperature was varied to achieve the desired temperature at the pipeline discharge. In a commercial operation, with a maximum lump size of 10 cm (4 in), one would normally encounter lumps smaller than the size used in this simulation. Such a lump size distribution would lead to a conservative estimate of lump digestion along the pipeline. Clearly, Figure 5.7 shows that lump digestion is strongly dependent on the slurry discharge temperature. At a 50 °C slurry discharge temperature, nearly all the lumps have been digested. At a 20 °C discharge temperature, however, nearly 50 % of the lumps remain undigested after travelling a distance of 4 km along the pipeline (a lump is considered to be digested when it is 1 mm in diameter). The strong dependence of lump digestion on temperature is simply due to the fact that bitumen viscosity is strongly dependent on temperature.

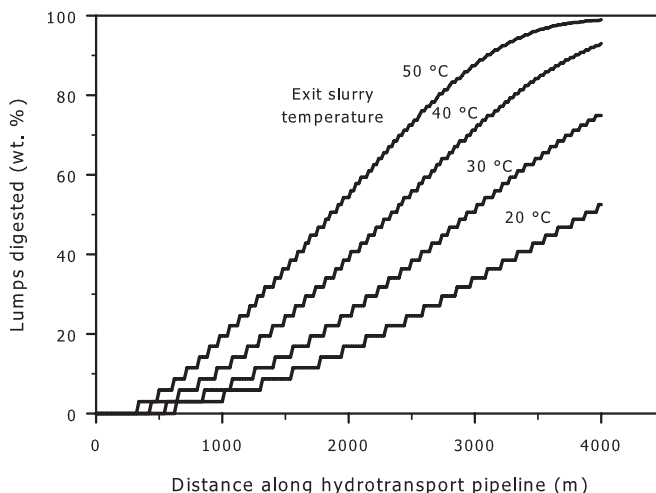


Figure 5.7 Effect of slurry temperature on lump digestion.

For a slurry discharge temperature of 40 °C, the effect of initial lump diameter is shown in Figure 5.8 for lump diameters in the range of 5 cm to 15 cm (2 to 6 in). The smaller lumps digest much faster than the larger lumps. This is because a given mass of oil sands ore in the form of smaller lumps will digest much faster than the same mass of ore in the form of larger lumps due to the larger surface area of the former. The plots of Figure 5.8 would indicate that introducing smaller lumps into the hydrotransport pipeline would require a shorter pipeline length. From an operational point of view, initial lump size and temperature and slurry discharge temperature are the major parameters dictating the required pipeline length for given lump digestion.

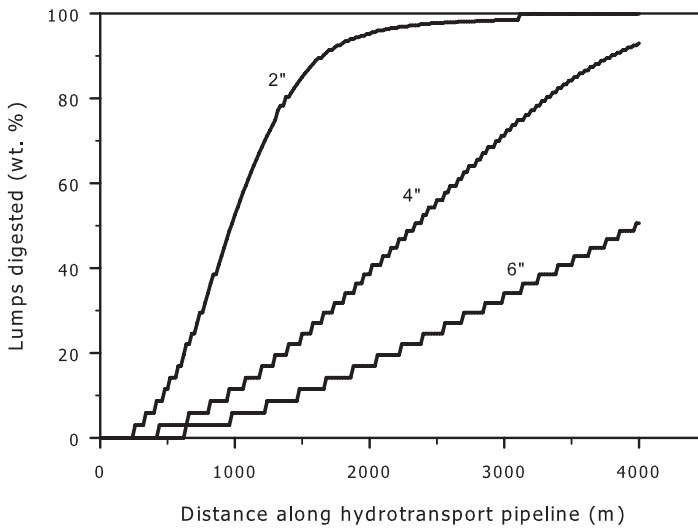


Figure 5.8 Effect of initial oil sands lump diameter on lump digestion.

The effect of the slurry density for given dry oil sand feed is shown in Figure 5.9 for an initial lump diameter of 10 cm (4 in) and a discharge slurry temperature of 40 °C. In this case, the feed flow rate of dry oil sand to that of water was 2000 kg/1150 kg, with a slurry discharge density of 1463 kg/m³. In other words, the water flow rate was increased from 950 kg/s to 1150 kg/s, while the dry oil sands feed was kept the same. Two important competing factors influence lump digestion. At the lower water flow rate of 950 kg/s, the total slurry flow rate is smaller than that at the higher water flow rate, leading to a longer residence time in the pipeline, albeit, with a higher shear rate in the moving bed. Figure 5.9 indicates that the digestion rate is slightly better at the higher slurry discharge density. Although a slurry discharge density of about 1550 kg/m³ is used in commercial operations, other considerations, relating to operational costs and pipeline integrity, are taken into account.

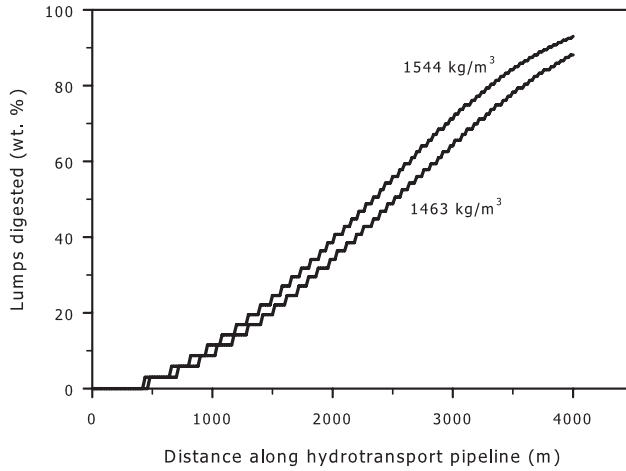


Figure 5.9 Effect of slurry density on lump digestion.

The effect of the pipeline diameter on lump digestion is shown in Figure 5.10. For the sake of comparison, the average velocity and the slurry density are kept the same. Figure 5.10 shows that the smaller pipeline diameter provides a faster lump digestion rate. In general terms, this can be attributed to higher energy dissipation per unit mass in the smaller diameter pipe, which leads to higher interparticle shear stresses and thus results in faster digestion. The pipe diameter size is dictated by the oil sands train capacity, capital and operating costs, operation safety, and pipeline availability.

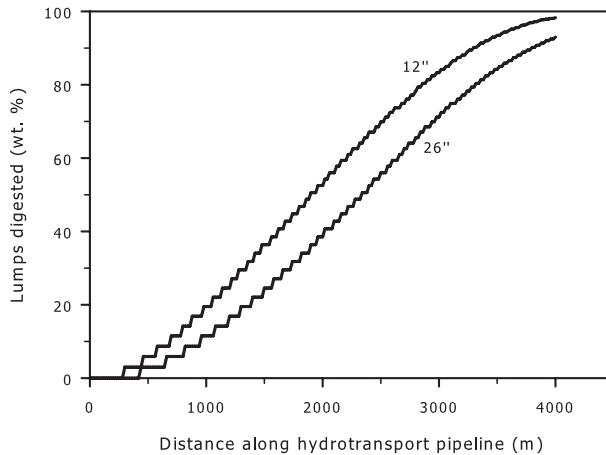


Figure 5.10 Effect of pipeline inner diameter on lump digestion.

5.2 Bitumen Liberation

In the previous section, we discussed oil sands lump size reduction using ablation concepts. The next essential step is the liberation of bitumen from the sand grains themselves and the subsequent attachment of the liberated bitumen to air that is present in the hydrotransport pipeline. A detailed analysis of bitumen liberation and aeration is given in Chapter 6. Here, we provide some brief observations.

Due to surface forces at the bitumen-water interface, the bitumen continuum surrounding the sand grains is broken (Takamura and Wallace 1988; Basu, Nandakumar, and Masliyah 1996). If the digestive slurry chemistry is favourable (e.g., low electrolyte concentration and high pH), the broken bitumen does not adhere to the sand grain surface, but rather recedes from it, forming a bitumen globule that eventually disengages from the sand grain (Moran 2001).

Chemical additives, pH, electrolyte and clay content in the digestive slurry, slurry temperature, and shear rate all play an important role in the liberation of bitumen from the sand grains. For example, the addition of NaOH raises the slurry pH and allows for the liberation of the natural surfactants in the bitumen, thereby decreasing the interfacial tension of the bitumen-water interface, increasing the repulsion between bitumen and silica, and decreasing the adhesion force between silica and bitumen (Liu, Xu, and Masliyah 2003; 2005a, 2005b). As well, moderate addition of NaOH decreases the wettability between the bitumen and the sand grains, allowing the bitumen to easily disengage from the sand grains (Bowman 1967; Baptista and Bowman 1969; Takamura and Chow 1983; Schramm, Smith, and Stone 1984).

A higher water temperature lowers the bitumen's viscosity, thereby allowing for quick bitumen recession from the sand grains. Clearly, applying shear to the digestive slurry aids in the detachment of the recessed bitumen from the sand grains. Model systems illustrating the effect of slurry pH and temperature are described below. A model system of bitumen recession from a microscope slide was investigated by Basu, Nandakumar, and Masliyah (1996, 1998, 2000) and by Basu et al. (1998; 2004). A microscope slide was coated with a bitumen film in the form of a disc. The disc was then immersed in a water bath of a given temperature and pH. The recession of the bitumen film to form a spherical cap was recorded using a video camera. Figure 5.11 shows the rate of bitumen film recession at a pH of 11 at two different water temperatures. Clearly, the bitumen droplet recession is complete at a much shorter time at a higher temperature. It is evident from Figure 5.11 that the temperature of the processing water plays a very important role in the time required for bitumen recession on a microscope slide.

Walker (2006) conducted studies on bitumen displacement from a microscope slide. A bitumen-coated microscope slide was placed in flowing water under controlled conditions. The bitumen recession rate was measured using the degree of darkness of the microscope slide as bitumen receded from the slide surface, an approach developed at Natural Resources Canada's CanmetENERGY facility (Friesen, Dabros, and Kwong 2004). Figure 5.12 shows that the time required for 50 % bitumen recession from the coated slide is much dependent on the water temperature—it is one order of

magnitude higher when the temperature is increased from 35 °C to 60 °C. The tests were conducted in industrial plant recycle process water with a pH of ~ 8.2. A study on the effect of temperature on bitumen liberation was carried out by Luthra et al. using a similar approach (2004).

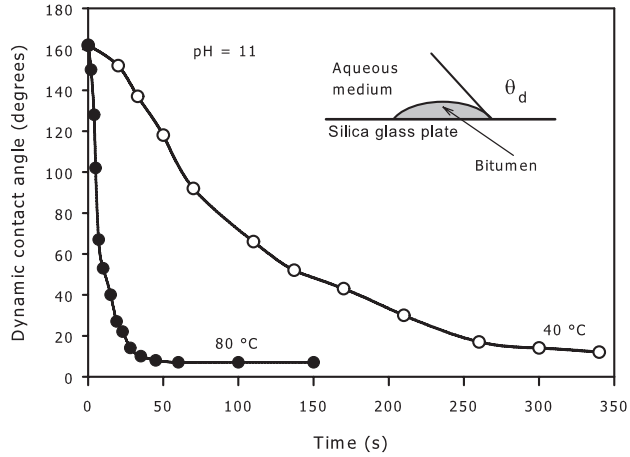


Figure 5.11 Recession of a bitumen film on a microscope slide, at pH 11, showing the effect of water temperature.

Source: Basu, Nandakumar, and Masliyah (1996).

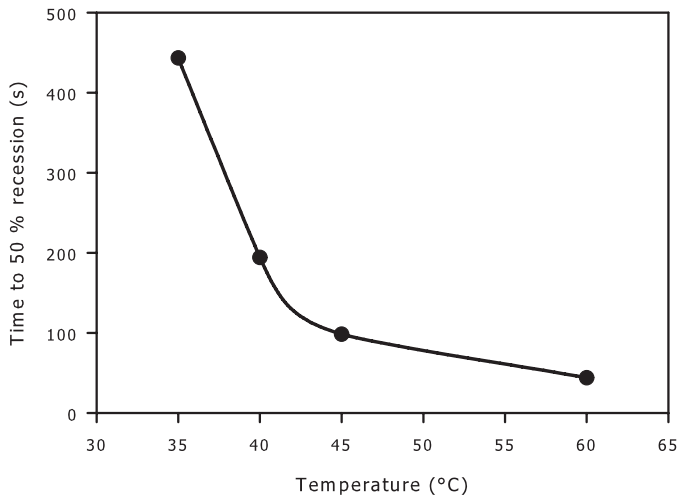


Figure 5.12 Recession of a bitumen film on a microscope slide, at pH 11, showing the effect of water temperature.

Source: Basu, Nandakumar, and Masliyah (1996).

Figure 5.13 compares the time required for 50 % recession to take place in an industrial plant recycle process water system and in a deionized water system (at varying temperatures). It also shows one test in which deionized water was doped with sodium, chloride, sulphate, bicarbonate, calcium, and magnesium ions at levels found in industrial plant recycle process water. This is referred to as *simulated process water*. The ‘recipe’ for this simulated process water is shown in Table 5.1. It can be noted that, although the industrial plant recycle water contains significant concentrations of calcium and magnesium ions, its overall performance is better than that of the deionized water, and ionic levels are comparable between the two. The pH of the deionized water was adjusted to 8.2 to match the pH of the industrial process water. The difference in the recession rate between the actual industrial recycle process water and the simulated process water is attributed to the presence of natural surfactants and bicarbonates. Naturally occurring surfactants have been shown to favourably influence the extraction process by suppressing the negative effects of calcium and magnesium on the formation of three-phase contact lines and on air-bitumen attachment (Schramm and Smith 1987). It is noted from the trends that the time required for 50 % recession for all water chemistries is roughly equivalent at low temperatures. This is because, as temperature decreases, the process of recession becomes dependent on bitumen viscosity, and the effects of water chemistry become less significant.

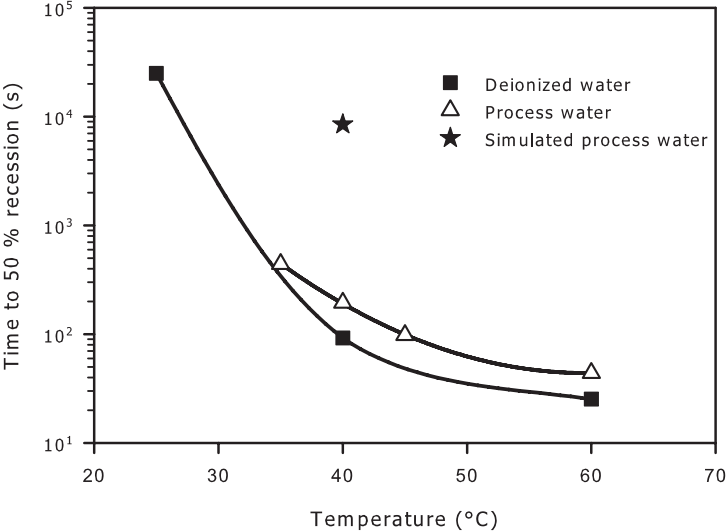


Figure 5.13 Comparison of industrial plant recycle process water with deionized water system.

Table 5.1 Simulated industrial recycle process water electrolyte concentrations

Component	meq/L
NaCl	9.0
Na ₂ SO ₄	4.2
NaHCO ₃	12.5
CaCl ₂ ·2H ₂ O	2.2
MgCl ₂ ·6H ₂ O	1.6

Once the bitumen disengages from the individual sand grains in the form of bitumen ‘entities,’ it is desirable for the entities to agglomerate, forming larger ones that can easily attach to air bubbles. The digestive slurry’s chemistry should be such that the disengaged bitumen entities do not agglomerate with the fine solids, thereby increasing their density and preventing them from floating to the top of gravity separation vessels. The factors that affect bitumen attachment to air bubbles or fine solids are determined by the type and quantity of fine solids in the oil sands ore and by the digestive slurry pH and its ions concentrations (Moran, Yeung, and Masliyah 2000). The presence of high amounts of Ca⁺⁺ and Mg⁺⁺ ions tends to cause the formation of fines-fines and bitumen-fines agglomerates (Takamura and Wallace 1987, 1988). There is little data available on the effects of digestive slurry composition on bitumen-air interaction. As well, it is not known when bitumen-air attachment takes place—whether it occurs during bitumen disengagement from a sand grain or after it has already disengaged. It should be recalled here that, as the density of bitumen is very close to that of water, bitumen-air attachment plays an important role in increasing the buoyancy needed for a bitumen entity to float in the digestive slurry under gravity.

After the digestion step in a hydrotransport pipeline, the slurry is diluted with water and introduced into a gravity separation vessel. The separation vessel is referred to as the *primary separation vessel* (PSV) by Syncrude, *sep cell* by Suncor, and *primary separation cell* (PSC) by others. In the gravity separation vessel, the bitumen entities, along with their associated air, float to the top of the separation vessel to form bitumen froth (about 60 % bitumen, 30 % water, and 10 % solids, by weight). The coarse solids, water, and some fugitive bitumen exit through the bottom of the vessel. A middlings stream (with a density of about 1200 kg/m³) is normally withdrawn from the vessel. Finally, flotation cells are used to recover bitumen from the middlings stream of the gravity separation vessel. The bitumen froth produced in the gravity separation vessel is first deaerated. In order to allow for the separation of the water and solids from the bitumen froth, the deaerated froth is diluted with a solvent to reduce its density and viscosity. In naphthenic froth treatment, inclined plate settlers, cyclones, or centrifuges are used to affect the separation of the water and solids from the hydrocarbon phase. When a paraffinic solvent is used, both at low and high temperature operations, asphaltenes are precipitated and they aid in removing the emulsified water and fine solids from the hydrocarbon phase (Gray, Xu, and Masliyah 2009).

5.3 References

- Baptista, M.V., and C.W. Bowman. 1969. The flotation mechanism of solids from the Athabasca oil sand. In *Proceedings of the 19th Canadian Chemical Engineering Conference*. Edmonton, Alberta, Canada: Canadian Society for Chemical Engineering.
- Barnea, E., and J. Mizrahi. 1973. A generalized approach to the fluid dynamics of particulate systems. Part 1: General correlation for fluidization and sedimentation in solid multiparticle systems. *The Chemical Engineering Journal* 5 (2): 171–189.
- Basu, S., W.C. Kanda, K. Nandakumar, and J.H. Masliyah. 1998. Effect of hydrophobic and hydrophilic clays on bitumen displacement by water on a glass surface. *Industrial & Engineering Chemistry Research* 37 (3): 959–965.
- Basu, S., K. Nandakumar, S. Lawrence, and J.H. Masliyah. 2004. Effect of calcium ion and montmorillonite clay on bitumen displacement by water on a glass surface. *Fuel* 83 (1): 17–22.
- Basu, S., K. Nandakumar, and J.H. Masliyah. 1996. A study of oil displacement on model surfaces. *Journal of Colloid and Interface Science* 182 (1): 82–94. *With erratum in Journal of Colloid and Interface Science* 196, 324.
- . 1998. A visual study of high grade oil sand disintegration process. *Journal of Colloid and Interface Science* 205 (1): 201–203.
- . 2000. A study on daughter droplets formation in bitumen/glass/water contact line displacement due to instability. *Fuel* 79 (7): 837–841.
- Bowman, C.W. 1967. Molecular and interfacial properties of Athabasca tar sands. In *Proceedings of the 7th World Petroleum Congress*. Mexico City, Mexico.
- COST. 1999. Lecture notes, Certificate in Oil Sands Technology, University Extension Centre, University of Alberta, Masliyah, J., B. Bara
- Fine Tailings Fundamentals Consortium (FTFC). 1995. *Advances in oil sands tailings research*. Edmonton: Alberta Department of Energy, Oil Sands Research Division.
- Friesen, W.I., T. Dabros, and T. Kwong. 2004. A bench-scale study of conditioning behaviour in oil sands slurries. *Canadian Journal of Chemical Engineering* 82 (4): 743–751.
- Fuhr, B., C. Powter, D. Taplin, and D. Rose. 1993. Catalogue of technologies for reducing the environmental impact of fine tails from oil sand processing. Paper read at Oil Sands: Our Petroleum Future Conference, Apr. 4–7, at Edmonton, Alberta, Canada.
- Gilles, R.G., C.A. Shook, and K.C. Wilson. 1991. An improved two layer model for horizontal slurry pipeline flow. *Canadian Journal of Chemical Engineering* 69 (11): 173–178.

- Gilles, R.G., and M. Small. 1996. Oil sand slurry pipeline studies. Phase 1: Pipeline hydraulics. Phase 2: Lump dispersion. Saskatoon: Saskatchewan Research Council, Process Development Division.
- Gray, M., Z. Xu, and J. Masliyah. 2009. Physics in the oil sands of Alberta. *Physics Today*, March, 31–35. *See also* Timblin, L.O. Jr., G. Stiles, E. Wood, M. Gray, Z. Xu, and J. Masliyah. 2009. Efficiency and environmental effects in the oil sands of Alberta. *Physics Today*, December, 8–9.
- Hines, A.L., and R.N. Maddox. 1985. *Mass transfer: Fundamentals and applications*. Englewood Cliffs: Prentice-Hall.
- Law, D.H.-S., J.H. Masliyah, and K. Nandakumar. 1987. Ablation of frozen oil sands under the influence of turbulent axisymmetric jets. *AOSTRA Journal of Research* 3: 177–182
- Liu, J., Z. Xu, and J.H. Masliyah. 2003. Studies on bitumen-silica interaction in aqueous solutions by atomic force microscopy. *Langmuir* 19 (9): 3911–3920.
- . 2005a. Interaction forces in bitumen extraction from oil sands. *Journal of Colloid and Interface Science* 287 (2): 507–520.
- . 2005b. Colloidal forces between bitumen surfaces in aqueous solutions measured with atomic force microscope. *Colloids and Surfaces A: Physicochemical and Engineering Aspects* 260 (1–3): 217–228.
- Long, J., Z. Xu, and J.H. Masliyah. 2005. On the role of temperature in oil sands processing. *Energy & Fuels* 19 (4): 1440–1446.
- Luthra, M., R. Lopetinsky, S. Sanders, K. Nandakumar, and J.H. Masliyah. 2004. A new device to determine bitumen extraction from oil sands. *Canadian Journal of Chemical Engineering* 82 (4): 752–762
- Moran, K.L. 2001. Micro-mechanics of emulsion drops. PhD diss., Department of Chemical and Materials Engineering, University of Alberta, Edmonton.
- Moran, K.L., A. Yeung, and J.H. Masliyah. 2000. Factors affecting the aeration of small bitumen droplets. *Canadian Journal of Chemical Engineering* 78 (4): 625–634.
- Schramm, L.L., and R.G. Smith. 1987. Two Classes of Anionic Surfactants and Their Significance in Hot Water Processing of Oil Sands. *Canadian Journal of Chemical Engineering* 65 (5): 799–811.
- Schramm, L.L., R.G. Smith, and J.A. Stone. 1984. A surface-tension method for the determination of anionic surfactants in hot water processing of Athabasca oil sands. *Colloids and Surfaces* 11 (3-4): 247–263.
- Takamura, K., and R.S. Chow. 1983. A mechanism for initiation of bitumen displacement from oil sands. *Journal of Canadian Petroleum Technology* 22: 22–30.

- Takamura, K., and D. Wallace. 1987. Experimental and theoretical studies of the hot water processability of different grades of Athabasca oil sands. In *Flocculation in biotechnology and separation systems*, ed. Y. A. Attia. Amsterdam: Elsevier.
- . 1988. The Physical chemistry of the hot water process. *Journal of Canadian Petroleum Technology* 27 (6): 98–106.
- Walker, J.R. 2006. The recession of bitumen from a silica surface under shear flow. Master's diss., Department of Chemical and Materials Engineering, University of Alberta, Edmonton.

Chapter 6

Bitumen Recovery

To understand the bitumen recovery process, let us briefly review the elementary steps in water-based bitumen extraction. For effective bitumen recovery from the oil sand–water slurry, the oil sand matrix must be disintegrated and the bitumen separated from the sand grains. This latter step is called *bitumen liberation*. Individual droplets of liberated bitumen collide with each other, and some of the collisions cause the droplets to fuse or coalesce into bigger ones. Simultaneously, the bitumen droplets collide with dispersed air bubbles. Some of these collisions result in *bitumen aeration*, i.e., the formation of air bubble–bitumen droplet aggregates. The aggregates have sufficient buoyancy to float to the surface of the separation vessel and form a froth. The rising velocity of the air-bitumen aggregates depends on their size and density (or air-to-bitumen volume ratio) and on the viscosity of the medium in which they rise. After the coarse solids have settled, this medium is composed of water, suspended fine solid particles (mostly clays), and fugitive bitumen (mostly in the form of fine droplets), and is referred to as *middlings* in the oil sands industry.

All of these elementary steps (liberation, coalescence, aeration, and flotation) are necessary for recovering bitumen. Anything that hinders any of these steps will have a negative impact on the overall bitumen recovery process. The water chemistry, especially the pH and the divalent ion content, and, to a lesser extent, the total salt content, has a profound effect on all of the elementary steps in bitumen recovery.

6.1 Bitumen Liberation

Bitumen liberation, defined as the separation or detachment of bitumen from sand grains in water, is an essential step in bitumen recovery. As shown in Figure 6.1, the bitumen liberation process can be broken down into two subprocesses: bitumen recession on the sand surface in water, and bitumen separation from the sand grain. During bitumen recession, the change in the bitumen-water interface as the bitumen forms droplets can be considered negligible. At the same time, the bitumen-sand

interface ($\gamma_{B/S}$) is replaced by a sand-water interface ($\gamma_{S/W}$). The energy change during bitumen recession is then given by

$$\frac{\Delta G}{\Delta A} = \gamma_{S/W} - \gamma_{B/S} \quad (6.1)$$

To quantify the free energy change associated with bitumen recession from a sand grain in water using Eq. (6.1), we must determine the interfacial tension of sand-water and of bitumen-sand, both of which cannot be measured directly. However, the difference between these two interfacial tensions is linked with the interfacial tension of bitumen-water (which can be measured directly) and with the contact angle (θ) by Young's equation,

$$\gamma_{B/S} - \gamma_{S/W} = \gamma_{B/W} \cos \theta \quad (6.2)$$

where θ is measured through the aqueous phase. Inserting Eq. (6.2) into Eq. (6.1) leads to

$$\frac{\Delta G}{\Delta A} = -\gamma_{B/W} \cos \theta \quad (6.3)$$

Since $\gamma_{B/W}$ is greater than zero, Eq. (6.3) shows that the critical condition for bitumen recession from a sand grain in water is a contact angle of less than 90° . Clearly, the hydrophobicity of solids plays a critical role in bitumen recession. The condition of a contact angle less than 90° for bitumen recession suggests that the interaction between the sand and water must be stronger than the interaction between the sand and bitumen, i.e., $\gamma_{B/S} > \gamma_{S/W}$. Eq. (6.3) indicates that increasing the aqueous pH is not favourable for bitumen liberation, as it reduces the bitumen-water interfacial tension. However, it is important to note that increasing aqueous pH can often increase the wettability of the sand (i.e., reduce contact angle) by increasing the hydrolysis of the sand surfaces. It can also lead to an increase in the production of natural surfactants, which reduces the bitumen-water interfacial tension. The smaller the θ , the more negative the $\Delta G/\Delta A$, and hence, the easier it is for bitumen to recess.

Following bitumen recession to a critical shape, bitumen droplets will detach from the sand grain, as shown in Figure 6.1B. In this process, the contact of bitumen with sand is changed to the contact of bitumen with water and the contact of sand with water. The interfacial energy associated with bitumen separation is then given by

$$\frac{\Delta G}{\Delta A} = \gamma_{S/W} + \gamma_{B/W} - \gamma_{B/S} \quad (6.4)$$

Inserting Young's equation into Eq. (6.4) leads to

$$\frac{\Delta G}{\Delta A} = \gamma_{B/W} (1 - \cos \theta) \geq 0 \quad (6.5)$$

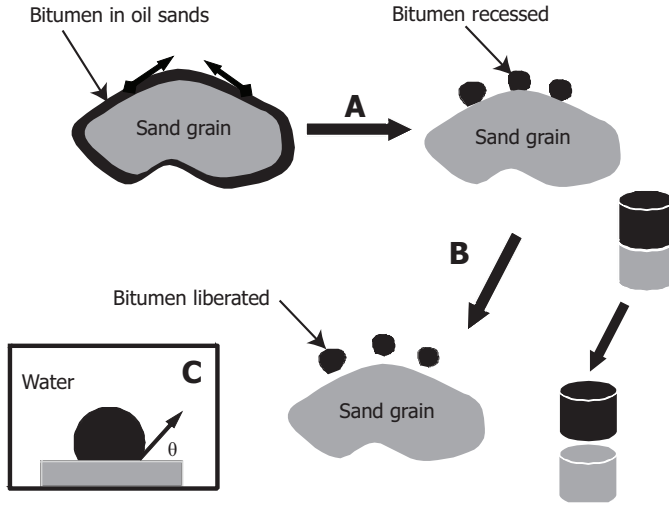


Figure 6.1 Bitumen liberation from a sand grain in two subprocesses: bitumen recession (A) and bitumen detachment (B), which are determined by the aqueous contact angle (θ) of bitumen on a sand grain (C).

Eq. (6.5) shows that bitumen detachment from a sand grain is thermodynamically unfavourable. For bitumen liberation to occur under static conditions, sand grains must be completely hydrophilic, i.e., they must have a contact angle of zero, regardless of the bitumen-water interfacial tension. Since a lower bitumen-water interfacial tension corresponds to a smaller positive free energy gain, increasing the pH to reduce the bitumen-water interfacial tension is expected to facilitate bitumen liberation. Eq. (6.5) also illustrates that, for bitumen to detach from sand grains, mechanical energy (such as fluid drag force, mechanical inertia force, and/or buoyancy force of the aerated bitumen) is required in order to compensate for the interfacial energy gain. In other words, bitumen liberation from sand grains arises mainly from hydrodynamic forces.

It is evident that the wettability of sands, measured by contact angle, plays a critical role in bitumen recession and separation. Based on Young's equation,

$$\cos \theta = \frac{\gamma_{B/S} - \gamma_{S/W}}{\gamma_{B/W}} \quad (6.6)$$

we see that in order to reduce the contact angle (increase $\cos \theta$), and hence, improve bitumen liberation, we must reduce the bitumen-water interfacial tension ($\gamma_{B/W}$) and increase $\gamma_{B/S} - \gamma_{S/W}$, i.e., increase the bitumen-sand interfacial tension and/or reduce the solid-water interfacial tension. In general, the bitumen-solid interfacial tension cannot be easily changed in operation, while the exposure of sand to water upon bitumen recession would allow for the sand-water interfacial properties to be controlled.

Increasing pH often reduces the sand-water interfacial tension, as it enhances hydrolysis and increases the charge of the sand surface, making the sand more hydrophilic at alkaline pH. In Chapter 4, we saw that the bitumen-water interfacial tension decreases with increasing aqueous pH (Figure 4.57). We can see that increasing the pH reduces contact angle, and hence is beneficial for bitumen liberation.

Basu, Nandakumar, and Masliyah examined the aqueous contact angle of bitumen on a glass slide as a function of pH (1996). As shown in Figure 6.2, the contact angle is less than 90° over the entire pH range of 2 to 11 studied, and decreases with increasing aqueous-phase pH. This finding confirms that a high pH is beneficial for bitumen liberation. It is interesting to note that increasing the temperature from 40 °C to 80 °C had little effect on contact angle. It is believed that, at 40 °C, bitumen is already fairly fluid-like, so that the natural surfactant transfer from the bulk bitumen to the bitumen-aqueous interface and bitumen globule formation were not affected over the time span of the experiments.

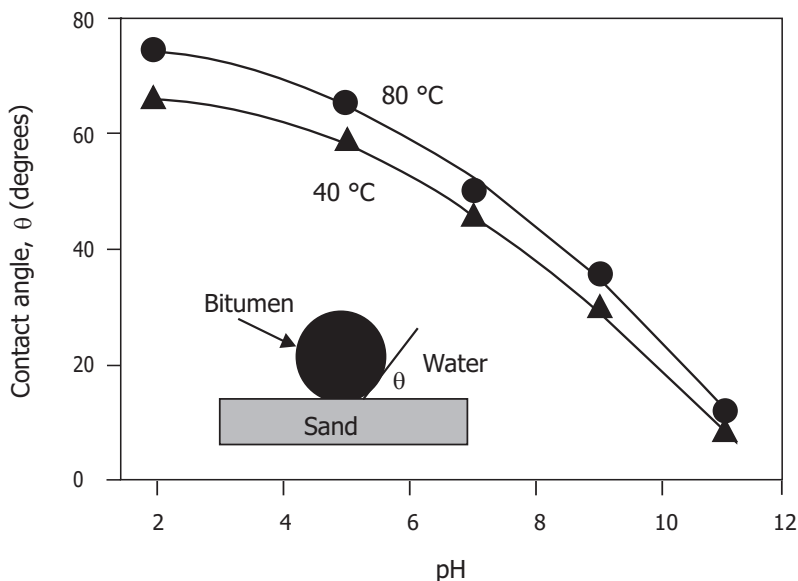


Figure 6.2 Aqueous contact angle of bitumen on glass (as model sand) surface as a function of pH at two different temperatures.

It is important to distinguish the contact angle of water in two different systems: water-solid-bitumen and water-solid-air. The same contact angle value in these two systems does not indicate the same hydrophobicity of the solids. In other words, for a given solid, the contact angles measured in these two systems are often very different. Readers should be aware of this when interpreting contact angle values.

From a molecular point of view, increasing the pH helps the ionization and transfer of natural surfactants from the bulk bitumen to the interface and then into the aqueous phase. High pH also enhances the hydrolysis ($\text{SiOSi} + \text{H}_2\text{O} \rightarrow 2\text{SiOH}$) and

charging ($\text{SiOH} + \text{OH}^- \rightarrow \text{SiO}^- + \text{H}_2\text{O}$) of the sand-water interface, making the sand more hydrophilic, and hence, is conducive to bitumen liberation. The effect of pH on bitumen liberation is summarized in Figure 6.3.

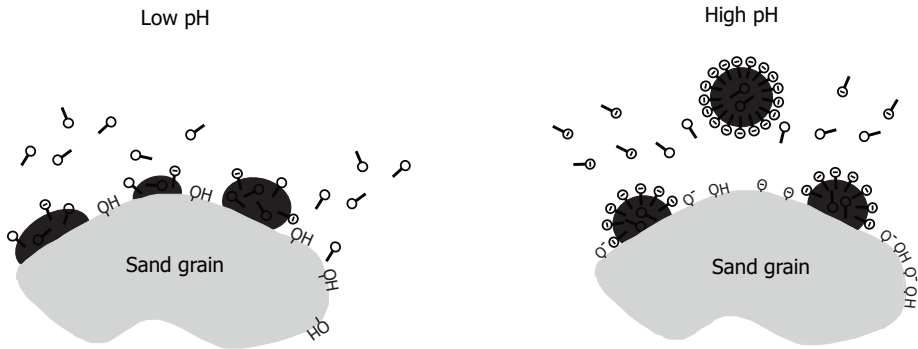


Figure 6.3 Effect of pH on bitumen liberation from a sand grain. At low pH, only a fraction of natural surfactant is extracted to the bitumen-water interface, and the bitumen-water interfacial tension is relatively high. The sand surface is less hydrolyzed with more siloxane oxygens (SiOSi), and hence, is more hydrophobic or less hydrophilic, leading to a high contact angle and less potential for bitumen liberation. At high pH, a large amount of natural surfactant is extracted to the bitumen-water interface and charged, reducing bitumen-water interfacial tension, while the sand surface is highly hydrolyzed to create mostly hydroxyl groups ($-\text{OH}$) and negatively charged sites ($-\text{O}^-$), leading to a small contact angle and helping the bitumen to dislodge from the sand grain.

The important role of the wettability of sands in bitumen liberation is clearly reflected by the tremendous difficulties encountered during the processing of weathered ores (Ren et al. 2009a). It was found that the weathering of oil sands ores led to a significant reduction in water wettability (an increase in the contact angle of water on solids from 42° to 65°) due to the contamination of solids by toluene-insoluble hydrocarbons on solid surfaces. Direct force measurements using an atomic-force microscope showed a corresponding increase in the adhesion force between bitumen and silica spheres in process water upon weathering of bitumen-coated sand grains, indicating the difficulties involved in liberating bitumen from contaminated hydrophobic solids. Poor liberation of bitumen from a weathered sand surface was confirmed experimentally by bitumen recession experiments using bitumen-coated glass slides with and without artificial weathering (Ren et al. 2009b). Slow bitumen liberation following artificial weathering was found to be partially responsible for the poor processability of weathered ores, leading to a low bitumen recovery and poor froth quality. It is interesting to note that hot-water washing (at temperatures above 65°C) was able to restore the wettability of contaminated solids and hence improve the processability of weathered ores, further justifying the use of hot water in industrial oil sands extraction operations to ensure a robust processing condition. A detailed

analysis on the effect of ore weathering on the wettability of solids and its role in ore processability will be provided in Section 6.4.1.

In view of the observed significant role of surfactants, water chemistry is expected to influence bitumen liberation, as it affects the soluble surfactant concentration. A recent study using atomic force microscopy showed a significant increase in adhesion force between a silica particle and bitumen in the presence of calcium and magnesium cations (Zhao et al. 2006). The presence of surfactants was found to alleviate the negative impact of divalent cations on bitumen liberation. A further study found that there was strong adhesion between bitumen and silica sand in simulated process water with no bicarbonate addition, while the addition of bicarbonate to the simulated process water was capable of reducing the adhesion more than tenfold, suggesting that bitumen liberation is much easier in the presence than in the absence of bicarbonate (Zhao et al. 2009). Bicarbonate is believed to scavenge calcium ions, so that the natural surfactant from bitumen remains effective, reducing the bitumen-water interfacial tension (as illustrated in Example 4.4 of Chapter 4), while the sand surface remains hydrophilic by eliminating calcium cation bridging through scavenging of calcium ions by bicarbonate. Bicarbonate addition also increases the pH of the slurry, which also facilitates bitumen liberation. It should be noted that thermodynamic analysis provides only the direction of liberation. To accurately predict the liberation process, one must consider the hydrodynamic conditions under which it occurs.

6.2 Bitumen Aeration

Bitumen aeration, the process of bitumen attachment to air bubbles, is another key step in bitumen recovery. The density of bitumen is similar to that of water. After liberation, bitumen droplets would remain suspended in the slurry if they were not aerated. Aeration reduces the apparent density of the bitumen-air mixture so that it is much lower than that of the separation medium, which causes the aerated bitumen to float to the top of the slurry in the separation vessel, where it can be recovered as a bitumen-rich froth. Bitumen aeration can occur in either hydrotransport slurry pipelines or flotation cells. In some cases, aeration of bitumen has been found to assist in bitumen liberation (Lelinski et al. 2004).

The strength of bitumen–air bubble attachment can be conveniently analyzed in terms of interfacial energies. In bitumen–air bubble attachment, described by A and C in Figure 6.4, the free energy change associated with the attachment is given by

$$\frac{\Delta G}{\Delta A} = \gamma_{B/A} - (\gamma_{B/W} + \gamma_{A/W}) \quad (6.7)$$

Young's equation for the system, on the other hand (Figure 6.4 D), is given by

$$\cos \theta = \frac{\gamma_{B/A} - \gamma_{B/W}}{\gamma_{A/W}} \quad (6.8)$$

where subscripts B , A , and W represent bitumen, air, and water, respectively. Replacing $(\gamma_{B/A} - \gamma_{B/W})$ in Eq. (6.7) with Eq. (6.8) leads to

$$\frac{\Delta G}{\Delta A} = \gamma_{A/W}(\cos \theta - 1) \quad (6.9)$$

Clearly, when the contact angle θ is greater than zero, $\Delta G/\Delta A$ is less than zero, i.e., bitumen–air bubble attachment is thermodynamically spontaneous. Eq. (6.9) shows that the larger the contact angle, the more negative the $\Delta G/\Delta A$, and hence, the more favourable it is for bitumen to attach to air bubbles.

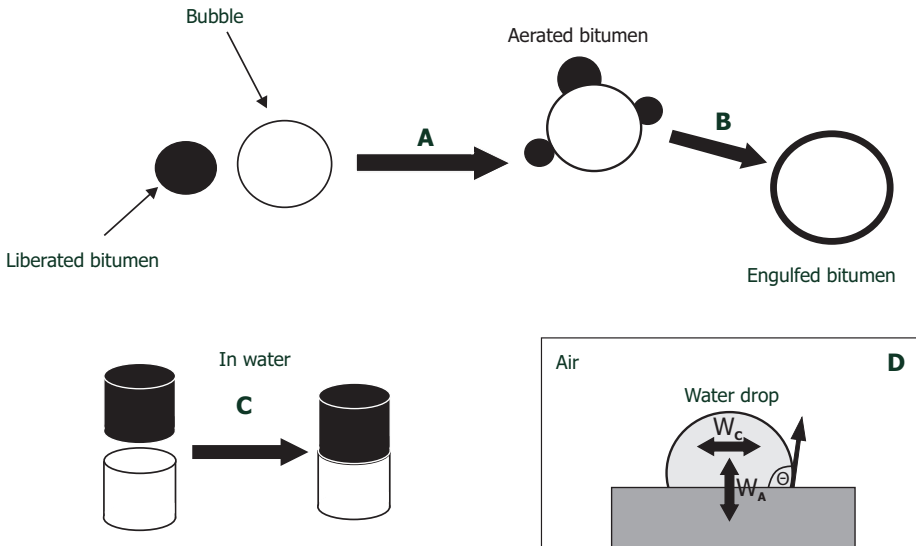


Figure 6.4 Schematic illustration of bitumen attachment to an air bubble (A) and subsequent engulfment (B) on the air bubble. The attachment process, simplified in C, is described by the equilibrium contact angle of water on bitumen (D).

The contact angle of water on bitumen as a function of pH, measured with the captive bubble method (Adamson and Gast 1997), is shown in Figure 6.5. The contact angle measured as such is more akin to a receding contact angle, indicating that equilibrium is reached by water receding from the bitumen surface as the air bubble advances. This process resembles the process of air bubbles attaching to bitumen, as encountered in flotation. It is interesting to note that increasing pH decreases the contact angle of water on bitumen, indicating that higher pH provides a less favourable condition for air bubble attachment to bitumen, as shown by the less-negative value of $\Delta G/\Delta A$ in Eq. (6.9). At pH above 11, the bitumen-coated bubble floats away from the bitumen surfaces, illustrating two important phenomena: i) bitumen spreads on an air bubble upon contact, and ii) the buoyancy force of a bubble is able to break the bitumen-bitumen contact, possibly due to a very low bitumen-water interfacial tension. Clearly, lower pH is more favourable for bitumen aeration and flotation.

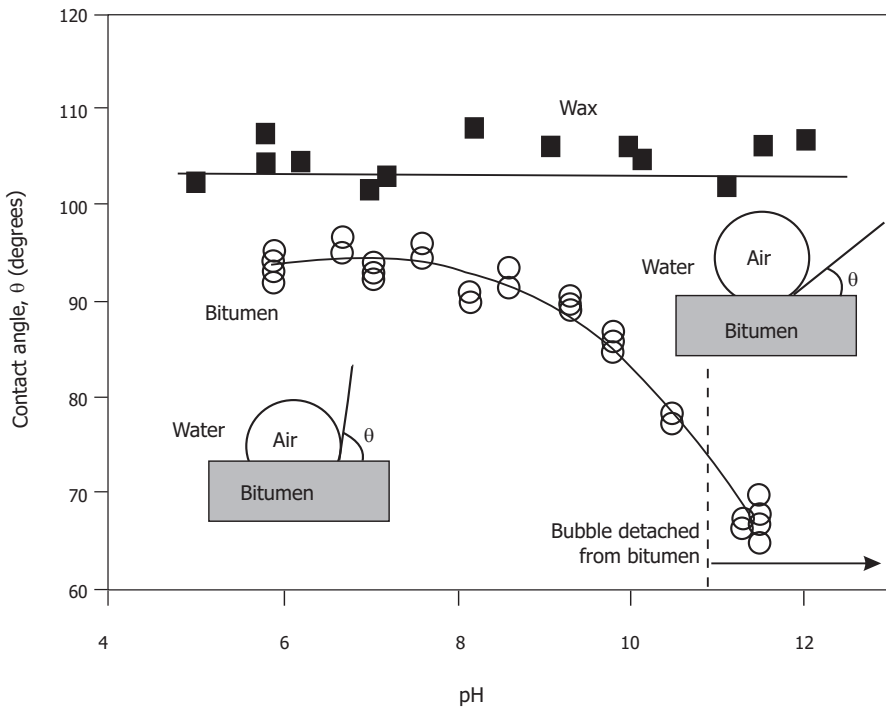


Figure 6.5 Contact angle of water on bitumen and paraffin wax, measured as a function of aqueous pH.

Source: Zhou, Xu, and Masliyah (2004a).

To understand the role of pH in controlling the contact angle of water on bitumen (and thus, bitumen aeration), the contact angle of water on paraffin wax was measured (Zhou, Xu, and Masliyah 2004a). The results, shown in Figure 6.5, indicate a constant

contact angle value of around 103° over the entire pH range of 5 to 12 studied. Clearly, pH has little effect on air-water and wax-water interfacial tensions due to the absence of surface-active components in paraffin wax. To understand the difference between the pH-dependence of water contact angle on bitumen and on paraffin wax, it is instructive to further investigate Young's equation (Eq. [6.2]), which governs the equilibrium contact angle (Figure 6.4D). For the given Young's equation, the surface tension of bitumen (30 mN/m) is slightly higher than that of paraffin wax (25.5 mN/m). Since there is a weaker interaction between water and paraffin wax than between water and bitumen, a higher interfacial tension of water with paraffin wax than with bitumen is expected, as implied by the extended Fowkes interfacial tension equations (Eqs. [4.20] and [4.21]), illustrated in Figure 4.56b. Therefore, one would expect $\gamma_{B/A} - \gamma_{B/W}$ to be higher than $\gamma_{P/A} - \gamma_{P/W}$ (in which subscript P represents solid paraffin wax), and thus, the contact angle of water on bitumen to be lower than on paraffin wax for a given air-water interfacial tension, as observed in Figure 6.5. The lower air-water interfacial tension in a bitumen-water system than in a paraffin wax-water system contributes to a slightly higher contact angle value of water on paraffin wax than on bitumen when the pH is between 5 and 8, and a *much* higher contact angle value when the pH is above 9.

To understand how interfacial properties can be optimized for bitumen liberation and aeration, it is instructive to examine Young's equation (Eq. [6.2]) for bitumen-sand-water and Eq. (6.8) for air-bitumen-water. Table 6.1 shows the desired trend of various interfacial tensions for this optimization. For practical purposes, when the surface tension of bitumen is given, there is little room to change the interfacial tension of bitumen-sand. The only interfacial properties that can be adjusted are those of bitumen-water, sand-water, and air-water. Increasing the pH of the process medium would lead to hydrolysis of the sand surfaces and ionization of the sand and bitumen surfaces, making both the bitumen and the solids more hydrophilic. This would decrease the interfacial tension of the sand-water and bitumen-water interfaces, a condition that is favourable for bitumen liberation.

Unfortunately, a reduction in bitumen-water interfacial tension is unfavourable for bitumen aeration. As shown in Figure 4.57b of Chapter 4, increasing the pH of the process medium in the presence of bitumen decreases the air-water interfacial tension, which is also undesirable for bitumen aeration. As we can see from Figure 4.57 and Table 6.1, a high pH is favourable for bitumen liberation, while a low pH is favourable for bitumen aeration. There is a clear conflict in the pH requirement, making caustic addition an important process variable. Current hot water-based oil sands extraction processes almost exclusively operate at pH values of between 8 and 8.5 to compromise between bitumen liberation and aeration. Novel ideas are clearly needed to either uncouple these two subprocesses through a two-stage processing option or to maximize the air-water interfacial tension for aeration. As shown in Figure 4.57b, increasing pH would inevitably reduce the air-water interfacial tension, leading to difficulties in aeration. An effective way to avoid this would be to use fresh bubbles where the air-water interfacial tension is at a maximum. In this respect, producing the bubbles in an area where contact between the bitumen droplets and the air bubbles could be made immediately would be ideal. This is the concept behind the aeration technology

used in modern flotation cells, such as the Microcell, the Jameson cell, and Canadian Process Technologies' cavitation cell.

From the molecular interaction point of view, the thermodynamic condition of the contact angle of water on bitumen being greater than zero can be thought of as the cohesion of water being stronger than the adhesion of water with bitumen. The work of adhesion, as defined by Eq. (2.6) for the current system, is given by

$$W_{ad} = \gamma_{A/W} + \gamma_{B/A} - \gamma_{B/W} \quad (6.10)$$

while the work of cohesion (Eq. [2.7]) is

$$W_{co} = 2\gamma_{A/W} \quad (6.11)$$

Inserting Eqs. (6.10) and (6.11) into Eq. (6.8) leads to

$$\begin{aligned} \frac{\Delta G}{\Delta A} &= \gamma_{B/A} - (\gamma_{B/W} + \gamma_{A/W}) = (\gamma_{A/W} + \gamma_{B/A} - \gamma_{B/W}) - 2\gamma_{A/W} \\ &= W_{ad} - W_{co} \end{aligned} \quad (6.12)$$

Eq. (6.12) shows that having $\Delta G/\Delta A < 0$ is equivalent to having $W_{ad} < W_{co}$, which is identical to the contact angle being greater than zero. A stronger cohesion of water to itself than its adhesion to bitumen, as illustrated in Figure 6.4D, pulls the water molecules together to form a water droplet on the bitumen. The extent of this action is determined by the difference between the two, which determines the value of the contact angle. Anything that weakens the work of adhesion of water on bitumen, i.e., increases the hydrophobicity of bitumen, will enhance bitumen-air attachment and improve flotation.

Table 6.1 Desired change of interfacial tensions for better performance of bitumen liberation and aeration, where the subscripts *B*, *S*, *A* and *W* represent bitumen, solid, air, and water, respectively.

Interfacial tension (mN/m)	$\cos \theta$	$\gamma_{B/S}$	$\gamma_{B/W}$	$\gamma_{B/A}$	$\gamma_{S/W}$	$\gamma_{A/W}$
Liberation	↑	↑	↓	-	↓	-
Aeration	↓	-	↑	↓	-	↑

Example 6.1

The surface tension of paraffin wax (γ_p) is determined to be 25.5 mN/m, while the surface tension of pure water (γ_w) is 72.8 mN/m. Using Eqs. (6.9) and (6.12), calculate

the contact angle of water on paraffin wax, the work of adhesion of water to paraffin wax, the work of cohesion of water in air, and the value of $\Delta G/\Delta A$ for air bubble–paraffin wax attachment.

Solutions:

In order to calculate the contact angle using Young’s equation (equivalent to Eq. [6.8]), one needs to know paraffin wax–water interfacial tension ($\gamma_{P/W}$), which is not given. Fowkes’ equation (Eq. [4.21]) can be used for this purpose. It is given by:

$$\begin{aligned}\gamma_{P/W} &= \gamma_W + \gamma_P - 2\sqrt{\gamma_W^{vdW} \gamma_P^{vdW}} \\ &= 72.8 + 25.5 - 2\sqrt{21.8 \times 25.5} = 51.14 \text{ mN/m}\end{aligned}$$

With $\gamma_{P/W}$ being known, Young’s equation (Eq. [6.8]) can be used as follows to

$$\cos \theta = \frac{\gamma_P - \gamma_{P/W}}{\gamma_W} = -0.3522 \rightarrow \theta = 110.6^\circ$$

calculate the contact angle:

This value is in excellent agreement with the values measured and shown in Figure 6.5. On the other hand, the work of adhesion and the work of cohesion, respectively, can

$$W_{ad} = \gamma_W + \gamma_P - \gamma_{P/W} = 72.8 + 25.5 - 51.14 = 47.2 \text{ mN/m}$$

be calculated using
and

$$W_{co} = 2\gamma_W = 2 \times 72.8 = 145.6 \text{ mN/m}$$

From Eqs. (6.9) or (6.12), we have

$$\frac{\Delta G}{\Delta A} = W_{ad} - W_{co} = 47.2 - 145.6 = -98.44 \text{ mN/m}$$

and

$$\frac{\Delta G}{\Delta A} = \gamma_W (\cos \theta - 1) = 72.8 \times (-0.3522 - 1) = -98.44 \text{ mN/m}$$

Clearly, the attachment of an air bubble to hydrophobic paraffin wax is thermodynamically favourable, and both methods (using Eqs. [6.9] and [6.12]) give the same value for $\Delta G/\Delta A$.

Example 6.2

The surface tension of bitumen at 25 °C is determined to be 30 mN/m. The surface tension of water in contact with bitumen at pH 8.5 and 10.5 is 71.5 mN/m and 68.3 mN/m, respectively. The bitumen-water interfacial tension, on the other hand, is measured to be 9.1 mN/m and 1.8 mN/m at pH 8.5 and 10.5, respectively. Calculate the contact angle of water on bitumen and $\Delta G/\Delta A$ for these two pH values.

Solutions:

Applying Young's equation (Eq. [6.8]) to the current system leads to

$$\cos \theta = \frac{\gamma_{B/A} - \gamma_{B/W}}{\gamma_{A/W}} = \frac{30 - 9.1}{71.5} = 0.2923 \rightarrow \theta = 73^\circ$$

at pH 8.5, and

$$\cos \theta = \frac{\gamma_{B/A} - \gamma_{B/W}}{\gamma_{A/W}} = \frac{30 - 1.8}{68.3} = 0.4129 \rightarrow \theta = 65^\circ$$

at pH 10.5.

The calculated contact angles predict the trend as measured experimentally (Figure 6.5). However, both are lower than the experimentally measured values of 90° and 78°, respectively. The difference is attributed to the spreading of bitumen on the air bubbles during experimental contact angle measurement, which leads to a smaller air-water interfacial tension, and hence, results in larger contact angle values.

The corresponding $\Delta G/\Delta A$ is calculated to be -50.6 mN/m and -40.1 mN/m for pH 8.5 and 10.5, respectively. These values indicate that bitumen-air attachment is thermodynamically favourable, although it would be easier at pH 8.5 than at pH 10.5.

The important role of bitumen surface hydrophobicity (measured by water contact angle on bitumen) in bitumen flotation is clearly illustrated by Zhou, Xu, and Masliyah (2004b). As shown in Figure 6.6, there exists a clear correlation between bitumen recovery and water contact angle on bitumen surfaces: a higher contact angle value corresponds to a higher bitumen recovery. A critical contact angle value of 65° appears to exist. Interestingly, this critical contact angle value for effective bitumen recovery corresponds well with the value required for effective mineral flotation (Fuerstenau and Han 2003).

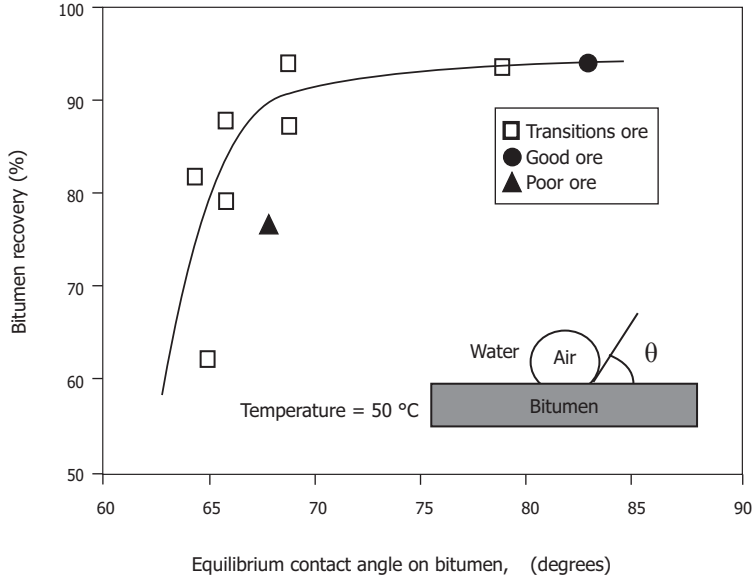


Figure 6.6 Correlation between bitumen recovery and contact angle of water on bitumen (measured by the captive-bubble method using centrifuged bitumen froth obtained from three different ores) in process water. A minimum contact angle of 65° is identified, below which a significant drop in bitumen recovery was observed.

Source: Zhou, Xu, and Masliyah (2004b).

After attaching to air bubbles, bitumen may spread quickly over them, completely covering them in a bitumen film and resulting in the formation of stable bitumen–air bubble composites. The extent and rate of bitumen spreading on an air bubble depend on the interfacial tension and the temperature of the system. The spreading process, shown in Figure 6.4B, can be predicted by the spreading coefficients defined in Eq. (2.8): $S_{B|W:A} = \gamma_{A/W} - (\gamma_{B/W} + \gamma_{B/A})$. With the interfacial tension values given in Example 6.1, the spreading coefficients are calculated to be 32.4 mN/m and 36.5 mN/m for pH 8.5 and 10.5, respectively, indicating the engulfment of bitumen on air bubbles in process water for both pH values. Rearranging Eq. (2.8) with Young’s equation leads to

$$S_{B|W:A} = \gamma_{A/W} (1 + \cos \theta) - 2\gamma_{B/A} \quad (6.13)$$

The spreading condition of bitumen on an air bubble is therefore determined by $S_{B|W:A} > 0$, i.e.,

$$\cos \theta > \frac{2\gamma_{B/A}}{\gamma_{A/W}} - 1 \quad (6.14)$$

Inserting the typical values of $\gamma_{B/A} = 30 \text{ mN/m}$ and $\gamma_{A/W} = 68 \text{ mN/m}$ for process water into Eq. (6.14), the critical contact angle value is calculated to be 97° . This value is greater than the contact angle values measured over the entire operating pH range, shown in Figure 6.5. It is therefore almost certain that the bitumen will spread on the air bubble upon attachment in the warm/hot water extraction process, which indicates that bitumen–air bubble attachment is the limiting step in bitumen flotation, provided that the viscosity of bitumen is not a limiting factor.

6.2.1 Wettability of Solids

It has been shown that the wettability of solids plays a critical role in bitumen liberation. Effective liberation requires solids to be highly hydrophilic and contact angle to be zero, ideally, as indicated by Figure 6.2. The hydrophobicity of solids also has an impact on froth quality, as solids can attach to air bubbles and be floated to the froth. The conditions for solids flotation, although undesirable in bitumen flotation, are similar to bitumen flotation as described above, and therefore, a similar analysis can be applied. To discourage solids flotation, it is important to learn the key factors that control solids wettability. For solids to be unable to float, the work of adhesion between water and solids must be larger than the work of cohesion of water (all in air), i.e., water must be more attracted to the solids than to itself. Coarse sands, mainly quartz (SiO_2), are generally hydrophilic when hydrolyzed, as described by Figure 4.14 (I) of Chapter 4. Increasing the pH of the aqueous slurry facilitates hydrolysis of the sand. More importantly, increasing the pH causes deprotonation, as shown in Figure 4.14 (III), and makes the sand more negatively charged, as indicated in Figure 6.7 by the increasingly more negative zeta potential of silica (representing sand) in a simple KCl electrolyte solution. The increase of negative surface charge makes the sand more hydrophilic, facilitating bitumen liberation and preventing sand flotation.

In the real world of oil sands processing, the sand is often contaminated by natural surfactants, especially when divalent cations, such as calcium and/or magnesium cations, are present. Although divalent calcium ions (Ca^{2+}) are able to adsorb on negatively charged silica surfaces (SiO^-) by electrostatic driving forces, as shown in Figure 4.14 (IV), the condensation of calcium monohydroxy ions (CaOH^+) on hydrolyzed sand (Figure 4.14 V) is much more effective, forming covalent SiOCa links and making the sand surface positively charged, at least locally, even at low calcium concentrations. The specific adsorption of calcium monohydroxy ions on silica has been experimentally verified, as shown by the results in Figure 6.7, where a much greater reduction in zeta potential values is seen at pH above 8.5, although the

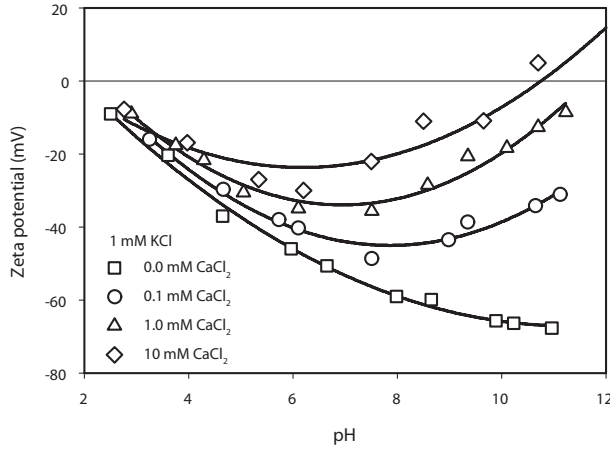


Figure 6.7 Variation of silica zeta potential with pH in the absence and presence of various amounts of calcium ions. The zeta potential is measured in 1 mM KCl background electrolyte solutions at room temperature.

higher-valence calcium ions (Ca^{2+}) are gradually transformed to lower-valence calcium monohydroxyls (CaOH^+). Based on the Stern-Grahame equation of adsorption, the adsorption (Γ_i) of species i from a solution of bulk concentration C_i at a solid-liquid interface is given by Fuerstenau (1982) as:

$$\Gamma_i = 2rC_i \exp\left(-\frac{\Delta G_{ads}^o}{RT}\right) \quad (6.15)$$

where r is the radius of the adsorbing species i , and ΔG_{ads}^o is the standard free energy of adsorption, given by

$$\Delta G_{ads}^o = \Delta G_{elec}^o + \Delta G_{chem}^o + \Delta G_{spec}^o + \Delta G_{solv}^o + \dots \quad (6.16)$$

Here, ΔG_j^o are contributions from mechanism j , such as electrostatic (*elec*), chemical reaction (*chem*), non-chemical but specific reaction (*spec*), solvation (*solv*), etc. In the case of calcium adsorption at pH lower than 8, electrostatic attraction is the major driving force, and

$$\Delta G_{ads}^o = \Delta G_{elec}^o = zF\psi_d \quad (6.17)$$

where F is the Faraday constant and ψ_d is the Stern potential, often approximated by

zeta potential (ζ). Since increasing pH makes silica surfaces increasingly more negative (i.e., makes ζ more negative), as shown in Figure 6.7, Eq. (6.17) shows that, for a given $z = 2$, the amount of calcium ions adsorbed increases as well. At pH 8, for example, the increased adsorption of divalent calcium ions from a 10 mM calcium ion solution on silica makes the silica surface less negative than at pH 6, even though the original surface is more negative at pH 8 than at pH 6. The adsorption of calcium ions also increases with increasing bulk concentration of calcium, as observed in Figure 6.7. However, the electrostatic mechanism alone does not account for the minimum on the zeta potential profiles and the zeta potential reversal at pH levels above 11, as shown in Figure 6.7. Based on the electrostatic adsorption mechanism, one would expect the zeta potential to level off with increasing pH for a given concentration of calcium ions.¹ It is evident that an additional driving force is operating at pH values above 8, corresponding to the minimal zeta potential value.

At pH values of above 8, calcium ions become increasingly hydrolyzed, forming corresponding monohydroxyl ions (CaOH^+). Although the z -value is reduced by half, the condensation reaction of calcium monohydroxy ions with silanol groups on the silica surface, given by Figure 4.14 (VI), provides an additional driving force, given by ΔG_{chem}^0 , i.e.,

$$\Delta G_{ads}^0 = \Delta G_{elec}^0 + \Delta G_{chem}^0 \quad (6.18)$$

In general, ΔG_{chem}^0 is much greater than ΔG_{elec}^0 and overcomes the loss of ΔG_{elec}^0 due to reduced zeta potential by the adsorption of positively charged calcium monohydroxy ions. In the current system, this is indicated by a further increase in zeta potential towards zero or even a charge reversal, where ΔG_{elec}^0 would be a negligible contributor or resistant to further adsorption of positively charged calcium monohydroxy ions. The dramatic increase in calcium adsorption on silica above pH 8 is well documented in literature (James and Healy 1972; Fuerstenau 1982).

Baptista and Bowman reported that surfactants that aid bitumen flotation also aid the flotation of fine minerals, leading to poor froth quality (1969). The adsorption of natural surfactants in bitumen on sand surfaces is possible through the activation of calcium ions, as described in Figure 4.14 (VI). The flotation of silica/quartz by anionic surfactants in the presence of calcium is well documented (Fuerstenau, Miller, and Kuhn 1985), although the pH range reported for effective flotation is higher than the incipient pH value for effective calcium adsorption (James and Healy 1972).

It should be noted that the above analysis is equally applicable to the reaction of other metal oxide minerals with other hydrolyzable multivalent cations. A common observation in literature is that activation is most effective at pH levels where monohydroxyl species dominate. For example, ferric ions (Fe^{3+}), aluminum ions (Al^{3+}), and magnesium ions (Mg^{2+}) would activate silica flotation at pH 2.5, 3.5, and 11, respectively, where respective monohydroxyl species start to dominate

¹ Note to reader: Why do you think this would be the case?

(Fuerstenau, Miller, and Kuhn 1985). Recently, the coagulation of bitumen or other model oils with quartz in the presence of hydrolyzable calcium, magnesium, and ferric ions was reported (Gan et al. 2007; Gan, Crozier, and Liu 2009). In these studies, the complexation of hydrolyzable metal ions using citric acid was found to be effective in preventing coagulation and improving bitumen recovery.

Mineralogical analysis of solids reported to bitumen froth from industrial operations has revealed that the froth is enriched with heavy minerals (e.g., titanium, zircon, calcite, pyrite). These heavy minerals are likely activated by hydrolyzable metal ions and rendered hydrophobic by natural surfactants in bitumen, such that they are floated independently or with bitumen to the froth. Although heavy minerals only account for a small amount of solids in oil sands (< 0.25 % to 0.5 %), industrial operations demonstrate that up to 90 % of heavy minerals can be recovered to bitumen froth, making the recovery of heavy minerals from froth treatment tailings economically feasible. The condensation reaction given in Figure 4.14 (V), however, requires the presence of surface hydroxyl groups. The effect of hydroxyl groups on solid surfaces, which is also highly pH-dependent, is less understood. More insight into this area would help provide some guidance for oil sands operating conditions that would maximize liberation and minimize the contamination of solids in bitumen froth through manipulation of the hydrolysis of solids.

6.3 Bitumen Flotation

Flotation is a versatile technology for separating solids from solids or solids from liquids in a slurry, liquids from liquids, and even ions from liquids. In flotation, air bubbles, used as carriers, are generated and attached to the target component(s) in a complex multiphase fluid system. Because the air bubble–solid or air bubble–liquid aggregates have a lower apparent density than the fluid, the target components are carried to the top of the slurry by the floating air bubbles, where they are collected as the product in the form of froth. The solids or the liquid droplets that are unable to attach to air bubbles remain in the pulp and are discharged as tailings. In oil sands extraction, flotation is used to float fugitive bitumen, often in the form of fine bitumen droplets, in the middlings stream of a primary separation vessel. Fine bitumen droplets of a density similar to that of the slurry to be recovered must attach to air bubbles so that the aerated bitumen, which has a significantly lower density than the slurry, can effectively float to the top of the slurry within a reasonable residence time. There are two major aeration methods in flotation: bubble-bitumen attachment in slurry (as in induced mechanical flotation cells) and bubble nucleation on bitumen (as in dissolved air flotation).

6.3.1 Induced Air Flotation

Figure 6.8 shows the essential components of a typical mechanical flotation machine. A mechanical flotation machine consists of the following attributes: (1) a mechanical agitator (impeller) hosted in a standpipe and used to suspend the solids and homogenize the slurry; (2) a feed mechanism to introduce the feed slurry into the machine; (3) a supplier of air/gas for the generation of bubbles; (4) a quiescent region for aerated bitumen to float; (5) a mechanism to remove the aerated bitumen froth; and (6) a tailings discharge mechanism to discharge tailings without short-circuiting the feed slurries.

The mechanical energy provided by the agitator is also used to break the air stream (3) into air bubbles of desired sizes to induce contact between the bubbles and the bitumen or solids and to provide inertia energy for breaking the liquid films between bubbles and bitumen/solids during attachment. Bubble generation, air-bitumen collision, and attachment are almost exclusively accomplished in a small region near the impeller and stator (diffuser), where intensive energy dissipation occurs. For flotation of bitumen to occur, selective attachment of air bubbles to bitumen is required, which includes the collision of bitumen droplets with air bubbles, the thinning of the liquid films intervening between the bitumen and the air bubbles, and the stable attachment of bitumen to air bubbles. Under a given hydrodynamic condition, the recovery rate also depends on the number of air bubbles available.

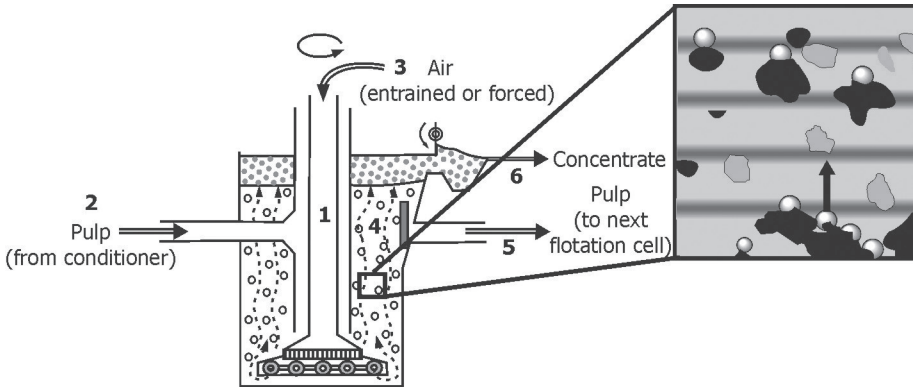


Figure 6.8 A schematic diagram of a mechanical flotation machine, illustrating all essential attributes. Detail shows aerated bubbles of hydrophobic coal particles (black) rising in a slurry of gangue particles (light grey) sinking under gravity.

Mathematically, the bitumen collection rate in the pulp zone of a mechanical flotation machine, $R_c(t)$, can be written as

$$R_c(t) = \frac{dn_p}{dt} = -k_s P_c P_a (1 - P_d) S_b n_p \quad (6.19)$$

where k_s is a flotation system parameter; P_c is the probability of collision; P_a is the probability of attachment; P_d is the probability of detachment; S_b is the bubble surface area flux; and n_p is the number of bitumen droplets. For a given oil sands flotation system, the hydrodynamics of a flotation machine determines the probability of air bubble-bitumen collision, P_c . At a given ratio of bubble-to-bitumen-droplet size, a stronger mixing would enhance the collision between air bubbles and bitumen droplets. Hydrodynamic analysis (Schulze 1984) shows that the collision is proportional to the square root of the energy dissipation rate. Therefore, the most collisions occur near the impeller and stator, where the energy dissipation is highest.

Upon collision, the attachment of an air bubble to a bitumen droplet depends on the thinning and rupture of the intervening liquid film to form a three-phase contact line, and the subsequent expansion of the three-phase contact line to a stable attachment. The time required for attachment to occur is known as the *induction time* of bubble-bitumen attachment. It is clear that, for attachment to occur, the contact time upon collision between bitumen droplets and air bubbles must be greater than the induction time. The study of induction time in flotation is therefore extremely important. It has been established that the thinning and rupture of the intervening liquid film between a bitumen droplet and an air bubble, and hence their attachment, is largely controlled by the interfacial properties of the bitumen-water and air-water interfaces, i.e., the wettability of bitumen and air by water.

As shown in Figure 6.9, when bringing an air bubble to a bitumen surface in a liquid (water) of contact angle θ on bitumen, the total energy change (ΔG) for the attachment is given by $\Delta G = \gamma_{A/W} (\cos \theta - 1)$. As long as the contact angle of water on bitumen is greater than zero, the interfacial energy change of the attachment process will lead to attachment. However, the affinity of the liquid film to bitumen droplets and air bubbles would create a barrier that would cause a resistance to the thinning of the liquid film, leading to a longer induction time. This resistant force, known as *disjoining pressure*, pushes the air bubble away from the bitumen droplets. As a result, the actual profile of interaction energy, shown in Figure 6.9, plays a critical role in determining the induction time (and hence, the attachment of bitumen droplets to air bubbles) upon contact.

For a system of a contact angle greater than zero, the critical parameter determining the thinning of the intervening liquid film is the magnitude of the energy barrier, E_b , as shown in Figure 6.9. The energy barrier can be calculated from the classic DLVO (Derjaguin, Landau, Verwey, and Overbeek) theory, which takes into consideration universal van der Waals forces and electrostatic double layer forces (Derjaguin and Landau 1941; Verwey and Overbeek 1948; Hunter 1986; Israelachvili 1990). The van der Waals forces for various geometrical systems are calculated using the equations given in Table 2.5, for which the key Hamaker constants are given in Table 2.6 or calculated using Eq. (2.32). It should be noted that the van der Waals forces in bitumen flotation systems, i.e., bitumen-air bubble interactions across an aqueous medium, are repulsive. More importantly, there is very little room to change/control the van der Waals forces in a given system.

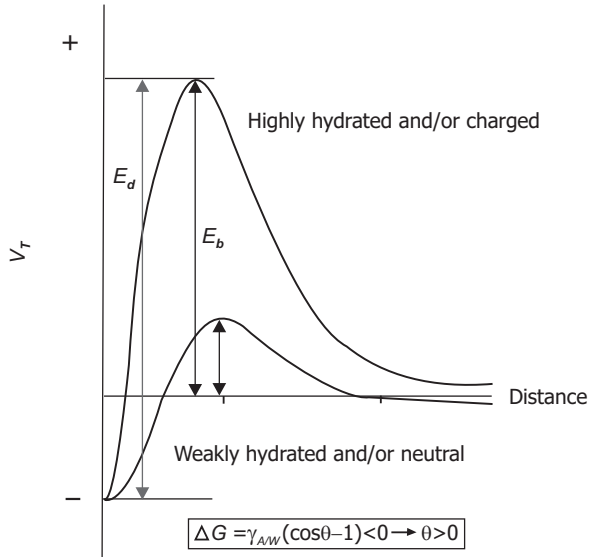


Figure 6.9 A schematic diagram of energy profiles (V_T) between a bitumen droplet and an air bubble as a function of distance between the two in an aqueous solution, illustrating energy barriers (E_b) and energy of detachment (E_d). For a given adhesion energy $\Delta G = \gamma_{AW}(\cos \theta - 1)$, the magnitude of the energy barrier determines the probability of attachment upon collision of the bitumen droplet with the air bubble.

The electrostatic double layer forces, on the other hand, are a strong function of the aqueous ionic strength and, even more so, of the valence of ions and the concentration of potential determining ions, which determine the magnitude of surface charges. The energy barrier can therefore be controlled by changing the potential ion concentrations (for example, by changing the pH, for the case of oxide and clays) or through the addition of high-valence electrolytes such as calcium or aluminum chloride. High-valence electrolytes, traditionally referred to as coagulants, induce the aggregation of particles by screening the particle surface charges in such a way that the van der Waals forces become dominant. The electrical double layer forces can be approximately calculated from Eq. (2.33) or Eq. (2.36) (depending on the required accuracy of the calculation) using the known surface potential or zeta potential value and the electrolyte concentration.

It should be noted that for some systems, the use of the classic DLVO theory is inadequate. In such cases, the DLVO theory can be extended to include repulsive hydration forces (Israelachvili 1990), repulsive steric forces (Sato and Ruch 1980), attractive hydrophobic forces (Israelachvili 1990; Churaev and Derjaguin 1985; Kitchener 1984; van Oss 2006), and/or attractive bridge forces (Ives 1978). In fact, attractive forces originating from surface hydrophobicities are the only driving force for bitumen-bubble attachment. In this case, the classic DLVO theory would not be appropriate, as it would predict an infinitely high energy barrier for negatively charged bubbles and for bitumen surfaces with repulsive van der Waals forces.

In a dynamic system, the probability of bitumen-bubble attachment can be calculated from the known energy barrier (E_b) and the kinetic energy imparted on

$$P_A = \exp\left(-\frac{E_b}{E_k}\right) \quad (6.20)$$

colloidal particles by mixing (E_k) using an analogue of the chemical reaction rate theory (Mao and Yoon 1997):

It is evident from Eq. (6.20) that the higher the energy barrier, the lower the probability of bitumen-bubble attachment. The typical variation of energy barrier (E_b) with surface potential (ψ) or electrolyte concentration is shown in Figures 2.18 and 2.19 of Chapter 2, respectively. When a system is at the condition for critical coagulation of its surface potential (a magnitude of surface potential of less than 11 mV in a 1-mM KCl solution or an electrolyte concentration of 2.58 mM KCl at a surface potential value of 15 mV), the energy barrier approaches zero and P_a becomes unity, i.e., every collision leads to attachment. Extreme caution must be exercised when calculating the energy barrier between bitumen droplets and air bubbles in an aqueous solution, as the classic DLVO theory used to calculate interaction energy profiles shown in Figures 2.18 and 2.19 is not applicable. The extended DLVO theory (Mao and Yoon 1997) must be established and used for calculating the interaction energies between bitumen droplets and air bubbles as encountered in bitumen flotation.

Upon attachment at the condition at which the induction time is less than the contact time of the collision (Schulze 1984), the successful collection of target particles (in this case, bitumen droplets) by air bubbles also depends on the strength of the attachment, as the hydrodynamic shear force can tear the bitumen droplets away from the air bubbles. This is known as the probability of detachment (P_d). There are two attachment models in bitumen flotation, depending on the temperature (Figure 6.10). At low temperatures, the bitumen droplets simply attach to air bubbles (as shown in Figure 6.10a) and are more susceptible to detachment. The energy required for detachment is given by E_d in Figure 6.9. Clearly, larger contact angle values of bitumen (i.e., more negative ΔG values), a higher surface tension of the fluid medium, and/or a larger energy barrier can lower the probability of detachment. In mathematical terms,

$$P_d = \exp\left(-\frac{E_d}{E_k}\right) = \exp\left(-\frac{E_b - \Delta G}{E_k}\right) \quad (6.21)$$

the probability of detachment is given by Mao and Yoon (1997) as:

where E_k is the kinetic energy exerted on bitumen-bubble aggregates by the local turbulence of fluids. In designing and operating a flotation machine, it is important to

have a hydrodynamic environment in the collection zone that maximizes bitumen collection by air bubbles under the constraint of $E_b < E_k < (E_b - \Delta G)$. This constraint implies that a high surface hydrophobicity of particles or bitumen droplets allows for improved tolerance to high local turbulence in flotation operations (and hence, a higher collision rate) without causing detachment.

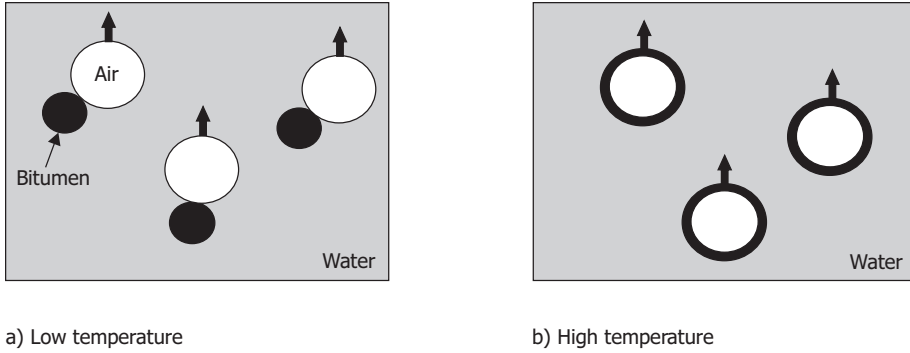


Figure 6.10 A schematic diagram of two aeration models: (a) bitumen droplet–air bubble attachment at low temperature; and (b) bitumen engulfing air bubbles upon attachment at high temperature.

At high temperatures, bitumen engulfs air bubbles, as shown in Figure 6.10b. In this case, the detachment of bitumen from the aerated air bubbles can be considered negligible, and P_d becomes zero. Nevertheless, the bitumen-engulfed air bubble may break up under severe hydrodynamic shear. The probability of a bitumen-engulfed air bubble breaking up depends on the bitumen–water interfacial tension. Even though the hydrodynamic shear is strong enough to break up the bitumen-engulfed air bubbles, the daughter bubbles remain engulfed by bitumen and lift the bitumen to the froth. The rising velocity in this case is lower due to the small sizes of the daughter bubbles. It is therefore safe to conclude that the rate of bitumen collection at elevated flotation temperatures is mainly determined by bitumen–bubble collision and attachment, with P_d being essentially equal to zero.

Another essential component of bitumen collection by air bubbles is the presence of bubbles, which is measured by bubble surface area flux (S_b , in Eq. [6.19]). For a given rate of air flow into a flotation cell, the higher the mixing intensity or local shear rate, the smaller the bubbles and the higher the S_b , which leads to a higher bitumen collection rate. Under a hydrodynamic condition for a given air flow rate, the addition of surface-active chemicals, known as frothers, leads to the production of much smaller bubbles due to lower air–water interfacial (surface) tension. Quantitatively, this is illustrated by the well-known Young–Laplace equation (Eq. [2.3]), in which ΔP represents the driving force for bubble formation in a solution of surface tension γ and bubble size r . It is evident that for a given air flow rate, the stronger the mixing and the lower the surface tension of a liquid, the smaller the bubble sizes and the larger the bubble surface area flux, leading to a higher bitumen collection rate, as

shown by Eq. (6.19). The addition of a frother to the flotation pulp also minimizes the coalescence of bubbles, stabilizing bubbles at small sizes. In bitumen flotation, the natural surfactant released from bitumen during conditioning is sufficient to produce the bubbles required for bitumen flotation. Therefore, a frother is rarely used for bitumen flotation in warm/hot water extraction processes. However, in low-temperature extraction processes (say, $< 30\text{ }^{\circ}\text{C}$), the addition of a frother may be necessary to generate suitable amounts and sizes of bubbles, a result of the reduced release rate of natural surfactant from bitumen at low processing temperatures. For example, kerosene and methyl isobutyl carbinol (MIBC) are used together as a process aid in the OSLO low-energy extraction process.

Hydrodynamic analysis of flotation shows that small bubbles are more effective in collecting small-size particles or bitumen droplets. In hydrodynamic analysis of collision by interception, the collision rate between air bubbles and bitumen droplets of diameters d_a and d_b , respectively, is scaled by $(d_b/d_a)^2$, i.e., small bubbles lead to a high collision rate (Yoon and Luttrell 1989). Moreover, small bubbles also facilitate bubble-bitumen attachment upon collision, which was recently confirmed using a novel experimental setup, shown in Figure 6.11 (Gu et al. 2004). In this setup, hydrogen or oxygen bubbles of desired size are obtained by coalescing a number of smaller bubbles generated by electrolysis. Once a bubble is of the desired size, it is released underneath a hanging bitumen droplet that is located a sufficient distance away from the bubble release point, allowing it to reach its terminal velocity prior to its contact with the hanging bitumen droplet. The rising bubble collides with the hanging bitumen droplet and slides upwards along it. The process of the bubble rising toward and sliding around the hanging bitumen droplet is recorded and analyzed to determine the bubble's rising velocity and the amount of time it spent sliding before it stopped, i.e., the induction time.

For a given water chemistry and temperature, large bubbles (0.31 mm or larger) slide or sweep away from the bitumen droplet, as shown by the results in Figure 6.12, even though the impact force of the collision of large bubbles is greater than that of small bubbles due to the higher rising velocity of the large bubbles. This is attributed to a shorter contact time (during sliding) than induction time required for the attachment. Small bubbles (of sizes less than 0.31 mm) stick/attach to the bitumen droplets, as the amount of time they spend in contact with the bitumen surface during the sliding is longer than the induction time. In fact, the results in Figure 6.12 show that smaller bubbles have a much shorter induction time, i.e., they stop sliding and stick to the bitumen droplet after a much shorter sliding time than the larger bubbles.

Under the force of buoyancy, a rising bubble in contact with a bitumen droplet can become deformed and flattened along the side in contact with the bitumen, as illustrated in Figure 6.13. It is well known that the pressure inside the bubble is higher than that outside of it by the amount given in the Young-Laplace equation ($P = 2\gamma_{A/W}/r$), balanced by the curved bubble surface. This pressure difference at the flattened area will cause an excess of pressure on the intervening liquid film between the bitumen surface and the air bubble, as shown in Figure 6.13. Such excess pressure is highly related to the curvature of the bubbles: the smaller the bubble, the higher the excess

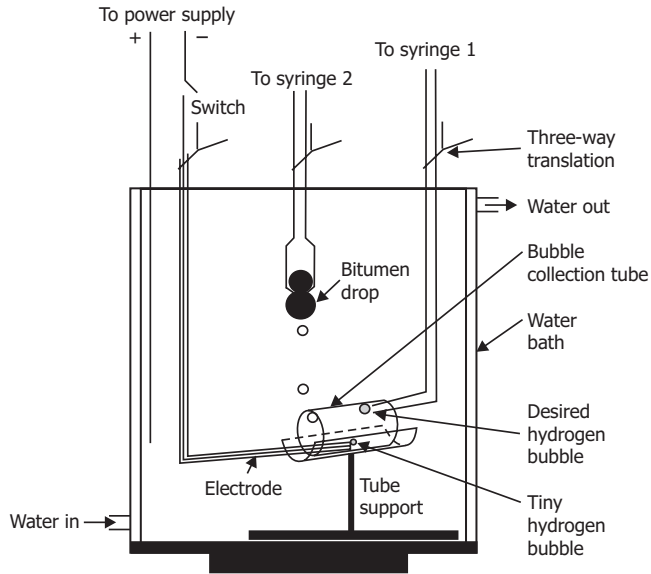


Figure 6.11 Experimental setup for recording bubbles rising towards and sliding around a hanging bitumen droplet, used to determine the induction time of bubble-bitumen attachment.

After Gu et al. (2004).

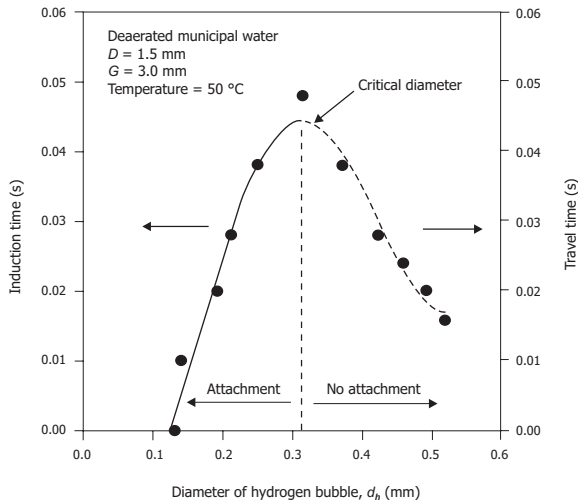


Figure 6.12 Induction of bitumen-bubble attachment as a function of bubble size, determined using the experimental setup shown in Figure 6.11. D is the diameter of bitumen droplets and G is the gap between bubble and bitumen droplet.

After Gu et al. (2004).

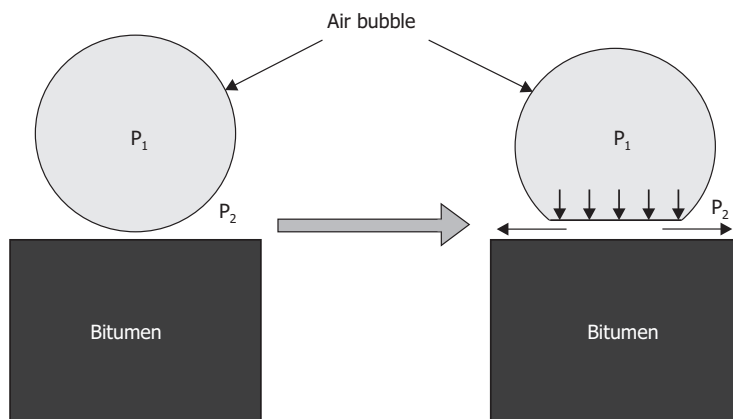


Figure 6.13 Illustration of excess pressure ($P = 2\gamma_{A/W}/r$) from a small bubble on the intervening liquid film between the bubble and bitumen droplet due to the deformation (flattening) of the bubble under buoyancy force.

pressure and the stronger the force that thins the intervening liquid film, resulting in a faster drainage and breakup of the film. The smaller contact area between bitumen and smaller bubbles can also contribute to a shorter induction time, a result of faster drainage of the intervening liquid film in the absence of dimple formation. Clearly, smaller bubbles are beneficial for bitumen flotation.

It is important to note the critical role of air bubble surface properties and the effective transport of aerated bitumen. Smaller bubbles feature a lower rising velocity, as predicted in Masliyah's generalization of the Stokes law, suitable for higher Reynolds numbers and hindered settling (Masliyah 1979). In this case, multi-bubble attachment is needed to lift large bitumen droplets effectively within a limited residence time. More importantly, the addition of a frother or any surfactant, although beneficial for generating small bubbles, would make the bubble surface less hydrophobic (with polar heads of the adsorbed surface-active molecules facing the liquid). For attachment to occur, an additional force is required to push the frother or surfactant molecules away from the contact zone. Such an effect would increase the energy barrier (E_b) of bitumen-bubble attachment (Figure 6.9). It is therefore extremely important to consider the multi-faceted effects of chemical process aids in bitumen flotation.

6.3.2 Flotation by Gas Nucleation/Precipitation

The analysis of flotation presented above shows that the collision of air bubbles with bitumen, and the subsequent attachment of the two, is necessary to induce bitumen flotation. Since bitumen has a density similar to that of water, which is used as the separation medium, the inertia or kinetic energy of bitumen needed to induce effective collision with bubbles is anticipated to be low. An effective resolution to this deficiency is to eliminate the need for collision through selective gas nucleation

or precipitation on hydrophobic bitumen surfaces. The gas nucleation or precipitation flotation (Edzwald 1995), known as *dissolved air flotation*, has been used extensively in the removal of solids from municipal wastewater and in the recovery of fibres from the pulp of waste newspaper. In conventional dissolved air flotation, gas bubbles are generated in situ on solid particles as the system goes through a pressure reduction by either gas pre-supersaturation of the slurry under pressure or vacuum flotation. Although the critical bubble diameter in homogeneous bubble nucleation follows the Young-Laplace equation, heterogeneous gas nucleation on hydrophobic surfaces can occur at a much smaller pressure drop, or a smaller gas nucleus can be produced on hydrophobic particles under a given local pressure drop, to minimize the system free energy.

Clearly, as the degree of gas supersaturation increases, gas nucleation becomes much easier and more gas nuclei are generated, in particular in the presence of hydrophobic particles. The driving force for gas nucleation is given by the pressure drop from gas saturation pressure (P_S) to an ambient pressure (P_A) under which the slurry is discharged to open flotation cells. With the operation under pure pressure release, the volume of gas released (\bar{V}_G) per unit volume (litre) of slurry during the pressure drop corrected to the standard temperature and pressure (STP) is given by

$$\left(\bar{V}_G \right) = f \frac{P_S - P_A}{k_H} \frac{22.4(\text{STP})}{M_G} \quad (6.22)$$

where f is gas saturation efficiency, k_H is Henry's law constant of saturation gas in water, and M_G is the molar mass of the saturation gas. At 25 °C, k_H is 4654 kPa/(g/L) for air and 67.7 kPa/(g/L) for CO₂. Eq. (6.22) gives the upper limit of gas volume released when the gases saturated in the slurry are in the form of gas molecules, using the saturation configuration of Figure 6.14A. For a given saturation pressure of 5 atm (505 kPa absolute) and a releasing pressure of 1 atm (101 kPa absolute) with a gas saturation coefficient of 1, for example, the calculated volume of gases dissolved in 1 litre of water would be 0.067 L (STP) for air and 3.04 L (STP) for CO₂.

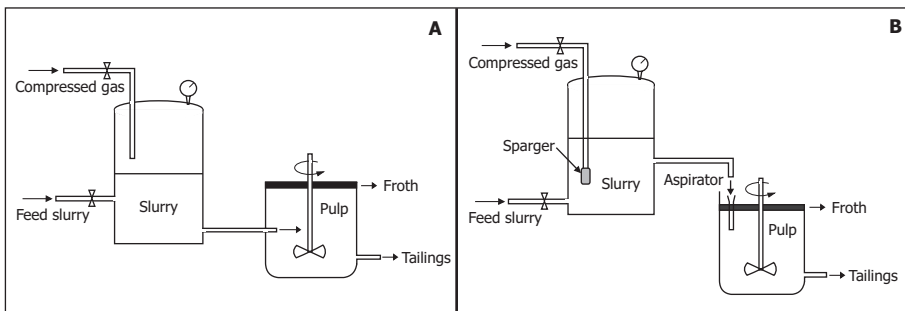


Figure 6.14 Dissolved air flotation systems: A) pressurized saturation with release of slurry without additional entrained air; and B) sparged saturation with release of slurry enhanced by additional entrained air.

It is evident that only a very small volume fraction of air (0.063) could be dissolved in a slurry under a saturation pressure of 5 atm. Such a small volume fraction alone is not sufficient for the recovery of bitumen from oil sands. For this reason, dissolved air flotation is rarely used in bitumen recovery, although it eliminates the collision step in bitumen collection by air bubbles. However, the role of dissolved air in activating bitumen recovery cannot be overlooked: a small amount of gas nuclei attached to bitumen can reduce the effective density of gas nucleus–frosted bitumen droplets and increase the hydrodynamic inertia, enhancing the subsequent collision of gas nucleus–activated bitumen droplets with conventional dispersed flotation bubbles. It is also established that upon collision, the gas nucleus–activated solid or bitumen droplets more easily attach to conventional flotation bubbles (Klassen and Mokrousov 1963; Mishchuk, Ralston, and Fornasiero 2006).

In contrast, if CO₂ is used as a processing gas, a much larger volume fraction of gas (0.75) is released effectively after gas saturation at 5 atm—an amount sufficient for recovering bitumen. Unfortunately, such an approach has not been explored in the oil sands industry. The challenge lies in the fact that, at equilibrium with 5 atm CO₂, the pH of the slurry would drop to about 3. At such a low slurry pH, the liberation of bitumen from sand would be very difficult.

To accelerate gas dissolution in water, different strategies can be adopted. For example, under the constraints of the limited solubility of gases such as air, the amount of gas dissolved could be improved by sparging the gases into the slurry, as shown in Figure 6.14B, instead of directly pressurizing them (Figure 6.14A). Increasing the air-water interfacial area by gas sparging increases the rate of air dissolution in water. A substantial amount of gases could be also introduced into the slurry in the form of Harvey gas nuclei (i.e., the gases trapped in or transferred to the crevices and cracks of hydrophobic solid particles in the slurry). When discharging the pressurized slurry to atmospheric pressures, the expansion of these Harvey gas nuclei not only enhances the amount of gases available for generating bubbles, but also facilitates the attachment of flotation bubbles to the particles frosted with gas nuclei.

With a local pressure drop of 500 kPa under hydrodynamic turbulence, bubbles as small as 10 μm could easily be generated (Zabel 1984). Bubbles are generated in situ on bitumen or solid particles when a pressurized slurry is fed into a separation vessel open to atmospheric pressures. Hydrodynamic cavitation of the gas-saturated slurry can enhance gas nucleation, causing a significant pressure fluctuation within highly turbulent regimes in the fast-flowing feed. The mechanism of bubble generation by hydrodynamic disturbances is very similar to the well-known foaming mechanism encountered on opening a pop bottle that has been shaken. With such an aeration mechanism, the rate-limiting collision of gas bubbles with bitumen droplets is no longer needed, provided that sufficient gas is available for the gas nucleus to grow. Gas nucleation and bitumen aeration can be significantly enhanced if the pressurized slurry is released into the pulp in the flotation tank through an aspirator, as shown in Figure 6.14B. In this case, the gas nuclei formed when the slurry is depressurized can grow rapidly to a size sufficient to lift bitumen effectively with the supply of air provided through the aspiration action. In fact, this concept has been explored in recent developments, such as the Jameson cell, the Microcell, and the hydrodynamic cavitation (also known as picobubble) flotation cell.

In oil sands processing, dissolved gas also plays a significant role in primary separation vessels. As shown in Figure 6.15, oil sands slurry is pumped through slurry hydrotransport pipelines at a linear velocity of 3 m/s to 5 m/s. There is a significant pressure drop from over 10 atm at the feed end to 1 atm (absolute) at the discharge end of the slurry hydrotransport pipeline, where the slurry enters primary separation vessels. In a slurry hydrotransport pipeline, a pump is used to provide the pressure required to transport the slurry. It is therefore anticipated that, when the slurry enters the pipeline, the gases dissolved within it will selectively precipitate on bitumen surfaces as the pressure drops along the pipeline under hydrodynamic disturbances. Air entrained during the slurring process is a major source of gases, although in some cases, additional gases are added into the slurry. To maximize the amount of gases introduced into the slurry, highly soluble gases can be forced in at the inlet of the feed pump, where the pressure is relatively low. However, it should be noted that too much gas trapped in the pump could reduce the pump efficiency significantly. A clear balance is need

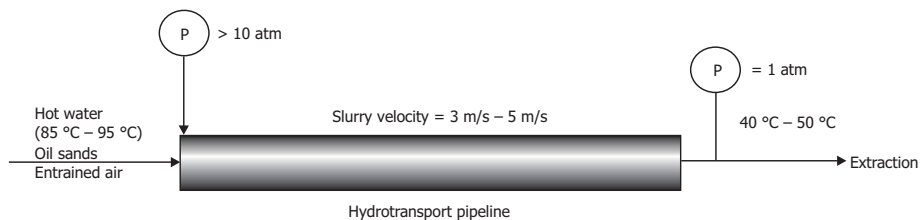


Figure 6.15 Operating conditions in a typical slurry hydrotransport pipeline in an oil sands operation, illustrating a significant pressure drop (> 9 atm) along the pipe. The pipe could be used as an air saturation system for the enhanced aeration of bitumen.

Source: Zhou et al. (2009).

6.3.3 Flotation Machines

Various types of flotation cells have been used in the mineral industry (Fuerstenau and Han 2003), including mechanical flotation cells, pneumatic flotation cells, and column flotation cells. Currently, the oil sands industry relies mainly on the Outokumpu and Dorr-Oliver tank cells for bitumen recovery from the middlings streams of primary separation vessels. Examples of two such mechanical flotation cells are shown in Figure 6.16. The Outokumpu cell features a unique impeller design to enhance slurry circulation and improve aeration (Wills and Napier-Munn 2006). With the impeller closed off on top by a horizontal plate, the slurry is accelerated and expelled through the tapered slots in the rotor, while the forced air stream introduced through the central shaft breaks down into small bubbles. These bubbles make contact with the bitumen

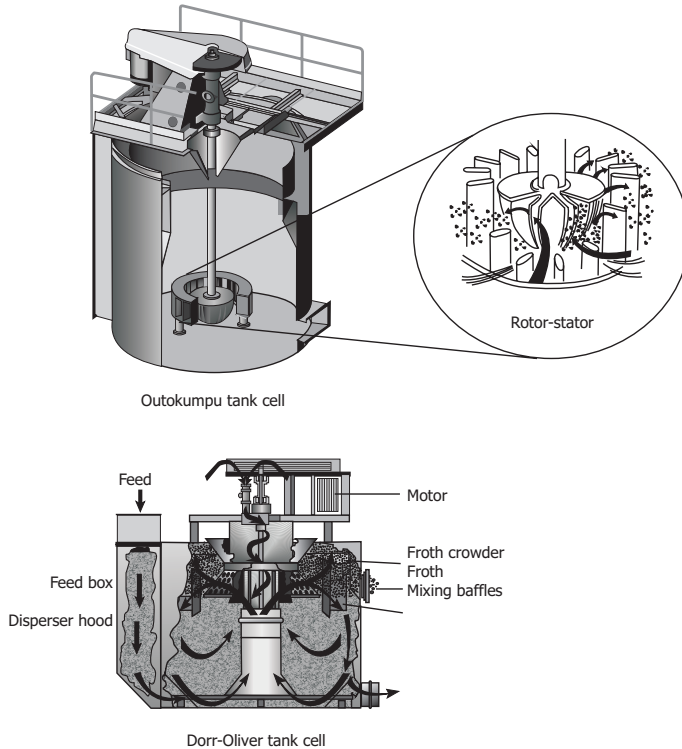


Figure 6.16 Two mechanical flotation cells used in the oil sands industry.

Source: redrawn from Outokumpu and Dorr-Oliver commercial brochures.

droplets within the clearance between the rotor and the stator. In this design, the impeller acts as a pump, drawing the slurry from the bottom of the rotor. The aerated slurry escapes the rotor-stator region through open slots in the stator and enters the quiescent separation zone.

The cylindrical Dorr-Oliver cell (Figure 6.16, bottom) features a hybrid draft tube with a bevelled cell bottom along with a froth crowder, mixing baffles, and a radial launder. The hybrid draft tube and bevelled tank are claimed to improve the hydrodynamics of mixing, while the mixing baffles and radial launder increase froth mobility and decrease froth residence time. The cylindrical configuration improves mixing and air dispersion while minimizing the turbulence in the separation zones, allowing for flexible operating conditions at optimized local energy input, aeration, and mixing. In Dorr-Oliver cells, the rotor-disperser consists of two portions. The upper portion of the rotor draws the air into the slurry through a central standpipe and the disperser breaks it down into small bubbles. The lower portion of the rotor draws the slurry upwards to provide the correct mix of particle momentum trajectory and recirculation and to maximize the slurry retention within the cell.

A common feature of mechanical flotation cells is the high-speed rotation of the impellers within the tank. Wear of impellers is often an issue, and shutdowns for the

replacement of worn impellers are a major concern in the oil sands industry. This is not an issue in pneumatic flotation cells. As shown in Figure 6.17 (left), in a Davcra cell, air is introduced into a fast-flowing slurry (Lynch et al. 2007). Through a cyclone-type nozzle, a high-velocity air-slurry mixture impinges onto a vertical baffle inserted into the tank. High-intensity mixing in this region breaks the air down into small bubbles that make intimate contact with the solids in the slurry. The aerated slurry flows over the baffle into a quiescent region, where separation of the aerated particles (bitumen droplets) from the pulp occurs. In a recent design of a pneumatic flotation cell by Imhof, known as the Imhoflot G-Cell, (Figure 6.17, right), a centrifugal force is imparted to enhance the separation of aerated solids from the slurry. It is, in essence, a centrifugal dissolved air flotation machine. The aeration is accomplished by self-aspiration of air into a fast-flowing slurry, very similar to the Jameson cell process, which will be discussed later. The aerated slurry is fed tangentially into a separating vessel to create the rotational speed desired for rapid separation, under a much higher g-force than in normal, gravity-based flotation devices. The enhanced radial velocity allows for the separation of aerated solid particles within a much shorter residence time, which makes it suitable for large throughput operations, such as those in the oil sands industry. The use of self-aspiration avoids the limitations imposed by the carrying capacity of air bubbles, as encountered in conventional dissolved air flotation.

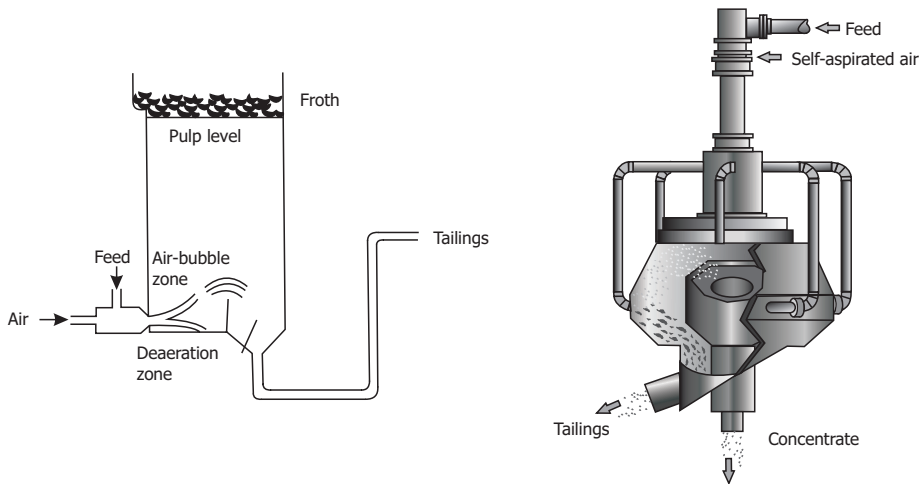


Figure 6.17 Two pneumatic flotation cells used in the mineral and coal industries (left: Davcra cell; right: Imhoflot G-cell).

Source: Lynch et al. (2007).

The Jameson cell (Clayton, Jameson, and Manlapig 1991; Finch 1995), shown in Figure 6.18 (left), uses self-aspiration as an aeration mechanism, which conveniently allows for the decoupling of aeration and separation by flotation. The slurry is introduced into the downcomer, which releases the slurry as a jet, creating a low-pressure region where air is supplied and then entrained into the slurry as tiny bubbles. Due to high

slurry velocity, gas nucleation is anticipated to occur within this region (Klassen and Mokrousov 1963), which further enhances solids aeration. The aerated slurry enters deep into the separation vessel, where the aerated solids are separated from the slurry as a froth. An interesting development in the flotation column is microbubble flotation, which first appeared in the Microcel (Yoon 1993). A modified version of the Microcel is shown in Figure 6.18 (right). In the Microcel, microbubbles are generated through the static mixer when the slurry is forced to flow through it with air addition. Highly turbulent conditions in the static mixer not only break the air down into small bubbles (known as microbubbles), but also encourage gas nucleation/precipitation selectively on hydrophobic particles under hydrodynamic cavitation conditions. As a result, the hydrophobic particles are effectively aerated within the static mixer and the aerated slurry is discharged into a column, where separation of aerated particles from the slurry occurs. To ensure a desired slurry velocity in the static mixer, required for microbubble generation and hydrodynamic cavitation, a portion of the tailings is pumped back to the static mixer. Such tailings recirculation acts as a scavenger of flotation tailings, ensuring high recovery. At the top of the column, washwater is often added to suppress the process water containing unwanted fine solids, improving the froth quality. The Microcel column is essentially a rougher/scavenger/cleaner flotation circuit, if operated properly.

Instead of using a static mixer, Xu, Quinn, and Stratton-Crawley (1996) used a venturi-type aerator for inline feed aeration. Fan and Tao (2008) extended the Microcel column to include a hydrodynamic cavitation tube. In situ bubble generation by hydrodynamic cavitation further improved flotation recovery for both fine and coarse particles by encouraging multi-bubble aeration.

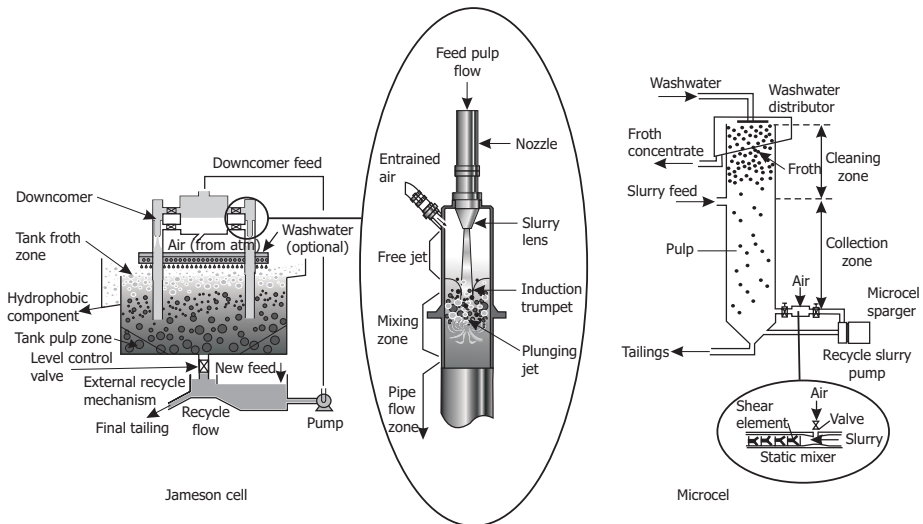


Figure 6.18 Two column-type flotation cells, with gas nucleation components as in dissolved air flotation, but in which gas nucleation is accomplished by hydrodynamic cavitation. These flotation cells are currently under evaluation in the oil sands industry.

Source: redrawn from Xstrata Technology and CISA commercial brochures.

Although not conventionally used in the oil sands industry, inline feed aeration systems, such as the Jameson cell or modified columns of static mixer or cavitation tube aeration mechanisms, are being tested on both the pilot and plant scales. These systems offer the incentive of a high bitumen recovery and froth quality. Since there are no moving parts in these systems, they are simple to operate and maintain, while the parts that are susceptible to wear, such as downcomers and static mixers, can be replaced without stopping the operation.

It should be noted that the flotation machines discussed above are just a few examples of the various types of flotation machines available. The reader is encouraged to consult Wills and Napier-Munn (2006), Fuerstenau and Han (2003), and Parts 1 and 4 of Fuerstenau, Jameson, and Yoon (2007) for a more extensive discussion on the subject.

6.3.4 Flotation Circuits

Regardless the type of flotation machine, flotation cells are often arranged in banks, as shown in Figure 6.19. Middlings from primary separation vessels are fed to bank 1, consisting of three cells, which acts as a rougher. The froths from each cell are collected as a secondary froth that is recycled back to primary separation vessels for further cleaning, or sent directly to froth treatment. The tailings from bank 1 flow into bank 2, known as the scavenger, to further recover remaining bitumen. The bitumen froth from bank 2 is usually of lower quality than that from bank 1 and is not suitable for sending to froth treatment or back to primary separation vessels. It is therefore sent to bank 1 for further cleaning. The tailings from bank 2 contain a minimum amount of bitumen and are discharged as final tailings. The objective in arranging the flotation cells into banks is to maximize bitumen recovery while ensuring bitumen froth quality by optimizing the operations of each cell.

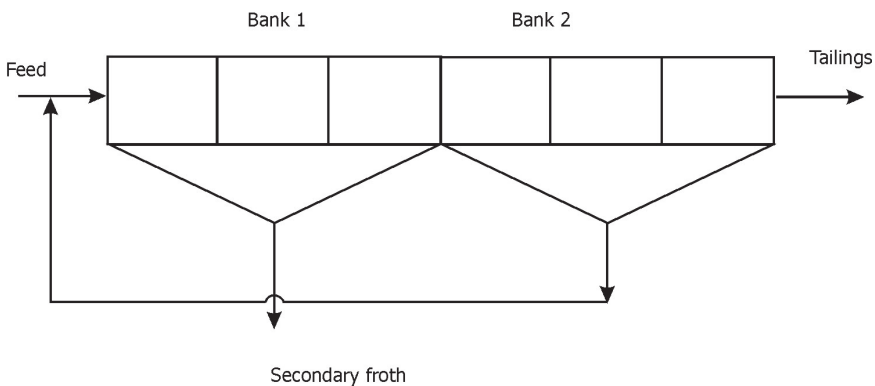


Figure 6.19 A typical flotation circuit, including a rougher (bank 1) and a scavenger (bank 2) in series.

Source: Wills and Napier-Munn (2006).

Within a given flotation cell, the system is considered to be well-mixed and the recovery rate, $R(t)$, is given by

$$R(t) = R_{\infty} \frac{kt}{1 + kt} \quad (6.23)$$

where R_{∞} is the ultimate flotation recovery, determined by ore characteristics, water chemistry, and conditioning systems; k is the flotation rate constant; and t is residence time. From cell to cell and bank to bank, the flotation system can be considered to be in a plug flow. Under the plug flow condition, the flotation recovery follows the first-order rate process, and can be described by the following rate equation:

$$R(t) = \frac{R_{\infty}}{1 - e^{-kt}} \quad (6.24)$$

For a bank of n number of flotation cells, the overall bitumen recovery, R , is given by

$$R = \sum_{i=1}^n R_i(t_i) = 1 - (1 - R_j)^n \quad (6.25)$$

where $R_i(t_i)$ is the bitumen recovery of the i^{th} cell of residence time t_i . The second equal sign in Eq. (6.25) assumes that i) all of the cells achieve the same unit recovery, R_j , over the same residence time; ii) the amount of froth removed from each cell is negligible compared to the remaining main slurry stream; and iii) the bitumen remaining in the flotation cell has the same flotation rate constant as in the previous cells. In reality, one would like to operate each cell independently to maximize the cell hydrodynamics and hence, the bitumen recovery. The size of flotation cells in volume V (given in m^3) is determined by the required residence time t (given in s) and the plant throughput Q (in m^3/s):

$$V = Q \times t \quad (6.26)$$

The residence time t is determined by the required bitumen recovery R of the known flotation rate constant. In the context of flotation cell design, the distance, H , that an aerated bitumen droplet must travel and the rising velocity of an aerated bitumen droplet, v_a , are used to determine the residence time:

$$t = \frac{H}{v_a} \quad (6.27)$$

The rising velocity (v_a) of the aerated bitumen–air bubble aggregates is a function of the effective size (d_a) and density (ρ_a) of the aerated bitumen droplets for a given slurry density. The subscript a here emphasizes the bitumen-air aggregates. H is

considered to be the distance from the feed point to the level of froth, provided that the bitumen froth removal is not a limiting step. Assuming a case of bitumen engulfing an air bubble, the rising velocity of bitumen-air aggregates can be estimated using the simple Stokes' law, or with more accuracy using Masliyah's hindered settling equation (Masliyah 1979). For the simplicity of discussion, let us estimate the rising velocity of bitumen-air bubble aggregates using Stokes' law for a low Reynolds number condition:

$$v_a = \frac{g(\rho_w - \rho_a)d_a^2}{18\mu} \quad (6.28)$$

Here, ρ_w and μ are the density and viscosity of liquid, i.e., water. The effective size and density of the aerated bitumen, on the other hand, depend on the size and density of the bitumen droplets and air bubbles. The size (d_a) and density (ρ_a) of an air bubble that is engulfed by a bitumen droplet of size d_p and density ρ_p are given by the equations

$$d_a = \sqrt[3]{d_p^3 + d_b^3} = d_p \sqrt[3]{1 + \left(\frac{d_b}{d_p}\right)^3} = d_p \sqrt[3]{1 + (\alpha)^3} \quad (6.29)$$

and

$$\rho_a = \frac{d_p^3 \rho_p + d_b^3 \rho_b}{d_p^3 + d_b^3} = \frac{\rho_p + \alpha^3 \rho_b}{1 + \alpha^3} \quad (6.30)$$

where α is defined as the dimensionless size of the air bubbles, i.e., the diameter ratio of air bubble and bitumen droplets. It is evident from Eq. (6.29) that, for a given dimensionless size of air bubble, the larger the bitumen droplet, the larger the bitumen-air bubble aggregates, and the larger the rising velocity of the aggregates. For a given size of bitumen droplet, increasing the size of the air bubble also increases the effective diameter and the rising velocity of the bitumen-air bubble aggregates.

Since the density of saturated air at ambient conditions (1.19 mg/cm³) is much lower than the density of bitumen (980 mg/cm³), which is close to that of water (1000 mg/cm³), Eq. (6.30) shows that increasing the dimensionless size of air bubbles reduces the effective density of the aggregates and increases their rising velocity. Since aggregate rising velocity is proportional to the square of the aggregate diameter and only to the linear of the aggregate density, increasing the effective diameter of the aggregates by increasing the size of the bubbles is most effective for the transport of aerated bitumen in a separation vessel. However, one has to consider the collision and adhesion of bitumen to air bubbles, an essential step for bitumen aeration. In this case, collision is more effective when bitumen droplets and air bubbles are of an equal

size, although small bubbles are more effective in attachment. It is evident that, to optimize bitumen flotation recovery, a comprehensive model must be developed to fully capture all of the ways in which the size and surface properties of air bubbles and bitumen droplets affect the different aspects of bitumen flotation, including collision, attachment, aggregate rising velocity, and flotation cell hydrodynamics.

6.4 Processability

6.4.1 Ore Processability

Now that we have established a solid foundation in interfacial sciences as applied to oil sands extraction systems, we will take a closer look at the physicochemical factors that affect ore processability. The most important of these are the properties of the ore.

Impact of Ore Grade

Bitumen content has been traditionally used as an indicator of ore processability. In fact, ores with a bitumen content of below 7 % were considered uneconomical for processing. To some extent, bitumen content has been linked with the geological environment of the oil sands formation. Oil sands ores formed in fluvial environments usually contain relatively higher bitumen content than oil sands ores formed in marine environments. A clear correlation has been shown between bitumen content and fines content in an oil sands ore, i.e., high-fines ores contain low bitumen content (Cameron Engineers 1978; Cuddy 2004). The effect of fines content on bitumen recovery varies depending on the type of fines and the water chemistry. This is clearly shown in Figure 6.20, where the depression of bitumen recovery from a good processing ore is observed only when 1 wt. % smectite clays are co-added with 40 ppm calcium ions. The addition of kaolinite or illite at the same level with calcium ions does not show substantial depression on bitumen recovery. After extensive laboratory tests using a wide variety of ores with a bitumen content of 8 wt. % to 12 wt. % and a fines content of 8 wt. % to 40 wt. %, Wallace et al. (2004) showed that the presence of degraded illite (of swelling characteristics) depresses bitumen recovery. The observed depression is attributed to slime coating, confirmed by zeta potential distribution and direct colloidal force measurements using an atomic force microscope.

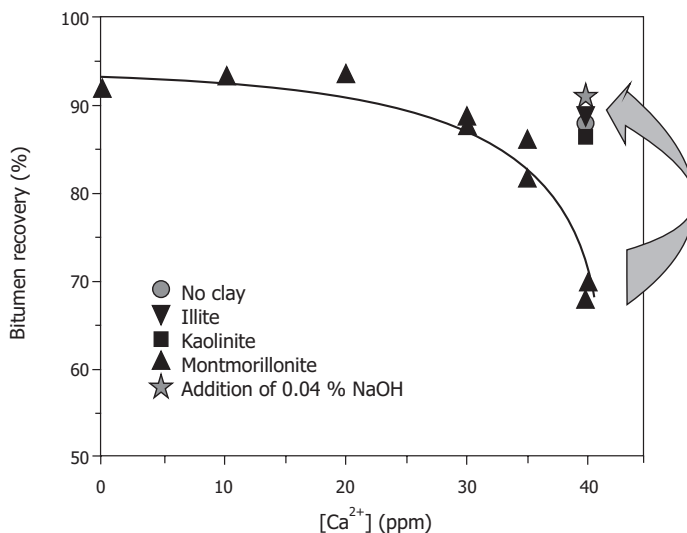


Figure 6.20 Effect of calcium ion concentration on bitumen recovery from a good processing ore doped with 1 wt. % fine clays. The flotation was conducted using a Denver flotation cell operated at 80 °C and at a slurry pH of 8.5.

Source: Kasongo et al. (2000).

Impact of Temperature

The processing temperature is considered to be vital for bitumen extraction from oil sands. A common notion regarding the role of temperature in oil sands extraction is that it reduces the viscosity of bitumen, which is true in many ways. However, a recent study by Long et al. (2007) showed that the effects of temperature are more profound, particularly in terms of the impact on the long-range forces and adhesion forces between bitumen and solids, as shown in Figure 6.21. At temperatures above 30.8 °C, the long-range repulsive forces between fine solids and bitumen increase, while the adhesion forces between bitumen and fine solids disappear (making bitumen retention on solid surfaces more difficult). Such changes in the adhesion and long-range repulsive forces cannot be directly linked with the reduction of bitumen viscosity with increasing temperature. The increase in repulsive forces indicates an increase in the charge of bitumen and/or solid surfaces with increasing temperature. It is conceivable that a decrease in bitumen viscosity with increasing temperature would facilitate the migration of natural surfactant from bulk bitumen to the surface, increasing the concentration of natural surfactant on bitumen, which is favourable for bitumen liberation (as shown in Figure 6.3). Increasing the temperature is also known to increase the hydrolysis of solid surfaces and decrease the hydrophobicity of solids, which can also improve bitumen liberation. In fact, Ren et al. (2009a) showed

that increasing the process temperature could restore the reduced wettability of solids resulting from ore weathering, improving bitumen recovery. Both the increased migration of natural surfactant in bitumen to the bitumen-water interface and the increased wettability by surface hydrolysis with increasing temperature will increase the degree of bitumen liberation and decrease the slime coating of fines.

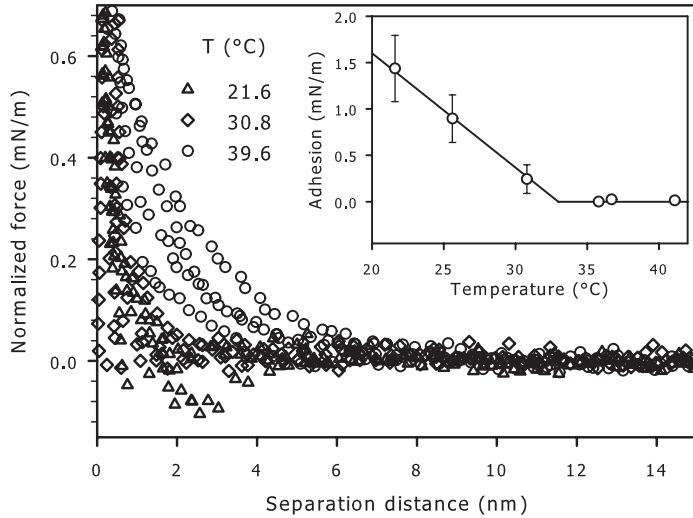


Figure 6.21 Effect of temperature on long-range and adhesion (inset) forces between fine solids and bitumen in tailings water at pH 8.5, showing a critical temperature of around 35 °C, above which there is no adhesion and surfaces are highly repulsive.

Source: Long et al. (2007).

Processing temperature also has a significant effect on bitumen aeration, as illustrated in Figure 6.22 by the decrease in induction time with increasing temperature. In the worst case of bitumen aeration in process water containing 50 ppm calcium ions and 0.5 wt. % fine solids, a reduction in induction time from 7000 ms at 25 °C to 1000 ms at 50 °C was observed (Gu et al. 2003). This level of induction time reduction with increasing temperature would contribute significantly to bitumen recovery, as shown by the results in Figure 6.23 (Long et al. 2007), where an increase in bitumen recovery from 10 % to above 90 % was observed when the processing temperature increased from 25 °C to 50 °C, regardless the nature of the ores. The sharp transition in the recovery curve as a function of temperature corresponds well with the sharp increase in the long-range repulsion forces and the sharp decrease in the adhesion forces between bitumen and fines, as well as the sharp reduction in induction time over a similar temperature range of 25 °C to 50 °C.

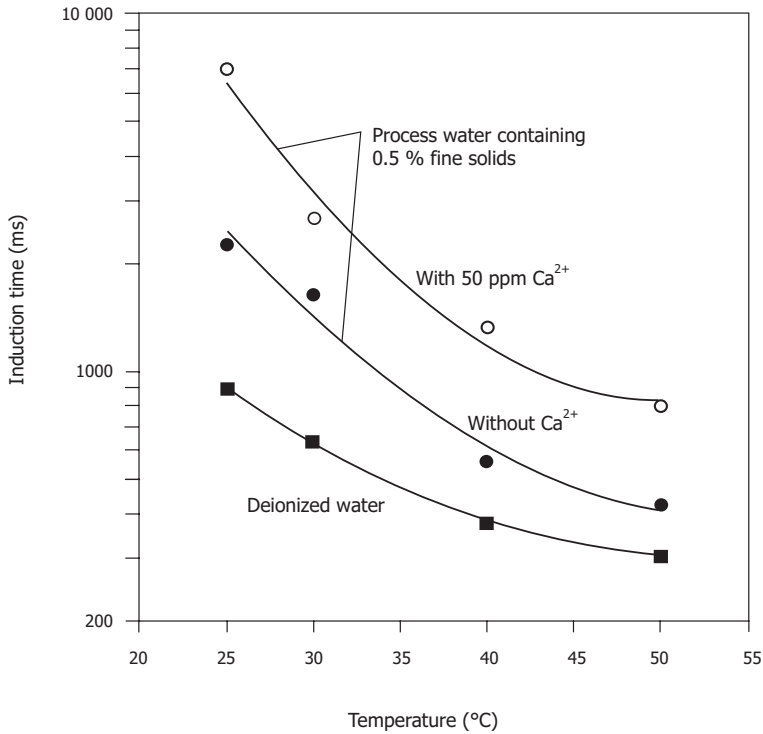


Figure 6.22 Induction time of air bubble–bitumen attachment as a function of temperature in process water containing 0.5 % fine solids. Deionized water is used as a reference.

Source: Gu et al. (2003).

Impact of Ore Acidity

Another important characteristic of an ore is its acidity, which is measured by the pH of the formation or slurry water. The acidity of an oil sands formation water ore can vary over a pH range of 4 to 8. Ding et al. (2006) showed a decrease in bitumen recovery when deionized water was used at lower processing pH—a result of illite addition. The reduction in bitumen recovery at lower processing pH is attributed to slime coating by the added illite on bitumen, as revealed by zeta potential distribution measurements. When plant process water with a substantial buffer capacity of pH ~ 8 was used, the addition of illite showed little effect on bitumen recovery. Kasongo et al. (2000) found that a suitable level of caustic addition could reverse the depression of bitumen recovery caused by the co-addition of 1 wt. % smectite clays and 40 ppm calcium ions (Figure 6.20). Caustic addition increases slurry pH, extracting more ionized natural surfactants from the bitumen and increasing its negative surface charge. Increasing pH also increases the dissolved CO₂ content, and hence the concentration of bicarbonate, which is known to scavenge calcium ions. The removal of calcium ions through the

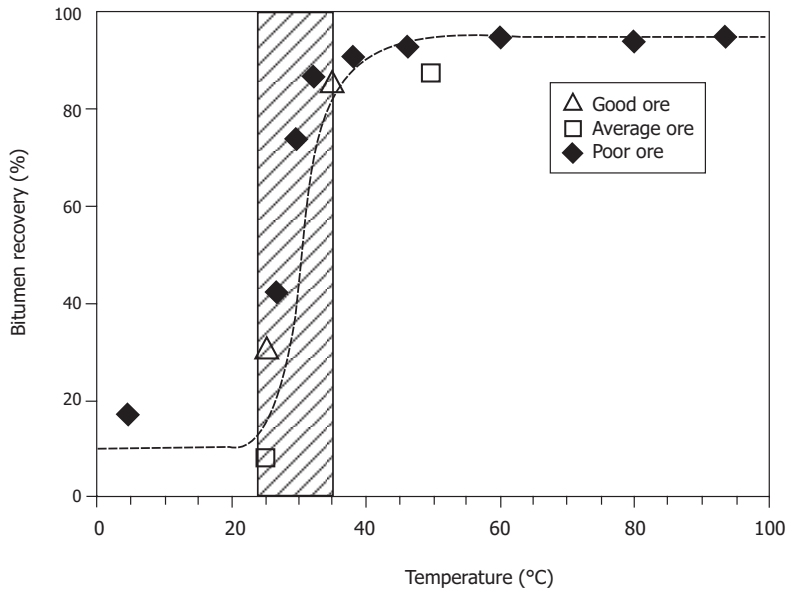


Figure 6.23 Effect of temperature on bitumen recovery in bench-scale tests.

After Long et al. (2007). Results were obtained from Ding et al. (2006) for good ore, Schramm et al. (2003) for average ore, and Bichard (1987) for poor ore.

formation of calcium carbonate helps restore negative charge on sand grains and clays while maintaining the desired level of natural surfactant. Collectively, these effects help avoid slime coating and enhance bitumen liberation, leading to an improved bitumen recovery and froth quality (Wallace et al. 2004).

Impact of Solids Wettability

Recently, Dang-Vu et al. conducted a systematic study on the role of solids wettability in oil sands processability (2009). Results obtained using a wide range of oil sands ores show a clear correlation between the wettability of fine solids in the ore and bitumen recovery and froth quality (Figure 6.24): higher wettability of fine solids (measured by shorter water drop penetration time) leads to a higher bitumen recovery and froth quality, as indicated by a high bitumen-to-solids ratio of froth. A similar correlation was also observed with coarse solids. As discussed earlier, the wettability of solids affects bitumen liberation and aeration. Solids of a lower affinity to water, i.e., high contact angle or longer water drop penetration time, hinder bitumen liberation, while slime coating by hydrophobic clay particles hinders aeration. The solids in naturally or artificially weathered ores of low formation water content were found to be more hydrophobic. It is interesting to note that weathering causes the loss of formation

water. As a result, electrolyte concentration in the remaining formation water increases, while the distance (or the thickness of water film) between the bitumen and solids decreases. A high concentration of electrolytes in formation water reduces the repulsion between bitumen and sands or clays, bringing the two surfaces much closer and allowing natural surfactant to adsorb on the solid surfaces, in particular in the presence of divalent inorganic cations such as calcium and/or magnesium ions. The adsorption of surfactant makes solids hydrophobic and is responsible for the observed decrease in their wettability and the poor processability of weathered oil sands ores.

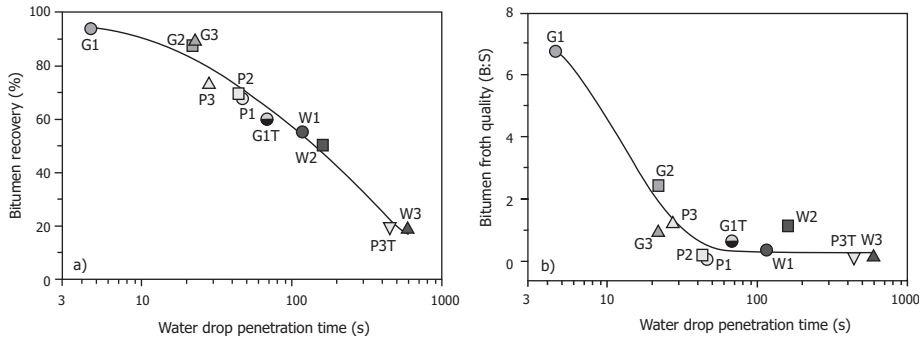


Figure 6.24 Effect of fine solids wettability on bitumen recovery (a) and froth quality measured by bitumen to solid ratio (B:S) (b), obtained from a number of good (G), poor (P), and weathered (W) oil sands ores, showing a decreasing bitumen recovery and froth quality with decreasing wettability of fine solids in the ores, as measured by a longer water-drop penetration time.

Source: Dang-Vu et al. (2009).

Impact of Water Chemistry

The chemistry of the processing water plays a significant role in determining the processability of oil sands ores, which is sensitive to the presence of both divalent cations and fine solids. As seen in Figure 6.25, the addition of calcium ions to clear process water leads to a noticeable decrease in the induction time (defined as the minimum contact time required for bitumen–air bubble attachment to occur), indicating that bitumen–air bubble attachment is easier with calcium ion addition (Gu et al. 2003). In the presence of fine solids in the processing water, the addition of calcium ions increases the induction time and makes bitumen–air bubble attachment more difficult. These results clearly illustrate the important role of water chemistry and of fine solids, whether they originate from the ore or are intentionally modified.

Traditionally, water chemistry was manipulated through the addition of caustic. Caustic is a chemical capable of softening water, dispersing clay, and adjusting pH. Increasing the pH of process water helps to release natural surfactants (Leja and Bowman 1968) and impart more negative charges to the surfaces of bitumen, sand,

and clays. It also promotes the precipitation of calcite, and can thus cause scaling on pipes and valves. High slurry pH has a direct and indirect impact on the properties of tailings and tailings water, and has significant environmental implications. Caustic has been used as a process aid in bitumen extraction since the very beginnings of the industry (Clark and University of Alberta 1929). With this multitude of various effects, it can be risky to focus on one or two specific roles of water chemistry or caustic addition without due attention to the others.

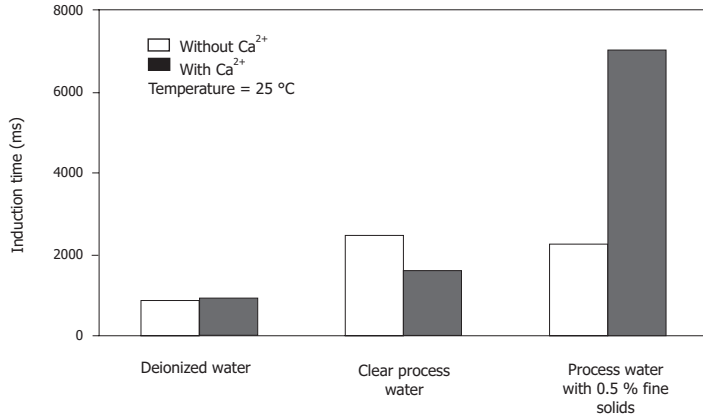


Figure 6.25 Induction time of bitumen–air bubble attachment, as affected by the addition of calcium ions to process water with and without fines at 25 °C and pH 8.5.

After Gu et al. (2004).

Effect of Clay and Calcium Addition on Bitumen Recovery

In Chapter 4, we saw that variation in the selectivity of divalent cation exchange with type of clay mineral plays an important role in oil sands extraction systems. As seen from the results in Table 4.3, montmorillonite undergoes the most swelling in the presence of divalent calcium cations in a solution, followed by illite and kaolinite. This variable impact is seen in early studies of bitumen recovery from a good processing oil sands ore doped with 1 wt. % clays of various kinds and with varying amounts of calcium ions, shown in Figure 6.20 (Kasongo et al. 2000). The addition of 1 wt. % of montmorillonite with 1 mM of calcium ions yields a more significant depression of bitumen recovery than the addition of the same amount of kaolinite or illite. This distinct difference between montmorillonite and illite/kaolinite is attributed to a stronger affinity of calcium ions to montmorillonite than to the latter two, as shown in Table 4.3. Kasongo (2006) determined calcium adsorption on these three types of clays and found that, during the flotation of good processing ores doped with 1 wt. % clays, the uptake of calcium is much higher with montmorillonite doping than with kaolinite or illite doping.

The adsorption of calcium ions on clay surfaces decreases the net surface charge of clay particles, as shown by the decrease in the magnitude of zeta potential in Figure 6.26. It is interesting to note that in bitumen extraction tests, when measured independently at pH 8.5, the impact of calcium addition on zeta potential was similar for all three types of clays. Yet, only montmorillonite clay was found to depress bitumen recovery when added with 1 mM calcium ions. Such a discrepancy may be related to the swelling nature of montmorillonite clays.

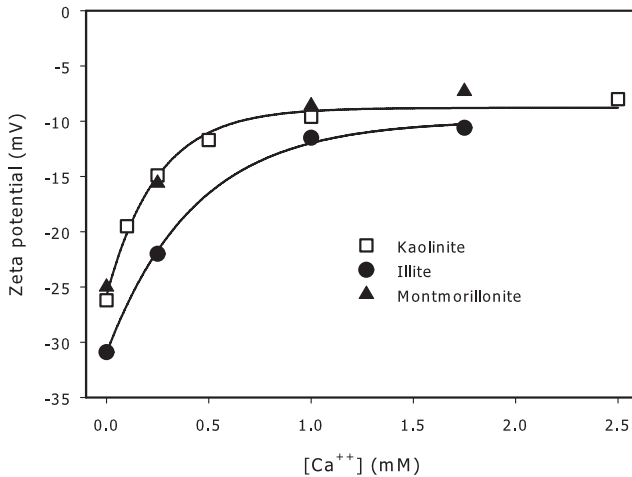


Figure 6.26 Effect of calcium ion concentration on zeta potential of clay particles in 1 mM KCl aqueous solutions of pH 8.5.

Replotted based on the results by Liu, Xu, and Masliyah (2004). The minerals were purchased from Ward's Natural Sciences (Rochester, NY).

Sludging of the Separation Vessel

As we discussed previously, the stability of a suspension is primarily controlled by the electrostatic, repulsive interaction between particles. On a micro scale, if the repulsion is not sufficiently strong, the particles will stick to each other after colliding due to agitation and/or particle Brownian movements. On a macro scale, however, the behaviour of the systems also depends on the amount of fines present or on the effective volume fraction of the fines. At low fines volume fractions, the aggregates (flocs) formed will settle to the bottom of the vessel, leaving clear water on top. This approach is used to remove fine solids from process-affected water and is a common procedure in water treatment plants, where the loading of fines in the feed water is low.

In bitumen extraction middlings, loading of fine solids in water is relatively high, such that when the repulsion between fines is weak (for whatever reasons), the

total volume of the flocculated solids can become comparable to the volume of the middlings layer in the separation vessel. If this happens, the individual flocs touch each other throughout the middlings layers, forming a superstructure that fills the entire cross-section of the vessel with a gel-like material. This material causes a dramatic increase in the viscosity of the middlings layers. Both the rising velocity of the aerated bitumen and the falling velocity of the sand grains decrease sharply. As a result, the density of the middlings increases. In extreme cases, no separation takes place at all and the vessel becomes “sludged.” The conditions that favour this phenomenon are a slurry of a high fines volume fraction and low repulsion between the fines. As calcium and magnesium ions tend to lower the surface charge of the fines, the danger of sludging in the separation vessel increases with increasing hardness of the process water. Common coping strategies are to cut back on the ore feed rate and/or to add more water, therefore lowering the total volume fraction of fines. Another common strategy is to add caustic, thus removing calcium and increasing the repulsive interactions between the fines through increased negative surface charges on the solids. The transition from a dispersed state (which is favourable for bitumen separation) to a flocculated state (which is preferred in tailings) will be discussed in more detail later and is shown schematically in Figure 6.31.

Slime Coating

The gelation (sludging) of fines by reduced repulsion between fine particles is not the only mechanism that affects bitumen recovery. The fines can also interact with other species present in the system. Their interaction with bitumen is especially important. When a small solid particle collides with a bitumen droplet, it can become permanently attached to the bitumen droplet, unless there is a sufficiently high energy barrier preventing this attachment from occurring. The source of repulsive interactions, and thus the source of this barrier, is the electric charge on the particle and bitumen surfaces. Both bitumen and fine solids have to carry like charges, and those charges have to be sufficiently high to prevent attachment. In mineral processing language, the coverage of a valuable mineral with fines is called *slime coating*. If a bitumen droplet is covered with clay fines, an approaching air bubble ‘sees’ the hydrophilic clays coating on the droplet surface rather than the hydrophobic bitumen underneath. Under such a condition, the bubble will not attach to slime-coated bitumen. Since attachment of the bitumen to air bubbles is a necessary condition for bitumen recovery, slime coating is detrimental. Masliyah et al. (2004) and Kasongo et al. (2000) have shown that the addition of smectite clay (montmorillonite) and calcium ions to oil sand slurry results in a dramatic drop in bitumen recovery. Both laboratory studies (Liu et al. 2002) and commercial operations (Liu, Masliyah, and Xu 2004) have shown that slime coating is, indeed, responsible for poor bitumen recovery.

The slime coating phenomenon is illustrated in Figure 6.27. The adsorption of cationic calcium ions on clay surfaces (I) triggers the adsorption of natural surfactant on clay surfaces (II), rendering them hydrophobic. The hydrophobized clay can float

by attaching to air bubbles, reducing bitumen froth quality. If the hydrophobized clay comes into contact with hydrophobic bitumen droplets, it can attach to them as well, leading to slime coating by clay on the bitumen (III). In this case, the slime-coated bitumen droplet remains hydrophobic and is able to attach to air bubbles for its recovery to bitumen froth, reducing froth quality without reduction in bitumen recovery. Alternatively, the calcium-activated clay can attach to the bitumen surface through anionic natural surfactant at the bitumen-water interface (IV), which again leads to slime coating of bitumen, but by hydrophilic clays. A bitumen droplet coated by hydrophilic clays will not be able to effectively attach to the air bubbles, resulting in reduced bitumen recovery.

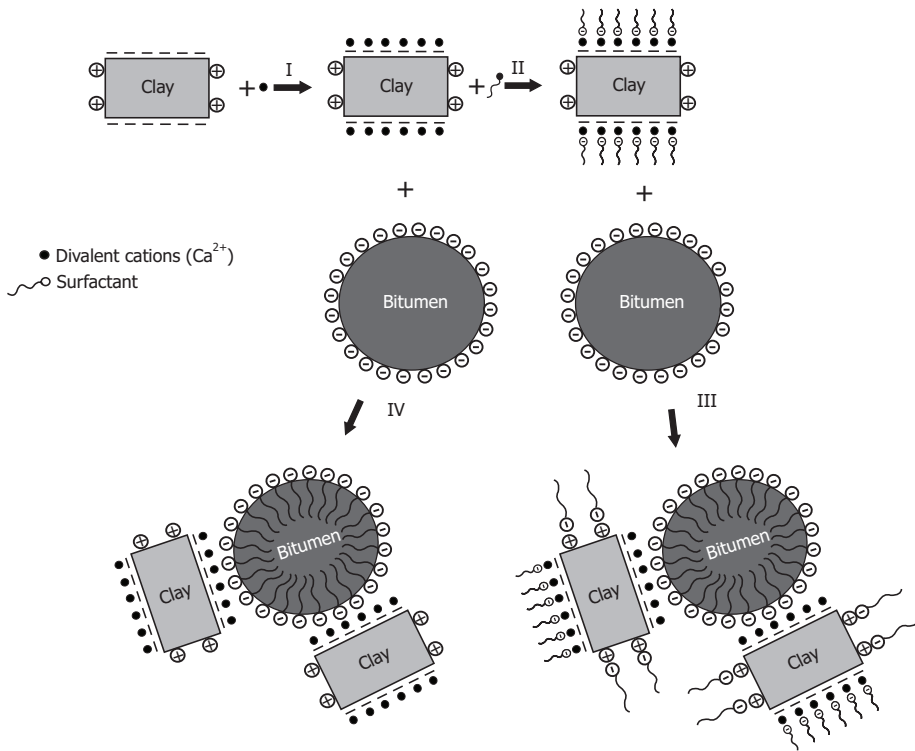


Figure 6.27 Schematic illustration of slime coating on bitumen surfaces triggered by divalent calcium cations acting as a bridge in two different operating modes: a) calcium cations adsorbed on the clay react with carboxyl groups on bitumen (IV), leading to slime coating of the bitumen droplet by hydrophilic clays; and b) calcium cations on the clay induce adsorption of anionic surfactant (II and III), making the clay hydrophobic and hence amenable to attachment to the hydrophobic bitumen surface, resulting in the bitumen droplet being coated by hydrophobized clays.

The detrimental effects of slime coating on bitumen in high-fines ores on bitumen recovery and froth quality were confirmed through zeta potential distribution measurements (Liu, Masliyah, and Xu 2004) and direct force measurements using an atomic force microscope (AFM) (Liu, Xu, and Masliyah 2005). The results of zeta potential distribution measurements conducted with bitumen and fines isolated from good and poor processing ores in corresponding processing tailings water are shown in Figure 6.28. For the good processing ore, zeta potential distributions of bitumen droplets and fines measured individually in the corresponding processing tailings water peaked at -71 mV and -45 mV, respectively, as shown in the upper left plate. When a mixture of bitumen droplets and fines in the processing tailings water was measured, two distinct zeta potential distribution peaks were observed at locations corresponding to those measured for bitumen droplets and fines individually, suggesting that bitumen and fines are separated from each other, as indicated in the lower left plate and its inset. Such an environment would lead to a good bitumen recovery, as observed experimentally by Liu, Xu, and Masliyah (2004).

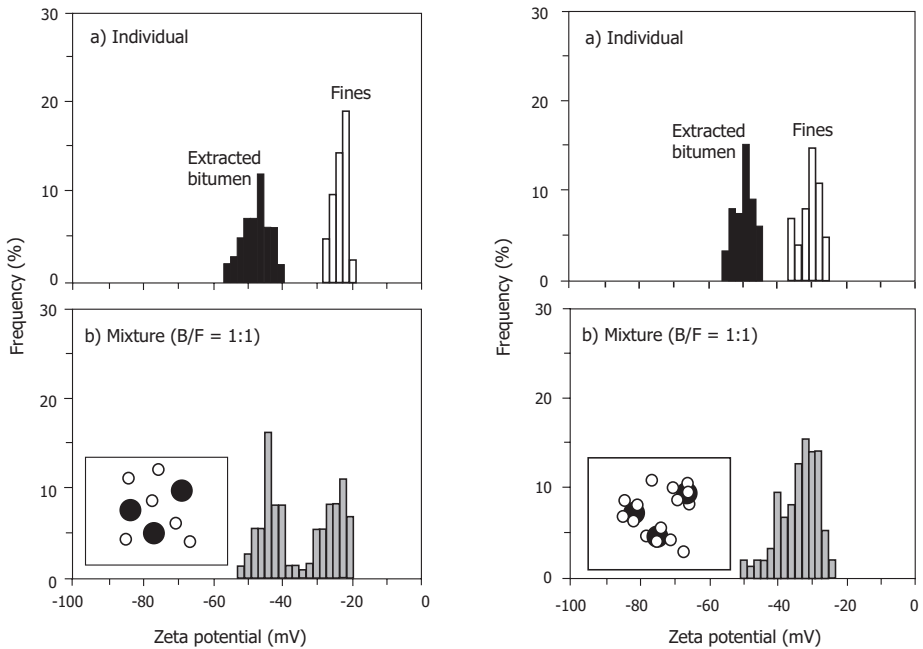


Figure 6.28 Zeta potential distribution of bitumen and fines isolated from good (left) and poor (right) processing ores in corresponding process tailings water of pH 8.5, measured individually (a) and in a mixture (b).

Source: Liu, Masliyah, and Xu (2004).

As shown in the upper right plate of Figure 6.28, when measured separately in the processing tailings water, the zeta potential distributions for bitumen and fines from the poor processing oil sands ores peak at -50 mV and -28 mV, respectively. These values are considerably lower than for the good processing ores, suggesting a significant suppression of negative surface charges on both bitumen and fines surfaces. This charge suppression is attributed to the adsorption of calcium that is present in the processing tailings water of the poor processing ores, as determined independently by an atomic absorption spectrophotometer (AAS). More importantly, when zeta potential distribution was measured using a mixture of bitumen droplets and fines in its processing tailings water, there was only one broad distribution peak, at the location corresponding to that for fines, as shown in the lower right plate of Figure 6.28. This type of zeta potential distribution suggests hydrophilic (or less hydrophobic) fines coating on the bitumen surface, as shown in the inset of the lower right plate of Figure 6.28. The coating of the bitumen by fines hinders the attachment of bitumen to air bubbles, resulting in lower bitumen recovery, as often experienced in the processing of high-fines ores.

The results of direct force measurements using AFM, shown in Figure 6.29 (left), indicate a purely repulsive force profile (i.e., positive in the force curve) and minimum adhesion (right) between bitumen and fines isolated from a good processing ore in corresponding processing tailings water. In contrast, a purely attractive force profile (i.e., negative in the force curve) with strong adhesion forces was determined between bitumen and fines isolated from a poor processing ore in its processing medium. These results reinforce the conclusions derived from zeta potential distribution measurements: an attractive-force profile and strong adhesion between bitumen and fines isolated from the poor processing ore leads to fines coating on bitumen surfaces and results in low bitumen recovery, while a repulsive-force profile with negligible adhesion between bitumen and fines isolated from the good processing ore leads to clean bitumen surfaces without fines coating and results in good bitumen aeration and recovery. The reduction of the electrical double layer repulsion between bitumen and fines with either increasing electrolyte concentration and/or decreasing processing water pH was found to be responsible for slime coating.

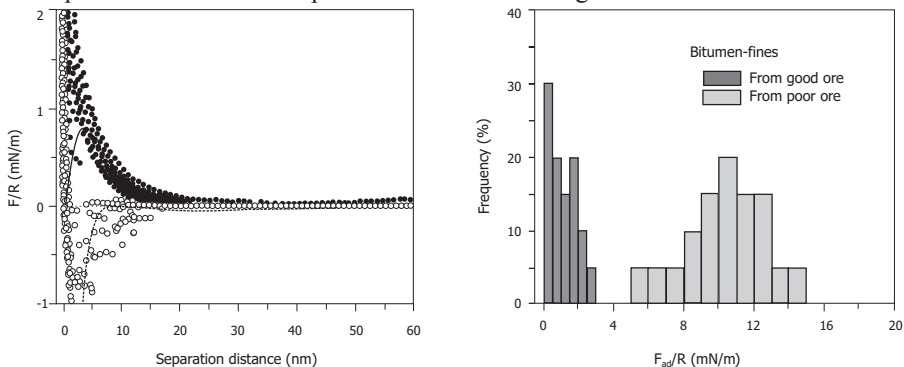
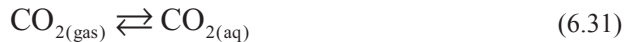


Figure 6.29 Interaction forces (left) and adhesion forces (right), in tailings water of pH 8.5, between bitumen and fines isolated from tailings of good and poor processing ores

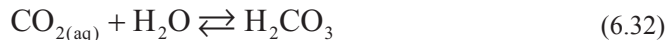
The addition of caustic can, to a certain extent, help us cope with poor recovery resulting both from sludging of the separation vessel and from the slime coating mechanism. In the past, it was common practice to try to increase caustic addition when the commercial operation suffered from lower-than-expected recovery. In both cases, the action of caustic is twofold: it decreases the concentration of calcium ions (as discussed in the next section, on water softening), and it increases the negative surface charge on both bitumen and fines. Both make fines flocculation and slime coating formation more difficult.

Water Softening

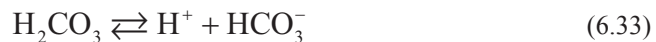
Water hardness is the result of dissolved multivalent cations; under normal conditions, these are almost exclusively calcium and magnesium ions, although sometimes, ferric ions may significantly contribute to the overall water hardness. Increasing the pH of water generally makes water softer, i.e., leads to a lower overall soluble divalent cation concentration. To understand how this works, it is beneficial to recall the basic equilibria in a system of water containing carbon dioxide and dissolved calcium ions. Usually, unless special precautions are taken, water is in equilibrium with air, i.e., it is saturated with all of the gases forming the air, including CO₂. Such a system is usually called “open” to reflect that it is able to exchange CO₂ with air.² Carbon dioxide dissolves in water as follows:



The dissolved CO_{2(aq)} reacts with water, forming carbonic acid:



Carbonic acid is a weak acid that dissociates into ions. The two-step dissociation reaction is:



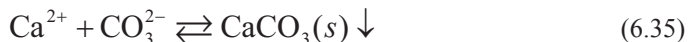
and



² It should be noted that hydrotransport slurry, being confined within the walls of the pipe, is not open to air and cannot exchange CO₂ with the atmosphere. A tailings pond can be considered to be an open system.

At any time, all of the above species are present in the system in quantities dependent on the amount of carbon dioxide in air, on the temperature, and on the pH of the water.

As the pH of the water increases (e.g., through the addition of caustic), the equilibria in reactions (6.31) to (6.34) shift to the right, with two important consequences: first, more carbon dioxide is allowed to dissolve; and second, the concentration of carbonate ions increases. When the product of calcium and carbonate ion concentrations in water exceeds the solubility product of calcium carbonate, i.e., $[Ca^{2+}][CO_3^{2-}] > K_{SP(CaCO_3)}$, calcium ions precipitate as calcium carbonate (calcite):



Thus, precipitation of calcium can be triggered by an increase in pH if the water can draw the necessary CO_2 from the air, which is a characteristic of an open system. In a closed system, e.g., when the water is confined within a vessel or a pipe, calcium precipitation can only occur if the water has a sufficient amount of already-dissolved CO_2 . Depending on the pH, the dominant carbonate species varies, from dissolved carbonic acid ($H_2CO_{3(aq)}$) at low pH to bicarbonate (HCO_3^-) or carbonate (CO_3^{2-}) ions at high pH. The total amount of dissolved carbonate species is often referred to as *carbonate alkalinity*. At operating plants that have used caustic as a process aid for a long time, recycle water has built up a considerable alkalinity or inventory of carbonate and bicarbonate ions. Bicarbonate ions, the dominant form of carbonic species at neutral and moderately alkaline conditions ($6 < pH < 10$), are present in the recycle water at about 500 ppm to 1000 ppm.

Figure 6.30 shows the precipitation onset for calcium carbonate, calcium hydroxide, and magnesium hydroxide as a function of aqueous pH. The first of the three straight lines represents the solubility limit of $CaCO_3$ in a system open to the atmosphere with 0.03 vol. % CO_2 , a typical value for CO_2 content in air. Magnesium carbonate solubility is substantially higher than that of calcium carbonate. This finding implies that adding bicarbonate or increasing pH is less effective in alleviating the detrimental effects of magnesium ions on bitumen recovery under the normal operating pH range. With increasing pH, magnesium hydroxide, rather than carbonate, would start to precipitate. The second and third straight lines show the solubility of $Mg(OH)_2$ and $Ca(OH)_2$, respectively.

Without any bicarbonate or carbonate ions, calcium would eventually precipitate as calcium hydroxide, but only at substantially higher pH values, as shown in the figure. Magnesium also contributes to overall water hardness, and is as detrimental to bitumen recovery as calcium is. However, because of the higher solubility of magnesium carbonate, unlike calcium, magnesium precipitates at high pH as magnesium hydroxide (Figure 6.30).

The family of curves in Figure 6.30 represents the solubility of calcium carbonate in a closed system, where precipitation of calcite consumes carbonate ions already present in the water. It should be noted that the onset of calcium precipitation depends on the initial concentration of bicarbonate ions, or the *carbonate alkalinity*. In water containing 1000 ppm bicarbonate ions, for example, calcium will start to precipitate at a pH that is 1.5 units lower than in water containing only 50 ppm bicarbonate.

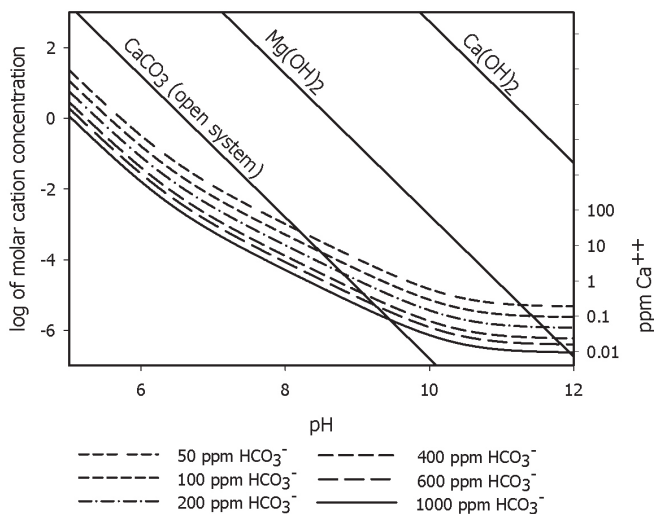


Figure 6.30 Solubility of selected calcium and magnesium species at various pH values. Precipitates are formed above corresponding lines.

Alternatively, at the same pH, increasing the bicarbonate level from 100 ppm to 1000 ppm lowers the equilibrium calcium level by a factor of ten. Since divalent ions, like calcium, are detrimental to bitumen extraction, the accumulated bicarbonate ion inventory is beneficial, and if it is lowered, it will increase the process demand for caustic or other process aids.

The presence of bicarbonate and carbonate ions in water has an important side effect. For instance, if a small amount of an acid is added to water containing both ions, the equilibria described by Eqs. (6.34) and (6.35) will shift to the left, converting some of the carbonate ions to bicarbonate ions with a negligibly small decrease in the water pH. Similarly, a small addition of a base will shift the equilibria to the right, again with little change in the water pH value. Chemists say that the water is buffered, i.e., its pH is relatively insensitive to small additions of a base or an acid. The amount of added acid or base that the water can tolerate without a marked change in pH depends on the total amount of carbonates present. A mixture of carbonates and bicarbonates buffers the water pH at about 8.5, which is close to the optimum value for oil sands conditioning and eventually, for bitumen recovery.

Since the bicarbonate/carbonate pair buffers water at moderate alkaline conditions, the accumulated total bicarbonate/carbonate inventory is called water carbonate alkalinity.³ Formally, the carbonate alkalinity is defined as the sum of bicarbonate and

³ The presence of precipitated species, such as CaCO_3 , adds to the total buffering capacity of the water, and in many cases, is the dominating contribution to the buffering capacity in natural river or lake waters. Because of this, aquatic scientists like to express the total water alkalinity in mg/L of CaCO_3 . This is often very confusing, especially in the context of calcite precipitation or water softening. The total alkalinity is measured by titration with an acid, and the shape of the titration curve allows differentiation between the total and the carbonate alkalinities.

carbonate ion concentration, expressed in chemical equivalents per litre. A chemical equivalent is equal to the molar mass divided by valence; thus for the bicarbonate ion, it is equal to its molar mass, and for the carbonate ion, it is equal to its molar mass divided by two.

The buffering capacity of the process water due to carbonate alkalinity has a positive impact on oil sand conditioning. It makes the process less sensitive to acidic ores, as the process water is to a certain extent capable of neutralizing acids that come with the formation water. It is very likely that the buildup of alkalinity in recycle waters was responsible for a decline in the demand for caustic as a process aid.

The recent introduction of consolidated/composite tailings (CT) technology for tailings disposal, where calcium is added in the form of gypsum, increases water hardness and decreases carbonate alkalinity. This may force operating companies to consider water softening technologies to cope with the detrimental effects of increased levels of calcium and magnesium in process waters. We must remember that water softening processes lower water carbonate alkalinity. Water softening through the addition of lime (Ca(OH)_2) lowers the alkalinity more than softening with NaOH, as lime supplies additional calcium that has to be precipitated at the expense of further depletion in the carbonate alkalinity. The difference in alkalinity decrease using lime and caustic softening is less than 30 % of the total, but should be considered in the overall picture while discussing various softening technology options.

It is worth adding two additional comments. First, it is well known that in oil sands tailings ponds, various bacteria utilize organics (such as hydrocarbons) as their energy source. The byproduct of the oxidation is carbon dioxide, which contributes to the total carbonate alkalinity. The extent of this contribution is difficult to quantify, but biogenic gas production within settling ponds has resulted in an increase in alkalinity over the years. The second comment is that in the past, caustic was added to the slurry in tumblers. Typical dosages were 100 g to 150 g for every ton of oil sands (0.01 wt. % to 0.015 wt. %), with a water-to-ore ratio of about 0.4 and a pH in excess of 10.5, so that both calcium and magnesium would precipitate as CaCO_3 and Mg(OH)_2 , respectively. The precipitates formed were removed from the water with the extraction tailings, and calcium and magnesium concentrations below 10 mg/L were standard. One may think of this process, with caustic addition at the conditioning stage, as a water-softening plant that produces bitumen froth at the same time, i.e., a coupled water-softening *and* bitumen extraction plant.

Impact of Natural Surfactants

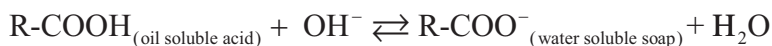
In conventional mineral processing, at least three types of surface-modifying chemicals are routinely added as process aids. *Frothers* are used to help create small air bubbles and to slow the bubbles' coalescence in order to assure the optimum bubble size distribution. *Collectors* are used to make the surfaces of the target mineral that is to be recovered selectively hydrophobic, thus promoting valuable mineral-air bubble attachment. Finally, *depressants* are used to make gangue (waste) minerals more

hydrophilic in order to decrease their attachment to air bubbles and thus, improve the quality of the concentrate. In the oil sands industry, we try to recover bitumen, a mineral that is naturally hydrophobic and possesses a natural affinity to air. Thus, under most conditions, no collector is required. Bitumen contains several classes of surface-active chemicals, some of which can be leached to the water phase, fulfilling the role of a frother and, to a certain extent, a depressant of hydrophobic fine solids. In many cases, as a result of these two fortunate properties of oil sand (i.e., its natural hydrophobicity and its natural surfactant content), no chemical addition is required for bitumen recovery. Unfortunately, such good-quality ores are not the most frequently encountered and, as it will be shown below, for the majority of ores, chemical aids (most frequently caustic) must be added to the oil sand slurry to maximize bitumen recovery.

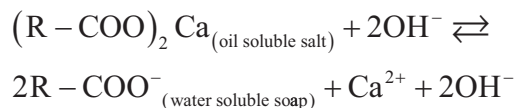
It is now well established that increasing the pH of the slurry helps in releasing the natural surfactants from bitumen to the aqueous phase. Sanford and Seyer showed that addition of NaOH to the oil sand–water slurry caused a decrease in the surface tension and an increase in the dissolved carbon content of the water (1979). Further studies of process water samples with varying amounts of caustic addition established that the titration curves for process water were very similar to the titration curve of sodium oleate, a type of soap. This was a strong indication that the addition of caustic helps to release the natural surfactants present in bitumen, and that these surfactants are likely to be carboxylic acid salts (Schramm, Stasiuk, and Turner 2003). It has been shown that the surfactants present in tailings and process recycle water are mostly the sodium salts of naphthenic acids.

Naphthenic acids are a class of carboxylic acids of a petroleum origin. Their sodium salts are thus chemically very closely related to the sodium salts of fatty acids or soaps. The difference is that conventional soaps, made by the saponification of animal fats, contain straight hydrocarbon chains of even numbers of carbon atoms. As such, they are easily biodegradable, as most bacteria that degrade fats have enzymes that cut two carbons at a time from a straight hydrocarbon chain. Any chain branching, an odd number of carbons, and/or a ring structure in the hydrocarbon part of the surface-active organic molecules significantly deteriorates the enzyme's effectiveness. Naphthenic acids have hydrophobic tails that are branched and can contain both rings and an odd number of carbon atoms. As a result, they are not only more difficult to biodegrade, but also toxic to many life forms.

Natural surfactants may be present in bitumen either in the form of free carboxylic acids (naphthenic acids) or as their calcium and/or magnesium salts, which are oil-soluble but are insoluble in water. In any case, an increase in the pH of water would assist with surfactant release, either by converting hardly water-soluble carboxylic acids into more soluble soaps:



or by converting an oil-soluble divalent salt into a water-soluble form:



In the latter case, if the water contained bicarbonate and/or carbonate ions, as is usually the case, the calcium ions would be precipitated as calcium carbonate (Dai, Chung, and Czarnecki 1992).

We must remember that water-soluble surfactants are not the only surfactants generated by increasing the pH of the oil sand slurry. Water solubility will be limited to surfactants with less than about 18 to 20 carbon atoms per molecule. The solubility of commercial sodium naphthenate samples, which typically have 15 to 18 carbon atoms, is similar to that of common soap. In Athabasca bitumen, the majority of naphthenic acids have 21 to 24 carbons per molecule and a molecular weight of 300 to 400 Daltons. The sodium salts of these acids have relatively low solubility in water and are likely to stay with the bitumen. Although they cannot be easily detected in process-water analysis, they certainly contribute to the surface properties of bitumen, especially its surface charge.

Ionic surfactants adsorb on the bitumen-water interface, charging it according to the charge of surfactant ions. Thus, the adsorption of anionic surfactants such as naphthenic acid salts would cause bitumen droplets to carry a negative electric charge. Since all carboxylic acids, including naphthenic acids, are weak acids, the pH of the solution controls the surface charge originating from adsorbed naphthenic ions. The bitumen surface charge would become more negative with increasing pH, similar to the surface charge response to pH for most oxide minerals, as discussed in Chapter 2. Under normal process conditions, bitumen droplets are negatively charged.

Bitumen-in-Water Emulsions

Emulsions are defined as a dispersion of one liquid in another immiscible liquid. Emulsification, i.e., emulsion formation, creates a large specific interfacial area, with the total energy change given by

$$\Delta G = \gamma_{O/W} \Delta A \quad (6.36)$$

where $\gamma_{O/W}$ is the oil-water interfacial tension. Since the interfacial tension is positive in general, an increase in the interfacial area by emulsification increases the system's energy, making the system thermodynamically less stable. To produce an emulsion, therefore, external energy is required to offset the gain of thermodynamic energy. In the case of oil sands processing under a given hydrodynamic condition, increasing pH reduces the bitumen-water interfacial tension (as shown in Figure 4.57a), a favourable condition for bitumen-in-water emulsification, as only a small amount of energy is required to create a given surface area. Pumps and slurry hydrotransport pipelines are the source of mechanical energy for bitumen emulsification.

Eq. (6.36) also shows that an emulsion system is thermodynamically unstable, as coalescence, i.e., the combination of two bitumen droplets in water to form a larger bitumen droplet, reduces the interfacial area and hence, the energy of the system. However, bitumen-in-water emulsions are found to be extremely stable in highly alkaline aqueous solutions, even though they are thermodynamically unstable. This is attributed to the presence of negatively charged hydrophilic groups at the bitumen-water interface. Excess energy is required to overcome the long-range electrostatic repulsion and short-range repulsive hydration forces to cause coalescence of bitumen droplets in highly alkaline pH slurry. In addition, extremely low interfacial tension (near zero) at high pH values can contribute to a stable emulsion.

The emulsification of bitumen in water causes difficulties in bitumen recovery because the collision frequencies of small bitumen droplets with air bubbles are extremely small. One of the major reasons that hot water-based oil sands extraction operates at a mildly alkaline pH of 8.5 is to allow for the best compromise between bitumen liberation and aeration.

Segregating and Non-Segregating Slurry

When a tailings slurry is discharged to a tailings pond, the sand sediments quickly out of the fines-loaded water, forming beaches, while the well-dispersed fines remain suspended. The fines, requiring much more time to settle, follow the water into the body of the pond. There, they settle slowly, forming a sludge known as fluid fine tailings (FFT) or mature fine tailings (MFT), composed mostly of fine solid particles (up to 30 wt. %). However, if the fines are flocculated, the sand grains tend to be trapped in the flocculated fines structures. As a result, a ‘non-segregating’ mixture can be formed. This is the basis for the composite or consolidated tailings (CT) technology of tailings disposal (Matthews et al. 2002). The transition from a segregating to a non-segregating regime depends on the effective volume fraction of the fine solids and on the interaction energy between the particles, as shown in Figure 6.31. At a low volumetric fraction of the suspended solids, when the particles attract each other, the formed flocs of low solids loading will segregate.

To form a non-segregating system, the effective volume fraction of the solids must be sufficiently high. In CT technology, this sufficiently high solids volume fraction is achieved by adding more fine solids in the form of fine fluid tailings or mature fine tailings, and/or by removing some water through cycloning. In addition, the attractive interaction between the particles must be sufficiently strong. In CT, this is achieved with the addition of calcium ions, which lower the electrostatic repulsion between the fines by lowering their negative surface charges.

The concept of segregating and non-segregating slurry is well established in the tailings community; however, it is not widely used by those involved in extraction. In order to have a working separation vessel, the segregating condition, as shown in the lower left part of Figure 6.31, must be maintained. Operators accomplish this condition by adding more water when they observe a decrease in separation. By doing

so, they lower the volume fraction of the solids, moving the system to the left in the diagram. Another action that is often taken is to increase the dosage of caustic, which results in stronger repulsion between the particles, as discussed above. The addition of caustic moves the point describing the system downwards in the diagram shown in Figure 6.31. Similar results can be obtained by adding other dispersants, e.g.,

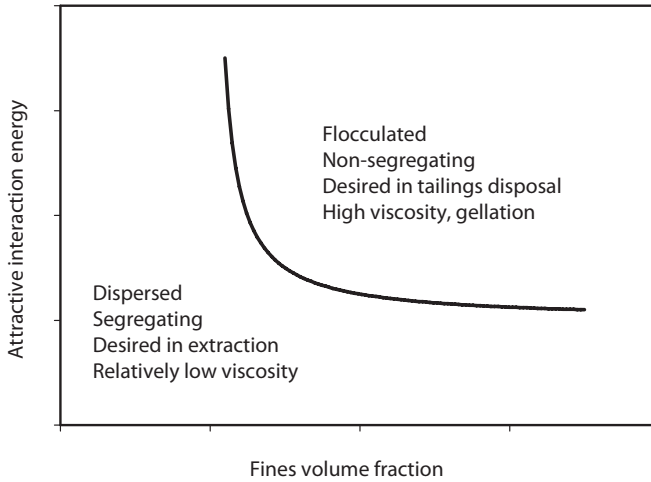


Figure 6.31 Transition from segregating to non-segregating fines suspension.

sodium hexa-metha-phosphate (also known as calgon) or sodium silicate, both popular dispersing agents.

As we can see, there are contradictory requirements between tailings treatment and extraction: in extraction, we would like to have well-dispersed fines, such that the separation of aerated bitumen and sand is promoted. In tailings treatment, we would usually like to have a non-segregating mixture of coarse solids and flocculated fines for enhanced fine solids capture. Therefore, in tailings treatment, we would prefer to have hard water with relatively high levels of calcium and magnesium at relatively low pH, as this would lower the required dosage of gypsum in making the CT. Thus, the addition of caustic in extraction makes tailings management more challenging. In extraction, soft water, a low fines level, and higher pH are all beneficial. Any hardness left in the recycle process water from tailings treatment is undesirable as it upsets the extraction. This is important to remember, especially while making any changes to either extraction or tailings procedures, as any such change can have a profound negative impact on the overall plant performance.

6.5 Concluding remarks

The discussion presented here is by no means a complete survey of the physicochemical properties affecting the processability of oil sands ores. Rather, it is intended to illustrate the complexity of oil sands extraction systems. We can see that ore characteristics, water chemistry, and temperature all have a significant impact on ore processability. It appears that we are still far from establishing a direct indicator of the processability of oil sands ores. The question itself of whether such a unique indicator exists remains to be answered. Nonetheless, we have demonstrated that colloidal science plays a key role in improving our current understanding of oil sands ore processability.

6.6 References

- Adamson, A.W., and A.P. Gast. 1997. *Physical Chemistry of Surfaces*. 6th ed. New York: Wiley.
- Baptista, M.V., and C.W. Bowman. 1969. The flotation mechanism of solids from the Athabasca oil sand. In *Proceedings of the 19th Canadian Chemical Engineering Conference*. Edmonton, Alberta, Canada: Canadian Society for Chemical Engineering.
- Basu, S., K. Nandakumar, and J.H. Masliyah. 1996. A study of oil displacement on model surfaces. *Journal of Colloid and Interface Science* 182 (1): 82–94. *With erratum in Journal of Colloid and Interface Science* 196, 324.
- Bichard, J.A. 1987. *Oil sands composition and behaviour research: The research papers of John A. Bichard, 1957–1965*, AOSTRA Technical Publication Series No. 4. Edmonton: Alberta Oil Sands Technology and Research Authority (AOSTRA).
- Cameron Engineers. 1978. Oil sands. In *Synthetic fuels data handbook: U.S. oil shale, U.S. coal, oil sands*, ed. G. L. Baughman. Denver: Cameron Engineers.
- Churaev, N.V., and B.V. Derjaguin. 1985. Inclusion of structural forces in the theory of stability of colloids and films. *Journal of Colloid and Interface Science* 103 (2): 542–553.
- Clark, K.A., and University of Alberta. 1929. Process and apparatus for separating and treating bituminous sands. Canadian Patent 289058, issued April 4, 1929.
- Clayton, R., G.L. Jameson, and E.V. Manlapig. 1991. The development and application of the Jameson cell. *Minerals Engineering* 4 (7–11): 925–933.
- Cuddy, G. 2004. Oil sands geology. Guest lecture notes for Chemical Engineering 534, Fundamentals of Oil Sands Extraction, January 7–9, at University of Alberta, Edmonton.

- Dai, Q., K.H. Chung, and J. Czarnecki. 1992. Formation of calcium carbonate in the bitumen/aqueous sodium hydroxide system. *AOSTRA Journal of Research* 8 (2): 95–101.
- Dang-Vu, T., R. Jha, S. Wu, D. Tannant, J. Masliyah, and Z. Xu. 2009. Effect of solid wettability on processability of oil sands ores. *Energy & Fuels* 23 (5): 2628–2636.
- Derjaguin, B.V., and L.D. Landau. 1941. Theory of the stability of strongly charged lyophobic sols and of the adhesion of strongly charged particles in solutions of electrolytes. *Acta Physicochem USSR* 14 (6): 633–662.
- Ding, X., C. Repka, Z. Xu, and J. Masliyah. 2006. Effect of illite clay and divalent cations on bitumen recovery. *Canadian Journal of Chemical Engineering* 84 (6): 643–650.
- Edzwald, J.K. 1995. Principles and application of dissolved air flotation. *Water and Science Technology* 31 (3–4): 1–23.
- Fan, M., and D. Tao. 2008. A study on picobubble enhanced coarse phosphate froth flotation. *Separation Science Technology* 43 (1): 1–10.
- Finch. 1995. Column flotation: A selected review. Part 4: Novel flotation devices. *Minerals Engineering* 8 (6): 587–602.
- Fuerstenau, D.W. 1982. Thermodynamics of surfaces, adsorption and wetting. In *Principles of Flotation*, ed. R. P. King. Johannesburg: South African IMM.
- Fuerstenau, M.C., and K.N. Han. 2003. *Principles of mineral processing*. Littleton, CO: Society for Mining, Metallurgy, and Exploration.
- Fuerstenau, M.C., G. Jameson, and R.H. Yoon, eds. 2007. *Froth flotation: A century of innovation*. Littleton, CO: SME Inc.
- Fuerstenau, M.C., J.D. Miller, and M.C. Kuhn. 1985. *Chemistry of flotation*. New York: SME.
- Gan, W., M. Cao, B. Crozier, and Q. Liu. 2007. Inhibiting quartz-bitumen coagulation by complexing agents. *Canadian Metallurgical Quarterly* 46 (3): 207–214.
- Gan, W., B. Crozier, and Q. Liu. 2009. Effect of citric acid on inhibiting hexadecane-quartz coagulation in aqueous solutions containing Ca^{2+} , Mg^{2+} and Fe^{3+} ions. *International Journal of Mineral Processing* 92 (1–2): 84–91.
- Gu, G., R. Sanders, K. Nandakumar, Z. Xu, and J. Masliyah. 2004. A novel experimental technique to study single bubble-bitumen attachment in flotation. *International Journal of Mineral Processing* 74 (1–4): 15–29.
- Gu, G., Z. Xu, K. Nandakumar, and J.H. Masliyah. 2003. Effects of physical environment on induction time of air-bitumen attachment. *International Journal of Mineral Processing* 69 (1–4): 235–250.
- Hunter, R.J. 1986. *Foundations of colloid science. Volume I*. Oxford: Clarendon Press.
- Israelachvili, J. 1990. *Intermolecular surface forces*. 2nd ed. San Diego: Academic Press.

- Ives, K.J., ed. 1978. *Scientific basis of flocculation*. NATO Advanced Study Institutes Series. Alphen aan den Rijn, The Netherlands: Sijthoff and Noordhoff.
- James, R.O., and T. Healy. 1972. Adsorption of hydrolyzable metal ions at the oxide-water interface (Parts I, II, and III). *Journal of Colloid and Interface Science* 40 (1): 42–52, 53–64, 65–81.
- Kasongo, T. 2006. Role of fine clays and ionic species in bitumen extraction from oil sands ores using the hot water extraction process. Ph.D diss., Department of Civil and Environmental Engineering, University of Alberta, Edmonton.
- Kasongo, T., Z. Zhou, Z. Xu, and J.H. Masliyah. 2000. Effect of clays and calcium ions on bitumen extraction from Athabasca oil sands using flotation. *Canadian Journal of Chemical Engineering* 78 (4): 674–681.
- Kitchener, J.A. 1984. Surface forces in flotation: a critique. In *Principles of mineral flotation: The Wark Symposium*, ed. M. H. Jones and J. T. Woodcock, 65–71. Victoria, Australia: Australia Institute of Mining and Metallurgy.
- Klassen, V.I., and V.A. Mokrousov. 1963. *An introduction to the theory of flotation*, Trans. J. Leja, and G.W. Poling. London: Butterworths.
- Leja, J., and C.W. Bowman. 1968. Application of thermodynamics to the Athabasca tar sands. *Canadian Journal of Chemical Engineering* 46: 479–481.
- Lelinski, D., J. Drelich, J.D. Miller, and J. Hupka. 2004. Rate of bitumen film transfer from a quartz surface to an air bubble as observed by optical microscope. *Canadian Journal of Chemical Engineering* 82 (4): 794–800.
- Liu, J., J.H. Masliyah, and Z. Xu. 2004. Interaction between bitumen and fines in oil sands extraction system: Implication to bitumen recovery. *Canadian Journal of Chemical Engineering* 82 (4): 655–666.
- Liu, J., Z. Xu, and J. Masliyah. 2004. Role of fine clays in bitumen extraction from oil sands. *AIChE Journal* 50 (8): 1917–1927.
- Liu, J., Z. Xu, and J.H. Masliyah. 2005. Interaction forces in bitumen extraction from oil sands. *Journal of Colloid and Interface Science* 287 (2): 507–520.
- Liu, J., Z. Zhou, Z. Xu, and J.H. Masliyah. 2002. Bitumen-clay interactions in aqueous media studied by zeta potential distribution measurement. *Journal of Colloid and Interface Science* 252 (2): 409–418.
- Long, J., J. Drelich, Z. Xu, and J. Masliyah. 2007. Effect of operating temperature on water-based oil sands processing. *Canadian Journal of Chemical Engineering* 85 (5): 726–738.
- Lynch, A.J., J.S. Watt, J.A. Finch, and G.E. Harbort. 2007. History of flotation technology. In *Froth flotation: A century of innovation*, ed. M. C. Fuerstenau, G. Jameson and R. H. Yoon. Littleton, CO: SME Inc.
- Mao, L., and R.H. Yoon. 1997. Predicting flotation rates using a rate equation derived from the first principles. *International Journal of Mineral Processing* 51 (1–4): 171–181.

- Masliyah, J.H. 1979. Hindered settling in a multi-species particle system. *Chemical Engineering Science* 34 (9): 1166–1168.
- Masliyah, J.H., Z. Zhou, Z. Xu, J. Czarnecki, and H.A. Hamza. 2004. Understanding water-based bitumen extraction from Athabasca oil sands. *Canadian Journal of Chemical Engineering* 82 (4): 628–654.
- Matthews, J.G., W.H. Shaw, M.D. MacKinnon, and R.G. Cuddy. 2002. Development of composite tailings technology at Syncrude. *International Journal of Mineral Processing* 16 (1): 24–39.
- Mishchuk, N., J. Ralston, and D. Fornasiero. 2006. Influence of very small bubbles on particle/bubble heterocoagulation. *Journal of Colloid and Interface Science* 301 (1): 168–175.
- Ren, S., T. Dang-Vu, H. Zhao, J. Long, Z. Xu, and J. Masliyah. 2009a. Effect of weathering on surface characteristics of solids and bitumen from oil sands. *Energy & Fuels* 23 (1): 334–341.
- Ren, S., H. Zhao, J. Long, Z. Xu, and J. Masliyah. 2009b. Understanding weathering of oil sands ores by atomic force microscopy. *AIChE Journal* 55 (12): 3277–3285.
- Sanford, E.C., and F.A. Seyer. 1979. Processability of Athabasca tar sand using a batch extraction unit: The role of NaOH. *CIM Bulletin* 72 (803): 164–169.
- Sato, T., and R. Ruch. 1980. *Stabilization of colloidal dispersions by polymer adsorption*. New York: Marcel Dekker.
- Schramm, L.L., E.N. Stasiuk, and D. Turner. 2003. The influence of interfacial tension in the recovery of bitumen by water-based conditioning and flotation of Athabasca oil sands. *Fuel Processing Technology* 80 (2): 101–118.
- Schramm, L.L., E.N. Stasiuk, H. Yarranton, B.B. Maini, and B. Shelfantook. 2003. Temperature effects from the conditioning and flotation of bitumen from oil sands in terms of oil recovery and physical properties. *Journal of Canadian Petroleum Technology* 42 (8): 55–61.
- Schulze, H.J. 1984. *Physico-chemical elementary processes in flotation*. Amsterdam: Elsevier.
- van Oss, C.J. 2006. *Interfacial forces in aqueous media*. Boca Raton: Taylor & Francis (CRC Press).
- Verwey, E.J.W., and J.T.G. Overbeek. 1948. *Theory of stability of lyophobic colloids*. Amsterdam: Elsevier.
- Wallace, D., R. Tipman, B. Komishke, V. Wallwork, and E. Perkins. 2004. Fines/water interactions and consequences of the presence of degraded illite on oil sands extractability. *Canadian Journal of Chemical Engineering* 82 (4): 667–677.
- Wills, B.A., and T.J. Napier-Munn. 2006. *Wills' mineral processing technology: An introduction to the practical aspects of ore treatment and mineral recovery*. 7th ed. Burlington: Butterworth-Heinemann (Elsevier).
- Xu, M., P. Quinn, and R. Stratton-Crawley. 1996. A feed-line aerated flotation column, Part I: Batch and continuous test work. *Minerals Engineering* 9 (5): 499–507.

- Yoon, R.H., and G.H. Luttrell. 1989. The effect of bubble size on fine particle flotation. *Mineral Processing and Extractive Metallurgy Review* 5 (1): 101–122.
- Yoon, R.H. 1993. Microbubble flotation. *Minerals Engineering* 6 (6): 619–630.
- Zabel, T. 1984. Flotation in water treatment. In *The scientific basis of flotation*, NATO Advanced Study Institutes Series, ed. K. J. Ives, 349–377. Boston: Martinus Nijhoff.
- Zhao, H., T. Dang-Vu, J. Long, Z. Xu, and J. Masliyah. 2009. Role of bicarbonate ions in oil sands extraction systems with a poor processing ore. *Journal of Dispersion Science and Technology* 30 (6): 809–822.
- Zhao, H., J. Long, J. Masliyah, and Z. Xu. 2006. Effect of divalent cations and surfactants on silica-bitumen interactions. *Industrial & Engineering Chemistry Research* 45 (22): 7482–7490.
- Zhou, Z., R.S. Chow, P. Cleyle, Z. Xu, and J. Masliyah. 2009. Dynamic bubble nucleation in flotation. In *Advances in Mineral Processing Science and Technology: Proceedings of the 7th UBC-McGill International Symposium on Fundamentals of Mineral Processing*, edited by C. Gomez, J. Nasset and R. Rao. Montreal: MetSoc.
- Zhou, Z., Z. Xu, and J.H. Masliyah. 2004a. Factors affecting bitumen surface hydrophobicity evaluated from contact angle measurements. In *NSERC Chair Program*.
- . 2004b. Factors affecting the recovery of bitumen from Athabasca oil sands in low temperature processes using flotation. In *NSERC Chair Program*.

Chapter 7

Froth Treatment Fundamentals

Froth produced in extraction operations typically contains ~ 60 vol. % bitumen, ~ 30 vol. % water, and ~ 10 vol. % solids. The water usually carries dissolved salts, which contribute to corrosion hazards in downstream operations. Coarse solids increase equipment wear, increasing overall operational costs, while fine solids plug reactor beds and contribute to emulsion stabilization. Pipeline networks also have strict specifications for acceptable levels of salt and solids content. Therefore, before bitumen can be fed to upgrading operations or to a pipeline, the solids and water have to be removed. The removal of water and solids is performed in the operation traditionally referred to as *froth treatment*. The first step in froth treatment is the addition of a light hydrocarbon solvent to dilute the bitumen and provide a density difference between the oil phase and the water necessary for water/oil separation. The addition of a solvent also lowers the oil phase viscosity, accelerating separation processes. The diluted bitumen is then fed to a system of stationary separators, such as inclined plate settlers (IPS), and rotary equipment, such as scroll and disk centrifuges. The industrial aspects of froth treatment operations will be discussed in Volume 2, in the chapter titled 'Froth Treatment.' Here, we will only cover the relevant fundamental science behind the froth treatment operation.

Most of the water and practically all of the coarse solids in froth are relatively easy to remove. Water forms big drops or lenses in bitumen, which, following dilution with a light solvent, quickly form a distinct heavy phase that easily separates in both inclined plate settlers and scroll centrifuges. However, some of the water is present in the form of a very stable emulsion, with droplets ranging from below 1 μm to up to 10 μm in diameter, and most having a diameter of about 3 μm . This emulsified water is very difficult to remove, and thus, the factors affecting the stability of water in diluted bitumen emulsions are of great interest for this chapter.

In Chapter 2, devoted to colloid and surface science, we briefly discussed emulsions as one kind of colloidal dispersion. Let us recall that an emulsion is a dispersion of a liquid in another immiscible liquid. From the froth treatment point of view, we are interested in water dispersion in a continuous oil phase. The oil phase consists of bitumen diluted with a hydrocarbon solvent, while the water usually

contains dissolved salts and suspended fine solids. Quite often, multiple emulsions are observed; that is, water droplets suspended in a continuous oil phase may sometimes contain even smaller oil droplets (Figure 7.1). The system we are dealing with is very complicated, containing several distinct phases: water, oil, and solids. The oil contains a large number of chemicals; many of them exhibit some surface activity and can thus contribute to emulsion stabilization. Fine solids can also stabilize emulsions. It is therefore not surprising that, despite the huge industrial importance of petroleum emulsions, there is no agreement in the scientific community on the leading mechanisms responsible for the stabilization of petroleum emulsions.

7.1 Emulsions and Emulsion Stability

7.1.1 Introduction

An emulsion is a dispersed system composed of two immiscible or partially immiscible liquids. Usually, one of the liquids is water and the other is a hydrocarbon liquid, conventionally referred to as oil. In the context of emulsion science, oil is understood as a liquid that does not mix well, or does not mix at all, with water. Thus, a wide variety of substances that do not mix with water, such as olive oil, benzene or toluene, or any hydrocarbon liquid, including all petroleum crudes and bitumen, can be classified as oils. Usually, one of the liquids forms a continuous phase, while the other is dispersed into small droplets. The droplet size typically ranges from a fraction of a micrometre to over 10 μm . On the upper end, emulsion droplets are larger than typical colloidal particles. Yet, as we will discuss below, emulsion stability is governed by the properties of a thin film—part of the continuous phase liquid—that separates dispersed droplets on their close approach. This film becomes increasingly thinner as the droplets approach. It eventually becomes so thin that the droplets start to interact with each other via surface forces, such as van der Waals attractive forces, repulsive forces resulting from double layer overlapping, or forces resulting from steric effects.¹ For the emulsion droplets to coalesce, they must overcome repulsive surface forces. Therefore, emulsion stability is controlled by surface forces. As such, emulsions are colloidal systems, even when some droplets may be much larger in size than typical colloidal particles.

If water forms a continuous phase in which oil is dispersed in the form of small emulsified droplets, the emulsion is referred to as an *oil-in-water (O/W) emulsion*. If water is dispersed in a continuous oil phase, the resulting dispersion is called a *water-in-oil (W/O) emulsion*. An emulsion mixes easily with the liquid that forms the continuous phase. Thus, an O/W emulsion can be easily diluted with water; while a W/O emulsion added to water will form large blobs of undiluted emulsion in the excess water. This is one of the methods used to distinguish between the two emulsion

1 All types of surface forces are discussed in Chapter 2 of Volume 1.

types. There are other methods; for instance, O/W emulsions usually show higher electric conductivity than W/O emulsions. Also, emulsions can be easily coloured using a dye that is soluble in the continuous phase liquid.

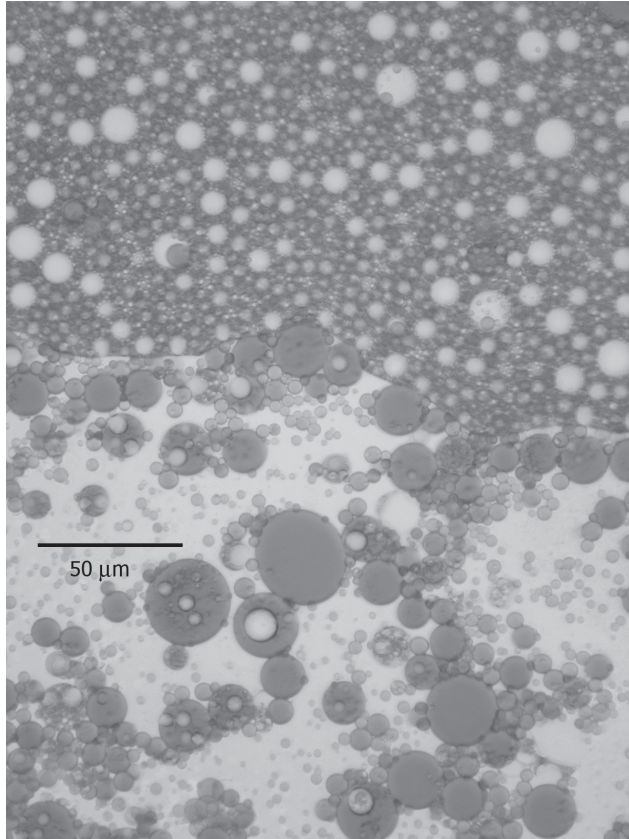


Figure 7.1 Photomicrograph of the interface between water (bottom) and oil (top) phases following centrifugation of naphtha-diluted bitumen.

Photo courtesy of Dr. X. Yang, Champion Technologies.

Figure 7.1 shows an interface between a water phase (bottom) and an oil phase (top) after centrifugation of naphtha-diluted bitumen. The boundary between the oil continuous and water continuous phases runs horizontally (more or less in the middle of the photograph). We can see a water-in-oil emulsion in the upper part of the picture and an oil-in-water emulsion at the bottom. Some of the oil droplets at the lower part of the photograph contain much smaller water droplets, confined in their interior. Upon careful examination, one can also find water drops containing smaller oil droplets in the upper part of the picture. Such systems are known as multiple emulsions. Their presence in petroleum emulsions adds to the overall complexity of problems and difficulties encountered in water-oil separation in the petroleum industry.

The most important property of any emulsion is its stability. Like all dispersed systems, emulsions are inherently unstable, as a large interfacial area increases the total system energy. Thus, phase separation, or emulsion breaking as it is also called, should occur spontaneously, because it results in decreasing the system energy. The fact that mayonnaise (a concentrated O/W emulsion) remains stable for weeks or months without any noticeable phase separation implies that the rate of the phase separation is extremely slow. This is called kinetic stabilization. *Kinetic stabilization* means that, although the system is intrinsically unstable, the phase separation is slowed down such that the emulsion appears to be infinitely stable. This stabilization is caused by surface forces.

High emulsion stability may be desired in many commercial emulsions, such as those in some food or cosmetic products, or can be highly detrimental, such as in the removal of water from oil in froth treatment operations. Here, we should distinguish between stability against coalescence and stability against flocculation. The former is a process of emulsion droplets fusing at contact, resulting in the formation of larger drops, which are easier to remove. This is always a preferred option if we want to break an emulsion. However, due to many factors, discussed below, it is not always possible. The other option is emulsion flocculation, where the droplets form large aggregates (usually under the influence of an added chemical aid or a change in the medium properties). Because of their larger size, the flocs are easier to remove than individual droplets. Sometimes, both flocculation and coalescence occur simultaneously. Eventually, the dispersed liquid will form a new continuous phase, separated from the other liquid by a single interface. This may take seconds or eons, depending on the system.

The most common emulsion stabilization is due to adsorption of surfactants on the water-oil interface. When two pure liquids are homogenized, the formed emulsion separates rapidly. However, the addition of a suitable surfactant can cause the resulting emulsion to become very stable. This surfactant is often called an *emulsifier* or *emulsifying agent*. An O/W emulsion can also be formed by adding oil to a surfactant solution in water, above the surfactant critical micelle concentration (CMC). The oil dissolves in the hydrocarbon interior of the micelles, causing them to swell. The resulting oil droplets, with the surfactant molecules at their surfaces, are indistinguishable from the ones that are formed when oil and water are agitated in the presence of added surfactant. Studies of equilibria in a three-component system (containing water, oil, and a surfactant) are a convenient way of gaining insight into emulsion structure and stability.

An ionic surfactant may stabilize emulsions by providing an electric charge to emulsion droplets. Charged droplets repel each other, which prevents them from colliding and coalescing. Non-ionic surfactants may stabilize emulsions by forming a steric stabilization layer, i.e., a layer that prevents a close droplet-to-droplet approach due to the protruding parts of the surfactant molecules. Similarly, many natural or synthetic polymers may stabilize emulsions via steric effects. Many emulsions are stabilized by small solid particles that are anchored at emulsion droplet surfaces due to their affinity to both liquids forming the emulsion.

All of the mechanisms mentioned above will be discussed in more detail below.

7.1.2 Surfactant-Stabilized Emulsions

Winsor Emulsion Types

As follows from above, surfactant-stabilized emulsions are systems containing at least three components: two immiscible liquids and a surfactant (also known as an emulsifier). If the surfactant dissolves well in the water phase, it tends to promote the formation of O/W emulsions. If it is mostly oil-soluble, it tends to support the formation of W/O emulsions. This experimental observation is known as one of Bancroft's rules, after Wilder D. Bancroft (1867–1953), an American physical chemist and a professor at Cornell University. Bancroft's work on emulsions resulted in a number of experimental rules, some of which did not survive later scrutiny, and some, such as the one mentioned above, that still serve as quick rules of thumb.

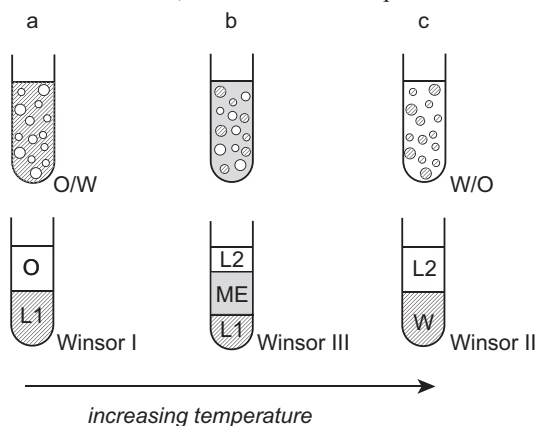


Figure 7.2 Influence of temperature on the type of emulsion formed in a non-ionic surfactant-oil-water system.

The solubility of some surfactants (especially non-ionic surfactants of the alkyl-polyethylene oxide, or $R-(CH_2-CH_2-O)_n-OH$, type) can be fine-tuned by changing temperature. At relatively low temperatures, the surfactant is mostly water-soluble. When a mixture of water, oil, and the surfactant is vigorously agitated, an O/W emulsion is formed, as shown in Figure 7.2a. Upon centrifugation, the system separates into a surfactant-rich aqueous phase (called L1) containing surfactant micelles and an almost pure oil phase. This is referred to as the *Winsor type I system*. At higher temperatures, when the polar oxy-ethylene head loses its hydrating water, surfactant solubility in water decreases and the solubility in oil increases, and a W/O emulsion is formed (Figure 7.2c). When centrifuged, the emulsion separates into almost-pure water and a surfactant-rich oil phase containing inverted micelles (L2). This is referred to as the *Winsor type II system*. Somewhere in between, when the surfactant solubility is almost the same in the oil and water phases, a different picture emerges. No visible

emulsion is formed, and after centrifugation, the system separates into three distinct phases: a water phase with micelles (L1) at the bottom; an oil phase (L2) on top; and a new phase (ME) in the middle separating the L1 and L2 phases and in equilibrium with both (Figure 7.2b). This is called the *Winsor type III system*. The middle phase is referred to as a *microemulsion* (ME). It is important to note that, contrary to ordinary emulsions, microemulsions are thermodynamically stable phases.

Figure 7.2 shows only a part of the complex phase equilibria that can be formed in surfactant-water-oil systems. It is shown here to illustrate the fact that there can be a continuous and smooth transition from oil-in-water (O/W) to water-in-oil (W/O) emulsions. Although in this case, the transition from an O/W to a W/O emulsion was induced by a change in temperature (and thus, changes in surfactant solubility), similar transitions can occur as a result of changes to the surfactant type or concentration, to the salinity and pH of the aqueous phase, or to other factors.

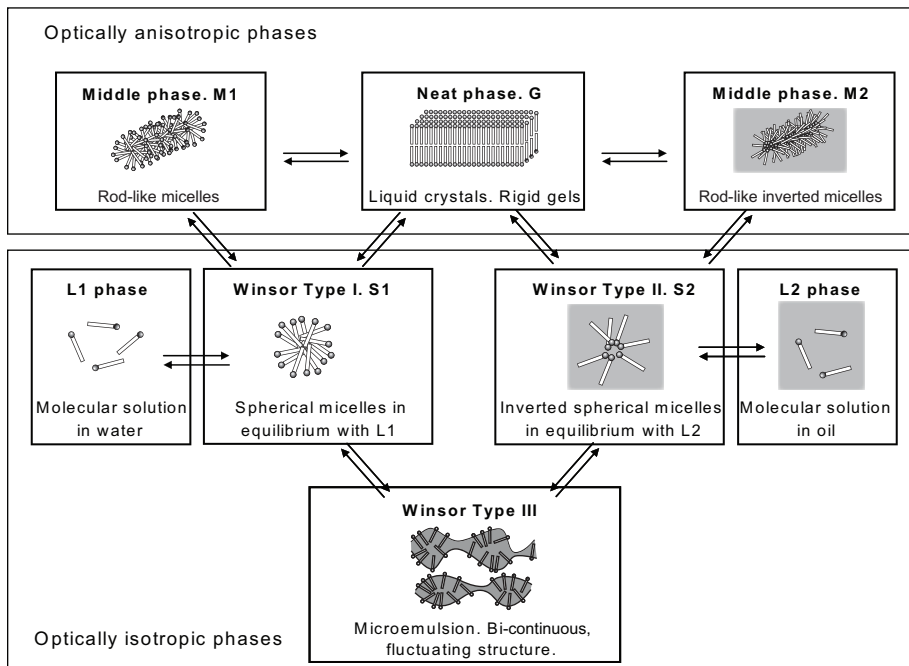


Figure 7.3 Self-organized surfactant structures

Surfactants are able to form a number of self-organized structures in water or oil media. Spherical micelles in water are just the simplest example of such self-organization. Figure 7.3 shows a few other common structures. All of these structures can be converted to different ones by changing the surfactant concentration, the temperature, or the salinity of the aqueous phase. Increasing surfactant concentration

in water, the L1 phase (being a simple molecular solution) is the first to form at low concentration. At CMC, spherical micelles are formed first, and the S1 phase appears. The addition of oil makes the micelles bigger as they solubilize the oil in their interiors. At higher surfactant concentrations, the initially spherical micelles elongate to form rod-like micelles, which align themselves parallel to each other to allow optimum packing. This is the M1 phase, which, because of the parallel orientation of the rods on large length scale, is optically anisotropic. At even higher surfactant concentration lamellar liquid crystal phase (G phase) is formed. In the presence of large amounts of oil, inverted phases S2, M2, and L2 are possible. Finally, under certain conditions, a bi-continuous microemulsion phase can be formed.

Many of these structures are encountered in biological systems, e.g., cell membranes are in fact bilayers formed by the self-organization of phospholipids, a natural surfactant group. Surfactant self-organization is thus of great interest for biology and medicine and for the pharmaceutical industry. It is also the basis of many phenomena utilized in so-called nanotechnology.

It is worth noting that, although the stability of both W/O and O/W emulsions may be quite high for systems far from microemulsion ranges, the stability of a 'macro' emulsion usually drastically decreases as it approaches microemulsion composition, just at the boundary of the microemulsion existence range, and this decrease in stability often results in phase separation. This mechanism is important for the petroleum industry, as it can be used in the removal of water from crude oils. Also, in conventional enhanced oil recovery, a surfactant injection is often performed in such a way that it results in the formation of a microemulsion in situ. Because microemulsions are characterized by very low interfacial tensions and relatively low viscosities, they allow for the additional recovery of oil that is trapped in porous reservoir rocks and cannot be moved using standard enhanced oil recovery techniques.

7.1.3 Impact of Fine Solids on Emulsion Stabilization

It is very well known that surfactants can be used as emulsifiers to aid in the formation of both water-in-oil (W/O) and oil-in-water (O/W) emulsions. It is much less recognized that fine solid particles can also stabilize emulsions, and that in many cases, the stability of solid-stabilized emulsions exceeds that of surfactant-stabilized ones. Solid particles attached to droplet surfaces form a steric barrier for the coalescence of droplets, as shown in Figure 7.4.

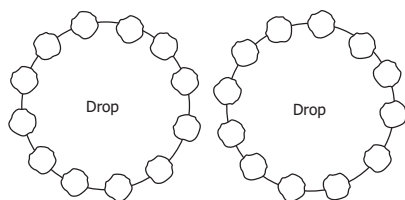


Figure 7.4 Steric stabilization barrier formed by solid particles.

There are many similarities between solid and surfactant stabilization mechanisms, and there are also significant differences. Because of the importance of solid-stabilized emulsions to the petroleum industry, we will briefly compare the two stabilization mechanisms. The ability of surfactants and solids to stabilize W/O and O/W emulsions is governed by their relative affinities to water and oil. In surfactants, this is conveniently described by their hydrophilic-lyophilic balance, or HLB (discussed in Chapter 2). In surfactants with *high* HLB values, the heads tend to have a larger cross-section than the tails. As a result, high-HLB surfactants promote the formation of curved interfaces that are concave towards the oil phase, and can therefore be used as O/W emulsifiers. Conversely, the heads of surfactants with *low* HLB values usually have a smaller cross-section than the tails. Low-HLB surfactants promote interfaces that are concave towards water, and they can thus be used as W/O emulsifiers.

In the case of solids particles, their affinity to oil or water phases can be described with the contact angle. Usually, contact angle is measured through the aqueous phase. If we follow this convention, hydrophilic particles are characterized by a contact angle $\theta < 90^\circ$. If a spherical hydrophilic ($\theta < 90^\circ$) particle is 'adsorbed' at the oil-water interface,² most of the particle resides in the water phase, as shown in Figure 7.5. For hydrophobic particles ($\theta > 90^\circ$), the opposite is true: most of the particle body is immersed in the oil phase. Hydrophilic particles ($\theta < 90^\circ$) thus form curved interfaces that are convex towards the oil phase and tend to promote the formation of O/W emulsions. Hydrophobic particles ($\theta > 90^\circ$), on the other hand, form interfaces that are convex towards water and promote the formation of W/O emulsions.

The biggest difference in the behaviour of solids and surfactants as emulsion stabilizers stems from the source of their energy of attachment to the interface. For surfactants, this energy originates from the lowering of the interfacial tension due to surfactant adsorption, as described by Gibbs' law. It is usually of an order of several kT units per surfactant molecule.

Solid particles at an interface do not lower the interfacial tension. However, they do lower the free energy of the system in a totally different way. To clarify this

2 We wrote that a solid particle is 'adsorbed' at the oil water interface. The term 'adsorption' is not strictly applicable to solid particles. Particles are not described by Gibbs' adsorption equation, which is only valid for ions and molecules dissolved in one or both neighbouring phases. Solid particles, even very small ones, still form a separate phase in the thermodynamic sense. They do not adsorb the same way molecules do. Instead, they get attached to the interface, forming a three phase contact line and finite contact angles. With this note, in mind, we will use the term 'adsorption' in connection with solid particles, but to stress the differences outlined here, we will continue using the single quotation marks.

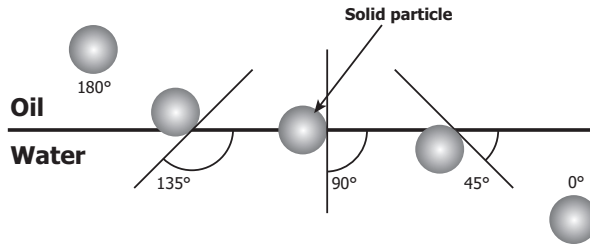


Figure 7.5 Influence of contact angle on the position of a solid particle at oil-water interface.

point, let us estimate the attachment energy of a spherical particle of radius r to an oil-water interface with the interfacial tension on $\gamma_{o/w}$. Let us assume that the particle is characterized by a contact angle of θ . We have to consider three contributions to the attachment energy: let us suppose that initially, the particle was totally immersed in water. After its ‘adsorption,’ a part of the particle surface is exposed to the oil. Let us take the surface area of the spherical cup of the particle now exposed to oil to be S . The system gains energy by creating this new solid-oil interface and the corresponding energy change is $\gamma_{s/o} \cdot S$. In the process of particle attachment, an equivalent amount of solid-water interface was lost, with the corresponding energy term of $-\gamma_{s/o} \cdot S$. The largest contribution to the energy balance is due to the fact that some of the oil-water interface is lost and replaced by the cross-section of the particle ‘adsorbed’ at the interface. The area of this cross-section depends on contact angle θ . The energy change for attachment of a single particle ΔE can thus be written as

$$\Delta E = \pi r^2 \gamma_{o/w} (1 \pm \cos \theta)^2 \quad (7.1)$$

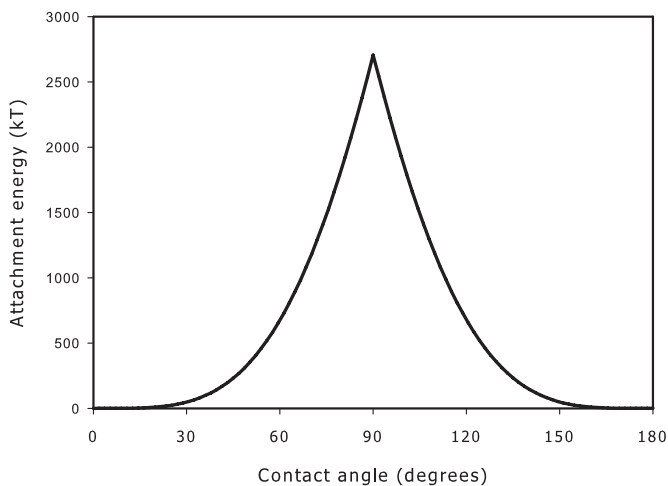


Figure 7.6 Attachment energy of a solid 10 nm spherical particle to toluene-water interface as a function of the particle contact angle, plotted according to Eq. (7.1).

where $\gamma_{o/w}$ is the oil-water interfacial tension and r and θ are the particle radius and contact angle, respectively (Binks 2002). The sign in the bracket is negative for particle attachment from the oil phase and positive for particle attachment from the water phase. When the above equation is plotted (Figure 7.6), we see that the particle is most strongly held at the interface at a contact angle of $\theta = 90^\circ$. On either side of 90° , the energy drops rapidly to negligibly small values for $\theta < 20^\circ$ and for $\theta > 160^\circ$.

For a particle with a 10-nm radius at a toluene-water interface ($\gamma_{o/w} = 36.1 \text{ mJ/m}^2$; see Table 2.2 in Chapter 2) at $\theta = 90^\circ$ and at 25°C , the attachment energy is about $2.7 \cdot 10^3 \text{ kT}$ units. For all practical reasons, this means that, once such a solid particle is attached to the interface, it is attached permanently or irreversibly ‘adsorbed.’

Particle attachment energy for a constant contact angle depends on the square of the particle radius. For very small particles, of less than 1 nm, the attachment energy for a hydrocarbon-water interface becomes several kT, which means that such particles are easily detached from the interface and cannot be effective emulsion stabilizers. It is perhaps worth noting that such small particles are of about the same size as surfactant molecules. It should also be noted that their attachment energy, calculated according to Eq. (7.1), more or less coincides with the adsorption energies for typical surfactants.

As W/O emulsion droplets coalesce, their combined surface area decreases. For instance, when two identical droplets coalesce, the area of the resulting drop is about 20 % lower than the combined surface areas of the two droplets before coalescence. Thus, if there were initially any solid particles on the droplet surfaces, their surface concentration would increase when the droplets coalesce, eventually forming full surface coverage and making any further droplet coalescence impossible. It is also interesting to note that a droplet covered with fine solid particles does not behave as a Laplacian body, meaning that when such a droplet is deflated or subjected to deformation due to gravity, its shape cannot be described by the Laplace equation. Therefore, conventional methods of interfacial tension measurements, which assume that the observed shapes have a Laplacian character, cannot be applied to sessile or pendent drops with ‘adsorbed’ fine solid particles.

In systems relevant to the petroleum industry, the fine solids capable of stabilizing emulsions are mainly inorganic clays whose surface properties have been modified by the adsorption of surfactants present in the oil. Clays with clean surfaces (with the exception of talc) are naturally hydrophilic and will not ‘adsorb’ at an oil-water interface unless made partially hydrophobic with a contact angle of close to 90° . Thus, clean clays and other inorganic particles do not contribute to emulsion stabilization unless their surfaces are altered by adsorption to make them partially hydrophobic. The substances present in oil that are involved in making clays partially hydrophobic are likely members of asphaltene and resin SARA fractions (see below) or naphthenic and humic acids and their salts.

We would like to add that the fine solid particles do not necessarily have to be inorganic. Any solid or solid-like particles would stabilize petroleum emulsions in the same way. Thus, asphaltene aggregates, coal particles, or any organic material insoluble in the parent oil may be involved. This adds to the tremendous complexity of emulsion stabilization in petroleum systems, which will be discussed in more depth in Section 7.2.

7.1.4 Emulsion Thin Liquid Films

When two droplets approach one another, a thin liquid film is formed between them, as shown in Figure 7.7a. Due to the concave curvature of the meniscus around the film, a capillary pressure difference arises between the meniscus and the flat film, causing the liquid to drain from the film out to the meniscus. As the liquid drains, the droplets' surfaces, which bind the film, begin to interact through van der Waals, steric, electrostatic, and other surface forces. The effect of these forces is often expressed in terms of disjoining pressure, which is the pressure acting normal to the film surfaces. A positive disjoining pressure is equivalent to the film surfaces repelling each other, thus increasing emulsion stability. Negative disjoining pressure causes spontaneous film drainage and thinning, which can eventually cause film rupture at a critical thickness. Often, as the film drains, the disjoining pressure gradually increases until it equals the capillary pressure at the edge of the film. At this stage, an equilibrium state is reached and a film of uniform thickness is formed. This film opposes further approach of the droplets and thus prevents their coalescence. In this sense, emulsion stability is controlled by the stability of the thin liquid films separating emulsion droplets.

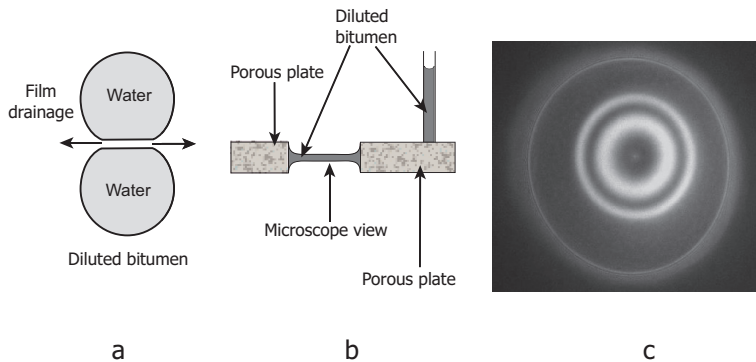


Figure 7.7 Emulsion thin liquid film and film pressure balance technique.

Scheludko-Exerowa Thin Film Balance Technique

In this technique, a single thin emulsion film is formed inside a hole drilled in a porous glass plate (Figure 7.7b). The plate is first filled with the oil phase and then submerged in water. A biconcave drop of oil is then formed by sucking out the oil from the hole through a capillary welded to the porous plate. The pressure is further reduced to create a flat thin oil film in between water above and below the film. The pressure in the capillary can be measured with any pressure transducer or with a water manometer.

Under equilibrium conditions, this pressure is equal to the disjoining pressure in the thin film. Therefore, measurements of the capillary pressure make it possible to evaluate the disjoining pressure.

The film formed in the porous plate models the film formed between two approaching water droplets. The bottom of the measuring cell is made of an optical-quality glass plate. The measuring cell with the porous-plate film holder inside (Figure 7.7b) is placed on an inverted microscope, allowing for direct observation of the film. An image of such a film is shown in Figure 7.7c. The light reflected from the upper film surface interferes with the light reflected from the lower film boundary. Using monochromatic light illumination and limiting the size of the image with suitable diaphragms or pinholes in the microscope optical path, one can calculate the film thickness at a selected film area from the measured light intensity. This can be done to an accuracy of about 0.2 nm for foam films and about 1 nm or better for emulsion films. The technique allows precise evaluation of the film thickness and disjoining pressure or the disjoining pressure as a function of the film thickness at constant temperature. It has been successfully used for experimental verification of the DLVO theory.

This method, developed by Scheludko and Exerowa, was named the Thin Liquid Film-Pressure Balance Technique (TLF-PBT) (Scheludko 1967; Platikanov and Exerowa 2005). Considerable knowledge has been obtained using this technique for foam films as well as for oil-in-water emulsion films. The technique was later adopted to study water-in-oil emulsion films (Khristov et al. 2000). In addition to pressure and optical measurements, the most recent modification of the technique permits simultaneous estimation of the dielectric properties of the film (Panchev et al. 2008).

7.2 Emulsions in Petroleum Systems

7.2.1 Introduction

Emulsions create problems and challenges in many industries, but it is in the petroleum industry, in particular, that these problems are very well recognized and dealt with on a large scale. Oil coming out of a well always contains some water—as little as below 1 % or as much as over 70 % of the total volume of the produced liquids. Some of that water is present in the form of large lenses and drops. This free water, as it is called, easily separates from the oil. Some of the produced water forms an emulsion with droplets of less than 5 μm in diameter. Water-in-crude oil (W/CO) emulsions are usually very stable and difficult to break. How these emulsions are formed is not exactly clear. Some emulsions may already be present in the oil reservoir, as oil migrating into the reservoir could occlude connate water. Most of the emulsions, however, are likely formed when the oil starts to flow from the reservoir into the well bore, or through turbulent flow on chokes and valves and especially on centrifugal pump impellers.

The same is true for the oil sands industry, both in in situ recovery methods and in the extraction of bitumen from mined oil sands ores. In addition, during bitumen extraction from mined ores, water can be emulsified into the oil when the oil sand–water mixture is subjected to vigorous agitation as it takes place at both the slurry preparation stage and during hydrotransport.

Salts carried with the emulsified water pose serious corrosion problems for pipelines and downstream refineries. Millions of dollars are spent daily on preventing the formation of W/CO emulsions or on breaking them once they have formed. Despite the enormous industrial significance of W/CO emulsions, their exact stabilization mechanism is not yet fully understood. The existing paradigm claims that W/CO emulsions are almost exclusively stabilized by asphaltenes, and hundreds of papers in scientific journals support this claim with experimental data. There are also numerous papers in scientific literature that claim that the most important stabilizing agents are fine solid particles. We will discuss both of these claims in more detail below.

7.2.2 Asphaltenes

Asphaltenes are defined as the fraction of crude oil that is insoluble in simple straight-chain alkanes, like pentane or heptane, but soluble in toluene. This definition describes asphaltenes as a solubility class and *not* as a specific family of chemicals with a common functional group. The only common property of a chemical that includes it into the asphaltene class is the chemical's insolubility in n-heptane or n-pentane, the solvents most commonly used to separate asphaltenes. Therefore, individual chemical molecules in the asphaltene group do have different functionalities, like acid, base, ether, ester, or other. They differ in molecular weight, composition, functionality, polarity, and just about any other property except their insolubility in n-alkanes. This is important to keep in mind, as general statements are often made referring to asphaltenes as the most heavy, polar, and surface-active components of crude oils. Asphaltenes may contain molecules that match those attributes, or at least some of them, but they also contain molecules that do not. Therefore, it is very difficult and perhaps futile to present a 'typical' asphaltene molecule. This is especially important when discussing the role of asphaltenes in petroleum emulsion stabilization, where a specific functionality rendering them surface-active is necessary.

SARA Analysis

SARA analysis of crude oil separates the oil into saturate, aromatic, resin, and asphaltene (SARA) fractions. The saturate fraction contains non-polar linear, branched, and cyclic hydrocarbons. The aromatic fraction contains molecules with one or more aromatic rings. Resins and asphaltenes, in addition to aromatic rings, also contain various polar groups. The difference between resins and asphaltenes is that

asphaltenes are insoluble in light hydrocarbon solvents, like heptane or pentane, while resins are pentane- and heptane-soluble. The polarizability of all SARA fractions increases from saturates to asphaltenes.

Oil fractionation into SARA fractions begins with the addition of large quantities of heptane (or pentane) to precipitate asphaltenes, usually at a ratio of 40:1. Precipitated asphaltenes are then washed with the solvent and dried. Once the asphaltenes are removed, the separation of the remaining SARA fractions is usually done by chromatography. Chromatography does not provide sharp differentiations between various fractions, and the yield of each of the fractions depends on the adsorbent and eluting force of the solvent. The amount of asphaltenes precipitated also depends on the aliphatic solvent used. Therefore, the boundaries between the SARA fractions are not sharp, and there is a substantial overlapping of the neighbouring fractions. Despite these ambiguities, SARA analysis is one of the most commonly used characteristics of crude oils. The popularity and usefulness of SARA analysis comes from two main sources: First, since asphaltenes precipitate when the parent oil is mixed with a paraffinic solvent, asphaltene precipitation can also occur when an oil with high asphaltene content is blended with a paraffinic crude. Asphaltene precipitation due to such ‘oil incompatibility’ may lead to the formation of solid deposits in pipelines, tanks or production wells resulting in flow restriction or, in extreme cases, plugging. Serious problems can be encountered in upstream production (when oils from different wells or strata are blended), during transportation, or in downstream refineries (when oils from different sources are mixed). Second, the asphaltene content correlates with oil’s propensity to form coke when heated. Obviously, the deposition of coke in heat exchangers and catalyst beds is highly detrimental.

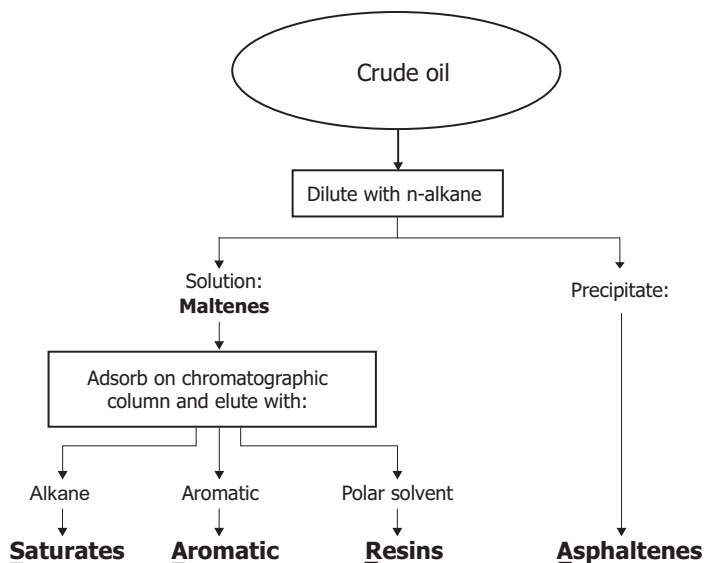


Figure 7.8 Basic flow sheet of SARA analysis. Details may vary from one laboratory to another. The standard protocol is described in ASTM D6560-00 (2005).

Traditional SARA analysis is initiated with asphaltene precipitation by adding light paraffinic solvent, followed by chromatography of the supernatant as described in the American Society for Testing and Materials (ASTM) Standard D6560-00 (2005). The whole procedure is tedious and time-consuming, requires large quantities of solvents, and is difficult to automate. There are numerous improved methods that rely on high-pressure liquid chromatography or thin-layer chromatography. The former method still requires asphaltene removal prior to chromatography. The latter is faster and easier to automate.

Table 7.1 Results of SARA analysis of various bitumen samples (wt.%)
Source: Strausz (1989).

	Atha- basca	Peace River	Wabis- kaw	Cold Lake	Vene- zuela
Asphaltene	17.2	20	19	16	22
Resins	44.8	44	48	44	38
Saturates	16.9	15	15	21	14
Aromatics	18.3	19	18	19	26

Table 7.1 shows the results of SARA analysis for bitumen from four different Alberta oil sands deposits and from one from Venezuela. As it can be seen, there is not much difference between individual samples. All of the Canadian oil sands bitumen contains 16 wt. % to 20 wt. % asphaltenes.

Asphaltene Chemistry

The results of elemental analysis of Athabasca asphaltenes, shown in Table 7.2, indicate that they consist mainly of carbon, hydrogen, nitrogen, oxygen, and sulphur. They also contain trace amounts of vanadium and nickel. The carbon-to-hydrogen ratio (C/H) is ~ 1.2. The data presented in the table are taken from Strausz (1989). Nuclear magnetic resonance (¹³C NMR) studies indicate that about 40 % of carbon atoms are in aromatic rings. Infrared (IR) and ¹H NMR studies show that about 90 % of hydrogen atoms are linked to saturated carbon atoms in methyl and methylene groups. This implies that most of the aromatic rings are condensed to polyaromatic structures containing several individual rings. Asphaltenes are rich in sulphur, which is mostly present in thiophenic groups and acyclic sulphides. The molecular structure of asphaltenes will be described in a separate section below.

Table 7.2 Elemental composition (wt. %) of Athabasca asphaltenes

C	H	N	S	O	H/C
79.9	8.3	1.2	7.6	3.2	1.24

Molecular Weight of Asphaltenes

Asphaltene association causes serious difficulties in the estimation of asphaltenes' molecular weight. Recent studies using modern analytical techniques indicate that the molecular weight of asphaltenes is confined in the range of 400 Da to 1500 Da, with the average weight at about 750 Da. Previous asphaltene molecular weight estimates, based on vapour pressure osmometry (VPO) and gel permeation chromatography (GPC), are much higher at 3000 Da to 10 000 Da. This difference, as we will see later, can substantially affect our understanding of asphaltene molecular structure, and consequently, its chemistry. For this reason, we will take a moment to describe how the molecular weight of asphaltenes is estimated.

Without going into much detail, in VPO, asphaltenes are dissolved in a good solvent (such as toluene), and the equilibrium vapour pressure of the solvent is measured. The equilibrium vapour pressure can be used to calculate the solute molar fraction.³ Knowing the solution's mass composition, one can then calculate the molecular weight of the solute—in this case, asphaltene. The problem with this seemingly simple method is that asphaltenes are known to strongly associate in their solutions, forming dimers, trimers, and so on. To estimate the 'true' molecular weight of the asphaltene, that is, the molecular weight of the monomer molecule, we need to work with highly diluted solutions, such that the degree of association is practically zero. At high dilutions, the vapour pressure of the solution is very close to that of a pure solvent, resulting in large experimental errors. Usually, a series of solutions of gradually increasing concentrations is prepared and the vapour pressure is measured for each of the solutions. The results are then extrapolated to infinite dilution (or zero concentration), where asphaltenes should only be present as monomers. Extrapolation outside the experimental range is always risky and should be avoided if at all possible, as it can seriously bias the final results. Here, the risk is further compounded by the fact that the experimental errors, as mentioned above, increase with dilution, adding another dimension to the uncertainty of the molecular mass estimation.

In gel permeation chromatography (GPC), molecular size is estimated based on the elution time of the investigated material from a column filled with a porous gel, of which the pore size distribution is known. Molecules that are small enough to enter the pores remain on the column longer than the large ones, which pass through the column quickly. Knowing the gel's pore size distribution, the geometrical size of the molecules can be estimated from the amount of time it takes for the sample to pass through the column. The GPC method gives the molecular weight distribution, whereas VPO provides only an average. However, GPC suffers from several uncertainties, some similar to those encountered in VPO. Association makes the molecules bigger; thus, the results for more concentrated solutions must be extrapolated to infinite dilution,

3 The equilibrium vapour pressure (p_{solvent}) over a diluted solution of a non volatile solute in a solvent is given by Raoult's law: $p_{\text{solvent}} = x_{\text{solvent}} p_{\text{solvent}}^0$ where x_{solvent} is the molar fraction of the solvent and p_{solvent}^0 is the pure solvent equilibrium vapour pressure. Lumping all of the individual chemicals forming the asphaltene fraction into a single pseudo component, we have $p_{\text{solvent}} = (m_{\text{solute}} M_{\text{solvent}} / m_{\text{solvent}} M_{\text{solute}}) p_{\text{solvent}}^0$ where m and M denote the mass and molecular weight of the components, respectively. From this equation (valid for diluted solutions), the molecular weight of the solute can be calculated.

with the consequences discussed above. Interaction of the studied molecules with the gel material cannot be eliminated, introducing new uncertainty into the picture.

Most of the modern methods for asphaltene molecular mass estimations use various mass spectrometry (MS) techniques. This is an obvious choice, as in mass spectrometry, the ratio of charge carried by a molecule to its mass is measured directly. The way a charge is applied to a molecule and the amount of energy a molecule is exposed to during the ionization process vary across the different MS methods, which include electric field ionization (FIMS), atmospheric pressure photo ionization (APPI), atmospheric pressure chemical ionization (APCI), laser desorption (LDMS), and electrospray ionization (ESI). In the gentlest method, ESI, a sample diluted in a suitable solvent is sprayed into a high vacuum via a nozzle that is connected to a high electric voltage source. The resulting droplets carry a negative or positive charge, depending on the polarization of the applied voltage. As the drops evaporate in the vacuum, their charge density increases until they disintegrate under the strong electrostatic repulsion of their charges. The smaller droplets formed in this charge-induced explosion evaporate further. Their surface charge density increases, they explode, and the cycle repeats a few times, such that at the end, we obtain single molecules carrying mostly one elementary charge. In this method, the energy applied to the molecules is too small to cause their fragmentation.

Mass spectrometry methods are not free of problems. The most serious is that individual molecules in complex mixtures, like asphaltene samples, differ in their ability to vaporize and to acquire an electric charge. Thus, most of the MS methods are very good in showing the molecular weight of the molecules present in the samples with high accuracy, allowing for the determination of the elemental composition of individual molecules. Molecular structure can then be inferred from the elemental composition; chemical analysis; and IR, NMR, and other spectroscopic methods. However, MS methods cannot be reliably used for evaluating the composition of a sample, as the relative abundances of the sample components, as evaluated by MS, do not depend solely on the components' concentrations. They also depend on the components' ability to vaporize and ionize, which changes from one molecule type to another.

Fluorescence depolarization measurements were also used to determine the molecular weight of asphaltenes (Groenzin and Mullins 2007). This technique is capable of working with highly diluted solutions of asphaltenes, such that it is safe to assume that all aggregates are fully dissociated. Here, the sample is illuminated with plane-polarized light, which is first absorbed by the molecules studied and then re-emitted. If, between the photon absorption and subsequent fluorescent emission, the molecule rotates due to Brownian rotary movements, the emitted light will be slightly depolarized; the degree of depolarization depending on the rotation rate, which in turn depends on the molecule size. The larger the molecule, the slower its rotary Brownian movement. Thus, time-resolved fluorescence depolarization (TRFD) spectroscopy allows for the estimation of molecular size or mass.

The values for the molecular weight of petroleum asphaltenes obtained using these modern techniques are in the range of 400 Da to 1500 Da, with an average value of about 750 Da. This is much less than the estimates obtained from the VPO and GPC techniques (3000 to 10 000 Da), which has led to a long-standing and vigorous

discussion on the matter. In this context, it is perhaps of value to present some typical positions within this controversy, as it is not uncommon to find authors on either side of the fence misquoting each other. We will come to this a bit later, presenting the discussion on molecular weight together with proposed molecular structures.

Asphaltene Aggregation

Before roughly 1980, asphaltenes were believed to be present in crude oils in the form of colloidal-sized aggregates containing several high-molecular-weight molecules. Asphaltenes were considered to be the most polar, and, with a molecular weight measured at several thousand Daltons, the heaviest, component of crude oils. Asphaltenes' polarity and formation of aggregates resulted in a notion that they are similar to surfactants (which are polar and aggregate into micelles). Consequently, asphaltene aggregates were likened to inverted surfactant micelles, often called 'asphaltene micelles,' which were believed to be kept in solution by resins of substantially lower molecular weight. The resins were assumed to surround the asphaltene core of the micelle, keeping the whole aggregate suspended in the oil. These two notions supported each other and led to the widespread opinion that a resin-asphaltene relationship is the key to understanding asphaltene aggregates and their properties.

This model of resins peptizing asphaltene aggregates was introduced by Nellensteyn (1924), based on observation of the Tyndall effect and Brownian movements of particles in oil. Nellensteyn's ideas were then refined by Pfeiffer and Saal (1940), resulting in the widely accepted 'colloidal model.' In this model, asphaltene aggregates were referred to as micelles and were considered to be similar in nature to the micelles formed in aqueous solutions of surfactants. There are numerous reports in scientific literature on measurements of critical micelle concentration (CMC) for asphaltenes in organic solvents (usually from surface tension vs. asphaltene concentration). However, the CMC concept, even with a very liberal interpretation of the micellization term, is not applicable for surfactants, nor for asphaltenes in organic solvents (Friberg 2007).

The colloidal model of asphaltenes in crude oils is widely used today, although it has been never scientifically validated (Selucky et al. 1981). In fact, it is unlikely that it has any validity at all. To illustrate this point, let us review briefly the analogies and differences between asphaltene association in crude oils and surfactant associations in water and hydrocarbon media.

Surfactant micellization in water, formation of inverted surfactant micelles in hydrocarbons, and asphaltene association in crude oils are described in depth by Stig Friberg, a leading authority in the field of surfactant self-associations (2007). Micellization in aqueous systems is driven by entropic effects resulting from the fatty surfactant 'tails' moving from water into the oily interior of the micelle, which causes a decrease in the free energy of the system. The formation of inverted micelles in hydrocarbons is driven by attractive interactions between polar surfactant 'heads' in the interior of the micelle, which always contains small amounts of water. The addition of a surfactant to a hydrocarbon solvent and the formation of inverted micelles in the presence of water cause only very small changes in surface tension

(Friberg et al. 1986). Therefore, surface tension should not be used in studies of association in non-aqueous systems. Friberg writes: "It cannot be overemphasized that surface tension measurements in nonpolar media cannot be expected to leave similar information about micellization as those in aqueous solutions" (2007, p. 194).

For the clarity of further discussion, let us note that in micellization, one has to consider not only the driving force for association, but also the factors that limit the size of the formed aggregate. Without this limit, association would lead to phase separation rather than to the formation of colloidal-sized aggregates. In aqueous surfactant systems, typical micelles contain about 50 to 100 individual surfactant molecules. Micelle size in water is limited by repulsive interactions between charged surfactant 'heads' and geometrical factors. Non-ionic surfactants, like polyoxyethylene alkyl esters, which lack charged heads, do not form finite-sized micelles; their association is infinite and results in phase separation, as expected.

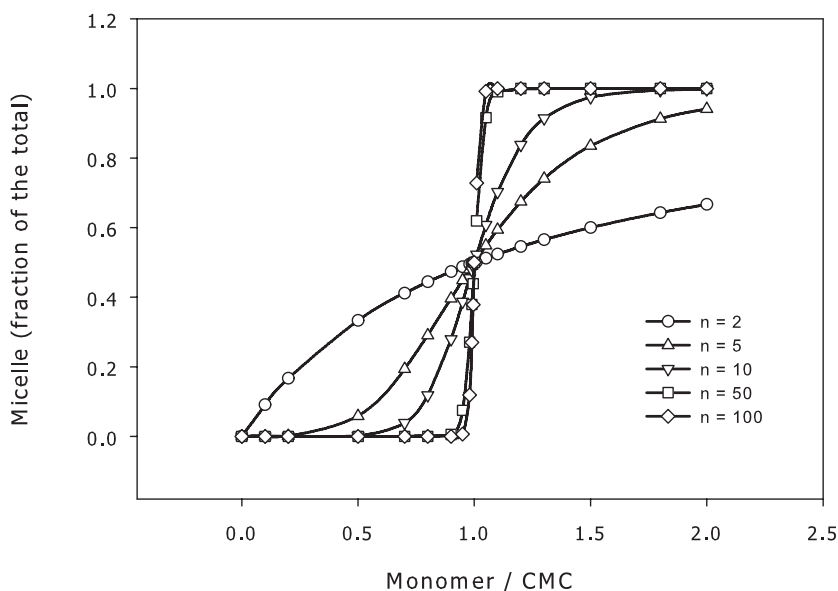


Figure 7.9 Micelle fraction dependence on aggregation number n .

The association of surfactants into inverted micelles in non-polar media is driven by attraction between polar 'heads,' usually mediated by the presence of trace amounts of water. The interactions between hydrocarbon 'tails' and hydrocarbon media are so small that their contribution can be neglected, at least in most cases. Figure 7.9 shows the ratio of the surfactant forming micelles to the total surfactant concentration present in the system for different aggregation number. For small aggregation numbers, say smaller than ten, as the surfactant concentration increases, there is a gradual increase in the aggregate concentration. Only for aggregation numbers of about 50 or more is the transition very sharp. For large aggregation numbers, as the surfactant concentration

increases, initially there are no micelles. Micelles first appear at the critical micelle concentration (CMC). Above CMC, practically all of the added surfactant ends up forming micelles. In hydrocarbon media, inverted surfactant micelles contain only a few individual monomer molecules. The asphaltene aggregates that are formed first contain two to six monomer molecules (Yarranton, Alboudwarej, and Jakher 2000). Because of this low aggregation number, there is no sharp transition between micellar and monomer states. In other words, there is no CMC in those systems—a point we strongly emphasize.

Inverted micelles have the capacity to solubilize large amounts of water (if it is present in the system) and they always contain some water in their interior. With increasing amounts of water, the inverted micelles grow bigger, incorporating more surfactant molecules. If there is a sufficient amount of water and the surfactant present, these swollen inverted micelles eventually become indistinguishable from emulsified water droplets that have been stabilized with an adsorbed surfactant layer.

There is no doubt that asphaltenes form colloidal-sized aggregates in crude oils. Asphaltenes are certainly not surfactants. They lack the amphiphilic properties of surfactants. They do not have easily identifiable hydrophilic polar heads and hydrophobic hydrocarbon tails. The driving force for their association cannot be tail-solvent interaction, as this is not even important for surfactant association in hydrocarbon media. Nor can it be interaction between polar heads, which asphaltenes do not have (though they do have polar groups distributed throughout their molecules). Their association is likely driven by their poor solubility in the parent oil (Sharma and Mullins 2007; Yarranton, Alboudwarej, and Jakher 2000). However, it is not certain yet what factors limit their size or prevent asphaltene precipitation as a separate phase, although steric effects due to the presence of hydrocarbon side chains are likely responsible.

The old Pfeiffer and Saal model of asphaltene aggregates (1940) is likely highly misleading. The first dent to that old paradigm was a result of the work of a University of Alberta group led by Otto Strausz (Selucky et al. 1981). They reported that the GPC molecular weight of diluted solutions of asphaltenes (0.01 wt. % to 0.05 wt. %) yielded an unexpected trimodal molecular weight distribution pattern indicating three different molecular weight domains—contrary to expectations stemming from the ‘colloidal model.’ As follows from Strausz’s pioneering work, the dissociation process of asphaltene aggregates is very slow and may take weeks or more to complete. Strausz and his collaborators reported that, over a period of up to several weeks, the smallest molecular weight domain increased, while the higher-molecular-weight fractions decreased, indicating slow dissociation of higher-molecular-weight aggregates into their low-molecular-weight components. The asphaltene aggregation process spreads over a long period of time, and a large concentration range is difficult to reconcile with the old Pfeiffer and Saal colloidal model (1940), which assumed that the resins adsorbing on the asphaltenic aggregates were preventing their further growth, implying a rather uniform molecular weight of the aggregates. In addition, asphaltenes dissolved in toluene form colloidal-sized aggregates in the absence of any resins (Cimino et al. 1995), which, according to the Pfeiffer and Saal model, are essential to keep them in suspension.

Therefore, we have to reject the idea of resin-asphaltene interactions as the mechanism responsible for asphaltene stabilization. Despite its obvious deficiency, the model of resins stabilizing asphaltenes in solutions is still widely used and resin-asphaltene interactions are considered to be the key to understanding crude oil behaviour, especially in connection with asphaltene precipitation and emulsion stabilization. There is still no complete understanding of the mechanism or mechanisms involved. The limiting factor in asphaltene aggregate growth may be steric repulsion from aliphatic chains attached to their aromatic core (Buenrostro-Gonzalez et al. 2001; Andreatta, Bostrom, and Mullins 2005).

Asphaltene Molecular Structure

The discussion on asphaltene molecular mass is closely linked to their molecular structure. Below, we will describe two main models existing in the literature, known as the *archipelago* and *island* (or hand-like) models.

Archipelago Model

The archipelago model was introduced by Strausz, Mojelsky, and Lown based on VPO and GPC molecular mass estimations and on extensive chemical studies (Strausz 1992). In this model, a typical asphaltene molecule has a molecular weight of about 2000 Da or more. It also has a loose flexible architecture, in which aromatic and naphthenic ring structures are attached to each other and to the core of the asphaltene molecule by alkyl chains of various length, and by –S– and possibly –C(O)–O– and –O– bridges. These structural elements may also be present as side chains.

Figure 7.10 shows the structure proposed in Strausz, Mojelsky, and Lown (1992). The molecule shown in the figure has a molecular weight of about 6200 Da. This molecule is very often shown at scientific seminars and printed in many papers. It has to be stressed that in the original paper, Strausz writes that the elemental composition of this molecule is close to that of Athabasca asphaltenes. In the same publication, he writes further:

The experimental molecular weight determined by vapor pressure osmometry in benzene solutions, 6000 daltons, represents the molecular weight of micellar aggregates rather than a single covalently bound molecule. However, this difference does not present conceptual difficulties, since the model molecule can be broken into smaller fragments in order to accommodate for aggregation requirement (Strausz 1992, p. 1362).

This statement, however, is almost never included while discussing the original 1992 paper, not only contributing to the long-standing controversy about the molecular weight of asphaltenes, but also doing a big disservice to the original authors.

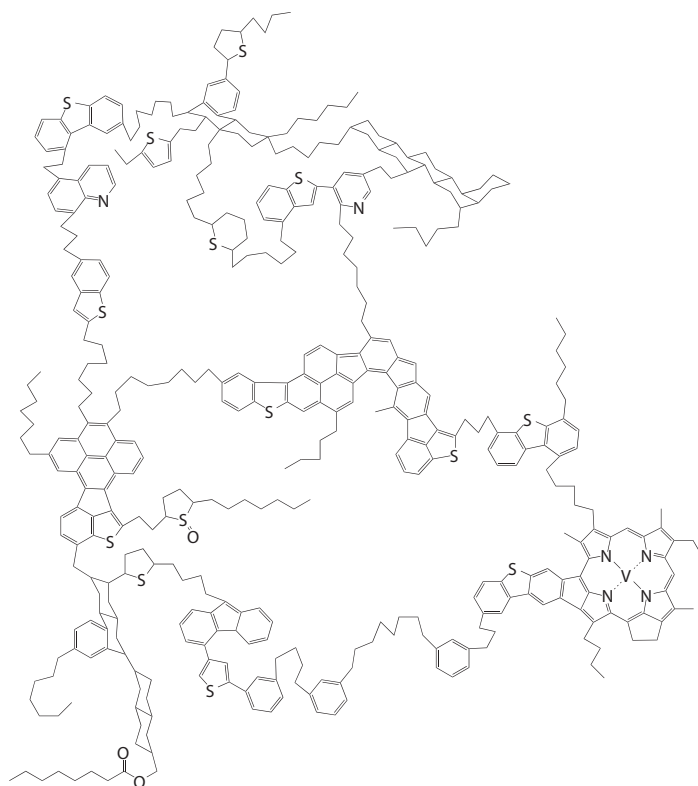


Figure 7.10 Hypothetical 'archipelago' asphaltene molecular structure. The molecular weight of the structure shown is about 6200 Da.

Redrawn from Strausz, Mojelsky, and Lown (1992).

The presence of alkyl bridges and side chains in asphaltene molecules has been indicated by ruthenium-ion-oxidation (RICO), which converts alkyl bridges and side chains to corresponding carboxylic acids:



or



The RICO cleaves the large molecule at the site of attachment of the side chain to an aromatic ring. If the resulting acid has one carboxylic group, it originated from a side chain. If it has two carboxylic groups at both ends of the molecule, it was a bridge in the original structure. Strausz reported that most of those dicarboxylic acids are short; however, some may have as many as over 20 carbon atoms, indicating the existence of relatively long alkyl bridges in the original asphaltene structures. The existence of dicarboxylic acids in RICO products is important for the justification of the archipelago model.

Removal of sulphur from sulphides can be done selectively by nickel boride reduction to H_2S . Such treatment will fragment the parent molecule at the original location of the alkyl sulphide sulphur atoms and, by necessity of the fragmentation, reduce its molecular weight. This was confirmed by the VPO and GPC methods. According to Strausz et al. (2008), after nickel boride reduction, the average molecular weight of Athabasca asphaltenes was reduced from about 4800 Da to 1200 Da.

According to the archipelago model, the typical molecule may have several different, relatively small aromatic ring systems connected to each other via alkyl or sulphide bridges. The ring structures may be substituted with functional groups, which may contain heteroatoms, mainly (thiophenic) sulphur and/or nitrogen. Some of the nitrogen compounds are complex porphyrin-like structures, containing coordinated metals such as vanadium, nickel, iron, or other trace elements.

Island or Like-Your-Hand Model

In the island or like-your-hand model (Groenzin and Mullins 2007), the typical asphaltene molecule is much smaller, with a molecular weight of 500 Da to 1500 Da. It has a polyaromatic core typically containing about seven condensed aromatic rings (palm) and several side alkyl and naphthenic side chains (fingers)—see Figure 7.11.

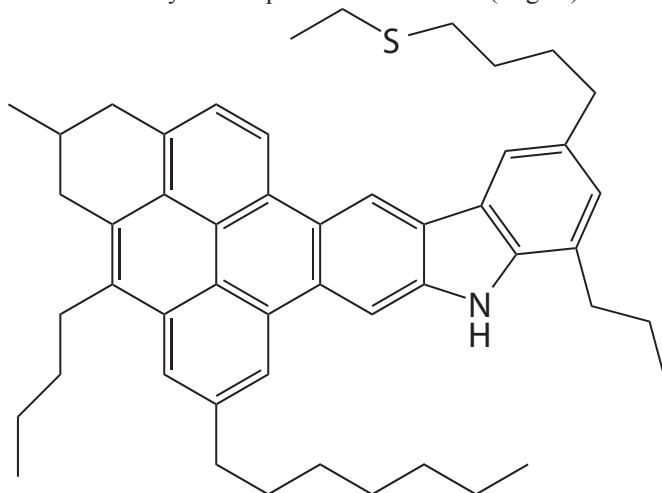


Figure 7.11 Hypothetical 'island' asphaltene molecular structure. The molecular weight of the structure shown is about 708 Da.

Redrawn from Groenzin and Mullins (2007).

The island model is based on asphaltene molecular weight estimation from several modern instrumental methods, including time-resolved fluorescence depolarization (TRFD), mentioned earlier. The island-like molecule has a molecular weight of about 400 Da to 1500 Da, with an average value of about 750 Da. The 'island' structure contains a fused aromatic ring system consisting, on average, of about seven members. This is further supported by optical absorption and fluorescence emission studies (Groenzin and Mullins 2007; Ruiz-Morales 2007). The central aromatic core facilitates the aggregation of asphaltenes via van der Waals attraction between them. The condensed ring systems tend to stack on top of each other. This stacking decreases asphaltene solubility, the defining property of asphaltenes. The attached aliphatic chains (fingers) limit the size of the formed aggregate, such that instead of undergoing phase separation, asphaltenes form small aggregates at low concentrations. These aggregates, consisting of a few of individual monomer molecules, are called *nano-aggregates*. At higher concentrations, nano-aggregates aggregate further to form even larger clusters.

Asphaltene Nano-Aggregation and Mullins' Model

The notion of asphaltenes forming nano-aggregates at low concentrations, followed by the formation of clusters at slightly higher concentrations that in turn associate further to form insoluble asphaltene particles is the basis of the extended Yen model of asphaltenes, proposed by Mullins. This model was supported by high-resolution transmission electron microscopy (HRTEM) studies (Sharma and Mullins 2007). In essence, the model suggests that asphaltene precipitate is formed from a hierarchical structure, composed of small nano-aggregates of a few individual monomer molecules, clusters of nano-aggregates, and finally, macroscopic-sized particles consisting of a number of nano-aggregates. There is a notion of CNAC (critical nano-aggregate concentration), another analogue to critical micelle concentration (CMC). The existence of CNAC for a species composed of just a few individual monomer molecules seems to be doubtful for reasons discussed in the section above on asphaltene aggregation. A small aggregation number necessarily implies a diffuse transition from a monomer to an aggregate state.

7.2.3 Role of Naphthenic Acids and Their Salts in Emulsion Stabilization

Strictly speaking, naphthenic acids are defined as carboxylic mono-acids of petroleum origin, with the general formula RCOOH, where R can be any cyclo-aliphatic group (Ese and Kilpatrick 2004). However, the term is also used in a more generic sense to describe all carboxylic acids present in crude oils, including acids of aromatic or paraffinic character.⁴ Naphthenic acids have been studied extensively, as they are

⁴ This usage is justified, as the acids are separated from the parent oil by first extracting them into an aqueous caustic solution, which converts the acids to their water soluble sodium salts. After the separation of the aqueous phase, a strong mineral acid is added, followed by extraction of the acids formed with an organic solvent. After removal of the solvent by evaporation, the residue is a mixture of any carboxylic acids initially present in the oil.

the main contributor to the total acid number (TAN), an important indicator of oil's characteristics, e.g., its corrosive propensity. Naphthenic acids are also the main source of toxicity in process-affected waters in oil sands operations.

Naphthenic acids are mainly C_{10} to C_{50} compounds with up to six fused ring structures, most of them saturated (Ese and Kilpatrick 2004). The carboxylic group is usually attached to the ring structure by a short aliphatic side chain. All crude oils contain some naphthenic acids, but the content varies widely. Heavy oils usually contain more naphthenic acids than light crudes. Naphthenic acids are believed to originate from the biodegradation of oils and are often used as markers of oil field biodegradation.

All carboxylic acids and their salts are surface-active. The sodium salts of the acids with 10 to 18 carbon atoms are surfactants. The group includes common soaps. The carboxylic acids of this moderate size, including naphthenic acids, have an HLB of about 3 to 6; thus, they are effective W/O emulsion stabilizers. In addition, it was shown that sodium salts of naphthenic acid can form liquid crystals (Horváth-Szábo, Czarnecki, and Masliyeh 2001). Friberg et al. have shown that the presence of liquid crystals dramatically increases foam and emulsion stabilities (Friberg et al. 1986; Friberg and Solans 1986). Calcium and magnesium form water-insoluble salts when mixed with naphthenic acids, which often cause serious production problems, especially in offshore operation

7.3 Fundamental Aspects of Paraffinic and Naphtha-Based Processes

Bitumen is extracted from mined Athabasca oil sands deposits by a modified flotation method, yielding froth typically containing about 60 wt. % bitumen, 30 wt.% water, and 10 wt. % solids. The water carries dissolved salts, including NaCl, which poses serious corrosion problems in downstream upgrading operations. Coarse solids increase the wear on pipes, pumps, and other equipment. Fine solids plug catalyst beds, increase the volume of produced coke, and increase fouling in heat exchangers and other equipment. Therefore, before froth can be passed over to upgrading operations, the water and solids must be removed. This is accomplished in froth treatment operations.

Because the density of bitumen at process temperatures is very close to that of water, froth treatment is not possible without the addition of a light hydrocarbon solvent. The dilution of froth with a light solvent lowers the oil phase density, facilitating various gravity- and centrifugation-based operations. Gravity settlers, centrifuges, and cyclones, used in all operating plants, depend on the density difference between oil and water. Thus, the main purpose of solvent addition is the lowering of bitumen density. It also lowers the oil viscosity and, as a result, accelerates water and solids separation from oil.

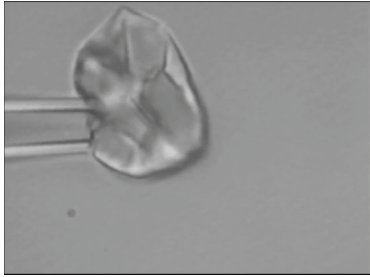
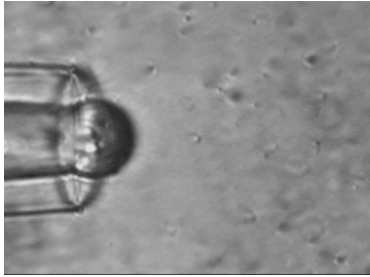
7.3.1 Learning from Past Research

As we have already discussed, the addition of diluent is a crucial operation in oil sands processing, making it distinctly different from most conventional and heavy oil recovery processes. It also provides some control over the composition of the oil phase. It is therefore not surprising that substantial research efforts have been devoted to determining how the nature and amount of diluent affects the ability of the oil phase to stabilize emulsions. In the mid-1990s, it was discovered that using a paraffinic diluent above a diluent-to-bitumen ratio (D/B) of about 2 could produce a very clean and dry product in froth treatment. This was a breakthrough discovery that led to the development of what is known as *paraffinic froth treatment* technology (Shelfantook 2004).

Critical Dilution Ratio

The results of extensive studies on the impact of the amount and nature of diluent added can be summarized as follows: There is a critical diluent-to-bitumen ratio at which a number of the system properties change dramatically (Yeung et al. 1999; Yang and Czarnecki 2002; Dabros et al. 1999). Some of these changes are listed in Table 7.3. For instance, in experiments using a micropipette to manipulate small emulsion droplets, Yeung et al. found that, at a high dilution ratio (low bitumen concentration), the interface between a water droplet and the diluted bitumen appears rigid and crumples when the droplets are deflated. At low dilutions (high bitumen concentrations), the deflated droplets preserve their spherical shape, indicating a flexible water-oil interface (Dabros et al. 1999).

Table 7.3 Selected water-oil interface properties above and below critical dilution

Above critical dilution Low bitumen concentration	Below critical dilution High bitumen concentration
<ul style="list-style-type: none"> • Rigid oil-water interface • Droplets crumple on deflation • Droplets flocculate • Paraffinic froth treatment operating regime 	<ul style="list-style-type: none"> • Flexible oil-water interface • Droplets preserve spherical shape on deflation • Emulsions form easily • Naphtha-based froth treatment operating regime
	

Alex Wu has developed a method for collecting the interfacial material (IM) that covers droplets in W/O emulsions in quantities sufficient enough to allow chemical analysis (2002). Wu's unique method allows for the extensive studies of emulsion stabilization mechanisms, and therefore deserves a brief description. When a stable emulsion is centrifuged, it yields a cake at the bottom of the centrifuge cell. The cake is composed mostly of the emulsion droplets, which do not coalesce due to high emulsion stability. The droplets carry with them whatever material was initially present on their surfaces; this material is the main source of the stability. The cake also contains some of the parent oil entrained between the droplets. Thus, it is not a good source of interfacial material for analysis, as it is impossible to distinguish between the chemicals originating from the entrained oil and those from the stabilizing layer on the droplet surfaces. Wu's method, illustrated in Figure 7.12, overcomes this problem. First, an emulsion of water in the studied oil is made using heavy water instead of ordinary water. A sample of this emulsion is placed on top of an ordinary water layer in a centrifuge cell (Figure 7.12, left) and then centrifuged. Emulsified heavy water droplets, having a density higher than that of water, break through the emulsion water interface and form a cake at the bottom of the cell in the water phase (Figure 7.12, right). Thus, contamination with the parent oil is greatly reduced. The cake is then collected, dried, and analyzed. Figure 7.13 shows a typical scanning electron microscope (SEM) photograph of the cake.

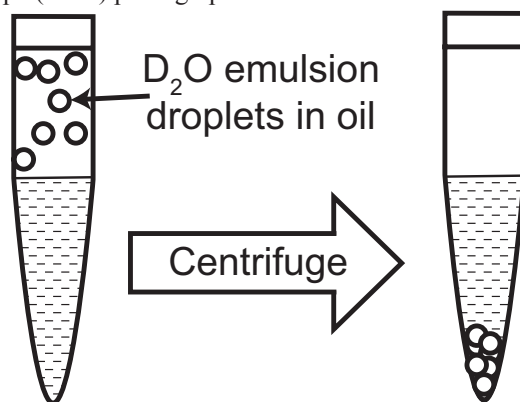


Figure 7.12 Alex Wu's method for collecting material from emulsified water droplets.

Source: Wu (2002).

Wu (2002) measured the H/C ratios for interfacial materials collected from a number of samples of bitumen diluted with heptol (1:1 mixture by volume of heptane and toluene) with increasing bitumen concentration ranging from 0.1 wt.% to 10 wt. %, as shown in Figure 7.14. For bitumen concentrations below 4 %, the H/C ratio was about 1.13, sharply increasing around 4 % bitumen to a value of 1.34 above 4 % bitumen. This sharp transition corresponded to a change in surface rheological properties and emulsion stability against flocculation. At low bitumen concentrations, the surfaces of emulsified droplets were rigid and the droplets flocculated. At high bitumen concentrations, approximately above 5 wt.%, the droplet surfaces were

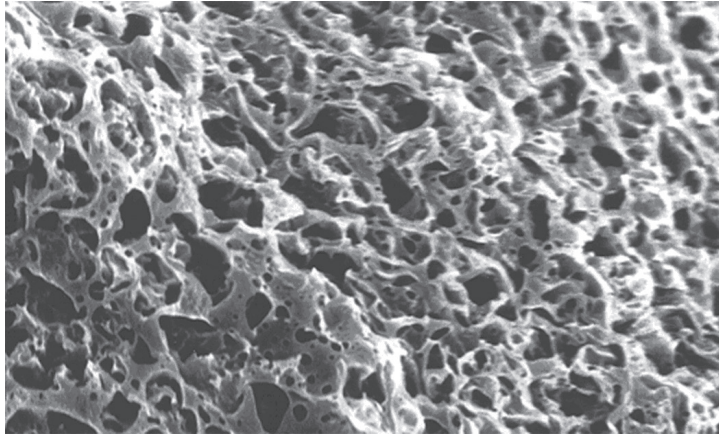


Figure 7.13 SEM photograph of surface material collected using Wu's method.

flexible and emulsion droplets were well dispersed. Although Wu has not reported any asphaltene precipitation in any of his samples, similar behaviour was reported for bitumen diluted with naphtha, where an onset of asphaltene precipitation was observed around critical dilution (Yang and Czarnecki 2002).

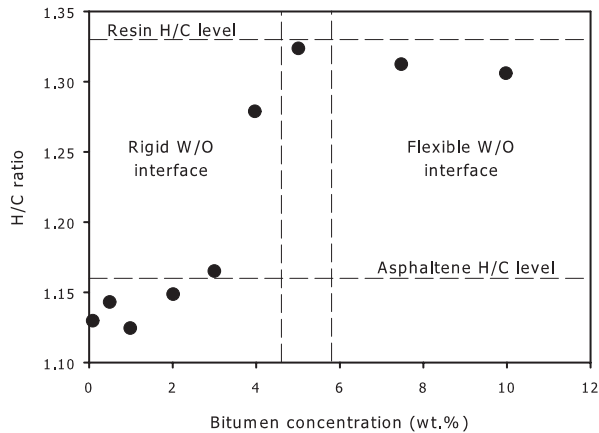


Figure 7.14 H/C ratio for interfacial material collected using Wu's method at different bitumen concentrations in heptol.

Based on data from Wu (2002).

Interfacial material collected using Wu's method was later analyzed using high-resolution mass spectrometry at the National High Magnetic Field Lab at Florida State University in Tallahassee. Most of the results and sample-handling protocol were published in Stanford et al. (2007).

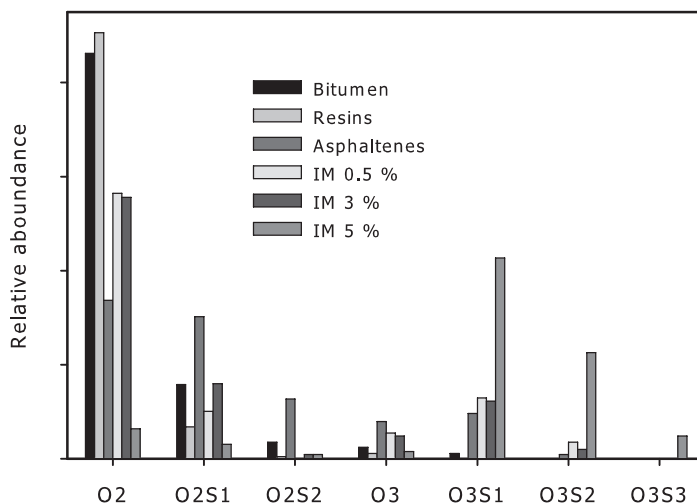


Figure 7.15 Negative-ion ESI selected OS class relative abundance for bitumen, asphaltenes, and resins, and for IM 0.5 %, IM 3 %, and IM 5 %.

Figure 7.15 shows the relative abundance of several selected chemical classes for IM 0.5 %, IM 3 % and IM 5 % (i.e., interfacial material prepared from emulsions in 0.5, 3, and 5 wt.% bitumen solutions, respectively). In addition, Figure 7.15 shows the mass spectrometry (MS) results for the parent bitumen and for samples of asphaltenes and resins separated from the parent bitumen. If one considers the mass spectrum to be a ‘fingerprint,’ the fingerprints of IM 0.5 % and IM 3 % are similar to each other but different from that of IM 5 %. This is to be expected, as both IM 0.5 % and IM 3 % were collected below critical dilution, while IM 5 % is the surface material collected above critical dilution. None of the IM material fingerprints are similar to that of asphaltenes, resins, or the parent bitumen. For instance, molecules containing 3 oxygen and 2 sulphur atoms in addition to carbon and hydrogen (O3S2 class) could only be detected in IM samples, and were below the detection limit in bitumen, asphaltenes, and resins samples. The O3S3 class could only be seen in the IM 5 % sample. Since the mass spectra of the materials collected from the emulsified droplet surfaces are not similar to that of asphaltenes, one must conclude that it is not asphaltenes that are responsible for emulsion stabilization.

The critical dilution ratio depends on the diluent composition. It increases with increasing diluent aromaticity. It was also found that the critical dilution coincides with the onset of asphaltene precipitation in the system (Czarnecki and Moran 2005). The critical dilution for a paraffinic diluent is about 1.8–2 (Xu et al. 1999). For the naphtha used as a diluent, as in Syncrude’s commercial operation, this critical D/B ratio is about 4 (Yang and Czarnecki 2002). Experiments with individual emulsion droplets manipulated with micropipettes showed that, above critical dilution, the oil-water interface is rigid (Yeung et al. 1999). Below critical dilution, i.e., at high bitumen concentrations, the oil-water interface is flexible (Dabros et al. 1999), and emulsions

are formed easily. This is the regime at which a conventional froth treatment process, using naphtha at a D/B of about 0.6–0.7, operates. Paraffinic froth treatment operates above critical dilution.

7.3.2 Industrial Implications

There are two technologies currently used in commercial froth treatment operations. In naphtha-based froth treatment, naphtha is usually added at a solvent-to-bitumen (S/B) ratio of 0.65–0.7 (by weight). This ratio is a compromise between cost-effectiveness, which forces the operators to use as low an S/B ratio as possible to lower capital and operating expenses, and the process requirements for a larger S/B ratio, at which water separation from bitumen is easier. The alternative technology, known as paraffinic froth treatment (employed at Albion Oil Sands), uses a paraffinic solvent, e.g., natural gas condensate, or a cut from the bitumen upgrading product containing mostly straight paraffinic hydrocarbons. Paraffinic solvent must be added above the onset of asphaltene precipitation, usually at an S/B ratio of about 2 or higher.

Naphtha-Based Froth Treatment

Naphtha-based froth treatment uses hydrotreated or untreated naphtha as froth diluent. The source of the naphtha is usually an integrated upgrading plant, where a light hydrocarbon cut can be produced to meet the froth treatment requirement for a solvent. It is mixed with froth at an S/B ratio of about 0.65–0.7 (by weight), resulting in the volume of diluted bitumen being almost half of that used for the paraffinic process at the same bitumen throughput. As a result, naphtha-based froth treatment requires significantly smaller equipment than that required for paraffinic diluent technology to treat the same amount of froth.

As the naphtha-based process operates below critical dilution, the oil-water interface is flexible and emulsions are easily made. Thus, any agitation of the diluted bitumen, such as that caused by pumps, valves, etc., disperses water into small droplets, contributing to the formation of a large number of very small droplets (about 3 μm in diameter), which are very difficult to remove. The combination of these effects causes the product quality of naphtha-based processes to be substantially lower than that of the paraffinic froth treatment process. The naphtha-based process makes it practically impossible to meet specifications for feedwater (or salt) content for downstream operations without using chemical aids (demulsifiers), which will be briefly discussed below and in more detail in in Volume 2.

Below critical dilution, where the naphtha-based froth treatment operates, there is no rejection of asphaltenes. Overall oil losses to tailings are thus much lower than in the paraffinic froth treatment, discussed below.

Paraffinic Froth Treatment

The paraffinic froth treatment process takes advantage of the fact that, when paraffinic solvent addition exceeds the onset of asphaltene precipitation, the precipitating asphaltenes act as flocculants for emulsified water droplets and fine solids (Long, Dabros, and Hamza 2007). The flocs that are formed contain water droplets, fine solids, and precipitated asphaltenes. They settle as a zone, forming a very sharp interface with clean, dry oil above. It is not clear what the mechanism behind this surprisingly sharp interface is, although it could be the result of a relatively narrow floc-size distribution and the fact that the free floc settling rate is higher than the hindered settling rate (T. Dabros, pers. comm.). Figure 7.16 shows the typical settling behaviour of bitumen froth diluted with paraffinic solvent. As the flocculated emulsion settles, the interface between the clean oil and the settling emulsion moves downwards, as illustrated by curve 1 in the figure. At the same time, an interface is formed between the settling emulsion and a consolidating cake is formed at the bottom (curve 2). After a certain amount of time, the two curves intersect. From that moment on, clean oil sits on top of the consolidating cake and the interface between the two zones moves downwards at a substantially slower pace. The settling rate of the flocculated emulsion is the most important parameter characterizing paraffinic froth treatment. It dictates the size of the settling vessels required for a given production level.

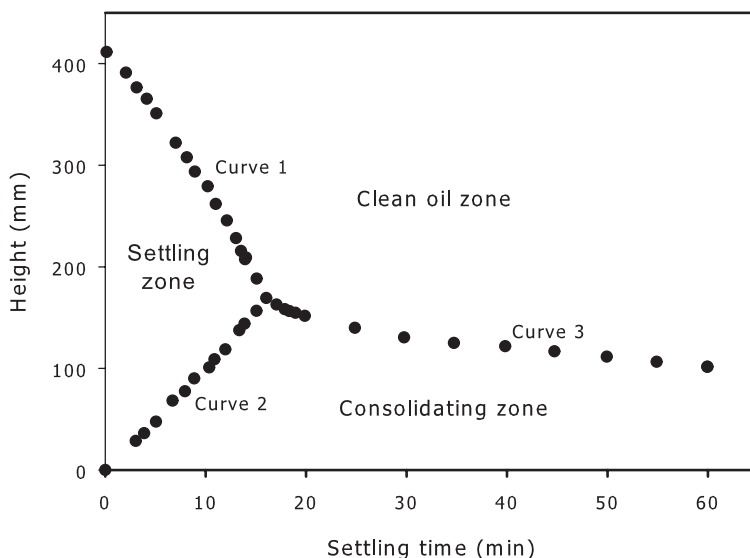


Figure 7.16 Zone settling curves for typical bitumen froth diluted with paraffinic solvent (1:1 n-pentane/n-hexane mixture). S/B = 2.8 by weight, at 22 °C.

Redrawn using data from Figure 20.15 in Long, Dabros, and Hamza (2007).

The main advantage of paraffinic froth treatment is that it produces a very clean and dry oil product. This makes it much easier to meet the feed specifications for a primary upgrading unit, especially if it is a catalytical hydrocracker. Since fine solids contribute significantly to catalyst deactivation, catalytical hydrocracking is much more sensitive to the fine solids level in the feed than coking technologies are. Paraffinic froth treatment requires an S/B wt. ratio of > 2 , resulting in higher volumes of diluted bitumen to be treated than in naphtha-based technology. Higher volumes require larger vessels, increasing the capital and operating costs of the process as compared to naphthenic froth treatment. In addition, paraffinic solvent is usually more expensive, further increasing operating costs. As well, oil losses to tails are greater in the paraffinic process, for two reasons. First, some of the parent hydrocarbon is rejected as precipitated asphaltenes. Second, some oil is lost due to its entrainment with the consolidated cake. There are claims that rejected asphaltenes would not contribute to liquid products in upgrading and that the material the technology rejects is therefore worthless. The validity of these claims is sometimes questioned, as perhaps some liquid hydrocarbons can be obtained from upgrading asphaltenes, although at a much lower yield than from the whole parent oil. Rejected asphaltenes always have some value as a fuel and can possibly be gasified to yield hydrogen for upgrading.

Overall, the benefits from an extremely dry and clean product often outweigh the drawbacks. The decision in selecting paraffinic or naphtha-based froth treatment technology in a 'green field' situation is always site-specific. It is driven by the configuration of the downstream upgrading plant and the current and projected cost of natural gas.

7.3.3 Summary

Both naphthenic and paraffinic solvent technologies have their pros and cons. Naphtha-based froth treatment works with smaller amounts of less expensive solvent. It sustains less oil loss to tailings. However, it uses rotary equipment (centrifuges), which adds to the operating complexity and cost. In addition, without the use of demulsifiers, the quality of the product does not meet pipeline specifications. The low quality of the product requires that the upgrading plant use coking as the primary upgrading technology.

The main advantage of the paraffinic process is that it yields a very clean and dry product without the need for rotary equipment. However, it requires a higher addition of more expensive solvent, resulting in the need for larger vessels with both capital and operating cost consequences.

Selection between the two technologies is site-specific, and companies analyzing 'green field' scenarios at more or less the same time have ended up with different conclusions based on their specific needs and conditions.

7.4 Demulsifiers and Other Chemical Aids

There are a number of chemicals used in the petroleum industry to achieve various goals. There are chemicals used to treat water (usually water softeners and clarifiers), corrosion inhibitors, scale deposition inhibitors, anti-foaming agents, chemicals to treat bacteria related problems, wax and asphaltene deposition inhibitors, hydrogen sulphide scavengers, and finally, emulsion breakers (often also called *demulsifiers*), which are of main interest in this chapter. The composition of commercial demulsifiers is tailored to address site-specific emulsion stabilization mechanisms, which are not always known. Demulsifiers may promote droplet coalescence, cause droplet flocculation, or displace the steric stabilization layer. Often, commercial demulsifier products are a mixture of various chemicals, such that the product can help with the emulsion problem regardless the physicochemical reason for high emulsion stability.

Use of chemicals for emulsion control is as old as the petroleum industry itself. Early-twentieth-century applications and patents dealt mostly with simple inorganic chemicals. These chemicals include agents that react with water, such as anhydrous calcium chloride or quick lime (calcium oxide, CaO); flocculate protective fine solids on droplet surfaces, such as multivalent salts (FeSO₄ or Na₂SO₄); neutralize negative surface charges on water droplets, such as sulphuric acid, acetic acid, or ferric salts; or disrupt organic films on water droplets, such as aggressive solvents like carbon disulphide, acetone, ether, or carbon tetrachloride. Reading old literature on the subject, one gets the impression that just about anything on a lab shelf was tested as an emulsion breaker, and that claims were made about just about every chemical being an effective demulsifier. Methods of chemical addition were also very primitive. A can with a chemical was hung from a manhole over a tank; a nail hole punched in the can would allow the chemical to slowly drip into the tank and mix with the incoming crude. Periodically, the water separating at the bottom of the tank would be drained and the chemical in the can refilled. How much water would separate without any chemical or how effective the chemical aid addition actually was is difficult to say. There was very little controlled experimentation and science behind those early practices.

Later on, after the Second World War, simple surfactants were introduced as emulsion breakers. At about the same time, the bottle test became the routine method for assaying demulsifiers' effectiveness. In the bottle test, several bottles or jars are filled with tested emulsion and the tested chemicals are added at known concentrations to each of the bottles. The bottles are shaken by hand and left for some time, after which any changes in appearance of the material are observed and recorded. When the best-performing chemical is found, another series of bottle tests is done to find the optimum chemical dosage, and, in many cases, to develop a chemical mixture for a particular field application. Bottle tests can be easily done in the field, allowing for a chemical and its dosage to be matched to a particular field problem. Because of its simplicity, the bottle test is still routinely used today, although in order to develop

complex chemical mixtures, the number of variables (type of individual components and their concentrations) requires that hundreds, if not thousands, of individual bottle tests are performed.

Modern demulsifiers are usually mixtures of polymer surface-active chemicals. As we have discussed above, the stability of W/O emulsions in petroleum systems is due to a stabilization layer on water droplet surfaces forming a ‘skin’ that is very difficult to disrupt. The nature of this skin is not fully understood yet. Regardless, whether the skin is formed by asphaltenes, fine biwetttable solids, natural surfactants, a mixture of all of the above, or some other agents, the chemical aid used to break the emulsion must be capable of destroying or at least substantially weakening it. To penetrate the skin or to adsorb at the water-oil interface, the chemical must be surface active. Various vendors offer many complex formulations to address specific requirements.

These formulations are usually site-specific and their exact composition is almost always confidential. Most of the active ingredients in the chemicals used as emulsion breakers are co-polymers of ethylene oxide (EO) and propylene oxide (PO) of various molecular weights and various EO-to-PO ratios.

Changing the EO/PO ratio changes the HLB number of the product. Increasing EO content increases the HLB value and makes the polymer more hydrophilic, while increasing PO makes it more oil-soluble. Polymers of low molecular weight usually act faster but may leave some water in the oil. High-molecular-weight polymers are slower-acting but usually yield a better product. Commercial compositions usually contain a blend of several polymers of different EO/PO ratios and of different molecular weights. The formulations also contain solvents, anti-freezing agents, and other additives.

7.4.1 Demulsifier Dosage

The dosage, that is the concentration of added demulsifier in the treated oil, is very important, not only because of economics, but also because of chemical performance. Starting from very low additions, the product quality improves with increasing dosage and then, after passing over the optimum dosage, deteriorates. This is counterintuitive, as we tend to think that if something is good, then more of it would be even better—not so with demulsifiers. Because the detrimental effects of overdosage are often not properly recognized, we will spend some time discussing their impact on chemicals that act by flocculating water droplets and on that which promote coalescence.

Flocculant-Type Chemicals

In order to analyze the action of flocculating chemical aids, we must first gather some information on the structure of the flocs formed under the chemicals’ influence. This can be done by microscopy, while taking care to ensure that the way the sample is handled does not affect the floc structure (for instance, by using rectangular cross-section glass capillaries with optical quality walls, known as microslides) (Czarnecki, Moran, and

Yang 2007). From microscopic images, the flocs' size, fractal dimension, porosity, and density can be evaluated. As an example, Figure 7.17 shows the density of such flocs as a function of the maximum floc radius. The flocs were formed in naphtha-diluted froth, under the influence of an added commercial flocculating chemical. It is clearly seen that higher flocculant concentration results in lower density flocs. This is to be expected because, at high chemical addition, the water droplets and fine solids form aggregates immediately on contact, resulting in 'fluffy' flocs. At lower chemical additions, the droplets and particles may still rotate and/or move a bit within the forming structure, establishing multiple bonds with their neighbours and thus forming denser flocs. Obviously, denser flocs would sediment faster than fluffier flocs of the same size.

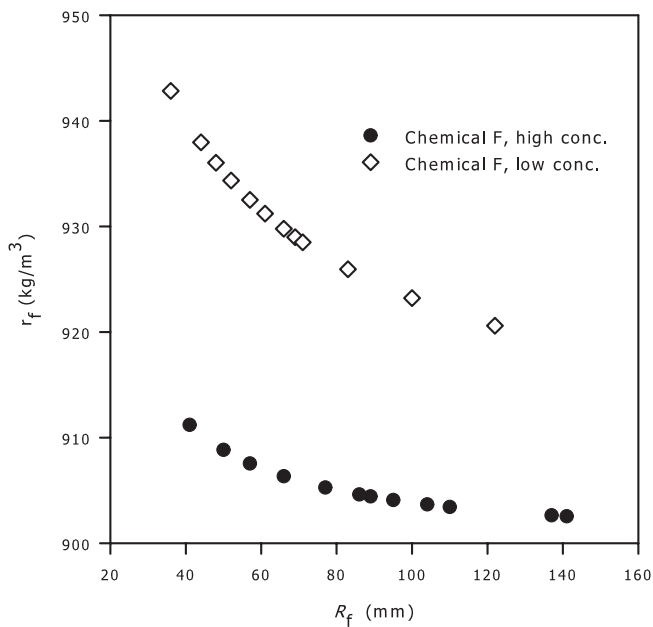


Figure 7.17 Density of flocs formed at high (open diamonds) and low (full circles) flocculant addition as a function of maximum floc radius.

In a separating vessel such as an inclined plate settler (IPS), we have to compare the flocs' settling velocity with the velocity of the fluid in the vessel. Transient settling velocities were calculated by solving partial differential equations using data from microscopy (Czarnecki, Moran, and Yang 2007). Figure 7.18 shows the instantaneous settling velocities of flocs formed at high and low dosages of a flocculating chemical and drops formed with the addition of a coalescing agent. We see from the figure that the terminal settling velocity is achieved within a few milliseconds.

Thus, it is sufficient to analyze only the terminal velocities, V_{ter} , given by

$$V_{ter} = \frac{2}{9} \frac{gR_f^2(\rho_f - \rho_o)}{\mu} \quad (7.2)$$

where g is acceleration due to gravity, R_f is the floc radius, ρ_f and ρ_o are the densities of the floc and the continuous oil medium, respectively, and μ is the dynamic viscosity of the medium. In the example shown in Figure 7.18, all velocities were scaled in respect to the fluid velocity in the separation vessel. It can be seen from the figure that increasing the flocculating agent concentration decreases the flocs' settling velocity such that, in the example shown, they will be carried over to the overflow. Of course, the individual flocs differ in their radii and densities, and therefore, some of them will settle and some will be carried over. The plot is shown here to illustrate the general trend: overdosing with flocculating agent makes for fluffier flocs, creating a situation in which some of the flocs will end up with the settler overflow, deteriorating the product quality.

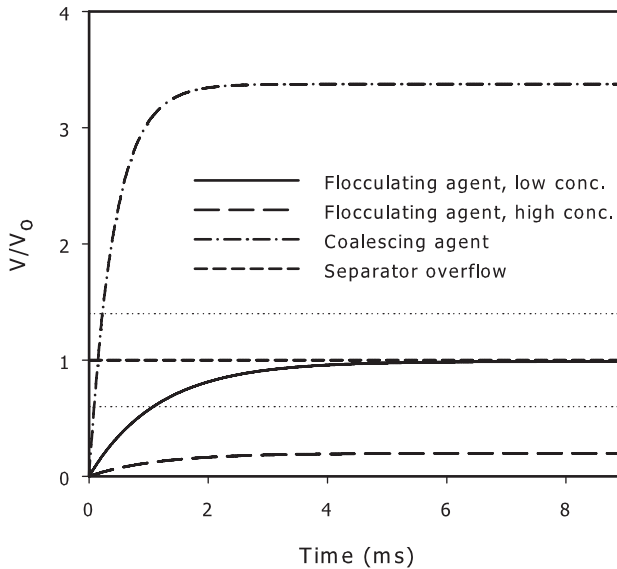


Figure 7.18 Settling behaviour of flocs and droplets.

Coalescing-Type Chemicals

Coalescing-type chemicals are often called ‘interface controllers,’ and their role is to promote the coalescence of small emulsified droplets, which results in faster settling of the larger drops formed.

The kinetics of the coalescence process is described by the same formalism as coagulation, discussed in Chapter 2. For shear-induced coagulation (or coalescence), the total number of droplets n_{tot} , as a function of time t , is given by combining Eq. (2.52) with Eq. (2.49) yielding the following approximate expression:

$$\frac{dn_{tot}}{dt} = -\frac{16}{3} a^3 G n_{tot}^2 \quad (7.3)$$

where a is the distance at which the droplets collide, equal to the sum of the colliding droplets’ radii, and G is the shear rate. Analysis of Eq. (7.3) indicates that, under favourable conditions, shear coalescence causes rapid growth of droplets and therefore quickly increases their sedimentation rate.

From Figure 7.18, it follows that droplets usually settle fast, as coalescence allows them to grow big enough. Thus, if the chemical is effective in creating conditions for droplet coalescence, it is only a question of time (i.e., the vessel residence time) before the drops grow big enough to settle faster than the fluid rising velocity.

Commercial Compositions Versus ‘Pure’ Systems

In a ternary system composed of a surfactant, oil, and water, when the surfactant content is increased, the system evolves from a water-in-oil, kinetically stable, ordinary emulsion to a thermodynamically stable microemulsion (see subsection on Winsor types in Section 7.1.2). It was found that, usually, the emulsion stability is drastically reduced just at the boundary between the emulsion and microemulsion. Therefore, if a demulsifier is added just at the right concentration, it can be very effective. Below and above this narrow concentration range, it is not effective at all. This is based on observations dealing with pure component systems with very well-defined properties. In industrial applications, we never deal with systems this pure. All of the pseudo-components in practical systems are mixtures of many individual chemicals, including natural emulsifying agents and added demulsifiers. The latter are usually a mixture of both coalescing and flocculating agents. This complex composition of industrial systems makes the range of emulsion destabilization wider, which is beneficial as it makes the concentration control of the added agent a little less stringent. At the same time, it also makes the destabilization effect slightly smaller. With this in mind, the main message still remains valid: the demulsifier dosage has an optimum, and using it both above and below the optimum dosage results in serious deterioration of the chemical’s performance.

7.5 Concluding Remarks

Emulsions cause serious problems in just about every branch of the petroleum industry. However, remarkable progress has been made over the last 80 years of the industry's modern history, and most emulsion-related problems in oil production today are efficiently controlled. Chemicals are almost always used in combination with various mechanical and electrical demulsification methods. Chemical companies have developed several families of effective demulsifiers, capable of treating most commercial streams. With the introduction of polymer demulsifiers, the chemicals' cost per barrel has dropped significantly as well, a result of the remarkable improvement in chemicals' performance.

In the realm of the basic science of petroleum emulsion stabilization mechanisms and emulsion breaking, the situation is, unfortunately, not as favourable. It is well known that some components of crude oils are natural emulsifiers. In some cases, they have been isolated and identified. Yet, variability in crude composition and field conditions makes any generalization practically impossible. Asphaltenes, resins, naphthenates, waxes, and fine solids have all been blamed as the main source of emulsion problems. It is likely that a combination of all of these components has an impact on emulsion formation and stability, with the dominant factor being difficult to identify and likely changing from case to case.

According to the most common belief, asphaltenes are the main source of emulsion stabilization in petroleum systems. Asphaltenes are defined as pentane or heptane insolubles, and thus are a solubility class. Their ability to associate at very low concentrations makes even estimation of their average molecular weight difficult. That seems to be an issue of relatively low importance, but without knowing how big asphaltene molecules are, it is even more difficult to determine their structure, and thus, their functionality. Vigorous discussion on asphaltenes' molecular weight, structure, association, precipitation, and interactions with other oil fractions has been taking place for many years in professional literature. Unfortunately, most published papers deal with specific issues and use custom laboratory protocols, making it almost impossible to draw any generally valid conclusions. Everybody agrees that standardization of laboratory methods, samples, sample collection, and handling would make progress much faster and easier. Yet very little, if anything, is done to achieve that goal.

Some progress, however, has been made, although perhaps slower than we would hope for. For example, recent progress in high-resolution mass spectrometry, combined with the application of modern instrumental analytical methods, is already making a significant impact. In the very least, the scientific community is converging to believe that the average asphaltene molecule is rather small, with a molecular weight of about 750 Da. This relatively low molecular weight and the elemental composition of asphaltenes mean that a single, small asphaltene molecule cannot have a multitude of functional and polar groups, as a molecule several times larger could. Therefore, some members of asphaltene solubility classes may have the ability to stabilize

emulsions, while others may not, supporting ideas that only a very small sub-fraction of asphaltenes are the ‘bad actors.’ This is only to illustrate the difficulties encountered in petroleum emulsion research.

There are many variables influencing petroleum emulsion formation and stability. Laboratory techniques for studying the problem are difficult, tedious, and in many cases, very expensive, such that it is much easier to rely on simple field testing (such as bottle tests) rather than on sophisticated scientific methods. Despite its simplicity, field testing has generated a vast practical knowledge on what works under specific conditions and what does not. This practical approach has become more of an art than a science. It contributes to the gap between very successful field practice and lagging scientific understanding. However, with recent progress in the basic science of petroleum emulsions and in modern demulsifier synthesis and selection, in the not-too-distant future, we will perhaps be able to make field decisions on a more fundamental basis.

7.6 References

- American Society for Testing and Materials (ASTM). 2005. *Standard test method for determination of asphaltenes (heptane insolubles) in crude petroleum and petroleum products*, ASTM D6560-00.
- Andreatta, G., N. Bostrom, and O.C. Mullins. 2005. High-Q ultrasonic determination of the critical nanoaggregate concentration of asphaltenes and the critical micelle concentration of standard surfactants. *Langmuir* 21 (7): 2728–2736.
- Binks, B.P. 2002. Particles as surfactants: similarities and differences. *Current Opinion in Colloid & Interface Science* 7 (1–2): 21–41.
- Buenrostro-Gonzalez, E., H. Groenzin, C. Lira-Galeana, and O.C. Mullins. 2001. The overriding chemical principles that define asphaltenes. *Energy & Fuels* 15 (4): 972–978.
- Cimino, R., S. Corraera, A.D. Bianco, and T. Lockhart. 1995. Solubility and phase behaviour of asphaltenes in hydrocarbon media. In *Asphaltenes: Fundamentals and applications*, ed. E. Sheu and O. Mullins. New York: Plenum.
- Czarnecki, J., and K. Moran. 2005. On the stability of water in diluted bitumen emulsions. *Energy & Fuels* 19: 2074–2079.
- Czarnecki, J., K. Moran, and X. Yang. 2007. On the ‘rag layer’ and diluted bitumen froth dewatering. *Canadian Journal of Chemical Engineering* 85: 748–755.
- Dabros, T., A. Yeung, J. Masliyah, and J. Czarnecki. 1999. Emulsification through area contraction. *Journal of Colloid and Interface Science* 210 (1): 222–224.
- Ese, M.-H., and P.K. Kilpatrick. 2004. Stabilization of water-in-oil emulsions by naphthenic acids and their salts: Model compounds, role of pH, and soap : Acid ratio. *Journal of Dispersion Science and Technology* 25 (3): 253–261.

- Friberg, S. 2007. Micellization. In *Asphaltenes, heavy oils, and petroleomics*, ed. O. Mullins, E. Sheu, A. Hammami and A. Marshall. New York: Springer.
- Friberg, S.E., I. Blute, H. Kunieda, and P. Stenius. 1986. Stability of hydrophobic foams. *Langmuir* 2 (5): 659–664.
- Friberg, S.E., and C. Solans. 1986. Surfactant association structures and the stability of emulsions and foams. *Langmuir* 2 (2): 121–126.
- Groenzin, H., and O. Mullins. 2007. Asphaltene molecular size and weight by time-resolved fluorescence depolarization. In *Asphaltenes, heavy oils, and petroleomics*, ed. O. Mullins, E. Sheu, A. Hammami and A. Marshall. New York: Springer.
- Horváth-Szábo, G., J. Czarnecki, and J. Masliyah. 2001. Liquid crystals in aqueous solutions of sodium naphthenates. *Journal of Colloid and Interface Science* 236: 233–241.
- Khristov, K., S.D. Taylor, J. Czarnecki, and J. Masliyah. 2000. Thin liquid film technique: Application to water-oil-water bitumen emulsion films. *Colloids and Surfaces A: Physicochemical and Engineering Aspects* 174 (1–2): 183–196.
- Long, Y., T. Dabros, and H. Hamza. 2007. Selective solvent deasphalting for heavy oil emulsion treatment. In *Asphaltenes, Heavy Oils, and Petroleomics*, ed. O. Mullins, E. Sheu, A. Hammami and A. Marshall. New York: Springer.
- Nellensteyn, F.I. 1924. The constitution of asphalt. *Journal of the Institution of Petroleum Technologists* 10: 211.
- Panchev, N., K. Khristov, J. Czarnecki, D. Exerowa, S. Bhattacharjee, and J. Masliyah. 2008. A new method for water-in-oil emulsion film studies. *Colloids and Surfaces A: Physicochemical and Engineering Aspects* 315 (1–3): 74–78.
- Pfeiffer, J.P., and R.N.J. Saal. 1940. Asphaltic bitumen as colloid system. *The Journal of Physical Chemistry* 44 (2): 139–149.
- Platikanov, D., and D. Exerowa. 2005. Thin liquid films. In *Fundamentals of interface and colloid science*, ed. J. Lyklema. Amsterdam: Academic Press.
- Ruiz-Morales, Y. 2007. Molecular orbital calculations and optical transitions of PAHs and asphaltenes. In *Asphaltenes, heavy oils, and petroleomics*, ed. O. Mullins, E. Sheu, A. Hammami and A. Marshall. New York: Springer.
- Scheludko, A. 1967. Thin liquid films. *Advances in Colloid and Interface Science* 1 4: 391–464.
- Selucky, M., S.S. Kim, F. Skinner, and O.P. Strausz. 1981. Structure-related properties of Athabasca asphaltenes and resins as indicated by chromatographic separation. In *Chemistry of asphaltenes. Advances in chemistry Series*, ed. J. W. Bunger and N. C. Li. Washington, D.C.: ACS.
- Sharma, A., and O. Mullins. 2007. Insights into molecular and aggregate structures of asphaltenes using HRTEM. In *Asphaltenes, heavy oils, and petroleomics*, ed. O. Mullins, E. Sheu, A. Hammami and A. Marshall. New York: Springer.

- Shelfantook, W.E. 2004. A perspective on the selection of froth treatment processes. *Canadian Journal of Chemical Engineering* 211: 704–709.
- Stanford, L.A., R.P. Rodgers, A.G. Marshall, J. Czarnecki, and X.A. Wu. 2007. Compositional characterization of bitumen/water emulsion films by negative- and positive-ion electrospray ionization and field desorption/ionization Fourier transform ion cyclotron resonance mass spectrometry. *Energy & Fuels* 21: 963–972.
- Strausz, O.P. 1989. Bitumen and heavy oil chemistry. In *AOSTRA Technical Handbook on Oil Sands, Bitumens and Heavy Oils: AOSTRA Technical Publication Series.*, ed. L. G. Hepler and C. Hsi. Edmonton: Alberta Oil Sands Technology and Research Authority (AOSTRA).
- Strausz, O.P., T.W. Mojelsky, and E.M. Lown. 1992. The molecular structure of asphaltene: an unfolding story. *Fuel* 71 (12): 1355–1363.
- Strausz, O.P., I. Safarik, E.M. Lown, and A. Morales-Izquierdo. 2008. A critique of asphaltene fluorescence decay and depolarization-based claims about molecular weight and molecular architecture. *Energy & Fuels* 22 (2): 1156–1166.
- Wu, X. 2002. Investigating the stability mechanism of water-in-diluted bitumen emulsions through isolation and characterization of the stabilizing materials at the interface. *Energy & Fuels* 17 (1): 179–190.
- Xu, Y., T. Dabros, H.A. Hamza, and W.E. Shelfantook. 1999. Destabilization of water in bitumen emulsion by washing with water. *Petroleum Science and Technology* 17 (9–10): 1051–1070.
- Yang, X., and J. Czarnecki. 2002. The effect of naphtha to bitumen ratio on properties of water in diluted bitumen emulsions. *Colloids and Surfaces A: Physicochemical and Engineering Aspects* 211 (2–3): 213–222.
- Yarranton, H.W., H. Alboudwarej, and R. Jakher. 2000. Investigation of asphaltene association with vapor pressure osmometry and interfacial tension measurements. *Industrial & Engineering Chemistry Research* 39 (8): 2916–2924.
- Yeung, A., T. Dabros, J. Czarnecki, and J.H. Masliyah. 1999. On the interfacial properties of micrometre-sized water droplets in crude oil. *Proceedings of the Royal Society of London A* 445: 3709–3723.

Chapter 8

Colloidal Science in Tailings Management

In a typical water-based oil sands extraction process, the production of one barrel of bitumen requires approximately 1.8 tons of oil sands ore mixed with 2.5 m³ of hot water and desired process aids, as shown in Figure 8.1. Unfortunately, after the bitumen has been recovered, approximately 3.3 m³ of tailings sludge is left behind, which is discharged to tailings ponds. While coarse solids (sands) settle quickly to form beaches along the tailings pond, the fines (mainly silts and clays) take a much longer time to settle. Even after a few years, the solids remain suspended in the process-affected tailings water in the form of a sludge, with no further noticeable densification for several decades. The sludge, which contains approximately 30 wt. % fine solids and about 70 % water, must be contained in the tailings ponds. This material is referred to as *fluid fine tailings* (FFT) or *mature fine tailings* (MFT).

The volume of MFT, which is dependent on the rate of bitumen production, accumulates at an alarming rate. For example, if production proceeds as projected, Syncrude will produce an estimated one billion cubic metres of fine tailings by 2025, while Suncor will accumulate 800 million cubic metres by 2033. The current tailings ponds occupy a total area of more than 130 km². To put the size of the accumulated tailings in perspective, a container of a similar volume would be large enough to hold the earth's population. The volume of fluid fine tailings accumulates at a rate of more than 20 % of the volume of oil sands excavated from the mine. Provision for the containment of fluid fine tailings represents a direct incremental operating cost and continues to be the source of major logistical and environmental concerns.

One of the principal considerations in tailings treatment is the quality of the release water recycled back to extraction, as water chemistry has been known to be a key physicochemical property affecting bitumen extraction (Zhao et al. 2009). The objective of tailings treatment is to increase the solid settling velocity and the rate of consolidation by optimizing the physicochemical conditions of the system. Therefore, the ability to treat fresh tailings and MFT requires an understanding of the colloidal behaviours of fine solids in process water.

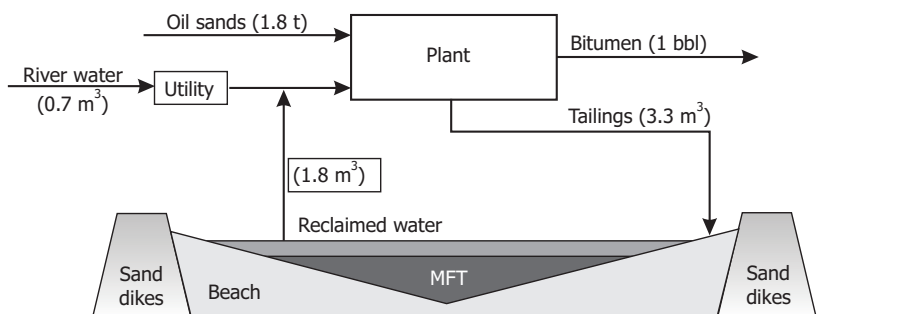


Figure 8.1 Traditional tailings disposal to a tailings pond and water balance in oil sands extraction.

Source: Cymerman et al. (1999).

Alternating between pumping from short- and long-term tailings containment structures and the storage of fluid fine tailings incur additional costs for oil sands operators. More importantly, a containment structure failure might lead to a catastrophic disaster. Effort has been made to treat MFT and process tailings in an attempt to reduce, and eventually eliminate, tailings ponds. Treating oil sands processing tailings reduces not only the size of tailings ponds, but also the intake of freshwater by maximizing the amount of recycle water used. Energy Resources Conservation Board (ERCB) regulations ensure that the maximum freshwater intake from the Athabasca River by an oil sands operator does not exceed 25 % of the total water flow in the Athabasca River at any given time. If fresh, warm tailings are treated as they are produced, the warm water, along with the residual chemicals in the process-affected water, can be recycled. This reduces the amount of energy required to heat the pond water for the warm water process and contributes to a higher energy efficiency and a lower carbon footprint. Furthermore, if a sufficiently high-density, self-supportive sludge is produced, it can be deposited back to the mined pit for immediate land reclamation, rather than being placed into a tailings pond, minimizing the land disturbance resulting from oil sands operations. It is therefore highly desirable to treat tailings when they are still fresh and to reduce (consume) existing MFT.

8.1 Impact of Water Chemistry

To address the impact of water chemistry on the dispersion of fine solids, it is beneficial to recall the basic science involved in this phenomenon, as discussed in Chapter 2. Individual solid particles interact with each other and with the medium in which they are suspended (usually water). There are two main sources of these interactions: van

der Waals forces, which are always attractive between particles of the same species, and electrical double layer interactions, which are usually repulsive.

As the suspended particles collide with each other due to their Brownian movements, the attractive van der Waals forces would cause them to stick to each other, destabilizing the suspension, if not for the electrostatic repulsive forces. The nature of electrostatic interaction forces between suspended solid particles was discussed in Chapter 2. Here, it is sufficient to recall that this electrostatic repulsion is due to overlapping of electrical double layers surrounding the charged particles. The higher the surface charge, the stronger the particle-to-particle repulsion. If a particle is situated outside a neighbouring particle at a distance much larger than the electrical double layer thickness (κ^{-1}), it sees the particle, along with its electrical double layer, as being electrically neutral. Any electrical interaction between these two particles can thus only occur if the ionic double layers of the interacting particles start to overlap. The bottom line is that the interaction energy between colloidal particles due to their surface charges decays exponentially with the distance between the particles, and the range of these interactions decreases with increasing salinity of the dispersing medium. Therefore, one can decrease the repulsion between suspended solid particles either by decreasing the electrical surface charge of particles or by decreasing the thickness of the electrical double layers.

Surface charge on suspended particles can be controlled by pH and adsorption of ions. Since most of the particles of importance for oil sands processing (like clays and silica) are oxides, the particles become negatively charged at neutral pH and their surface charge becomes more negative as the pH increases. The higher the surface charge, the stronger the electrostatic repulsion between the particles. Thus, the stability of a clay suspension in water will increase as the pH increases. This can be achieved by the addition of any base, including caustic. Agents that increase the stability of a suspension (which is a dispersed system) are called *dispersants* or *dispersing agents*. Thus, caustic is a dispersing agent, as it increases the electrostatic repulsive forces between suspended particles through the mechanism described above.

The same dispersing effect can be achieved by adding any base, such as sodium carbonate or bicarbonate, sodium silicate, sodium methaphosphate (calgon), or ammonia. Negatively charged silicate and phosphate anions tend to form poly-ions, which very strongly adsorb on clays or silica surfaces and, therefore, are stronger dispersing agents than caustic on a per-mol basis. However, they also tend to be more expensive, as they are often made using caustic (e.g., sodium silicate). The addition of sodium carbonate or bicarbonate also adds to the total carbonate alkalinity, which is often beneficial. This must be kept in mind when considering the use of Geosol, a proprietary process aid, which contains sodium carbonate and bicarbonate as its main active components. Its beneficial role may be rationalized for cases when the slurry water has low alkalinity, especially when the feed ore is acidic. (As we discussed earlier, carbonates increase water buffering capacity, making the system less sensitive to the addition of acids that come with the acidic ores.)

Multivalent cations, such as calcium or magnesium, adsorb on the surface of oxides. As they are positively charged, their effect is opposite to that of silicate or phosphate anions. They lower the solid's negative surface charge, thus lowering the repulsive interaction between solid particles and promoting fines flocculation.

Calcium is used in CT technology for this very reason. The impact of added divalent cations is twofold: they lower surface charge and they contribute to an increase in the total salinity, thereby decreasing the thickness of the electrical double layer (i.e., the distance at which particles repel each other via electrostatic forces). In terms of the impact of calcium and magnesium ions on fine solids dispersion, their ability to lower the surface charges of particles is far more important than their ability to decrease the thickness of the electrical double layer.

8.2 Characteristics of Fluid Fine Tailings

Given a sufficient period of time, oil sands processing tailings in tailings ponds separate into three distinct zones along the depth of a tailings pond: a clear water layer on top (around 3 m thick), a layer of settling fines, known as the transition zone (around 1 m thick), and a fluid fine tailings zone on the bottom, which consists of fine clays, fine sands, and residual bitumen, known as *fluid fine tailings*. This zone, which contains 85 % water, 13 % clays, and 2 % bitumen, can be as thick as 40 m, and eventually becomes mature fine tailings (MFT). The extremely low settling rate of fluid fine tailings following the Clark Hot Water Extraction (CHWE) process is attributed to the dispersed nature of fine and ultrafine particles in the tailings water, caused by the use of caustic during extraction, although the gelation of ultrafines has also been proposed as the cause of MFT formation. The type and content of the clays, the geochemistry of the oil sands ores, and the water chemistry of the tailings sludge are all known to play a major role in the settling and densification of fluid fine tailings. The surface charge of fine particles has been identified as a key measure for the stable suspension of fluid fine tailings. A critical electrokinetic mobility of $-2 (\mu\text{m/s})/(\text{V/cm})$ was determined as the transition point from rapid to slow settling of tailings from both CHWE and OSLO hot water extraction (OHWE) processes (Fine Tailings Fundamentals Consortium [FTFC] 1995a). Since caustic is not used in the OHWE process, the fine tailings from OHWE naturally settle faster than those from CHWE (Sury and Stone 1995).

The main reason for the poor consolidation of fluid fine tailings is the undesired coagulation and gelation of ultrafine clays, which lead to excessively high viscosity. Ultrafine clays, ranging from 50 nm to 400 nm in size, are considered to be responsible for gel formation, trapping coarser solids in the gel as it is formed. Although the bulk of fine particles in fluid fine tailings is made up of kaolinite and illite clays (80 wt. % and 15 wt. %, respectively) and fine quartz particles, the ultrafine clays are mainly kaolinite and mica, delaminated to a layer thickness of only a few atoms, with an aspect ratio of 30:1 (FTFC 1995a). These clays are highly negatively charged in tailings water. Investigations using a scanning electron microscope revealed that clays in fluid fine tailings from the CHWE process are oriented predominantly in

an edge-to-edge configuration, forming a local lamellar structure (FTFC 1995a). In contrast, clays in fluid fine tailings from the OHWE process are mostly randomly oriented. The structural differences resulting from ultrafine clay interactions are shown schematically in Figure 8.2.

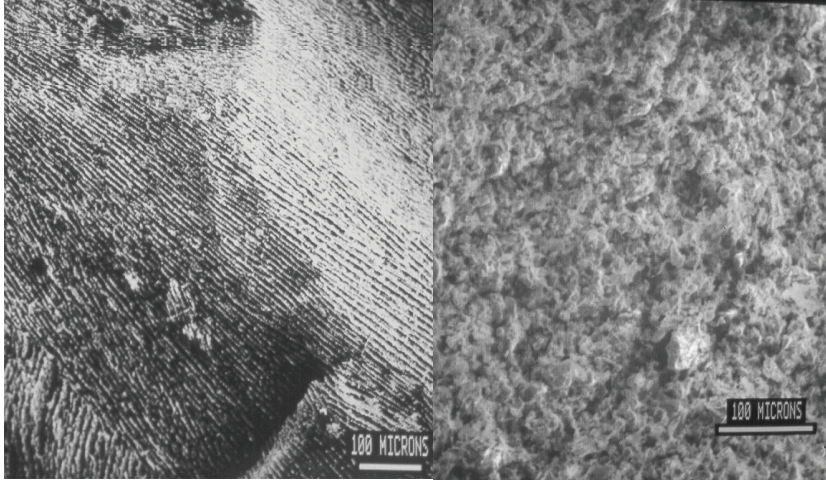


Figure 8.2 Scanning electron micrographs of MFT from CHWE (left) and OHWE (right), showing lamellar and random orientation, respectively.

Source: (Mikula and Zrobok 1999).

To explain the observed structure of fine clays in the MFT, it is instructive to calculate the interaction energy of clays in various orientations in the MFT tailings water, such as clay basal plane-to-basal plane (C_B-C_B), edge-to-edge (C_E-C_E), and edge-to-basal plane (C_E-C_B), using the classic DLVO theory. Based on the charging mechanism, which charges the basal planes through isomorphous substitution and the edge surfaces through the hydrolysis of broken Si-O and Al-O bonds, the basal plane can be considered to maintain a constant surface charge density and the edges to maintain a constant surface potential as the surfaces approach each other. The van der Waals contributions (V_A) to the interaction energy of two spherical particles of radii a_1 and a_2 in a medium 3 as a function of separation distance H can be calculated using the following equation:

$$V_A = -\frac{A_{132}}{6H} \frac{a_1 a_2}{(a_1 + a_2)} \quad (8.1)$$

where A_{132} is the combined Hamaker constant for a given system, which can be calculated using Eq. (2.32). Kar, Chander, and Mika (1973) reported the following three equations for calculating the contributions of electrical double layers forces (V_E)

for the conditions of constant potential (ψ - ψ), constant charge density (σ - σ), and constant potential–constant charge density (ψ - σ), respectively:

$$V_E^{\psi-\psi} = \frac{\pi\epsilon_0\epsilon_r a_1 a_2}{(a_1 + a_2)} \left\{ \begin{array}{l} 2\psi_1\psi_2 \ln \left[\frac{1 + \exp(-\kappa H)}{1 - \exp(-\kappa H)} \right] \\ + (\psi_1^2 + \psi_2^2) \ln [1 - \exp(-2\kappa H)] \end{array} \right\} \quad (8.2)$$

$$V_E^{\sigma-\sigma} = \frac{\pi\epsilon_0\epsilon_r a_1 a_2}{(a_1 + a_2)} \left\{ \begin{array}{l} 2\psi_1\psi_2 \ln \left[\frac{1 + \exp(-\kappa H)}{1 - \exp(-\kappa H)} \right] \\ - (\psi_1^2 + \psi_2^2) \ln [1 - \exp(-2\kappa H)] \end{array} \right\} \quad (8.3)$$

$$V_E^{\psi-\sigma} = \frac{\pi\epsilon_0\epsilon_r a_1 a_2}{(a_1 + a_2)} \left\{ \begin{array}{l} 2\psi_1\psi_2 \left[\frac{\pi}{2} - \tan^{-1}[\sinh(\kappa H)] \right] \\ - (\psi_2^2 - \psi_1^2) \ln [1 + \exp(-2\kappa H)] \end{array} \right\} \quad (8.4)$$

In these equations, ϵ_0 and ϵ_r are the permeability of the vacuum and the relative permeability of the medium, respectively, and ψ is the Stern potential, often substituted by the zeta potential as an approximation, with subscripts 1 and 2 representing particles 1 and 2, respectively. The symbol κ in the above equations represents the decay length of the electrical double layer, a property of the solution, given by Eq. (2.26). It should be noted that in Eq. (8.4), particle 1 is at constant potential and particle 2 at constant charge density. The total interaction energy using the classic DLVO theory is the summation of V_A and V_E , i.e.,

$$V_T = V_A + V_E \quad (8.5)$$

For illustrative purposes, we will simplify the calculation by considering only a simple electrolyte solution of 1 mM KCl at pH 8.5, where the basal plane has a negative zeta potential of -35 mV and the edge surfaces carry a slightly negative surface charge equivalent to a surface potential of -5 mV. Using Eqs. (8.1) to (8.5) and a Hamaker constant of 8×10^{-21} J, the energy profiles are calculated. The results in Figure 8.3 show that at a CHWE tailings water pH of 8.5, there is a weak attraction between slightly negatively charged edge surfaces (C_E - C_E), a strong repulsion between strongly negatively charged basal planes (C_B - C_B), and an energy barrier between edge surfaces and basal planes (C_E - C_B), leading to the observed edge-to-edge attachment orientation. The strong repulsion between basal planes of constant charge density (C_B - C_B) leads to substantial gaps between the lamellae stacks, which is likely responsible for holding a substantial volume of water in MFT. It is important to note that the above calculation is very much simplified, as real water chemistry contains various types of divalent

cations and natural surfactants released from bitumen, and has conditions that are far more complex than those used in this calculation. The presence of these cations would compress the electrical double layer and change the surface charges at the Stern layer through specific adsorption, making accurate calculation more difficult. A more accurate prediction would require information about the surface charge of the clay basal planes and edges in real processing tailings water, which is extremely difficult, if not impossible, to obtain. Furthermore, fine clays are likely to be contaminated with surface-active organic molecules from bitumen, which may induce attractive hydrophobic forces. Nevertheless, the simple calculation above provides a valuable, semi-quantitative explanation for the observed structure of fines in MFT resulting from the CHWE process.

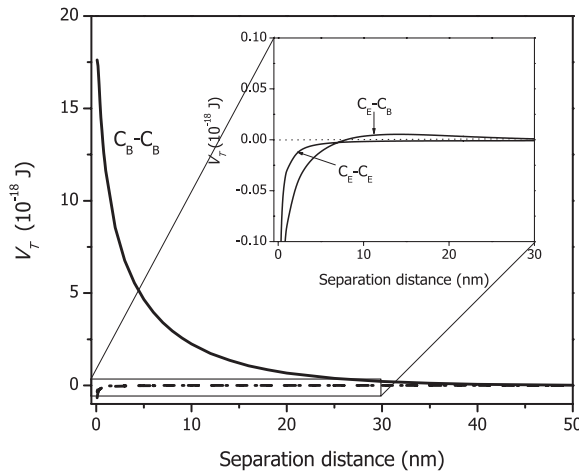


Figure 8.3 Interaction energy profiles between clay surfaces in 1 mM KCl solutions at pH 8.5, calculated using Eqs. (8.1) to (8.5). The Stern (zeta) potential of the clay edges and basal planes are -5 mV and -35 mV, respectively. The edges (C_E) and basal planes (C_B) are considered to be at constant potential and constant charge density, and are 0.1 μm and 2 μm in diameter, respectively. The combined Hamaker constant of clay-water-clay is taken to be 8×10^{-21} J.

The settling velocity of solids in a slurry, v_a , is governed by the hindered settling equation

$$v_a = \frac{(\rho_s - \rho_l)d^2g}{18\mu} f(\alpha_s, \text{Re}) \quad (8.6)$$

where ρ_s and ρ_l are the density of the solids and liquid, respectively; d is the diameter of the solids; μ is viscosity of the liquid; α_s is the volume fraction of solids in the suspension; and Re is the Reynolds number of the particles. The difficulty in treating fine tailings arises from the slow settling velocity of solids due to their small sizes, d .

For a given system, the physical parameters, such as ρ_s , ρ_p , μ , and α_s are more or less fixed, and the settling rate can be increased if the apparent size of the solids can be increased through aggregation of the fine particles. There are two approaches available for aggregating fine particles: coagulation (resulting from the addition of inorganic salts or from pH adjustment) and flocculation (resulting from polymer addition). In some literature, these two terms are used interchangeably, even though the mechanisms responsible for fine particle aggregation are very different in each, as will be discussed.

8.3 Hydrodynamics of Particle Aggregation

To achieve attachment, particles must first make contact with each other. This process, known as particle collision, is controlled largely by hydrodynamics, which depends on the nature of the system. For suspensions of extremely small-sized particles (of less than a few microns), the collision is largely controlled by Brownian motion, and aggregation is known as *perikinetic aggregation*. The collision kernel of perikinetic aggregation, β_B , is given by Eq. (2.48). For a monodisperse colloidal suspension, the perikinetic aggregation kernel is simplified to

$$\beta_B = \frac{4kT}{3\mu} \quad (8.7)$$

where k is the Boltzmann constant, T is the absolute temperature, and μ is the viscosity of the fluid (Yusa 1977). Eq. (8.7) shows that for the aggregation of small particles, increasing the temperature and/or reducing the viscosity of the liquid would promote collision by Brownian motion.

For a suspension of large particles in a laminar flow environment, shear-induced *orthokinetic aggregation* dominates. The collision kernel β_G in this case is given by Eq. (2.49), i.e., the collision rate is proportional to the shear rate, G , and to the particle diameter to the third power. In a turbulent environment, the collision kernel of

$$\beta_T = 12\pi k_e \left(\frac{\varepsilon}{\mu} \right)^{\frac{1}{2}} d^3 \quad (8.8)$$

suspensions consisting of large monodisperse particles, β_T is given by where k_e is an empirical coefficient and ε is the intensity of energy dissipation. From a collision point of view, a system with a high energy dissipation rate is favourable. High turbulence would also lead to the densification of formed aggregates by the exudation of the dispersing medium trapped in the aggregates, a phenomenon known as *syneresis*. However, excessive turbulence would lead to a shear force that is high

enough to tear the aggregates apart. It is therefore critical to carefully design mixing systems in order to achieve a desired level of turbulence, to maximize the orthokinetic collision and mechanical syneresis while minimizing the breakage of aggregates.

It is important to note that, although the aggregation of fine particles is initially controlled by perikinetic collision in fluid fine tailings, orthokinetic aggregation will become dominant as fine particles aggregate to form larger aggregates of appreciable sizes. In a highly polydisperse colloidal system, such as that in oil sands processing tailings, both perikinetic and orthokinetic collision mechanisms must be considered to accurately describe aggregation kinetics. Overall, high shear rate and temperature and low viscosity are desired in fine particle aggregation. Although particle collision is essential for particle aggregation, particle attachment upon collision is equally important for the success of particle aggregation, which is largely controlled by colloidal forces between colliding particles.

8.3.1 Coagulation

In a suspension of fine solids, individual particles are stabilized by repulsive forces, often arising from long-range electrostatic, steric, electrosteric, and/or short-range hydration forces. The nature of these forces and the corresponding governing equations are discussed in great detail in Section 2.7 of Chapter 2. A brief description is given here. Electrostatic repulsion arises from the overlap of electrical double layers around particles. Steric repulsion, on the other hand, arises from overlapping brushes (loops and/or tails) of adsorbed non-ionic polymers. Electrosteric repulsion originates from the overlapping of ionic polymers adsorbed on solid surfaces. Short-range hydration repulsion results from the excess energy required to displace hydrated ions or/and molecules on solids when two particles are brought into close proximity. The objective of coagulation is to depress or destroy these repulsive forces through the addition of chemicals (often inorganic multivalent cations) to such an extent that the attractive van der Waals forces become predominant and are able to bring and hold the particles together. The chemicals used for this purpose are referred to as *coagulants*. As illustrated in Figure 2.19, coagulants compress the electrical double layer, which is governed by the Schulze-Hardy rule (given by Eq. 2.39). The compression of the electrical double layer reduces the energy barrier that prevents the particles from approaching each other, leading to a higher probability of particles overcoming the energy barrier for particle attachment, given by the stability ratio defined by Eq. (2.59). At the critical coagulation concentration (CCC), the energy barrier becomes zero, which leads to a stability ratio of 1, indicating successful attachment of particles upon collision, a condition of rapid aggregation (coagulation).

Eq. (2.39) shows a strong dependence (z^{-6}) of critical coagulation concentration on the valence (z) of electrolytes. This is the reason why gypsum is used in the production of non-segregating tailings (NST), also known as composite or consolidated tailings

(CT)¹. Divalent calcium in gypsum acts as a coagulant. It is important to note that, very often in a real system, a much lower level of calcium ions than the critical coagulation concentration (calculated using Eq. 2.39) is sufficient to induce effective coagulation, due to the specific adsorbing nature of calcium ions on clays and sands. In this case, the Schulze-Hardy rule overestimates the concentration of coagulation. It should be noted that an overdose of gypsum could be detrimental, as excess calcium ions of a specific adsorbing nature could reverse the charge of fine clay particles, inducing a repulsive force. In this case, one would see a maximum in the settling rate with increasing gypsum dosage. A more effective method to induce coagulation is to change the concentration of the potential determining ions, such as hydrogen (H^+) or hydroxyl (OH^-) ions, and hence reduce the electrical surface potential. At the point of zero charge where the electrical surface potential is zero, the particles become purely attractive by van der Waals forces, as shown in Figure 2.19, leading to rapid coagulation. In contrast to coagulation by gypsum, inducing coagulation by changing the potential determining ion concentration and hence, the surface potential, avoids the introduction of calcium ions to the recycle water, which is known to be detrimental to bitumen extraction (Kasongo 2006). Unfortunately, such an approach is not practical in oil sands tailings management, as it requires a large amount of acids and bases for pH adjustment and a limited operating pH range to optimize bitumen recovery.

Another way in which particle aggregation can be enhanced is through heterocoagulation with oppositely charged particles, i.e., through the aggregation of different types of particles. The alteration of the electrical surface charge of coarse silica sand (Si) to 5 mV (Si^+), as shown in the inset of Figure 8.4, results in only a marginal improvement in the attractive energy between coarse sands and clay edge surfaces (Si^+-C_E). The negatively charged basal planes of clay particles will be strongly attracted to the positively charged sand particles (Si^+-C_B), even if the sand particles are only marginally charged at 5 mV, leading to heterocoagulation. This energy profile is in great contrast to a strong repulsion ($Si-C_B$) without activation. Such an approach is feasible, as one can make the sand particles positively charged with low levels of divalent cation addition. From a practical point of view, one can treat the coarse solids from hydrocyclone underflow with low levels of divalent ferrous ions or lead ions at a pH of 8.5, where ferrous or lead monohydroxy cations are dominant, to render the coarse particles positively charged by specific adsorption (Fuerstenau, Miller, and Kuhn 1985). The activated coarse solids are then added to the hydrocyclone overflow with fluid fine tailings, where heterocoagulation of fine solids with activated coarse sands (as implied by the energy profile in the inset of Figure 8.4) will lead to non-segregating tailings (NST), enhancing fine particle settling and consolidation. This concept can be easily implemented as shown by the process in Figure 8.5, which is comparable to the CT process, but treats both MFT and fresh tailings simultaneously. The main advantage of this approach (as compared with the CT process) is that it requires only low levels of divalent cation addition to a small volume of hydrocyclone underflow of high coarse sands content, not only reducing chemical costs, but also reducing the detrimental effects of process-affected recycle water from tailings treatment on bitumen extraction.

1 Both terms are standard in the industry and refer to the same process; Syncrude uses the former term; Suncor prefers the latter.

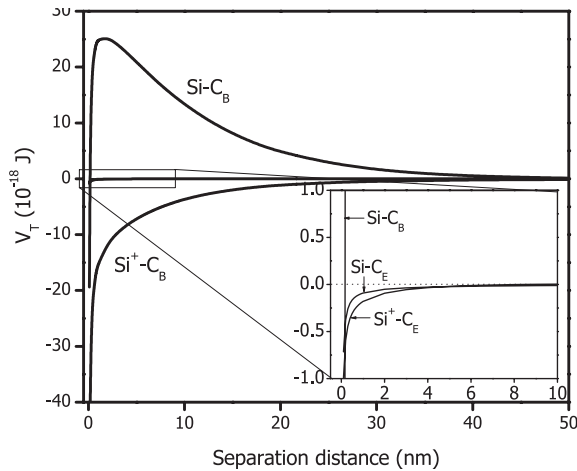


Figure 8.4 Interaction energy profiles between clay surfaces and a coarse sand particle in 1 mM KCl solutions at pH 8.5, calculated using Eqs. (8.1) to (8.5). The surface (zeta) potential of the clay edges (C_E) and basal planes (C_B) is -5 mV and -35 mV, respectively. The surface (zeta) potential of the sand with and without positive charge activation by divalent metal monohydroxy cations is 5 mV and -35 mV, respectively. The edges and basal planes are considered to have a diameter of $0.1 \mu\text{m}$ and $8 \mu\text{m}$ and to be at constant potential and constant charge density, respectively, while the sand particles are considered to be $200 \mu\text{m}$ in diameter and to be at constant potential. The combined Hamaker constant of clay-water-sand is taken to be 8×10^{-21} J.

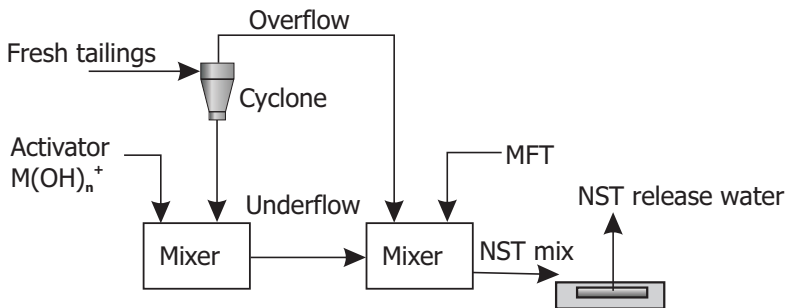


Figure 8.5 A novel tailings treatment process in which coarse solids in the hydrocyclone underflow are activated by metal monohydroxy cations and then mixed with fine solids in the hydrocyclone overflow and/or with mature fine tailings.

A careful examination of the energy profile under the critical coagulation condition shown in Figure 8.6a reveals that particles in coagulation make contact with each other. As a result, the aggregates formed by coagulation are usually relatively compact, as schematically shown in Figure 8.7a.

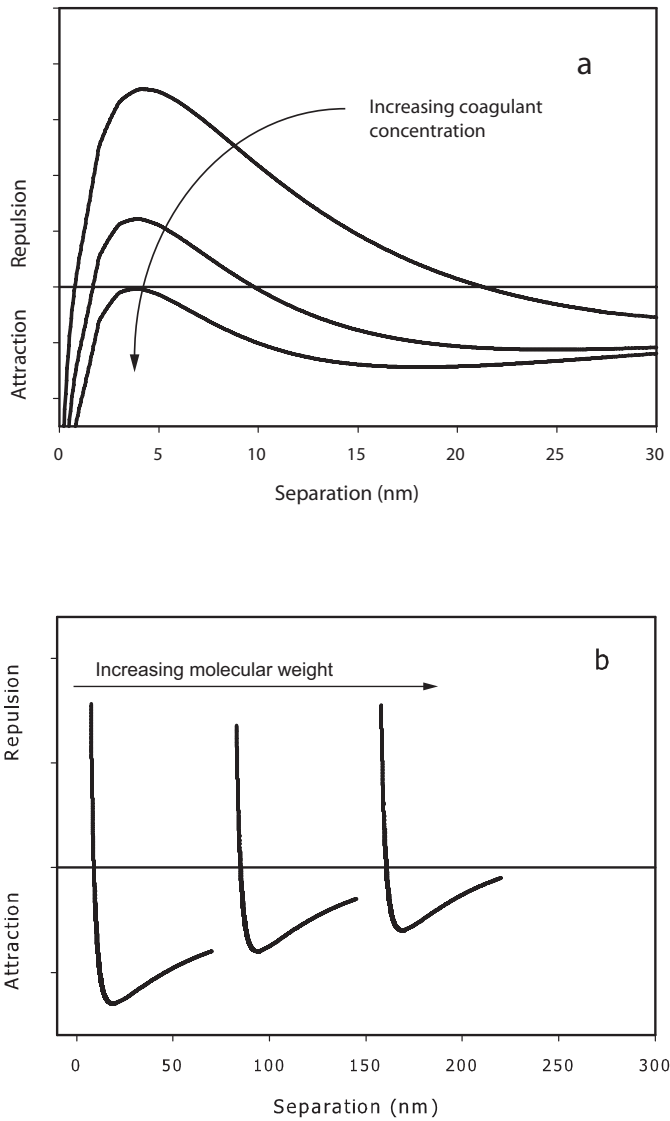


Figure 8.6 Schematic energy profiles between two fine particles in the absence (a) and presence (b) of polymeric flocculants, corresponding to coagulation and flocculation conditions, respectively.

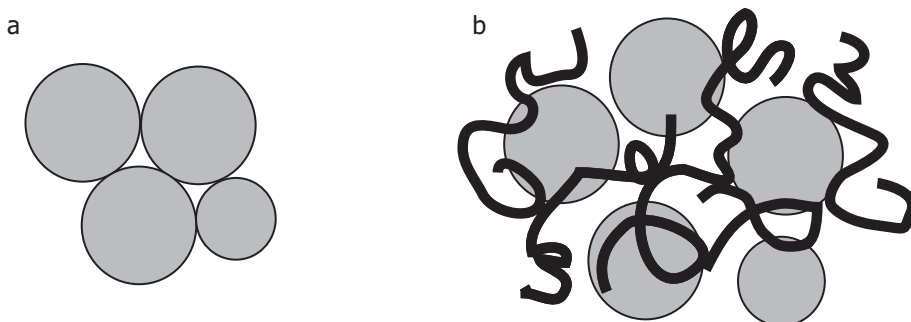


Figure 8.7 Schematic comparison of the aggregates formed by coagulation (a) and flocculation (b) processes. The aggregates formed by coagulation are usually much more compact and smaller than those formed by flocculation, where polymer bridging combines more particles per floc.

Flocculation

In contrast to coagulation, which relies on the reduction of repulsive forces between aggregating particles, flocculation involves the addition of a polymer in order to bridge particles into large flocs, as shown in Figure 8.7b. In flocculation, it is not necessary to reduce the repulsive forces between aggregating particles, as the polymer bridge can extend beyond the range of electrical double layer repulsion, as shown in Figure 8.6b. In flocculation, there is a long-range attraction, followed by a strong repulsion that results from compressing polymer strings (loops) bridging the particles. Flocculation, therefore, largely relies on the optimal adsorption of polymer molecules on multiple particles, mainly through hydrogen bonding and corresponding molecular configurations. The aggregates formed by flocculation are more open in structure than those formed by coagulation due to the molecular characteristics of polymer flocculants, which trap a large amount of water within the aggregates.

In flocculation, a flexible polymer molecule is desired, and control of polymer adsorption is critical. An effective flocculant often has a molecular weight of over a few million daltons. To achieve effective flocculation, a polymer flocculant must: i) be well dispersed throughout the suspension; ii) diffuse toward particle surfaces; iii) adsorb on particle surfaces; and iv) bridge the particles with loops and tails of the adsorbed flocculants, as shown in Figure 8.8a. To achieve a desired configuration of polymers for effective bridging, controlling intramolecular interactions by controlling the charge density of the polymer and the solvent quality (solution chemistry) is critical. At optimal charge density, a polymer flocculant would have sufficient flexibility to form loops when adsorbed on a solid surface with moderate binding forces, as shown in Figure 8.8a, allowing effective bridging between the particles. A higher-than-optimal charge density would lead to a stiff polymer flocculant chain, as shown in Figure 8.8b

and c, while a lower-than-optimal charge density would lead to a collapsed polymer configuration, as shown in Figure 8.8d, both leading to poor bridging flocculation or even steric stabilization, as shown in Figure 8.8e. Polymer adsorption is generally effective due to its multi-point anchor, mainly through hydrogen bonding of a single molecule on a solid surface, as shown schematically in Figure 8.8a. However, the charge density of an anionic polymer flocculant hinders its adsorption on a negatively charged solid surface due to electrostatic repulsion. It should be noted that too strong of an interaction of flocculant with solid particles is not desirable for flocculation, as it leads to poor bridging due to the adsorption of polymer molecules on single particles, as shown in Figure 8.8b.

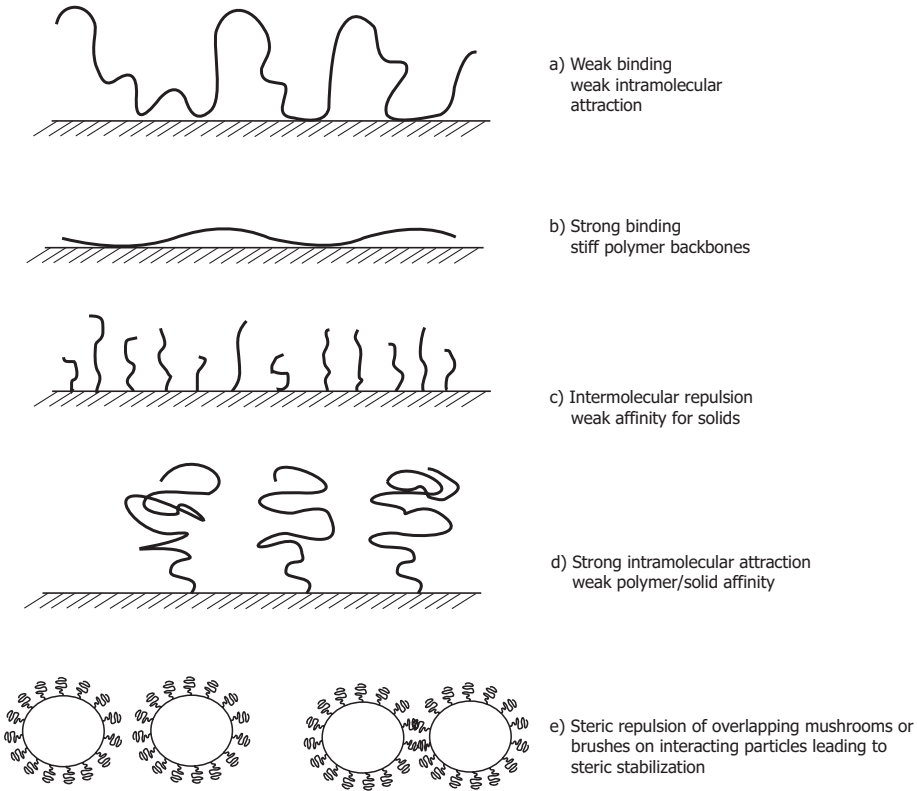


Figure 8.8 Configuration of polymer flocculant adsorbed on solids: a) ideal configuration, with extending loops and tails for bridging particles; b) stiff polymer flocculant of strong intramolecular repulsion, strongly adsorbed on solid surfaces showing minimal propensity for bridging particles; c) stiff polymer flocculant of weak affinity to solid surfaces, leading to formation of polymer brushes; d) collapsed polymer mushrooms of strong intramolecular attraction, adsorbed on solids showing limited bridging of particles; and e) strong adsorbing and/or overdosed polymer flocculant on particle surfaces, causing steric stabilization of fine particles.

It is important to recognize that the local concentration of polymer flocculant is extremely critical for effective flocculation. A pair of particles of few adsorbed loops and tails will have a smaller probability of attaching to each other, while a pair of particles whose surfaces are fully covered with loops and tails are likely to be stabilized by steric stabilization, as illustrated in Figure 8.8e. Statistically, the bridging of a particle with other particles is proportional to the surface coverage of the particle with polymer flocculant, Θ , defined as the ratio of surface area of a particle covered by loops/tails to the total surface area available for full coverage by loops/tails. For a full surface coverage of $\Theta = 1$, for example, contact at any uncovered area of a neighbouring particle will lead to bridging with the particle, provided that the contact is made on an unoccupied surface of the other particle. For a zero surface coverage ($\Theta = 0$), on the other hand, contact at any point will not lead to bridging unless it is made on a polymer-covered area of the other particle. To ensure bridging upon contact of two particles, the loops and tails adsorbed on one particle must find an empty space on the other particle. The probability of particle bridging by flocculant, P_B , is therefore proportional to the surface coverage by flocculant on one particle (Θ) and the empty space on the other particle ($1 - \Theta$). Mathematically, it is given by:

$$P_B = \Theta(1 - \Theta) \quad (8.9)$$

Physically, Eq. (8.9) represents the probability of loops/tails on one particle (Θ) finding an empty spot on the other particle ($1 - \Theta$). From Eq. (8.9), one can readily show that the maximum efficiency of particle bridging is achieved at $\Theta = 0.5$, i.e., when half of a particle's surface is covered by flocculant. An important practical implication of this analysis is that, if flocculant is added in concentrated solutions, it can lead to a local overdose, leading to low flocculation efficiency and steric stabilization of fine particles, even if the overall flocculant dosage is far below the overdose concentration. A local overdose can be avoided by adding flocculant in the form of dilute solutions or by stepwise addition under well-mixed conditions to distribute the polymer flocculant quickly over the entire suspension.

Example 8.1

Let us evaluate the effect of particle aggregation by coagulation and flocculation on the settling velocity of an aggregate in an infinite medium. Let M_s be the mass of the primary solid particles in an aggregate and n be the number of the primary solid particles in the aggregate. We will assume that the primary solid particles are spherical, with a diameter d and a density ρ_s . The mass of the solids in an aggregate is given by

$$M_s = n \frac{\pi d^3}{6} \rho_s \quad (8.10)$$

Assuming that there is no internal fluid flow within the aggregate during its settling in the fluid (water) and that the aggregate is settling in an infinite medium (i.e., in the absence of hindered settling), we can write the Stokes settling velocity of an aggregate, V_a , as

$$V_a = \frac{g(\rho_a - \rho_f)d_a^2}{18\mu_f} \quad (8.11)$$

where g is the acceleration due to gravity, μ_f is the dynamic fluid viscosity, d_a is the aggregate diameter, ρ_f is the surrounding fluid density, and ρ_a is the density of the aggregate, which is given by

$$\rho_a = \rho_s\alpha_s + \rho_f(1 - \alpha_s) \quad (8.12)$$

The α_s in Eq. (8.12) is the volume fraction of the primary solid particles in the aggregate. It is assumed that the effective gravity force is given by the difference between the densities of the aggregate and the surrounding fluid, $\rho_a - \rho_f$. From Eq. (8.12), we can write

$$\rho_a - \rho_f = (\rho_s - \rho_f)\alpha_s \quad (8.13)$$

The diameter of the aggregate, d_a , is given through the definition of the volume fraction of primary solid particles in the aggregate, i.e.,

$$\alpha_s = \frac{n(\pi/6)d^3}{(\pi/6)d_a^3} = \frac{nd^3}{d_a^3} \quad (8.14)$$

Eq. (8.14) indicates that for an aggregate consisting of n primary solid particles of diameter d , the aggregate diameter, d_a , is a function of the solids volume fraction, α_s , within the aggregate. For a given n and d , the solids volume fraction is inversely proportional to d_a^3 , i.e., the smaller the size of the aggregate, the higher the α_s , and hence, the more compact the aggregate.

Making use of Eqs. (8.10), (8.13), and (8.14), the Stokes settling velocity can be given in different forms:

$$V_a = \frac{g(\rho_s - \rho_f)d^2}{18\mu_f} \left[\alpha_s^{1/2} n^{2/3} \right] \quad (8.15)$$

$$V_a = \frac{g(\rho_s - \rho_f)d^2}{18\mu_f} \left[\frac{nd}{d_a} \right] \quad (8.16)$$

$$V_a = \frac{g(\rho_s - \rho_f)d^2}{18\mu_f} \left[\frac{6M_s}{\pi d^2 \rho_s d_a} \right] \quad (8.17)$$

The value of terms in the square brackets is a multiplier that gives the settling velocity enhancement resulting from the formation of aggregates (rather than the settling velocity of a single solid particle).

Let us discuss the settling velocity implication as provided by Eqs. (8.15) to (8.17). To simplify the discussion, we assume that the primary solid particles diameter, d , is fixed.

Eq. (8.15) indicates that, for a given number of primary particles in an aggregate, the aggregate settling velocity increases with increasing volume fractions of primary solid particles within the aggregate. This is due to the fact that the aggregate density increases with increasing volume fractions of solids, thereby leading to an increase in the difference between the densities of the aggregate and its surrounding fluid, $\rho_a - \rho_f$ as shown by Eq. (8.13). Such an increase in the settling velocity with α_s occurs in spite of the fact that the aggregate diameter, d_a , decreases with increasing α_s , as shown in Eq. (8.14).

Eq. (8.16) indicates that for an aggregate consisting of a given number of primary particles of a given diameter, a smaller aggregate diameter would provide a larger settling velocity enhancement. A smaller aggregate diameter of fixed d and n gives a higher α_s value, and hence, a larger gravity driving force.

Eq. (8.17) shows that for a given solids mass in an aggregate, a smaller aggregate diameter would provide a higher settling velocity enhancement. Again, this conclusion is simply due to the fact that for an aggregate of fixed n and d , a smaller aggregate diameter gives a denser aggregate and, hence, a higher driving force for settling. Let

$$d = 10 \mu\text{m};$$

$$n = 50 \text{ and } 100;$$

$$\rho_s = 2600 \text{ kg/m}^3;$$

$$\rho_f = 1000 \text{ kg/m}^3; \text{ and}$$

$$\mu_f = 0.001 \text{ Pa}\cdot\text{s}.$$

Eq. (8.16) is used for the evaluation of the Stokes settling velocity of an aggregate as a function of the solids volume fraction in the aggregate. The results are presented in Figure 8.9.

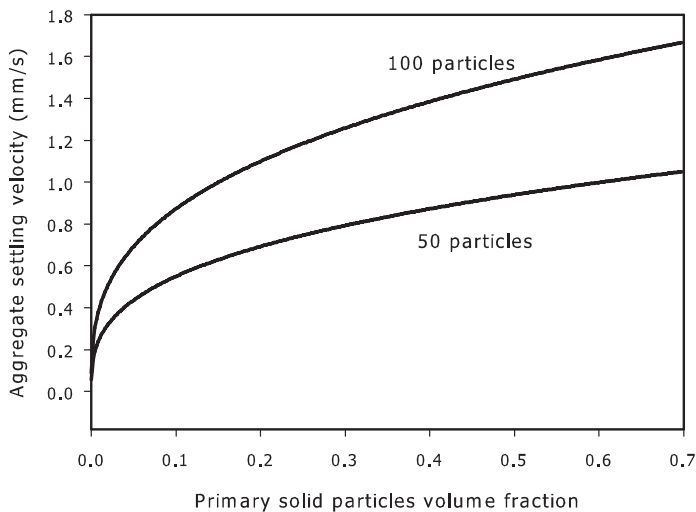


Figure 8.9 Variation of aggregate settling velocity with aggregate solids volume fraction.

The results in Figure 8.9 show that increasing the volume fraction of solids in an aggregate (i.e., increasing α_s) leads to a higher settling velocity. This finding suggests that for a given number of primary particles in an aggregate, the more compact aggregates (resulting from charge neutralization, as shown in Figure 8.7a) are favourable for solids settling. However, increasing the number of particles from $n = 50$ to $n = 100$ increases the free settling velocity of the aggregates much more significantly for a given particle compaction, i.e., for a given α_s . Flocculation using polymers often leads to a larger number of particles in an aggregate, but also results in a more ‘fluffy’ (loosely packed) configuration. The best practice, therefore, is to use a combination of coagulation and flocculation under well-controlled hydrodynamics to maximize both n and α_s for the best achievable settling.

It is important to recognize that, although there is a substantial increase in the settling velocity of an aggregate in the unhindered regime, the aggregate settling velocity is substantially reduced in the hindered settling regime at higher solids aggregate concentrations. However, it is valuable to analyze the settling velocity enhancement by only considering the terms in the square brackets of Eqs. (8.15) to (8.17). For interest, the settling velocity enhancement factor is provided in Figure 8.10. For $n = 50$, it is as large as 10 for $\alpha_s = 0.4$, i.e., representing a tenfold decrease in settling time.

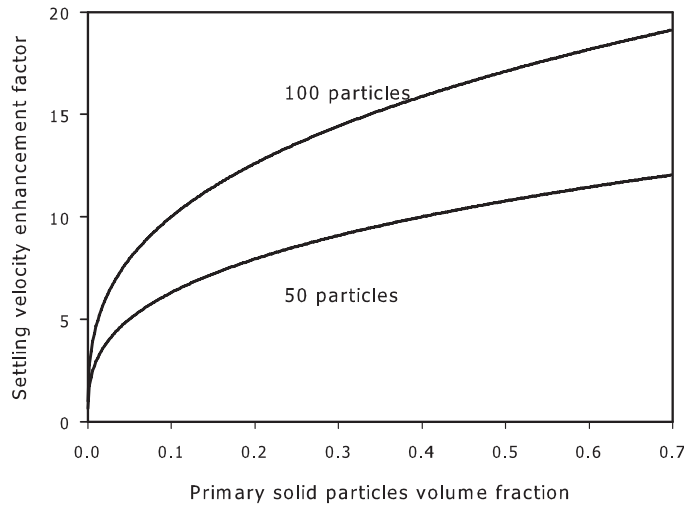


Figure 8.10 Variation of settling velocity enhancement factor with aggregate solids volume fraction.

The results in Figures 8.9 and 8.10 clearly show the importance of forming compact aggregates of a given number of primary particles. Aggregates can be made more compact through charge neutralization in flocculants or through the use of flocculants of charges opposite to those of fine particles, as well as through syneresis, which occurs when uneven stress is applied to the aggregates (Yusa 1977). However, excess turbulence from mixing breaks the aggregates, reducing the number of primary particles in the aggregates. Careful design of the mixing tank for optimal performance of flocculation and aggregate compaction is therefore extremely important. The maximum intensity of turbulence an aggregate can sustain without breaking up is strongly dependent on the strength of particle bridging. Polymer flocculants whose properties can be fine-tuned based on their application would be highly desirable in the industry. Focus should be directed in this area to resolve many of the issues associated with oil sands tailings.

Although the addition of coagulant and/or flocculant is capable of increasing the particle settling rate by particle aggregation (as shown by the results in Figures 8.9 and 8.10), particle aggregation does not necessarily improve sediment densification. Research done by FTFC (1995a) indicates that, although solids settle more quickly and are easier to compact following flocculation and/or coagulation, the compaction of sediments to a desired level of self-support after discharge cannot be achieved through the natural force of gravity alone. Sand compaction may be a viable solution for the consolidation of non-segregating fluid fine tailings. A typical settling curve of MFT after dilution to 5 wt. % solids with flocculant addition is shown in Figure 8.11 (Alamgir, Masliyah, and Xu 2010). The flocculants used in this set of experiments were Magnafloc 1011 (MF) from Ciba Specialty Chemicals and in-house synthesized Al-PAM. MF is a partially hydrolyzed polyacrylamide with a molecular

weight of 17 million daltons and an anionic charge density of 27 %. Al-PAM is an inorganic-organic, $\text{Al}(\text{OH})_3$ -PAM hybrid copolymer of low cationic charge density (Wang et al. 2010).

The settling curves for both polymers in Figure 8.11 indicate a common feature: rapid settling followed by slow densification. In contrast, the blank diluted MFT without polymer flocculant addition does not indicate any noticeable settling within the experiment time span. Although the enhancement in settling is more significant with 10 ppm MF addition than with 50 ppm Al-PAM addition, there is very little difference in solids densification. Both resulted in a final solids content of around 30 wt. % in the sediments, a value close to the solids content of the original MFT. It is clear that flocculation helps the diluted MFT reach its final sediment state over a much shorter settling period, but has little effect on the release of additional water from the MFT. Additional external forces are required to force the release of the trapped water from the sediments, for example that resulting from the weight of overlaying coarse sands or centrifugation.

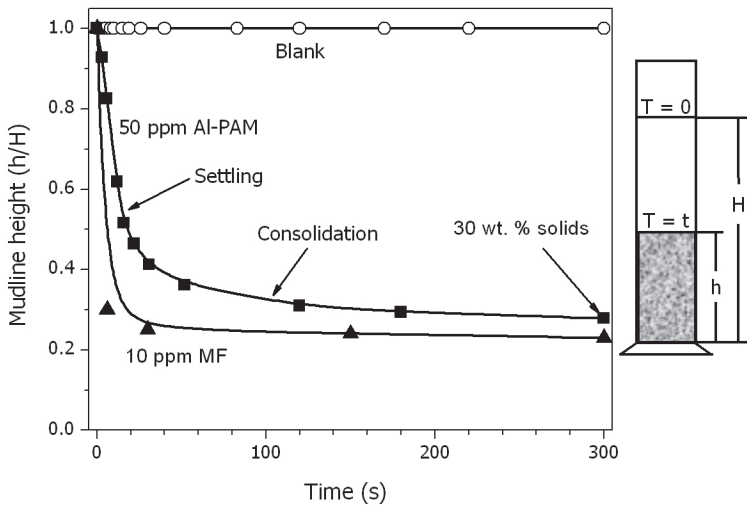


Figure 8.11 Settling of MFT after dilution to 5 wt. % of solids with and without flocculant addition. Magnafloc 1011 (MF) is a commercially available partially hydrolyzed polyacrylamide, and Al-PAM is an $\text{Al}(\text{OH})_3$ -PAM hybrid polymer, synthesized in-house.

Source: Alamgir, Masliyah, and Xu (2010).

8.4 Rheology of Fine Particle Slurries

Rheology focuses mainly on the deformation or flow characteristics of complex fluids (suspensions) in response to applied stress. The rheology of a slurry is a critical physical property to consider in the transport of mature fine tailings (MFT) and thickened tailings (TT), and during the deposition of thickened tailings in oil sands. In tailings transport, for example, it is desirable for the slurry to have fluid-like characteristics and a low viscosity at the highest possible solids content, while the deposition of the thickened tailings or paste requires the slurry to flow as it is being deposited and the deposits to be stationary during the freeze-thaw and/or drying process.

Understanding the rheological properties of clay suspensions is also of critical importance to bitumen extraction due to the gelation of fine clays in primary separation vessels and froth treatment equipment such as thickeners and inclined plate settlers. Although a rigorous, mathematical treatment of rheological properties is beyond the scope of this book, it is instructive to highlight a few basic concepts of rheology, which will provide a foundation for understanding some important rheological characteristics of oil sands slurries and thickened tailings, mostly from a colloidal science point of view (Johnson et al. 2000).

The typical rheological characteristics of concentrated suspensions, known as flow curves, are summarized in Figure 8.12. The basic terms used to describe the deformation of materials are shown and defined in Figure 8.13. The shear stress, σ , is defined as a force applied parallelly (tangentially) to a unit surface of a material (suspension), i.e., $\sigma = F/A$. The shear strain, γ , is the relative displacement of materials under an applied shear stress, defined by $x(t)/y_0$. The shear rate or strain rate, $\dot{\gamma}$ is then given by $\dot{\gamma} = d\gamma/dt = dv_x/dy$, where v_x is the velocity of the flowing fluid. For liquids, the second term is traditionally used for calculating shear rate, and the general definition of viscosity, μ_x , is given by:

$$\mu = \frac{\sigma}{\dot{\gamma}} \quad (8.18)$$

The various flow curves can be described by the following general relation:

$$\sigma = \sigma_y + \mu_p \dot{\gamma}^n \quad (8.19)$$

where σ_y is the yield stress; μ_p is the consistency; and n is the flow index. When $\sigma_y = 0$ and $n = 1$, as for flow curve 1, μ_p is equal to μ , which is the viscosity of the

fluid (suspension) and is a measure of the resistance to the flow of a fluid under either a shear stress or an extensional stress. In this case, the flow curve passes through the origin, and the viscosity is independent of the shear rate. The fluid (suspension) is then known as a Newtonian fluid. Most diluted, stable (non-interacting) fine particle suspensions are of Newtonian fluid characteristics.

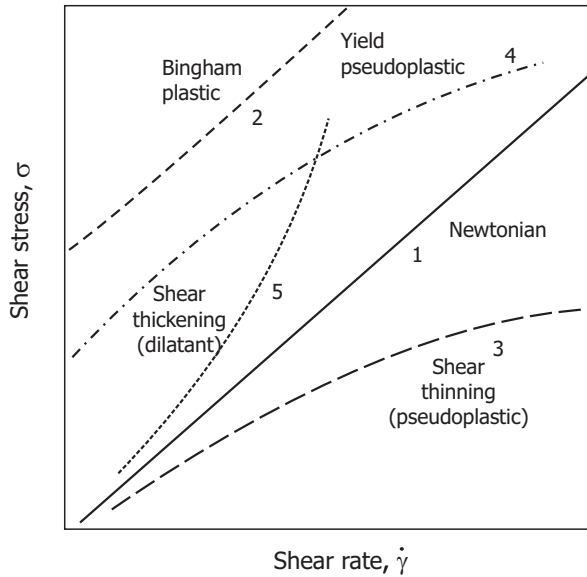


Figure 8.12 Types of flow curves for various complex fluids/suspensions.

Source: Kelly and Spottiswood (1989).

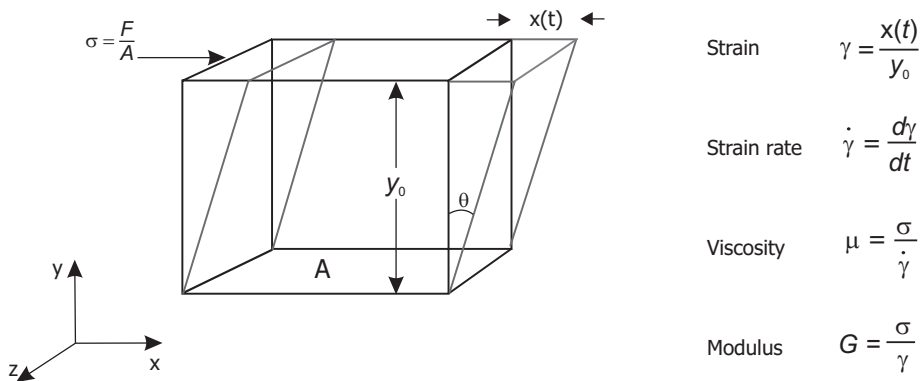


Figure 8.13 Free-body diagram of a fluid element under shear, defining various terminologies and corresponding definitions.

For a suspension of $n = 1$, but of a finite σ_y , the suspension of flow characteristics 2 (Figure 8.12) is known as a Bingham plastic fluid. In this case, suspension will not flow until the applied stress exceeds the yield stress, σ_y , after which the suspension behaves like a Newtonian fluid of shear rate-independent viscosity. This type of suspension, when rested, is of a three-dimensional structure that is sufficiently rigid to resist any stress that is lower than its yield stress, i.e., $\dot{\gamma} = 0$ for $\sigma < \sigma_y$. The shear yield stress is indicative of the material transitioning from solid-like to liquid-like (Johnson et al. 2000). In a slurry, the number of particle contacts (bonds) and the strength of these bonds determine the magnitude of yield stress: a large number of stronger bonds leads to a higher yield stress.

A suspension of flow characteristics like the one indicated by curve 3 in Figure 8.12 is known as a *pseudoplastic*. In this case, there is no yield stress ($\sigma = 0$), but n is less than 1, indicating a decrease in viscosity with increasing shear rate. This type of flow is seen in suspensions of weak flocculation (gelation). The increased shear breaks down the flocs, reducing their resistance to the flow, in a process referred to as *shear thinning*. Clay suspensions are often pseudoplastic. For such suspensions, the structures take time to recover once they are broken down. Some pseudoplastic fluids (suspensions) also show a yield stress ($\sigma_y \neq 0$), as shown by flow curve 4 of Figure 8.12, which indicates a stronger association of particles or structures.

In contrast to pseudoplastic suspensions, dilatant suspensions show a shear thickening, i.e., an increase in viscosity with shear rate, as shown by flow curve 5. In this case, $\sigma_y = 0$ and $n > 1$. This usually occurs in suspensions concentrated enough to reach close packing, or in the case of shear-induced coagulation/flocculation.

Some suspensions, known as *thixotropic* suspensions, exhibit a time-dependent viscosity that often decreases with prolonged shear. When the viscosity increases with shearing time, it is referred to as *rheopexy*. When the flow of a fluid (suspension) varies with the rate at which the stress is applied—elastic at very fast applied stress rate and plastic at slow applied stress rate—this fluid is referred to as being *viscoelastic*, showing both elastic and plastic properties. In this case, the shear stress is a function of both shear rate and strain, given by:

$$\sigma = G\gamma + \mu\dot{\gamma} \quad (8.20)$$

where G is the shear modulus of the slurry when $\dot{\gamma}$ is held constant. Sometimes, the testing is done with a sinusoidal strain of $\gamma = \gamma_0 \sin \omega t$, where γ_0 is the amplitude of shear strain and ω is angular frequency. The shear modulus has two components, G' and G'' , known as the storage modulus and the loss modulus, respectively. The magnitude of the storage modulus reflects the elastic behaviour, while that of the loss modulus reflects the viscous behaviour of the fluid (suspension). G' represents the capacity of the material to resist deformation and store an applied stress, while G'' represents the viscous properties of the material, which is a measure of the energy dissipated per cycle of deformation. In a frequency sweep test, when G' is higher than

G'' , the material shows less energy dissipation due to applied deformation and has stronger elastic (solid-like) properties. This may indicate gel formation.

Figure 8.14 shows the flow characteristics of kaolinite clays ($D_{50} = 4 \mu\text{m}$) at their natural pH of 7.5–7.8 (for clays from Albian deposit) and different solids contents (Zhou et al. 2010). The slurries containing kaolinite particles ranging from 38 wt. % to 45 wt. % all exhibit non-Newtonian, shear-thinning characteristics. Figure 8.14 also shows a significant increase in the viscosity of the slurry with increasing solids content, as expected: at a given shear rate, the viscosity increases linearly with increasing solids content, as shown in the inset of the figure. With increasing shear rate, the increase in viscosity with increasing solids content becomes less significant, as indicated by the declining slopes in the inset of Figure 8.14. Boger (2009) reported a similar dependence of viscosity on solids content for red mud. Also interesting to note is a significant increase in the viscosity of the slurry containing 40 wt. % total solids of 99 wt. % kaolinite and 1 wt. % montmorillonite. In fact, the measured viscosity of the slurry containing 40 wt. % total solids of the mixture is much higher than the viscosity of the slurry containing 45 wt. % kaolinite alone. This finding clearly illustrates that the type of clay (e.g., montmorillonite), even in small quantities, plays a significant role in determining the slurry viscosity, and hence has an impact on oil sands processing and tailings management.

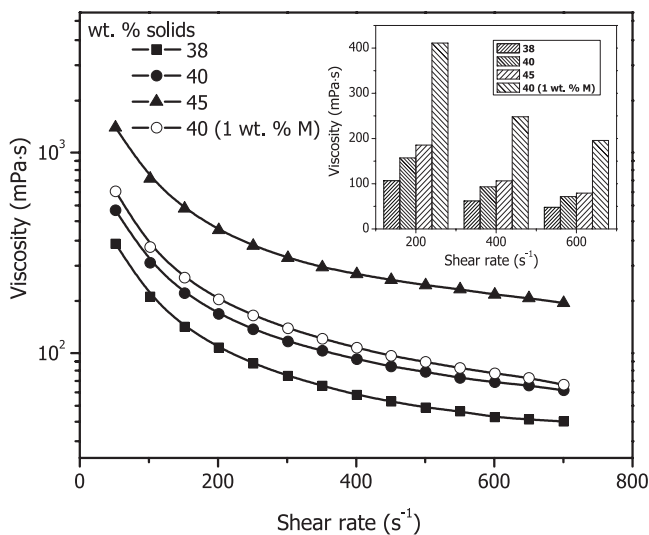


Figure 8.14 Viscosity of kaolinite slurry of varying solids contents, from 38 wt. % to 45 wt. %, as a function of shear rate, all at their natural pH of 7.5–7.8. One of the tests was performed using a slurry of 40 wt. % total solids containing 99 wt. % kaolinite ($D_{50} = 4 \mu\text{m}$) and 1 wt. % montmorillonite ($D_{50} = 2 \mu\text{m}$). The inset shows the effect of solids content and montmorillonite doping on the viscosity of slurry at three different shear rates.

Source: Zhou et al. (2010).

The effect of water chemistry on the viscosity of kaolinite slurry at pH 11 is shown in Figure 8.15 (Zhou et al. 2010). As seen in the figure, the addition of 1 mM Ca^{2+} significantly increased the viscosity of the slurry over the entire shear-rate range studied. This effect is attributed to the reduced repulsion between clay particles (resulting from a charge neutralization and a compression of the electrical double layers), which leads to coagulation and eventually, gelation. An increase in kaolinite slurry viscosity is not conducive to bitumen recovery, as it hinders the flotation of aerated bitumen, but is favourable for the production of non-segregating tailings (NST), as used in the CT process. As shown by the results of Figure 8.15, bicarbonate ion addition can reverse the increase in the viscosity of the kaolinite slurry resulting from calcium ion addition, and can even make the slurry less viscous than it was originally. As a result, the addition of bicarbonate ions (HCO_3^-) improves bitumen recovery, but creates difficulties in tailings management. The observed impact of bicarbonate ions on clay suspension viscosity is attributed to two aspects. Bicarbonate ions are known to react with calcium ions, scavenging calcium ions from the slurry and eliminating the enhanced viscosity of clay suspensions by calcium ion addition. They are also known to specifically adsorb on kaolinite surfaces, increasing its negative charge, which in turn increases the electrostatic repulsion and stability of clay suspensions, leading to a lower viscosity than that of the original suspension.

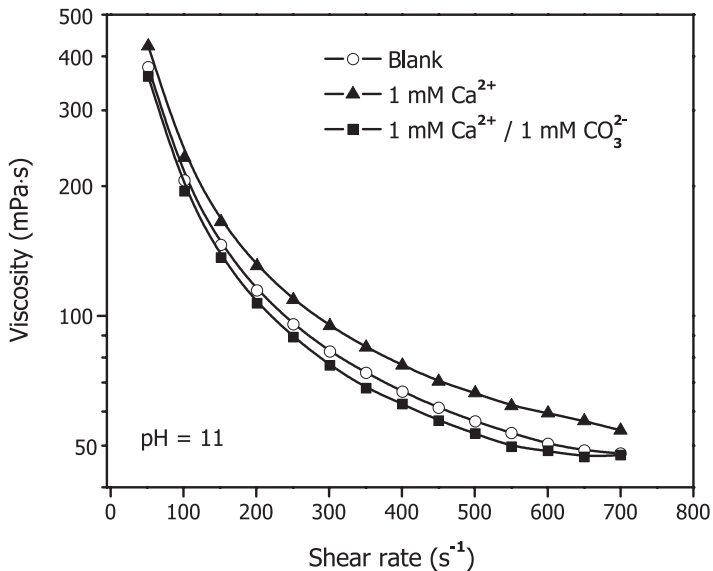


Figure 8.15 Effect of water chemistry on viscosity of kaolinite slurry (40 wt. % solids) at pH 11.

Source: Zhou et al. (2010).

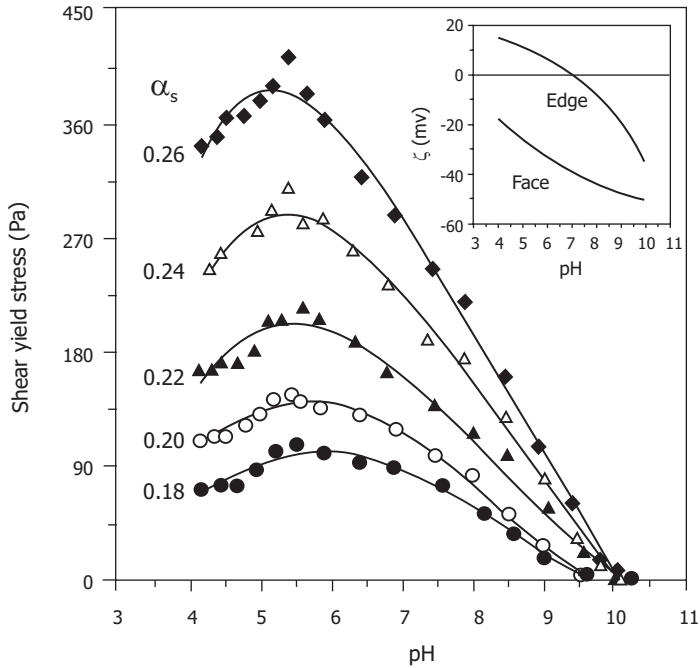


Figure 8.16 Shear yield stress of kaolinite clay slurries as a function of pH and volume fraction (α_s) of solids (given in the figure). The inset shows the zeta potential of kaolinite faces and edges as a function of pH.

Source: Johnson et al. (2000).

Johnson et al. (2000) conducted an extensive study on the effect of water chemistry on the yield stress of kaolinite slurries. Their results, shown in Figure 8.16, indicate that yield stress reaches a maximum at a pH of around 5.5 and decreases at both ends of this optimal pH. The maximum yield stress was also found to increase significantly with an increasing volume fraction of kaolinite particles in the slurry, as anticipated. The inset of Figure 8.16 shows the zeta potential of faces and edges of the kaolinite used in the study. The anisotropic zeta potential of the kaolinite faces and edges is believed to be responsible for their characteristic rheological behaviour. At pH 5.5, the difference in zeta potential between the oppositely charged faces and edges of kaolinite is the most significant. The attraction between these two edge and face surfaces is strong, resulting in the card-house structure of kaolinite by heterocoagulation. At pH lower than 5.5, the attraction between the faces and edges diminishes slightly. The repulsion between the face surfaces (C_B-C_B) also decreases, and there is a slight attraction between the edges (C_E-C_E), as shown by the results in Figure 8.3. Such characteristics of colloidal interactions between various pairs of surfaces in clay suspensions with decreasing suspension pH lead to a more lamellar-like arrangement of faces, as shown in Figure 8.2 (left), causing a slight reduction in yield stress with reducing slurry pH. At pH above 5.5, the attraction between faces and edges diminishes quickly and even

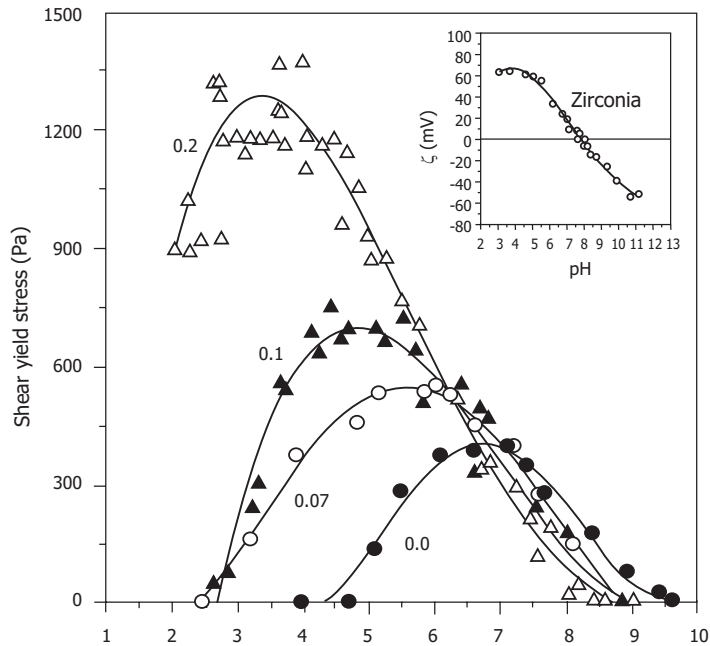


Figure 8.17 Shear yield stress of zirconia suspensions containing 18.4 % solids by volume as a function of pH with various levels of sodium dodecyl sulphate addition (indicated in the figure as percent of dry solids weight). Inset shows zeta potential of zirconia as a function of pH in the absence of SDS.

Source: Johnson et al. (2000).

becomes repulsive with increasing slurry pH, progressively disrupting the card-house structures and leading to a much more significant reduction in shear yield stress with increasing slurry pH. The slurry becomes fluid-like without noticeable yield stress at pH above 10, at which the forces between faces and edges, faces and faces, and edges and edges are all strongly repulsive. The increase of shear yield stress with increasing kaolinite solids content is attributed to the increase in particle-particle bonds (contacts) with increasing particle concentration, which require larger force to break down.

In oil sands processing, fines are mostly contaminated by hydrocarbons, resulting in additional attractive forces known as hydrophobic forces. Figure 8.17 shows the effect of surface hydrophobization by surfactant adsorption on the shear yield stress of zirconia. The figure also shows the zeta potential of zirconia as a function of pH (inset). In the absence of an anionic surfactant (sodium dodecyl sulphate, SDS), the isoelectric point of zirconia was determined to be around pH 7.5, where a maximum shear yield stress of 400 Pa was determined for a suspension containing 18.4 % solids by volume. It is interesting to note that the shear yield stress has a symmetrical bell shape, a result of the decreased aggregation of particles with increasing electrostatic repulsion that occurs as the particles move away from the isoelectric point on both sides.

Adding SDS to zirconia suspensions containing 18.4 wt. % solids not only lowered the pH where maximum shear yield stress was present, but also markedly increased the value of the maximum shear yield stress. This increase in maximum shear yield stress with increasing SDS addition is attributed to the increased aggregation of particles with increasing hydrophobicity of particles, resulting from the adsorption of anionic SDS molecules on positively charged zirconia particles. The lower pH where the maximum shear yield stress exists with increasing SDS concentration is attributed to the shift in the isoelectric point with specific adsorption of SDS on positively charged zirconia particles. It is also interesting to note the overlap of shear yield stress curves at pH values above the original isoelectric point of zirconia (pH 7.5), suggesting a minimal effect of SDS addition on the shear yield stress of zirconia suspensions (at pH above zirconia's isoelectric point). This is attributed to the minimal adsorption of anionic SDS on negatively charged zirconia particles.

The Fine Tailings Fundamentals Consortium characterized the rheological properties of MFT (1995a). The minimum values of the elastic modulus and yield stress (and thus, the most stable conditions for MFT) were found to occur at pH 9 for Syncrude MFT and at pH 9.5 to 10.5 for Suncor MFT. Away from these pH values, the MFT became progressively coagulated/flocculated. The yield point disappeared when the solids content of the MFT became less than 26 wt. % (Syncrude) and 21 wt. % (Suncor), indicating highly dispersed fine particles in fine tailings (the higher value for Syncrude reflects a higher caustic dosage in its CHWE process). For OHWE fine tailings, the yield stress and elastic modulus were determined when the solids concentration was as low as 8 wt. % for MFT from both Syncrude and Suncor ores, indicating a substantial aggregation of fine particles.

Following this early work, Adeyinka et al. (2009) measured the yield stress of fractionated MFT. The D_{50} for each of the three solids fractions (F1, F2, and F3; separated by sedimentation and centrifuging) was 6 μm , 0.14 μm , and 0.16 μm , respectively. The measured yield stress of the fractionated MFT as a function of solids content is shown in Figure 8.18. The coarse-size solids fraction of MFT (F1) did not show any gelation until 20 wt. % solids, and significant gelation was observed when the solids content was greater than 33 wt. %. In contrast, the fine-size solids fraction (F2) showed strong gelation at a solids content of around 15 wt. %. The most surprising finding from this study was with regard to the strong gelation characteristics of suspensions made of solids from fraction 3 over the entire solids concentration range studied, although the particle size and the mineralogy of solids from fraction 3 are similar to that of solids from fraction 2. A detailed thermal gravimetric analysis and Fourier transform infrared (FTIR) spectroscopy characterization revealed a higher hydrocarbon contamination and a much higher contact angle value of solids in fraction 3 than in fraction 2 (Samiei 2007). The observed gelation and the high yield stress of the suspension made of solids from fraction 3 are attributed to stronger hydrophobic coagulation and particle association. Following removal of hydrocarbon contamination by hydrogen peroxide washing, the rheological characteristics of solids in fraction 3 were found to be similar to those of the solids in fraction 2, further confirming the detrimental role of fine solid surface contamination by hydrocarbons in

oil sands processing and tailings management (Adeyinka et al. 2009). The dispersion of these fine solids is of critical importance for improved bitumen recovery and froth cleaning. In tailings management, the focus is on making the fine solids amenable to coagulation and/or flocculation.

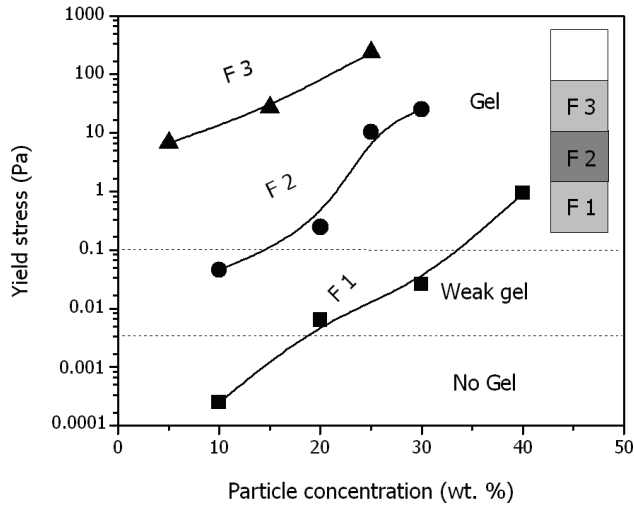


Figure 8.18 Yield stress of fractionated fine solid suspensions from mature fine tailings.

Source: Samiei (2007).

8.5 Non-Segregating Tailings

Following the coagulation and/or flocculation of fluid fine tailings, additional forces must be used to further densify the low-density sediments in order to release the maximum amount of water and produce trafficable (solid-like) deposits.

One approach to achieving this objective is to use the natural weight of the coarse sands produced during oil sands processing to compact the sediments. This is the basis for the production of non-segregating tailings (NST), which calls for the right mix of coarse sands and fluid fine tailings with the appropriate water chemistry. NST production is illustrated in Figure 8.19, which shows the settling of a model tailings sample containing 25 wt. % total solids of 75 wt. % coarse sands solids ($D_{50} = 197 \mu\text{m}$) and 25 wt. % kaolinite fines ($D_{50} = 8 \mu\text{m}$), representing a sand-to-fines mass ratio (SFR) of 3, as encountered in some oil sands extraction fresh tailings. This SFR is similar to the SFR used in the composite/consolidated tailings process. The photograph shown in the figure was taken following 10 minutes of settling. Without flocculant addition, at a natural pH of 7.8, the coarse sands settled quickly through the fine clay suspension and the fine clays segregated from the coarse sands, although there is visible settling of fine clays. With 2 ppm Magnafloc 1011 addition, the fine

clays remained segregated. A close examination of the settled solids reveals that the volume of coarse sediments on the bottom increased and the fine clay fraction settled much faster with 2 ppm Magnafloc addition, indicating flocculation of the fine clays. In this case, some of the flocculated fine clays may have settled within the coarse sand sediments. Non-segregating settling occurred when 10 ppm of Magnafloc 1011 was added. In this case, the overall sediment volume further decreased by 16 %. From the uniform darker colour of the sand across the whole sediment, it appears that either the fine clays completely heteroflocculated with the coarse sands, or that the flocs formed by the fine clays had a similar settling velocity to that of the coarse particles, producing a non-segregating sediment of 61 wt. % solids within 100 seconds, as shown by the settling results in Figure 8.20. Clearly, for model clays of SFR 3, Magnafloc 1011 is an effective flocculant for producing NST with a clear supernatant layer that can be recycled back to the extraction process.

Here, we provided a basic scientific understanding of how coagulation and flocculation can enhance particle aggregation in the development of non-segregating tailings from mature fine tailings mixed with coarse solids. Two notable applications based on this concept are the composite/consolidated tailings process and paste technology, which will be discussed in more detail below.

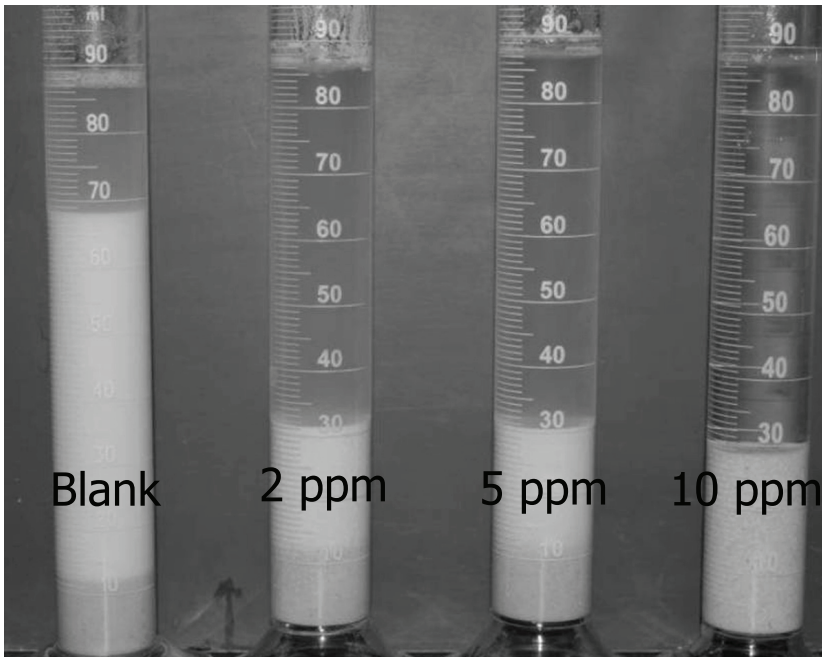


Figure 8.19 Settling of a model CT slurry containing 25 wt. % total solids of 75 wt. % coarse sand solids ($D_{50} = 197 \mu\text{m}$) and 25 wt. % kaolinite fines ($D_{50} = 8 \mu\text{m}$), with the addition of various amounts of Magnafloc 1011, at natural pH of 7.8. Photos were taken after 10 minutes of settling.

Source: Wang (2009).

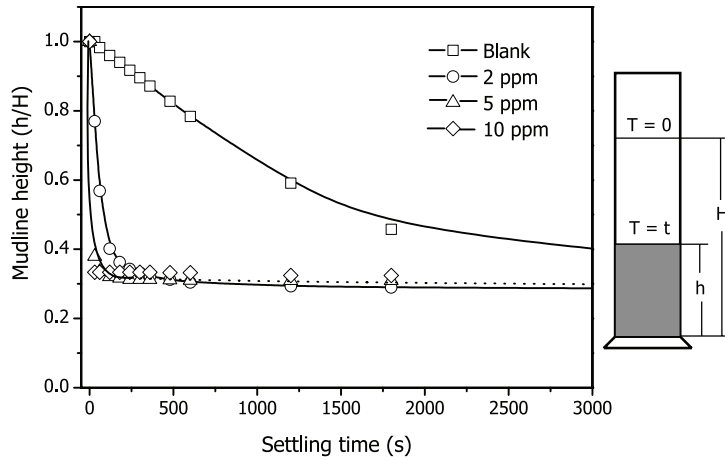


Figure 8.20 Settling curve of a model CT slurry containing 25 wt. % total solids of 75 wt. % coarse sand solids ($D_{50} = 197 \mu\text{m}$), and 25 wt. % kaolinite fines ($D_{50} = 8 \mu\text{m}$), with the addition of various amounts of Magnafloc 1011, at natural pH of 7.8.

Source: Wang (2009).

8.5.1 CT Process

The objective of the composite/consolidated tailings process, also known as the CT process or the NST process, is to produce a slurry mix that does not segregate during transport, discharge, and deposition. Three key parameters are known to control the segregation of a coarse-fine slurry mix: the total solids content, the fines content, and chemical treatment (Matthews et al. 2002). The segregation boundary for a Syncrude extraction tailings sample is given in Figure 8.21. The solids composition of the slurry below the boundary curve represents a segregating slurry, while that above the boundary represents a non-segregating mix. For example, a slurry of 63 wt. % total solids, with 23 % fines in the solids and without any chemical treatment (point A in Figure 8.21), is a segregating mix. Densification of the mix to 68 % solids (for example, through the use of a hydrocyclone) with no change to the SFR would make it a non-segregating mix (point B in Figure 8.21). The non-segregating condition can also be met by increasing the fines content of the solids to 28 % without changing the total solids content of the mix (point C in Figure 8.21). Adjusting these physical parameters changes either the density or the viscosity of the slurry, slowing down the settling of the coarse solids. A dramatic shift of the segregating boundary can be achieved through chemical treatment, such as gypsum addition, as shown by the dotted line in Figure 8.21. The flocculation of solids can also cause a shift in the slurry mix from a segregating to a non-segregating settling regime, as shown by the results in Figure 8.19.

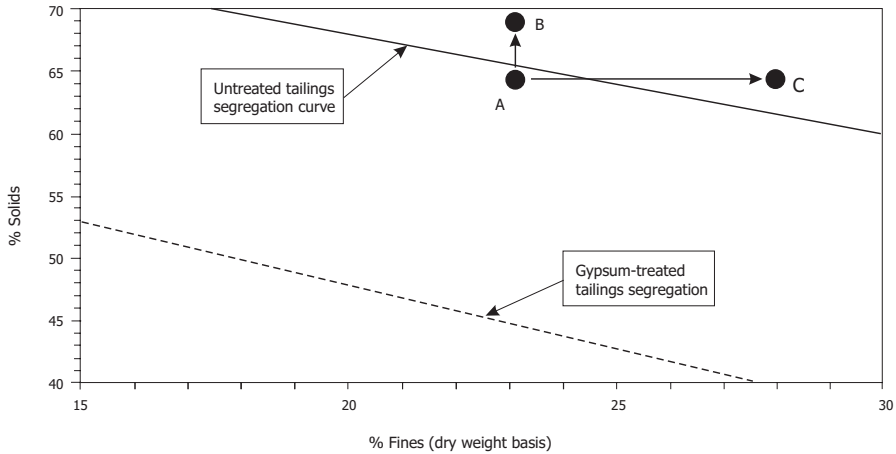


Figure 8.21 Segregation curve of raw and gypsum-treated CT slurry.

Source: Matthews et al. (2002).

The fact that increasing the fines content in the slurry mix can shift a settling regime from segregating to non-segregating provides an important practical means for reducing MFT inventory, as the MFT can be mixed with the coarse solids segregated from fresh tailings by a hydrocyclone. This is the basis for the CT process.

The CT process, implemented in 2000, represents the first commercially successful tailings treatment for MFT reclamation (Matthews et al. 2002). Figure 8.22 shows a flow diagram for a typical CT process. The fresh extraction tailings are classified by hydrocyclones. The densified coarse solids in the underflow of the cyclones are mixed with the MFT along with a coagulant, while the fines in the overflow of the hydrocyclones are discharged to settling ponds, where they settle to make new MFT. The mix of cyclone underflow and MFT is controlled to achieve an SFR greater than 3, (ideally, 4) to obtain an optimal consolidation rate and adequate geomechanical performance. The purpose of the coagulant or flocculant is to change the particle size distribution of the slurry mix (preferably through heterocoagulation or heteroflocculation) in order to reduce the size differences among particles and avoid the differential settling of solids. Various coagulants and flocculants, such as lime, H_2SO_4 , gypsum, alum ($Al_2(SO_4)_3 \cdot 14.3H_2O$), fly ash, CO_2 , and organic polyelectrolytes (such as Percol LT27A from Allied Colloids Ltd.), have been shown to be effective. The design target for the CT process is for the water to release rapidly, without segregation of the fine solids from the coarse fractions, during the deposition of the slurry. Because the CT mix usually contains around 60 wt. % solids and has a fluid nature, it flows like a viscous slurry and must be contained in the CT deposit site, where further consolidation occurs to release any remaining CT-affected water. The slope of the CT deposit is usually sufficient to allow the release water to flow along the surface to the foot of the deposit.

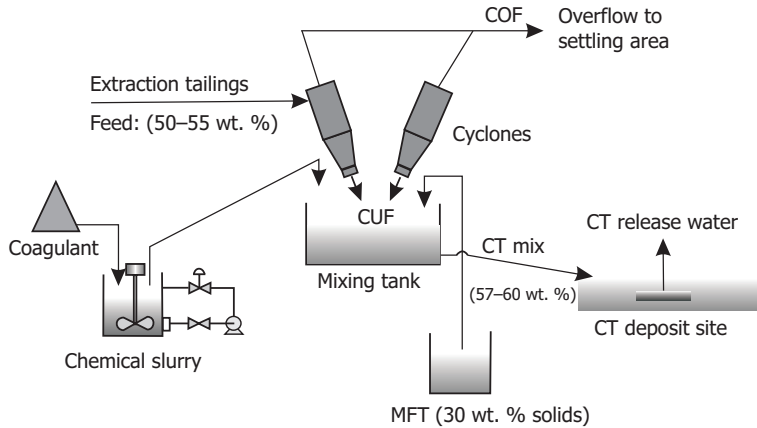


Figure 8.22 Schematic diagram of a typical CT process.

Source: MacKinnon et al. (2001).

After considering the segregational, depositional, and geotechnical characteristics of the CT mixes formed with various chemical aids, Syncrude and Suncor chose gypsum, at 1200 g to 1400 g per cubic metre of CT slurry, as the preferred coagulant for their CT process operations (Matthews et al. 2002). The runoff water released from CT process is generally free of mineral solids. Unless treated, the release water from the CT process contains high concentrations of calcium ions (due to the addition of gypsum), which is known to be detrimental to the extraction of certain types of oil sands ores (Kasongo et al. 2000; Liu et al. 2002; Wallace et al. 2004), as shown in Figure 6.20, and can cause scaling in pipes, valves, and other processing equipment. The general increases in the salinity, the sodium and sulphate content, the pH, and the alkalinity of release water from the CT process also pose challenges to the reclamation of a CT-affected area (MacKinnon et al. 2001).

Mikula, Zrobok, and Omotoso (2004) studied the settling behaviour of a CO₂-CT mix. At a low clay-to-water ratio (0.11) and total solids content of 52 wt. %, CO₂-CT was found to dewater more rapidly than gypsum-CT, producing non-segregating CT. Matthews et al. (2002) showed a significant shift of the non-segregating boundary of CO₂-CT towards a much lower solids and fines content. The mechanism of the CO₂-CT process has been attributed to an increase in the viscosity of the slurry with CO₂ addition (Mikula, Zrobok, and Omotoso 2004), caused by CO₂-induced coagulation most likely resulting from a reduction in slurry pH and hence, a reduction in the electric charges of particles. An increase in calcium ion concentration by CO₂ bubbling may contribute to fines-clay coagulation. Approximately 75 t to 200 t of CO₂ were estimated to be sequestered by one Mt of CT, depending on the initial pH of the CT water (Mikula, Zrobok, and Omotoso 2004). Compared with the release water from the gypsum-CT process, the release water from the CO₂-CT process was found to contain noticeably lower concentrations of calcium ions and magnesium ions, accompanied by higher carbonate and bicarbonate ion concentrations and a lower

slurry pH, indicating the sequestration of CO₂ in the form of bicarbonate in pore and release water. High carbonate concentration and lower calcium ion concentration in the CO₂-CT release water are suitable for recycle to bitumen extraction.

Although organic polymer flocculants, such as partially hydrolyzed polyacrylamides (e.g., Magnafloc 1011 in Figure 8.19) have been tested as effective chemical aids for producing NST, and have a negligible effect on the quality of clarified water due to their low residual concentrations, the CT deposits produced by flocculation do not seem to meet geotechnical standards. As a result, their use in the CT process remains to be investigated. Its success largely relies on the discovery of a robust polymer flocculant capable of sustaining geomechanical stress upon deposition.

8.5.2 Thickened Tailings (or Paste) Technology

The CT process, as shown in Figure 8.22, has the potential to reduce the volume of MFT already present in tailings ponds. However, new fluid fine tailings are produced from fines in the hydrocyclone overflow. Rapid densification of fluid fine tailings from the hydrocyclone overflow can be accomplished through flocculation, as practiced at one of the current oil sands operations for the purpose of warm water recycling to improve energy efficiency (Liu, Lord, and Krishnaumurthi 2000). After a desired level of flocculant addition, the cyclone overflow of fresh oil sands extraction tailings is thickened in an in-ground thickener of a 90-m diameter. The underflow from the thickener has a solids content of 25 wt. % to 30 wt. %, which is disposed of in a contained area. This process is known as the *thickened tailings* (TT) process.

The type, molecular weight, charge density, and concentration of polymer flocculant; the mineralogy and particle size of the solids; the pH and water chemistry of the slurry; and the feed dilution and hydrodynamic conditions of the flocculation systems all affect the flocculation performance of fluid fine tailings. Results from early studies show that diluting the feed and optimizing the hydrodynamic conditions with stepwise flocculant addition at starvation dosages can significantly improve flocculation performance (Xu and Cymerman 1999). Higher-molecular-weight anionic polymers with a moderate density charge, such as Percol 727, can more effectively flocculate oil sands tailings, leading to a higher settling rate. However, this type of flocculation is very sensitive to the dosage of Percol 727, showing overdosing stabilization. After single-stage flocculation and clarification, the supernatant still contains a relatively high solids content. The addition of inorganic cations or cationic polymers can improve the clarity of supernatants.

Flocculation performance is also highly dependent on mixing conditions. For certain flocculants, such as polyethylene oxide (MW: 8×10^6 g/mol), suitable mixing conditions were found to improve the distribution of the polymer in the flocculating suspension, resulting in less polymer being required to obtain good flocculation (Sworska, Laskowski, and Cymerman 2000).

Compared with the gypsum-CT process, the use of polymer flocculants has a negligible effect on the chemistry of release water for recycle. TT technology offers a possible solution for treating fine tailings arising from present and future oil sand processing plants, eliminating the need for large MFT storage ponds. However, at the

Albian Sands Energy operation, a conventional thickener (not a paste thickener) has been implemented, which produces a low-density sludge of thickened underflow that requires containment.

Yuan and Shaw (2006) conducted extensive laboratory and pilot-scale tests on a number of TT process configurations. Their study showed that the simple flocculation of extremely fine tailings, using a single flocculant or coagulant in a thickener, is ineffective, as it produces an overflow containing 1 wt. % to 4 wt. % fine solids. The clarified water, as such, is not suitable for recycling back to bitumen extraction, as the presence of fines at this level will interfere with bitumen recovery, in particular when there is an excess of divalent cations in the process water.

During their tests, Yuan and Shaw (2006) developed the three-stage process of flocculation-coagulation-flocculation (FCF). An anionic flocculant of high molecular weight (12 to 24 million Da) and a moderate charge density (20 % to 30 %), and a cationic coagulant of low molecular weight (5 to 50 thousand Da) and a high charge density (100 %), were used. The FCF process resulted in a much higher initial settling rate of flocs formed from the hydrocyclone overflow of marine ore extraction tailings, and produced, on average, an overflow stream and an underflow stream containing 0.12 wt. % and 20.8 wt. % solids after 10-min and 60-min settling, respectively.

The initial addition of flocculant at 250 g/ton to 300 g/ton normally bridges the relatively large particles together, resulting in the formation of large flocs, while the fines remain dispersed. The addition of oppositely charged coagulant at 250 g/ton induces coagulation by compressing the electrical double layer of the dispersed fine particles, forming small aggregates while eliminating individual fine particles, and produces clear, clarified water for recycling. A small amount of flocculant at 60 g/ton is then added to flocculate the large flocs formed in the first stage with the small aggregates formed in the second stage by flocculation, leading to much faster settling of the resulting composite aggregates/flocs. The FCF process generates the largest possible aggregate size and releases clear water for recycle. Unfortunately, the sediments produced by FCF remain fluid and cannot be self-contained.

It would be attractive to combine the CT process with fresh fluid fine tailings if the fluid fine tailings could be densified. Such an approach would eliminate the need for new fluid fine tailings ponds, while immediate treatment of fresh tailings would allow for the recovery of thermal energy and process chemicals from warm process water during recycling. A proposed scheme for such an approach is shown in Figure 8.23. In this process, the fine tailings that would traditionally be sent to the tailings ponds are mixed with an appropriate level of MFT and coarse sands to control the desired SFR in the thickener feed tank. After appropriate dilution of the slurry mixture with the thickener overflow water, the desired level of flocculant is added to the prepared slurry in stages through the inline mixers. The slurry is then sent to a deep-cone thickener, where the flocculated CT solids are separated rapidly from the clarified water by natural gravity. By controlling the density of the underflow stream of the deep-cone thickener, either CT or a pumpable paste of up to 60 wt. % solids could be produced, depending on the downstream deposition options, while the clarified warm water (overflow) from the thickener could be used for CT feed dilution and recycled back to extraction.

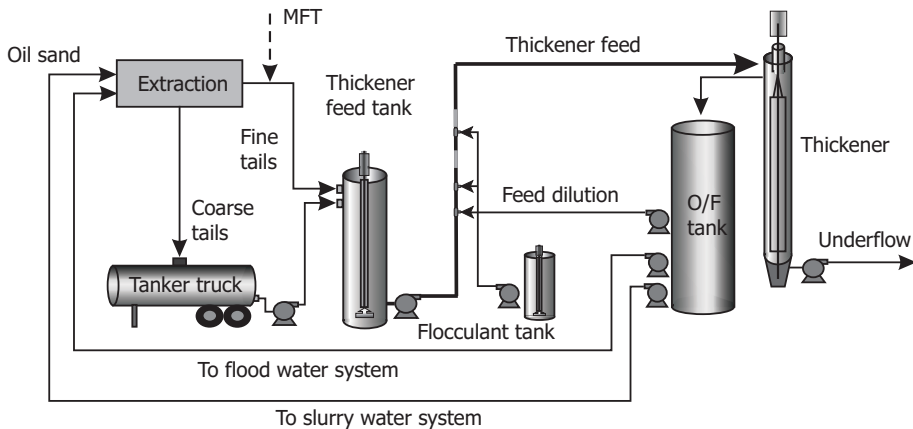


Figure 8.23 Schematic description of a novel thickened tailings (TT) process.

Source: Cymerman (1999).

8.6 Integration of Fines Flocculation with Bitumen Extraction

In certain types of oil sands ores, such as high-fines and high-electrolyte ores, slime coating has been shown to interfere with bitumen recovery and to decrease the quality of bitumen froth, as illustrated schematically in Figure 6.27. Long-range attraction and strong adhesion forces between fines and bitumen in process tailings water (Figure 6.29) are considered to be the cause of the deteriorated processability of these types of ores. The impact of slime coating on bitumen recovery and froth quality, as depicted in Figure 8.24a, has been experimentally verified through zeta potential distribution measurements (Figure 6.28). Selective flocculation of fine clays, as depicted in Figure 8.24b, leads to the formation of large fines flocs, which reduce the tendency for slime coating. Thus, the addition of flocculant not only provides a practical means of improving ore processability, but also plays a critical role in tailings management.

The use of polymeric flocculant as a process aid in bitumen extraction was tested in the laboratory by Li et al. (2008). Using a Syncrude transition ore, they tested two different types of polymers (a commercial anionic polyacrylamide [Percol 727, manufactured by Ciba; MW = 17.5 million daltons; 27 % charge density] and an in-house synthesized cationic, inorganic-organic hybrid copolymer [Al-PAM, an $\text{Al}(\text{OH})_3$ colloid-polyacrylamide]) in a laboratory hydrotransport extraction system (Wallwork, Xu, and Masliyah 2004). Here, we will refer to these two polymers as polymers A and B, respectively.

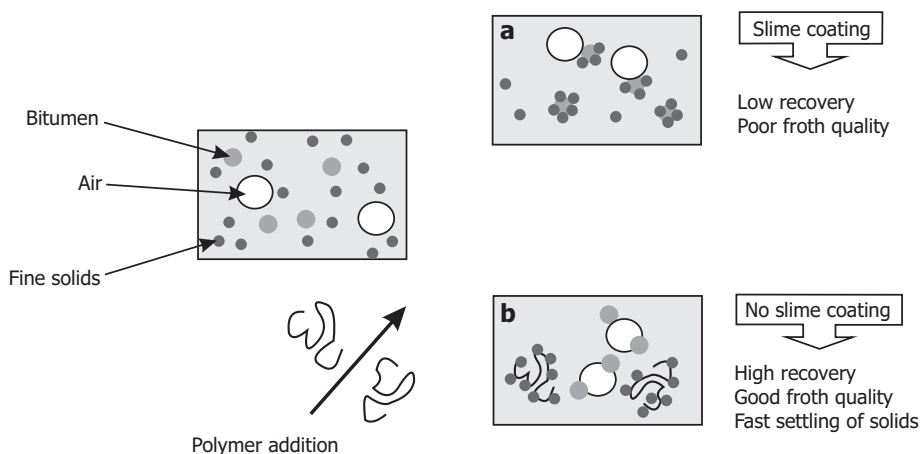


Figure 8.24 Novel concept of using polymeric flocculant as a process aid for both bitumen extraction and tailings management

As shown in Figure 8.25, the addition of 20 ppm of polymer A improved bitumen recovery from 50 % to almost 70 %. It also led to a reduction in bitumen froth quality, measured by the bitumen-to-solids ratio (Figure 8.26). In contrast, the addition of 5 ppm Al-PAM, determined to be the optimal dosage, decreased bitumen recovery slightly, from 50 % to 45 %, but improved the bitumen froth quality, increasing the bitumen-to-solids ratio from 1.5 to 1.7, as shown in Figure 8.26. The observed reduction of bitumen recovery is attributed to the induced agglomeration of bitumen by Al-PAM. Both polymers improved solids settling significantly, as shown in Figure 8.27. With the addition of 20 ppm of polymer A, more than 70 % of the volume became clear water after 30 minutes of settling, in comparison to 17 % in the control (without polymer addition). Compared with polymer A, polymer B was slightly less effective at flocculating fines, resulting in 68 % of the volume becoming clear water.

In view of the potential of polymers A and B to improve ore processability in terms of bitumen recovery and froth quality, respectively, a combination of both polymers, at 5 ppm each, was tested. The results in Figures 8.25, 8.26, and 8.27 show an overall improvement in bitumen recovery, bitumen froth quality, and fine solids settling in tailings, respectively, all comparable to the top performance for each respective category. Colloidal force measurements using an atomic force microscope showed a significant increase in the long-range repulsive forces between bitumen and clays, as well as a reduction in the adhesion forces to almost zero, following the addition of 5 ppm each of polymers A and B (Li et al. 2008). The long-range repulsion and adhesion forces between bitumen and bitumen decreased from 6–7 mN to 0.36 mN, while the long-range attractive and adhesion forces between silica sand and clays increased. These colloidal force measurements provide a scientific basis for the observed improvements in bitumen recovery, bitumen froth quality, and solids settling in tailings water.

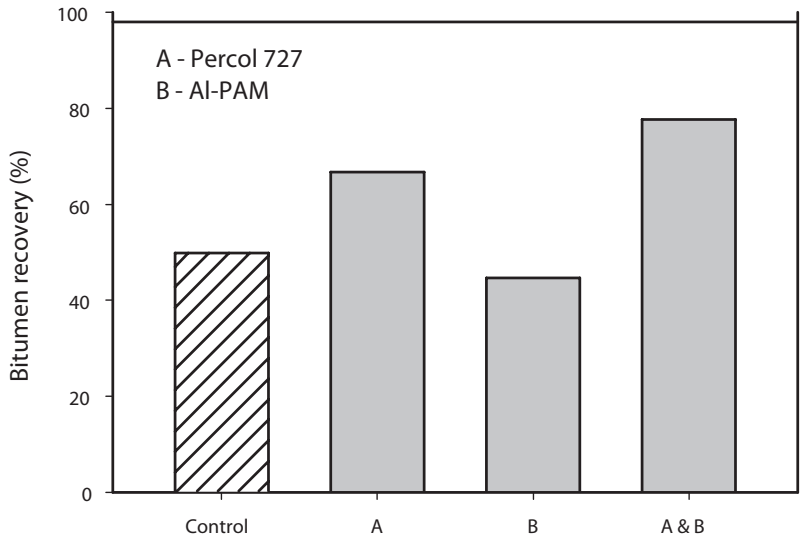


Figure 8.25 Effect of addition of 20 ppm polymer A (A), 5 ppm polymer B (B) and 5 ppm polymer A + 5 ppm polymer B (A&B) on bitumen recovery from a high-fines ore at pH 8.5 and 35 °C.

Source: Li et al. (2008).

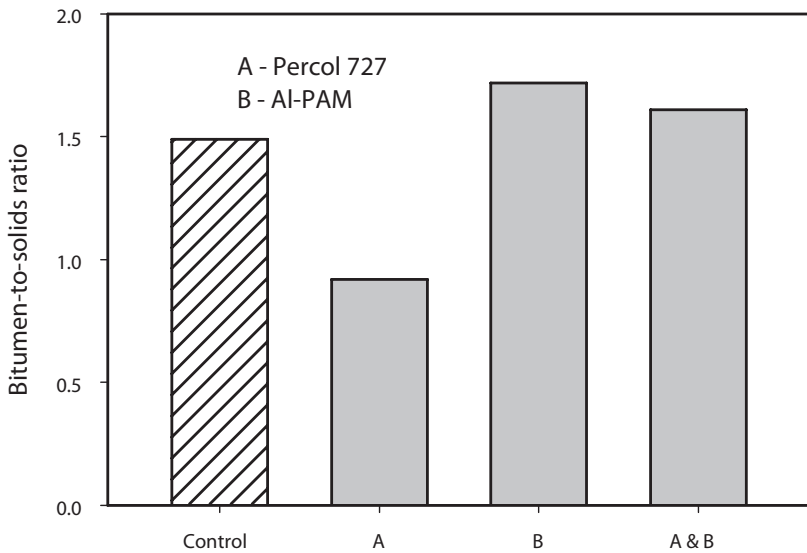


Figure 8.26 Effect of addition of 20 ppm polymer A (A), 5 ppm polymer B (B) and 5 ppm polymer A + 5 ppm polymer B (A&B) on the quality of bitumen froth obtained from a high-fines ore at pH 8.5 and 35 °C.

Source: Li et al. (2008).

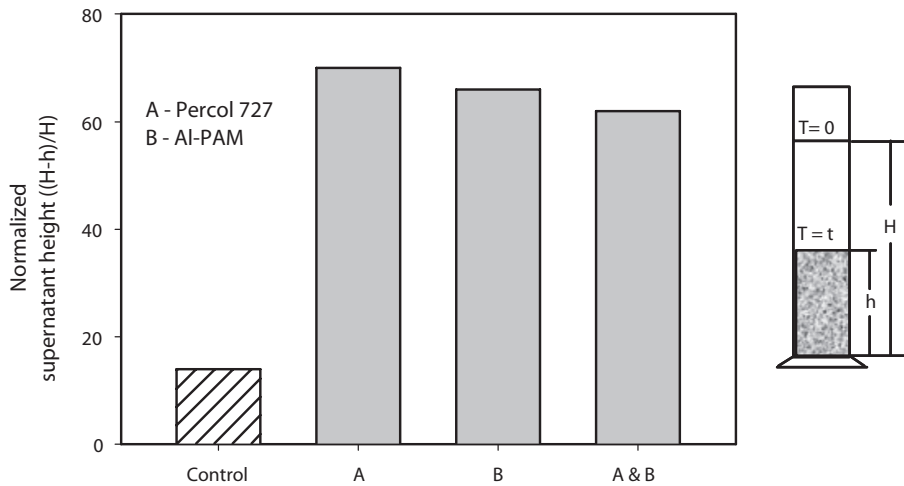


Figure 8.27 Effect of addition of 20 ppm polymer A (A), 5 ppm polymer B (B) and 5 ppm polymer A + 5 ppm polymer B (A&B) on solids settling in tailings obtained from a high-fines ore at pH 8.5 and 35 °C; measurement taken following 30 minutes of settling.

Source: Li et al. (2008).

The photographs in Figure 8.28 show a clear improvement in bitumen froth quality with the addition of 5 ppm each of polymers A and B (top right), in comparison to the control case, where no polymer was added (top left). The improvement in the bitumen froth is attributed to reduced clay entrainment by flocculation of fine clays. As a result, the settling of fines in the tailings is also improved, as shown in the bottom two photographs of the figure. Without polymer addition (bottom left), the tailings suspension remains stable, in contrast to the clear supernatant layer that forms after 30 minutes of settling when 5 ppm each of polymers A and B are added (bottom right). The results clearly demonstrate the feasibility of integrating oil sands tailings management with bitumen extraction.

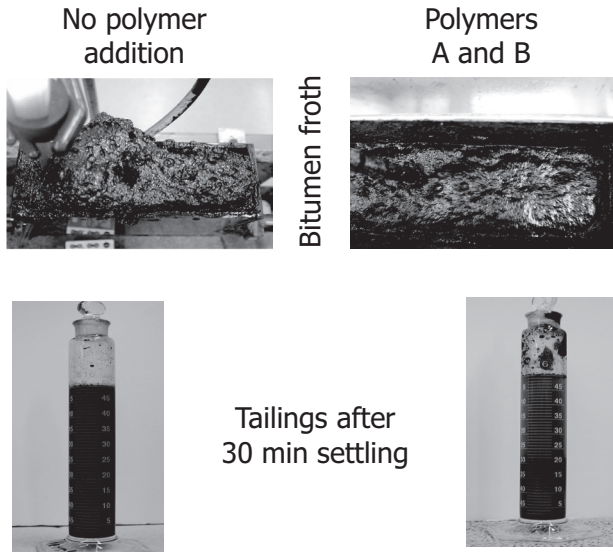


Figure 8.28 Visual evidence of improvement in bitumen froth quality and solids settling in tailings water following the addition of 5 ppm each of Percol 727 (A) and Al-PAM (B).

Source: Li et al. (2008).

8.6.1 Stackable Deposits

Both the consolidated tailings process and thickened tailings (or paste) technology are capable of increasing the settling rate of fine solids in a tailings stream, leading to the rapid release of warm water for recycling. However, the sediments produced by both processes remain fluid, and their containment in a deposit site is essential. Simply containing the paste or CT mix, however, does not mitigate the liability associated with tailings ponds. Further consolidation of the paste and CT mix, to produce self-supportive dry tailings, or stackable deposits, is desired. Producing stackable dry tailings allows for the immediate recycling of the maximum amount of warm water to the extraction plant. It also provides the opportunity for the immediate land reclamation of consolidated dry tailings in a mined pit. Several consolidation technologies have been developed for oil sands tailings, including the freeze-thaw process, centrifugation, natural drying, and filtration. These technologies will be described briefly here, and in more detail in Volume 2 of this handbook.

8.6.2 Freeze-Thaw Process

In the freeze-thaw process, fluid fine tailings deposits are naturally dried, without any energy input, when the ground freezes during the winter and thaws during spring and summer. As the deposit freezes in thin layers, its volume increases due to the expansion

that occurs as ice forms from the pore water in the void spaces between clay particles (Dawson, Sego, and Pollock 1999). The negative pore-water pressure between the unfrozen water surrounding the clay particles and the ice causes the water to migrate to the growing ice crystals, forming distinct reticulate ice that is segregated from the fine clay peds. The formation of ice crystals, on the other hand, forces the clays together, collapsing the floc structure and releasing trapped water (FTFC 1995a). During the thawing of the frozen deposit and the settling of the clay peds, water is released from the reticulate ice formed during freezing, developing a thaw strain and leading to a significant reduction in deposit volume and a release of water.

Post-thaw loading can cause further densification of the freeze-thawed deposit. A typical densification resulting from the freeze-thaw process is shown in Figure 8.29 for two types of oil sands processing tailings. The fluid fine tailings from the OHWE and CHWE processes experience the freeze-thaw cycle differently, though both show a significant volume strain of thaw, defined as the reduction of tailings volume. For example, during the first freeze-thaw cycle, the solids content of CHWE fluid fine tailings increased from 30 wt. % to 36 wt. %. In contrast, in the OHWE fine tailings, the solids content increased from 22 wt. % to 44 wt. %, indicating a much more significant consolidation (FTFC 1995b). The freeze-thaw process is easier with OHWE fine tailings as a result of the less dispersive characteristics of the fines.

Figure 8.29 also shows the potential for further freeze-thaw densification for both CHWE and OHWE cases following the first freeze-thaw cycle.

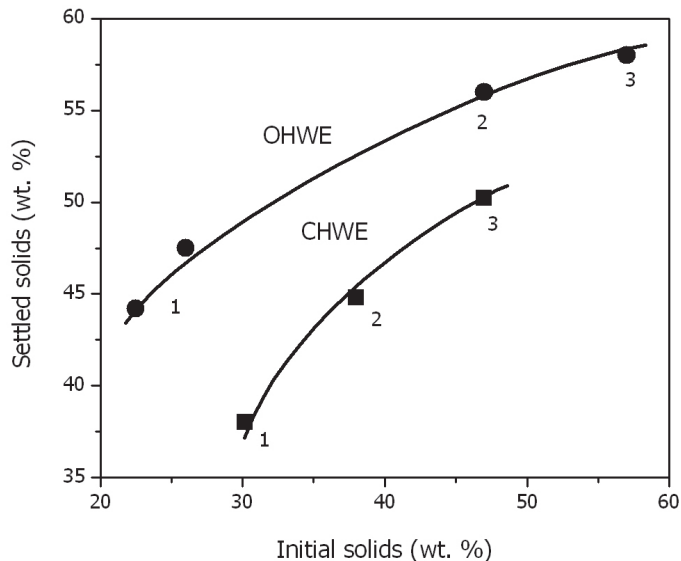


Figure 8.29 Consolidation of MFT by sequential freeze-thaw dewatering.

Source: (FTFC 1995b).

The freeze-thaw process requires the deposition of fluid fine tailings, layer by layer, onto a large open area in winter. The thickness of each layer (normally 15 cm) is determined in such a way that the deposited layer is able to freeze before the next layer is deposited. Based on thermal consideration (Dawson, Segó, and Pollock 1999), it is possible to obtain a total frozen thickness of 2 m to 4.5 m in a typical Fort McMurray winter. However, the total thaw thickness of frozen fluid fine tailings over one year is limited to only 3 m to 4.5 m, depending on whether ambient or warm-water thaw is employed. In Fort McMurray, therefore, the freeze-thaw is limited by thaw to 3 m under ambient thaw conditions. After five years of freeze-thaw operations, a total volume strain of 65 % is feasible.

It is important to note that the freeze-thaw process increases the ionic strength of the remaining pore water, contributing to a disruption of aggregate structure. As a result, the water released from freeze-thaw has a relatively low ionic strength. Although the freeze-thaw dewatering of MFT has not been practiced on an industrial scale, several trial tests have been conducted at oil sands sites, where MFT was deposited into small, shallow ponds in winter and underwent thawing and evaporation in summer (Dawson, Segó, and Pollock 1999). The results are promising. Using the freeze-thaw method, Suncor processed over 75 000 m³ of oil sands fine tailings in the winters of 1992 and 1993, producing a 3-m thick stackable deposit containing 75 wt. % solids from fluid fine tailings of 30 wt. % solids (Mikula et al. 1996). However, to scale this process to a level of industrial production would require enormous surface area for land and pond accommodation.

8.6.3 Natural Drying

Drying by natural sunlight has been practiced since ancient times. Drying fluid fine tailings or MFT using solar energy makes sense. A typical curve of MFT evaporation with varying deposit thickness (lift) is shown in Figure 8.30. In bench tests, for deposits of 2-cm, 5-cm, and 10-cm thickness on a slope of 4 %, the MFT was dewatered to 80 wt. % solids after 7.5, 14, and 20 days of evaporation, respectively, when it was mixed with hydrated lime and gypsum. These materials are used as process aids to adjust the viscosity of the MFT for optimal deposition (flow) on the slope and to maintain sufficient strength to support deposits of a thickness of 8 cm to 10 cm. The amount of process aids needed depends on the properties of the original MFT and on the slope of the deposit. Figure 8.30 shows a faster drying time for thinner deposits. This approach is known as *thin lift drying* technology. When the deposit thickness is greater than 10 cm, natural drying becomes less effective, leading to a deposit solids content of less than 70 %.

For Suncor's MFT, 20 g of hydrated lime and 20 g of gypsum per kilogram of MFT slurry were found to be sufficient to produce 8-cm thick deposits, leading to effective release of clear water from the deposits on the slope. The final fine tailings, dewatered by drying, are in the form of a polygonal crust, which is well below the plastic limit (Wells and Riley 2007). The optimal dewatering was observed at an MFT deposit thickness of 9 cm over an evaporation period of April 1 to November 1,

leading to a maximum MFT disposal volume of 1.55 m³ per square metre of deposition area. The observed limit of evaporation is attributed to the formation of surface crusts.

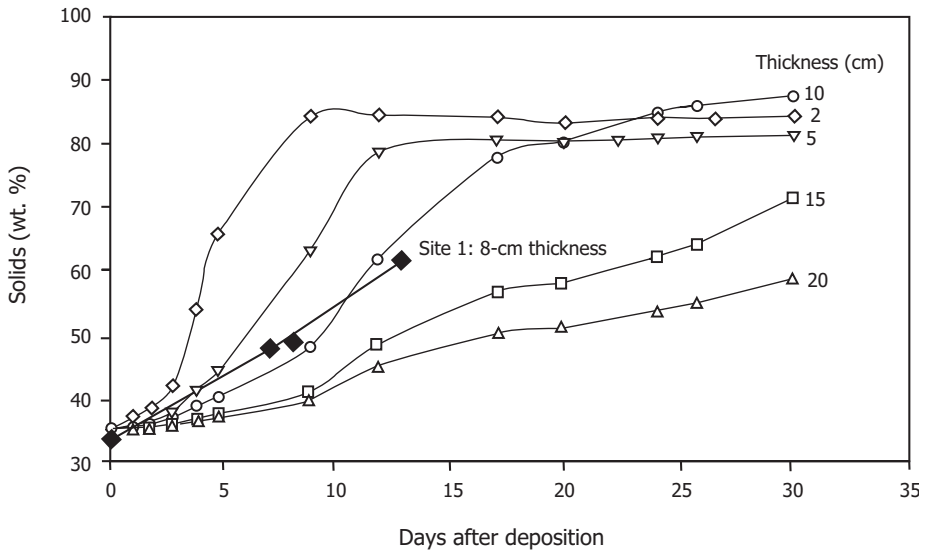


Figure 8.30 Comparison of drying curves obtained in laboratory bench tests (open symbols) with desiccation/drying in pilot deposition.

Source: Wells and Riley (2007).

In a field trial, conditioned fluid fine tailings were deposited on a sand bed with a slope of 4 % contained on three sides, as shown in Figure 8.31a. There was substantial dewatering following 8 days of natural drying. After 14 days' drying, the deposit dried to 80 wt. % solids, sufficient to support a person walking on it, as evidenced by Figure 8.31b. Once it has reached a solids content of 68 wt. % or more, the dried deposit is ready for another deposition.

As shown in Figure 8.30, the drying rates observed in field-scale tests are comparable to those obtained in bench-scale tests. The field tests by Wells and Riley (2007) showed that the amount of lime required decreases significantly with increasing solids content of MFT. If the source MFT contains more than 40 wt. % solids, lime addition is not necessary and gypsum alone is sufficient to reduce the drying time of the deposits. On the other hand, if the original MFT contains less than 30 wt. % solids, it is unlikely that a deposit of MFT on a 4 % slope would be stable, suggesting the need for pre-consolidation, either through the CT process or through TT technology. As the deposition slope is reduced to 2 %, the lime and gypsum dose can be reduced while maintaining a sufficient slope for positive water runoff.

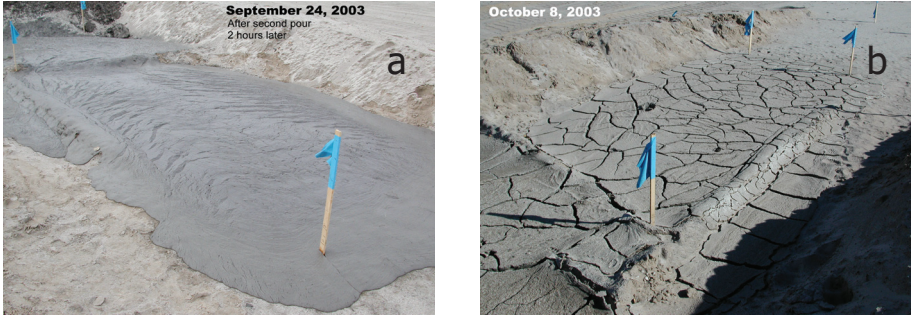


Figure 8.31 Fresh MFT deposit (a), and MFT deposit following 14 days of natural drying (b).

Source: Wells and Riley (2007).

Both the freeze-thaw approach and natural drying are attractive as they utilize natural solar energy. However, they are less practical in the winter season, when the drying time is at a minimum, and both are rather limited by the amount of land they require to handle large volumes of MFT inventory. They should be considered as a complement to other technologies, discussed below.

A combination of natural drying and the freeze-thaw approach could be effective in winter. The optimal gain would be for the freeze-thaw process to leave behind a deposit of a thickness no greater than that which could be dried in a given time. Suncor is currently considering this combined technology for tailings reduction in its new operations.

It is important to note that the evaporative drying process does not recover water from the MFT, as it is released into the atmosphere as water vapour. As a result, the salts contained in the MFT and added to the process remain concentrated in the dried crust. During rainfall, there is a risk that they may seep into and contaminate the groundwater.

8.6.4 Centrifugation

Using a centrifuge to consolidate fluid fine tailings relies on the enhanced gravity forces applied on fine solids aggregates. In a centrifugal field, the instantaneous velocity of particles/aggregates is equal to its terminal velocity by a factor of $r\omega^2/g$, where r is the radius of rotation and ω is the angular velocity (Wakeman and Tarleton 2005). In a centrifuge operating at a few hundred revolutions per minute (rpm), particles of a few microns in diameter settle quickly to form a sediment. The g-force of rotation is then applied to consolidate the sediment by squeezing the aggregates at a force a few hundred times the natural g-force.

For oil sands applications of separating solids from fluid fine tails, the decanter centrifuge is the most suitable (Mundy and Madsen 2009). As shown in Figure 8.32, a decanter centrifuge consists of a horizontally driven bowl to induce accelerated sedimentation. A conveyor transports the separated solids up a conical beach, where solids are discharged in the form of a cake. The clarified liquid is discharged over weir plates at the other end of the centrifuge. Since the objective of MFT dewatering is to achieve a dry cake and an effluent (centrate) that is sufficiently free of solids for recycle, while operating under conditions of high solids loading, polymer is added to the MFT to enhance the separation by particle flocculation. Unfortunately, the solids flocculated by polymer cause the sediments to behave like a cake, hindering the drainage of liquid trapped in the sediments. Running the centrifuge with a deep layer of solids at low differential conveyor speed would minimize this effect.

In designing and running a decanter centrifuge for MFT dewatering, the level of shear must be controlled for effective distribution of flocculant in the feed to the decanter. A low shear environment in the decanter leads to the driest cake and the highest quality of centrate. It is important to note that the operation of a centrifugal decanter is sensitive to the solids content in the feed. A reduction in the solids content of the feed to the decanter will lead to a reduction in the dryness of the cake. It is therefore desirable to operate a centrifuge decanter together with a thickener in order to control the solids content in the feed to the decanter. With a polymer flocculant dosage of 600 g/ton of dry solids cake, 270 m³/h of MFT containing less than 30 wt. % solids (54 dry tons of solids per hour) can be treated by a single centrifuge decanter (operating at 8000 rpm) to produce a decanter cake of 60 wt. % solids and centrate of less than 1 wt. % solids, suitable for recycle back to bitumen extraction. The decanter cake remains pumpable by a positive displacement pump. After deposition, further dewatering of the centrifuge decanter cake (shown in Figure 8.33) by natural drying or freeze-thaw processes is needed to produce stackable solids for final land reclamation.

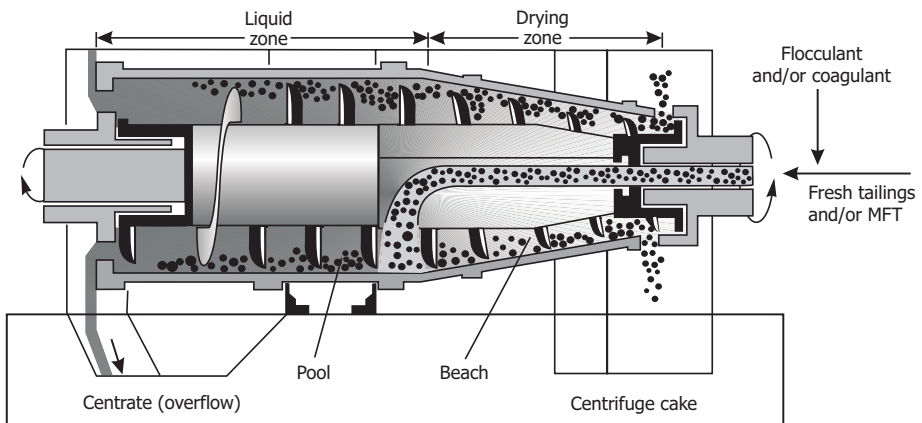


Figure 8.32 A horizontal decanter centrifuge for dewatering flocculated MFT.

Source: Mundy and Madsen (2009).



Figure 8.33 Deposited centrifuge cake following flocculation of diluted MFT.

Source: Lahaie (2008).

A recent laboratory study using fluid fine tailings of a high fines content showed that the addition of 600 g/ton of a polyacrylamide flocculant of high molecular weight and medium charge density and centrifugation at 500-g (2400 rpm) improved both the clarity of the centrate and the strength of the centrifuge cake (Mikula, Muñoz, and Omotoso 2009). Significant dilution was found to be necessary in order to effectively mix the polymer flocculant with the tailings.

Although centrifugation is capable of producing dry stackable tailings and reducing the net usage of water per barrel of oil produced (from over 4 barrels of water to about 2), this tailings treatment option may be prohibitively expensive at low percent solid feed rates. Using a thickener to prepare a centrifuge feed of around 30 wt. % solids was proposed as an economical option. For a feed of 5.1 wt. % solids, a thickener-centrifuge combination is capable of producing a centrifuge cake of 52.7 wt. % solids and a centrate of less than 0.2 wt. % solids, even with a limited centrifugal force of 500-g. It is anticipated that a larger centrifuge at higher g-force would produce a cake of higher solids content and a centrate of lower solids content.

In the context of pumping the centrifuged cake, Ahmed et al. (2009) determined the yield stress of MFT at different levels of solids content and flocculant addition. A combination of fine-sized particles, clay mineralogy, pore water chemistry, solids content, and flocculant dosage causes unsheared centrifuge cake to exhibit unusually high yield stress compared to other base metal mine waste pastes. For sheared

centrifuge cake, the yield stress decreases, particularly at high flocculant dosages. The centrifuge cake exhibits paste-like flow characteristics, following the Bingham plastic model. Following shearing in a mixer, the centrifuge cake can be pumped by a positive displacement pump and deposited as an intermediate cone, forming a flowing paste pile of sloped deposition. Pumping a flocculated centrifuge cake containing 54.5 wt. % solids through a pipe of 200-mm diameter at a flow velocity of 1.4 m/s leads to ~ 10 kPa/m friction loss.

Centrifuging MFT and/or fresh fluid fine tailings after they have been treated in a thickener with flocculant addition provides an option for oil sands tailings management, not only reducing water demand and energy intensity used in bitumen production by recycling of the warm, process-affected water, but also eliminating the need for dike construction and fluid fine tailings storage, hence shortening the time between oil sands mining and land reclamation. The commercialization of thickener-centrifuge technology for oil sands fine tailings management remains to be justified due to its high capital and operating costs, which are a result of high maintenance and centrifuge wear. There remain incentives to develop a robust and economical technology for oil sands tailings management.

8.8.1 Filtration

An alternative to centrifugation for the production of dry, stackable oil sands tailings is filtration. In the filtration process, liquid in a suspension is forced to flow through the interstitial voids of a formed filter cake through the application of pressure, a vacuum, centrifugal force, or a combination of the above. During batch filtration, the volumetric flow rate of the filtrate depends on the driving force (e.g., pressure drop) across, and the resistance of, the cake and the filter medium, as shown by the well-known Darcy's law:

$$\frac{t}{V} = \frac{\mu\phi\alpha_s}{2PA^2}V + \frac{\mu\phi L_m}{PA} \quad (8.21)$$

where t is the filtration time (s); V is the filtrate volume (m³); μ is the viscosity of the fluid (Pa·s); ϕ is the specific resistance to filtration (m/kg); α_s is the fractional solids content per unit volume of filtrate (kg/m³); P is the pressure applied (Pa); A is the area of filter press (m²); and L_m is the thickness of the filter medium (m). Eq. (8.21) shows a linear relationship between t/V and V , where the slope is given by $\mu\phi\alpha_s/2PA^2$, the first term on the right-hand side of Eq. (8.21).

It is evident that a larger slope corresponds to a slower filtration rate. For a filtration system where μ , P , A , and α_s are constant, a larger value of slope corresponds to a larger value of specific resistance to filtration (SRF), ϕ , as shown in Eq. (8.21). The SRF is a function of the slurry characteristics and the filter medium, and is independent of filtration measurement for an incompressible suspension. It is the radii of the capillaries of the voids in a filter cake, not simply the cake porosity, that determines the

containing a large amount of fine particles, such as that encountered in oil sands processing tailings or MFT, would have a high cake resistance, as the fine particles in the slurry would block or reduce the size of the capillary channels through which the filtrate flows. For this reason, fluid fine tailings are known to be difficult to filter without any chemical treatment. This is clear from the results shown in Figure 8.34. Using fresh laboratory samples of oil sands extraction tailings of varying fines contents (obtained by blending fine [$D_{50} = 3 \mu\text{m}$] and coarse [$D_{50} = 140 \mu\text{m}$] tailings at different ratios), the filtration was performed in a pressure filter press of a 10-cm diameter and 15-cm height (1000-cm³ capacity) at 150 kPa pressure and room temperature (Xu, Dabros, and Kan 2008). As shown in Figure 8.34, the SRF increases sharply by four orders of magnitude as the fines content of solids (indicated by open symbols) increases from 4.3 wt. % to 20 wt. %. Beyond 20 wt. % fines, the SRF levels off at a very high value of 2×10^{13} m/kg, indicating that all the passages in the cake are most likely blocked by fines.

From a practical point of view, without tailings pretreatment, filtration is applicable to coarse oil sands extraction tailings that have a fines content of less than 4.3 wt. % in the solids. A slurry pH of between 7 and 8.4 was found to have a negligible effect on the SRF in the filtration of fresh oil sands extraction tailings.

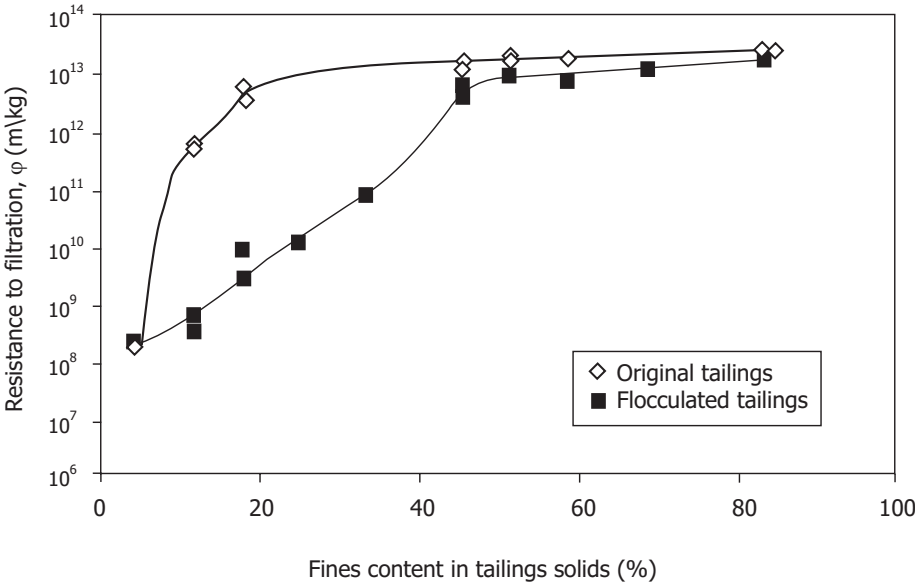


Figure 8.34 Specific resistance to filtration as a function of fines content in tailings solids with and without flocculation at pH 8.4 and 150 kPa pressure.

Source: Xu, Dabros, and Kan (2008).

Following flocculation using a high-molecular-weight, medium-charge density polyacrylamide flocculant at optimal dosage, the filterability of flocculated sediments from tailings containing an intermediate fines content of 10 wt. % to 20 wt. % was improved drastically, as shown in Figure 8.34 (solid symbols). For tailings with 12 % fines, for example, the SRF was reduced from 4×10^{11} m/kg in the original tailings to 4×10^8 m/kg (an improvement of about three orders of magnitude) with as little as 10 g/ton of flocculant. Similarly, the SRF of oil sands tailings containing 18 wt. % fines of solids decreased from 6×10^{12} m/kg to about 2×10^9 m/kg with 30 g/ton of flocculant addition. These tailings are almost impossible to filter without flocculation.

The results clearly demonstrate the significant effect of flocculation on the filtration of tailings containing a moderate amount of fines. For high-fines tailings with a fines content of more than 50 wt. %, flocculant addition led to only a marginal improvement in filterability and a small reduction in the SRF. In this case, a pressure increase from 50 kPa to 150 kPa was found to have a negligible effect on the SRF. For coarse tailings containing only 4 wt. % fines, on the other hand, the addition of flocculant showed a negligible improvement, as anticipated. This is attributed to a very low SRF of 2×10^8 m/kg for the original fresh coarse tailings. For such materials, filtration can be applied without prior flocculation.

Since the flocculation of fines dramatically improved the filterability of oil sands fine tailings containing a moderate amount of fines, as shown in Figure 8.34, the degree of flocculation, determined by polymer dosage, is also thought to play a role in improving the filterability of oil sands fine tailings. Figure 8.35 (top) shows the results of filtration tests for fresh oil sands extraction tailings of 18 wt. % fines content at 50 kPa pressure. There is a rapid reduction in the SRF, by more than three orders of magnitude, with increasing polymer dosage (up to 40 g/ton dry solids), indicating a significant improvement in the filterability of these tailings. The SRF levels off as the polymer dosage is further increased beyond 40 g/ton, suggesting an optimal flocculation at this dosage. Accompanied with SRF reduction is a reduction in the water content of the filter cake, as shown in Figure 8.35 (bottom). The water content reaches a minimum of 11.5 wt. % at a flocculant dosage of 55 g/ton, after which a slight increase in the water content of the filter cake is observed with further increasing flocculant dosage. The optimal dosage of flocculant for this tailings appears to be between 42 g/ton to 55 g/ton of dry solids.

Recently, Wang et al. (2010) performed a systematic study of an organic-inorganic hybrid flocculant, Al-PAM, as a filtration aid for oil sands processing tailings. Fresh tailings of 0.8 wt. % bitumen and 13.5 wt. % total solids containing 40 wt. % fines less than 44 μm in size were obtained from the extraction of a high-fines ore using a laboratory hydrotransport extraction system (LHES). This high level of fines represents almost the upper limit of fines content in fresh oil sands extraction tailings. Two polymers were used as settling and filtration aids: Magnafloc 1011, formally sold as Percol 727, of high molecular weight (17.5 million Da) and medium anionic charge density (27 %), and in-house synthesized cationic Al-PAM, of medium molecular weight (around 1 million Da). The results in Figure 8.36 show a marginal settling of the blank fresh tailings. The photograph in Figure 8.37 indicates segregation of the coarse sands from the suspended fines.

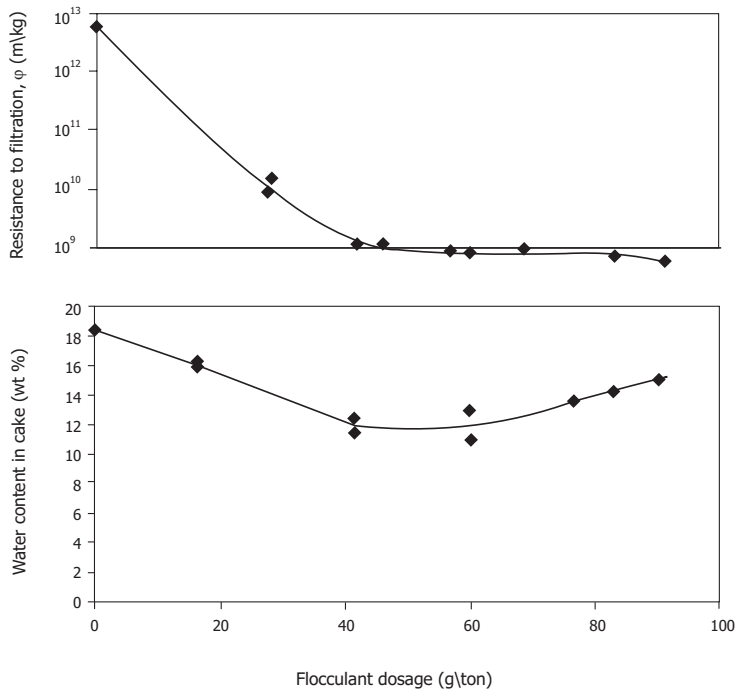


Figure 8.35 Specific resistance to filtration and filter cake water content of MFT filtration at 50 kPa pressure as a function of flocculant dosage.

After Xu, Dabros, and Kan (2008).

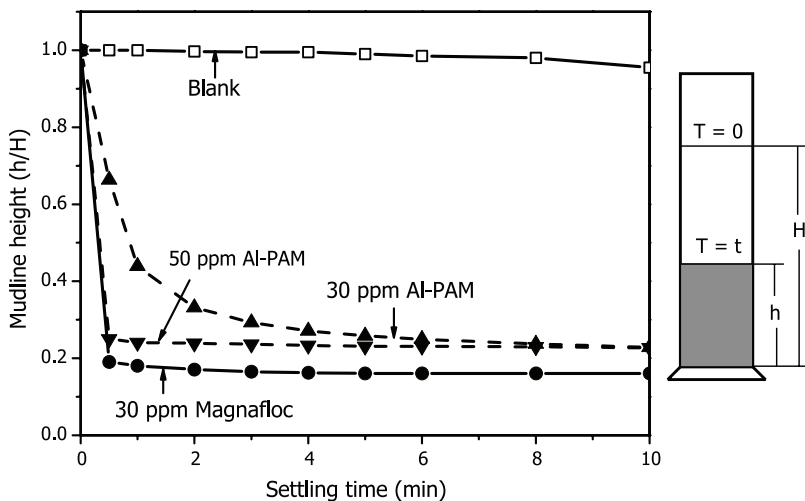


Figure 8.36 Effect of flocculant addition on the settling of solids in fresh extraction tailings of a high-fines ore.

Source: Wang et al. (2010).

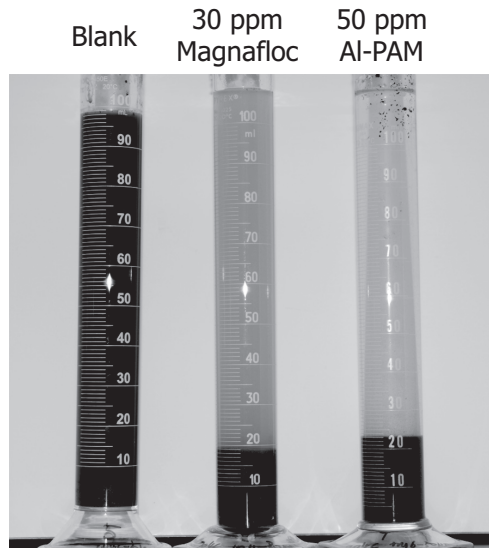


Figure 8.37 Settled tailings of a high-fines ore without and with flocculant addition.

Source: Wang (2009).

Following the addition of Magnafloc at an optimal dosage of 30 ppm, a dramatic improvement in solids settling was observed. Within less than 30 seconds, the solids reached the densification stage. With Al-PAM, a higher dosage (50 ppm) was required to reach a similar initial solids settling rate (Figure 8.36). More importantly, as shown in Figure 8.37, the flocs formed using Magnafloc were more compact, leading to a normalized initial slurry sediment height (h/H) of 0.16 (compared to 0.22 using Al-PAM) following 10 minutes of settling and densification. Figure 8.37 also shows that the supernatant of tailings treated with Al-PAM is much clearer than that treated with Magnafloc (both at their corresponding optimal dosages).

The filtration characteristics of fresh oil sands extraction tailings with and without flocculant addition were determined with a filter press at 15 kPa pressure, using filter papers of an area of 45.8 cm² and 2- μ m to 5- μ m pore size. The results in Figure 8.38 show that, without flocculant addition (blank), fresh tailings did not filter well. In fact, within the specified filtration time of 3 minutes, filtration of these high-fines tailings did not lead to the formation of the integral filter cake. This finding is in excellent agreement with results obtained by Xu, Dabros, and Kan (2008).

Surprisingly, the addition of 30 ppm Magnafloc to the fine tailings did not improve filtration performance, although effective flocculation was observed, as shown in Figures 8.36 and 8.37. In fact, with Magnafloc addition, filtration performance was even worse than in the blank case, in which there was no flocculant addition. The deteriorating filtration performance with the flocculation of fines is attributed to the incomplete flocculation of ultrafine particles, along with the rapid buildup of the filter cake by rapid settling of flocculated aggregates with the water trapped inside the flocs.

The remaining suspended ultrafine particles, as indicated by the darker supernatant in Figure 8.37 (centre), compounded with the residual bitumen in the tailings, quickly block (blind) the passages of the formed solids bed on the filter press, preventing the flow of the filtrate. This observation is in line with recent observations of the extremely low filterability of flocculated tailings containing more than 40 wt. % fines (Xu, Dabros, and Kan 2008).

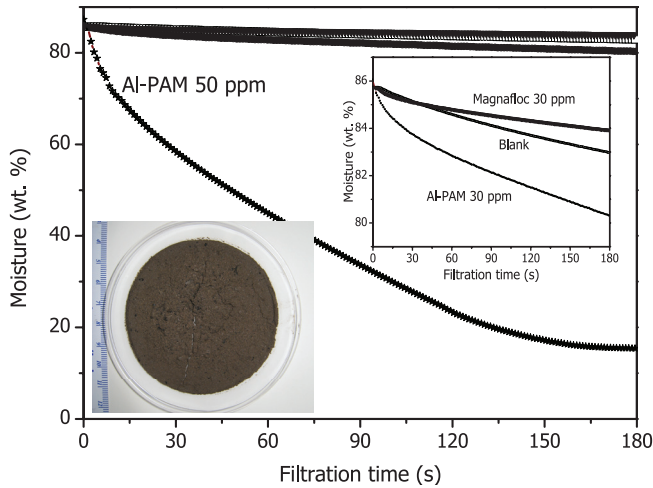


Figure 8.38 Filtration characteristics of fresh oil sands extraction tailings, with and without flocculation by Magnafloc and Al-PAM. Inset is a photograph of filter cake obtained by filtering flocculated tailings with Al-PAM.

Source: Wang et al. (2010).

In contrast to Magnafloc, Al-PAM at its optimal flocculation dosage led to rapid filtration. Within 3 minutes, a filter cake containing less than 18 wt. % moisture formed. A photograph of this wet filter cake is shown in the inset of Figure 8.38. Clearly, the filtration of oil sands tailings with proper flocculation of fines is capable of producing dry, stackable solids for safe deposition and quick land reclamation. The results in Figure 8.39 clearly show a significant drop in the SRF (from 2×10^{12} m/kg to 9×10^{10} m/kg) with 50 ppm Al-PAM addition at 500 rpm mixing, in contrast to an increase in the SRF (from 2×10^{12} m/kg to 7×10^{12} m/kg) with 30 ppm Magnafloc addition. The SRF can be further reduced to 4×10^9 m/kg when the flocculation mixing is optimized at 700 rpm.

The reduction in specific resistance to filtration (SRF) with Al-PAM addition is attributed to the effective flocculation of fine particles by Al-PAM, which leads to a high clarity of the supernatant, as shown in Figure 8.37 (right). The formation of more fluffy flocs, as shown by the larger sediment height in Figures 8.36 and 8.37, may also contribute to larger pores among the flocs in the sediments (filter cake), contributing to the observed low SRF value. Furthermore, Al-PAM is known to attach to negatively charged bitumen due to its cationic nature, flocculating finely dispersed

bitumen droplets in the tailings, which are known to blind the filter medium. Overall, Al-PAM shows great promise as a filtration aid for managing fresh oil sands tailings, even those of high fines content.

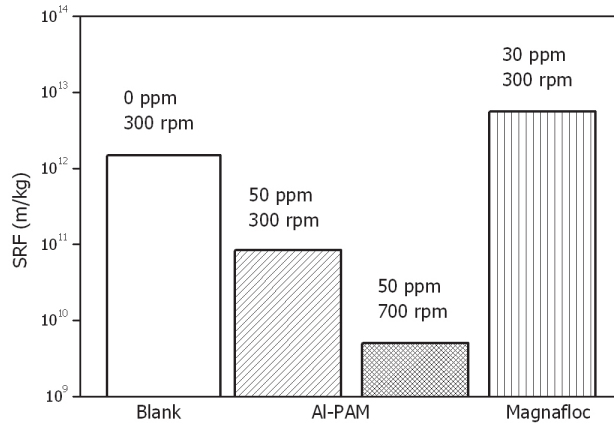


Figure 8.39 Effect of flocculant type, flocculant dosage, and mixing on specific resistance to filtration of a high fines tailings sample.

Source: Wang (2009).

Given the excellent performance of Al-PAM and the solid scientific foundation supporting its working mechanism (Wang et al. 2010), the use of Al-PAM as a filtration aid for treating MFT was attempted (Alamgir, Masliyah, and Xu 2010). It was found that the addition of Al-PAM has a negligible effect on the settling of solids in MFT when the MFT is not diluted. This lack of response of MFT to flocculant addition is attributed to the high viscosity of the MFT, which hinders the distribution of the Al-PAM. A potential local overdose of flocculant can compound the problem by inducing steric stabilization and further impeding flocculant distribution. Initial dilution of the MFT was therefore found essential in order to achieve any flocculation and filtration.

Figure 8.40 shows the effect of dilution of MFT on its response to the addition of Al-PAM at optimal dosages. Without Al-PAM addition, simple dilution of MFT with its mother aliquot, obtained by ultracentrifugation, did not lead to any significant improvement in solids settling. A significant improvement in particle settling was observed upon Al-PAM addition. For example, as shown in Figure 8.41, a 2:1 water-to-MFT dilution ratio (which yielded a total solids content of 10 wt. %) led to an increase in the initial settling rate, from 0.02 mm/s to 0.7 mm/s. Although an additional fivefold increase in dilution, along with an optimal Al-PAM dosage of 1000 ppm on a dry MFT solids basis, further increased the initial settling rate to above 1.1 mm/s, it did not lead to the release of additional water. With 750 ppm Al-PAM addition, the solids content in the sediments was 31.6 wt. % at 5:1 dilution and 32 wt. % at 2:1 dilution. After one hour of settling, both 5:1 and 2:1 dilutions produced supernatants of turbidity less than 160 NTU (nephelometric turbidity unit), in comparison to no

dilution, which, with 833 ppm Al-PAM addition, produced a blank supernatant with a turbidity exceeding the instrument limit of 500 NTU. As there is a much larger volume of diluted MFT at a 5:1 dilution (5 wt. % solids) than at a 2:1 dilution (10 wt. % solids), a larger thickener would be required to concentrate the solids from the MFT diluted at 5:1 ratio than at 2:1 ratio. Furthermore, the optimal Al-PAM dosage on a dry solids basis is higher at a 5:1 dilution ratio than at a 2:1 dilution ratio. The 2:1 dilution of MFT to a total solids content of 10 wt. % is more beneficial, and is therefore the method that has been used in subsequent filtration tests.

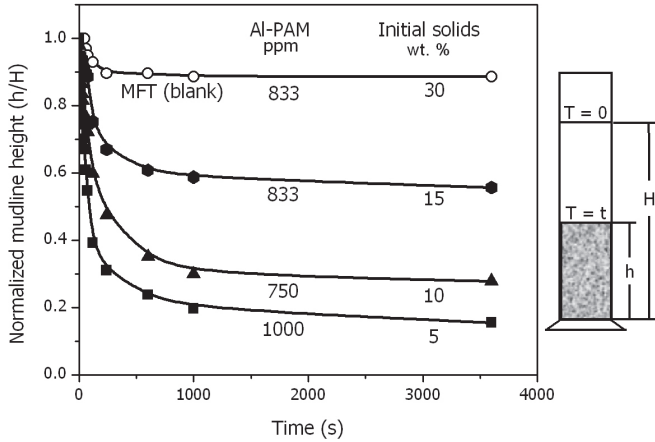


Figure 8.40 Effect of MFT dilution on solids settling (with Al-PAM flocculant at corresponding optimal dosages).

Source: Alamgir, Masliyah, and Xu (2010).

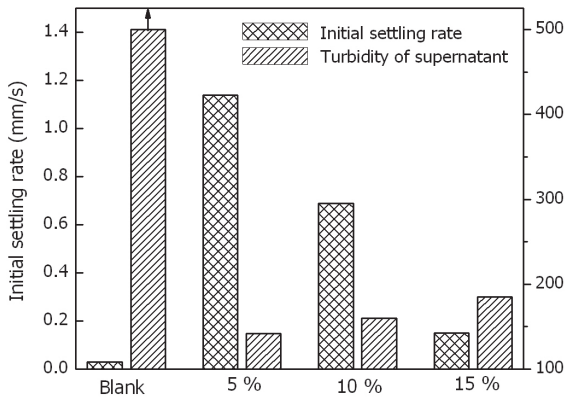


Figure 8.41 Effect of MFT dilution on initial settling rate of solids and supernatant clarity after 1 hour settling (with Al-PAM flocculant at corresponding optimal dosages).

Source: Alamgir, Masliyah, and Xu (2010).

Since MFT dilution with flocculation by Al-PAM did not improve the densification of sediments, an attempt was made to filter the diluted MFT after flocculation (Alamgir, Masliyah, and Xu 2010). In this case, the target was to produce a stackable filter cake of less than 24 wt. % water. The time required to reach this 24 wt. % moisture content target, referred to as the filtration time, was used as the indicator for assessing the filtration performance. The results, shown in Figure 8.42, indicate a significant reduction in filtration time, from more than 8 hours for undiluted MFT with 833 ppm Al-PAM addition, to 45 minutes at a 1:1 dilution with 833 ppm Al-PAM addition. Increasing the dilution to 2:1 and 5:1 at corresponding optimal Al-PAM dosages of 750 ppm and 1000 ppm further reduced the filtration time to 24 minutes and 20 minutes, respectively. It is important to note that, for a given volume of MFT, a 5:1 dilution requires the filtration of twice the amount of diluted MFT as a 2:1 dilution. Furthermore, a much higher Al-PAM dosage is required at a higher dilution ratio to achieve optimal filtration. A 2:1 dilution is therefore considered to be optimal.

To reduce the amount of liquid passing through the filter cake, the filtration of sediments was compared with the filtration of whole diluted MFT, both following flocculation by Al-PAM at optimal dosage. The results showed a significant reduction in filtration time (from 24 minutes to 10 minutes) when sediments, instead of whole diluted MFT, were filtered (Figure 8.43). The filtration converted fluid sediments containing 32 wt. % solids into a stackable filter cake of 76 wt. % solids, as shown in the inset of Figure 8.43. The photographs in Figure 8.44 show a very clear filtrate and a turbid supernatant. The solids content in the supernatant, however, is below 0.5 wt. %—suitable for recycle back to extraction (Xu and Cymerman 1999; Cymerman et al. 1999).

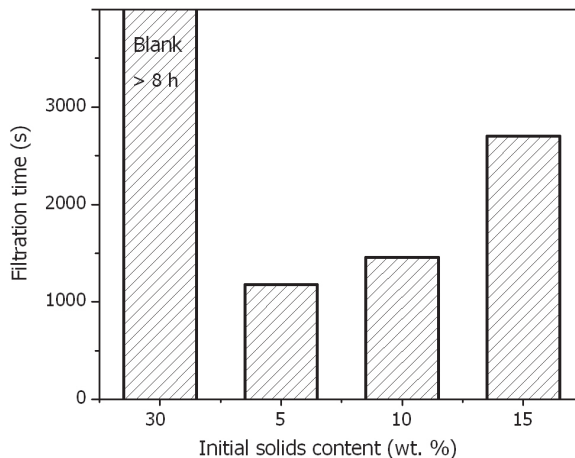


Figure 8.42 Effect of MFT dilution on filtration of flocculated MFT at corresponding optimal flocculant dosages of 833, 1000, 750, and 833 ppm Al-PAM, respectively, from left to right.

Source: Alamgir, Masliyah, and Xu (2010).

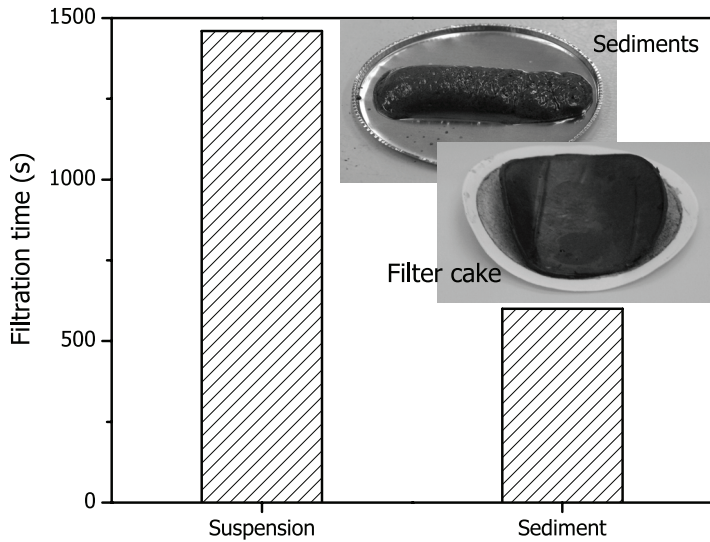


Figure 8.43 Filtration of flocculated MFT suspension and its sediments after 2:1 dilution at 750 ppm Al-PAM addition. Inset shows photographs of sediments containing 32 wt. % solids and filter cake containing 76 wt. % solids.

Source: Alamgir, Masliyah, and Xu (2010).

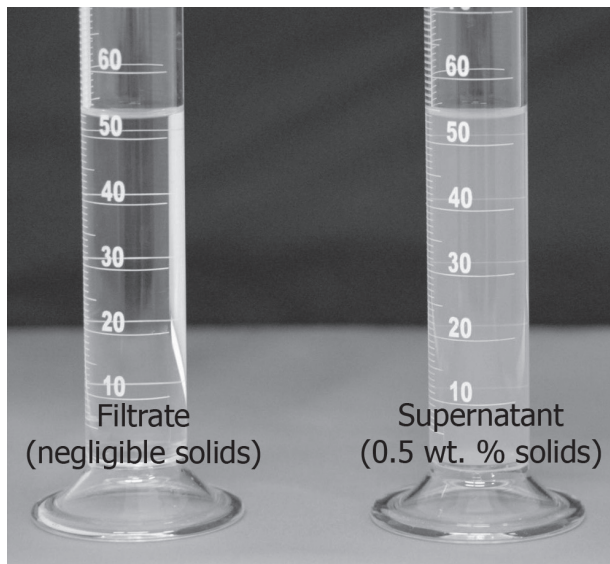


Figure 8.44 Comparison of filtrate with supernatant after dilution of MFT at 2:1 ratio with 750 ppm Al-PAM addition.

Source: Alamgir, Masliyah, and Xu (2010).

The study by Alamgir, Masliyah, and Xu (2010) clearly demonstrates the potential of filtration as a practical means of managing MFT (with Al-PAM used as a filtration aid). Considering the need for MFT dilution prior to flocculation by Al-PAM and filtration, we propose a hypothetical process, as shown in Figure 8.45. In this process, supernatant from the thickener and a portion of the filtrate are combined to form dilution water, to which 75 ppm of Al-PAM flocculant is added to facilitate flocculant distribution and hence, effective flocculation. The dilution water is mixed with raw MFT of around 30 wt. % solids and then fed to a thickener, in which the flocculated fine solids settle quickly to form sediments. The clarified water is recycled back as dilution water, while the sediments are sent to filtration. The resulting filter cake, of more than 76 wt. % solids, is self-supportive (stackable), as shown in the inset of Figure 8.43, and is ready for backfill into a mined pit. The clear filtrate is suitable for recycle, although a small portion of it may be needed to obtain a sufficient amount of dilution water for a 2:1 MFT.

Alamgir, Masliyah, and Xu investigated the suitability of supernatant as dilution water (2010). The results in Figure 8.46 show a slight decrease in filtration time for the first two rounds of recycling of the clarified supernatant as dilution water. The reduced filtration time is attributed to the residual Al-PAM in the recycled supernatant, which helped optimize the flocculation. After three rounds of recycling, the filtration time increased slightly, which may be attributed to a slight overdose of Al-PAM due to its accumulation in the recycle water. If this is the case, it may be possible to reduce Al-PAM dosage and stabilize the process, a prospect that requires further investigation. Nevertheless, thickening followed by filtration appears to be an emerging technology for managing both fresh and mature oil sands fine tailings, and in particular for blending MFT with fresh tailings, which contain some coarse solids, to further enhance the filterability of MFT alone. The challenge is to scale up this process from a laboratory concept to one that is capable of handling many million cubic metres of MFT and fresh tailings.

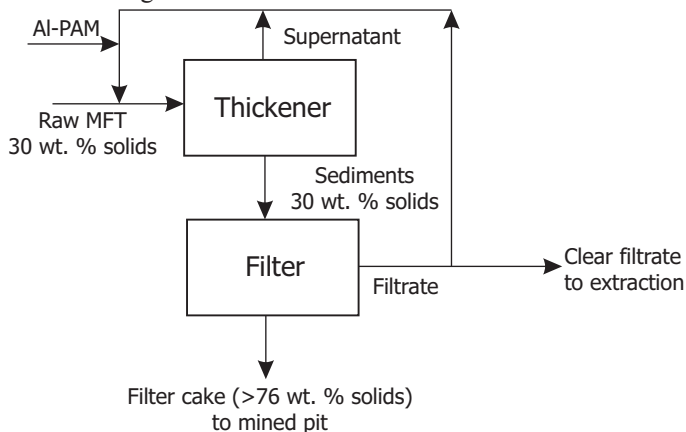


Figure 8.45 Conceptual process of flocculation-assisted MFT filtration that consumes MFT while producing clear filtrate for recycle and stackable solids for backfill of mined pits and for rapid land reclamation.

Source: Alamgir, Masliyah, and Xu (2010).

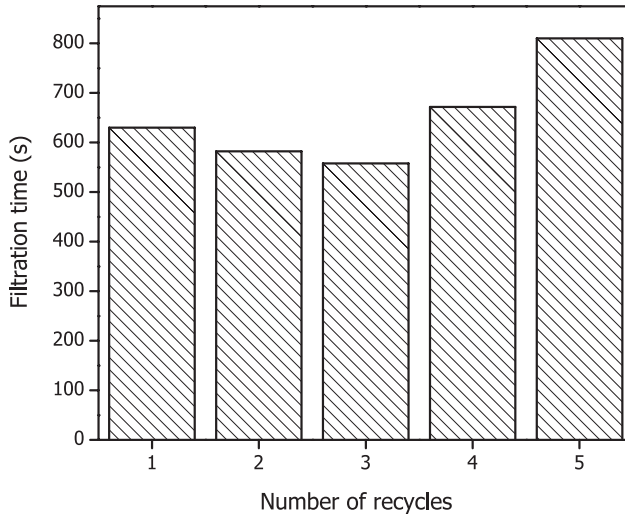


Figure 8.46 Effect of residual flocculant in supernatant and filtrate used as dilution water on filtration of diluted MFT.

Source: Alamgir, Masliyah, and Xu (2010).

8.7 Concluding Remarks

Although tremendous effort has been devoted to developing oil sands tailings management solutions, and many technologies, as discussed in this chapter, have been explored for this purpose, there is no single mature commercial technology capable of economically resolving the challenges posed by fluid fine tailings. Among the available options, filtration appears to be the most promising, as it not only provides tailings for immediate land reclamation, but also uses flocculant, which is conducive to overall bitumen recovery, to resolve issues related to recycle water chemistry, while minimizing the intake of freshwater for oil sands processing and maximizing the use of thermal energy from warm recycle water. However, more research is necessary before filtration or any of the other technologies for managing fluid fine tailings can be fully commercialized in the oil sands industry, and this research largely relies on an understanding of the fundamentals of fluid particles and interfacial sciences, as presented in this book. In filtration, for example, the development of a robust polymer flocculant that can withstand the turbulence of the processing environment while maintaining a high selectivity to fines flocculation is critical for the application of flocculation in an integrated approach that combines bitumen extraction and tailings management. Designing high-capacity filters, capable of handling large volumes of oil sands fluid fine tailings, incorporated with high-capacity and high-efficiency

clarifiers such as hydrocyclones or deep-cone thickeners, will facilitate the large-scale implementation of filtration in oil sands tailings management. In this regard, the recent development of the hyperbaric centrifuge filter in fine-coal dewatering (Asmatulu, Luttrell, and Yoon 2005) is worth further investigation.

8.8 References

- Adeyinka, O.B., S. Samiei, Z. Xu, and J.H. Masliyah. 2009. Effect of particle size on the rheology of Athabasca clay suspensions. *Canadian Journal of Chemical Engineering* 87 (3): 422–434.
- Alamgir, A., J. Masliyah, and Z. Xu. 2010. Al-PAM assisted filtration of mature fine tailings. Paper read at 2nd International Oil Sands Tailings Conference: IOSTC 2010, at Edmonton.
- Asmatulu, R., G.H. Luttrell, and R.H. Yoon. 2005. Dewatering of fine coal using hyperbaric centrifugation. *Coal Preparation* 25 (3): 117–127.
- Boger, D.V. 2009. Rheology and the resource industries. *Chemical Engineering Science* 64 (22): 4525–4536.
- Cymerman, G., T. Kwong, E. Lord, H. Hamza, and Y. Xu. 1999. Thickening and disposal of fine tails from oil sand processing. In *Polymers in mineral processing, Proceedings of the UBC-McGill Bi-Annual International Symposium on Fundamentals of Mineral Processing*. Montreal.
- Dawson, R.F., D.C. Sego, and G.W. Pollock. 1999. Freeze-thaw dewatering of oil sands fine tails. *Canadian Geotechnical Journal* 36 (4): 587–598.
- Fine Tailings Fundamentals Consortium (FTFC). 1995a. Vol. I. Clark hot water extraction: fine tailings. In *Advances in oil sands tailings research*, ed. H. Hamza. Edmonton: Alberta Department of Energy, Oil Sands and Research Division.
- . 1995b. Vol. III. Volume reduction of Clark hot water extraction fine tailings. In *Advances in oil sands tailings research*, ed. D. E. Sheeran. Edmonton: Alberta Department of Energy, Oil Sands Research Division.
- Fuerstenau, M.C., J.D. Miller, and M.C. Kuhn. 1985. *Chemistry of flotation*. New York: SME.
- Johnson, S.B., G.V. Franks, P.J. Scales, D.V. Boger, and T.W. Healy. 2000. Surface chemistry-rheology relationships in concentrated mineral suspensions. *International Journal of Mineral Processing* 58 (1): 267–304.
- Kar, G., S. Chander, and T. Mika. 1973. The potential energy of interaction between dissimilar electrical double layers. *Journal of Colloid and Interface Science* 44 (2): 347–355.

- Kasongo, T. 2006. Role of fine clays and ionic species in bitumen extraction from oil sands ores using the hot water extraction process. Ph.D diss., Department of Civil and Environmental Engineering, University of Alberta, Edmonton.
- Kasongo, T., Z. Zhou, Z. Xu, and J.H. Masliyah. 2000. Effect of clays and calcium ions on bitumen extraction from Athabasca oil sands using flotation. *Canadian Journal of Chemical Engineering* 78 (4): 674–681.
- Kelly, E.G., and D.J. Spottiswood. 1989. *Introduction to mineral processing*. New York: Wiley.
- Lahaie, R. 2008. New tailings concepts. Paper read at International Oil Sands Tailings Conference, Dec. 7–10, at Edmonton.
- Lahaie, R., I. Ahmed, M. Labelle, and R. Brown. 2009. Paste pumping and deposition field trails and concept on Syncrude's dewatered mature fine tailings (centrifuge cake). Paper read at Tailings and Mine Waste, Nov. 1–4, at Banff, AB.
- Li, H., J. Long, Z. Xu, and J. Masliyah. 2008. Novel polymer aids for low-grade oil sand ore processing. *Canadian Journal of Chemical Engineering* 86 (2): 168–176.
- Liu, B., E. Lord, and K. Krishnamurthi. 2000. Depositional and geotechnical properties of thickened oil sands tailings. In *Transportation and Deposition of Thickened/Paste Tailings: Proceedings*. Edmonton.
- Liu, J., Z. Zhou, Z. Xu, and J.H. Masliyah. 2002. Bitumen-clay interactions in aqueous media studied by zeta potential distribution measurement. *Journal of Colloid and Interface Science* 252 (2): 409–418.
- MacKinnon, M.D., J. Matthews, W. Shaw, and R.G. Cuddy. 2001. Water quality issues associated with composite tailings (CT) technology for managing oil sands tailings. *International Journal of Mining, Reclamation and Environment* 15 (4): 235–256.
- Matthews, J.G., W.H. Shaw, M.D. MacKinnon, and R.G. Cuddy. 2002. Development of composite tailings technology at Syncrude. *International Journal of Mineral Processing* 16 (1): 24–39.
- Mikula, R., and R. Zrobok. 1999. Oil sands tailings reclamation via manipulation of clay behaviour: the role of rheology. In *Meeting of the Engineering Foundation*. Hawaii.
- Mikula, R., R. Zrobok, and O. Omotoso. 2004. The potential for carbon dioxide sequestration in oil sands processing streams. *Journal of Canadian Petroleum Technology* 43 (8): 48–52.
- Mikula, R.J., K.L. Kasperski, R.D. Burns, and M.D. MacKinnon. 1996. Nature of fate of oil sands fine tailings. In *Suspensions: Fundamentals and applications in the petroleum industry*, ACS Advances in Chemistry Series No. 251, ed. L. L. Schramm, 677–723. Washington: American Chemical Society.
- Mikula, R.J., V.A. Muñoz, and O. Omotoso. 2009. Centrifugation options for production of dry stackable tailings in surface-mined oil sands tailings management. *Journal of Canadian Petroleum Technology* 48 (9): 19–23.

- Mundy, P., and B. Madsen. 2009. The development of centrifugal separation technology for tailings treatment. In *Tailings and Mine Waste 2009*, 397–403.
- Samiei, S. 2007. Role of ultra-fine solid fractions on rheology of oil sands suspensions. Master's diss., Department of Chemical and Materials Engineering, University of Alberta, Edmonton.
- Sury, K., and J. Stone. 1995. Non-Clark extraction processes and their tailings characteristics.
- Sworska, A., J.S. Laskowski, and G. Cymerman. 2000. Flocculation of the Syncrude fine tailings: Part II. Effect of hydrodynamic conditions. *International Journal of Mineral Processing* 60 (2): 153–161.
- Wakeman, R., and S. Tarleton. 2005. *Solid/liquid separation: Principles of industrial filtration*. Oxford: Elsevier.
- Wallace, D., R. Tipman, B. Komishke, V. Wallwork, and E. Perkins. 2004. Fines/water interactions and consequences of the presence of degraded illite on oil sands extractability. *Canadian Journal of Chemical Engineering* 82 (4): 667–677.
- Wallwork, V., Z. Xu, and J. Masliyah. 2004. Processability of Athabasca oil sand using a laboratory hydrotransport extraction system (LHES). *Canadian Journal of Chemical Engineering* 82 (4): 687–695.
- Wang, X. 2009. Polymer aids for settling and filtration of oil sands tailings. Master's diss., Department of Chemical and Materials Engineering, University of Alberta, Edmonton.
- Wang, X., X. Feng, Z. Xu, and J. Masliyah. 2010. Polymer aids for settling and filtration of oil sands tailings. *Canadian Journal of Chemical Engineering*. In press.
- Wells, P.S., and D.A. Riley. 2007. MFT drying-case study in the use of rheological modification and dewatering of fine tailings through thin lift deposition in the oil sands of Alberta. In *Proceedings of the Tenth International Seminar on Paste and Thickened Tailings Paste*, edited by A. Fourie and J. R.: Australia Centre for Geomechanics.
- Xu, Y., and G. Cymerman. 1999. Flocculation of fine oil sand tails. In *Proceedings of the 3rd UBC-McGill Bi-Annual International Symposium on Fundamentals of Mineral Processing*. Quebec City.
- Xu, Y., T. Dabros, and J. Kan. 2008. Filterability of oil sands tailings. *Process Safety Environmental Protection* 86 (4): 268–276.
- Yuan, X., and W. Shaw. 2006. Novel processes for treatment of Syncrude fine transition and marine ore tailings. In *6th UBC-McGill-UA International Symposium on Fundamentals of Mineral Processing: Interfacial Phenomena in Fine Particle Technology*, edited by Z. Xu and Q. Liu. Montreal: MetSoc.
- Yusa, M. 1977. Mechanisms of pelleting flocculation. *International Journal of Mineral Processing* 4: 293–305.

- Zhao, H., T. Dang-Vu, J. Long, Z. Xu, and J. Masliyah. 2009. Role of bicarbonate ions in oil sands extraction systems with a poor processing ore. *Journal of Dispersion Science and Technology* 30 (6): 809–822.
- Zhou, Z., O. Worku, L. Wang, Z. Xu, and J. Masliyah. 2010. Effect of electrolytes and montmorillonite addition on the viscosity of kaolinite and illite clay suspensions. In *8th UBC-McGill-UA International Symposium on the Fundamentals of Mineral Processing: Rheology and Processing of Fine Particle Systems*, edited by M. Pawlis and B. Klein. Montreal: MetSoc.

Index

A

- AAS. *See* atomic absorption spectrophotometer
- acidification, **31, 48**
- acid rain, **31**
- adhesion energy, **60–61, 308**
- adsorption, **59, 69–81 passim, 101, 103, 120, 122, 187, 228, 230, 249–265 passim, 302–304, 328–332, 334, 340, 344–346, 352, 356–358, 393–404 passim, 417–418**. *See also* Gibb's adsorption equation; Langmuir's adsorption isotherm; Stern-Graham equation of adsorption
- AERI. *See* Alberta Energy Research Institute
- aerosols, **52–53**
liquid, **53**
- Aerosol OT **114**
- AFM. *See* atomic force microscope
- aggregates, **100–116 passim, 157, 232, 237, 268, 289, 305, 309, 321–323, 330, 352, 358, 365–369, 372, 383, 387–388, 398–409 passim, 425, 432, 434, 441**.
See also asphaltenes, nanoaggregates and Mullins' model; mineral solids, clays, peds
- aggregation: kinetic, **398–399**
perikinetic, **398–399**
- air bubbles. *See* bubble
- Alberta Chamber of Resources, **22, 47**
- Alberta Energy Company Ltd., **20**
- Alberta Energy Research Institute (AERI), **37, 48–49, 264**
- Alberta Oil Sands Technology and Research Authority (AOSTRA), **127, 170, 259–264, 287, 343, 389**
- Alberta Research Council (ARC), **20, 47, 260**
- Albian, **10, 15, 20–21, 26, 30, 40, 43–45, 177, 267–268, 378, 425**
- Albian Sands Energy Inc. *See* Albian
- alkanes, **26, 96, 212, 214, 233–235, 361–362**
- American Petroleum Institute (API)
gravity scale. *See* API gravity
- American Society for Testing and Materials (ASTM), **362–363, 387**
- amine unit, **27–28**
- ammonia, **28, 32, 77, 393**. *See also* plants, ammonia;
- ammonium sulphate, **28, 32**
- AOSP. *See* Athabasca Oil Sands Project
- AOSTRA. *See* Alberta Oil Sands Technology and Research Authority (AOSTRA)
- API. *See* API gravity
- API gravity, **1, 38–39, 204–205, 209, 227**
- ARC. *See* Alberta Research Council
- aromatics, **229–232, 235, 241, 361–363, 369, 371–372, 377**
- asphaltenes, **13, 25–30 passim, 220–235 passim, 241, 259–260, 265, 268, 285, 358–389 passim**
aggregation **366**
chemistry of, **363–364**
colloidal model, **366, 368**
molecular mass, **364–366, 372, 386**
molecular structure of, **364, 369–371, 386**
archipelago model, **369–371**
island (like-your-hand) model, **369, 371–372**
nano-aggregates and Mullins' model, **372**
precipitation, **13, 233, 259–260, 268, 362–363, 368–369, 376–380**
- ASTM. *See* American Society for Testing and Materials
- association, **106, 118–119, 232, 364, 366–368, 386, 388–389, 413, 418**
- Athabasca formation, **179, 196**
- Athabasca oil sands (area) (OSA), **1–9, 13–16, 18, 47, 173–182 passim, 197, 219, 224, 241, 259–264 passim, 287–288, 345–347, 363, 378, 414, 450**
- Athabaska. *See* Athabasca
- Athabasca Oil Sands Project (AOSP), **15, 18, 30–36, 44–45**

Athabasca River, **4, 8, 40–47, 201, 203, 392**

flow zones, **42–43**

atomic absorption spectrophotometer (AAS), **334**

atomic force microscope (AFM), **287, 323, 333–334, 427**

B

Bancroft: rules, **353**

Wilder D., **353**

basal planes, **184, 186–191, 395–397, 400–401**

basal water sands (BWS), **6, 41, 198, 201**

Batchelor's coefficient, **168**

batch settling, **145–147, 154, 156–157**

benzene, **62, 95, 126, 207, 212–213, 231, 235, 241, 350, 369**

BET isotherm, **77–78**

bicarbonate, **173, 176, 196–197, 201, 203, 250–255 passim, 284, 294, 326, 336–338, 340, 347, 393, 415, 423–424, 452**

Bingham plastic fluid, **412–413, 437**

bitumen:

aeration, **176, 182, 236–237, 242–249 passim, 255, 258–259, 268, 282, 289, 294, 296–298, 310, 315–327 passim, 334, 341**. See also bitumen, froth; bubble; flotation, aeration methods
temperature effect on, **325–326**

chemical characterization of, **228–230**

chemical structure approach, **229**

elemental composition approach, **227–230**

solubility and adsorption class approach, **228, 230**

chemical properties of, **173, 176, 228–230**

content. *See* bitumen grade; bitumen saturation

crude, **1–2, 5–17, 24–37 passim, 44, 224**

deasphalted, **26, 30, 44, 217–218, 230–231, 268**

density of, **1, 25, 204–207, 227, 285, 294, 322, 373**

temperature effect on, **205–207**

diluted, **25–29, 31, 105, 165, 217, 349, 351, 359, 374, 378, 380, 387, 389**

extraction of, **20–30 passim, 39–40, 60–61, 79, 103, 154, 172, 174, 207, 236, 255–256, 260–263, 267–269, 279, 284, 287, 289, 297, 302, 305, 311, 323–324, 329–330, 337–346 passim, 349, 361, 391–392, 394, 400, 411, 419–427, passim, 429, 435, 448–452**

caustic use in, **20, 80, 255–256, 267, 297, 326–342 passim, 372, 393–394, 418**

slime coating, impact of, **91, 182, 237, 323, 325–327, 331–335, 426–427**

temperature impact, **61, 124, 174, 176, 223–224, 267, 270, 279–280, 282, 287, 309–311, 324–327, 343, 345–347**

water use in, **24, 39–46**

froth, **25–26, 159, 165, 176, 214, 216, 237–238, 246, 253, 268, 285, 289, 293–294, 301–306 passim, 310–322 passim, 327–328, 332–333, 338, 349, 373, 378–379, 383, 387, 419, 426–430**. *See also* bitumen, aeration; bitumen, froth treatment; bubble; frothers

froth treatment, **13, 25–28, 30, 52, 91, 105, 116–117, 174, 182, 196, 214, 234, 268–269, 305, 320, 349, 352, 373, 378–380, 389, 411**. *See also* bitumen, froth; naphtha; plants, bitumen froth treatment

naphthenic, **25–27, 214, 234, 268, 285, 374, 378, 380**

paraffinic, **25–26, 111, 233, 268, 285, 374, 378–380**

recovery of heavy minerals from, **305**

grade, **7, 173, 177–178, 180, 192–197, 323**

liberation, **124, 174, 186–187, 236–237, 242–259 passim, 268–270, 282–302 passim, 324–325, 327, 341**

hydrodynamic forces in, **291**

recession, **282, 289–291, 293**

separation, **20, 39, 174, 176, 289–291, 331**

- solids wettability role in, **302–305**
 - temperature effect on, **282–285, 292–293, 324**
 - production of, **10, 13, 15–17, 22–24, 26, 32–45** passim, **235, 238, 269, 391, 437**
 - recovery, **9–14** passim, **24, 91, 104, 124, 173–187** passim, **196, 205, 235–238, 246, 253–256, 259, 267, 269, 289, 293–294, 300–301, 305, 315–345** passim, **400, 415, 419, 425–428, 448**
 - acidity impact on, **326–327**
 - effect of clay and calcium addition, **329–330**
 - in situ, **8–23** passim, **37, 361**
 - open-pit or surface mining, **5–21** passim, **38, 173**
 - steps in, **267–269**
 - thermal, **12, 14–15, 23, 37**
 - refractive index, **217–218, 260, 265**
 - reserves of, **2, 9–14, 31**
 - established, **12–15**
 - initial established, **2, 9–15**
 - in situ, **14**
 - remaining established, **9–11, 13–15, 31**
 - ultimate potential recoverable, **9–12**
 - specific gravity of, **29, 204**
 - SARA analysis of, **363**
 - saturation, **6–8, 11, 173, 180, 192**
 - sulphur content, **5, 27, 227**
 - upgraded. *See* synthetic crude oil
 - upgrading of, **15, 23–31** passim, **40, 176, 182, 227, 269, 373, 378**
 - primary, **30, 380**
 - secondary, **30**
 - viscosity of, **1, 25, 61, 124, 176, 207–217, 235, 262, 268, 270, 276–285,** passim, **302, 324**
 - reduction, **212, 215**
 - temperature effect on, **208–211, 214–215, 263, 270, 324**
 - volume(s) of, **7, 9–14**
 - initial in-place, **7, 9–11, 13–14**
 - ultimate in-place, **9–12**
 - bitumen-in-carbonate rocks, **2**
 - bitumen-in-clastic sands, **2, 5**
 - bituminous sands. *See* oil sands
 - Boltzmann's constant, **83, 97, 99, 110, 125, 398**
 - Boltzmann's equation, **83–84**
 - Boycott effect, **166**
 - Brownian movement(s), **57, 108, 110, 330, 365–366, 393, 398**
 - Brownian motion. *See* Brownian movement(s)
 - brucite, **183–184, 190–191**
 - Brunauer, Stephen, **77**
 - bubble:
 - attachment, **258, 270, 285, 294–313** passim, **328–329, 331, 338–339**
 - induction time, **261, 307, 309, 311–313, 325–326, 328–329, 344**
 - generation, **258, 305–306, 315, 319**
 - bulk properties, **51, 176**. *See also* bitumen, density of; bitumen, viscosity of; heat of combustion; specific heat; viscosity, dynamic
 - BWS. *See* basal water sands
- ## C
- calcium carbonate, **95, 182, 222, 253–254, 305, 326, 329, 336–337, 340, 343** calcium ions, **101, 103, 186, 250–257** passim, **284, 286, 294, 302–304, 323–345** passim, **393, 399–400, 415, 423–424, 450** calcium sulphate. *See* gypsum
 - calcite. *See* calcium carbonate
 - California, **37, 39, 47**
 - California thermal enhanced oil recovery, **39**
 - Canadian Centre for Energy Information (CCEI), **5, 47**
 - Canadian Oil Sands Trust, **22, 25, 47**
 - CanmetENERGY, **20, 282**
 - CanMET Energy Technology Centre. *See* CanmetENERGY
 - Canadian Natural Resources. *See* CNRL
 - carbon, **28, 35, 75, 116, 118–119, 203, 227–230, 233, 235, 339–340, 363, 371, 373, 377**

carbonate alkalinity, **336–338, 393**
carbonate bitumen deposits, **2–3, 11**
carbonate ions, **254, 336–338, 340, 423–424**
carbon dioxide, **24, 27, 30, 33, 56, 212, 255, 314–315, 326, 335–336, 338, 422–424, 450**
 emission of, **24, 30, 33–35, 39**. *See also* equivalent carbon dioxide
carbonic acid, **254, 335–336**
carbon imprint, **35**
carbon-to-hydrogen ratio (C/H), **363**
carboxylic acids, **113, 244, 246, 255–256, 339–340, 370–373**. *See also* naphthenic acids
cation exchange capacity (CEC), **184–185, 189–191**
caustic, **20, 80, 255–256, 267, 297, 326–342 passim, 372, 393–394, 418**
cavitation, **298, 315–316, 319–320**. *See also* flotation cells, cavitation
CCC. *See* critical coagulation concentration
CCEL. *See* Canadian Centre for Energy Information
CEC. *See* cation exchange capacity
centrate, **435–436**
centrifuges, **25, 165, 268, 285, 349, 373, 375, 380, 434–437, 449–450**
cetene number, **227**
C/H. *See* carbon-to-hydrogen ratio
chemical equivalent, **338**
chlorite, **182–185, 188, 190–191**
chromatography, **230, 235, 362–364, 368–369, 371**
 gel permeation (GPC), **364–365, 368–369, 371**
 high-pressure liquid, **363**
 thin-layer, **363**
CHWE. *See* Clark Hot Water Extraction
Clark, Dr. Karl, **20**
Clark Hot Water Extraction (CHWE), **267, 394–397, 418, 431, 449**
Claus sulphur and tail gas units, **27–28**
clay minerals, **173–192 passim, 329, 436**. *See also* mineral solids, clays; illite; kaolinite; montmorillonite; smectite
clays. *See* mineral solids, clays
Clearwater Formation, **4–6**
CMC. *See* critical micellization concentration
CNAC. *See* critical nano-aggregate concentration
CNRL (Canadian Natural Resources Limited), **6, 15, 20–22, 25, 40, 43, 47, 177–178, 181, 197, 203, 214, 234, 260, 268**
 Horizon (Oil Sands) Project, **6, 15, 20, 47, 177–178, 197, 260, 268**
coagulant, **103, 308, 399, 409, 422–423, 425, 435**
coagulation, **100–112 passim, 305, 309, 344, 346, 385, 394–409 passim, 413–423 passim, 425**. *See also* critical coagulation concentration
 Brownian or perikinetic, **110–111**
 orthokinetic, **110**
 rapid, **107–109, 111, 400**
 slow, **107, 112**
coalescence, **268, 289, 311, 338, 341, 352, 355, 358–359, 381–382, 385**
coal-to-liquid technology (CTL), **39**
cogeneration, **39**
cohesion energies, **60–61**
coke, **13, 26–31, 220–222, 225, 235, 260, 362, 373**
coker, **26–32, 216, 227**
coking, **26–29, 38, 380**
Cold Lake oil sands (area) (OSA), **1–2, 6–7, 14–16, 20–21, 206, 209, 211, 213, 363**
collectors, **26, 125, 338–339**
colloid, **51–52, 77, 84, 89, 91, 98, 103–106, 122, 127, 169–170, 172, 260–265, 286–287, 343–346, 349, 387–389, 422, 449–450**
colloid science, **51–53, 344, 388, 411**
colloidal aggregates, **366–368**
colloidal dispersions, **51–53, 91, 107, 127, 171–172, 346, 349**
colloidal force, **129–130, 144, 156, 169, 287, 323, 399, 427**
colloidal model. *See* asphaltene(s), colloidal model

- colloidal particles, **84, 91–103** passim, **113, 116, 144–145, 157–158, 309, 350**
- colloidal suspensions, **81, 169, 172, 398**
- colloidal systems, **51–52, 91, 98, 103, 121, 350, 399**
- conservation of mass and energy, **271, 274**
- contact angle, **57–69** passim, **105, 122, 127, 176, 186, 236, 238, 290–302** passim, **307, 309, 327, 347, 356–358, 418**
- critical value, **300–302**
- hysteresis, **59**
- methods of measuring, **69**
- bubble captive method, **296, 301**
- contact line, **54, 57, 61, 238, 284, 286, 307, 356**
- cooling towers, **40**
- costs, capital and labour, **24**
- Cottrell's model, **175**
- critical coagulation concentration (CCC), **101–103, 399, 401**
- critical dilution, **374, 376–378**
- critical micellization concentration (CMC), **116–121, 352, 355, 366–368, 372**. *See also* Krafft point; micelles
- critical nano-aggregate concentration (CNAC), **372**
- crude. *See* bitumen, crude; oil, crude
- CSS. *See* cyclic steam stimulation
- CT. *See* tailings, consolidated
- CTL. *See* coal-to-liquid technology
- cyclic steam stimulation (CSS), **14, 20**
- cyclohexane(s), **217–218, 239–241**
- cyclones, **165, 268, 285, 373, 401, 422–424**. *See also* hydrocyclones
- D**
- Darcy's law, **437**
- D/B. *See* diluent-to-bitumen ratio
- deasphalting, **30, 338**
- Debye parameter, **84, 86, 88**
- deformation, **69, 137, 313, 358, 411, 413–414**
- demulsifiers, **105, 116, 378, 380–382, 385–387**
- bottle test for, **381–382, 387**
- dosage of, **382–385**
- depressants, **338–339**
- Derjaguin, B.V., **98, 126, 307–308, 343–344**
- detergency, **113, 122–123, 125**
- diesel, **1, 17–18, 34, 37–39, 47**
- ultra-low sulphur (ULSD), **37, 47**
- diffusion coefficient(s), **108, 111, 169**
- digestion. *See* oil sands, lumps, digestion
- digestion model development, **271–278**
- dilbit, **37–39**
- diluent, **25–31, 38–39, 174, 176, 214, 217, 268, 374, 377–378**
- naphthenic, **268, 377**
- paraffinic, **25, 268, 374, 377–378**
- diluent recovery unit (DRU), **27–29**
- diluent-to-bitumen ratio (D/B), **374, 377–378**
- dimers, **112, 364**
- disjoining pressure, **307, 359–360**
- dispersants, **342, 393**
- dispersing agents. *See* dispersants
- dispersions, **51–53, 57, 91, 107, 116, 121–127** passim, **171–172, 263, 287, 317, 340, 346–350** passim, **387, 392, 394, 419, 452**. *See also* colloids; colloidal systems; phases
- distillation, **1, 27, 30–31**
- atmospheric, **30–31**
- vacuum, **28, 30–31**
- DLVO theory, **84, 91, 98, 112, 122, 307–309, 360, 395–396**
- downcomers, **318–320**
- drag coefficient, **130–133, 135–138, 170**
- drag force, **129, 130, 169, 171, 291**
- DRU. *See* diluent recovery unit
- DSPW. *See* simulated process water, doped
- Dupré equation, **60–61**
- E**
- Edmonton, **15, 20–21, 24, 29**

electric double layer, **81–91, 96–107**
passim, **113, 157, 174, 258, 307–308, 334, 350, 393–403** passim, **415, 425, 449**. *See also* surface forces, double layer overlapping

electrokinetic phenomena, **79, 82, 86–88, 90–91**
electro-osmosis, **87, 89**
electrophoresis, **87–89, 91**
sedimentation potential, **87, 90**
streaming potential, **87, 89, 91**

electrolyte concentration(s), **85–86, 98, 100–103, 106, 282, 285, 308–309, 327, 334**

electrolytes, **86, 100–101, 103, 126, 173, 186, 196, 202, 308, 328, 344, 399, 422, 452**. *See also* coagulant

emulsification, **121–122, 246, 340–341, 386–387**

emulsifiers, **122, 352–353, 355–356, 385–386**. *See also* demulsifiers

emulsifying agents. *See* emulsifiers

emulsions, **52–53, 57, 68, 91, 105, 121–122, 127, 182, 235, 246, 260, 263, 287, 340–341, 349–361** passim, **369, 372–389** passim
microemulsions, **354–355, 385**
multiple, **351**
oil-in-water (O/W), **53, 116, 122, 350–353, 352–356, 360**
solid, **52–53**
solid-stabilized, **355–356**
stability, **350–352, 355, 359, 361, 374–375, 381, 385–387**. *See also* stabillization, kinetic; stabilization, mechanisms
surfactant-stabilized, **353, 355–356**
temperature effect on, **353–354, 373**
thin liquid film, **358–360, 388**
water-in-crude oil (W/CO), **360–361**
water-in-oil (W/O), **53, 116, 122, 350–360** passim, **373, 375–376, 382, 385**
Winsor types, **353–354, 385**

emulsion breaking. *See* phase separation

Emmett, Paul, **77**

energy barrier, **100–102, 112–113, 307–309, 313, 331, 396, 399**

energy demand, **23**

energy intensity, **33, 35–36, 437**

Energy Resources Conservation Board (ERCB), **1–2, 7–18, 22, 31, 47, 392**

environmental issues, **23–24, 269, 329**

Eo. *See* Eötvös number

EO. *See* ethylene oxide

EO/PO ratio, **116, 382**

Eötvös number (Eo), **137–141**

equilibrium constants, **76, 120, 246–255** passim

equivalent carbon dioxide, **33–37, 39**

ERCB. *See* Energy Resources Conservation Board

ethylene oxide (EO), **115–116, 382**

F

Faraday constant, **125, 304**

FCF. *See* flocculation-coagulation-flocculation

FGD. *See* flue gas desulphurization

FFT. *See* tailings, fluid fine

film. *See* emulsions, thin liquid film

finer. *See* mineral solids, fines

fine solids, **26–27, 156, 173–180** passim, **220, 222, 253, 263, 268, 285, 319, 324–331, 339, 341–342, 349–350, 355, 358, 361, 373, 379–386** passim, **391–392, 394, 399–401, 419–434** passim, **447**

Fine Tailings Fundamentals Consortium, **267, 269, 286, 394–395, 409, 418, 431, 449**

Firebag, **20–23, 34, 44–45**

flocs, **330–331, 341, 352, 379, 382–384, 403, 413, 420, 425–426, 431, 441–442**

flocculants, **379, 383, 402–410** passim, **419–426** passim, **435–448** passim. *See also* polymers
Al-PAM, **410, 426–430, 439–447**
Magnafloc 1011 (MF), **409–410, 419–421, 424, 439, 440–443**
Percol 727, **424, 426, 428–430, 439**

flocculation, **100, 105, 107, 111, 130, 144, 156, 253, 288, 331, 335, 344, 352, 375, 381, 394–413** passim, **419–429** passim,

- 435–452 *passim*
 flocculation-coagulation-flocculation (FCF), 425
- flotation, 20, 52, 57, 61, 96, 107, 122, 124–125, 174, 179, 182, 187, 253, 259–265 *passim*, 286, 289, 296–324 *passim*, 329, 343–347, 373, 415, 449–450. *See also* bitumen, aeration; bitumen, froth; bubble aeration methods, 305–316
 induced air, 268, 306–313
 dissolved air, 305, 314–315, 318–319, 344
 circuits, 319–323
 rougher bank, 319–320
 scavenger bank, 319, 320
 machines. *See* flotation cells
 microbubble, 319, 347
 rate constant, 320
- flotation cells, 25–26, 125, 159, 255, 268, 285, 294, 298, 305, 310, 314, 316–324 *passim*
 cavitation, 298, 316
 column, 316, 319–320
 Denver, 324
 Jameson, 298, 315, 318–320, 343
 mechanical, 305–306, 316–317
 Dorr-Oliver tank, 316–317
 Outokumpu tank, 316–317
 Microcell, 298, 315, 319
 pneumatic, 316, 318
 Davcra, 318
 Imhofflot G-cell, 318
- flow:
 horizontal, 129, 169
 slurry, 129, 152–154, 169, 176, 278, 280, 318
 vertical, 129, 150, 152–153, 169
- flow curve, 411–413
 flue gas desulphurization (FGD), 30, 32
 fluidization, 147, 149, 169, 171, 286
 foams, 52–53, 114, 127, 360, 373, 388
 solid, 52–53
- Fort McMurray, 5, 15, 20–22, 24, 29, 31, 48–49, 432
- Fourier transform infrared (FTIR) spectroscopy, 418
 Fowkes equation, 242–243, 297, 299
 fractionation, 228, 231–232, 362
 freshwater intake, 40, 43–46, 392, 448
 froth. *See* bitumen, froth
 frothers, 125, 310–311, 313, 338–339
 FTIR. *See* Fourier transform infrared (FTIR) spectroscopy
- ## G
- Ga. *See* Galilei number
 Galilei number (Ga), 134–135, 137, 144, 150, 152
 gangue, 124–125, 306, 338
 gases:
 flue, 27–28, 30–32
 greenhouse, (GHGs), 33–35, 37–38, 49
 natural, 1, 23–33 *passim*, 39, 224, 378, 380
 sour, 27–28, 31
 sweet fuel, 27–28
 gas nucleation. *See* flotation, aeration methods, dissolved air
 gasoline, 1, 34, 37–39, 89, 207, 225, 229
 GCOS. *See* Great Canadian Oil Sands
 gelation, 182, 188, 331, 394, 411, 413, 415, 418
 GHGs. *See* gases, greenhouse
 Gibbs, J. Willard, 70
 adsorption equation, 72, 74–75, 120–121, 244–246, 356
 dividing plane, 71–74
 law, 356
 Good and Girifalco parameter, 242
 GPC. *See* chromatography, gel permeation
 Grand Rapids Formation, 6
 Grashof number, 167
 Great Canadian Oil Sands (GCOS), 15–16, 20
 gypsum, 27–28, 32, 111, 268, 338, 342, 399–400, 421–424, 432–433

H

- Hamaker constant(s), **94–96, 99, 101–102, 104, 124, 307, 395–397, 401**
- Harvey gas nuclei, **315**
- H/C or H:C. *See* hydrogen-to-carbon ratio
- heat conduction equation, **275**
- heat of combustion, **176, 224–225**
- heat transfer coefficient, **276**
- heavy metal(s), **1, 5, 27–28, 230**
- Henry's constant, **79, 255**
- Henry's isotherm, **78–79**
- Henry's law, **255, 314**
- heptanes, **62, 95, 205, 217–218, 228, 233–235, 243, 361–362, 375, 386–387**
- heteroatoms, **28, 227, 231, 235, 371**. *See also* nitrogen; oxygen; sulphur
- heterocoagulation, **346, 400, 416, 422**
- heteroflocculation, **422**
- hexane, **62, 95, 214, 239, 242–243, 257–258, 262**
- HHV. *See* heat of combustion higher heating value (HHV). *See* heat of combustion
- high-resolution transmission electron microscopy (HRTEM), **372, 388**
- hindered settling. *See* settling, hindered; Masliyah's hindered settling equation
- HLB (hydrophilic-lipophilic balance), **115–116, 126, 244, 249, 356, 373, 382**
group numbers, **115**
- horizontal wells, **9, 20**
- hot water flotation process, **20, 264**
- HRTEM. *See* high-resolution transmission electron microscopy
- 'huff and puff' technique. *See* cyclic steam stimulation
- hydration, **80, 104, 106, 186, 244, 308, 341**
- hydrocracking, **29, 31, 38, 380**
- hydrocyclones, **25, 268, 400, 421–425**
passim, **448**. *See also* cyclones
- hydrodynamic forces, **129–130, 145, 169, 291**
- hydrodynamics, **307, 317, 321, 323, 398, 408**
- hydrodynamic volume factor, **157–158**
- hydrogen, **1, 27–31, 40, 79–81, 106, 118–119, 185, 187, 201, 227–230, 239, 242–243, 254, 311–312, 363, 377, 380–381, 400, 403–404**
- hydrogen-addition upgrading technology, **30–31**. *See also* plant, hydrogen
- hydrogen-to-carbon ratio (H/C or H:C_a), **1, 28, 229, 363, 375–376**
- hydrogen peroxide washing, **418**
- hydrogen sulphide, **28, 31, 106, 118**
- hydrolysis, **186–187, 250, 256, 290, 292, 297, 302, 305, 324–325, 395**
- hydrophilic-lipophilic balance. *See* HLB
- hydrophilic sand, **174, 291–294**
- hydrophobic forces, **106–107, 308, 397, 417**
- hydrophobicity, **186, 236, 261, 290, 292, 298, 300, 302, 310, 324, 339, 347, 418**
- hydrophobic sand, **174, 293**
- hydroprocessing, **30**
- hydrotransport pipelines. *See* pipelines
- hydrotreater units, **27–30**
- hydrotreating, **26, 28–29, 31, 227**

I

- IEP. *See* isoelectric point
- IFN. *See* instream flow needs
- IFT. *See* interfacial tension
- illite, **182–192** passim, **222, 262, 323–330**
passim, **344, 346, 394, 451–452**
- IM. *See* interfacial material
- impellers, **306–307, 316, 318, 360**
- Imperial Oil, **20–21, 181, 192, 194, 197, 261**
- induction time. *See* bubble, attachment, induction time
- infrared (IR), **80, 363, 365**
- instream flow needs, **42, 47–48**
- interaction energy, **53, 92–104** passim, **239–240, 307, 309, 341–342, 393–401** passim
- interfacial area, **51–53, 98, 107, 315, 340–341, 352**. *See also* surface area
- interfacial material (IM), **375–377**
Wu's method of collecting, **375–376**

interfacial properties, **127, 174, 176, 235–238, 246, 259, 264, 286, 291, 297, 307, 374, 389**. *See also* interfacial tension; surface charge; surface tension; wettability

interfacial tension (IFT), **53–69** passim, **116, 124, 127, 139, 141, 176, 238–249** passim, **256, 282, 290–301** passim, **310, 340–341, 346, 355–358, 389**. *See also* Fowkes equation

measurement of using:

- drop shape methods, **67, 69**
- drop weight (volume) method, **68**
- Du Noüy ring method, **66, 239**
- micropipette methods, **68–69**
- spinning drop (bubble) method, **67**

intermolecular forces, **51, 53–54, 69, 92, 238–242** passim. *See also* surface forces, van der Waals

IR. *See* infrared

isoelectric point (IEP), **188–189, 417–418**

isomorphic substitution, **186, 188–191, 395**

isotherm. *See* BET isotherm; Henry's isotherm; Langmuir's adsorption isotherm

J

Jacobs Consultancy, **37, 39, 48**

K

kaolinite, **182–192, 222, 265, 323–324, 329–330, 394, 414–421** passim, **452**

kinetic energy, **241, 309, 313**

Krafft point, **117–118**. *See also* critical micellization concentration

Kyoto targets, **24**

L

laboratory hydrotransport extraction system (LHES), **426, 439, 451**

Landau, L. D., **98, 126, 307, 344**

land reclamation, **392, 423, 430, 435, 437, 442, 447–448**

Langmuir's adsorption isotherm, **75–78**

Laplace problem, **67**

Laplacian body, **358**

LCA. *See* life cycle analysis

LC-Fining, **26, 30**

LHES. *See* laboratory hydrotransport extraction system

life cycle analysis (LCA), **35, 37, 39**

tank-to-wheels (TTW), **37**

well-to-tank (WTT), **35, 37**

well-to-wheels (WTW), **37–38**

lime, **338, 381, 422, 432–433**

liquid crystals. *See* phases, liquid crystal lumps. *See also* oil sands, lumps

M

magnesium ions, **124, 190, 250, 284, 305, 328, 331, 335–336, 393–394, 423**

maltenes, **218, 225, 230–231, 362**

Masliyah's hindered settling equation, **322**

mass action model, **120**

mass spectrometry (MS) methods, **365, 376–377, 386, 389**

electrospray ionization (ESI), **365, 377**

mass flow rate, **150, 153, 223, 271–274**

McMurray Formation, **4–6, 198**

MF. *See* flocculants, Magnafloc 1011

MFT. *See* tailings, mature fine

methane, **33, 224–225, 229, 233**

micelles, **113, 116–118, 120–121, 352–355, 366–368**. *See also* critical micellization concentration

inverted, **353–354, 366–368**

middlings, **25, 52–53, 159–160, 162, 285, 289, 305, 316, 320, 330–331**

mineral solids, **8, 39, 41, 158, 160–161, 173–181** passim, **192, 194–195, 268–274** passim, **423**. *See also* particle, size distribution

clays, **27, 41, 67, 80, 103, 106, 173–196** passim, **204, 230, 237, 260–262, 286, 289, 308, 323–332** passim, **345, 358, 391–400** passim, **411–420** passim, **426–431** passim, **450**. *See also* clay minerals; illite; kaolinite; montmorillonite; smectite

ion exchange importance, **185–186, 189**

peds, **431**

ultrafine, **394–395**
fines, **67, 104, 175, 179–182, 192–196, 235, 237, 256, 261, 268, 285, 323–335** passim, **341–346** passim, **391, 394, 397, 417–431** passim, **436, 438–443, 448, 451**. See also percent fines; tailings, fluid fine; tailings, mature fine

Mo. See Morton number

molar mass, **1, 230, 232, 235, 240, 265, 314, 338**

molecular interactions, **54, 69, 93, 238, 240–242, 298, 403**. See also surface forces, van der Waals

molecular mass, **5, 96, 105, 116, 212, 227, 232, 235, 340, 361, 364–372** passim, **382, 386, 389, 403, 410, 424–425, 436, 439**

of asphaltenes, **364–366**

monomer(s), **109, 112, 120–121, 364, 367–368, 372**

montmorillonite, **182–192** passim, **222, 265, 286, 324, 329–331, 414, 452**

Morton number (Mo), **139–140**

MS. See mass spectrometry

N

n-alkane. See alkane(s) nano-aggregates. See also asphaltenes, nanoaggregates and Mullins' model; critical nanoaggregate concentration (CNAC)

naphtha, **25, 28–29, 38, 205, 214–218, 225, 234, 239, 268, 351, 373–383** passim, **389**. See also bitumen, froth treatment

naphthenic acids, **203, 253, 339–340, 358, 372–373, 387**. See also carboxylic acids

National Energy Board (NEB), **9–11, 21–23, 27, 48–49**

Natural Sciences and Engineering Research Council of Canada (NSERC), **20, 347**

NEB. See National Energy Board

Newtonian fluid, **129, 207, 412–413**

Newton regime, **133**

Newton's law of viscosity, **277**

Nexen/OPTI, **23**

n-heptane. See heptanes

nickel, **5, 227, 230, 235, 363, 371**

nitrogen, **5, 28, 30, 32, 77, 106, 227–230, 235, 363, 371**

NMR. See nuclear magnetic resonance

North Saskatchewan River, **43–45**

n-pentane. See pentanes

NSERC. See Natural Sciences and Engineering Research Council of Canada

NST. See tailings, consolidated nuclear magnetic resonance (NMR), **363, 365**

O

octane, **62, 95, 214, 227**

OWHE. See OSLO hot water extraction oil:

conventional, **1, 5, 37–39, 355, 374**

crude, **1, 4–5, 9, 13, 18, 37, 49, 53, 67, 196, 235, 260, 350, 355, 360–373** passim, **386, 389**

extra-heavy, **1**

heavy, **1, 37, 205, 211, 227, 374**

light, **204, 227**

light-medium, **1**

light sour, **18, 34**

light sweet, **18, 27, 34**

medium, **204**

mining, **37–38**

recovery of, **355, 374**

sour, **18, 227**

sweet, **227**

synthetic (SCO). See synthetic crude thermal, **37–38**

oil sands, **1–53** passim, **103, 123–124, 170–201** passim, **219–224, 226, 235–307** passim, **315–347** passim, **373–374, 391–394, 399–400, 409–452** passim: areas (OSAs), **1–5, 7, 11, 13–15, 21, 31**

Athabasca Wabiskaw-McMurray. See Athabasca oil sands (area) (OSA)

Cold Lake Clearwater. See Cold Lake oil sands (area) (OSA)

Peace River Bluesky-Gething. See Peace River oil sands (area) (OSA)

- components. *See* oil sands constituents
- constituents, **173–174, 220–222, 235, 238**
- deposits, **1–2, 22, 47, 363, 373**
- development:
 - forces driving demand for, **23–25**
 - history of, **18–22, 174, 268**
- leases, **6, 20, 22, 40, 47, 177–179, 186, 196–197, 200–202**
- lumps, **25–26, 153, 226, 267–282, 287, 364**
 - ablation, **269, 273–274, 276, 282**
 - digestion, **268, 270–271, 277–281, 285**
- mineral composition of, **181–182**
- operators, **21–22, 25, 32, 43, 392**. *See also* CNRL; Imperial Oil; Nexen/OPTI; Shell Canada; Suncor (Energy Inc.); Syncrude (Canada Ltd.)
- ore(s), **8–9, 173–177 passim, 182, 192, 196–197, 201, 209, 226, 241, 246, 256, 265, 268, 285, 293, 301, 323, 326–329, 334, 339, 342–346, 361, 391, 394, 423, 426, 428–429, 450**.
See also bitumen, grade; oil sands, ore processability, impact of grade
- regions. *See* Athabasca oil sands (area); Cold Lake oil sands (area); Peace River oil sands (area)
- ore processability, **174, 180, 263, 288, 293–294, 323, 327–328, 342–344, 346, 426–427, 451**
- impact of acidity, **326–327**
- impact of grade, **323–324**. *See also* bitumen, grade
- impact of natural surfactants, **338–340**. *See also* surfactants, natural
- impact of solids wettability, **327–328**.
See also bitumen, liberation, solids wettability role in
- impact of temperature, **324–326**. *See also* bitumen, density, temperature effect on; bitumen, aeration, temperature effect on; bitumen extraction, temperature impact; bitumen, liberation, temperature effect on; bitumen, viscosity, temperature effect on; emulsions, temperature effect on
- impact of water chemistry, **328–329**.
See also water, chemistry
- Orinoco Belt, **1**
- OSA. *See* oil sands area
- OSLO low energy extraction, **311**
- OSLO hot water extraction (OHWE), **394–395, 418, 431**
- Ostwald ripening, **55, 57**
- Overbeek, J.T.G., **98, 127, 307, 346**
- O/W. *See* emulsions, oil-in-water
- oxygen, **3, 28, 106, 182–186 passim, 203, 227–230, 235, 293, 311, 363, 377**
- ## P
- PADD. *See* Petroleum Administration for Defense District
- paraffinic froth treatment. *See* bitumen, froth treatment, paraffinic; diluent, paraffinic
- particle:
 - attachment, **237, 357–358, 398–399**
 - bridging. *See* polymer, bridging
 - collision, **107, 398–399**
 - recovery, **164–166, 168, 319**. *See also* bitumen, recovery of
 - size distribution (PSD), **176, 179–180, 192, 422**
- paste technology, **105, 420, 424, 430**. *See also* tailings, thickened
- pdi. *See* potential determining ion
- Peace River oil sands (area) (OSA), **1–2, 7, 14–16, 21, 363**
- pentanes, **5, 62, 95, 214, 230–233, 235, 361–362, 379, 386**
- percent energy input, **35–36**
- percent fines, **179–181, 192–196**. *See also* mineral solids, fines
- Petro-Canada, **21–22, 29, 49, 203**
- Petroleum Administration for Defense District (PADD), **38–39**
- phase, **51–61 passim, 70–71, 73, 79–81, 87, 90, 98, 104, 117–122 passim, 129, 137, 169–174, 236–246 passim, 255–263 passim, 284–285, 290, 292, 305, 307, 339, 349–359 passim, 367–375 passim, 387**

boundary, **52–54, 57, 70–71**
continuous, **51–53, 137, 139, 350–352**
dispersed, **51–53, 55, 137**
liquid crystal, **117, 354–355, 373, 388**
oil, **349–359** passim, **373–374**
solids, **350**
surface. *See* surface region
water, **80, 104, 122, 173–174, 339, 351–358** passim, **375**
phase separation, **118, 121, 352, 355, 367, 372, 386**
phosphate, **114, 344, 393–394**
physical constants, **125**. *See also* Boltzmann's constant
physical properties, **71, 116–117, 120, 134, 144, 168, 173, 176, 235, 260, 346**
pipelines, **24, 150–152, 176, 212, 254, 267–278** passim, **286–287, 349, 361–362, 380**
hydrotransport, **21, 25, 129, 159, 176, 179, 223–224, 226, 254, 267–268, 270, 279–285** passim, **294, 316, 341**
tailings, **129, 176, 179**
plants:
ammonia, **28**
bitumen froth treatment, **25, 27–28, 268**
extraction, **20, 25–33** passim, **40, 267, 269, 338, 430**
hydrogen, **27, 31**
industrial, **283–284**
power, **20, 39**
utilities, **27**
PNK theory, **167–168**
PO. *See* propylene oxide
point of zero charge (PZC), **80–81, 187, 189–190, 400**
Poisson's equation, **83–84**
polymers, **80, 104–107, 116, 122, 352, 382, 386, 398–410** passim, **424–430** passim, **435–436, 439, 449**. *See also* flocculant bridging, **100, 105, 403–405, 409**
loops/tails, **104–105, 399, 403–405**
porosity, **7–8, 11, 69, 143, 146, 383, 438**
pore volume, **7–8, 11**
potential determining ion (pdi), **187, 308,**

400

precipitation flotation. *See* flotation, aeration methods, dissolved air
primary separation cells (PSC). *See* vessels, separation
primary separation vessels (PSV). *See* vessels, separation
probability of detachment, **307, 309–310**
propylene oxide (PO), **115–116, 382**
PSC. *See* vessels, separation
PSD. *See* particle size distribution
pseudoplastic, **412–413**
PSV. *See* vessels, separation
PZC. *See* point of zero charge

R

Rault's law, **364**
Re. *See* Reynolds number
relative velocity equations, **144–145, 147, 150, 153–156, 158**
repulsive forces. *See* surface forces
residence time, **226, 267, 280, 305, 313, 317–318, 321, 385**
resins, **230–232, 241, 361–369** passim, **377, 386, 388**
Reynolds number (Re), **131–145** passim, **150, 155–157, 167, 212, 214, 313, 322, 397**
rheology, **411–419**
Richardson and Zaki power, **157**
Richardson-Zaki index, **145, 156, 158**
RICO. *See* ruthenium-ion-oxidation
rising velocity, **289, 310–311, 313, 321–323, 331, 385**
rotary breakers, **25, 226, 268**
rougher. *See* flotation, circuits, rougher bank
ruthenium-ion-oxidation (RICO), **370–371**

S

SAGD. *See* steam-assisted gravity drainage
sand-to-fines mass ratio (SFR), **419–422, 425**
SARA, **230–232, 241, 358, 361–363**

Saskatchewan Research Council, **278, 287**
 saturates, **230–232, 235, 241, 361–363**
 S/B. *See* solvent-to-bitumen (S/B) ratio
 scanning electron microscope (SEM), **375–376, 394**
 scavengers, **186, 326, 381**. *See also*
 flotation, circuits, scavenger bank
 Schulze-Hardy rule, **103, 399–400**
 Scientific and Industrial Research
 Council of Alberta (SIRCA). *See*
 Alberta Research Council
 SCO. *See* synthetic crude oil
 SDS. *See* sodium dodecyl sulphate
 SEM. *See* scanning electron microscope
 sep cells. *See* vessels, separation
 settlers:
 gravity, **373**
 inclined plate, **25, 129, 165–166, 168, 268, 285, 310, 349, 383–384, 411**
 vertical, **160, 162, 164, 167–168**
 settling:
 batch. *See* batch settling
 hindered, **143, 155–158, 170–171, 313, 322, 345, 379, 397, 406, 408**. *See also*
 Masliyah's hindered settling
 equation
 rate, **146, 167–168, 172, 379, 394, 397, 400, 409, 424–425, 430, 441, 443–444**
 velocity, **135, 145–147, 157, 166, 383–384, 391, 397, 405–409, 420**
 SFR. *See* sand-to-fines mass ratio
 SG. *See* specific gravity
 shear, **57, 82, 88, 110–111, 261, 264, 282, 288, 385, 398, 435**
 force, **189, 309–310, 398**
 modulus, **413, 418**
 loss, **413**
 storage, **413**
 rate, **110, 207–209, 277, 280, 282, 310, 385, 398–399, 411–415**
 strain, **411–413**
 stress, **270–281 passim, 411–413, 416–418**
 thickening, **412–413**
 thinning, **208, 412–414**
 Shell Albian Sands. *See* Albian
 Shell Canada **15–22 passim, 31, 32–36, 44–45, 49, 177, 264**
 silicate(s), **230, 342, 393**
 simulated process water (SPW), **243, 245, 284, 294**
 doped (DSPW), **243, 245**
 SIRCA. *See* Alberta Research Council
 SI units, **125–126, 207**
 slime coating. *See* bitumen, slime coating
 sludge. *See* tailings, fluid fine; tailings, mature fine
 sludging. *See* gelation
 slurry, **25–26, 125, 129, 138, 150, 152–154, 159, 165, 169, 172–185 passim, 196, 222–224, 237–238, 246, 254, 267–289 passim, 294, 302, 305–306, 314–341 passim, 361, 393, 397, 411–426 passim, 432, 437–438, 441**. *See also*
 flow, slurry; streams, slurry; tailings, slurry
 discharge, **279–280**
 segregating/non-segregating, **341–342, 421, 423**
 temperature, **222–224, 274, 277–280, 282**
 viscosity, **185, 414–415, 421, 423**
 smectite, **182–191 passim, 323, 326, 331**
 Smoluchowski:
 continuity equation, **109–111**
 Marian, **88, 108, 127**
 theory, **88–89, 108–109**
 sodium dodecyl sulphate (SDS), **114–116, 119, 257–258, 417–418**
 solids. *See* fine solids; mineral solids, fines
 sols, **52–53, 103**
 solubility class(es), **230, 361, 386**
 solubilization, **117, 120, 121**
 solvents, **25–27, 68, 72, 74, 113, 121, 176, 205–218 passim, 228, 230–235, 259–260, 268, 285, 349, 361–368, 372–373, 378–382, 388, 403**
 solvent-to-bitumen (S/B) ratio, **233–234, 378–380**

SOR. *See* steam-to-oil ratio

sour liquid, **28**

speciation diagram, **247, 249, 254**

specific gravity (SG), **5, 29, 204**

specific heat, **176, 218–223, 225–226, 260, 264, 274–275**

specific resistance to filtration (SRF), **437–440, 442–443**

spreading coefficient, **61, 124, 301**

SPW. *See* simulated process water

SRF. *See* specific resistance to filtration

SSB. *See* sweet synthetic blend; Syncrude Sweet Blend

stability ratio, **107, 112–113, 399**

stabilization:

- kinetic, **352**. *See also* emulsions, stability
- mechanisms, **52, 98, 121–122, 350, 356, 361, 369, 375, 381, 386**. *See also* emulsions, stability

static mixers, **319–320**

steam-assisted gravity drainage (SAGD), **9, 14–15, 23, 37–39**

steam-to-oil ratio, **23, 38**

stearic acid, **246–253**

steric effects, **350, 352, 368**

steric repulsion, **104, 106, 308, 369, 399, 404**. *See also* steric stabilization

steric stabilization, **104–105, 122, 352, 356, 381, 404–405, 443**. *See also* steric repulsion

Stern-Graham equation of adsorption, **303**

Stern potential, **304, 396–397**

Stokes' law, **132, 313, 322**

Stokes' regime, **132–137** *passim*, **142–148** *passim*, **154–162** *passim*

Strausz, Otto P., **368–371, 389**

streams:

- bitumen froth, **159, 165**
- input, **159**
- middlings, **25, 159–160, 285, 305, 316**
- output, **40, 159**
- overflow, **160–164, 425**
- slurry, **159, 165, 274, 321**
- slurry feed, **159, 162**
- tailings, **159, 180, 430**
- underflow, **160–164, 425**

sulphur, **5, 27–31, 38–39, 227, 229–231, 235, 363, 371, 377**

sulphur dioxide, **28, 30–33**

- emission of, **30, 32–33**

sulphur recovery unit, **29**

Suncor (Energy Inc.), **10, 15–49** *passim*, **177, 192–193, 214, 223–234, 264, 267–268, 285, 391, 399, 418, 423, 432, 434**

supercooling, **55–56**

superheating, **55, 56**

surface area, **13, 51–52, 54, 73–81** *passim*, **167, 184–185, 188, 280, 307, 310, 340, 357–358, 405, 432**. *See also* interfacial area

surface charge, **73, 79–87** *passim*, **96, 102–103, 106, 144, 176, 186–190, 235, 237–238, 256, 258–259, 265, 302, 308, 326–335** *passim*, **340–341, 381, 393–397, 400, 403**. *See also* electric double layer

density, **74, 80–81, 85, 97, 258, 365, 395–397**,

surface energy, **57, 67, 123, 126, 238, 241**

surface excess, **70–76, 78, 120–121**

surface forces, **51, 84, 91–92, 104, 106–107, 129, 144, 156, 282, 344, 345, 350, 352, 359**. *See also* critical coagulation concentration; DVLO theory

double layer overlapping, **91, 96–98, 106, 350**

electrosteric, **399**

electrostatic, **122, 174, 187, 302–303, 330, 341, 359, 365, 393–394, 399, 404, 415, 417**. *See also* electric double layer; surface forces, double layer overlapping

hydration, **399**

steric, **359, 399**. *See also* steric repulsion

van der Waals, **91–96, 124, 239, 242–243, 307–309, 350, 359, 392–393, 395, 399–400**. *See also* van der Waals

dipole-dipole interaction, **92**

dipole-induced dipole interaction, **92–93**

- dispersive interaction, **93**
 - surface potential, **73, 84–91** passim, **97–103** passim, **308–309, 395–397, 400–401**
 - surface region, **70–71**
 - surface science, **51–53, 122, 349**
 - surface tension, **53–75** passim, **116–121** passim, **126, 176, 238–246, 263, 297–298, 300, 309–310, 339, 366–367**
 - dynamic, **64**
 - measurement of using
 - capillary rise method, **62–63**
 - drop shape methods, **67, 69**
 - drop weight (volume) method, **68**
 - maximum bubble pressure method, **64–65, 68**
 - Wilhelmy plate method, **65–66**
 - surfactants, **105, 113–124** passim, **138, 176, 187, 230, 244–259** passim, **264–265, 282–294** passim, **302, 304–305, 313, 326, 328, 338–340, 347, 352–356, 358, 366–368, 373, 381–387** passim, **396**. *See also* HLB; tailings, surfactants in
 - amphiphilic nature of, **113, 115, 244, 255–256, 368**
 - anionic, **113–114, 119, 263–264, 287, 304, 332, 340, 417**
 - cationic, **113–114, 119, 250**
 - ionic, **119, 122, 246, 340, 352**
 - strong-acid, **246**
 - weak-acid, **246, 250, 255**
 - weak-base, **246, 255**
 - natural, **114, 122, 187, 244, 246, 253, 255–259, 282, 284, 290, 292–294, 302, 304–305, 311, 324–332** passim, **338–340, 355, 382, 396**
 - non-ionic, **113–114, 119–120, 246, 352–353, 367**
 - self-organized structures, **354–355**. *See also* critical micellization concentration; micelles
 - temperature effect on, **353**
 - suspensions, **52–53, 57, 80–81, 91, 101, 103, 109–110, 127, 129–130, 142–172** passim, **255, 262, 264–265, 277, 330, 342, 368, 393–405** passim, **411–419** passim, **424, 429, 437, 446, 449–452**
 - solid, **52–53, 419**
 - sweet synthetic blend (SSB), **33**
 - Syncrude (Canada Ltd.), **10, 15–49** passim, **177, 192–193, 201, 214, 220–223, 225, 234, 267–268, 285, 346, 377, 391, 399, 418–426** passim, **450–451**
 - Syncrude Sweet Blend (SSB), **24, 45, 205, 224–225**
 - syneresis, **398, 409**
 - synthetic crude oil (SCO), **1, 13–45** passim, **205, 225**
 - systems:
 - ideal, **130, 142, 144, 154, 156, 158**
 - non-ideal, **130, 156, 158**
- ## T
- tailings:
 - composite. *See* tailings, consolidated
 - consolidated (CT), **28, 101, 104, 257, 268, 338, 341–342, 346, 394, 399–401, 409, 415, 419–425, 430, 433, 450**
 - consolidation technologies:
 - centrifugation, **430, 434–437**
 - filtration, **430, 437–449**
 - freeze-thaw, **430–432, 434–435**
 - natural drying, **430, 432–435**
 - containment structures, **392**
 - discharge from bitumen flotation, **305–306, 314, 318–320**
 - disposal, **338, 341–342, 392**
 - extraction, **26, 338, 421–425, 438–442**
 - flocculation of, **105, 111, 439**
 - fluid fine (FFT), **182, 341, 391** passim, **409, 419, 424–425, 430–438** passim, **448**
 - fresh, **391, 400–401, 419, 422, 425, 435, 439, 441, 443, 447**
 - management, **91, 103, 105, 182, 196, 237–238, 342, 391, 400, 414–415, 419, 426–427, 429, 437, 448–449, 451**
 - mature fine (MFT), **24, 26–28, 41, 180, 182, 268, 341, 391–401** passim, **409–411, 418–426** passim, **431–450** passim

- non-segregating (NST). *See* tailings, consolidated
- oil sands processing, **392, 394, 399, 431, 438–439, 443, 447**
- oil losses to, **378, 380**
- pipelines. *See* pipelines, tailings
- ponds, **12, 24–32** passim, **40–45** passim, **180, 182, 201, 255, 257, 268–269, 335, 338, 341, 391–392, 394, 424–425, 430**
- processing, **333–334, 392, 394, 397, 399, 431, 438–439**. *See also* tailings, ponds; tailings, water
- recovery of heavy metals from, **305**
- settling of fines in, **427, 429**
- slurry, **26, 129, 153, 268, 341**
- stackable, **430, 432, 436–437, 442, 447, 451**
- streams. *See* streams, tailings
- surfactants in, **339**
- thickened (TT), **268, 409, 411, 423–433** passim, **450–451**
- treatment, **342, 391–392, 400–401, 422, 436, 438, 451**
- water, **26, 40, 196, 325, 329–334** passim, **391, 394–397, 426–427, 430**. *See also* tailings, ponds; tailings, processing
- TAN. *See* total acid number
- tar sands. *See* oil sands
- Teller, Edward, **77**
- temperature. *See* bitumen, density, temperature effect on; bitumen, aeration, temperature effect on; bitumen extraction, temperature impact; bitumen, liberation, temperature effect on; bitumen, viscosity, temperature effect on; emulsions, temperature effect on; surfactants, temperature effect on
- terminal velocity, **130–143** passim, **148, 155, 158, 170, 177, 311, 434**
- thermal conductivity, **226, 262, 275**
- thermal cracking, **28, 30**
- thermal energy, **28, 35, 99–100, 208, 218, 223–225, 267, 271, 274, 425, 448**
- thermodynamics, **58, 70, 72, 120, 123, 261, 344–345**
- thermal gravitational analysis, **418**
- thickeners, **26, 33, 268–269, 411, 424–426, 435, 444, 447, 449**
- thin lift drying technology, **432**
- Thin Liquid Film-Pressure Balance Technique (TLF-PBT), **359–360**
- time-resolved fluorescence depolarization (TRFD), **365, 372, 388**
- TLF-PBT. *See* Thin Liquid Film-Pressure Balance Technique
- toluene, **62, 95, 205, 212–213, 217–218, 232, 234, 239, 242–244, 265, 293, 350, 357–358, 361, 364, 368, 375**
- total acid number (TAN), **373**
- tumblers, **223, 226, 267–268, 338**
- TRFD. *See* time-resolved fluorescence depolarization
- truck-and-shovel method, **9, 21, 267**
- turbidity, **117, 120, 443–444**
- TT. *See* tailings, thickened
- TTW. *See* life cycle analysis, tank-to-wheels
- Tyndall effect, **366**
- ## U
- ULSD. *See* diesel, ultra-low sulphur
- University of Alberta, **20, 47, 49, 181, 260, 263, 287–288, 329, 343, 345, 368, 450–451**
- upgrader(s), **17, 28, 38, 40**
 Scotford, **15, 17, 29–33, 43–44, 49**
 Suncor, **17**
 Sturgeon, **29, 49**
 Syncrude, **17–18**
- ## V
- vacuum distillation unit (VDU), **27–28**
- vanadium, **5, 227, 230, 235, 363, 371**
- van der Waals:
 attraction, **99, 102, 104–106, 372**. *See also* surface forces, van der Waals
 energy, **94, 96, 98, 104**. *See also* surface forces, van der Waals
 Johannes, **92**
- vapour pressure osmometry (VPO),

232, 364–365, 369, 371, 389
 VDU. *See* vacuum distillation unit
 velocity. *See* rising velocity; settling, velocity; terminal velocity
 Verwey, E.J.W., 98, 127, 307, 346
 vessel(s):
 pressure, 26
 separation, 25–26, 129, 154–165
 passim, 171, 180, 182, 185, 268, 285, 289, 294, 305, 315–322 passim, 331, 341, 383–384, 411. *See also* settlers
 settling, 26, 379–380. *See also* settlers
 viscosity:
 bitumen. *See* bitumen, viscosity of
 dynamic, 88, 207, 209–210, 214, 216, 384, 406
 fluid, 69, 110–111, 130, 133, 137, 143, 155, 162, 167, 207–208, 398, 406, 411–413, 437
 liquids, 68–69, 133, 212, 322, 397–398, 411
 kinematic, 207, 214, 216, 263
 oil, 141, 207, 211, 373
 reduction, 212, 215
 slurry. *See* slurry, viscosity
 suspension, 277, 415
 synthetic crude, 27
 water, 141, 145, 150, 207, 210, 277, 322
 viscometer, 207–208, 210
 viscous dissipation, 208–209
 viscous heating, 207–208, 264
 VPO. *See* vapour pressure osmometry

W

water :
 chemistry, 100, 103–105, 124, 174, 176, 238, 246, 250, 255, 261, 284, 289, 294, 311, 321, 323, 328–329, 343, 391–396 passim, 415–416, 419, 424, 436, 448
 deionized, 284, 326, 329
 flow rate, 40, 147, 280
 formation, 40, 173–174, 176, 196, 198, 326–328, 338

process, 33, 238, 243, 250, 253, 257, 262, 268, 283–285, 293–294, 301–302, 319, 325–331 passim, 338–339, 342, 391, 425
 simulated, 243, 284–285, 294
 recycle, 26, 33, 40, 267–268, 283–285, 336, 338–339, 392, 400, 424–425, 437, 447–448
 release, 391, 401, 422–424, 431
 softening, 335, 337–338
 temperature, 56, 176, 223–224, 279, 282–283. *See also* bitumen, density, temperature effect on; bitumen, extraction, temperature impact; bitumen, liberation, temperature effect on; bitumen, viscosity, temperature effect on; emulsions, temperature effect on; surfactants, temperature effect on
 use, 24, 39–46
 Water Management Framework, 42
 W/CO. *See* emulsions. water-in-crude oil
 WCSB. *See* Western Canada Sedimentary Basin
 Western Canada Sedimentary Basin (WCSB), 4, 47
 wettability, 63, 105, 122, 124, 176, 235–238, 246, 259, 262, 282, 290–294 passim, 302, 307, 325, 327–328, 344
 W/O. *See* emulsions, water-in-oil
 WTT. *See* life cycle analysis, well-to-tank
 WTW. *See* life cycle analysis, well-to-wheels

Y

yield stress, 411, 413, 416–419, 436–437
 Young-Laplace equation, 54–55, 57–58, 62, 64, 68–69, 310–311, 314
 Young's equation, 58, 238, 290–291, 294, 297, 299–301
 Young, Thomas, 58

Z

zeta potential, 79, 87–91, 103, 187–190, 253–262 passim, 302–304, 308, 323–334 passim, 345, 396–397, 401, 416–417, 426, 450
 zirconia, 417–418

